Journal of Engineering for Gas Turbines and Power

Published Quarterly by ASME

VOLUME 126 • NUMBER 1 • JANUARY 2004

(**Contents continued on inside back cover**)

Transactions of the ASME, Journal of Engineering for Gas Turbines and Power (ISSN 0742-4795) is published quarterly (Jan., April, July, Oct.) by The American Society of Mechanical Engineers, Three Park Avenue, New York, NY 10016. Periodicals postage paid at New York, NY and additional mailing offices. POSTMASTER: Send address changes to Transactions of the ASME, Journal of Engineering for Gas Turbines and Power, c/o THE AMERICAN SOCIETY OF MECHANICAL ENGINEERS, 22 Law Drive, Box 2300, Fairfield, NJ 07007-2300.
CHANGES OF ADDRESS must be received at Society headquarters seven weeks before they are to be effective. Please send old label and new address.
STATEMENT from By-Laws. The Society shall not be responsible for statements or opinions advanced in papers or ... printed in its publications (B7.1, par. 3).

INDEXED by Applied Mechanics Reviews and Engineering Information, Inc. Canadian Goods & Services Tax Registration #126148048

This journal is printed on acid-free paper, which exceeds the ANSI Z39.48-1992 specification for permanence of paper and library materials. ♾™
♻ 85% recycled content, including 10% post-consumer fibers.

(**Contents continued**)

Journal of Engineering for Gas Turbines and Power **JANUARY 2004**

Volume 126, Number 1

(**Contents continued on facing page**)

Journal of Engineering for Gas Turbines and Power

Editorial

Power was certainly in the world's news during the past year, 2003. The great electrical blackout of August 15, 2003 occurred in the U.S. Northeast and Midwest, and in neighboring Canada. In the UK, parts of London and the entire underground train system suffered an electrical power shutdown. During a hot summer, the Finnish capital of Helsinki had a blackout, as did other European cities.

Our modern society has become so dependent on electrical power, that a power failure immediately focuses everyone's attention. The public's attitude concerning electrical power can be likened to the awareness of one's own health: *When you have it, you don't think about it, but when you don't have it, that's all you can think about*.

Reasons for the blackouts of 2003 will be discovered. It is a safe bet that long-term prevention of future blackouts will come not from the politicians and lawmakers, but from solid research and development on the production and control of electrical power, as reported and archived in technical journals such as our *Journal of Engineering for Gas Turbines and Power*.

The state of the Journal is sound and it should continue to thrive. Current technical challenges in the electrical power industry (e.g., preventing blackouts) should lead to more research—and more journal papers. While aviation technology research has accounted for many of the Journal's gas turbine papers published up until now, that may change as the key role of gas turbines in the electrical power market continues to grow. One can expect to see more non-aviation gas turbine research papers in the future, as gas turbines and combined cycle systems become a more important (and possibly dominant) part of the electrical power grids.

As Associate Editor Dennis N. Assanis wrote last year in the Journal's April 2003 issue, the internal combustion engine (ICE) is still the dominant fuel energy converter in our own society. The entire April issue was devoted to a selection of the highest quality ICE papers, selected through ASME's three-reviewer process from papers presented at ASME meetings and from those submitted directly to the Journal.

In the recent past, the Journal's paper backlog has been significant, with nearly two years elapsing between papers' presentation at an ASME conference and their publication in the Journal. Working with Judith Sierant, ASME Production Coordinator, and the ASME Publications Committee, we obtained 300 cumulative additional journal pages for the past four issues. The January 2003 issue had a record 400 pages, making it the largest issue ever published of any of ASME's eighteen journals. This has helped to reduce our current backlog, allowing publication of journal papers one year after conference presentation. We are working to further reduce this time-to-publication.

ASME Technical Publishing has developed an electronic web-based tool to process papers submitted on the internet to the Journal by authors. As announced in the October 2003 issue, I scheduled the Journal to start using the new web tool on November 1, 2003. The new submission process can be accessed at ⟨http://journaltool.asme.org⟩ and is self-guiding. I encourage authors to make use of the new web tool, but will continue to accept papers for review by the traditional method, until more authors (and reviewers) have become accustomed to the web tool and the many advantages it offers. However, starting July 1, 2004, the Journal will only accept paper submission on the ASME web tool.

As a service to the Journal's readership we have included in this January 2004 issue, a book review of the latest edition of the text, *Engineering Fundamentals of the Internal Combustion Engine*. It is my intent to have such book reviews on topics related to energy and power conversion, in future issues. The number and occurrence will depend on what is submitted to the Journal by publishers for review and my ability to find a good reviewer in each case.

Lee S. Langston
Editor

Thermodynamic Analysis of Zero-Atmospheric Emissions Power Plant

Joel Martinez-Frias
e-mail: martinezfriasl@llnl.gov

Salvador M. Aceves

J. Ray Smith

Lawrence Livermore National Laboratory,
7000 East Avenue, L-644,
Livermore, CA 94551

Harry Brandt
Clean Energy Systems, Inc.,
2530 Mercantile Drive, Suite A,
Rancho Cordova, CA 95742
e-mail: hbrandt@cleanenergysystems.com

This paper presents a theoretical thermodynamic analysis of a zero-atmospheric emissions power plant. In this power plant, methane is combusted with oxygen in a gas generator to produce the working fluid for the turbines. The combustion produces a gas mixture composed of steam and carbon dioxide. These gases drive multiple turbines to produce electricity. The turbine discharge gases pass to a condenser where water is captured. A stream of pure carbon dioxide then results that can be used for enhanced oil recovery or for sequestration. The analysis considers a complete power plant layout, including an air separation unit, compressors and intercoolers for oxygen and methane compression, a gas generator, three steam turbines, a reheater, two preheaters, a condenser, and a pumping system to pump the carbon dioxide to the pressure required for sequestration. This analysis is based on a 400 MW electric power generating plant that uses turbines that are currently under development by a U.S. turbine manufacturer. The high-pressure turbine operates at a temperature of 1089 K (1500°F) with uncooled blades, the intermediate-pressure turbine operates at 1478 K (2200°F) with cooled blades and the low-pressure turbine operates at 998 K (1336°F). The power plant has a net thermal efficiency of 46.5%. This efficiency is based on the lower heating value of methane, and includes the energy necessary for air separation and for carbon dioxide separation and sequestration. [DOI: 10.1115/1.1635399]

Introduction

The main contributor to increasing atmospheric carbon dioxide (CO_2) concentration is the combustion of fossil fuels for electricity generation, transportation and industrial and domestic uses. Fossil fuels (coal, oil, and natural gas) have underpinned the development of the economies in the industrialized countries around the world. The demand for energy is expected to grow in the developed countries and in particular in the developing countries as they strive to obtain a higher standard of living. This increase in energy demand will increase the carbon dioxide concentration in the earth's atmosphere.

Carbon dioxide capture and geologic storage offer a new set of options for reducing greenhouse gas emissions that can complement the current strategies of improving energy efficiency and increasing the use of nonfossil energy resources.

Production of electric power with zero-atmospheric emissions is one of the goals of the Vision 21 Program of the U.S. Department of Energy (DOE), [1]. A decade ago, such a concept would not have been considered to be viable. However, recent research, [2–10], has addressed technical and economic issues associated with the concept, making it a viable option.

The power plant concept uses a Rankine cycle to drive three turbines connected in series. However, unlike conventional steam power plants, the plant does not use a boiler to generate steam. Use of a boiler presents two disadvantages to the efficiency of the Rankine cycle. First, the maximum cycle temperature is limited by the maximum metal temperature that boiler components can withstand; and second, 10 to 15% of the available energy in the fuel is lost by the exhaust gases that are vented to the atmosphere.

In this study, the turbine working fluid is produced in a gas generator by the stoichiometric combustion of natural gas and oxygen. Hence, the maximum operating temperature of the Rankine cycle is no longer controlled by the maximum operating temperature of a boiler. Rather, the maximum operating temperature that the turbines can withstand becomes the efficiency-limiting temperature. The hydrocarbon fuel does not need to be natural gas, but could, for example, be syngas derived from coal, or gas derived from biomass.

The adiabatic flame temperature of the stoichiometric combustion of methane and oxygen at a pressure of 2.07 MPa (300.2 lb/in^2) is 3460 K (5768°F), [11]. No turbines are available that can operate at this temperature. Therefore, in the gas generator, water is premixed with the natural gas and oxygen before the mixture enters the combustion chamber. In addition, the gas generator, [8–10], has several sections in which water is added to the combustion products to bring the gas temperature to a level acceptable to available turbines.

The turbine discharge gases pass to a condenser where water is captured as liquid and gaseous carbon dioxide is pumped from the system. The carbon dioxide can be compressed for enhanced recovery of oil or coal-bed methane, or the compressed carbon dioxide can be injected for sequestration into a subterranean formation. The technology described in this paper is the subject of several US patents, [12–21].

The next section describes the specific plant configuration analyzed in this paper. The analysis section discusses the methodology used for analyzing the power plant.

Power Plant Configuration

Figure 1 presents the power plant configuration analyzed in this paper. The power plant has four major sections: methane compression, air separation and oxygen (O_2) compression, power generation, and carbon dioxide separation and sequestration. Each of these sections consists of multiple components as shown in the figure. For the analysis, the plant is assumed to operate on methane that is combusted with oxygen. Methane is compressed to the operating pressure of the gas generator (12.4 MPa, 1800 lb/in^2, point 22, Fig. 1). Part of the methane is compressed to a pressure of 1.38 MPa (200 lb/in^2) for a reheater that is installed between the high-pressure turbine and the intermediate-pressure turbine

Contributed by the Advanced Energy Systems Division of THE AMERICAN SOCIETY OF MECHANICAL ENGINEERS for publication in the ASME JOURNAL OF ENGINEERING FOR GAS TURBINES AND POWER. Manuscript received by the AES Division July 2002; final revision received March 2003. Associate Editor: G. M. Reistad.

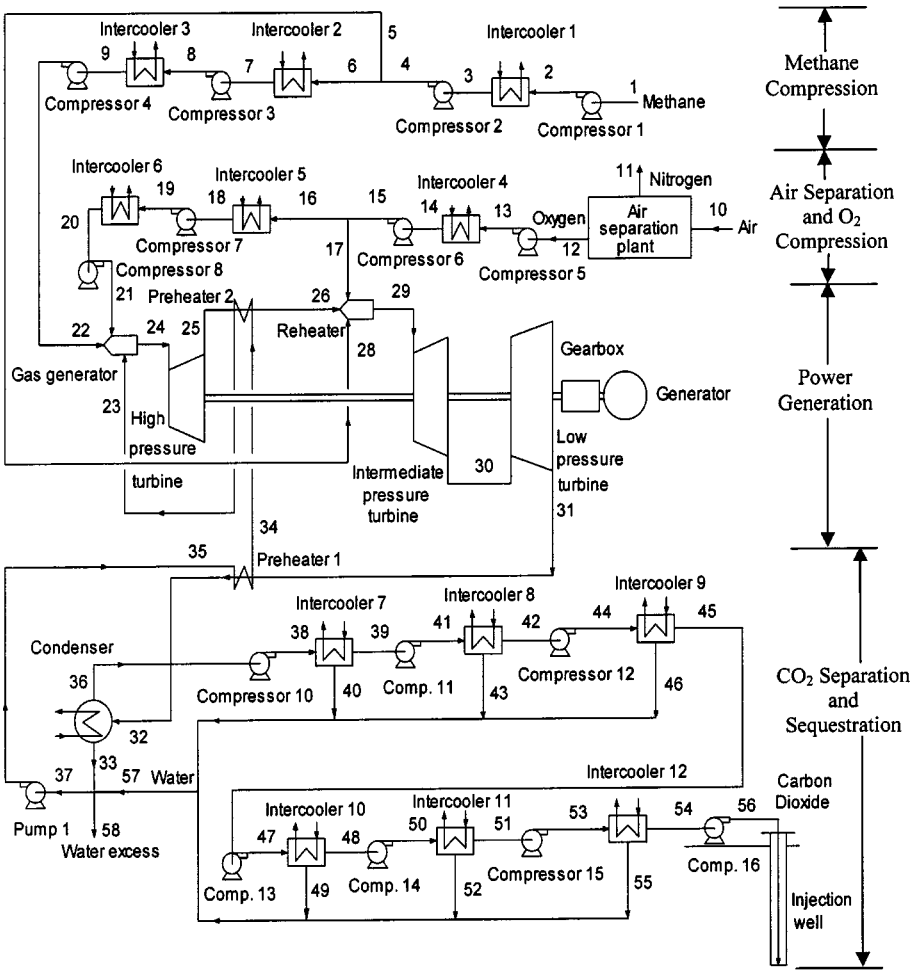

Fig. 1 Schematic of the zero-atmospheric emissions 400 MW power plant

(point 28). The compression system for methane consists of four compressors (Compressors 1 to 4) and three intercoolers (Intercoolers 1 to 3). Oxygen is generated in an air separation plant and is compressed to feed the gas generator and the reheater. The oxygen compression system consists of four compressors (Compressors 5 to 8) and three intercoolers (Intercoolers 4 to 6).

The water for this cycle is generated by the cycle itself. The water leaving the condenser is heated in Preheaters 1 and 2 before the water is injected into the combustion products in the gas generator. These preheaters increase the efficiency of the cycle.

In this study, the preheaters are located in the discharge lines of both the high-pressure turbine and the low-pressure turbine. The preheaters heat the water that is routed from the condenser to the gas generator where the water is evaporated to cool the combustion products in the gas generator. If the water were not preheated, a smaller amount of water would be required to cool the gases in the gas generator. However, taking thermal energy out of the discharge of the drive gas from the low-pressure turbine reduces the energy that is delivered to the condenser. As a result, less heat is transferred in the condenser to the condenser cooling water. This reduced condenser cooling water heat loss increases plant efficiency. The location of the preheaters, the amount of heat removed from the turbine drive gas and the temperature of the cooling water entering the gas generator, all affect cycle efficiency. How this increase in efficiency is obtained is not a priori clear, but is determined from optimization studies of the entire cycle.

Combustion products from the gas generator are delivered to the high-pressure turbine (point 24) where the mixture of steam and carbon dioxide expands, thereby producing power in the turbine and electrical generator system. The mixture consists of a 0.88 mass fraction of steam and 0.12 mass fraction of carbon dioxide. After the steam and carbon dioxide mixture leaves the high-pressure turbine, the mixture is heated by a reheater (point 26). The reheater increases the temperature of the mixture before it enters the intermediate-pressure turbine. After the reheater, the working fluid entering the intermediate-pressure turbine consists of a 0.79 mass fraction of steam and a 0.21 mass fraction of carbon dioxide. After leaving the intermediate-pressure turbine, the mixture enters a low-pressure turbine for its final expansion (point 30). The exhaust from the low-pressure turbine flows through Preheater 1 to preheat the water that was separated from the turbine working fluid in the condenser.

Most of the water that is generated in the cycle is separated from the turbine working fluid mixture in the condenser. Liquid water is extracted from the condenser by Pump 1 and is recycled to the system. The water temperature is increased in Preheaters 1 and 2, before the water goes to the gas generator (point 23) to control the temperature of the combustion products.

A mixture consisting primarily of carbon dioxide, but containing a substantial amount of moisture, is extracted from a port (point 36) at the top of the condenser. The carbon dioxide with the remaining moisture from the condenser is then delivered to several compressors and intercoolers to obtain high-pressure carbon dioxide with almost no moisture. The compression-sequestration system consists of seven compressors (Compressors 10 to 16) and six intercoolers (Intercoolers 7 to 12).

Table 1 Values of the parameters used in the base case simulation of the zero-atmospheric emissions power plant

System Parameters	Value
Preheater effectiveness	0.85
Condenser effectiveness	0.90
Intercooler effectiveness	0.85
Ambient temperature	288 K
Isentropic efficiency of the high-pressure turbine	90%
Isentropic efficiency of the intermediate-pressure turbine	91%
Isentropic efficiency of the low-pressure turbine	93%
Isentropic efficiency of the compressors	85%
Efficiency of the water pump	85%
Efficiency of the electric generator	98%

Analysis

The power plant system consists of a gas generator, three turbines, a reheater, a condenser, an oxygen separation plant, 15 compressors, a pump to recirculate the water from the condenser to the gas generator and a pump for the condenser cooling water, 12 intercoolers, two preheaters, and an electric generator. Energy and mass conservation laws are applied to every system component. The equations used to describe the power plant components are solved simultaneously in a computer code. A computer code using F-Chart software, [22], was developed to analyze plant efficiencies. Individual system components are described next.

Gas Generator and Reheater. Methane and oxygen are combusted in the gas generator to produce the turbine drive fluid. The temperature of the combustion products of methane with oxygen is controlled by adding water to the combustion products in the gas generator. The mass flow rate of water into the gas generator depends on the desired inlet temperature of the working fluid for the high-pressure turbine.

A reheater is used to increase the temperature of high-pressure turbine exhaust to the desired temperature for the intermediate-pressure turbine. The reheater produces this temperature increase by burning methane with oxygen and mixing the combustion products with the high-pressure turbine exhaust.

In the gas generator and the reheater, assuming an adiabatic process, the rate of change with time of the absolute enthalpy (including both sensible enthalpy and enthalpy of formation) of the products is equal to the rate of change of the absolute enthalpy of the reactants. Complete combustion is considered in the gas generator and in the reheater.

Turbines. Turbines are modeled by the equation of isentropic efficiency, [23], which is defined as the ratio of the power generated for the actual expansion of the gases in the turbine ($\dot{W}_a$) and the power generated in an isentropic expansion of the gases in the turbine ($\dot{W}_s$). For the three turbines the following equation is used for turbine efficiency:

$$\eta_t = \frac{\dot{W}_a}{\dot{W}_s} = \frac{\dot{H}_{in} - \dot{H}_{\text{out},a}}{\dot{H}_{in} - \dot{H}_{\text{out},s}}. \tag{1}$$

The turbine efficiencies for the high-pressure turbine, the intermediate-pressure turbine, and the low-pressure turbine were assumed to be 90%, 91%, and 93%, respectively (see Table 1). The efficiency of the high-pressure turbine takes into account the use of short blades; the efficiency of the intermediate-pressure turbine takes into account the blade cooling losses. These efficiencies compare to values of 93% used by Bannister et al. [24], 85% used by Bolland et al. [25], and 93% by Aoki et al. [26].

Heat Exchangers. To determine the performance of the heat exchangers (intercoolers, preheaters, and condenser) an effectiveness equation is used. The heat exchanger effectiveness is defined as the ratio of the actual rate of heat transfer in a given heat exchanger to the maximum possible rate of heat exchange. If the heat capacity rate of the warmer fluid ($\dot{m}_h c_{ph}$) is smaller than the heat capacity rate of the colder fluid ($\dot{m}_c c_{pc}$) then the equation for effectiveness, ε is

$$\varepsilon = \frac{\dot{Q}}{\dot{Q}_{\max}} = \frac{\dot{H}_{h,in} - \dot{H}_{h,\text{out}}}{\dot{H}_{h,in} - \dot{H}_{c,in}}. \tag{2}$$

If the heat capacity rate of the colder fluid ($\dot{m}_c c_{pc}$) is smaller than the heat capacity rate of the warmer fluid ($\dot{m}_h c_{ph}$) then the effectiveness equation is

$$\varepsilon = \frac{\dot{Q}}{\dot{Q}_{\max}} = \frac{\dot{H}_{c,\text{out}} - \dot{H}_{c,in}}{\dot{H}_{h,in} - \dot{H}_{c,in}}. \tag{3}$$

This analysis assumes an effectiveness of 85% for intercoolers and preheaters (see Table 1), [25]. The temperature of the environment and cooling water is assumed to be 288 K (59°F) to be consistent with the environment temperature used in the analysis of combined cycle plants.

Compressors. Compressors are modeled by the equation of isentropic efficiency [23] defined as the ratio of power needed to compress gases in an isentropic process and the actual power needed in the compression of the gases. For all compressors, the following equation is used for compressor efficiency, η_{comp},

$$\eta_{\text{comp}} = \frac{\dot{W}_s}{\dot{W}_a} = \frac{\dot{H}_{\text{out},s} - \dot{H}_{in}}{\dot{H}_{\text{out},a} - \dot{H}_{in}}. \tag{4}$$

The compressors were assumed to have an isentropic efficiency 85%. Previous researchers, [24,26], have used compressor efficiencies in the range of 85–89%.

Water Recirculation Pump. The isentropic efficiency of the water pump is assumed to be 85%. Previous researchers, [24,26], have used pump efficiencies in the range of 85–99%.

Oxygen Separation Plant. The power to operate the oxygen separation plant, 0.22 kWh per kg of oxygen, was obtained from data presented the literature, [27], for a cryogenic air separation plant. Advances in oxygen separation are expected to reduce this power, especially when ion transport membrane (ITM) technology matures.

Computational Assumptions. Complete combustion was assumed in the gas generator. This assumption is justified because the gas generator uses platelet injectors that provide extremely uniform mixing of oxygen, fuel, and water. In addition, bench-scale tests recently made at the University of California at Davis show an absence of hydrocarbons in the exhaust and only minor concentrations of carbon monoxide. These results are in agreement with predictions based on the use of the chemical kinetics code Chemkin-II, [28,29].

Pressure drops are considered negligible in all pipelines. Heat transfer losses to the environment from lines connecting plant components are also considered to be negligible. Heat losses to the environment from heat exchangers are neglected. In a conventional power plant, natural gas would be used instead of pure methane. Natural gas typically may contain about 1% nitrogen. Similarly, a commercial oxygen separation plant for this type of application would produce an oxygen stream that contains about 1 to 2% argon. In this analysis, the contributions of the nitrogen and argon in the turbine working fluid are neglected. Addition of nitrogen and argon to the working fluid mixture of steam and carbon dioxide makes the convergence of the iterative computations more complex. Studies show that these non-combustible gases do not

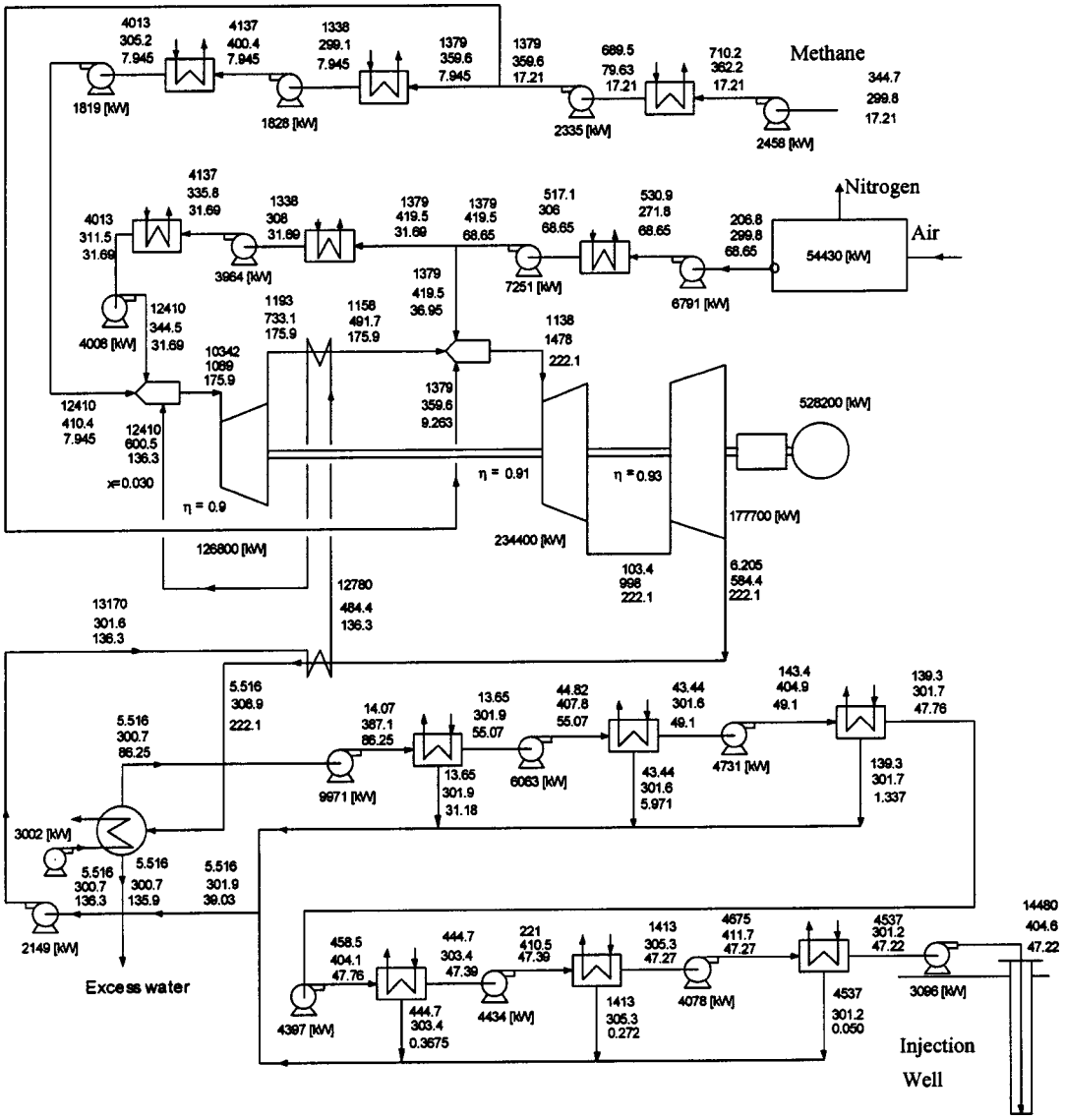

Fig. 2 Zero-atmospheric emissions power plant data for base-case analysis. Notation: pressure—kPa, temperature—K, mass flow—kg/sec. Input Power=860.4 MW, LHV, electric power generated=528.2 MW, parasitic power=128.2 MW. Net electric power=400.0 MW, net LHV thermal efficiency=0.4649.

change significantly the efficiency calculations, but primarily change the output power due to the change in molecular weight of the working fluid.

The system of equations is solved with an iterative equation solver, [22], by using computer-based tables of properties for all the substances involved (water, oxygen, methane, and carbon dioxide). The thermodynamic properties of water were obtained from the 1995 data of the International Association for the Properties of Water and Steam, [30]. Carbon dioxide properties were obtained from a fundamental equation of state by Span and Wagner [31]. Properties for methane were obtained from the 1991 equation of state by Setzman and Wagner [32]. Properties of oxygen were obtained from Sonntag and Van Wylen [33].

Table 1 shows the values of the system parameters used in the analysis.

Results

Figure 2 shows the results for the base case power plant analysis. Figure 2 shows pressures, temperatures and mass flow rates for this power plant at more than fifty locations. In Figure 2, power is given in kW, pressures in kPa, temperatures in K, and mass flow rates in kg/s. The base case assumes a high-pressure turbine with an inlet temperature of 1089 K (1500°F) and isentropic efficiency of 90%. The intermediate-pressure turbine operates at 1478 K (2200°F) and isentropic efficiency of 91%, and the low-pressure turbine operates at an inlet temperature of 998 K (1336°F) and isentropic efficiency of 93%. Steam turbines operating at these temperatures are being designed by a major U.S. manufacturer.

This power plant configuration has a net thermal efficiency of 46.5% and a net electrical output of 400 MW. The net thermal efficiency is based on the lower heating value of methane, and includes the energy required to separate oxygen from air and the energy required to compress the carbon dioxide for underground sequestration at a pressure of 14.5 MPa (2100 lb/in^2). This sequestration pressure is sufficient to inject the carbon dioxide either into an oil zone for enhanced oil recovery, or into a subterranean aquifer at an approximate depth of 1200 m (3937 ft).

Figure 3 presents the net thermal efficiency of the power plant as a function of two important power plant parameters: turbine inlet temperature and turbine isentropic efficiency. Figure 3 shows the efficiency advantage of being able to operate the power plant

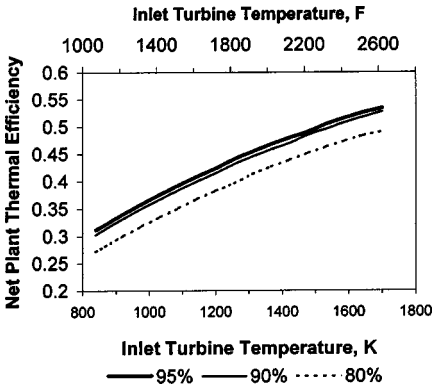

Fig. 3 Net thermal efficiency of the zero-atmospheric emissions power plant as a function of inlet turbine temperature for three values of turbine isentropic efficiency (95%, 90%, and 80%). Data shown in this figure are obtained for the same inlet temperature of both the high-pressure turbine and the intermediate-pressure turbine.

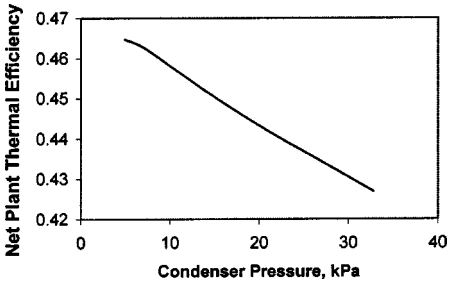

Fig. 4 Net thermal efficiency of the zero-atmospheric emissions power plant as a function of condenser pressure. The data were obtained for the base-case conditions shown in Fig. 2 and Table 1. The high-pressure turbine inlet temperature is 1089 K (1500°F), and the intermediate-pressure turbine inlet temperature is 1478 K (2200°F).

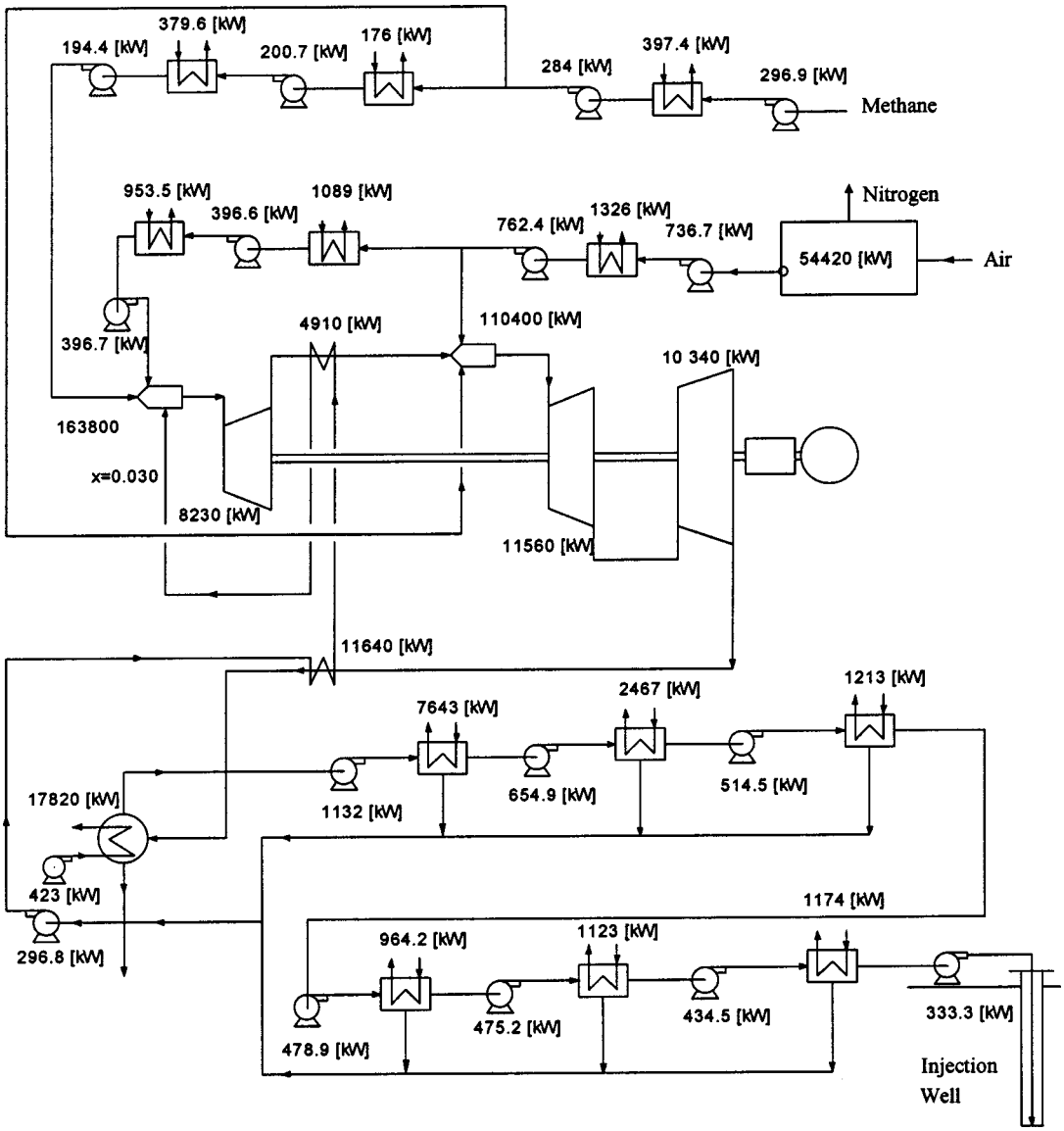

Fig. 5 Irreversibilities in components of the zero-atmospheric emissions power plant. Input power =860.4 MW LHV, electric power generated=528.2 MW, parasitic power=128.2 MW, net electric power =400.0 MW, net LHV thermal efficiency=0.4649.

with advanced-technology high-temperature turbines. The thermal efficiency is close to 50% for 90% turbine efficiency and 1644 K (2500°F) turbine inlet temperature. This is an excellent value considering that no regulated, or greenhouse gas emissions are emitted into the atmosphere.

Figure 4 shows the effect of variations in the condenser pressure on net plant thermal efficiency. Although lowering condenser pressure will increase the power required to pump the water and the carbon dioxide from the condenser, the increase in efficiency of the Rankine cycle more than offsets this pumping power increase, thereby giving a net increase in overall plant efficiency.

A second-law analysis, [34], of the power plant was conducted as a part of this study. Irreversibilities were calculated for all components of the power plant, operating at the base-case conditions (Fig. 2). Figure 5 shows the calculated irreversibilities in kW. Figure 5 shows that the main source of irreversibilities is the combustion process. This is typical of existing power plants. The exergy lost in the gas generator and the reheater is 274 MW, which is 32% of the total exergy fed into the power plant. This irreversibility can be reduced by increasing the operating temperature of the gas turbine. However, this is difficult to accomplish due to the limits of operating temperature of current turbine materials. The second most important source of irreversibility is the air separation plant, where 54.4 MW of power is lost. This points to alternative methodologies to cryogenic air separation as important for improving the efficiency of this power plant. A possible alternative methodology is ion transport membrane (ITM). On the other hand, little exergy is consumed in carbon dioxide separation and sequestration. This process only generates 18.6 MW of irreversibility, which corresponds to 2.2% of the exergy input to the system. This is one of the main advantages of this cycle: carbon dioxide sequestration can be accomplished with little additional work.

Finally, it is worth noticing that the capital cost of a typical power plant accounts for more than half of the electricity cost. Although plant efficiency is a major factor in the cost of electricity generation, the reduced capital cost of the power plant described in this paper will result in reduced electricity cost. The reader is referred to previous publications, [8,9,35], for electricity costs per kWh and a comparison of the costs of the current technology with the electricity costs of combined cycle plants with exhaust gas clean up.

Conclusions

This paper presents a thermodynamic analysis of a zero-atmospheric emissions power plant. The simulation considers the compression process of methane and oxygen to feed the gas generator and the reheater, a Rankine cycle with three turbines and the carbon dioxide separation and sequestration processes.

The analysis predicts a 46.5% net thermal efficiency in a zero-atmospheric emissions 400 MW power plant that can be constructed with turbine technology that is under current development. The net thermal efficiency is based on the lower heating value of methane, and includes the energy required to separate oxygen from air and the energy required to compress the carbon dioxide for underground sequestration. A thermal efficiency of more than 50% is expected in a system that uses future high-temperature turbine technology.

The separation and sequestration process of the carbon dioxide demands only a small part of the auxiliary power of the system. Current research and development of the air separation technology is expected to reduce the energy required to separate oxygen from air. This would increase the efficiency of the power plant.

Acknowledgments

This work was performed under the auspices of the U.S. Department of Energy by the University of California, Lawrence Livermore National Laboratory under Contract No. W-7405-Eng-48. Some of the concepts in this publication are based on the intellectual property of Clean Energy Systems, Inc.

Nomenclature

c_p = constant pressure specific heat, kJ/(kg K)
H = rate of absolute enthalpy (includes enthalpy of formation), kW
LHV = lower heating value, kJ/kg
$\dot{m}$ = mass flow rate, kg/s
P = pressure, kPa
$\dot{Q}$ = heat transfer rate, kW
T = temperature, K
v = specific volume, m^3/kg
$\dot{W}$ = power, kW
ε = effectiveness (Intercoolers, preheaters, and condenser)
η = efficiency

Subscripts

a = actual
c = cold side in the heat exchanger
comp = compressor
h = hot side in the heat exchanger
in = inlet condition in the power plant component
max = maximum
out = outlet condition in the power plant component
s = isentropic process
t = turbine

References

[1] DOE, 1999, ''Vision 21 Program Plan: Clean Energy Plants for the 21st Century,'' US Department of Energy, Federal Energy Technology Center, Pittsburgh, PA.
[2] Bilger, R., D., 1999, ''Zero Release Combustion Technologies and the Oxygen Economy,'' *Proceedings of the Fifth International Conference on Technologies and Combustion for a Clean Environment*, Research Group on Energy and Sustainable Development, Portugal.
[3] Falk-Pederson, O., and Dannström, H., 1997, ''Separation of Carbon Dioxide From Offshore Gas Turbine Exhaust,'' Energy Convers. Manage., **38**, pp. S81–S86.
[4] Herzog, H., Drake, E., and Adams, E., 1997, ''CO_2 Capture, Reuse, and Storage Technologies for Mitigation Global Climate Change,'' Final Report No. DE-AF22-96PC01257, U.S. Department of Energy, Washington, DC.
[5] Stevens, S. H., and Gale, J., 2000, ''Geologic CO_2 Sequestration May Benefit Upstream Industry,'' Oil Gas J., **98**, pp. 40–44.
[6] Wildenborg, T., 2000, ''Costs of CO_2 Sequestration by Underground Storage,'' Greenhouse Issues, International Energy Agency Greenhouse Gas R&D Program, (47), pp. 2–4.
[7] Wong, S., and Gunter, B., 1999, ''Testing CO_2-Enhanced Coalbed Methane Recovery,'' Greenhouse Issues, International Energy Agency Greenhouse Gas R&D Program, (45), pp. 1–3.
[8] Anderson, R., E., Brandt, H., Mueggenburg, H., H., Taylor, J., and Viteri, F., 1998, ''A Power Plant Concept Which Minimizes the Cost of Carbon Dioxide Sequestration and Eliminates the Emission of Atmospheric Pollutants,'' *Proceedings of the Fourth International Conference on Greenhouse Gas Control Technologies*, P. Reimer, B. Eliasson, and A. Wokaun, eds., Interlaken, Switzerland, Pergamon, London.
[9] Anderson, R. E., Brandt, H., Doyle, S. E., Mueggenburg, H. H., Taylor, J., and Viteri, F., 2000, ''A Unique Process for Production of Environmentally Clean Electric Power Using Fossil Fuels,'' *Proceedings of the 8th International Symposium Transport Phenomena and Dynamics Rotating Machinery* (ISROMAC-8), Pacific Center of Thermal-Fluids Engineering, Honolulu, HI.
[10] Smith, J. R., Surles, T., Marais, B., Brandt, H., and Viteri, F., 2000, ''Power Production With Zero Atmospheric Emissions for the 21st Century,'' *Proceedings of the 5th International Conference on Greenhouse Gas Control Technologies*, CSIRD Publishing, Cairns, Queensland, Australia.
[11] Glassman, I., 1977, *Combustion*, Academic Press, San Diego, CA.
[12] Viteri, F., 1993, ''Turbomachinery for Modified Ericsson Engines and Other Power/Refrigeration Applications,'' U.S. Patent 5473899.
[13] Viteri, F., 1997, ''Turbocharged Reciprocation Engine for Power and Refrigeration Using the Modified Ericsson Cycle,'' U.S. Patent 5590528.
[14] Viteri, F., 1997, ''Clean Air Engines for Transportation and Other Power Applications,'' U.S. Patent 5680764.
[15] Beichel, R., 1998, ''Reduced Pollution Hydrocarbon Combustion Gas Generator,'' U.S. Patent 5709077.
[16] Beichel, R., 1998, ''Reduced Pollution Power Generation System,'' U.S. Patent 5715673.
[17] Beichel, R., 1999, ''Reduced Pollution Power Generation System Having Multiple Turbines and Reheater,'' U.S. Patent 5956937.

[18] Beichel, R., 1999, ''Reduced Pollution Hydrocarbon Combustion Gas Generator,'' U.S. Patent 5970702.
[19] Viteri, F., Taylor, J. P., Brandt, H., and Anderson, R. E., 2000, ''Hydrocarbon Combustion Power Generation System With CO_2 Sequestration,'' U.S. Patent 6170264.
[20] Mueggenburg, H., 2001, ''Steam Generator Injector,'' U.S. Patent 6206684.
[21] Viteri, F., 2001, ''Clean Air Engines for Transportation and Other Power Applications,'' U.S. Patent 6247316.
[22] Klein, S. A., and Alvarado, F. L., 2002, ''Engineering Equation Solver,'' F-Chart Software, Madison, WI.
[23] Wilson, D. G., and Korakianitis, T., 1998, *The Design of High-Efficiency Turbomachinery and Gas Turbines*, Prentice-Hall, Englewood Cliffs, NJ.
[24] Bannister, R. L., Newby, R. A., Yang, W. C., 1999, ''Final Report on the Development of a Hydrogen-Fueled Combustion Turbine Cycle for Power Generation,'' ASME J. Eng. Gas Turbines Power, **121**, pp. 38–45.
[25] Bolland, O., Kvamsdal, H. K., and Boden, J. C., 2001, ''A Thermodynamic Comparison of the Oxy-Fuel Power Cycles Water-Cycle, Gratz-Cycle and Matiant-Cycle,'' International Conference of Power Generation and Sustainable Development, Liège, Belgium.
[26] Aoki, S., Uematsu, K., Suenaga, K., Mori, H. H., and Sugishita, H., 1998, ''A Study of Hydrogen Combustion Turbines,'' *Proceedings of the International Gas Turbines & Aeroengines Congress & Exhibition*, Stockholm, Sweden, ASME, New York.
[27] Kobayashi, H., and Prasad, R., 1999, ''A Review of Oxygen Combustion and Oxygen Production Systems,'' Praxair Technology, Inc.
[28] Kee, R. J., Rupley, F. M., and Miller, J. A., 1991, ''Chemkin-II: A Fortran Chemical Kinetics Package for the Analysis of Gas Chemical Kinetics,'' SAND89-8009B, UC-706, Sandia National Laboratories, Albuquerque, NM and Livermore, CA.
[29] Bowman, C. T., Frenklach, M., Wang, H., Goldberg, M., Smith, G. P., Golden, D. M., Hanson, R. K., Davidson, D. F., Gardiner W. C., Jr., and Lissianski, V., 1997, ''GRI-MECH2.11–An Optimized Detailed Chemical Reaction Mechanism for Natural Gas Combustion and NO Formation and Reburning,'' *Proceedings of the American Institute Chemical Engineers*, Los Angeles, CA, AIChE, New York.
[30] IAPWS, ''Formulation 1995 for the Thermodynamic Properties of Ordinary Water Substance for General and Scientific Use,'' The International Association for the Properties of Water and Steam (IAPWS).
[31] Span, R., and Wagner, W., 1996, ''A New Equation of State for Carbon Dioxide Covering the Fluid Region From the Triple-Point Temperature to 1100 K at Pressures up to 800 MPa,'' J. Phys. Chem. Ref. Data, **25**(6), pp. 1509–1596.
[32] Setzman, U., and Wagner, W., 1991, ''A New Equation of State and Tables of Thermodynamic Properties for Methane Covering the Range From Melting Line to 625 K and Pressures up to 1000 MPa,'' J. Phys. Chem., **20**(6), pp. 1061–1155.
[33] Sonntag, R. E., and Van Wylen, G., J., 1986, *Fundamentals of Classical Thermodynamics*, John Wiley and Sons, New York.
[34] Moran, M. J., 1982, *Availability Analysis: A Guide to Efficient Energy Use*, Prentice-Hall, Englewood Cliffs, NJ.
[35] Simbeck, D., 1998, ''A Portfolio Selection Approach for Power Plant CO_2 Capture, Separation and R&D Options,'' *Fourth International Conference on Greenhouse Gas Control Technologies*, Interlaken, Switzerland, P. Reimer, B. Eliasson, and A. Wokaun, eds., Interlaken, Switzerland, Pergamon, London.

Thermal Characteristics of Gaseous Fuel Flames Using High Temperature Air

A. K. Gupta
Department of Mechanical Engineering,
University of Maryland,
College Park, MD 20742
e-mail: akgupta@eng.umd.edu

Recent advances on high temperature air combustion (HiTAC) have demonstrated significant energy savings, higher and uniform thermal field, lower pollution, and smaller size of the equipment for a range of furnace applications. The HiTAC technology has evolved from the conception of excess enthalpy combustion (EEC) to high and ultra-high preheated air combustion. In the HiTAC method, combined heat regeneration and low oxygen methods are utilized to enlarge and control the flame thermal behavior. This technology has shown promise for much wider applications in various process and power industries, energy conversion, and waste to clean fuel conversion. For each application the flow, thermal, and chemical behavior of HiTAC flames must be carefully tailored to satisfy the specific needs. Qualitative and quantitative results are presented on several gas-air diffusion flames using high-temperature combustion air. A specially designed regenerative combustion test furnace facility, built by Nippon Furnace Kogyo, Japan, was used to preheat the combustion air to elevated temperatures. The flames with highly preheated combustion air were significantly more stable and homogeneous (both temporally and spatially) as compared to the flames with room-temperature combustion air. The global flame features showed the flame color to change from yellow to blue to bluish-green to green over the range of conditions examined. In some cases hybrid and purple color flame was also observed. Under certain conditions flameless or colorless oxidation of the fuel has also been demonstrated. Information on global flame features, flame spectral emission characteristics, spatial distribution of OH, CH, and C_2 species and emission of pollutants has been obtained. Low levels of NO_x along with negligible levels of CO and HC have been obtained using high-temperature combustion air. The thermal and chemical behavior of high-temperature air combustion flames depends on fuel property, preheat temperature, and oxygen concentration of air. Waste heat from a furnace in high-temperature air combustion technology is retrieved and introduced back into the furnace using regenerator. These features help save energy, which subsequently also reduce the emission of CO_2 (greenhouse gas) to the environment. Flames with high temperature air provide significantly higher and uniform heat flux than normal air, which reduces the equipment size or increases the process material throughput for same size of the equipment. The high-temperature air combustion technology can provide significant energy savings (up to about 60%), downsizing of the equipment (about 30%), and pollution reduction (about 25%). Fuel energy savings directly translates to a reduction of CO_2 and other greenhouse gases to the environment. [DOI: 10.1115/1.1610009]

1 Introduction

The principle conception of excess enthalpy combustion was originated almost three decades ago for the combustion of low heating value fuels [1]. In excess enthalpy combustion the thermal energy released is fed back to the fresh reactants so that the temperatures obtained with excess enthalpy combustion are much higher than its counterpart with normal temperature air. However, in high-temperature air combustion (HiTAC) technology high-temperature combustion air at low oxygen concentration is used in the combustion chamber. High temperature of the air is obtained by preheating the air with the exhaust gases from a furnace or reactor. The peak temperature in the flame zone is much reduced with the use of diluted low oxygen concentration combustion air even though the air is preheated to high temperatures. This low oxygen concentration (or diluted) air is obtained from the exhaust gases by recirculating part of the combustion products into the incoming hot combustion air. The combustion air is preheated to temperatures in excess of 1000°C, depending on the application, using honeycomb-type or ceramic ball-type heat exchangers. Honeycomb type heat exchangers are more effective than the ceramic-ball type heat exchangers [1]. Most of the previous research activities have been focussed on gaseous fuels, such as methane, propane, liquefied petroleum gas (LPG), and process gases, [1–9]. The HiTAC technology has also been demonstrated to provide significant benefits with other gas, liquid solid, and waste fuels, [1–30], for applications to various processes, and industrial and power systems.

Combustion researches are always concerned with meeting various industrial, societal, and national needs. An example of this can be seen from the excess enthalpy concept that was used for the combustion of low heating value fuels without using any auxiliary fuel. Global environmental problems, including acid rain, particulate, ozone layer destruction, and global warming from greenhouse gases, such as CO_2 and methane, are now recognized to cycle between atmosphere and the earth. Simultaneous requirements of both environment protection and energy conservation require rapid development of combustion science and technology for various applications. The science and technology of combustion has made significant progress during the past century, in particular after World War II. For the furnaces area, HiTAC technology has shown revolutionary demonstration for energy conserva-

Contributed by the Fuels and Combustion Division of THE AMERICAN SOCIETY OF MECHANICAL ENGINEERS for publication in the ASME JOURNAL OF ENGINEERING FOR GAS TURBINES AND POWER. Manuscript received by the F&C Division January 2000; final revision received April 2003. Associate Editor: S. Gollahalli.

tion, reduction of pollution generation including NO_x and CO_2, far uniform thermal field and higher heat flux than previously possible, to give superior quality product, [10,30]. Higher heat flux is due to increase of both convective and radiative heat transfer. The increase in convective heat transfer is due to increased flow velocity as well as higher and very uniform temperatures in the entire combustion chamber.

In this paper, recent progress on HiTAC is first reviewed. Both qualitative and quantitative data from flames are presented using several different gaseous fuels. The major emphasis is placed on (1) characteristics of these flames using CH_4, C_3H_8, LPG, CO, H_2, and C_2H_2 as the fuels, (2) role of highly preheated combustion air having low levels of oxygen concentration (dilution of air with nonoxidative gas, such as, N_2 or CO_2), (3) formation and emission of pollutants, in particular NO_x, and (4) heat flux distribution in flames. These data are obtained from laboratory scale investigations.

In addition to the above, several other issues of interest include: flow field, temperature distribution, efficiency, combustion stability, and flame emissivity. Description of highly preheated air combustion (HiTAC), including the concept of excess enthalpy combustion, is also provided. The motivations and objectives of HiTAC are discussed so that the relationship between environmental issues and energy conservation can be clarified. Recent research progress on HiTAC in laboratory scale experiments are then discussed which has, for most part, been centered on determining the structure of flames under various input and operational conditions. Some experiences from field trials are also given. Numerous field test demonstrations in industrial furnaces have shown significant energy savings. The focus has been on (1) heat transfer enhancement, which is affected by flow velocity and temperature distribution (for both convective and radiative heat transfer), (2) flowfield, which affects the main motion of flame and the flame volume occupied, (3) reaction mechanisms, which may be responsible for the observed flame structure, and (4) pollution formation and emission.

2 High-Temperature Air Combustion Technology (HiTAC)

2.1 Motivation of HiTAC. Fossil fuels, such as, coal, oil and gas, have been used by the society for millions of years. These fuel sources have never been considered exhaustible until recently. Rapid industrialization and growth of human society has resulted in rapid utilization of natural resources on the earth. This then leads to the reality that in the very near future the fossil fuels, which encompassed our main energy consumption cycle, will run out. Although the nuclear and solar energy may provide more promise for future, fossil fuel cannot be quickly replaced for all applications, at least in the near future because of their unique advantages including mature utilization technologies, nonradioactivity, safety, high conversion efficiency and cost effectiveness. However, when one considers the negative impact of fossil fuels, besides the limited reserves, concerns over environmental issues is quite serious.

In this century more and more attention has been given to fossil fuel utilization because of the problem of air pollution to the atmosphere. Pollutants such as CO, CO_2, NO_x, hydrocarbons, soot and particulate, metals, polycyclic aromatic hydrocarbons, dioxins, and furans have been on the priority list. Global warming is a direct result of the greenhouse gases, such as, CO_2, NO_x, and methane.

In 1992 the United Nation Conference on Environment and Development (the Earth Summit) provided global efforts to protect our environment. At the 1997 Kyoto protocol, efforts by many developed countries were discussed to reduce carbon emissions by 7% below the 1990 level over the next ten years. High temperature air combustion technology provides an opportunity to achieve this goal with significant gains from major energy consumption sectors.

Thermodynamic considerations suggest that high temperature combustion air increases flame temperature, combustion intensity and efficiency, and heat transfer. However, with the usual air preheat NO_x will increase. Controlled combustion can reduce pollution emission, including NO_x. Our focus is on reducing energy consumption, and pollution formation and emission.

HiTAC is one of the most promising combustion techniques that provide solution for energy savings and pollution formation and emission. HiTAC is particularly attractive for processes that require uniform temperature, and higher and uniform heat flux distribution in the combustion zone. Controlled flame behavior results in uniform thermal field, significantly lower emissions and combustion noise, and smaller chamber size for processing the same material or increased material throughput for same furnace size. However, in order to explore further the full potential of high-temperature air combustion technology, one must have good understanding on the detailed structure of highly preheated air flames so that the results can be translated to wide applications.

2.2 Benefits of Combustion With High Temperature Air

(1) Energy Saving. High-temperature air combustion technology uses regenerative heat exchangers to extract thermal energy from the waste gases in the combustion products. Ceramic honeycomb or balls have been shown to provide good energy storage heat media heat exchangers. Honeycomb-type heat exchanger is more effective than ceramic ball type as this provides larger surface area, low-pressure drop and high efficiency. Exhaust gases from industrial furnaces and processes represent one of the major heat losses from the system. The regenerative media used in the HiTAC devices recovers large amounts of thermal energy from the exhaust gases and transports it back to the combustion zone. The amount of energy recovered translates directly into fuel saving. In the ''High Performance Industrial Furnace Development'' project, [2,30], the objective was to demonstrate significant energy savings (about 30%) using regenerative media, reduce physical size of the equipment by about 25%, reduce pollution emission (including CO_2) by about 30%. This goal has been successfully demonstrated using over 167 field demonstration tests, [19,21,30].

(2) CO_2 Reduction. The role of CO_2 in global warming phenomena is now widely recognized. The demands for reducing CO_2 emission are higher than ever before. All fossil fuels contain carbon, which generate CO_2 as a byproduct during the combustion of carbon so that any efforts to reduce energy consumption will directly translate to reduction of CO_2 emission. Good correlation between fuel consumption and CO_2 production suggests that CO_2 reduction should be nearly the same as energy saving, [30].

(3) NO_x Reduction. Emission of NO_x is now known to be responsible for the destruction of ozone layer in the upper atmosphere. NO_x (NO, NO_2, N_2O, N_2O_4, N_2O_5, etc.) involves the complicated reaction mechanisms, which result in accelerating the ozone depletion in the oxygen cycle on earth. Therefore, combustion engineers have focussed their attention to develop various strategies to reduce NO_x emission and improve the combustion process. HiTAC is one of the most advanced techniques because of low levels of NO_x formation and emission, significant energy savings and uniform thermal properties in the entire combustion space, [19,21,30].

(4) Reduction of Equipment Size. Higher and far uniform thermal field and heat flux distribution is obtained with HiTAC technology as compared to any other known method for combustion, such as, combustion with room-temperature air, [13,14,30], or air preheated to some moderate temperature using recuperators. The ignition delay time is different as compared to that obtained using room temperature air for combustion, [5,6]. This means that many industrial combustion equipment has potential for reduced size, better product quality from the process and material's con-

Table 1 Various methods of heat recirculation used in combustion systems

Heat Recirculation Methods	Internal Recirculation Methods	Steady	Convection	Central toroidal recirculation (swirl flows, wake flows) flames, comer recirculation zone flame (comb. Eng.) (internal-external recirculation)
			Conduction	Combustion in porous media
			Radiation	Cyclone combustors
		Unsteady	Convection	Pulse combustion
			Conduction	No trials
			Radiation	No trials
	External Recirculation Methods	Steady	Convection	No trials
			Conduction	**Swiss roll burner** Burner with heat exchanger
			Radiation	Porous media Rotary regenerators
		Unsteady	Convection	No trials
			Conduction	No trials
			Radiation	Regenerative combustion

servation with high-temperature combustion air technology [15,21,30]. Simultaneous realization of the above benefits was considered impossible before. The unique flame features associated with HiTAC assists in utilizing this technology for wider range of applications than initially envisioned, [10,30].

3 Basic Principle of HiTAC Technology

3.1 Thermodynamic Consideration of Combustion Process. Flame temperature is one of the important factor for considering combustion efficiency and energy conversion efficiency. Weinberg [1] provided initial concept of excess enthalpy combustion. In his study, limitations on combustion temperature were discussed, including both positive and negative factors associated with combustion temperatures in a certain range. Heat circulation from the exhaust gases, using high-efficiency heat exchanger, was adopted in order to increase the combustion temperature thus allowing the combustion of low heating value fuels that could otherwise not be combusted without using auxiliary fuel. However, combustion engineers have to pay attention to the upper limit of combustion temperature because of materials constraints used in the equipment and/or pollution formation at higher temperatures, in particular NO_x. Various possibilities on enthalpy intensification have been described, [2]. From the economic point of view, it is of course better to use thermal energy generated by combustion process itself to heatup the oxidant or fuel, which is often of low thermal energy, than via the use of electrical or mechanical energy.

The amount of combustion-generated energy circulated into the combustion process is given as, [1],

$$\int_{T_0}^{T_t} C_p dT = Q_c + Q_a = H_t - H_0$$

where T_f is the final temperature, T_0 is the initial temperature, Q_c is the heat release by chemical energy conversion, Q_a is the energy added, and H_t and H_0 are the enthalpy at two states. The circulation part of thermal energy from combustion-generated products will increase the combustion temperature so that enthalpy of the reaction zone will be above the conventional combustion level. This has resulted in the use of term called ''excess enthalpy combustion.''

Increase in thermodynamic efficiency must be coupled with other desirable characteristics, such as low NO_x formation, reliability of the equipment and refractory material, and spatial uniformity of temperature. Nonetheless the heat circulation and excess enthalpy methods provide new light on next generation of advanced energy conversion technology and combustion chamber design. This method provides new ideas to control temperature in the combustion zone. The method is independent of the fuel composition, and can simultaneously satisfy the demands of high-combustion intensity and reduced pollutant formation from fuels, including low-grade fuels.

3.2 Basics of Excess Enthalpy Combustion Design. Excess enthalpy combustion can be realized by internal or external circulation or their suitable combination. In all cases the heat circulation strategy is adopted for combustion improvement, see Table 1. Most designs for internal heat circulation use bluff body, porous media or swirl to the flow. Most of these are aimed at flame stabilization, [16], and are very effective. Advanced methods are being sought for increased concern on pollution reduction and energy conservation. Internal heat circulation relies on heat convection and species circulation so that pool of hot and active radicals in reaction zone can be maintained, which also assists in flame stabilization.

The external circulation methods use heat exchanger to transfer the thermal energy via conduction between combustion products and solid media so that heat can be exchanged to the cool reactants. Most of the enthalpy contained in hot combustion products can be recirculated back to the combustion process. This allows one to utilize much of the waste energy for flame stabilization, control the reaction process, and achieve desirable composition.

3.3 Application of Excess Enthalpy Combustion in High-Temperature Air Combustion (HiTAC). Thermodynamic considerations suggest that preheating the oxidant to very high temperatures (not fuel due to possible fuel decomposition and safety) increases the cycle thermal efficiency. Air preheats add enthalpy to the combustion zone. From the point of pollutant formation, especially NO_x, high temperature of combustion has been recognized to be one of the most important parameter for high levels of NO_x emission. This then requires method to control the emission of NO_x. One method of maintaining the same temperature in the

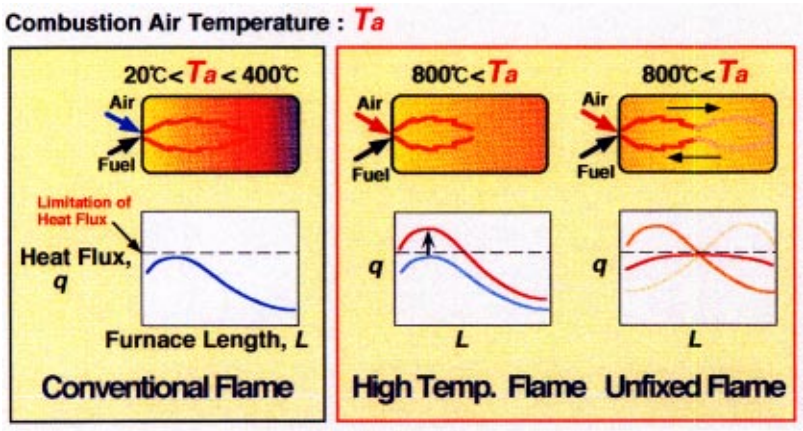

Fig. 1 A schematic diagram of flame and heat flux distribution in a furnace with low temperature combustion air, high temperature air, and HiTAC combustion conditions

combustion zone is to dilute the incoming combustion air with hot combustion products to cause MILD combustion condition. Partial recirculation of hot products into the incoming combustion air dilutes the inlet concentration of oxygen in the air. This diluted air will lower the peak flame temperatures and also lower the oxidation of N_2. Further examples of this depiction are given in Refs. [2], [4], [17], [30].

Efforts made by Nippon Furnace Kogyo Kaisha Ltd. (NFK) starting from the early 1990s, under the leadership of late President Ryoichi Tanaka of NFK, were focused on efficiency and pollution from furnaces and boilers. The goal was to demonstrate significant pollution reduction from industrial furnaces (by about 25%), enhance efficiency and achieve fuel energy savings (by about 30%), and reduce equipment size (by about 25%) using honeycomb-type regenerative burners that can be classified to operate using excess enthalpy principles. In the North American design, ceramic balls have been used in the regenerators to preheat the combustion air with hot gases exiting the furnace. The use of ceramic balls in a packed bed provided higher combustion air temperatures; however, the regenerator efficiency is not so high as compared to honeycomb-type regenerator. Nonetheless the air preheat temperatures were much higher than those achieved previously with the use of recuperators. In the high-temperature air combustion (HiTAC) technology of NFK a honeycomb-type regenerator is used. The honeycomb regenerator is much more compact than a bed packed with ceramic balls, have high specific surface area, low thermal inertia and provides very low-pressure drop, [2,15]. In the HiTAC technology low oxygen concentration air at high temperatures is used for combustion air. In conventional burners increasing the air preheat temperature increases NO_x emission levels. However, with high temperature combustion air the temperature of combustion gases in the furnace or reactor is small (only about 50 to 100°C above the incoming high-temperature combustion air). The oxygen concentration in the combustion air is very low (only about 2 to 5% by volume, depending on the application). Under these conditions the thermal field in the combustion zone is very uniform, [14,29,30]. The peak temperatures in the combustion zone are suppressed to result in very low NO_x emission levels. The heat flux from the flame with high-temperature combustion air is also very high, [13,14,30]. A schematic diagram of the flame and heat flux distribution with normal temperature air and high-temperature combustion air (called HiTAC flame) is shown in Fig. 1. The HiTAC flame results in very uniform thermal field, and uniform and high heat flux in the combustion zone.

Major thrust in all kinds of furnaces used in melting, reheating, soaking, heat treatment, boilers, etc., is to reduce product costs and improve product quality. Fuel costs represent a major cost element in furnace operation. Furthermore the furnace design must also offer low pollution. Treatment of exhaust gases to reduce pollution emission is not desirable as this increases the capital investments of the equipment in addition to the added equipment maintenance. Combustion with high temperature air provides a practical solution.

Most of the studies on HiTAC flames have been carried out using gaseous fuels (LPG, propane, methane, and low heating value gases). Recently, some studies have also been carried out using heavy fuel oil, [18], light oils, [14], and solid-waste fuels, [11]. The fundamental studies conducted provide an insight on the thermal, chemical, and fluid dynamical behavior of the flames, [17,20], while the applied research provide optimal utilization of the technology for some specific application, e.g., heating, melting, heat treatment, soaking, boiler, [19–21,30].

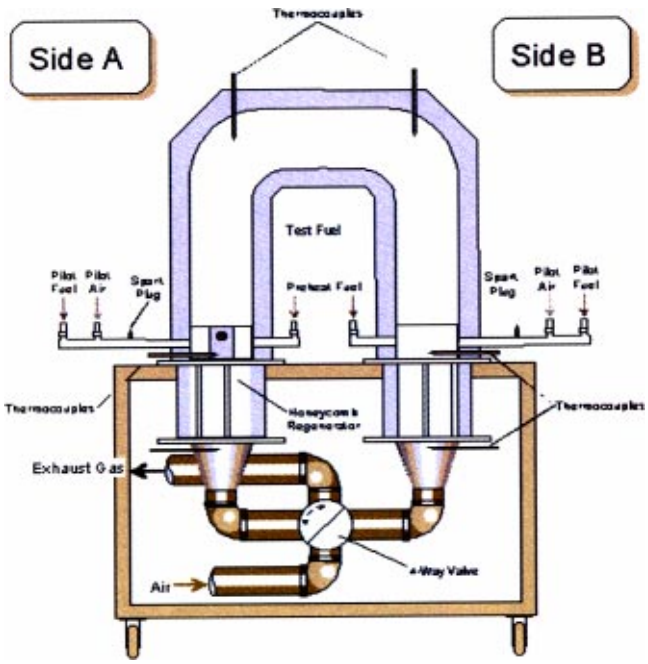

Fig. 2 A schematic diagram of the experimental test facility

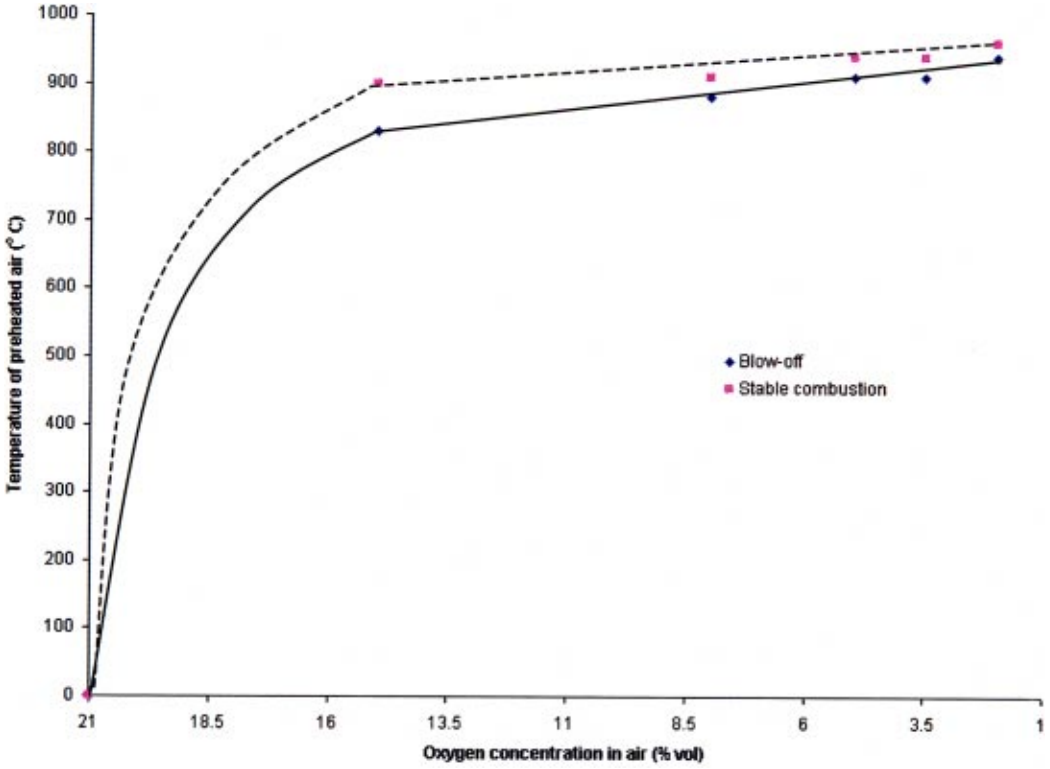

Fig. 3 Stability limits of propane flames at high temperature and different oxygen concentration in air

4 Flame Characteristics With High Temperature Air

4.1 The Experimental Facility. A high-temperature air test furnace facility, developed and built by NFK, Japan, has been used to determine the characteristic features of flames produced with high temperature combustion air (HiTAC flames), see Fig. 2. The two main components of the facility are: furnace section and control unit. The furnace has two combustion chambers; each equipped with a ceramic-type honeycomb regenerator at upstream section of the respective burners. Each combustion chamber in the furnace is equipped with a burner (one each for the two combustion chambers), each firing section A and B of the furnace, respectively, in some sequence. The other component is the computer control unit with flow and switching sequence controllers. Further details on this test facility are given in Ref. [2]. When burner in furnace section A is firing, heatup fuel at ambient temperature is supplied to burner A. The hot gases from furnace section A heat up the regenerator located at upstream section of burner B, before the gases are exhausted to the environment. After a prescribed time duration (about 30 s) the system is switched so that the burner in chamber B is firing and the regenerator located upstream of the furnace section A gets heated. The regenerators therefore act as thermal heat storage for the gases released from the two furnace sections. The exhaust gases, after passing through the regenerator, are released to the environment via a four-way valve. The above process is repeated again with the burner A firing while the regenerator B gets heated up. By repeating this cycle several times, more and more heat is stored in the regenerators. When the desired temperature of the regenerator is achieved the desired composition of air is passed over the regenerator. This air gets heated up to the desired high temperature after passing through the regenerator. The air with this facility can be heated to temperatures close to the furnace temperature. The test fuel is then introduced into section A of the furnace to examine the flame characteristics.

4.2 Flame Stability and Characteristics. The flame characteristics of propane fuel and high temperature combustion air have been examined in the test furnace facility using several advanced diagnostics. The flame stability limits as a function of air-preheat temperature and oxygen concentration in air is shown in Fig. 3. The flame stability limits increase significantly at high air preheats. It is to be noted that very wide flame stability limit occurs even with low oxygen concentration air. Under HiTAC conditions (high temperature and low oxygen concentration) the flame stability are infinite. The results also suggest that it is possible to use exhaust gases from a furnace as oxidant since these gases often contain several percent of oxygen.

The flame structure was found to depend on air preheat temperature and oxygen concentration. The diagnostics used here include direct flame photography, spectrometry, gas analyzers for NO_x, CO, CO_2, and hydrocarbons, and flame signatures for OH, CH, C_2 using ICCD camera fitted with narrow band filters. In this paper experimental data on several non-premixed gas-air flames are presented using high-temperature combustion air.

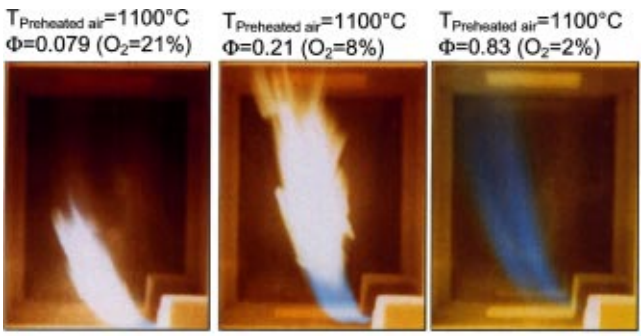

Fig. 4 Flame photographs with combustion air temperature of 1100°C and O_2 concentration (from left to right) of 21%, 8% and 2% (nitrogen as dilution gas)

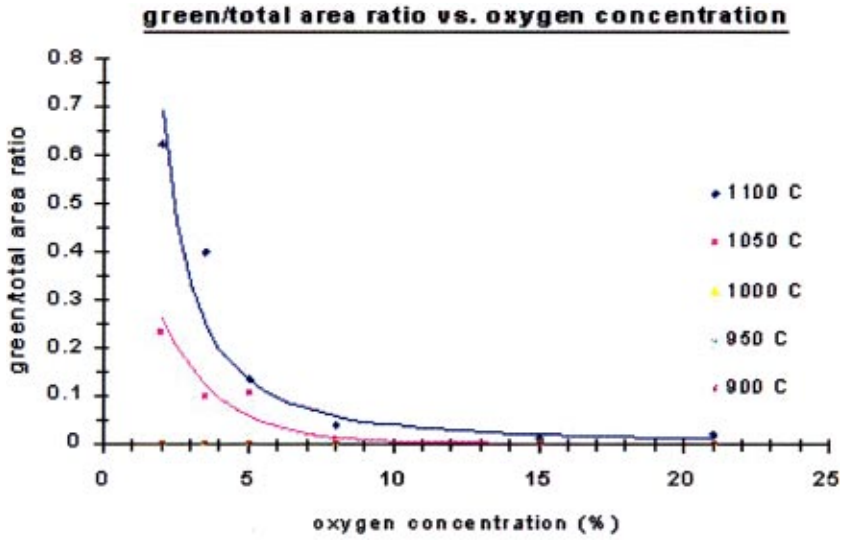

Fig. 5 Increase in green flame volume with decrease in O_2 concentration and increase in air-preheat temperature

The regenerator can preheat the incoming combustion air to temperatures in excess of 1100°C. Furthermore, it is possible to dilute the air with any gas or gas mixtures thus simulating exhaust gas recirculation (EGR). The fuel was injected via a fuel nozzle (about 1 mm diameter) in a direction normal to the preheated airflow so that the initial mixing between the fuel and air is in the form of jet in cross-flow. This form of jet mixing is known to be very efficient. The momentum of the gas jet was maintained constant when examining other gaseous fuels. For a constant cross-flow (hot air) the Patrick number (momentum ratio between the two jets) was thus maintained constant. This then means constant mixing between various cases. The oxygen concentration in the air was varied from 21% (normal air) down to about 2%. Thus the equivalence ratio was varied from $\phi = 0.83$ (with 2% O_2) to $\phi = 0.079$ (with 21% O_2) for the propane-air flames examined here. This provided similarity in mixing between the fuel and air. The equivalence ratio was, therefore, different between fuels for the same oxygen concentration. As an example, changing the fuel from propane to methane and maintaining the same momentum of the fuel jet changed the equivalence ratio to 0.3 (for 2% O_2 in air) and 0.03 (for 21% O_2). All the results presented are with constant fuel jet momentum, and hence the Patrick number.

The combustion air supplied to the test section of the furnace was preheated to temperatures ranging from 900°C to 1100°C with oxygen concentration ranging from 21% (normal air) to 2% (diluted air). Flame photographs were obtained with a still camera using short exposure times. From the flame photographs the flame area and flame color was analyzed using a computer program. Propane flame photographs with air preheat temperature of 1100°C and oxygen concentration of 21, 8, and 2% in combustion air are shown in Fig. 4. The overall equivalence ratio, ϕ, of these flames are 0.079, 0.21, and 0.83, respectively. These flames show several distinct colors (yellow, blue-yellow, and green). Under certain conditions colorless flame (flameless oxidation of fuel) has also been observed, [3,5,22,30]. The green color observed for propane flames at low oxygen concentration and high air-preheat temperatures has not been observed before. Furthermore the green color was not observed with methane fuel over the range of conditions examined, [3,10,12,22]. This suggests significant role of fuel property on the flame thermal signatures and heat transfer characteristics.

The size and color of these flames depend on air preheat temperature and oxygen concentration (or the amount of gas recirculation) in the combustion air. In addition it also depends on the fuel property, [3]. All flames showed very different flame structure as the air-preheat temperature was increased and the oxygen concentration in air was reduced from 21% to less than 5%. The flame volume was found to increase with increase in air preheat temperature and decrease in O_2 concentration in the combustion air. At any fixed temperature, the total flame volume decreased with increase in oxygen concentration from 2% (lowest value examined here) to 21%. No yellow color flame was found at temperatures below 950°C and oxygen concentrations below 15%. The size of blue color region in the flame decreased with increase in oxygen concentration (up to about 15%) and temperature. The flames were of blue color for air preheats temperature between 900° to 950°C and O_2 concentrations between 5 to 15%. For very fuel-lean mixtures at high air preheat temperature (1100°C), the luminosity of the flame (and hence the heat flux) was found to be very high. Further discussions on flame features are given in Refs. [3], [10], [21], [30].

At high air-preheat temperatures and low oxygen concentration of about 2–5% in air, the flame was found to of green color. The green flame color pronounced at higher air preheats and low oxygen concentration in the combustion air. This suggests high levels of C_2 species (swan band) produced from within the flames under these conditions. The results in Fig. 4 also show a dramatic increase in the flame volume under conditions of low oxygen concentration and high-temperature combustion air.

No flame color could be observed at very low O_2 concentration in air (less than about 2%). We describe this condition as colorless or flameless oxidation of fuel (also called FLOX). The nature of the species formed under colorless condition requires further examination. Determination of pertinent species under colorless/flameless oxidation conditions will allow one to determine the mechanistic pathways of the fuel undergoing chemical reactions. The fuel chemical property has a significant effect on the flameless oxidation of fuel, [3,21–23,30]. The thermal and chemical behavior of flameless oxidation condition requires further examination.

The extent of change to the flame color was obtained by using a specially developed computer program sensitive to color in flame photographs. The program allowed determination of flame length and volume associated with different colors in the flame. The results on the effect of oxygen concentration in air are shown in Fig. 4, while that for the air preheats temperature are shown in Fig. 5. The yellow color of the flame volume increases with increase in O_2 concentration in the air. Over the range of tempera-

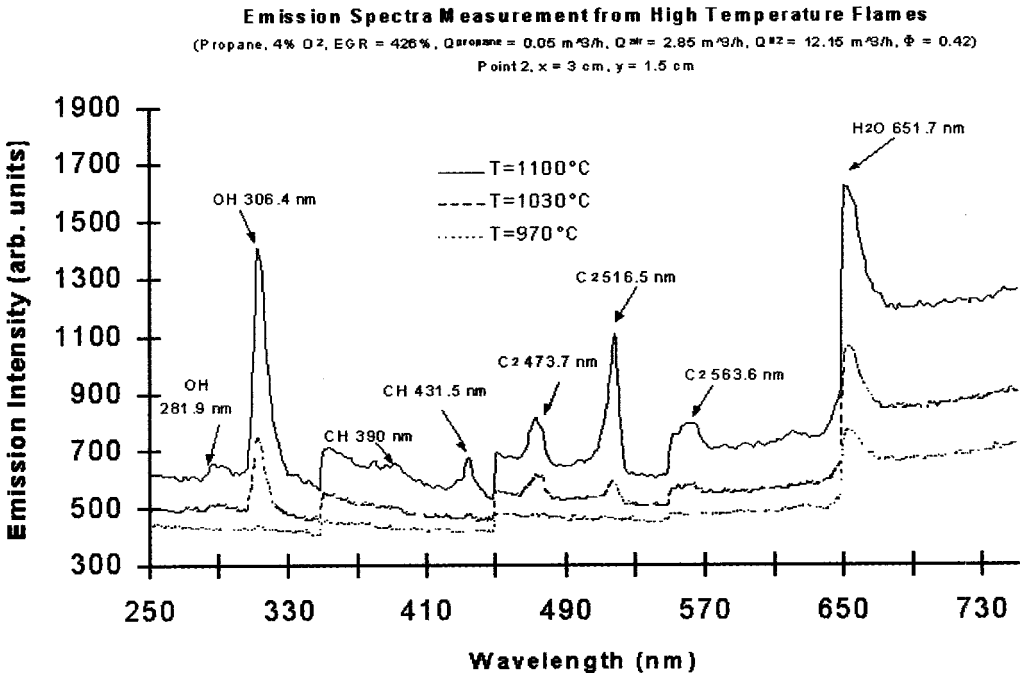

Fig. 6 Flame emission spectra at one point in the flame ($x=3$ cm and $Y=1.5$ cm) and three air-preheat temperatures (nitrogen as the dilution gas)

tures examined, the increase in flame temperature increases yellow fraction of the flame at high O_2 concentrations in air. Figure 5 shows that flame volume associated with green color of the flame increases rapidly at O_2 concentrations less than 5% in the combustion air. Similarly the flame volume associated with other colors in the flame was determined. The flame radiation associated with different flame colors is different. In some applications high radiative heat flux is desirable while for others it is not. The flame standoff distance from the nozzle exit (ignition delay) was found to decrease with an increase in air-preheat temperature. The information presented here, therefore, assists in providing design guidelines on the use of high-temperature air combustion (HiTAC) technology for various applications, [28]. Further recent activities on HiTAC technology include the clean gas energy conversion from solid wastes, biomass, coals and low-grade fuels, fuel reforming, and utilization of clean gas energy in stationary gas turbine combustion, [30].

4.3 Emission Spectra. The spatial distribution of C_2, OH, and CH emission from within the flames, obtained using a ICCD camera and narrow-band optical filter, appropriate for the desired specie to be detected, showed significant effect of oxygen concentration and air preheats temperature on the spatial distribution of above species in flames, [3,5]. At high air preheats and low oxygen concentration the propane flame had two high regions of C_2 concentration, [3,5], both regions being near to upstream portions of the flame. With increase in oxygen concentration in combustion air the flame structure became more symmetrical. It was observed that flame fluctuations were negligible at high air preheats and low oxygen concentration combustion air, [4,14,17,27,29]. Quantitative data on flame fluctuation at high air preheats and low oxygen concentrations are given in Refs. [23], [24], [29].

Emission spectra of various species in HiTAC flames have been determined for different operational conditions at selected positions in the flames. Sample results with 4% O_2 concentration and air preheats of 970°C, 1030°C, and 1100°C taken at one location in the flame ($X=3$ cm and $Y=1.5$ cm) are shown in Fig. 6. These results correspond to simulated exhaust gas recirculation (EGR) of 426%. These results were obtained using a spectrometer by scan-

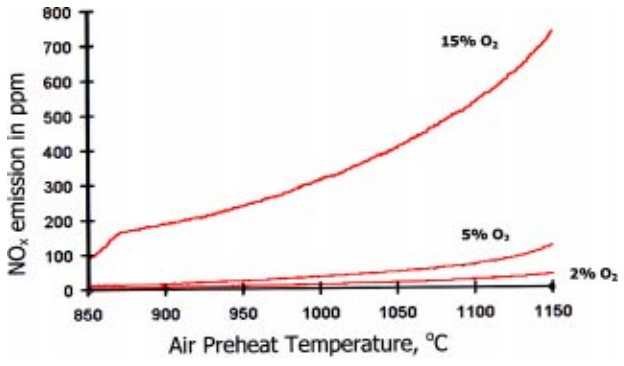

Fig. 7 Emission of NO_x as a function of air-preheat temperature and O_2 concentration in air using propane as the fuel (nitrogen as the dilution gas)

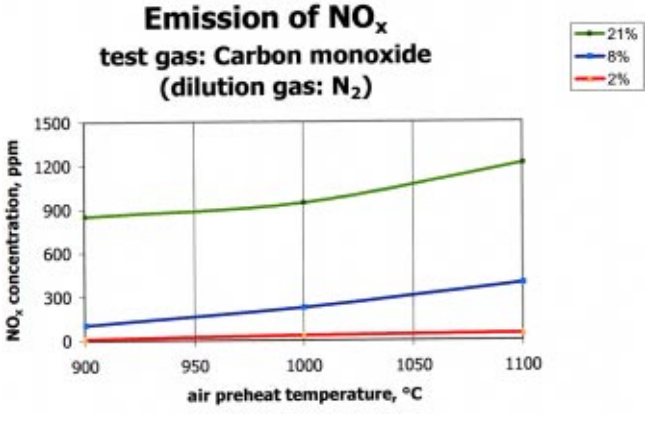

Fig. 8 Emission of NO_x as a function of air-preheat temperature and O_2 concentration in air using carbon monoxide as the fuel (nitrogen as the dilution gas)

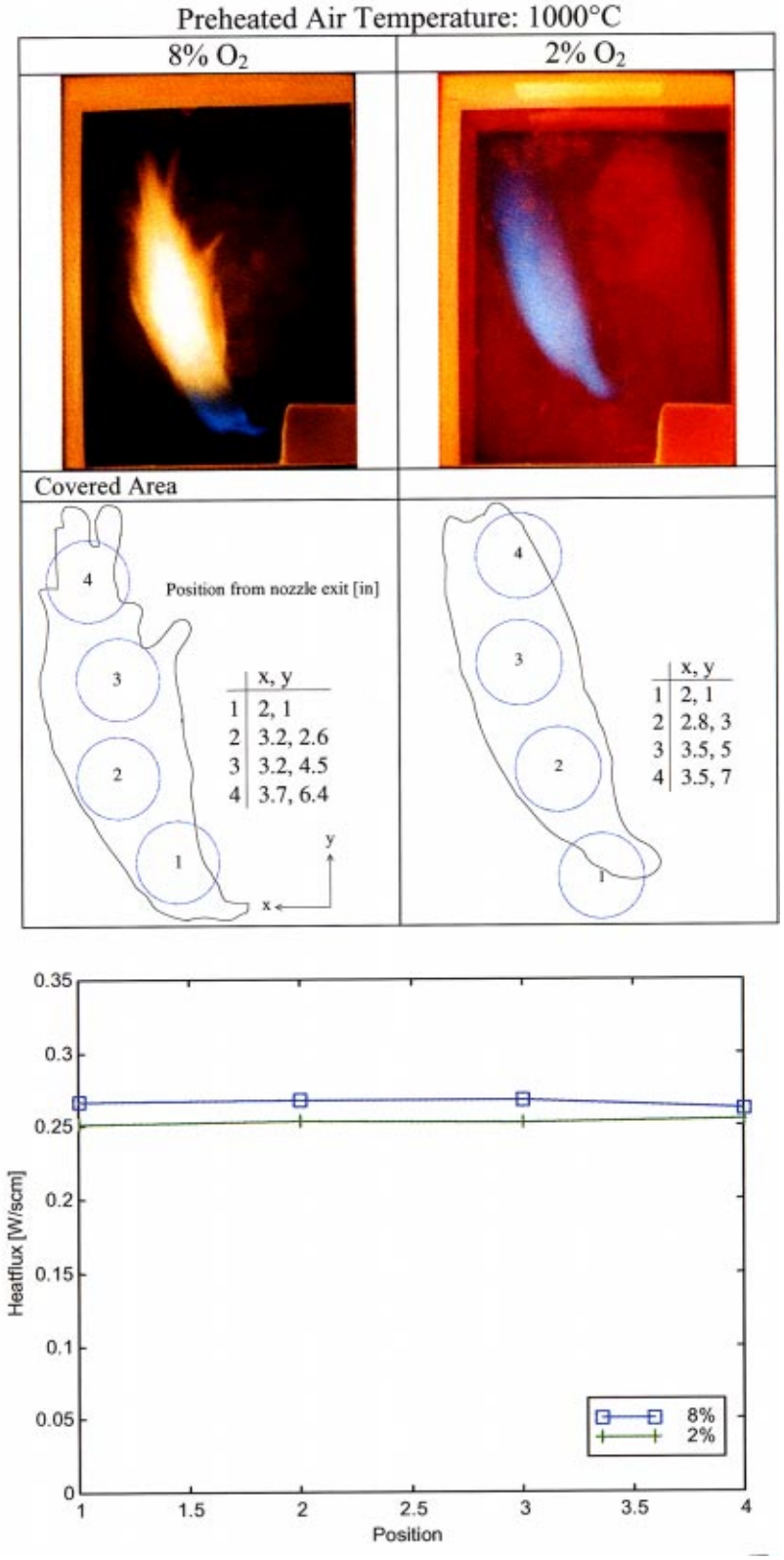

Fig. 9 Heat flux variation along the flame using propane as the fuel, T_{air} = 1000°C (sensor at 6.5 in. from the center axis of flame), arbitrary unit of heat flux

ning the flame in 100 nm wavelength intervals in order to provide enhanced resolution. Thus, one flame condition required five scans for 250–750 nm ranges. No significant species were found beyond 750 nm for the examined flames. The results show a significant increase of OH, CH, C_2, and H_2O emissions with increase in air preheats temperature. The relative amount of various species present at other positions in the flame was different. Global observations of the flame showed change in flame color from blue to bluish-green to green with increase in air preheat temperature at low oxygen concentration in air. This is attributed to the

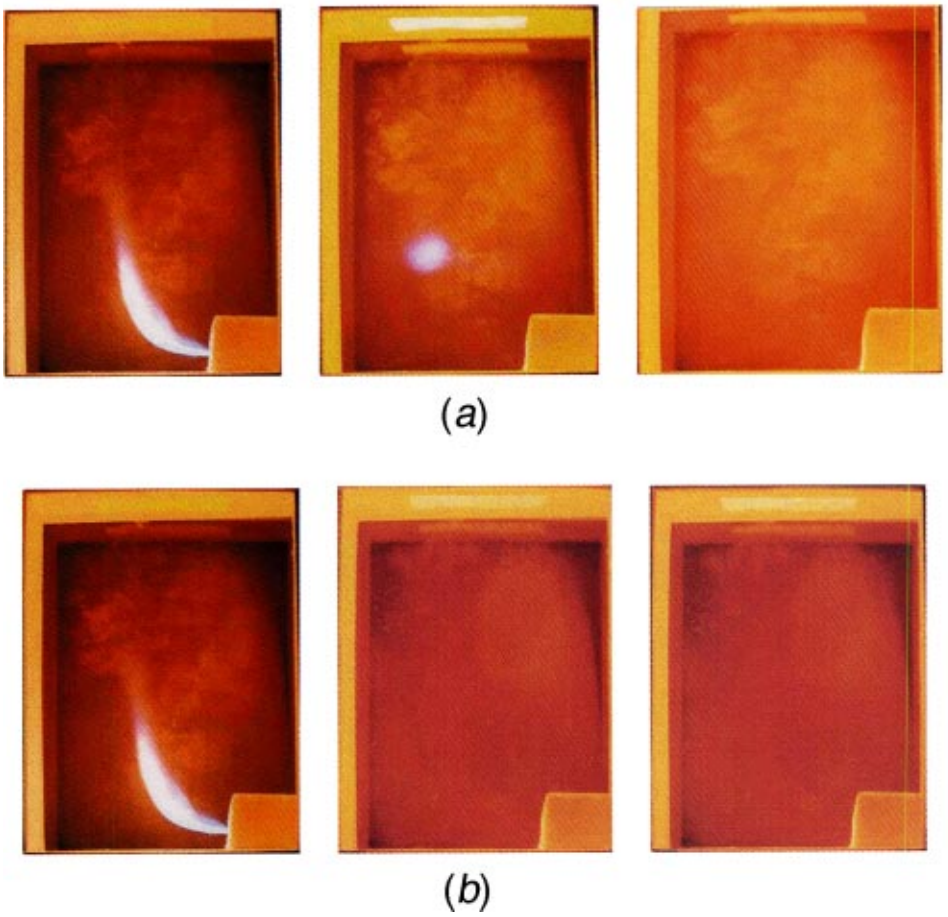

Fig. 10 (*a*) **Methane flame photographs with combustion air temperature of 1000°C and oxygen concentrations (from left to right) of 21%, 8%, and 2%, respectively (nitrogen as dilution gas).** (*b*) **Methane flame photographs with combustion air temperature of 1000°C and oxygen concentrations (from left to right) of 21%, 8%, and 2%, respectively (carbon dioxide as dilution gas).**

increase of C_2 emission. At 516.5 nm the increase factor is 1.9 from 970°C to 1030°C and 2.4 from 970°C to 1100°C. Similar results were found for other species, [5]. The green color of the flame is directly attributed to the increase of C_2 (swan band) emission. The ratio of CH and C_2 is important as this directly relates to the change of flame color from blue to green. Further downstream of the flame negligible amounts of CH and C_2 species were detected.

4.4 NO_x Emission. In order to determine whether high-temperature combustion air would adversely affect pollution emission, measurements were made of various gaseous species. Figure 7 shows the NO_x emission levels for propane flame as a function of air preheats at 15, 8, and 2% O_2 concentration in air. The emission of NO_x increases with air preheats temperature under normal combustion conditions. This was also true for HiTAC conditions but the rate of increase was small. Very low NO_x emission is observed under high temperature and low oxygen concentration combustion conditions. NO_x emission at air preheat temperature of 1150°C decreased from 2800 ppm at 21% O_2 to 40 ppm at 2% O_2. The emission of CO and UHC was negligible (below the detection limits). Figure 8 shows low NO_x emission with CO as the fuel. In general, therefore, HiTAC conditions results in low NO_x emission.

4.5 Heat Flux Distribution. The uniformity of heat flux distribution from within the flames was determined for a range of experimental conditions. The variation of heat flux along the flame for three O_2 concentrations of 21%, 8%, and 2% is given in Fig. 9. The corresponding flame photographs and the measurement locations are also shown in the figure. The results show very uniform heat flux distribution from the flames. The actual value of heat flux at each position in the flame may not be precise, as the measured results require calibration. Nonetheless the distribution of the heat flux in the flame will remain unchanged. The results were also obtained with normal air temperature and O_2 concentration. The distribution of heat flux showed a bell shaped curve, having low value near to the burner exit, peaked downstream of the burner exit, and then decayed further downstream from the burner exit. Furthermore, the absolute value was much lower than that found for the HiTAC flames. High heat flux in HiTAC flames is due to high velocity of the air in the test section, which increases the convective heat flux. In addition the radiative heat flux is higher due to enhanced radiation heat flux from the furnace walls. It can, therefore, be concluded that the heat flux from HiTAC flames is much higher and uniform. This can be translated to uniform heating of the material to be heated and reduced energy requirement.

4.6 Effect of Fuel Property on Global Flame Characteristics. Several different fuels have been examined to determine the effect of fuel property on the flame characteristics. Sample results with methane and acetylene fuels are given in Figs. 10 and 11, respectively. Two different gases for diluting the O_2 concentration in combustion air are nitrogen and CO_2. For all cases the fuel jet momentum was held constant to provide similarity in mix-

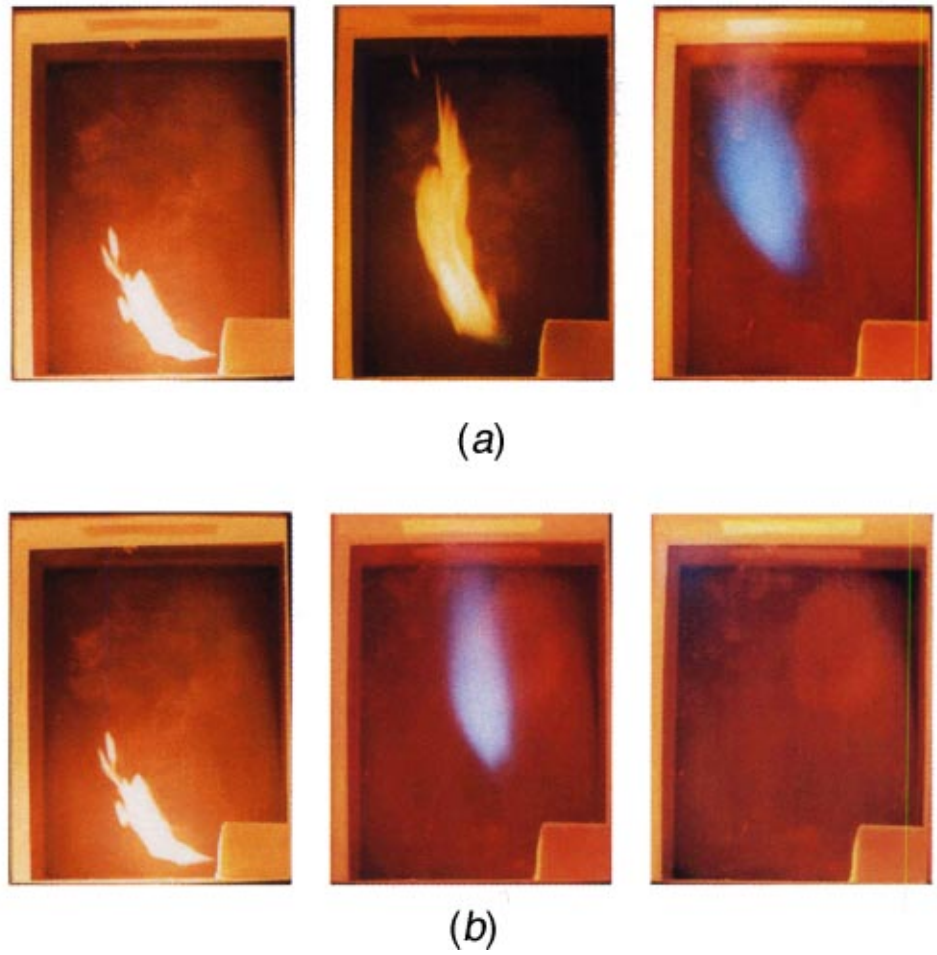

Fig. 11 (*a*) **Acetylene flame photographs with combustion air temperature of 1000°C and oxygen concentrations (from left to right) of 21%, 8%, and 2%, respectively (nitrogen as dilution gas). (*b*) Acetylene flame photographs with combustion air temperature of 1000°C and oxygen concentrations (from left to right) of 21%, 8%, and 2%, respectively (carbon dioxide as dilution gas).**

ing patterns between fuel jet and cross flow. The flame features of methane and acetylene fuels are much different than those observed for propane flames. The results also show that the dilution air significantly affects the flame features. In all cases a larger flame volume is observed under HiTAC conditions. The results showed flameless oxidation conditions under certain HiTAC conditions using methane as the fuel. Both the fuels provided no evidence of the presence of green color flame for the range of conditions examined. This suggests that the combustion mechanism is much different with different fuels. Flameless oxidation with methane as the fuel has been observed, [3]. Flame spectra measurements with methane fuel showed no pronounced peaks at the swan band.

5 Applications of Combustion With High Temperature Air

Most of the HiTAC technology efforts so far have been for furnaces, boilers and waste fuels, [30]. The technology has tremendous potential for many other applications. Some of the near term applications include:

- furnaces used for melting, heat treatment, soaking, petrochemical reforming heater, glass melting, steel reheating, process heater, aluminum melter, drying, boilers, ceramic heater, and domestic boilers and heaters.
- waste incineration/waste thermal destruction of solid and liquid wastes including wastes produced from municipal, industrial, yard, animals, and chicken. The technology is attractive for gasifying wastes, biomass fuels, and mixed wastes so that the gaseous fuel produced is clean and environmentally benign energy. High temperature steam gasification provides further benefits of higher heating value, higher hydrogen content, and destruction efficiency.
- fuel reforming and energy transformation to cleaner fuels for use in fuel cells, and other propulsion and power applications.
- power production using micro-gas turbines with the combustion of low to medium gas produced from wastes.
- destruction of odors and certain pollutants.
- production of nano-materials.

Further systematic fundamental and applied studies will allow further insights into the HiTAC technology. It is anticipated that additional applications will evolve with further R&D efforts on high temperature air combustion technology. Several efforts are now in place on the use of light and heavy fuel oils and solid fuels. They have provided useful insights for practical applications.

6 Summary

Recent developments on high-temperature air combustion have shown significant potential of HiTAC technology. The green flame

color observed with propane and certain other fuels occur only under certain conditions. Fuel property has a significant effect on the flame thermal and chemical signatures. The green flame color with propane fuel increases with increase in air preheats temperature and decrease in oxygen concentration. The observed yellow flame color was found to increase with increase in temperature and oxygen concentration in air. This is contrary to that observed for normal combustion conditions. Blue flame color predominates at air preheat temperature of up to 1000°C and O_2 concentration from 5 to 15%. The flame size increases with decrease in oxygen concentration and increase in air temperature. The flame standoff distance from the nozzle exit (ignition delay) was found to decrease with an increase in air preheat temperature. The emission of NO_x was significantly lower at high temperatures and low oxygen concentration air as compared to normal combustion air at low temperatures. Flameless oxidation of the fuel (colorless flame) has been observed under certain conditions. Thermal uniformity of flame is significantly enhanced at high air preheats and low oxygen concentration of air. Flame signatures can be significantly changed with changes in EGR, air preheats and O_2 concentration in air. This allows one to design and develop high temperature air combustion technology for various applications. The heat flux distribution from flames with high temperature air is much higher and uniform than those obtained with normal temperature air. High heat flux and energy recovery from the exhaust gases results in significant energy savings. Some of the near term potentials of this HiTAC technology presented here reveals significant future applications of this technology.

Acknowledgments

Support of this project by NASA and NSF, and NFK Japan is greatly appreciated. The experimental facility used here was design and built by NFK, Japan. Technical discussions, support and friendship provided by Mr. Toshiaki Hasegawa, Director of Basic Technology at NFK and late Mr. R. Tanaka, President of NFK is gratefully acknowledged. The author would also like to acknowledge the assistance provided by S. Bolz and K. Jagnow, and Z. Li.

References

[1] Weinberg, F. J., 1971, Nature (London), **233, Sep. 24**, pp. 239–241.
[2] Hasegawa, T., Tanaka, R., and Kishimoto, K., 1995, ''High Temperature Excess-Enthalpy Combustion for Efficiency Improvement and NO_x Abatement,'' Paper No. 9E, paper presented at the 1995 AFRC Japan-USA Meeting, Hawaii, Oct.
[3] Gupta, A. K., and Li, Z., 1997, ''Effects of Fuel Property on the Structure of Highly Preheated Air Flames,'' *Proc. Intl. Joint Power Generation Conference (IJPGC)*, Nov. 2–5, Denver, CO.
[4] Hasegawa, T., 1997, *Proc. Intl. Joint Power Generation Conference*, **1**, ASME, New York, ASME EC-Vol. 5, pp. 259–266.
[5] Gupta, A. K., Boltz, S., and Hasegawa, T., 1999, ''Effect of Air Preheat and Oxygen Concentration on Flame Structure and Emissions,'' ASME J. Energy Resour. Technol., **121**, pp. 209–216.
[6] Tanigawa, T., et al., 1998, ''Experimental and Theoretical Analysis Results for High Temperature Air Combustion,'' *Proc. Intl. Joint Power Generation Conference*, **1**, ASME, New York, ASME FACT-Vol. 22, pp. 207–214.
[7] Taniguchi, H., et al., 1998, ''Heat Transfer Analysis for High Temperature Preheated Air Combustion in Furnace,'' *Proc. Intl. Joint Power Generation Conference*, **1**, ASME, New York, ASME FACT-Vol. 22, pp. 215–225.
[8] Gupta, A. K., and Li, Z., 1997, ''Effect of Fuel Property on the Structure of Highly Preheated Air Flames,'' , 1998, *Proc. Intl. Joint Power Generation Conference*, **1**, ASME, New York, ASME EC-Vol. 5, pp. 247–258.
[9] Kitagawa, K., et al., 1998, ''Two-Dimensional Distribution of Flame Fluctuation During Highly Preheated Air Combustion,'' *Proc. Intl. Joint Power Generation Conference*, **1**, ASME, New York, ASME FACT-Vol. 22, pp. 239–242.
[10] Gupta, A. K., 2000, ''Flame Characteristics and Challenges With High Temperature Air Combustion,'' *Proc. 2nd International Seminar on High Temperature Air Combustion*, Jan. 17–18, Stockholm, Sweden.
[11] Yoshikawa, K., 2000, ''High Temperature Gassification of Coal, Biomass, and Solid Wastes,'' *Proc. 2nd Intl. Seminar on High Temperature Air Combustion*, Jan. 17–18, Stockholm, Sweden.
[12] Shimo, N., 2000, ''Fundamental Research of Oil Combustion With Highly Preheated Air,'' *Proc. 2nd Intl. Seminar on High Temperature Air Combustion*, Jan. 17–18, Stockholm, Sweden.
[13] Weber, R., Verlann, A. L., Orsino, S., and Lallemant, N., 1999, ''On Emerging Furnace Design That Provides Substantial Energy Savings and Drastic Reductions in CO_2, CO and NO_x Emissions,'' J. of the Institute of Energy, UK, Sept. pp. 77–83.
[14] Ahadi-Osuki, T., 2000, ''Heat Flux From Highly Preheated Air Combustion and Swirl Combustion,'' MS thesis, University of Maryland Combustion Laboratory, Feb.
[15] Hasegawa, T., 2000 ''Environmentally Compatible Regenerative Combustion Heating System,'' *Proc. 2nd International Seminar on High Temperature Air Combustion*, Jan. 17–18, Stockholm, Sweden.
[16] Gupta, A. K., Lilley, D. G., and Syred, N., 1984, *Swirl Flows*, Abacus Press, Tunbridge Wells, Kent, England.
[17] Hasegawa, T., and Mochida, S.; 1999, ''Highly Preheated Air Combustion Characteristics and Development of a Combustion Diagnostic on Advanced Industrial Furnace Making,'' *Proc. Intl. Joint Power Generation Conference*, San Francisco, CA, July 25–28, 1999, **1**, ASME, New York, ASME FACT-Vol. 23, pp. 457–466.
[18] Chang, Rey-Chein, and Chang, Wen-Chiang; 2000, ''Research of High Temperature Air Combustion Fired Heavy Oil,'' *Proc. 2nd International Seminar on High Temperature Air Combustion*, Jan. 17–18, Stockholm, Sweden.
[19] Suzukawa, Y., Sugiyama, S., and Mori, I., 1996, ''Heat Transfer Improvement and NO_x Reduction in an Industrial Furnace by Regenerative Combustion System,'' *Proc. 1996 IECEC Conference*, Paper No. 96360, pp. 804–809.
[20] Hasegawa, T., and Tanaka, R.; 1997, ''Combustion with High Temperature Low Oxygen Air in Regenerative Burners,'' paper presented at the 1997 ASPACC, Osaka, Japan.
[21] Katsuki, M., and Hasegawa, T., 1999, ''The Science and Technology of Combustion in Highly Preheated Air,'' *Proc. 27th Symposium (Intl.) on Combustion*, The Combustion Institute, Pittsburgh, PA, pp. 3135–3146.
[22] Gupta, A. K., and Hasegawa, T.; 1999, ''Air Preheat and Oxygen Concentration Effects on the Thermal Behavior of Propane and Methane Diffusion Flames,'' *Proc. High Temperature Air Combustion Symposium*, Jan. 20–22, Kaohsiung, Taiwan.
[23] Ishiguro, T., Tsuge, S., Furuhata, T., Kitagawa, K., Arai, N., Hasegawa, T., Tanaka, R., and Gupta, A. K., 1999, ''Homogenization and Stabilization During Combustion of Hydrocarbons With Preheated Air,'' *Proc. 27th Symposium (Intl.) on Combustion*, The Combustion Institute, Pittsburgh, PA, pp. 3205–3213.
[24] Kitagawa, K., Konishi, N., Arai, N., and Gupta, A. K., 1998, ''Two-Dimensional Distribution of Flame Fluctuation During Highly Preheated Air Combustion,'' *Proc. ASME Intl. Joint Power Generation Conference (IJPGC)*, ASME, New York, ASME FACT-Vol. 22, pp. 239–242.
[25] Gupta, A. K., 2001, ''High Temperature Air Combustion: Experiences From the USA-Japan Joint Energy Project,'' invited keynote lecture at the 4th High Temperature Air Combustion and Gasification Symposium, Nov. 27–30, Rome Italy.
[26] Gupta, A. K., 2002, ''Flame Length and Ignition Delay During the Combustion of Acetylene in High Temperature Air,'' invited paper, Proc. 5th High Temperature Air Combustion and Gasification (5th HTACG), Oct. 28–31, Yokohama, Japan.
[27] Konishi, N., Kitagawa, K., Arai, N., and Gupta, A. K., 2002, ''Two-Dimensional Spectroscopic Analysis of Spontaneous Emission From a Flame Using Highly Preheated Air Combustion,'' J. Propul. Power, **18**, pp. 199–204.
[28] Hasegawa, T., Mochida, S., and Gupta, A. K., 2002, ''Development of Advanced Industrial Furnace Using Highly Preheated Combustion Air,'' J. Propul. Power, **18**, pp. 233–239.
[29] Kitagawa, K., Konishi, N., Arai, N., and Gupta, A. K., 2003, ''Temporally Resolved 2-D Spectroscopic Study on the Effect of Highly Preheated and Low Oxygen Concentration Air on Combustion,'' ASME J. Eng. Gas Turbines Power, **125**, pp. 326–331.
[30] Tsuji, H., Gupta, A. K., Hasegawa, T., Katsuki, M., Kishimoto, K., Morita, M., 2003, *High Temperature Air Combustion: From Energy Conservation to Pollution Reduction*, CRC Press, Boca Raton, FL, 401 pp.

Y. Hino
Materials and Processing Research Center,
NKK Corporation,
1 Kokan-cho, Fukuyama,
Hiroshima 721-8510, Japan
e-mail: y-hino@lab.fukuyama.nkk.co.jp

S. Sugiyama
NK Techno Service Corporation,
1-1 Minamiwatarida-cho, Kawasaki-ku,
Kasawaki 210-0855, Japan

Y. Suzukawa

I. Mori

Fukuyama Works,
NKK Corporation,
1 Kokan-cho, Fukuyama,
Hiroshima 721-8510, Japan

N. Konishi
Department of Molecular Design and Engineering,
Graduate School of Engineering,
Nagoya University,
Nagoya 464-8603, Japan

T. Ishiguro
Department of Applied Chemistry,
Graduate School of Engineering,
Nagoya University,
Nagoya 464-8603, Japan

K. Kitawawa
Research Center for Advanced Energy Conversion,
Nagoya University,
Furo-cho, Chikusa-ku,
Nagoya 464-8603, Japan

A. K. Gupta[1]
Department of Mechanical Engineering,
University of Maryland,
College Park, MD 20742
e-mail: akgupta@eng.umd.edu

Two-Dimensional Spectroscopic Observation of Nonluminous Flames in a Regenerative Industrial Furnace Using Coal Gas

Thermal and chemical characteristics of the flames obtained from an industrial size regenerative combustion furnace have been obtained spectroscopically. The combustion characteristics of diffusion or premixed flames in the regenerative high-temperature air combustion facility have been examined using coal gas as the fuel. The fuel gas composition consisted of H_2, hydrocarbon, CO, and N_2. Monochromatic images of the flames have been observed in the emission mode using a CCD camera fitted with an optical band pass filter at the desired wavelength. The two-dimensional temperature distribution in the furnace has been determined using the two-line method by utilizing the Swan emission bands from within the flame. The emission intensity profiles of NO, as well as OH and CH radicals have also been observed spectroscopically. The results showed quite uniform two-dimensional temperature distribution and emission intensity of OH and CH radical species for the diffusion flame case as compared to the premixed case using high-temperature combustion air. The premixed flame case showed high local values and large fluctuations in the combustion zone for both emission intensity and temperature distribution. The temperature distribution of soot particles in the premixed flame was also determined using the two-color optical method. The results showed high local value of temperature, similar to that found for the gas temperature using signatures for C_2 species at two different wavelengths. In contrast the distribution of temperature for soot particles was different. The location of the maximum soot temperature shifted to downstream positions of the flame as compared to the maximum gas temperature regions measured from the C_2 species. The experimental results are discussed in conjunction with those obtained from the heat simulation analyses. [DOI: 10.1115/1.1610010]

Introduction

Recovery of heat from the exhaust gases in any energy conversion plant is important from the point of view of system efficiency, energy conversion, environmental problems, and costs. Thermal energy loss from the stack of a plant represents one of the major energy losses from any kind of power plant. Therefore, any efforts to recover energy from the stack gases translate directly into an increase in efficiency of the power plant and subsequent energy savings and costs to operate the power plant. The conventional approach has been to recover some of this thermal energy from the stack using a recuperator that is then used to preheat the combustion air for use in the power plant to combust the fuel. However, the degree of air preheats achieved using this method is rather small so that the efficiency gains of the plant are rather small. Recently significant attention has been given in the steel and aluminum industry to recover heat from the exhaust gases as this industry is quite energy intensive. The basic idea of the combustion technology with high temperature air is to recover

[1]To whom correspondence should be addressed.

Contributed by the Fuels and Combustion Division of THE AMERICAN SOCIETY OF MECHANICAL ENGINEERS for publication in the ASME JOURNAL OF ENGINEERING FOR GAS TURBINES AND POWER. Manuscript received by the C&F Division November 2001; final revision received April 2003. Associate Editor: S. Gollahalli.

most of the energy from the stack gases prior to their discharge to the atmosphere and combust the fuel with very high-temperature combustion air that contains very low oxygen concentration under controlled conditions, [1–10]. In industrial furnaces, the waste heat recovered from the stack gases can be utilized to preheat the combustion air, which subsequently results in significant savings of energy. Furthermore, uniform thermal characteristics are obtained in the combustion zone using high temperature air at low oxygen concentration.

Recent developments in regenerative combustion systems using high-temperature combustion air have resulted in significant improvement of efficiency and lower emission of pollutants, including NO_x, noise, and CO_2, from many different kinds of industrial furnaces and heating systems, [1–7]. Comprehensive information on the combustion science and technology using high-temperature air is provided in the recently book on this subject, [1]. It has been reported that combustion with very high air preheats, up to 1500 K, the temperature distribution in the furnace becomes very uniform. The high and uniform temperature distribution in the furnace gives higher heating capacity of the industrial furnaces, [1,3,5]. The high temperature air is generated efficiently by recovering heat from exhaust gases of the furnace using high-efficiency regenerators. In addition high heat flux is obtained due to high velocity of the gas flow. This enhances convective heat transfer and reduces the time available for NO_x formation in the combustion zone. Since the temperature in the combustion zone are low and very uniform, the formation of thermal NO_x is suppressed.

Combustion with high temperature air having normal 21% oxygen concentration results in high levels of NO_x emission because of the high flame temperatures caused by higher enthalpy of the combustion air. It is to be noted that NO_x emission increases exponentially with temperature so that at higher flame temperatures (above 1500 K) the thermal NO_x emission levels are significantly increased. At higher temperatures the thermal NO_x increases significantly so that if one were to use air preheat temperatures in excess of 1000°C the thermal NO_x formed will be excessive. In order to overcome this problem of increased NO_x, highly preheated combustion air containing low oxygen concentration (sometimes also called diluted air) is used, where fresh combustion air is mixed with the exhaust gases prior to its introduction into the combustion chamber. The use of low oxygen concentration combustion air suppresses the local increase in combustion temperatures. Furthermore, the combustion volume expands due to the decrease in reaction rate. The combined effect results in decreased NO_x emission levels. In addition, highly preheated air extends the lower flammability limit of the flame for a given fuel-air mixture so that stable flame can be obtained at extremely lean mixtures without the use of any auxiliary fuel or additional thermal energy. The results obtained with high temperature combustion air show very wide flame stability limits, [1,4,5,8,9].

Recently, regenerative burner systems have been developed that use honeycomb-type heat exchanger for efficient heat recovery from the exhaust gases. The honeycomb heat exchangers possess many fold superior heat exchange characteristics as compared to the ceramic ball type heat exchangers, [3–5]. The regenerative combustion system utilizes high-temperature air at low oxygen concentration for combustion so that the temperature rise from combustion and peak temperatures in the combustion zone is small. This type of combustion system has been shown to provide very low NO_x emission levels as compared to the conventional combustion system using normal air and temperature, [1–3]. In addition the noise levels from flames using high-temperature air for combustion are very low since the combustion occurs under mild conditions. The temperature and heat flux distributions in the furnace are very uniform. Results obtained with this technology from many field test studies have clearly demonstrated the multifold advantages of high-temperature air combustion technology. Some of the advantages include: high and uniform heat flux distribution in the furnace, low noise emission levels (quieter flame), reduced NO_x emission levels (in excess of 25%), significant energy savings (in the range of 10 to 60%) as compared to conventional furnaces, reduced size of the furnace or higher throughput of the material for the same size of the furnace (about 25%), and reduction of CO_2 emission due to reduced fuel consumption, [1,3].

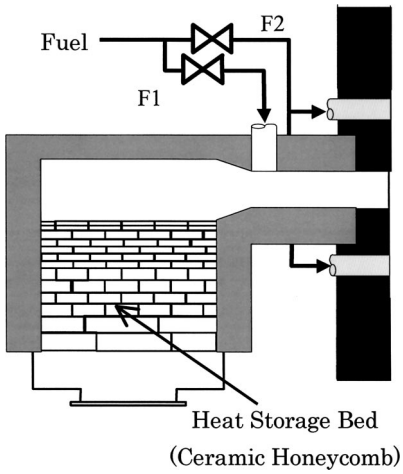

Fig. 1 A schematic diagram of the regenerative burner

In this study, diffusion and premixed flames produced with the combustion of coal gas (consisting of H_2, hydrocarbon, CO, and N_2) in highly preheated combustion air have been examined in an industrial size test furnace using regenerative combustion process. The data have been obtained for temperature, NO_x, and several radical species concentration using nonintrusive spectroscopic technique. The spatial distribution of emission from the radical species and C_2 vibrational temperature has been obtained by measuring the monochromatic two-dimensional images of the flames. The soot temperature distribution from the luminous premixed flame was also measured with the two-color optical method. The soot temperature was compared with the gas temperature distribution obtained from the intensity measurement of C_2 species. The results are discussed in conjunction with combustion and heat transfer characteristics.

Experimental

The Test Furnace. The combustion furnace facility used in this study was equipped with a pair of regenerative burners and had a test section of 4 m wide, 3 m high, and 8 m long. Figure 1 shows a schematic of the regenerative burner, which incorporates a honeycomb-type regenerator. The function of this regenerator is to extract thermal energy from the exhaust gases prior to their discharge to the atmosphere. This thermal energy is then fed back into the furnace section. The regenerative burners (in pair) are placed at the two opposite sidewall of the furnace. These regenerative burners operate in pair so that when one burner is firing the honeycomb in the other burner gets heated up to store the thermal energy from the exhaust gases emanating from the first burner prior to the discharge of gases to the atmosphere.

The operational principles of regenerative burners involve firing of one of the regenerative burners while the other burner serves to exhaust gases from the test section. This then heats the regenerator located in the second burner that also allows exiting the waste gases from the furnace. The combustion between the two pair of burners is switched at a preselected time interval (every 30 seconds) so that after this time duration the combustion occurs from the other (second) burner and the gases pass through the regenerator located in the first burner. The regenerator in the first burner thus heats up. This regenerator therefore serves to

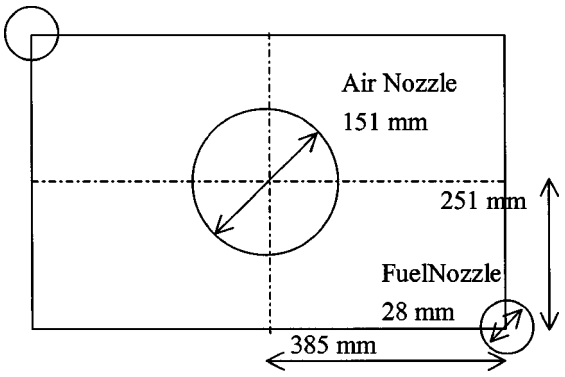

Fig. 2 Schematic diagram of the burner, as well as air and fuel nozzle in the furnace

extract the thermal energy from gases and then allow the gases to exit. The burner has a central port that allows admission of the highly preheated air to the combustion zone.

The facility incorporates two types of fuel injection ports into the burner. The fuel injection port F1 is for premixed combustion while port F2 is for diffusion combustion. Figure 2 shows a schematic diagram of these ports. The diffusion mode F2 nozzles are designed so as to retard mixing between the fuel and highly preheated combustion air injected from the central port. When the combustion air passes through the honeycomb regenerator, it is preheated to a temperature close to the gas temperature exiting from the test furnace. The furnace dimensions thermal rating of the burner, typical inlet velocities associated with highly preheated combustion air and fuel are listed in Tables 1 and 2.

Coal Gas Fuel. The fuel gas used in this study was a mixture of several gases that represent characteristic composition of coal gas and thus referred to here as ''coal gas.'' The coal gas is produced as a byproduct during the steel making process. The composition of the fuel, given in volume percent, is given in Table 3. The heating value of the fuel is estimated to be 11.9 MJ/m^3. The flow rates of air and fuel were kept constant throughout the experiments. The normalized air to fuel ratio was regulated at 1.15 so that the mixture contained 15% excess air. For these combustion conditions the flame was found to be nonluminous. The flame luminosity, length, and volume depend on the thermal conditions, fuel property, and firing conditions.

Spectroscopic Observation. The furnace was heated so that steady-state conditions were achieved in the furnace prior to performing any tests. After the furnace temperature reached the steady-state value, the spectroscopic observations of the flames were made in the test section of the furnace. These flames were observed with a 12-bit CCD camera (Santa Barbara) fitted with narrow band pass optical filter and an appropriate neutral density filter. The camera had 256×400 pixels and provided a measurable

Table 1 Dimensions of the test furnace

Length	8 m
Width	4 m
Height	3 m

Table 2 Specifications of the burner

Burner capacity	820 kW
Air nozzle diameter	151 mm
Fuel nozzle diameter	28 mm
Combustion air inlet velocity	84 m/s
Fuel inlet velocity	70 m/s

Table 3 Composition of coal gas fuel

CH_4	C_2H_2	CO	CO_2	H_2	H_2O	N_2
12.9%	1.2%	23.7%	10.6%	25.5%	1.3%	24.8%

wavelength range of 200–1000 nm. The system was used to observe the emission from C_2, CH, OH, and NO using different narrow band filters placed in front of the camera. The center band wavelengths of the filters used are given in Table 4.

A schematic diagram of the spectroscopic measurement system is shown in Fig. 3. A lens is placed adjacent to the quartz window in the furnace, which allowed us to focus the light emitted from test region in the furnace. Our objective was to determine the emission intensity of selected species and radicals from flames in the furnace. This was achieved by passing the total signal collected through a narrow band filter centered at the desired wavelength onto a CCD camera. The detected signal was then used to determine two-dimensional spectral intensity image of the specie of interest. The influence of background radiation was removed by subtracting the image observed without the presence of any flame. The two-dimensional image intensity becomes higher with increase in temperature and/or radical species concentration in the flame. An exposure time of 0.01 sec (shortest shutter speed was available on the CCD camera used) was used to acquire the instantaneous intensity distribution. Much shorter shutter speed of only a few milliseconds can be available if an image intensifier is attached to the CCD camera. However, this was difficult under the harsh conditions of noise and intense radiation from the furnace. Time duration of ten seconds was used to determine the time-averaged intensity distribution. The long time duration provides information on the mean properties while the instantaneous exposure provides information on the deviation from the mean value from which rms value of fluctuation can be determined.

Vibrational Temperature of C_2. The two wavelengths of C_2 emission (well known as Swan band, [10]) were observed consecutively by changing the optical band pass filters located in front of the cameras. Based on the Boltzmann distribution law, the intensity ratio of the two vibrational bands is given by the following equation

Table 4 Optical band pass filters used. (B.G.=Background)

	λ (nm)	Bandwidth (nm)
C_2	469.5	25.0
C_2	515.5	21.0
B.G.	490.0	28.0
NO	231.0	22.2
OH	306.4	15.0
CH	434.0	20.0
Soot	490.0	28.0
Soot	531.0	9.0

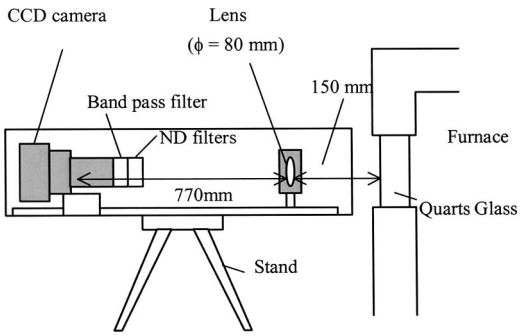

Fig. 3 Configuration of the CCD camera

$$\frac{I_1}{I_2}=\frac{\sum_i S_i \nu_i A_{\text{rel } i} \exp[-E_i/kT]}{\sum_j S_j \nu_j A_{\text{rel } j} \exp[-E_j/kT]} \tag{1}$$

where, S_i and S_j represent the instrument factor that account for the wavelength dependency of the CCD detector sensitivity, the transmittance of the optics used, etc., ν represent the frequency, $A_{\text{rel } i}$ and $A_{\text{rel } j}$ represent the relative transition probability for the individual vibrational emission line of the i and j Swan band, E the excitation energy, k the Boltzmann constant, and T the absolute temperature, [11,12]. Thus, the spatial distribution of C_2 vibrational temperature can be obtained from the intensity ratio of the respective spectral bands that incidents on the pixels of the CCD camera, provided the instrument factors are known or determined. The calibration was conveniently made by comparing the results obtained with Eq. (1) to that measured using a thermocouple at the same point in the furnace. The detailed discussion on the calibration between the C_2 vibrational temperature and that obtained using thermocouple is provided in Ref. [10]. Although there are some differences between these two measured temperatures in their absolute value, they are correlated.

Soot Temperature. The luminous flames represent the presence of soot in flames. To date, the soot has been assumed to be in local thermal equilibrium (LTE) with the surrounding gases, which means that the soot temperature is identical to that of the surrounding gas temperature in a small spatial region, [13–16]. In this study, non-LTE was experimentally found between these temperatures. The distribution of soot temperature (strictly speaking the soot surface temperature) has been determined in two dimensions using the CCD cameras at the appropriate wavebands and is also based on the two-color thermometry.

The emission from soot or its precursors in a luminous flame has a continuum spectrum based on the gray body radiation, or the Planck's law with a constant emissivity, [14–16]. The continuum radiation is emitted from soot particles and weak molecular band is from the diatomic molecules. The temperature of soot is determined from the ratio of spectral intensity at the two wavelengths where the band spectra do not exist. The spectral intensity and their ratio at two wavelengths is given by

$$I_\lambda=\varepsilon \frac{8\pi hc}{\lambda^5}\frac{1}{e^{ch/\lambda kT}-1}$$
$$\frac{I_{\lambda_1}}{I_{\lambda_2}}=\left(\frac{\lambda_2}{\lambda_1}\right)^5 \frac{e^{ch/\lambda_2 kT}-1}{e^{ch/\lambda_1 kT}-1}. \tag{2}$$

Thus, by measuring the intensity at some prescribed wavelengths the soot surface temperature can be measured from knowledge of the calibration system. For detailed discussion on the discrepancy from the gray body behavior that can give error in the determination of soot temperature, the dependence of the emissivity on the wavelength and temperature should be taken into account, [7,10]. This topic is currently under investigation and will be reported in a future paper by the investigators.

Results and Discussion

Temperature Distribution From C_2 Species. Figure 4 shows the distribution of temperature in the diffusion flame (see also tables) using highly preheated combustion air as the oxidant. The flow of gases in the flame is from left to right. The top figure shows that the temperature distribution (averaged over 10 seconds) obtained at the 800×500 mm grid points in the furnace using 1-mm diameter R-type thermocouples. The calibration was based on a black body furnace and the correction made for the radiation losses. The bottom figure shows the distribution of C_2 vibrational temperature determined that was obtained on the basis of Eq. (1).

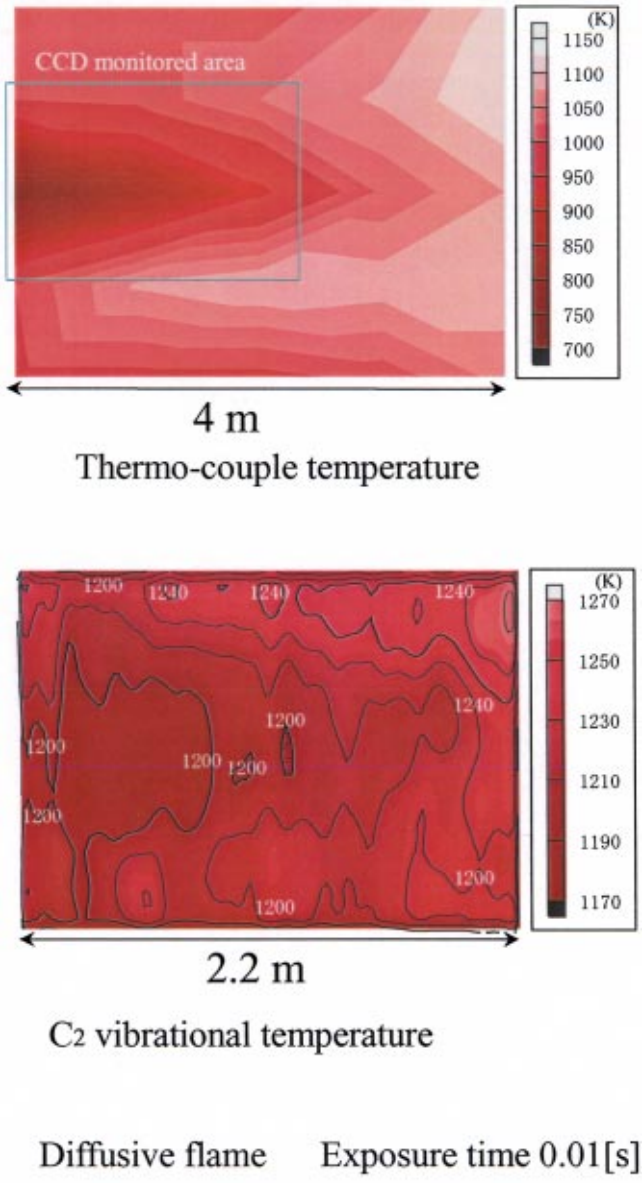

Fig. 4 Temperature distribution

The results show that the C_2 vibrational temperature based on Eq. (1) is higher than that measured using thermocouple at all points in the furnace. However, the temperature distribution pattern obtained from the two very different diagnostic techniques is similar. The vibrational temperature distribution has the advantage of high spatial resolution, which helps to visualize and illustrate the detailed structure of the flame. The low-temperature region is observed to be located near to initial region of the flame along the central axis of the burner. The high-temperature region surrounds this low-temperature region. The difference can be recognized from both the thermocouple and spectroscopically measured temperatures. It is to be noted that the calibration was made only at a point in the flame under premixed flame conditions. The spectroscopically determined temperature is based on the vibrational motion of C_2 molecules, which is more affected by combustion reaction mode, such as favored transfer of chemical reaction and heat. However, the thermocouple temperature reflects an average temperature of translational, vibrational, and rotational tempera-

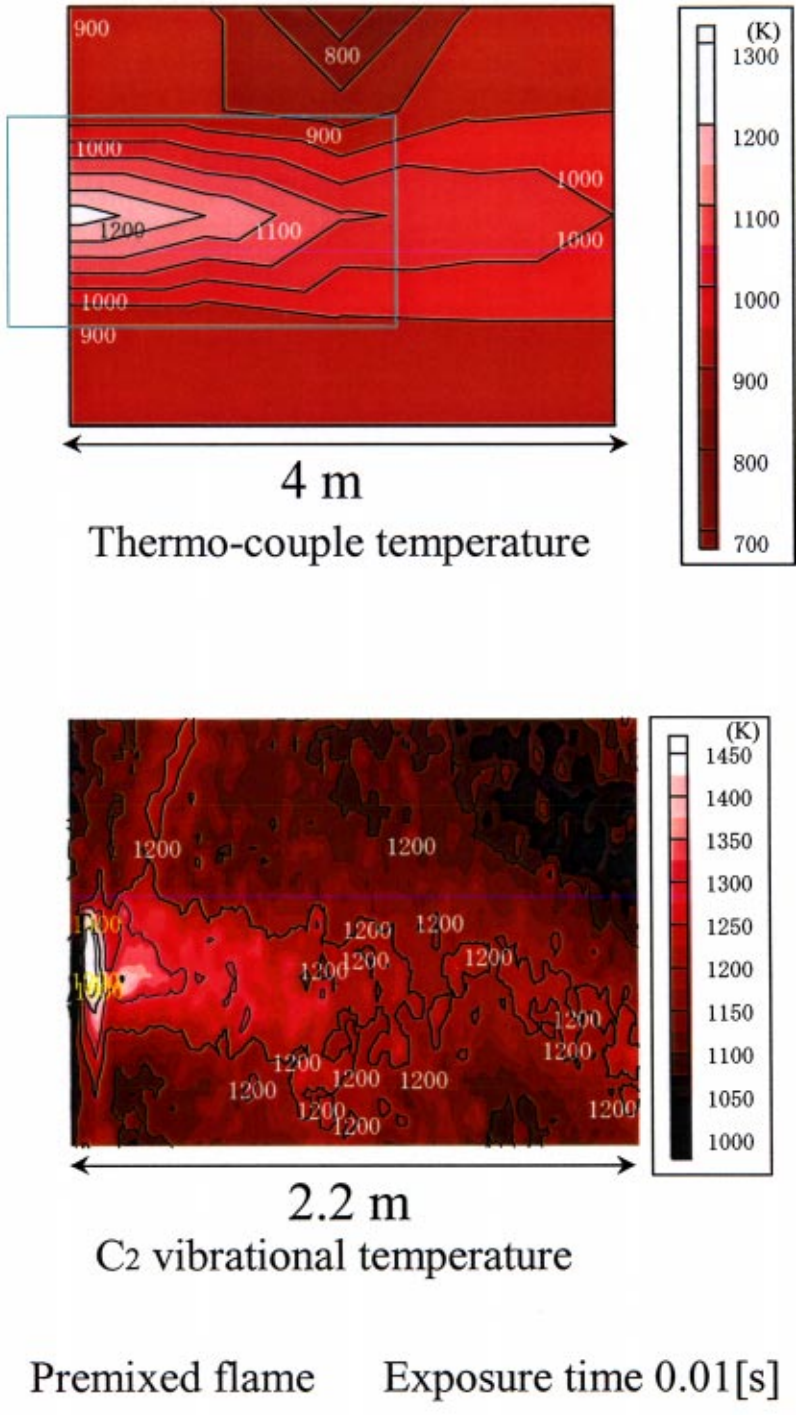

Fig. 5 Temperature distribution, premixed flame

tures (gas temperature). This results in differences between the translational and vibrational temperatures, which are called non-LTE (local thermal equilibrium).

Figure 5 shows the distribution of temperature for the premixed combustion case using high-temperature air as the oxidant for combustion. The premixed flame structure was unstable as compared to the diffusion flame case. Therefore, a relatively long exposure time of 10 sec was used to obtain the time-averaged profile for the premixed flame case. In this premixed case, 80% of the fuel was supplied from the F1 nozzle and the rest of the fuel was supplied from the F2 nozzle. Local high-temperature regions (above 1400 K) in the flame near to the injector exit (upstream region of the flame) along the central axis of the burner can be seen from Fig. 5. During the premixed combustion such high local temperatures and sharp pressure drop are caused by rapid combustion of the fuel-air mixture at elevated temperatures. In contrast for the diffusion combustion case with high-temperature air, the combustion proceeds more gradually over a larger volume in the furnace.

Figure 6 shows the instantaneous temperature distribution of soot obtained with the two-dimensional two-color thermometry during premixed combustion condition. A comparison of the soot temperature with the C_2 vibrational temperature shows that the soot temperatures are lower by about 100 K than the C_2 vibra-

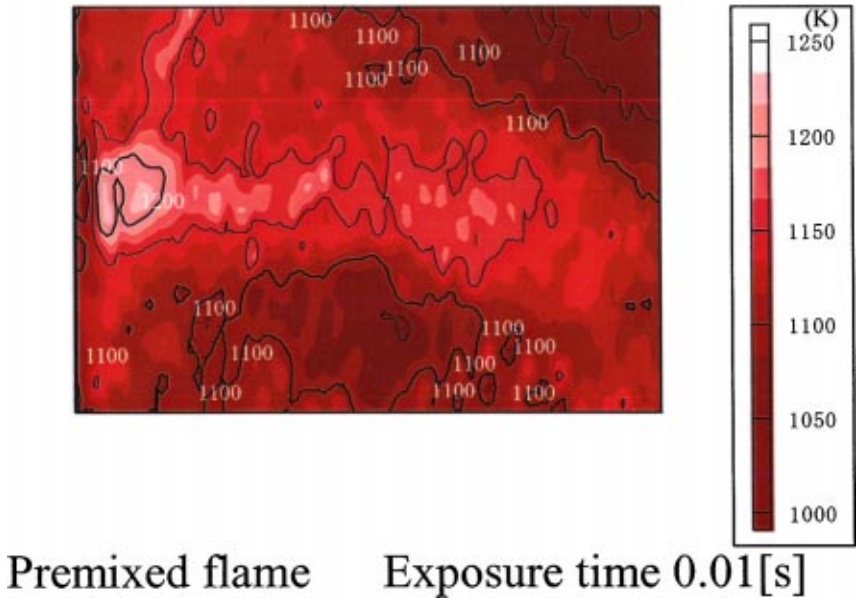

Fig. 6 Temperature distribution in premixed flame

tional gas temperatures in the combustion zone. This difference in temperature is probably due to the local thermal equilibrium (LTE) assumption, which may not be strictly applicable between the C_2 molecules and the soot/precursors. This is also reflected from the difference in temperature distribution. The discrepancy in temperature between that shown in Fig. 5 (at the bottom) and Fig. 6 suggests that the location of maximum temperature of soot is displaced and extends toward downstream regions as compared to the C_2 vibrational temperature. This suggests that the heat generated from combustion first influences the gaseous C_2 molecules and then transfers to the carbon clusters along with their formation. Furthermore, the soot temperature is expected top be somewhat lower than the surrounding gas temperature due to energy radiation from soot particles. Part of the heat is also lost by radiation during the formation of soot because of its relatively high emissivity. Consequently, the soot temperature is lower than the initial temperature of gaseous C_2 molecules. Since the rate of soot formation is slower than the molecular reactions, the zone of high soot temperature spreads out towards the combustion zone.

Maximum Heat Input. Most conventional burners used in industrial size furnaces employ diffusion combustion because of concern on safety issues associated with premixed combustion. The flame temperature depends on the equivalence ratio in premixed flames. However, in diffusion flames, local high temperature is obtained so that the temperature close to the burner exit can become quite high. At higher thermal loadings overheating of the furnace can occur. This can result in local regions of high stress in the furnace, which can adversely affect furnace reliability, durability, and performance. In some cases the product quality from the furnace can also be affected.

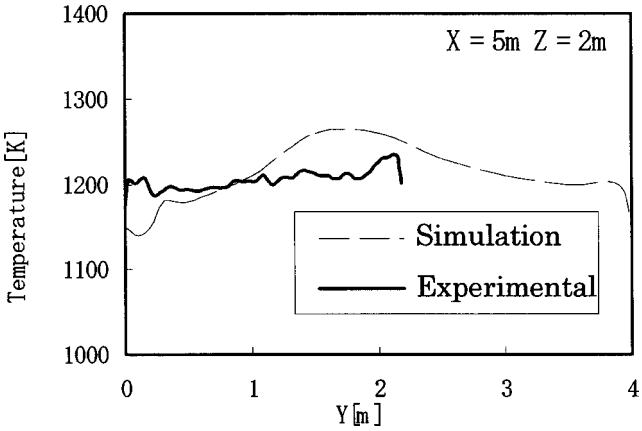

Fig. 7 Comparison of temperature distribution

The regenerative combustion system examined here operates in a switching mode between the two burners so that much of the local heating problem in the furnace can be alleviated. However, the high NO_x problem can still be an issue as that often encountered in conventional furnaces. The input energy to attain the same maximum temperature in the furnace is 1086 kW for diffusion combustion mode and 671 kW for the premixed combustion case. It can be clearly seen that much more energy can be introduced in the furnace for the diffusion case for the same maximum temperature. Since the furnace walls are thermally insulated, the radiative heat transfer takes place at predominantly bottom section of the furnace where the steel slabs are introduced for their heating process. Consequently, the heating process capability is much higher for the diffusion combustion mode because of the higher amounts of energy input.

Figure 7 shows a comparison of the C_2 vibrational temperature distribution, determined spectroscopically, with that obtained from the numerical simulation using the PDF (probability density function) model based on the combination of mixing rate and chemical reactions (see Refs. [6], [7], [17], [18] for more details on the model). The PDF simulation model predicts a temperature variation of about 100 K along the flame axis, [7]. In contrast, the measured C_2 vibrational temperature is quite uniform. In the PDF simulation the heat generated during combustion is determined from the mixing of oxidant with fuel. The maximum temperature shown in Fig. 7 suggests that the mixing rate has its peak value at a position of about 1.8 m downstream from the air outlet. This discrepancy also shows the non-LTE and that PDF simulation must be modified for better prediction of the temperature distribution in the furnace by taking into account different kinds of the temperatures.

Emission Intensity Distributions for NO, OH, and CH. Figure 8 shows the emission intensity distributions of NO from within the furnace flame. It can be clearly seen from these distributions that the NO intensity levels are very low during diffusion combustion as compared to the premixed combustion mode. These emission results for the diffusion combustion case are in good general agreement with those reported earlier on the NO_x

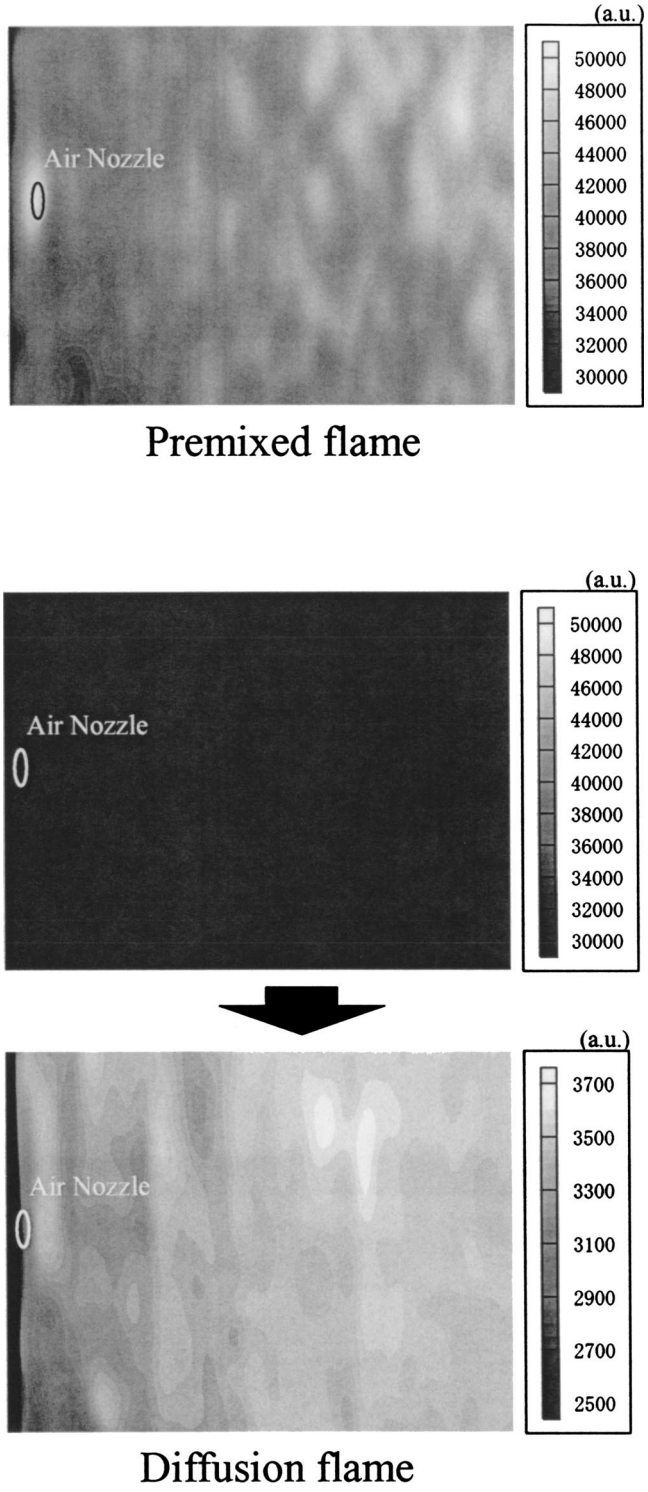

Fig. 8 NO emission intensity for premixed and diffusion flames

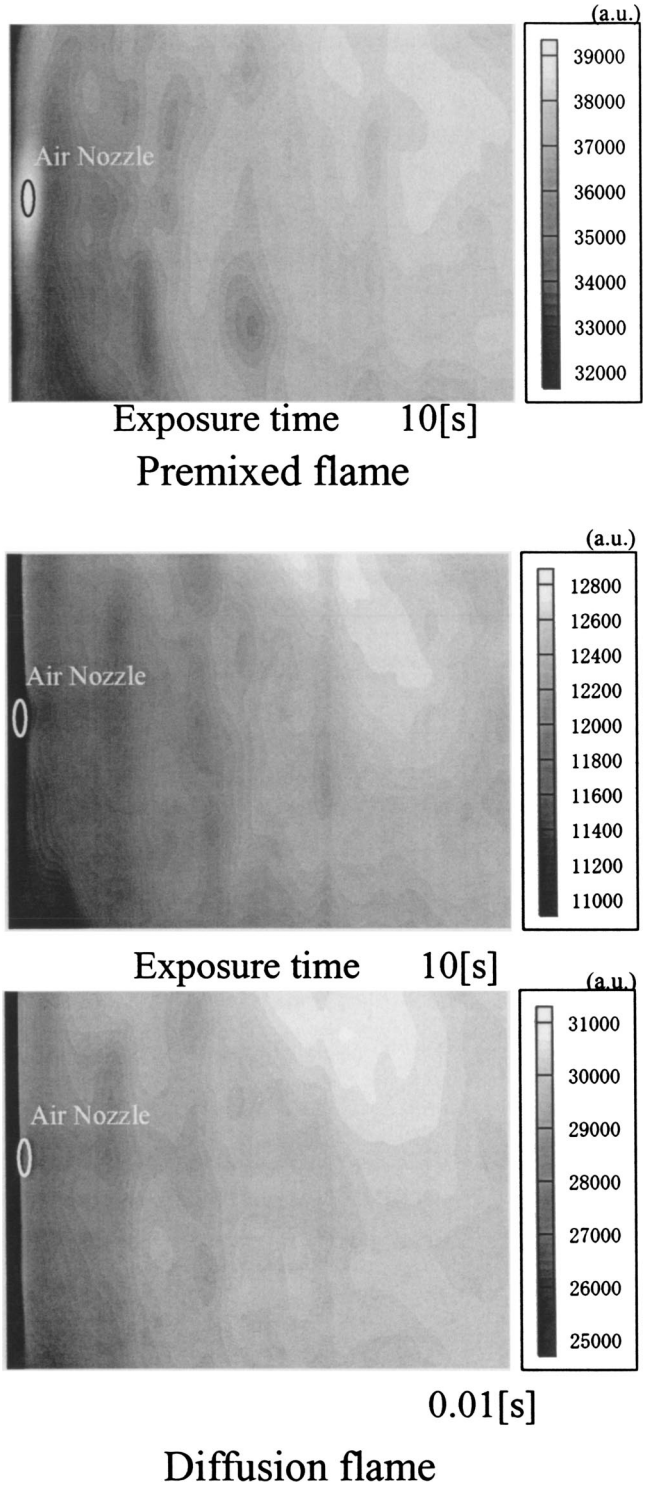

Fig. 9 OH emission intensity for premixed and diffusion flame

emission levels measured in the exhaust gas under high-temperature air combustion conditions, [3,4,8]. In this study, the NO_x concentration in the exhausted gas was also determined using a chemiluminescence NO_x analyzer. Indeed, the emission of NO_x in the diffusion flame case was much lower as compared to the premixed case (60 vppm for diffusion case as compared to 110 vppm for the premixed case, both at 11% O_2 in the flue gas). The uniform temperature distribution during the diffusion combustion leads to lower NO_x emission levels. In contrast the localized high-temperature regions near the injector for the premixed flame is probably the main cause of high NO_x emission. In fact, the spectral intensity of NO emission is very high around the centrally located injector nozzle while it is found to be very low during the diffusion combustion case, compare the distribution of NO around the nozzle shown in the top and bottom figures in Fig. 8.

The intensity of NO increases towards the downstream regions for both the diffusion and premixed combustion conditions. However, it should be noted that the spectral emission level is much lower (less than about one-tenth) during the diffusion combustion

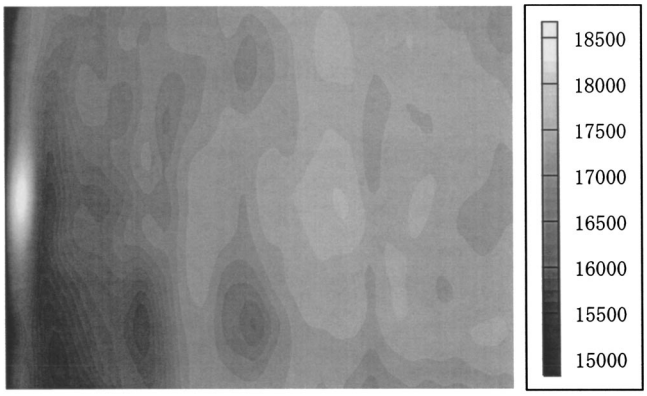

Fig. 10 CH emission intensity for premixed flame

condition as compared to the premixed condition. It should also be noted that although the vibrational temperature distribution reflects the shape of the flame, the intensity distribution of NO does not only correspond to the shape of flame (see the complex island structures in Fig. 8) but also complex processes of mixing and reactions that occur during such combustion conditions.

Figure 9 shows the intensity distribution of OH for both the premixed and diffusion flames. The premixed flame has strongintensity distribution as compared to the diffusion flame case. This suggests that combustion reactions for the premixed case occur with high gas density in a limited volume, or around the central injector along the axis. This is in good qualitative agreement with the high local value of temperature distribution given above for the premixed combustion case. In the diffusion combustion case, no significant differences are observed between the images taken over 10 and 0.01 sec time duration. This suggests good temporal stability of the flame during the diffusion combustion case using high temperature air.

Figure 10 shows the intensity distribution of CH for the premixed combustion case. The increase in intensity gradually shifts to downstream locations of the furnace. This reflects the initial reaction zone at the upstream region where the thermal decomposition takes place to produce the CH radical during the initial oxidation stage, followed by extended oxidation reactions at downstream regions.

Conclusions

The two-dimensional spectroscopic observation has been applied to observe thermal and chemical behavior of flames using an industrial size furnace. This is the first time someone has attempted to provide such details in an industrial size furnace. The spectral emission intensities from C_2 radicals as well as the distribution of vibrational temperature of C_2 gas phase species and soot temperature have been measured. During diffusion combustion using highly preheated air, the vibrational temperature distribution of C_2 was uniform. In contrast a local high temperature region was observed during the premixed combustion condition using the same degree of high temperature air for combustion. The diffusion combustion with highly preheated combustion air can utilize more fuel than the premixed flame case to give the same peak temperature. Using PDF method for combustion analysis showed more uniform two-dimensional temperature distribution during the diffusion combustion using high-temperature combustion air. The intensity distribution of NO, OH, and CH emission had no specific structure; the intensity gradually increased towards downstream region of the furnace. The significantly low spectral intensity of NO suggests lower NO_x emission with diffusion combustion as compared to the premixed combustion case. The exhaust gas analysis using a chemiluminescence analyzer showed good agreement with the low NO_x level observed spectroscopically. Spectroscopic observations of C_2 vibrational and soot temperature measurement in flames have been made in two dimensions that provides higher spatial resolution than the temperature measured using thermocouples. The soot temperature was found to be lower than the surrounding gas phase temperature.

Table 5 Fuel input under diffusion and premixed conditions

	Fuel (kW)
Diffusion	1086
Pre-mixed	671

Acknowledgments

New Energy and Industrial Technology Development Organization (NEDO) supported this research under the project ''Development of Higher Thermal Efficiency New Industrial Furnaces.'' One of the authors (AKG) would like to acknowledge the research support provided by NSF and NASA. He would also like to acknowledge the support provided by NFK, Japan and Mr. Hasegawa, Director of basic technology at NFK.

References

[1] Tsuji, H., Gupta, A. K., Hasegawa, T., Katsuki, M., Kishimoto, K., and Morita, M., 2003, *High Temperature Air Combustion: From Energy Conservation to Pollution Reduction*, CRC Press, Boca Raton, FL.

[2] Ishiguro, T., and Tsuge, S., Furuhata, T., Kitagawa, K., Arai, N., Hasegawa, T., Tanaka, R., and Gupta, A. K., 1998, ''Homogenization and Stabilization During Combustion of Hydrocarbons With Preheated Air,'' *Proc. Twenty-Seventh Symposium (International) on Combustion*, The Combustion Institute, Pittsburgh, PA, pp. 3205–3213.

[3] Katsuki, M., and Hasegawa, T., 1998, ''The Science and Technology of Combustion in Highly Preheated Air,'' *27th Symposium (Intl.) on Combustion*, The Combustion Institute, Pittsburgh, PA, pp. 3135–3146.

[4] Gupta, A. K., 2001, ''High Temperature Air Combustion: Experiences from the USA-Japan Joint Energy Project,'' Invited Keynote Lecture at the 4th High Temperature Air Combustion and Gasification Symposium, Rome, Italy, Nov. 27–30.

[5] Hasegawa, T., Mochida, S., and Gupta, A. K., 2002, ''Development of Advanced Industrial Furnace Using Highly Preheated Air Combustion,'' J. Propul. Power, **18**(2), pp. 233–239.

[6] Ishii, T., Zhang, C., and Sugiyama, S., 1997, ''Numerical Analysis of NO_x formation Rate in a Regenerative Furnace,'' *Proceedings of the ASME International Joint Power Generation Conference* (IJPGC97), ASME, New York, pp. 267–278.

[7] Zhang, C., Ishii, T., Hino, Y., and Sugiyama, S., 2000, ''The Numerical and Experimental Study of Non-Premixed Combustion Flames in Regenerative Furnace,'' ASME J. Heat Transfer, **122**, pp. 287–293.

[8] Gupta, A. K., Bolz, S., and Hasegawa, T., 1999, ''Effect of Air Preheat and Oxygen Concentration on Flame Structure and Emission,'' ASME J. Energy Resour. Technol., **121**, pp. 209–216.

[9] Gupta, A. K., and Li, Z., 1997, ''Effect of Fuel Property on the Structure of Highly Preheated Air Flames,'' *Proc. Intl. Joint Power Generation Conference* (IJPGC), ASME, New York, ASME EC-Vol. 5, pp. 247–258.

[10] Konishi, N., Kitagawa, K., Arai, N., and Gupta, A. K., 2002, ''Two-Dimensional Spectroscopic Analysis of Spontaneous Emission From a Flame Using Highly Preheated Air Combustion,'' J. Propul. Power, **18**, pp. 199–204.

[11] Tien, C. L., 1968, *Thermal Radiation Properties of Gases* (Advances in Heat Transfer, Vol. 5), Academic Press, New York, pp. 253–324.

[12] Heitler, W., 1954, *The Quantum Theory of Radiation*, Oxford University Press, New York, pp. 136–174.

[13] Sarofim, A. F., and Hottel, H. C., 1978, ''Radiative Transfer in Combustion Chambers: Influence of Alternative Fuels,'' *Proceedings of the Sixth International Heat Transfer Conference*, Hemisphere, Washington, DC, **6**, pp. 199–217.

[14] Foster, P. J., and Howarth, C. R., 1968, ''Optical Constants of Carbons and Coals in the Infrared,'' Carbon, **6**, pp. 719–729.

[15] Millikan, R. C., 1961, ''Optical Properties of Soot,'' J. Opt. Soc. Am., **51**, pp. 698–699.

[16] Millikan, R. C., 1961, ''Sizes, Optical Properties and Temperatures of Soot Particles,'' *The Fourth Symposium on Temperature, Its Measurement and Control in Science and Industry*, **3**, pp. 497–507.

[17] Weber, R., 1996, ''Scaling Characteristics of Aerodynamics, Heat Transfer and Pollutant Emission in Industrial Flames,'' *Proceedings of the 26th Symposium International on Combustion*, The Combustion Institute, Pittsburgh, PA, pp. 3343–3354.

[18] Johnson, R. C., 1927, ''The Structure and Origin of the Swan Band Spectrum of Carbon,'' Philos. Trans. R. Soc. London, Ser. A, **226**, pp. 157–231.

Modeling the Performance Characteristics of Diesel Engine Based Combined-Cycle Power Plants—Part I: Mathematical Model

Stan N. Danov
Fluor Canada, Inc.,
55 Sunpark Plaza, SE,
Calgary, Alberta T2X 3R4, Canada
e-mail: stan.danov@fluor.com

Ashwanti K. Gupta
Department of Mechanical Engineering,
University of Maryland,
College Park, MD 20742
e-mail: akgupta@eng.umd.edu

In this two-part series publication, a mathematical model of the energy conversion process in a diesel engine based combined-cycle power plant has been developed. The examined configuration consists of a turbocharged diesel engine (the topping cycle), a heat recovery steam generator (HRSG) and a steam turbine plant (the bottoming cycle). The mathematical model describes the processes that occur simultaneously in the diesel engine cylinders, turbocharger, air filter, air inlet pipes, exhaust pipes, HRSG, steam turbine, and the associated auxiliary equipment. The model includes nonlinear differential equations for modeling the energy conversion in the diesel engine cylinders, fuel combustion, gas exchange process, energy balance in the turbocharger, inlet pipes and exhaust system, heat balance in the HRSG, and steam turbine cycle. The fifth-order Kuta-Merson method has been applied for numerical solution of these simultaneous equations via an iterative computing procedure. The model is then used to provide an analysis of performance characteristics of the combined-cycle power plant for steady-state operation. The effect of change in the major operating variables (mutual operation of diesel engine, HRSG, and steam turbine) has been analyzed over a range of operating conditions, including the engine load and speed. The model validation and the applications of the model are presented in Part II (Results and Applications) of this two-part series publication. [DOI: 10.1115/1.1635396]

Introduction

Diesel engines provide the advantages of high thermal efficiency and reliability for industrial power and propulsion systems for use over land and sea. These benefits are key factors in cost effective industrial power and propulsion. Designers and researchers continue to seek ways to further improve the performance characteristics of diesel power plants via theoretical and experimental studies. The designers and manufacturers have to ensure reliability of the power plant operation, reduce the fuel consumption (kJ/kW-hr) and provide an environmentally benign operation.

A schematic flow diagram of the power plant examined is shown in Fig. 1. The topping cycle is represented by a turbocharged diesel engine, where part of the fuel energy supplied to the cycle is converted into electricity or propulsion power. The heat rejected from the topping cycle is utilized in the bottoming cycle. Figure 1 shows that the exhaust heat from the diesel engine is utilized in a HRSG to raise steam, which is then used to produce power in the bottoming cycle arranged as a steam turbine plant. Higher energy conversion efficiency is achieved in such a combined-cycle power plant with greater fuel energy conservation, therefore, heat recovery systems with turbo-generators are widely used in both stationary diesel power plants and marine propulsion plants.

Utilizing the heat from the exhaust gases of diesel engine provides electrical power at nominal and partial power outputs. However, difficulties occur when operating the turbo-generators at partial operating conditions of diesel engines. The power plants operate at partial operating conditions for some 80%–85% of the run-time, resulting in lower thermal efficiency. Therefore, the performance characteristics have to be predicted for the whole spectrum of operating conditions at the design stage.

In order to analyze and predict the performance of the plant as a whole, it is necessary to estimate the mutual operation of diesel engine, as a source of power and waste heat (exhaust gases) and heat recovery system as a consumer of rejected engine heat. Mathematical modeling studies can be a very powerful tool for better design and understanding of diesel engine based combined-cycle power plants with improved performance characteristics. Baykov [1] provides a comprehensive book concerning the mutual operation of a diesel engine and a turbocharger in the frame of a turbocharged engine. Danov, Yamamoto and Arai [2,3] recently developed a mathematical model of a turbocharged diesel engine. Danov and Gupta [4–6] have provided specific problems concerning the combustion process and energy conversion in diesel engines and model validation. The theoretical basis and computational tools developed in these studies are now used to investigate the mutual operation between a turbocharged diesel engine and a HRSG in combined-cycle power plants.

Objectives

The overall objective of this study is to provide numerical analysis of the performance characteristics of a diesel engine based combined-cycle power plant operating over a whole spectrum of conditions, including the engine load and speed. Some specific objectives are to:

- develop a full set equations to model the mutual operation between the main diesel engine as a source of power and waste (rejected) heat and the steam turbine plant as a consumer of waste heat from the flue gases,

Contributed by the Fuels and Combustion Division of THE AMERICAN SOCIETY OF MECHANICAL ENGINEERS for publication in the ASME JOURNAL OF ENGINEERING FOR GAS TURBINES AND POWER. Manuscript received by the F&C Division April 2002; final revision received February 2003. Associate Editor: S. Gollahalli.

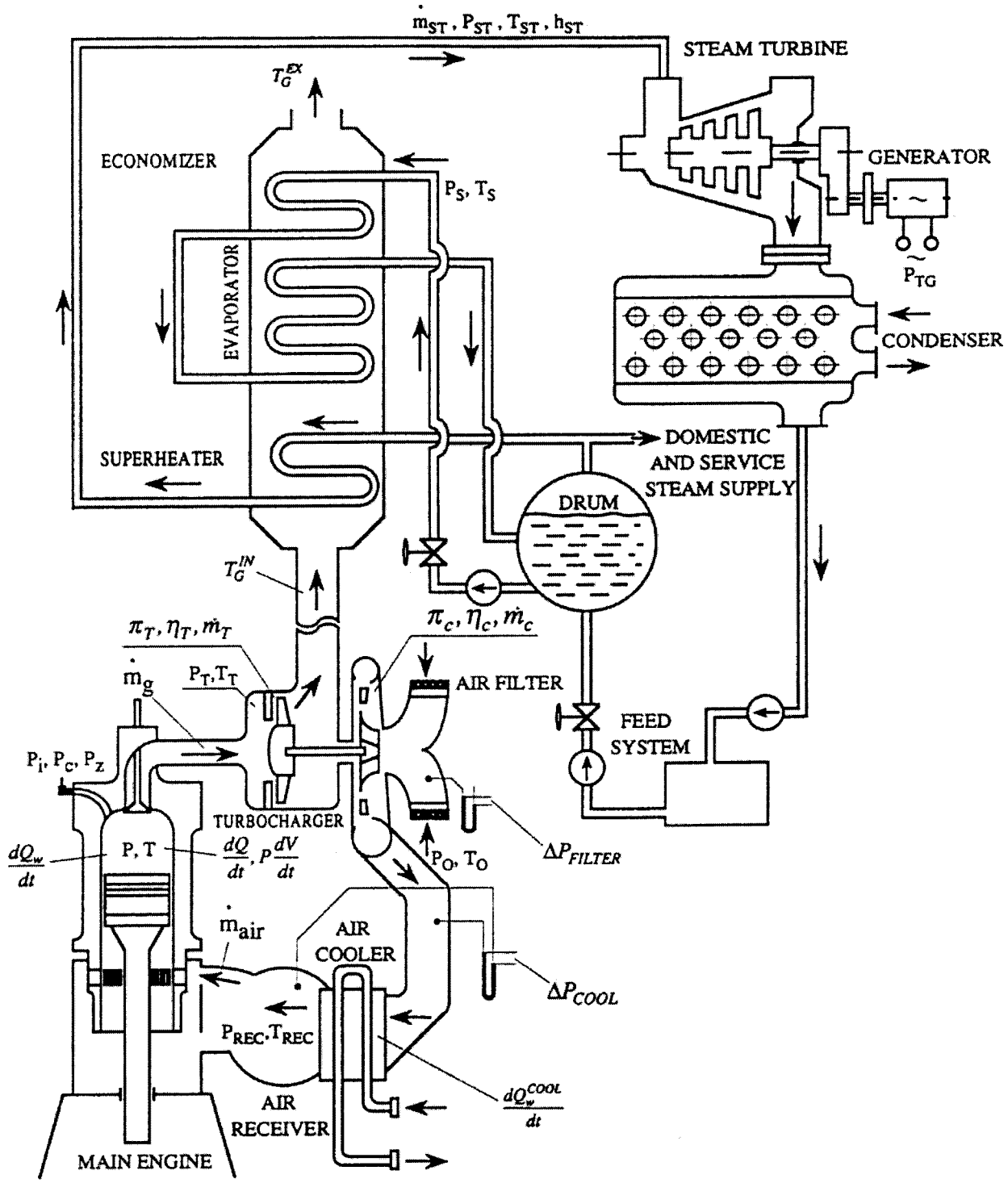

Fig. 1 Schematic flow diagram of a combined-cycle power plant based on turbocharged diesel engine

- develop algorithms and computational tools for numerical solution of the mathematical model,
- validate the model, and
- analyze the performance and efficiency of the combined-cycle power plant over a range of operating conditions. Also determine the effect of fluid flow, heat transfer and thermodynamics on engine operation.

Mathematical Model

The final set of equations for modeling the energy conversion processes in a turbocharged diesel engine can be presented as follows, see Refs. [1–7]:

$$M\left[c_v(v,T)+T\sum_{i=1}^{3}\frac{dc_{v_i}}{dT}\right]\frac{dT}{dt} = m_c Q_f \frac{df_b}{dt} - M\left(\frac{\partial u}{\partial r_1}\frac{\partial r_1}{\partial f_b}+\frac{\partial u}{\partial r_2}\frac{\partial r_2}{\partial f_b}+\frac{\partial u}{\partial r_3}\frac{\partial r_3}{\partial f_b}\right)\frac{df_b}{dt} - M\left[\frac{\partial u}{\partial r_3}\frac{\partial r_3}{\partial f_v}\frac{df_v}{dt}-\frac{\partial u}{\partial v}\left(\frac{1}{M}\frac{dV}{dt}-\frac{V}{M^2}\frac{dM}{dt}\right)\right] + (h-u)\frac{dM}{dt}-\frac{dQ_w}{dt}-\frac{dQ_{ev}}{dt}-\frac{dQ_d}{dt}-p\frac{dV}{dt} \quad (1)$$

$$\frac{df_v}{dt}=\frac{D_t}{p}\left(\frac{0.5T+0.5T_d}{273}\right)^2\frac{6}{\rho D_{SM}}f_i^{1/3}(f_i-f_v)^{5/3}\frac{\lambda-f_v}{1.15f_v} \quad (2)$$

$$\frac{df_p}{dt}=A_o\frac{m_c}{V_i}f_{vi}\{\exp[\varphi_o(t-t_{SC})]\}(f_{vi}-f_o)\Big|_{\text{from } f_o=0}^{\text{to } f_o=f_{vi}} \quad (3)$$

$$\frac{dfd}{dt}=\psi\frac{df_v}{dt}+A_1\frac{m_c}{V}(f_v-fb)^2fb \quad (4)$$

$$\frac{df_b}{dt}=\frac{d\left(\frac{m_b}{m_c}\right)}{dt}=\frac{d\left(\frac{m_p}{m_c}\right)}{dt}+\frac{d\left(\frac{m_d}{m_c}\right)}{dt} \quad (5)$$

$$u(v,T)=u_o(T)+\frac{3}{2}\frac{a}{b}\frac{1}{\sqrt{T}}\ln\left(\frac{v}{v+b}\right) \quad (6)$$

$$h(v,T)=h_o(T)+\frac{3a}{2b}\frac{1}{\sqrt{T}}\ln\left(\frac{v}{v+b}\right)+\frac{bRT}{v-b}-\frac{a}{(v+b)\sqrt{T}} \quad (7)$$

$$c_v(v,T)=c_{v_o}(T)-\frac{3}{4}\frac{a}{b}T^{-3/2}\ln\left(\frac{v}{v+b}\right) \quad (8)$$

$$c_p(v,T)=c_v(v,T)+T\left(\frac{R}{v-b}+\frac{a}{2v(v+b)T^{3/2}}\right)^2\times\left(\frac{RT}{(v-b)^2}-\frac{a(2v+b)}{v^2(v+b)^2\sqrt{T}}\right)^{-1} \quad (9)$$

$$\left(p+\frac{a}{v(v+b)\sqrt{T}}\right)(v-b)=RT \quad (10)$$

$$\frac{dp}{dt}=-p\frac{ka}{V}\left(\psi_{ex}Cd_{ex}A_{ex}-\psi_{in}\sqrt{\frac{k_{in}}{k}}\frac{a}{a_{in}}Cd_{in}A_{in}\right)-p\frac{k}{V}\frac{dV}{dt} \quad (11)$$

$$\frac{dp_t}{dt}=\frac{k_{ex}R_g}{A_{ex}a_{ex}\frac{l_{ex}}{a_{ex}+\Delta w}}\left[\sum_1^w(\psi_{ex}Cd_{ex}A_{ex}a_{ex}\rho_{ex}T)-\psi_tCd_tA_ta_t\rho_tT_t-\frac{c_t^2}{2}\frac{\dot m_T}{c_{pt}}+\frac{A_ta_{ex}}{R_gk_{ex}}(p_{to}-p_t)\right] \quad (12)$$

$$\frac{dT_t}{dt}=\frac{k_{ex}R_g}{A_{ex}a_{ex}\frac{l_{ex}}{a_{ex}+\Delta w}}\frac{T_t}{p_t}\left\{\sum_1^m(\psi_{ex}Cd_{ex}A_{ex}a_{ex}\rho_{ex}T)-\psi_tCd_tA_ta_t\rho_tT_t-\frac{c_t^2}{2}\frac{\dot m_T}{c_{pt}}+\frac{A_ta_{ex}}{R_gk_{ex}}\left(p_{to}-p_t\frac{T_t}{T_{to}}\right)-\frac{T_t}{k_{ex}}\left[\sum_1^m(\psi_{ex}Cd_{ex}A_{ex}a_{ex}\rho_{ex}-\psi_tCd_tA_ta_t\rho_t)\right]\right\} \quad (13)$$

$$\frac{dp_{\text{rec}}}{dt}=\frac{k_{\text{rec}}R_{\text{rec}}T_{\text{rec}}}{V_{\text{rec}}}\left[\dot m_C-\sum_1^Z(\psi_{in}Cd_{in}A_{in}\rho_{in})\right] \quad (14)$$

$$\frac{dn_{TC}}{dt}=9.549\frac{(P_T-P_C)}{J_{TC}\omega_{TC}} \quad (15)$$

$$P_T=\dot m_T\eta_T\frac{k_g}{k_g-1}R_gT_T^*(1-\pi_T^{*^{-(k_g-1)/k_g}}) \quad (16)$$

$$P_C=\dot m_C\frac{1}{\eta_C}\frac{k_{\text{air}}}{k_{\text{air}}-1}R_{\text{air}}T_o^*(\pi_C^{*^{(k_{\text{air}}-1)/k_{\text{air}}}}-1) \quad (17)$$

$$\pi_C,\eta_C=f\left(\frac{\dot m\sqrt{T_o^*}}{p_o^*},\frac{n_{TC}}{\sqrt{T_o^*}}\right) \quad (18)$$

$$(CdA)_T,\eta_T=f(\bar H_T). \quad (19)$$

The symbols in these equations are described in the nomenclature used. Eqs. (1)–(19) have the following physical meaning:

Equation (1) represents the energy balance in the engine cylinder according to the first law of thermodynamics. This differential equation describes the energy conversion in a diesel engine cylinder from the beginning of real compression process till the opening of exhaust valves/ports. This equation assumes real gas as the working medium and takes into account the imperfections in the working media due to the high pressures. This gives some advantages to model the indicator process of forced diesel engines with high peak pressure in the cylinder. During the indicator process (compression, combustion, expansion) the gas-exchange valves/ports are closed ($dM_{in}/dt=0; dM_{ex}/dt=0$)—i.e., there is no mass transfer and energy transfer through the inlet and exhaust valves/ports. The mass balance during the indicator process can be presented as

$$\frac{dM}{dt}=m_c\frac{df_i}{dt}=\frac{dM_L}{dt}, \quad (20)$$

i.e., the change of mass in the cylinder is caused by the fuel injection $m_c.df_i/dt$ and gas leakage through piston rings dM_L/dt.

Equation (2) represents the fuel vaporization rate. This equation allows one to define the instantaneous rate of fuel vaporization and mixing with respect to the current values of pressure, temperature, A/F equivalence ratio, Sauter mean diameter (D_{SM}) and concentrations. It should be noted that in spite of denoting df_v/dt as rate of vaporization, Eq. (2) has more comprehensive physical meaning—it represents the rate of preparing the fuel for combustion via atomization, vaporization, and mixing under the conditions of variable temperature, pressure and concentrations, and also take into account the diffusion (D_t) and turbulence (k_t). From this point of view df_v/dt is called 'vaporization rate' for simplicity, but its real meaning is rate of preparing the fuel for diffusion combustion. Equation (2) plays a very important role for defining the diffusion combustion rate.

Equation (3) represents the non-dimensional combustion rate under the conditions of premixed flame. This equation is valid only in the interval $0<f_o<fv_i$, where f_o is an integral sum of the right side of Eq. (3) from the beginning of combustion to the current moment of time:

$$f_o=\int_{t=t_{SC}}^{t}A_o\frac{m_c}{V_i}f_{vi}\{\exp[\varphi_o(t-t_{SC})]\}(f_{vi}-f_o)dt \quad (21)$$

where A_o is a constant depending on the physicochemical properties of the fuel; V_i is the volume of cylinder at the moment of ignition. For diesel fuels Semenov [8] suggests the value to be: $A_o=47-52$, $\varphi_o=5900-6200$. The following values were used for the simulation: $A_o=49$, $\varphi_o=6100$.

Equation (4) represents the non-dimensional combustion rate under the diffusion flame conditions. The first term on the right-hand side is valid until the end of vaporization process ($df_v/dt=0$), when the last fuel droplet is vaporized ($f_v=1$), but there are some unburned fuel vapors. Their percentage is $1-f_b$. The combustion of this amount of fuel can be represented only by the second term on the right side. However, this amount of fuel burns under conditions that cannot be considered as a diffusion flame because there is no atomization and vaporization. For these conditions this process cannot be considered as a premixed flame. While the premixed combustion in the engine cylinder is characterized with very high heat-release rate, the fraction of fuel, which has not yet been burned after the end of vaporization, burns at a low rate. At this stage of the process the premixed combustion

does not exist ($df_p/dt=0$) and therefore the combustion rate here is equal to the overall combustion rate (df_b/dt). In order to use Eq. (4), one needs data on the fuel injection rate and mean droplet size in the terms of Sauter mean droplet diameter, D_{SM} (see below).

Equation (5) represents the overall combustion rate (premixed plus diffusion). The final differential equation for the overall combustion rate (OCR) can be written by substituting Eq. (3) (for the premixed combustion rate, PCR) and (4) (for the diffusion combustion rate, DCR) into Eq. (5), as given here:

$$\frac{df_b}{dt}=A_o\frac{m_c}{V_i}f_{vi}\{\exp[\varphi_o(t-t_{SC})]\}(f_{vi}-f_o)\Big|_{\text{from } f_o=0}^{\text{to } f_o=f_{vi}}+\psi\frac{C}{p}\left(\frac{0.5T+0.5T_d}{273}\right)^2\frac{6}{\rho D_{SM}}f_i^{1/3}(f_i-f_v)^{5/3}\frac{\lambda-f_v}{1.15f_v}+A_1\frac{m_c}{V}(f_v-f_b)^2f_b. \tag{22}$$

The first term on the right-hand side describes the combustion rate of fuel vapors vaporized during the self-ignition delay period under the premixed flame conditions. The second term on the right-hand side expresses the combustion of fuel in which the burning rate is controlled by the rate of vaporization, and this is the main component of the diffusion combustion rate. The third term on the right-hand side describes the rate of combustion of fuel vapors and products of incomplete combustion which have not burned up to the current moment of time with the exception of fuel vapors vaporized during the self-ignition period. From the beginning of combustion process up to the moment $f_b=f_{vi}$, all three terms on the right-hand side of the equation are involved in the modeling process. From the moment $f_b=f_{vi}$ to the moment $f_v=1$ the second and third terms take part in the modeling process. Finally, after the end of vaporization process ($f_v=1$) only the last (third) term on the right side describes the combustion process, which takes place under the conditions of late combustion., $D_{SM}=68$ microns was used for the simulation.

Equations (6)–(9) represent mathematical dependencies between the caloric parameters (specific internal energy *u*, specific enthalpy *h*, isochoric specific heat capacity c_v and isobaric specific heat capacity c_p) and thermal parameters (*P, T, v*). These equations have been created in a previous study, [3], using the generalized relations of thermodynamics in partial derivatives, in conjunction with the equation of state of Redlich-Kwong [9] for real gases. These equations have been applied to the various products encountered during the combustion of fuel, such as nitrogen, N_2, oxygen, O_2, carbon dioxide, CO_2, carbon monoxide, CO, hydrogen, H_2, water vapor, H_2O, etc., and the gas mixture as a whole. These equations describe the thermodynamic behavior of real gases in the engine cylinder under conditions of high pressures and temperatures, which occur during the combustion process. A comparison between the numerical and experimental data is provided in Refs. [5], [7].

Equation (10) represents the equation of state of Redlich-Kwong for real gases, [9]. The coefficient *a* and *b* in this equation has been quantitatively evaluated in a previous work, [3], using the fact that all partial derivatives are equal to zero at the critical point, in conjunction with the equation of Planck-Gibbs for the critical point, [9]. Equation (20) is used to model the indicator process in the cylinder during the compression, combustion and expansion. The thermodynamic behavior of the air/gas mixture during the gas-exchange process in the cylinder, air receiver, exhaust pipes and the turbocharger is described by equation of state for ideal gases ($Pv=RT$), because pressure in these processes is low.

Equation (11) describes the energy balance in the engine cylinder during the gas exchange processes, i.e., without combustion. The pressure during these processes is much lower. This allows one to use the equation of state for ideal gas for this part of the process. Correspondingly, the current values of internal energy, enthalpy and heat capacities are defined with respect to the temperature and gas mixture composition only, i.e., the effect of pressure on these parameters is negligible.

Equations (12) and (13) express the energy balance in the exhaust pipe before the gas turbine. These equations describe the energy conservation in terms of enthalpy and kinetic energy of the gas flow. The heat transfer from exhaust pipe to the surrounding is considered to be negligible. In this case the exhaust gas collector is considered as an open thermodynamic system due to the mass exchange caused by the gas flow through exhaust valves and gas turbine. In Eqs. (12) and (13), Δw is an increase of the flow velocity for the selected time interval Δt. The front of pressure wave propagates with the current sonic speed, and the following values get an increase, defined under the conditions of the average parameters for the current part of the system:

$$\Delta w=\frac{\Delta p_t}{\Delta p_t}\frac{l}{k_{ex}\Delta t} \tag{23}$$

where Δt is the time interval.

Equation (14) describes the energy balance in the air receiver (after the compressor, and before the inlet ports).

Equations (15)–(17) represent the instantaneous power balance in the turbocharger in terms of the power of gas turbine P_T, compressor P_C, and momentum of inertia of turbocharger's rotor in Lagrangian formulation. This equation specifies the instantaneous rotating speed n_{TC} of the turbocharger. The instantaneous speed is needed for interpolating the compressor map (Eq. (18)). Equations (16) and (17) express the instantaneous power of compressor and turbine with respect to the current values of pressure ratios (π_c and π_t), mass flow rates ($\dot{m}_C$ and $\dot{m}_T$) efficiencies (η_C and η_T) inlet temperatures (T_o^* and T_T^*) and thermophysical properties ($R_g, R_{\text{air}}, k_g, k_{\text{air}}$).

Equations (18) and (19) represent correspondingly the compressor and turbine maps, [1,10]. Equation (18) defines the instantaneous values for the air mass flow rate, $\dot{m}_C$, in the compressor and the efficiency η_C with respect to the current pressure ratio π_c and rotating speed n_{TC}. Equation (19) defines the effective flow area $(CdA)_T$ and efficiency $\underline{\eta_T}$ of turbine with respect to the dimensionless enthalpy head H_r.

In addition to the above equations, additional equations are used to close the system of differential equations. The mass flow rate of fuel injected through the nozzle dm_f/dt, and hence the nondimensional fuel injection rate df_i/dt is modeled by the Hiroyasu's equation, [11]. The instantaneous heat transfer rates dQ_w/dt are modeled via the equations of Woschni [12,13] for the cylinder head and piston, and Dent [14] for the cylinder walls. The rate of dissociation dQ_d/dt is modeled by the equation of Gonchar [15]. The mass leakage rate dM_L/dt through the piston rings is modeled by the equation of Danov [3]. In order to integrate Eq. (2), one needs to know the values of Sauter mean diameter. These values are defined via the empirical formula of Hiroyasu and Kadota [16]. The equation of Hardenberg and Hase [17] is used to model the duration of the ignition delay period. This is needed to model the nondimensional fuel mass fraction f_{vi} vaporized during the self-ignition delay period.

For modeling the processes in HRSG, one needs the inlet temperature of flue gases. The following dependence has been used for defining this temperature:

$$T_g^{IN}=\frac{\Sigma_{i=1}^N(\Delta m_i c_{Pi}T_{Ti})}{\Sigma_i^N(\Delta m_i c_{Pi})}-\Delta T_{\text{loss}} \tag{24}$$

where Δm_i is instantaneous mass flow rate of gases through the gas turbine for an time interval Δt—the step of integration of differential Eqs. (1)–(19); T_{Ti}—instantaneous temperature of gasses behind the gas turbine; c_p—instantaneous value of the isobaric specific heat of gases behind the gas turbine; *N*—number of intervals used for numerical solution of Eqs. (1)–(19). ΔT_{loss} is tem-

perature drop due to cooling of gases during their movement from gas turbine to the boiler inlet. Usually $\Delta T_{\text{loss}}=8-10$ K. Having the values of gas mass flow rate $\dot{m}_g$, gas temperature at boiler inlet T_g^{in} and gas mixture composition, one can calculate the heat transfer in the heat recovery system for the specified geometry of convection coils. The flue gas composition is defined via the overall air/fuel equivalence ratio for the corresponding operating conditions of the diesel engine (load and rotating speed). For the heat transfer calculations the pressure and temperature of the superheated steam at boiler outlet (i.e., steam turbine inlet) are also needed. The thermodynamic properties of water and steam are defined from the charts of Rivkin [18] via equations derived by means of least-square techniques. This includes mathematical relations between the saturated pressure and temperature, enthalpy of the saturated water and steam, and enthalpy of the super-heated steam as a function of steam temperature and pressure.

According to Fig. 1, the HRSG consists of three heat-exchange coils—economizer, evaporator and super-heater, and also a circulating pump. The heat transfer in each coil is modeled via simultaneous consideration of the following equations, [19]:

$$\dot{Q}_{st}=\dot{m}_{st}(h_{st}^{EX}-h_{st}^{IN}) \tag{25}$$

$$\dot{Q}_g=\dot{m}_g(h_g^{IN}-h_g^{EX}) \tag{26}$$

$$\dot{Q}_c=h_c\Delta T_{LMT}A \tag{27}$$

where Eq. (25) represent the heat transfer rate via the differences in enthalpies of steam after h_{st}^{EX} and before h_{st}^{IN} the corresponding heat transfer unit (super-heater, evaporator, or economizer) for steam mass flow $\dot{m}_{st}$. Equation (26) represents the heat transfer rate corresponding to the differences in enthalpies of the gases before h_g^{IN} and after h_g^{EX} the corresponding heat exchanger for a mass flow rate $\dot{m}_g$ of gases. Equation (27) expresses the convective heat transfer rate in the corresponding heat exchanger, where h_c is the overall heat transfer coefficient, ΔT_{LMT} is the log mean temperature difference between the gases and steam/water, and A is the heat transfer surface area. The heat balance for the separator (drum) can be written as, [19]:

$$h_{FW}+(k_C-1)h'=k_Ch_{SEP} \tag{28}$$

where h_{FW} is the enthalpy of feed water; h' is enthalpy of the saturated water, corresponding to the pressure in the drum; h_{SEP} is enthalpy of the water in the drum, and k_C is a ratio between the circulating pump discharge and steam production ($k_C=m_{CP}/m_{ST}$).

Computational Procedure

The performance characteristics of the combined cycle power plant are simulated for steady-state operation. The simulation involves two independent models—i.e., the detailed model of the turbocharged diesel engine (Eqs. (1)–(24)) is used in conjunction with the model of heat recovery steam generator and steam turbine (Eqs. (25)–(28)). The inputs of the diesel engine to the HRSG are the temperature, pressure, and flow rate of exhaust gas. For this reason, the model of turbocharged diesel engine is executed independently. For a set of operating conditions (rotating speed and load/engine power) the results are stored in a separate output file. This approach minimizes repetitive computations for the engine.

The mathematical model of energy-conversion processes in a turbocharged diesel engine is a quasi-steady zero-dimensional global model. The parameters of working media (pressure, temperature, concentrations) are considered to be independent of any coordinate system and they change only with respect to time. For a fixed moment of time the properties of the working media are one and the same for the whole volume (cylinder, air receiver, gas collector). This model does not take into account the momentum transfer in the flow. The change of parameters is due to the energy and mass exchange. For this purpose an assumption of a momentary mixing is accepted. This assumption, however, leads to some requirements with respect to integrating over a step interval of time, Δt. For a time interval Δt the following condition must be met:

$$a\Delta t \gg \Delta l \tag{29}$$

where a is sonic speed, and Δl is length of the computational domain, i.e., part of air receiver, gas collector, or cylinder. According to Eq. (29) the distance over which the sonic wave passes for a time interval Δt should be longer than the length of the computational domain. For this reason, the long domains must be divided into several parts and for each part the conditions of Eq. (29) must be satisfied.

The fifth-order Kuta-Merson method, [20,21], has been applied for numerical solution of the system of differential Eqs. (1)–(19). The final solution of this system of differential equation does not depend on the initial values of the iterative parameters. These values may affect only the rate of convergence of the computational procedure. The final solution depends only on the operating conditions and geometry (bore, stroke, combustion chambre) of engine. The input data include:

- engine geometry
- compressor and turbine maps—Eqs. (18) and (19)
- instantaneous values of the effective flow area of valves and ports against crank angle
- operating conditions: engine speed, amount of fuel per cycle per cylinder, fuel calorific value, cooling fluid temperature, ambient pressure and temperature
- thermophysical constants and properties of working media
- initial conditions, including apriori assigned values for the following iterative parameters:
  - pressure and temperature in the engine cylinder at the beginning of compressing stroke,
  - pressure and temperature in the gas collector (before turbine),
  - pressure and temperature in the air receiver (after compressor and air cooler), and
  - rotating speed of turbocharger.

The numerical solution (integration) of the system of differential equations is carried out as a function of the crank angle (degrees). Since the proposed governing equations for the combustion rate are presented with respect to time, a change of the independent variable is also carried out: $dP/dt=dP/d\varphi \cdot d\varphi/dt$, where P is any parameter. The connection between these independent parameters (crank angle φ and time t) is the angular velocity, $\omega=d\varphi/dt$. The step $\Delta\varphi$ of integration is variable. Its initial value is 0.2 deg of crank angle rotation, but the algorithm has the ability to reduce the step automatically during the computational process depending on the current truncation error of the Kutta-Merson process, [20]. The current truncation error is estimated via the rule of Collatz [22].

There are 7 unknown (but desired) parameters for the heat recovery system (see Fig. 1):
For the water/steam side:

- temperature of water-stream mixture in the drum,
- water temperature at the outlet of economizer,
- mass flow rate of superheated steam, and
- enthalpy of superheated steam.

For the exhaust gases:

- temperature of gases at the outlet of superheater,
- temperature of the gases at the outlet evaporator, and
- temperature of gases at the outlet of economizer.

From Eqs. (25)–(27), upon substitution, one can derive two nonlinear algebraic equations for each of the heat-exchange unit (economizer, boiling section, and super heater). Together with Eq.

(28) for the heat balance in the drum, the total number of equations is also 7. Thus this system of seven nonlinear algebraic equations can be solved via an iterative computing procedure.

The algorithm for modeling is realized via a Fortran 90 program for use both on PC and UNIX workstation. For a CPU with 650 MHz the iterative computational procedure for one operating condition (engine speed and load) takes 40–50 minutes for converged solution. The computational time changes insignificantly with respect to the values of the initial conditions of the iterative parameters. The model is used as a desktop design tool for accurate predictions of cycle performance, as well as insight into design trends.

Conclusions

A mathematical model for modeling the diesel engine based combined-cycle power plant has been developed. The model can be used as a desktop design tool, which can make accurate predictions of cycle performance, as well as insight into design trends. A full set of equations is composed for modeling the mutual operation of a diesel engine as a source of power and waste heat, and a HRSG utilizing the rejected heat from diesel engine. The model can simulate the mutual operation of turbocharged diesel engine and a HRSG with a steam turbine in the whole power-speed spectrum of diesel engine. This gives an opportunity to obtain an optimization with respect to the operating variables. For details on the model validation and the applications of the model see Part II (Results and Applications) of this two-part series publication.

Nomenclature

a = speed of sound (see the subscripts), m/s
a = coefficient in the Redlich-Kwong's equation of state, $N.m^4.kg^2$
A = area, m^2 (see the subscripts)
A_o = constant depending from the physico-chemical properties of the fuel (applied for premixed combustion)
A_l = constant depending from the physico-chemical properties of the fuel (applied for diffusion combustion)
b = coefficient in the Redlich-Kwong's equation of state
c_t = gas velocity, m/s
bsfc = brake specific fuel consumption, g/kW-hour
c_v = specific isochoric heat capacity, J/kg.K
Cd = discharge coefficient (see the subscripts)
c_p = specific isobaric heat capacity, J/kg.K
D_{SM} = Sauter mean droplet diameter (SMD), m
D_t = coefficient of diffusion, m^2/sec
f = branching coefficient of chain reactions
f_b = overall nondimensional fuel mass fraction burned up to the current moment of time
f_d = nondimensional fuel mass fraction burned up to the current moment of time under the conditions of diffusion flame
f_i = nondimensional fuel mass fraction injected up to the current moment of time
f_o = see Eq. (21)
f_p = nondimensional fuel mass fraction burned up to the current moment of time under conditions of premixed flame
f_v = nondimensional fuel mass fraction vaporized up to the current moment of time
f_{vi} = nondimensional fuel mass fraction vaporized during the self-ignition delay period
g = breaking coefficient of chain reactions
$g.n$ = rate of breaking of the chains
h = specific enthalpy of air/gas mixture, J/kg
J_{TC} = momentum of inertia of turbocharger rotor, $N.m.s^2$
k = adiabatic index: $k=c_p/c_v$ (see the subscripts)
k_t = coefficient of turbulence
l_{ex} = length of the engine exhaust system from exhaust valves to the gas turbine inlet, m
LHV = lower heating value of fuel (kJ/kg)
$\dot{m}$ = mass flow rate (see the subscripts), kg/s
m_b = mass of fuel burned up to the current moment, kg
m_c = total fuel mass injected per cycle per cylinder, kg
m_d = fuel mass burned up to the current moment under the conditions of diffusion flame, kg
m_p = fuel mass burned up to the current moment of time under the conditions of premixed flame, kg
m_v = fuel mass vaporized up to the current moment, kg
M = current mass of air/gas mixture in the cylinder, kg
n = engine rotating speed, rpm
n_{TC} = turbocharger rotating speed, rpm
p = pressure (see the subscripts), N/m^2
P = power (see the subscripts), kW
$\dot{Q}$ = heat transfer rate, kW
Q = heat loss due to fuel vaporization, dissociation and heat transfer (see subscripts)
Q_f = fuel calorific value, J/kg
r_i = ($i=1,2,3$) mass fractions of ''pure air,'' ''pure gases'' and fuel vapors
R = gas constant (see the subscripts), J/kg.K
$\tilde{R}$ = universal gas constant (8.3143 J/mol.K)
t = time, sec
t_{SC} = time at the moment of the beginning of combustion
T = temperature (see the subscripts), K
T_d = surface temperature of the liquid fuel droplets, K
u = specific internal energy, J/kg
v = specific volume of air/gas mixture, m^3/kg
V = volume (see the subscripts), m^3
Vi = volume of the cylinder at the moment of ignition, m^3
w = increase of the flow velocity (Δw) for the selected time interval Δt

Greek Symbols

η_c = efficiency of compressor
η_T = efficiency of turbine
φ_o = total branching coefficient ($\varphi_o=f-g$)
ρ = density (see the subscripts), kg/m^3
ρ_a = density of air, kg/m^3
λ = air/fuel equivalence ratio, $\lambda=(A/F)_{actual}/(A/F)_{stoichiometric}$
π_c = compressor pressure ratio
π_T = turbine pressure ratio
τ_{id} = ignition delay (time between the start of injection and the start of detectable heat release)
Ψ = coefficient of mass flow rate (see the subscripts)
ω_{TC} = turbocharger angular velocity, s^{-1}

Subscripts

b = fuel burned
c = compressor, cycle, convective
c = cylinder
d = diffusion
d = dissociation
d = droplet
ev = evaporation
ex = exhaust
f = fuel
g = gasses
i = injection
in = inlet
liq = liquid fuel
o = initial, originating value
p = premixed flame
st = steam
Σ = overall, sum
sm = notation for Sauter mean diameter
v = fuel vaporized

t = turbulence, turbine
TC = turbocharger
w = cylinder wall

Definitions, Acronyms, Abbreviations

(A/F)=air/fuel ratio
air/fuel equivalence ratio $=(\mathrm{A/F})_{\mathrm{actual}}/(\mathrm{A/F})_{\mathrm{stoichiometric}}$
CA=crank angle

Nondimensional fuel mass fractions (accumulated percentages):

$f_d = m_d/m_c$ nondimensional fuel mass fraction burned up to the current moment of time under the conditions of diffusion flame

$f_p = m_p/m_c$ nondimensional fuel mass fraction burned up to the current moment of time under the conditions of premixed flame

$f_b = m_b/m_c$ overall nondimensional fuel mass fraction burned up to the current moment of time:

$m_b/m_c = m_p/m_c + m_d/m_c$, i.e., $f_b = f_p + f_d$, $(m_b = m_p + m_d)$

$f_i = m_i/m_c$ nondimensional fuel mass fraction injected up to the current moment of time

$f_v = m_v/m_c$ nondimensional fuel mass fraction vaporized up to the current moment of time

Nondimensional rates:

$DCR = df_d/dt = d(m_d/m_c)/dt$	diffusion combustion rate, 1/sec
$FIR = df_i/dt = d(m_i/m_c)/dt$	fuel injection rate, 1/sec
$FVP = df_v/dt = d(m_v/m_c)/dt$	fuel vaporization rate, 1/sec
$PCR = df_p/dt = d(m_p/m_c)/dt$	premixed combustion rate, 1/sec
$OCR = df_b/dt = d(m_b/m_c)/dt$	overall combustion rate, 1/sec

References

[1] Baykov, B. P., et al., 1975, *Turbochargers for Diesel Engines*, ''Mashinostroenie,'' 1975 (in Russian).

[2] Danov, S., Yamamoto, T., and Arai, N., 1998, ''Modeling the Power-Economic Characteristics of Diesel-Steam Combined Cycle in the Whole Spectrum of Operating Conditions,'' *Proc. ASME International Joint Power generation Conference*, Baltimore MD, ASME, New York, (**1**), pp. 275–286.

[3] Danov, S., 1997, ''A Differential Equation of the First Law of Thermodynamics for Modeling the Indicator Process of a Diesel Engine,'' Proc. ASME International Design Engineering Technical Conferences, Computers in Engineering Conference, Sacramento, CA, ASME Paper DETC97/CIE-4429.

[4] Danov, S., and Gupta, A. K., 2000, ''Effects of SMD on the Combustion Related Parameters in Heavy-Duty Diesel Engines,'' AIAA J. Prop. and Power, **16**(6), pp. 980–987.

[5] Danov, S., and Gupta, A. K., 2001, ''Influence of Imperfections in Working Media on Diesel Engine Indicator Process,'' ASME J. Eng. Gas Turbines Power, **123**, pp. 231–239.

[6] Danov, S., and Gupta A. K., 1997, ''Understanding of Diesel Engine Combustion Process,'' ASME International Design Engineering Technical Conferences, Computers in Eng. Conference, Sacramento, CA, ASME Paper DETC97/CIE-4430.

[7] Danov, S., Furuhata, T., and Arai, N., 1998, ''Effects of Thermo-Physical Properties of Products of Burning on the Combustion Characteristics in a Diesel Engine,'' *Proc. 63rd Annual Meeting of the Society of Chemical Engineers*, Osaka, Japan, Paper E106, p. 101.

[8] Semenov, N. N., *Theory of Chain Reactions and Heat Ignition*, Znanic Publisher, Moscow (in Russian).

[9] Wark, K., 1995, *Advanced Thermodynamics for Engineers*, McGraw-Hill, New York.

[10] Shliakhin, P. N., 1974, *Steam and Gas Turbines*, Energia Publisher, Moscow (in Russian).

[11] Hiroyasu, H., 1985, ''Diesel Engine Combustion and its Modeling,'' *Diagnostics and Modeling of Combustion in Reciprocating Engines*, Proceedings of the Symposium COMODIA'85, Tokyo, pp. 53–75.

[12] Woschni, G., 1967, ''Universally Applicable Equation for the Instantaneous Heat Transfer Coefficient in the Internal Combustion Engine,'' SAE Paper 670931, SAE Trans., **76**.

[13] Woschni, G., and Anisits, F., 1974, ''Experimental Investigation and Mathematical Presentation of Rate of Heat Release in Diesel Engines Dependent Upon Engine Operating Conditions,'' SAE Paper No. 7400086.

[14] Heywood, J. B., 1988, *Internal Combustion Engine Fundamentals*, McGraw-Hill, New York.

[15] Gonchar, B. M., 1969, ''Numerical Modeling of Diesel Engine Cycle,'' D.Sc. thesis, Moscow (in Russian).

[16] Hiroyasu, H., and Kadota, T., 1983, ''Fuel Droplet Size Distribution in Diesel Combustion Chamber,'' SAE Trans., **83**.

[17] Hardenberg, H. O., and Hase, F. W., 1979, ''An Empirical Formula for Computing the Pressure Rise Delay of a Fuel From Cetane Number and From the Relevant Parameters of a Direct-Injection Diesel Engines,'' SAE Paper 790493, SAE Trans., **88**.

[18] Rivkin, S., and Alexandrov, A., 1978, *Thermodynamic Properties of Water and Steam*, Sofia, Technika Publisher.

[19] Enin, V., 1978, *Marine Steam Generators*, Transport Publisher, Moscow.

[20] Dorn, W. S., and McCracken, D. D., 1972, *Numerical Methods With Fortran 4 Case Studies*, John Wiley and Sons, New York.

[21] Fox, L., 1962, *Numerical Solution of Ordinary and Partial Differential Equations*, Pergamon Press, Oxford.

[22] Ralston, A., 1962, ''Runge-Kutta Methods with Minimum Error Bounds,'' *Mathematics of Computation* pp. 431–437.

Modeling the Performance Characteristics of Diesel Engine Based Combined-Cycle Power Plants—Part II: Results and Applications

Stan N. Danov
Fluor Canada, Inc.,
55 Sunpark Plaza, SE,
Calgary, AL T2X 3R4, Canada
e-mail: stan.danov@fluor.com

Ashwani K. Gupta
Department of Mechanical Engineering,
University of Maryland,
College Park, MD 20742
e-mail: akgupta@eng.umd.edu

In this two-part series publication a mathematical model of the energy conversion process in a diesel engine based combined-cycle power plant has been developed and verified. The examined configuration consists of a turbocharged diesel engine (the topping cycle), a heat recovery steam generator (HRSG) and a steam turbine plant (the bottoming cycle). The model is then used to provide an analysis of performance characteristics of the combined-cycle power plant for steady-state operation. Numerous practical performance parameters of interest have been generated, such as the mean indicated pressure, specific fuel consumption, hourly fuel consumption, brake horsepower of diesel engine, mass flow rate, pressure, and temperature of gases and air, respectively, through the gas turbine and compressor (in the frame of a turbocharger), temperature of flue gases at boiler inlet and outlet, mass flow rate of exhaust gases through the convection coils, and mass flow rate, temperature, pressure, and enthalpy of superheated steam. The performance maps have been derived. The effect of change in the major operating variables (mutual operation of diesel engine, HRSG, and steam turbine) has been analyzed over a range of operating conditions, including the engine load and speed. The model is used as a desktop design tool for accurate predictions of cycle performance, as well as insight into design trends. [DOI: 10.1115/1.1635397]

Model Validation

Comprehensive work on validating the model has been carried out in our previous publications [1–5]. Given below are only comparisons between the integral parameters of the heavy-duty diesel engines used for simulating the performance characteristics of a combined-cycle power plant. Table 1 shows a comparison between the model and experiment for the mean indicated pressure, compression pressure, and peak pressure in the cylinder and the specific indicated fuel consumption. The experiments are for a two-stroke marine turbocharged diesel engine. The operating conditions are as follows: engine speed $n=140$ rpm, fuel lower heating value (LHV) 42.39 MJ/kg, start of fuel injection 11°BTDC, fuel amount 0.03785 kg/cycle/cylinder, ambient pressure 740 mm Hg, and ambient temperature 27°C. The ''noise'' in the experimental curve is filtered by means of a windowing method for filtration, [4].

The results show a very good agreement between the model and experiment values. The relative differences between the experimental and theoretical values (Table 1) are commensurate with the error of experiment. Table 2 shows a comparison between the major integral parameters of a heavy-duty diesel engine with bore=74 cm and stroke=160 cm for various loads and rotating speeds. These results confirm that the model can be used to analyze the performance characteristics of diesel engine based combined-cycle power plants over a range of engine operating conditions.

Contributed by the Fuels and Combustion Division of THE AMERICAN SOCIETY OF MECHANICAL ENGINEERS for publication in the ASME JOURNAL OF ENGINEERING FOR GAS TURBINES AND POWER. Manuscript received by the F&C Division April 2002; final revision received February 2003. Associate Editor: S. Gollahalli.

Results and Applications

The mathematical model, algorithms, and computational tools can be used to generate actual operating characteristics of combined-cycle power plants. This includes both instantaneous values (histories) and integral parameters. For instance, the histories with respect to the crank angle degree include the following parameters: pressure p_{REC} and temperature T_{REC} in the air receiver, pressure p, temperature T and gas mixture composition in the cylinder, pressure p_T, and temperature T_T in the gas collector before the gas turbine, power consumption P_C, pressure ratio π_C and efficiency η_C of turbocharger compressor, power output P_T, pressure ratio π_T and efficiency η_T of turbocharger gas turbine and rotating speed n_{TC} of turbocharger. By composing corresponding integral sums, the following integral parameters of the turbocharged diesel engine can be defined:

- mean indicated pressure
- specific indicated fuel consumption
- mechanical loss/mechanical efficiency
- brake specific fuel consumption
- compression pressure
- peak pressure of the cycle
- overall air/fuel equivalence ratio
- hourly fuel consumption
- brake power
- average gas pressure before the gas turbine
- average gas temperature before the gas turbine
- gas mass flow rate through gas turbine
- gas temperature after gas turbine
- pressure drop across the air filter
- air pressure and temperature before and after the air cooler
- pressure drop across the air cooler
- mass flow rate of air through the compressor

Table 1 Comparison between predicted and experimental parameters of direct injection marine diesel engine (bore =66 cm, engine speed=140 rpm)

Parameter	Modeling	Experiment
Mean indicated pressure, (MPa)	1.572	1.554
Compression pressure, (MPa)	8.970	8.953
Peak pressure (MPa)	11.284	11.150
Specific indicated fuel consumption, (kg/kW.h)	0.181	0.183

Some of the above integral parameters obtained from the engine modeling appear as input data for modeling the energy conversion process in the heat recovery system.

The model is used to provide an analysis of performance characteristics of the combined-cycle power plant for steady-state operation. The system is based on a heavy-duty diesel engine with bore=74 cm and stroke=160 cm, and a HRSG utilizing the exhaust gas heat from the engine. The heat exchange surfaces of the boiler are as follows: superheater 74.3 m^2, evaporator 535.0 m^2, economizer 172.1 m^2. The average free flow area for flue gases through the convection coils is 1.05 m^2. For all the numerical experiments the discharge of circulating pump is 9000 kg/hour and the pressure of steam in the drum is 0.68 MPa. The ambient pressure and temperature are correspondingly 98.7 kPa and 298 K. For any set of input data the solution provides the practical performance parameters of interest. One convenient way to present the operating characteristics of a diesel engine power plant over its full load and speed is to plot the parameters of interest, e.g., power output dependency as a function of engine speed (see below).

Along with the parameters of interest, Figs. 1–5 also show the limiting curve for the diesel engine. Such a limiting characteristic does not necessarily represent the maximum rated power of diesel engine. It represents limitations in terms of pressures and temperatures in the cylinder, torque output from the crankshaft, and temperature of gases at the turbocharger turbine inlet. The maximum cylinder pressure achieved during combustion generates high stress in many mechanical components. The temperature limitations are related to the metal temperature profiles at various critical components, such as piston, exhaust valves, cylinder head and liner, and turbine blades. Therefore, the limiting characteristic shows the allowable operating conditions in terms of engine load and speed. The upper envelope of the limiting curve corresponds to maximum allowable amount of fuel per cycle per cylinder,

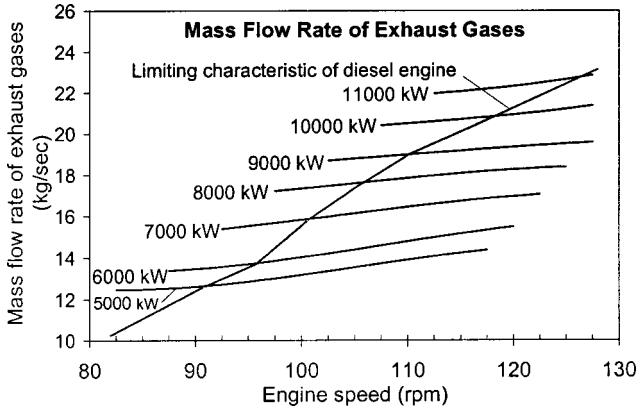

Fig. 1 Mass flow rate of exhaust gases for various loads and rotating speed for diesel engine (bore=74 cm, stroke =160 cm)

which corresponds to the highest brake mean effective pressure and crankshaft torque. Points below this curve define the part-load. The diesel engine manufacturer provides the limiting characteristic.

As the power plant under consideration includes a turbocharged diesel engine, Fig. 1 is a result of the matching between the airflow of the diesel engine and the turbocharger on one side, and matching the engine to the load on the other side. The matching procedure is based on the equations provided in [6]. The airflow rate through the diesel engine is a function of the engine speed, compressor delivery air density and the pressure differential between intake and exhaust manifolds during the period of valve overlap. Figure 1 shows the effect of engine load and speed as a function of the mass flow rate of gases. If the engine is run at constant speed (e.g., as for electricity generation), but steadily increasing load, then the mass flow rate increases approximately with the increasing charge density. The mathematical model provides the airflow rate through the engine superimposed on the turbocharger compressor characteristics. Since an intercooler is employed, [6], as the load increases, the cooling effect increases the charge density more rapidly for a corresponding boost pressure. As a result, the slope of the constant engine speed airflow line on the compressor characteristic will be less steep. This affects the compressor efficiency. Figure 1 also shows that if the engine is run at constant load (i.e., torque or break mean effective pressure), but increasing speed, the volumetric airflow rate also increases. The effective flow area of the turbocharger turbine re-

Table 2 Comparison between the theoretical and experimental parameters for a direct injection turbocharged marine diesel engine (bore=74 cm, stroke=160 cm) for different rotating speeds and loads

	Condition 1		Condition 2		Condition 3		Condition 4	
	$m_C=0.0237$ kg/cycle $n=96$ rpm		$m_C=0.0312$ kg/cycle $n=109$ rpm		$m_C=0.0380$ kg/cycle $n=120$ rpm		$m=_C=0.04116$ kg/cycle $n=124$ rpm	
Parameters	Experiment	Model	Experiment	Model	Experiment	Model	Experiment	Model
P_C, Mpa	3.589	3.391	4.325	4.312	5.246	5.248	5.639	5.682
P_Z, Mpa	5.482	5.267	6.139	5.993	6.806	6.748	7.051	7.099
P_i, Mpa	0.657	0.637	0.849	0.831	1.010	1.008	1.069	1.091
P_{REC}, Mpa	0.141	0.142	0.167	0.164	0.184	0.184	0.192	0.194
ΔP_F, mm H_2O	12.50	12.20	21.00	21.20	30.00	32.60	35.00	38.60
ΔP_{COOL}, mm H_2O	135.0	129.8	200.5	199.5	257.0	268.7	275.5	296.4
T_T, °C	342.5	345.1	390.0	395.4	438.0	441.0	461.0	461.6
T_{cyl}, °C	293.0	284.6	344.0	344.7	391.0	399.0	406.0	418.2
bsfc, kg/W.hour	0.217	0.221	0.216	0.220	0.217	0.219	0.221	0.218
P, kW	5040	4945	7570	7430	10075	9980	11080	11220

Notations (Table 2): n–engine rotating speed; m_C–amount of fuel per cycle per cylinder; P_C–compression pressure; P_Z–maximum pressure of the cycle; P_i–mean indicated pressure; P_{REC}–air pressure in the air receiver; ΔP_F–pressure drop of the air filter; ΔP_{COOL}–pressure drop of the air cooler; T_T–average temperature of gases before gas turbine; T_{CYL}–temperature of gases after the cylinder; bsfc–brake specific fuel consumption; P–brake power of engine.

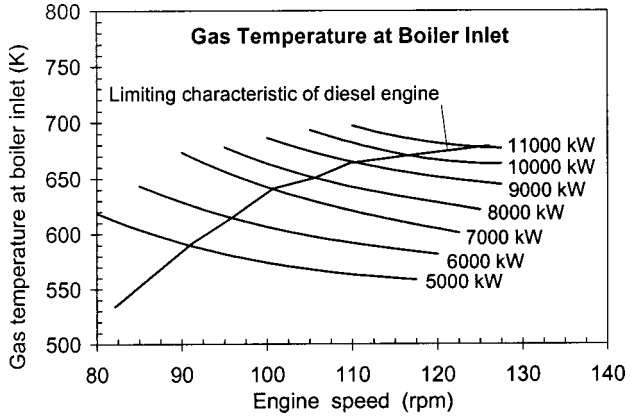

Fig. 2 Gas temperature at boiler inlet for various power and rotational speed of diesel engine (bore,=74 cm,stroke =160 cm)

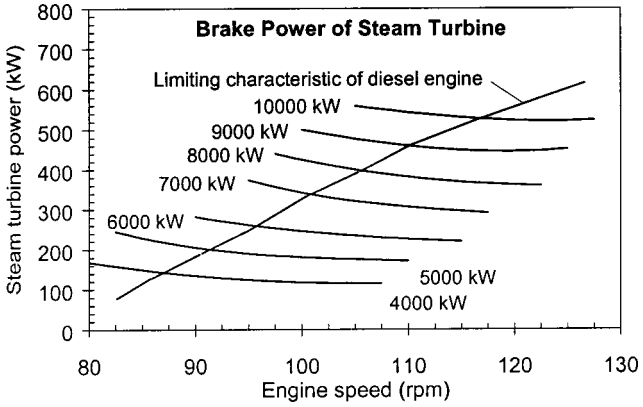

Fig. 5 Brake power of steam turbine in the whole load-speed spectrum of diesel engine (bore=74 cm,stroke=160 cm)

mains almost constant, which subsequently results in increased turbine inlet pressure. This results in increased available energy for expansion through the turbine and hence increased boost pressure at the compressor. Thus the constant load airflow line of the engine does not lie horizontally on the compressor characteristics, but rises with engine speed. The results shown in Fig. 1 demonstrate that, if the diesel engine operates at constant power but at different rotating speeds, the mass flow rate of exhaust gases increases with increase in the engine speed, which is favorable for the HRSG and steam turbine power output. However, the increase in engine speed at constant power leads to decreased gas temperature at boiler inlet (Fig. 2). The flue gas composition, estimated via the overall air/fuel equivalence ratio, varies in the power-speed spectrum of diesel engine (Fig. 3), which causes variations in the specific enthalpy of gases due to the variations in the gas composition. The variations in the mass flow rate and temperature of flue gases cause variations in the flue gas velocity through the convection sections, which subsequently affect the Reynolds number and the overall heat transfer coefficients in the convection coils. As a result the gas temperature at boiler outlet slightly decreases with increase in engine speed at constant engine power (Fig. 4). This is favorable for increasing the steam turbine power output, however, for light loads and higher rotational speeds the temperature of flue gases at boiler outlet gets closer to the dew-point which may cause corrosion, especially for fuels with high sulfur content.

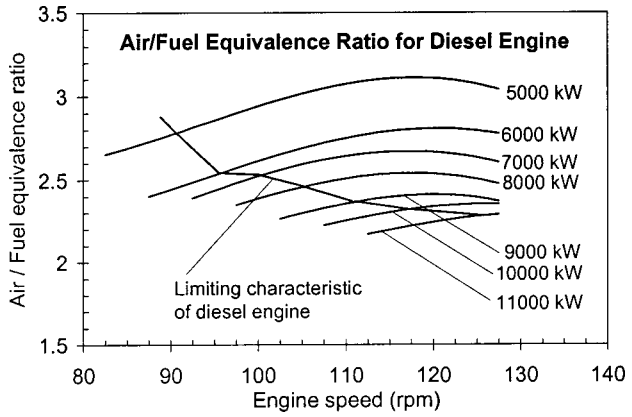

Fig. 3 Air/fuel equivalence ratio for diesel engine (bore =74 cm,stroke=160 cm) in the whole load-speed spectrum

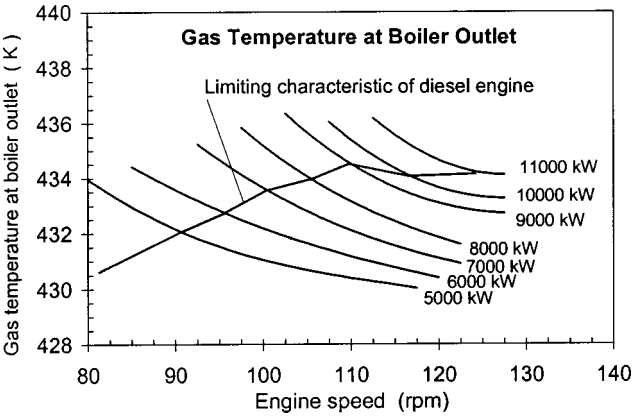

Fig. 4 Gas temperature at boiler outlet for various loads and rotational speed of diesel engine (bore=74 cm,stroke =160 cm)

Figure 5 shows the power of the steam turbine in the whole power-speed spectrum of diesel engine. The increase in engine speed at constant power ultimately causes a slight decrease in power output of the steam turbine. This indicates that the negative impact of decreased temperature of flue gases at boiler inlet dominates the positive impact of increased mass flow rate of flue gases. Having both the steam turbine power (Fig. 5) and the specific fuel consumption of the diesel engine (Fig. 6) for the whole power-speed layout, one can calculate the efficiency and specific fuel consumption of the combined diesel-steam power plant (see Figs. 7 and 8). The curves shown in Fig. 8 can be transformed into contours of constant brake specific fuel consumption (b.s.f.c.) for

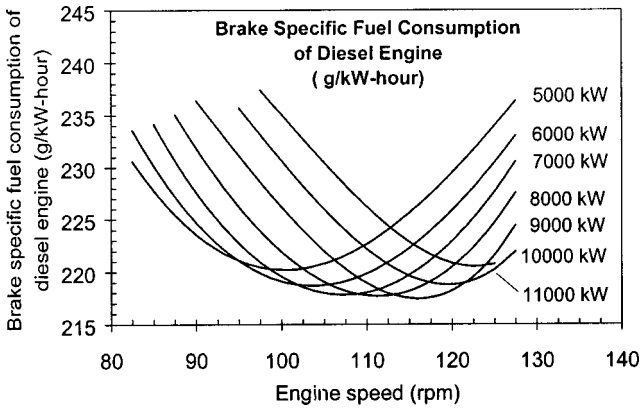

Fig. 6 Brake specific fuel consumption of diesel engine (bore=74 cm,stroke=160 cm) in the whole load-speed layout.

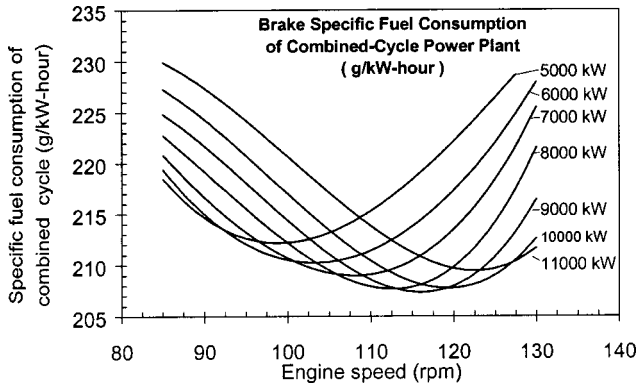

Fig. 7 Effects of engine load and rotational speed on the brake specific fuel consumption of diesel engine based combined-cycle power plant

the power plant as a whole (Fig. 9). This figure represents the plot of brake specific fuel consumption on a graph of power output versus engine speed. Therefore, this figure is a performance map of the combined-cycle power plant and can be used to solve a wide range of operational problems and for plant optimization.

The plots presented above can be understood in terms of variations in engine volumetric efficiency, air/fuel ratio, and the importance of heat losses and friction change as affected by the load and

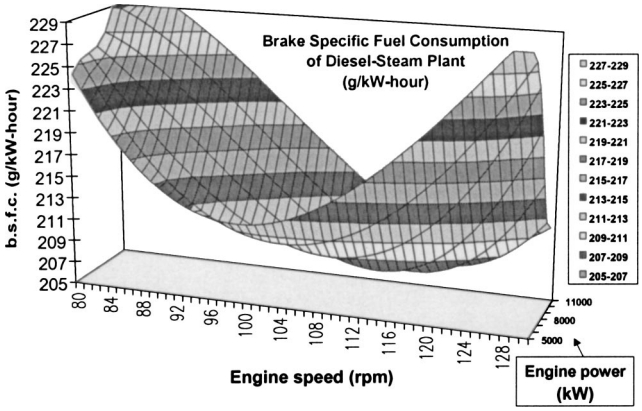

Fig. 8 Three-dimensional plot of brake specific fuel consumption of diesel engine based combined-cycle power plant as affected by the engine load and speed

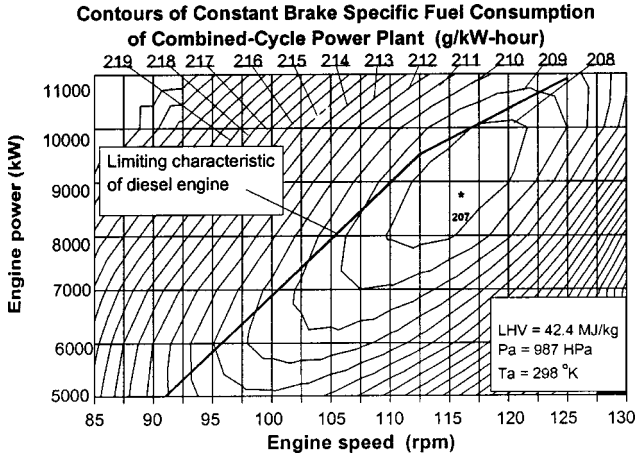

Fig. 9 Performance map of diesel engine based combined-cycle power plant

engine rotational speed. The minimum brake specific fuel consumption (b.s.f.c.) for the investigated power plant is 207 g/kW-hr at 116 rpm with 8900 kW power output. The contours of b.s.f.c. (Fig. 9) has the following explanation: Starting at the above-mentioned minimum b.s.f.c. point, increasing speed at constant load increases b.s.f.c. primarily due to the increased friction loss at higher speeds, i.e., decreased the mechanical efficiency. Decreasing speed at constant load increases b.s.f.c., primarily due to the increased importance of heat transfer per engine cycle. Friction decreases, increasing the mechanical efficiency, but this is secondary. Any mixture enrichment required to maintain a sufficiently repeatable combustion process at low engine speed contributes as well. Increasing load at constant speed from the minimum b.s.f.c. point increases b.s.f.c, primarily due to the mixture enrichment required to increase torque as the engine becomes increasingly airflow limited (see Fig. 3 for the air/fuel ratio). Decreasing load at constant speed increases b.s.f.c., primarily due to the increased magnitude of friction and decreased pump work, the increased relative importance of friction, and increased importance of heat transfer.

The heat rate and thermal efficiency of the plant can be easily derived via the above values of b.s.f.c. The plant heat rate (HR) is the ratio of heat addition to the net power output. Because the rate of heat addition is proportional to the fuel consumption rate, the heat rate is a measure of fuel utilization rate per unit of power output (kJ/kW-hr):

$$\mathrm{HR} = \mathrm{b.s.f.c.} * \mathrm{LHV} \tag{1}$$

where LHV (kJ/kg) is the lower heating value of the fuel used, and b.s.f.c. is in (kg/kW-hr). The gross fuel conversion efficiency can be calculated according to

$$\eta_t = \frac{3600}{\mathrm{HR}} = \frac{3600}{\mathrm{b.s.f.c.} * \mathrm{LHV}}. \tag{2}$$

The island of minimum b.s.f.c. is located in the range of 84%–93% of maximum speed, with some 71%–92% of the maximum power output for this particular power plant as shown in Fig. 9.

Conclusions

A mathematical model for modeling the diesel engine based combined-cycle power plant has been developed. The model is used as a desktop design tool, which can make accurate predictions of cycle performance, as well as insight into design trends. The model can simulate the mutual operation of turbocharged diesel engine and a HRSG with a steam turbine in the whole power-speed spectrum of diesel engine. A numerical analysis of performance characteristics of combined diesel-steam power plant over a range of operating conditions with respect to the diesel engine power and speed has been carried out. The performance parameters of the combined power plant have been derived for the whole range of engine load and speed. This gives an opportunity to obtain an optimization with respect to the operating variables. It should be noted that the most important prerequisite for higher efficiency of a combined-cycle power plant is the utilization of a highly efficient topping cycle, i.e., highly efficient diesel engines. The efficiency of the advanced diesel engines is comparable to that of gas turbines of equal power capacity. Diesel engine based combined-cycle power plants may appear to be the optimum option for smaller to medium power outputs, e.g., up to 35–40 MW.

References

[1] Danov, S., and Gupta, A. K., 2000, "Effects of SMD on the Combustion Related Parameters in Heavy-Duty Diesel Engines," AIAA J. Propul. Power, **16**(6), pp. 980–987.

[2] Danov, S., and Gupta, A. K., 2001, "Influence of Imperfections in Working Media on Diesel Engine Indicator Process," ASME J. Eng. Gas Turbines Power, **123**(1), pp. 231–239.

[3] Danov, S., and Gupta A. K., 1997, "Understanding of Diesel Engine Combustion Process," ASME International Design Engineering Technical Confer-

ences, Computers in Eng. Conference, Sacramento, CA, ASME Paper DETC97/CIE-4430.
[4] Rabiner, L., and Gold, B., 1975, *Theory and Application of Digital Signal Processing*, Prentice-Hall, Englewood Cliff, NJ.
[5] Danov, S., 1997, ''A Differential Equation of the First Law of Thermodynamics for Modeling the Indicator Process of a Diesel Engine,'' Proc. ASME International Design Engineering Technical Conferences, Computers in Engineering Conference, Sacramento, CA, ASME Paper DETC97/CIE-4429.
[6] Danov, S., and Gupta, A. K., 2004, ''Modeling the Performance Characteristics of Diesel Engine Based Combined-Cycle Power Plants Part 1: Mathematical Modeling,'' ASME J. Eng. Gas Turbines Power, **126**, pp. 28–34.

Adaptive Selection of Aircraft Engine Technologies in the Presence of Risk

B. A. Roth

M. D. Graham

D. N. Mavris

School of Aerospace Engineering,
Georgia Institute of Technology,
Atlanta, GA 30332-0150

N. I. Macsotai

GE Aircraft Engines,
Cincinnati, OH 45215

The objective of this paper is to describe a method for selecting optimal engine technology solution sets while simultaneously accounting for the presence of technology risk. This method uses a genetic algorithm in conjunction with technology identification, evaluation, and selection methods to find optimal combinations of technologies. The unique feature of this method is that the technology evaluation itself is probabilistic in nature. This allows the performance impact and associated risk of each technology to be quantified in terms of a distribution on key engine technology metrics. The resulting method can best be characterized as a concurrent genetic algorithm/Monte Carlo analysis that yields a performance and risk-optimal technology solution set. This solution set is inherently a robust solution because the method will naturally strive to find those technologies representing the best compromise between performance improvement and technology risk. Finally, a practical demonstration of the method and accompanying results is given for a typical commercial aircraft engine technology selection problem.
[DOI: 10.1115/1.1639006]

Introduction

The identification and selection of key technologies needed for next-generation aircraft engines is one of the most challenging problems faced by engine designers. This is because all parts of an aircraft gas turbine engine are tightly integrated together such that a technology introduced into one part of the system tends to have a ripple effect that impacts many other portions of the system. The results of this rippling effect can be difficult to predict, let alone predict quickly and inexpensively. Yet quick, accurate, and inexpensive evaluations are exactly what the marketplace is demanding in order for manufacturers to remain competitive today.

Moreover, each generation of systems tend to evolve into more complex and intricate designs than the previous generation. As a result, the difficulty in designing and building each successive generation of ever-more capable and sophisticated machines rises exponentially with time. The upshot of this is an increasingly urgent need to find new methods capable of quickly and accurately modeling these complex systems and their associated interactions. This need is categorically prevalent throughout the aerospace industry, but is particularly acute in the aircraft gas turbine industry.

It is axiomatic that the best combination of technology options is inherently a balance of many conflicting objectives and there are typically many more technology options available than resources to develop them. One could therefore characterize engine technology selection as a highly constrained multi-objective combinatorial optimization problem for which traditional gradient-based optimization methods are of little use. However, evolutionary search methods used in conjunction with advanced technology analysis methods are known to be very adept at solving complex engine technology selection problems and have been successfully applied to this end (Roth, Graham, and Mavris [1] and Roth and Mavris [2]).

In their present state, these advanced technology selection methods only address a limited aspect of the technology decision-making process. Specifically, they focus primarily on modeling the ''benefit'' of the technology impact and have only crude models for the impact of technology risk on the selection of technology concepts. The focus of this research is to integrate a more sophisticated model for technology risk into the existing engine technology selection method. The utility of this method is then demonstrated for a typical commercial engine technology selection problem.

Technology Identification, Evaluation, and Selection Method

The technology identification, evaluation, and selection (TIES) method is a generic technology evaluation method intended to enable rapid and accurate evaluations of technologies in *any* complex system (Kirby and Mavris [3]). The fundamental premise of the TIES approach is the use of technology metrics (the so-called K-factors) as a generic means to quickly and accurately model the impact of a technology at the sub-system level. These subsystem impact estimates can then be used as a basis for estimating the system-level impact through the use of a technology impact forecasting (TIF) environment. This TIF is often a metamodel created based on detailed-physics-based models, but can, in theory, be almost any model that links fundamental technology metrics to system level performance figures of merit (FoMs). Construction of a TIF usually involves selecting a set of system performance figures of merit (FoMs) and setting up a detailed analytical model for the baseline system. This model is used in conjunction with response surface methods to create a set of response surface equation metamodels that are a compact representation of a much more complex model. These metamodels are collectively referred to as a TIF environment.

The TIES method has been applied to aircraft gas turbine engine technology selection problems with considerable success. TIES implemented in conjunction with a genetic algorithm (GA) optimization routine (as described by Goldberg [4]) has proven particularly adept at finding the best possible set of technologies to meet any prescribed objective, regardless of system complexity, the number of technology concepts considered, or the number of objectives. This technique is a very valuable tool to assist engine designers in selecting the best possible subset of technologies

Contributed by the International Gas Turbine Institute (IGTI) of THE AMERICAN SOCIETY OF MECHANICAL ENGINEERS for publication in the ASME JOURNAL OF ENGINEERING FOR GAS TURBINES AND POWER. Paper presented at the International Gas Turbine and Aeroengine Congress and Exhibition, Amsterdam, The Netherlands, June 3–6, 2002; Paper No. 2002-GT-30623. Manuscript received by IGTI, Dec. 2001, final revision, Mar. 2002. Associate Editor: E. Benvenuti.

Table 1 Technology readiness level scores

TRI	Description
9	Actual system flight proven on operational flight
8	Actual system tested and flight qualified
7	System prototype demonstrated in flight
6	Model of prototype demonstrated in a relevant environment
5	Component validation in a relevant environment
4	Component validation in a laboratory environment
3	Analytical and/or experimental proof-of-concept
2	Technology concept formulated
1	Basic principles observed and reported
0	No concept formualtion—only basic ideas

from a pool of technology options. Moreover, the method is inherently fast and accurate if implemented properly.

Modeling Technology Risk

One of the simplest methods for analyzing technology risk and readiness is NASA's technology readiness level (TRL) scoring system. A TRL is subjective score that rates technologies on a scale of one to nine, with a score of one being highest risk and lowest readiness, while a score of nine is lowest risk and highest readiness. Each score is associated with a specific type of analysis or test activity which is intended to be a reflection of the level of research and development confidence in the technology, as shown in Table 1.

The principal advantages of the TRL scoring system are that it is simple to use, universally recognized/understood in industry, and bases readiness scores on a standardized scale. The principal disadvantages of the TRL scoring system are (1) inherent subjectivity in the scores; (2) the scores themselves are based primarily on the level of testing accomplished (which does not always accurately indicate the true level of risk); (3) TRL scores do not directly model the true nature of risk (i.e., uncertainty in ultimate benefit); and (4) TRL scores do not account for the myriad of nontechnical factors that contribute to technology risk. Therefore, the TRL scoring system should be regarded as a crude but inexpensive proximal treatment of the general technology risk problem.

TRL scores can be very useful in selecting technologies for complex systems, especially in the early phases of the design process where detailed information is rare and timely decisions are of the essence. One can typically obtain good estimates on TRL scores for a variety of technologies in very short order by polling technology experts on their perceptions of a given technology's readiness. These scores essentially categorize technologies according to the perceived risk posed by each.

This TRL rating system can be used directly in the GA-TIES analysis method as a crude model for risk by using the TRL (in conjunction with other performance figures of merit) as a component in a composite objective function. The resulting technology solution set is optimal in that the performance benefits are balanced against the TRL score in proportion to user-specified weights applied to the objective function. This approach was implemented and demonstrated in Ref. [1] on a commercial aircraft engine technology selection problem using a GA-TIES method and was shown to be capable of finding solutions that are difficult or impossible to obtain using conventional perturbation-based technology selection methods.

However, the GA-TIES method as demonstrated in Ref. [1] has a critical drawback. The simple model for technology risk based strictly on TRL scores does not capture the fundamental nature of technology risk, which is essentially degradation of expected benefit. In other words, the higher the risk, the more the expected benefit must be discounted. What is required is a *simple, compact* model for technology risk that captures the degradation of expected benefit, such as the K-σ risk model described in the following section.

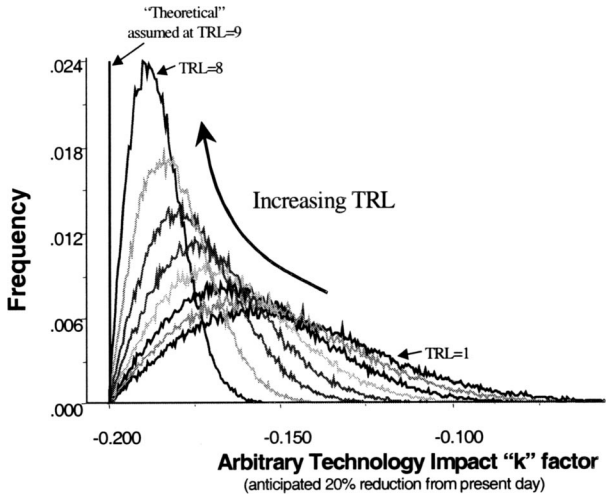

Fig. 1 K-σ model for technology readiness (from Kirby and Mavris, Ref. [5])

The K-σ Technology Risk Model

The K-σ model was for technology risk was first proposed by Kirby and Mavris and could be characterized as an *indexed benefit degradation model* based on TRL score (Kirby and Mavris [5]). In other words, the K-σ model probabilistically degrades expected technology benefit as a function of TRL score. To understand this, consider Fig. 1, which shows the expected benefit in terms of a single technology metric (K-factor) for some arbitrary technology. If this technology were at a TRL of 9, one would expect that its benefit relative to the baseline would be precisely known with very high confidence. In the example of Fig. 1, the technology benefit at a TRL of nine is shown as a 20% improvement over the baseline technology.

If the TRL of the technology in Fig. 1 were less than nine, one would intuitively expect that the point estimate on K-factor benefit would not be as precisely known and might better be described as a probability distribution. For the sake of argument, presume that the upper bound of the K-factor range is given by the baseline case (if it were higher, this would imply a trivial solution—the baseline case would be a better performer than the one with technology). Similarly, presume that the lower limit is given by the actual benefit at a TRL of 9. A probability distribution describing the expected benefit must be bounded by these extremes, and the TRL score of that technology dictates the skewness of the distribution towards one limit or the other. This is shown in Fig. 1 as a series of skewed probability distributions, with the distribution being skewed increasingly towards the left as TRL increases.

The distribution used in the K-σ readiness model is usually a Weibull because it can easily be skewed through use of parameters inherent to the distribution, though other distributions could be used if desired. The general form of the equation describing a Weibull distribution on K-factors as a function of TRL is given by

$$k_i(x)\big|_{T_i} = \begin{cases} \left(\frac{2}{\alpha}\right)\left(\frac{x-k_i}{\alpha}\right)\exp\left(-\left(\frac{x-k_i}{\alpha}\right)^2\right) & x \geqslant k_i \\ 0 & x \leqslant k_i \end{cases} \quad (1)$$

where α is a scale parameter,

$$\alpha\big|_{k_i,T_i,L=k_i,\beta=2} = |30\%k_i| - (\mathrm{TRL}-1)\frac{(|30\%k_i| - |5\%k_i|)}{8}.$$

Note that the bounds prescribed in the above equation could be changed if desired and will likely depend on the specifics of the

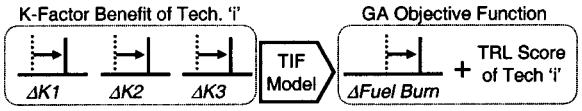

Fig. 2 Typical TIES representation of technology in terms of point estimates on K-factor deltas

problem being considered. However, the settings given above are generally a good starting point for any given K-factor.

The K-σ model offers a realistic means of simulating the impact of technology risk through probabilistic degradation of benefit. It is very flexible and simple, and though the example given here is applied to a single K-factor, it is easily extended to more complex technology models involving multiple K-factors. Note that the K-σ model is slightly conservative in its allowance for technology benefit, due primarily to the considerable degradation in K-factor benefit in moving from a TRL of 9 to 8. The bounding model assumed in this example can be modified to reach outside the baseline and nominal benefit limits if so desired. This paper will implement this technology readiness model as part of the GA-TIES technology selection method.

K-σ/GA-TIES Analysis Method

The K-σ technology risk model can be integrated into the TIES methodology in a fairly straightforward manner. To understand how this can be done, first consider the GA-TIES method as it is used today. Typically, when a TIES study is used to find an optimal technology set, the first step is to decide on a set of technology K-factors that will be used to model the technologies. Next, a pool of promising technology concepts is created and the impact of each technology under consideration is quantified in terms of deltas in these K-factors. This is usually achieved via a delphi-type exercise involving a group of technology experts. The resulting K-factor data is then assembled into a technology impact matrix (TIM). Once this is done, technology incompatibilities and enabling relationships are identified and encoded in the form of a compatibility matrix and an enabling matrix. Finally, each of the technologies is scored on a TRL rating scale (again, see Mavris and Roth [1] for a detailed discussion on the mechanics of the TIES analysis method).

At this point, all of the basic characteristics of the technologies have been encoded into a few matrices of numbers that embody the fundamental nature of each technology. These matrices can be quickly and accurately evaluated to calculate benefit of any arbitrary combination of technologies, provided that a technology impact forecasting (TIF) model is available. As mentioned previously, a TIF is essentially nothing more than a set of response surface equations for the system performance FoMs as a function of the K-factors.

The technology representation for any given technology in the candidate pool consists of a vector of point estimates on K-factor deltas as illustrated in Fig. 2. These point estimates can be plugged into the TIF model to yield point estimates on how each technology impacts overall system performance. This information can then be used in conjunction with the TRL scores as components in an objective function for GA optimization. The GA operates on the TIES model by picking various combinations of technologies, analyzing the results, and comparing their fitness using an objective function that is a weighted linear combination of the various FoMs:

$$\text{obj} = \alpha\left(\sum_i 10 - \text{TRL}_i\right) + \beta(\text{FoM1}) + \gamma(\text{FoM2}) + \ldots \quad (2)$$

where the sum of the weights α, β, γ, etc., would generally be 1.0.

The K-σ model for technology risk builds on this basic process by using the TRL scores as a basis to introduce a probabilistic degradation of the K-factor vectors associated with each technology. The lower a technology's TRL, the more the K-vector is degraded from the nominal benefit. This concept is illustrated in Fig. 3, which shows the K-vector for a given technology being expressed in terms of distributions on the K-factor deltas. The resulting performance will necessarily be a distribution of values as well. Since the technology readiness is explicitly encoded into the TIES model, it is not necessary to use TRL as a component in the GA objective function. Instead, the objective function can now be a pure linear function of performance FoMs:

$$\text{obj} = \beta(\text{FoM1}) + \gamma(\text{FoM2}) + \delta(\text{FoM3}) + \ldots . \quad (3)$$

The primary difference in the two formulations as far as the genetic algorithm is concerned is that in the former scheme, the objective function was purely deterministic—the TIES model always returns the same value for technology benefit for a given the set of technology inputs. The K-σ model will *never* return the same value for technology benefit twice, even if identical technology inputs are evaluated repeatedly. This is because the distributions on K-factors effectively introduce an element of random noise into the objective function evaluation.

The advantage of a GA-enabled technology selection is that it works on *populations* of designs that are evolved over many generations. Thus, the presence of noise in the objective function evaluation does not impede the GA's march toward a global optimum. Even though no single comparison between two technology sets will yield precisely the same result, the GA will still find the set of technologies that optimizes the objective function *in the mean*. Moreover, this final solution will naturally tend towards the most *robust* solution, which is the solution that exhibits the best compromise between minimum design variation and maximum performance benefit.

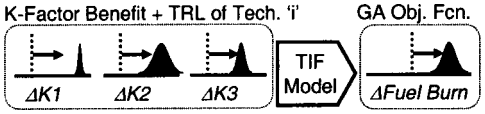

Fig. 3 Calculation of technology benefit using the K-σ technology readiness model

Application to a Typical Commercial Engine Technology Selection Problem

Perhaps the most expedient means of illustrating this model and its advantages is to demonstrate it on a typical technology selection problem of current interest. The objective of this section is to do precisely that. It should be noted that this problem is quite representative of those encountered in industrial practice, and is in fact based on a larger study conducted by the authors for GE Aircraft Engines.

Problem Description. The technology study considered is based on that described in Ref. [1] and consists of a set of 40 technology concepts. This includes ten high pressure compressor technologies, four combustor technologies, nine high pressure turbine technologies, seven frame/sump/bearing technologies, and ten low pressure spool technologies. These technologies were selected and evaluated in conjunction with experts from GE Aircraft Engines. The technology metrics used to evaluate technology impact consist of 11 factors, listed in Ref. [1], and were assembled into a 11×40 TIM such that each row contained all information necessary to evaluate a single technology in the TIF model.

The baseline engine is a current state-of-the-art high bypass commercial turbofan engine and the baseline aircraft is a notional twin-engine long-range wide-body commercial transport. The primary performance figure of merit of interest for this problem is change in 6,000 nmi mission fuel consumption relative to the baseline (no technologies) configuration. In addition, each tech-

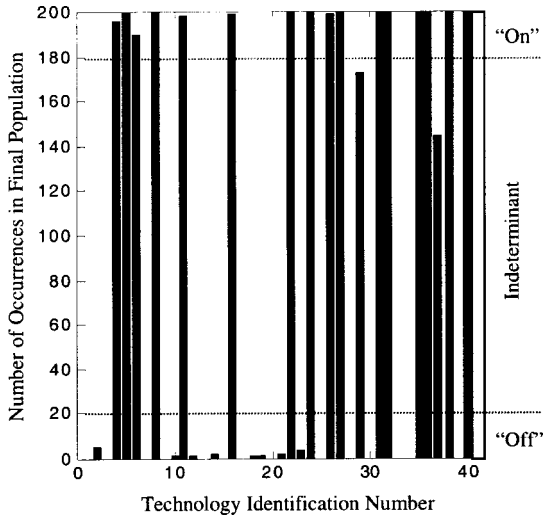

Fig. 4 Converged technology solution set for shop cost+fuel burn objective function

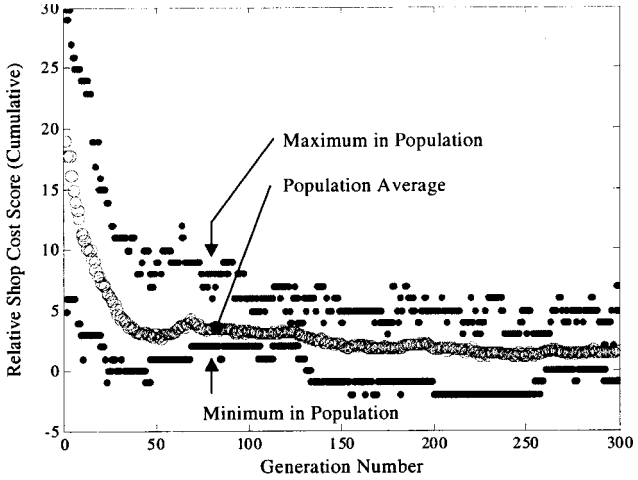

Fig. 6 Relative shop cost convergence history for 50% shop cost+50% fuel burn objective weights

nology was rated using TRL scores for technology risk and a "relative shop cost score." The former was described previously, while the latter is an ordinal ranking on manufacturing cost of each technology relative to the current technology baseline. For example, a score of "0" would indicate a technology of comparable manufacturing cost to current methods, a "+1" would indicate slightly higher cost, "+2" is much more costly, etc. The analysis model and setup is described in detail in Ref. [1].

Results. The 40-technology problem described previously was evaluated for several scenarios such that the differences in results could be compared to deduce the impact of implementing the K-σ technology risk model. Specifically, three scenarios are evaluated: a reference case in which the technology selection was based purely on 6 K fuel burn and relative shop cost only (meaning TRL is not used in the objective function); a simple TRL treatment wherein TRL is used as one of the components in the GA objective function; and a final case wherein the K-σ model is used.

One might intuitively expect that the "no-risk model" reference case would tend to be the solution incorporating the most technologies. This is because the objective function only forces the GA to balance the undiscounted technology benefit against relative shop cost. In the other extreme, if TRL is included in the objective function with a weight equal to both shop cost and 6 K fuel burn, one would expect that any technology with a low TRL score would be eliminated quite readily unless it showed exceptional potential for improving either shop cost or performance.

The analysis results for these two cases indicate that this is precisely the case. The results for the no-TRL case are shown in Fig. 4 and typical convergence histories for fuel burn and shop cost as a function of number of generations is shown in Fig. 5 and Fig. 6, respectively. Figure 4 is a bar chart showing which technologies were selected by the GA. The abscissa of this chart is a technology label, numbered from 1 to 40. The ordinate of the chart shows the number of occurrences each technology was present in the final (converged) population. In this case, the population size was set at 200, so a technology having a score of 200 in Fig. 4 indicates that that technology was uniformly present in the converged population. Similarly, a score of zero indicates that the technology was extinct from the final population, implying that it was not desirable for improving the objective function.

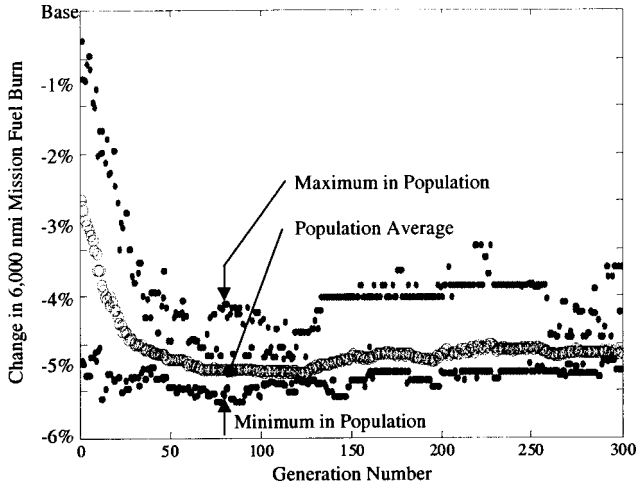

Fig. 5 6000 nmi mission fuel burn convergence history for 50% shop cost+50% fuel burn objective weights

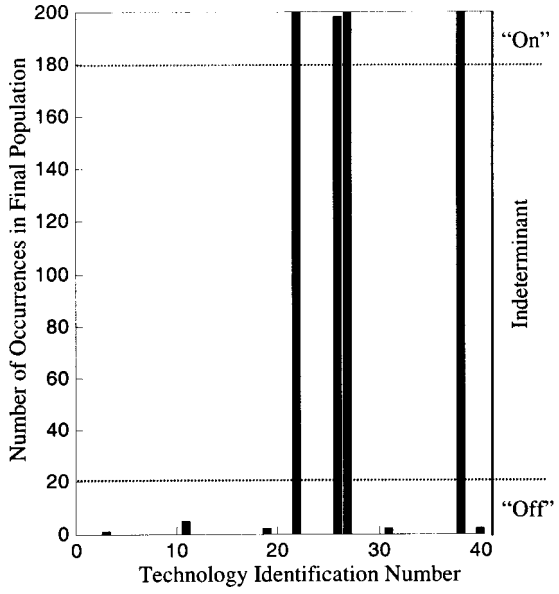

Fig. 7 Converged technology solution set for 33% shop cost +33% fuel burn+33% TRL objective weights

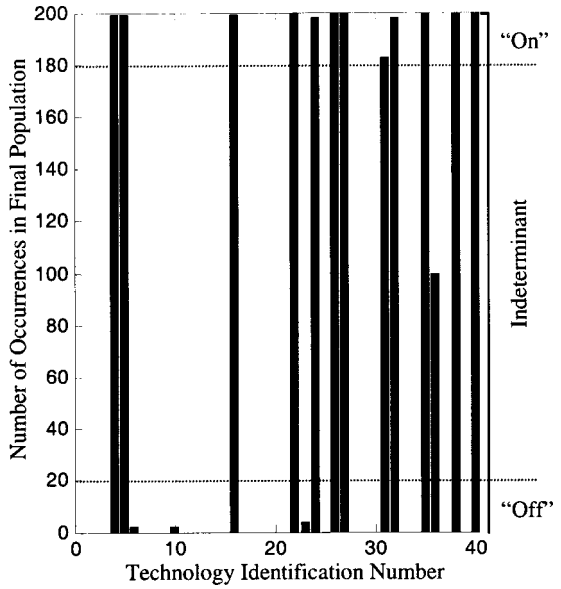

Fig. 8 Converged technology solution set for shop cost+fuel burn objective function with K-σ risk model

Since the genetic algorithm injects mutations into the population with a relatively high probability (20% in this case), there is some degree of random noise in the final solution. Consequently, a technology that is present in 90% or more of the final population (i.e., a score of greater than 180) is taken to be part of the optimal technology solution set whereas any technology not present more than 10% of the time is taken to be excluded from the optimal set. Scores of between 10% and 90% are indeterminate. Thus, Fig. 4 indicates that technologies 4, 5, 6, 8, 11, 16, 22, 24, 26, 27, 31, 32, 35, 36, 38, and 40 are part of the optimal technology solution set if relative shop cost and fuel burn are the only considerations in the objective function. Technologies 29 and 37 are indeterminate.

The convergence histories given in Fig. 5 and Fig. 6 give some insight as to how the GA arrived at this solution. These figures show a precipitous drop in both objective functions during the first 50 generations, indicating that the GA is finding technology combinations that benefit both objectives. After generation 50, the solution is largely converged, as evidenced by the relatively narrow average dispersion between the minimum, maximum, and average objective in the population. One can see that in the last 150 generations the average shop cost decreases slightly at the expense of a slight increase in fuel consumption, indicating that the GA is finding it desirable to trade some performance in the interest of reduced cost.

The solution for the shop cost/fuel burn/TRL case is shown in Fig. 7. In this case, TRL is given an objective weighting equal to fuel burn and shop cost (i.e., 1/3 weight on each). The change in the optimal technology solution set is precipitous, as evidenced in Fig. 7. In this case, only technologies 22, 26, 27, and 38 are selected, with all others being rejected. The convergence history for this case is similar to that shown in Fig. 5 and Fig. 6 and is not shown in the interest of brevity.

The results for the GA solution incorporating the K-σ model are shown in Fig. 8. As one might expect, the results are somewhat intermediate relative to the previous scenarios. In this case, technologies 4, 5, 16, 22, 24, 26, 27, 31, 32, 35, 38, and 40 are optimal relative to the objective function, which includes only fuel burn and relative shop cost. The impact of the K-σ model in practice is to degrade the fuel burn benefit obtained from the technologies, so it is perhaps no surprise that the results obtained with this model are intermediate.

The end result of this analysis is a technology set that can serve as a starting point to begin more detailed technology trade studies. In this regard, the method described herein could be thought of as a screening tool for technologies not unlike the perturbation-based technology analysis methods used today. However, the methods described herein also account for risk as well as the various compatibility and enabling relationships amongst technologies, whereas classical methods do not. For small studies involving only a handful of technology options, it is possible to devise ''one-on'' and ''one-off'' perturbation studies that account for these relationships. However, as the number of technologies under consideration increases, the classical methods become increasingly limited in the scope and accuracy of their results. The present method has no such limitation.

Conclusions

- The solution obtained using the K-σ model for technology risk is truly the robust solution: the optimal compromise between technology uncertainty and performance benefit.
- The K-σ model provides a good compromise between expediency (available with the TRL approach) and accuracy (enabled through mapping of distributions to TRLs).
- K-σ model as implemented herein should provide a slightly conservative estimate of which technologies benefit a given objective function. This is useful in determining which subsets of technologies are most promising to be carried forth into detailed product development.
- The applicability of the GA–Monte Carlo method is broader than technology risk. The technique can be used to find a robust solution to *any* engine design problem.
- This research provides a first step towards the development of even more sophisticated and capable analysis methods that would have provisions for other factors that must be considered in technology selection, particularly technology impact on *budget, schedule,* and *manpower/resources available*.

Acknowledgments

The authors would like to thank Dr. Michelle Kirby for her contributions to this paper, particularly with regard to development of fundamental theoretical principles used herein. We would also like to acknowledge the support of GE Aircraft Engines and the Office of Naval Research.

References

[1] Roth, B. A., German, B. J., and Mavris, D. N., 2001, ''Adaptive Selection of Engine Technology Solution Sets From a Large Combinatorial Space,'' 2001 AIAA/ASME/SAE Joint Propulsion Conference, Salt Lake City, UT, July 8–11, Paper No. AIAA2001-3208.

[2] Roth, B., and Mavris, D. N., 2001, ''Commercial Engine Architecture Selection in the Presence of Uncertainty and Evolving Requirements,'' 15th International Society of Air Breathing Engines, Bangalore, India, Sept. 2–7, Paper No. ISABE2001-1169.

[3] Kirby, M. R., and Mavris, D. N., 2000, ''A Method for Technology Selection Based on Benefit, Available Schedule and Budget Resources,'' 5th World Aviation Congress and Exposition, San Diego, Oct., Paper No. AIAA2000-01-5563.

[4] Goldberg, D., 1989, *Genetic Algorithms in Search, Optimization, & Machine Learning*, Addison-Wesley, Reading, MA, p. 27.

[5] Kirby, M. K., and Mavris, D. N., 1999, ''Forecasting Technology Uncertainty in Preliminary Aircraft Design,'' 4th World Aviation Congress and Exposition, San Francisco, CA, Oct. 19–21, Paper No. SAE1999-01-5631.

Characterization of Ceramic Matrix Composite Fasteners Exposed in a Combustor Linear Rig Test

M. J. Verrilli
Materials Research Engineer

D. Brewer

NASA Glenn Research Center,
21000 Brookpark Road
Cleveland, OH 44135-3191

Combustion tests on SiC/SiC CMC components were performed in an aircraft combustion environment using the rich-burn, quick-quench, lean-burn (RQL) sector rig. SiC/SiC fasteners were used to attach several of these components to the metallic rig structure. The effect of combustion exposure on the fastener material was characterized via microstructural examination. Fasteners were also destructively tested, after combustion exposure, and the failure loads of fasteners exposed in the sector rig were compared to those of as-manufactured fasteners. Combustion exposure reduced the average fastener failure load by 50% relative to the as-manufactured fasteners for exposure times ranging from 50 to 260 hours. The fasteners exposed in the combustion environment demonstrated failure loads that varied with failure mode. Fasteners that had the highest average failure load, failed in the same manner as the unexposed fasteners. [DOI: 10.1115/1.1639005]

Introduction

A major focus of NASA's enabling propulsion materials (EPM) program was development of advanced ceramic matrix composites (CMC's) for turbine engine combustor liners. CMC's offer great potential to improve turbine engine performance by reducing cooling requirements and NOx emissions by operating at higher temperatures than materials used typically for hot structures, such as Ni-base superalloys. A melt-infiltrated SiC fiber reinforced SiC matrix material (MI SiC/SiC) was the result of the collaborative efforts of NASA, General Electric, and Pratt & Whitney under the EPM program, [1].

Concurrent with EPM material development activities, a combustion rig was designed to test MI SiC/SiC components. The rich-burn, quick-quench, lean-burn (RQL) sector rig was designed and fabricated to demonstrate the structural durability of the SiC/SiC liners in a combustion environment where stresses, temperatures, and pressures would accurately reflect the operating conditions found in a turbine engine, [2,3]. The design of the RQL sector rig includes several different MI SiC/SiC component geometries for the combustor liner set, employing three different configurations to attach the CMC's to the metallic back structure. Attachments and fasteners are critical design features, requiring detailed attention and understanding for the successful insertion of CMC components into gas turbine engines.

In this paper, characterization of one fastener concept used in the sector rig, the Miller fastener, [4], is discussed. The effect of combustion exposure on the fastener material was characterized via microstructural examination. Properties of fasteners exposed to a combustion environment for up to 260 hours during operation of the RQL sector rig were obtained through destructive testing and are compared to those of as-manufactured fasteners.

Material

Fasteners were machined from eight-ply MI SiC/SiC composite panels, manufactured by Honeywell Advanced Composites. The panels consisted of a slurry-cast, melt-infiltrated SiC matrix, reinforced with Sylramic SiC fibers in a $[0/90]_s$ lay up. The fiber tows were woven into 5-harness satin weave cloth. Fiber tow spacings of 18 and 22 ends per inch were utilized to manufacture the panels, resulting in a nominal fiber volume fraction of 35 and 42%, respectively. More details on the material can be found in Ref. [1].

Fastener Configuration

The Miller fastener was developed to attach nozzle and combustor structural CMC components in an aircraft gas turbine engine, [4]. The configuration used for the MI SiC/SiC combustor liners is shown in Fig. 1. A schematic of the combustor liner attachment system is shown in Fig. 2. The combustor liners are reinforced with additional plies in the region of the fastener hole. The Miller fastener assembly consists of a metallic threaded clevis that supports a pin through the CMC shank. A Belleville washer provides compliance between the back structure and the threaded clevis. The assembly is completed with metallic nut to draw the CMC liner to the back structure. Three-dimensional finite element analyses were used to develop the fastener design, [4]. Benchmark mechanical tests were conducted to minimize head design angle, hole diameter, and distance of the hole to the end of the fastener.

Combustion Exposure

The RQL sector rig was designed by Pratt & Whitney under the HSR program and was installed at NASA Glenn in 1998. The rig contains two rich zone liner cans transitioning to a 60° sector lean burn zone. Figure 3 is a schematic of the rig, along with images of

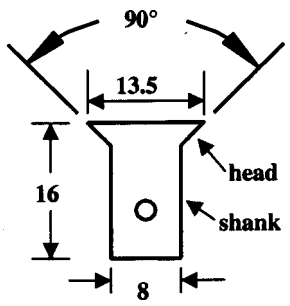

Fig. 1 Schematic of SiC/SiC fasteners. Dimensions are in mm.

Contributed by the International Gas Turbine Institute (IGTI) of THE AMERICAN SOCIETY OF MECHANICAL ENGINEERS for publication in the ASME JOURNAL OF ENGINEERING FOR GAS TURBINES AND POWER. Paper presented at the International Gas Turbine and Aeroengine Congress and Exhibition, Amsterdam, The Netherlands, June 3–6, 2002; Paper No. 2002-GT-30459. Manuscript received by IGTI, Dec. 2001, final revision, Mar. 2002. Associate Editor: E. Benvenuti.

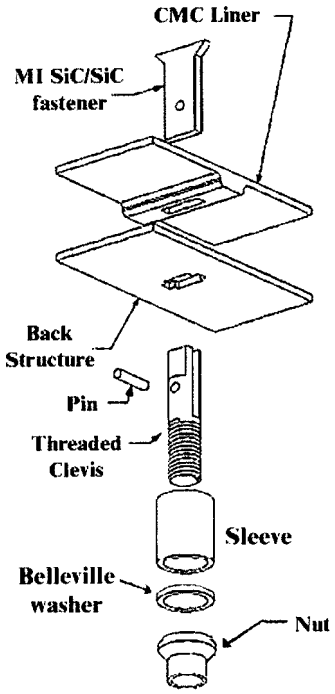

Fig. 2 Combustor liner fastener assembly

the individual components. A full liner set consists of 28 liners of 6 different part geometries. Testing was conducted using a cycle designed to approximate the pressures, temperatures, and flow rates of an aircraft turbine engine combustor, [5].

Several liners were removed from the sector rig after 115 hours to conduct post-exposure analyses, [3]. The rig was reassembled and 145 hours of additional testing was conducted. In addition, a few liners were removed during rig operation when periodic inspections revealed potential damage. After completion of 260 hours of operation, the rig was disassembled and all MI SiC/SiC combustor liners were removed.

The liner set included Miller fasteners that held 17 of the 28 components in the rig. As a result of the events described above, the liner set available for analyses included fasteners exposed for 53, 115, 145, 207, and 260 hours.

Fig. 3 Configuration of the rich-burn, quick-quench, lean-burn (RQL) SiC/SiC sector rig

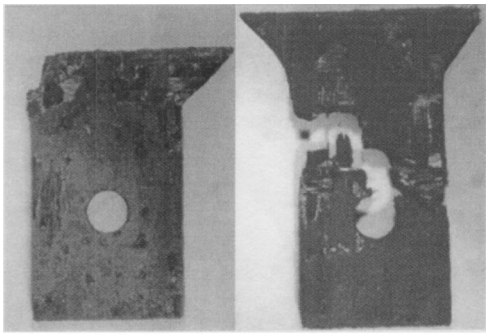

Fig. 4 Damage of fasteners after removal from the sector rig

Post-Exposure Examination

All fasteners were visually inspected to document their post-exposure condition. Damage in the head of the fastener was observed for about 60% of the fasteners removed intact. An extreme example of the observed damage mode is shown in Fig. 4(*a*). This particular fastener could not be subjected to post-exposure destructive testing, but the majority of fasteners with cracks and chipping in the ''ears'' such as this had less severe damage and thus could be tested. Other fasteners failed in the shank region (Fig. 4(*b*)). Damage in the shank was most often observed when

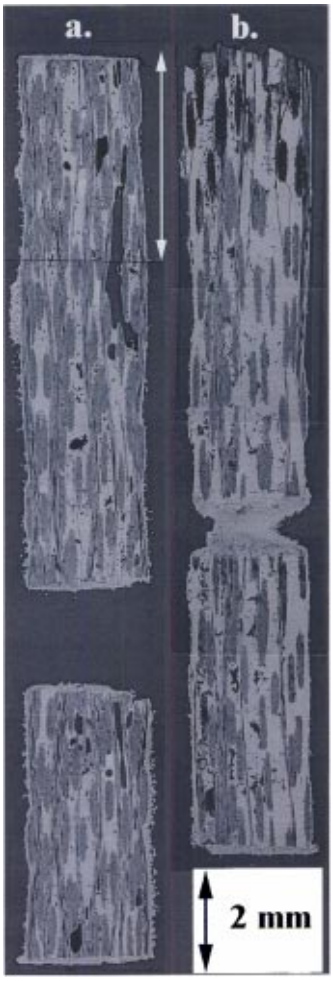

Fig. 5 Cross sections of SiC/SiC fasteners, (*a*) as-manufactured, (*b*) exposed for 145 hours. The arrow indicates the head region of both fasteners.

difficulties were encountered while removing the metallic nut from the threaded clevis (Fig. 2). About 25% of the total fastener set was not suitable for destructive testing because of either severe ''ear'' damage such as in Fig. 4(*a*) or failure while attempting to remove them from the rig.

Several fasteners were mounted for microscopic examination. The fasteners were held under vacuum to enable pores and cavities to out-gas. The metallurgical samples were then submerged in epoxy. The specimens were then placed in a pressure chamber and held at 10 MPa in a nitrogen environment to force epoxy into the pores and damage locations. After curing, the fasteners were then sectioned and lapped in preparation for final polishing, prior to examination.

A comparison of the microstructures of an as-manufactured fastener and one that was exposed in the combustion environment for 145 hours is shown in Fig. 5. The longitudinal, through-thickness cross sections reveal porosity in both fasteners. The large pore, in the as-manufactured fastener, exists in the head region. The most notable feature can be seen in the head of the exposed fastener in the form of fiber and composite damage. The dark regions indicate locations where fibers tows are missing due to preferential attack of the Sylramic fibers. This attack is due to the reaction of the boron nitride fiber interface with water vapor, present in the combustion gases, [1,6]. Recession of SiC in a combustion environment can also occur due to SiO_2 scale volatility, [7].

Mechanical Testing of Fasteners

As-manufactured and exposed fasteners were destructively tested at room temperature to measure their failure loads using a servo-hydraulic test machine. A fixture was machined from a superalloy with the same fastener hole geometry of the CMC combustor liners (Fig. 6). A clevis and pin, machined for fastener attachment in sector rig, were used to connect the fasteners to a pull rod. Both ends of the fixture were gripped using the wedge grips of the test machine. Fasteners were tensile tested to failure under load control at a rate of 20 N/sec.

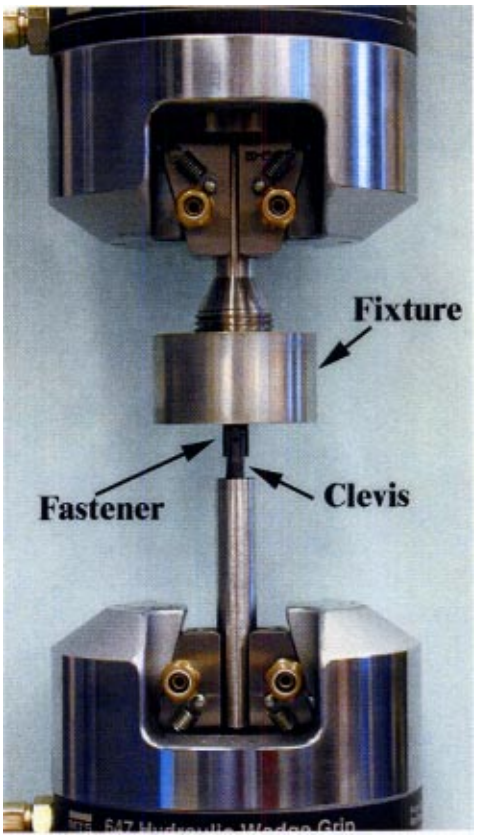

Fig. 6 Configuration for tensile testing of SiC/SiC fasteners

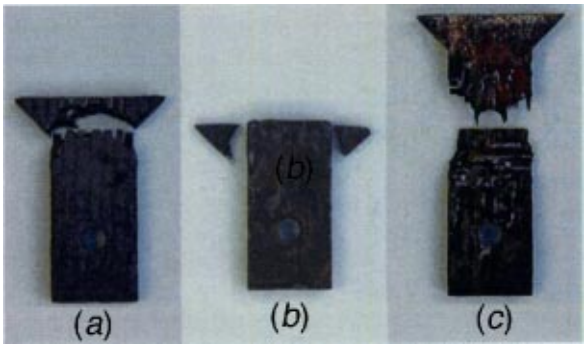

Fig. 7 Failure modes of tensile-tested SiC/SiC fasteners, (*a*) as-manufactured material, (*b*) ''ear'' shear failure of exposed material, (*c*) failure associated with pre-existing cracks

Discussion

The tensile failure mode observed for all the as-manufactured Miller fasteners is shown in Fig. 7(*a*). Approximately 17% of the combustion-exposed fasteners failed in the same manner, which is the desired failure mode, [4]. Failure of the fastener through shear failure of the ''ears'' of the head occurred in 70% of the exposed fasteners (Fig. 7(*b*)) and was associated with observed ''ear'' damage documented prior to destructive testing. The failure mode of the rest of the exposed fasteners was associated with pre-existing cracks, such as seen in Fig. 7(*c*).

The average failure load for the Miller fasteners as a function of failure mode is shown in Fig. 8. The as-manufactured fasteners failed at an average load of about 1900 N, while combustor-exposed fasteners that failed in the same mode had a 25% lower failure load. Failure of the fastener through ''ear'' shear failure yielded a failure load of 900 N. Those fasteners that failed due to pre-existing cracks had the lowest average failure load, 550 N.

The effect of exposure time can be seen by examining data for fasteners that attached one combustor liner part, the lean transition liner (LTL). The RQL sector rig liner set consisted of twelve

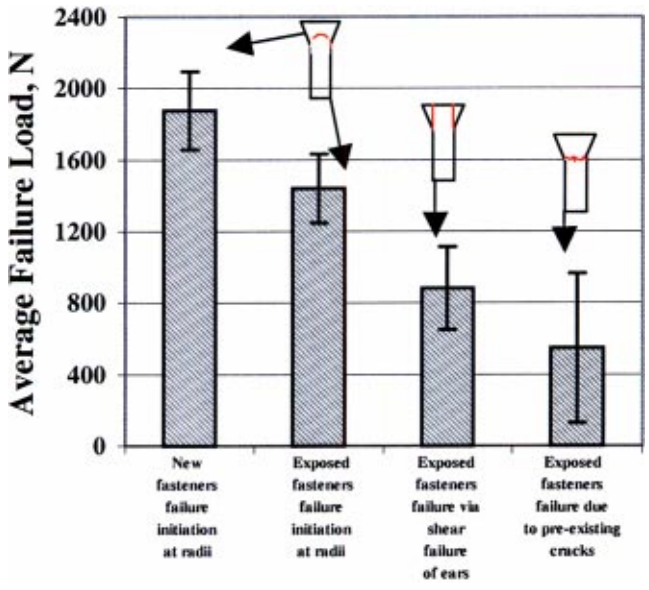

Fig. 8 Failure mode versus failure load for SiC/SiC fasteners tensile tested at 25°C

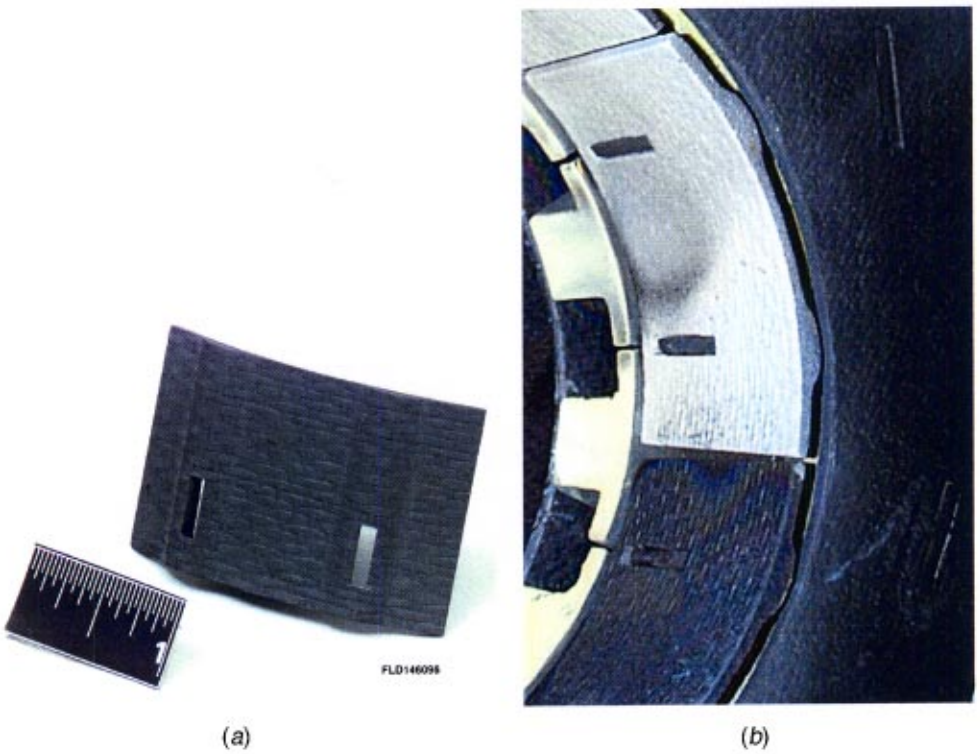

Fig. 9 Lean transition liners, (*a*) as-manufactured part, (*b*) installed in the sector rig

LTL's, each held in place with two Miller fasteners, Fig. 9. The exposure temperatures of the different liner parts in the sector rig varied. In addition, combustion gas chemistry and flow rate varied in different regions of the rig. Examination of fastener data for only one part can eliminate potential failure load differences due to varying exposure conditions. During the course of the 260 hours of rig operation, several of the LTL's and their fasteners were removed for reasons described earlier, resulting in the largest number of fasteners exposed for different times from a single part type. To eliminate the effect of failure mode on failure load, only data for LTL fasteners that failed via shear of the ''ears'' is shown as a function of exposure time in Fig. 10. Data for the as-manufactured fasteners is shown as well. Exposure of 50 hours reduced failure loads by 50% relative to the as-manufactured fasteners. The average fastener failure load of about 900 N was the same for all exposure times, up to the maximum of 260 hours. Note that during sector testing, LTL fasteners reached a maximum temperature of about 1200°C at the head surface subjected to combustion flow.

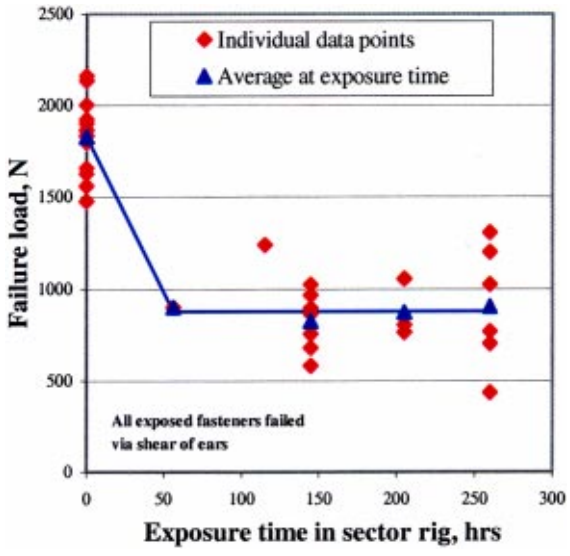

Fig. 10 Lean transition liner fastener failure loads after exposure in the sector rig

Comparing data for as-manufactured and for exposed fasteners that failed in the same manner as unexposed ones, an assessment of the material degradation due to combustion exposure can be made. As shown in Fig. 8, a 25% reduction in failure load was measured for fasteners after combustion exposure. Additional damage as described above was likely responsible for the switch of failure mode and further reduction of average strength for exposed fasteners.

Summary and Conclusions

Damage observed in fasteners removed from the sector rig was due to several factors. Loads imposed during fastener installation and/or removal likely caused some cracking. Rig mechanics had no prior experience with CMC hardware and may have accidentally induced damage during liner installation.

Also as stated earlier, difficulties were sometimes encountered while removing the metallic nut from the threaded clevis, resulting in overloading of CMC fasteners. Material recession due to the combustion environment exposure also occurred, as indicated by Fig. 5. A combination of installation damage and water vapor reaction may have resulted in damage that manifests itself as fasteners with low post-exposure failure loads. Reduction of the tensile loads imposed by the metallic clevis and nut during combustor testing likely resulted loosening of some of the Miller fasteners. Damage in the ''ears'' of the head due to relaxation of the nut torque was observed in fasteners after hot acoustic testing of CMC nozzle liners [8]. Despite the observed cracking and material recession, the Miller fasteners held the CMC liners in place

during combustion testing and thus displayed the desired damage tolerance of a CMC component while operating in a harsh environment.

References

[1] Brewer, D., 1999, ''HSR/EPM Combustion Materials Development Program,'' Mater. Sci. Eng., A, **261**, pp. 284–291.

[2] Brewer, D., Ojard, G., and Gibler, M., 2000, ''Ceramic Matrix Composite Combustor Liner Rig Test,'' Proceedings of Turbo Expo 2000: ASME Turbo Expo, Land, Sea & Air, May 8–11, Munich, Paper No. TE00CER03-03.

[3] Ojard, G., Stephan, R., Naik, R., Gibler, M., Cairo, R., Linsey, G., Hornick, J., and Brewer, D., 2000, ''NASA Rich Burn Quick Quench Lean Burn Sector Rig SiC/SiC CMC Testing,'' Proceedings of 24th Annual Conference on Composites, Materials, and Structures, Cocoa Beach, FL., Jan.

[4] Miller, R. J., Moree, J. C., and Jarmon, D. C., 1998, ''Design and Validation of High Temperature Composite Fasteners,'' Proceedings of the 39th AIAA/ASME/ASCE/AHS/ASC Structures, Structural Dynamics, and Materials Conference, Long Beach, CA., Apr. 20–23, 1998, AIAA Paper 98-1998.

[5] Verrilli, M., Martin, L., and Brewer, D., 2002, ''RQL Sector Rig Testing of SiC/SiC Combustor Liners,'' NASA Technical Memorandum 2002-211380, Mar.

[6] More, K. L., Tortelli, P. F., and Walker, L. R., 2001, ''Effects of High Water Vapor Pressures on the Oxidation of SiC-Based Fiber-Reinforced Composites,'' Mater. Sci. Forum, **369–372**, Part I, pp. 385–393.

[7] Robinson, R. C., and Smialek, J. L., 1999, ''SiC Recession Caused by SiO_2 Scale Volatility Under Combustion Conditions: I, Experimental Results and Empirical Model,'' J. Am. Ceram. Soc., **82**(7), pp. 1817–1825.

[8] Verrilli, M., 1998, unpublished data.

T. Fett
D. Munz
G. Thun

Forschungszentrum Karlsruhe,
Institut fur Materialforschung II,
Postfach 3640,
D-76021 Karlsruhe, Germany

Fracture Toughness Testing on Bars Under Opposite Cylinder Loading

Bars loaded by opposite concentrated forces via rollers are appropriate test specimens for the determination of the fracture toughness, K_{Ic}, and the crack resistance curve (R-curve) of ceramic materials. In this paper stress solutions for the proposed test specimens are provided, as well as the stress intensity factor and the T-stress solutions. As practical applications, R-curves are determined for a soft PZT ceramic and several alumina ceramics. [DOI: 10.1115/1.1639003]

Introduction

Various failure modes are responsible for failure and finite lifetimes of ceramic materials. Spontaneous failure occurs when the applied stress reaches the strength of the material or, in terms of fracture mechanics, when the stress intensity factor, K_I, the loading quantity in linear-elastic fracture mechanics, reaches or exceeds the fracture toughness, K_{Ic}, of the material for the most severe crack in a component. Therefore, for the fracture mechanics approach K_{Ic} must be known for the spontaneous failure behavior to be assessed. In the case of ideally brittle materials, the fracture toughness is independent of the crack extension and, consequently, identical with the stress intensity factor, K_{I0}, necessary for the onset of stable crack growth. It is a well-known fact that failure of several ceramics is influenced by an increasing crack growth resistance curve (R-curve). For piezoelectric ceramics the crack growth resistance behavior is substantially more complex than for other ceramics. In the polarized state and especially in the case of an externally applied electrical field, the R-curve is affected via electrical-mechanical coupling.

The measurement of fracture toughness requires test specimens with atomistically sharp cracks. In metals such cracks are introduced as fatigue cracks starting from a notch. In ceramics the creation of such cracks is more difficult.

A possibility to create a sharp crack in ceramics is the so-called bridge method, [1,2]. In principle, this procedure may be used not only for crack generation, but also for the determination of R-curves. Unfortunately, the friction conditions and the pressure distribution at the contact area between the bridge ends and the upper surface of the test specimen are not well defined. The same holds for the contact area between the test specimen and the supporting structure.

As a modification of the bridge method, loading via rollers separated by a short distance, d, is proposed (Fig. 1). This test device avoids any uncertainties in interpretation of the support conditions by use of a symmetrical force application via four symmetrically arranged rollers. The measurements can be carried out with simple bending bars (3×4×45 mm) or fragments of shorter length.

Stresses Caused by Two Pairs of Forces

The stresses in a strip of width W and thickness t, loaded by opposite concentrated forces P, have been computed by Filon [3] (see also [4]). Superposition of the results given for one pair of concentrated forces enables the computation of the loading problem illustrated in Fig. 1 (without crack).

We obtain the stress solution for the symmetry line ($x=0$)

$$\sigma_x = -\frac{8P}{\pi W t}\int_0^\infty \frac{\sinh u - u\cosh u}{\sinh 2u + 2u}\cos\frac{ud}{W}\cosh\frac{2uy}{W}\,du - \frac{8P}{\pi W t}\int_0^\infty \frac{2uy}{W}\frac{\sinh u}{\sinh 2u + 2u}\cos\frac{ud}{W}\sinh\frac{2uy}{W}\,du. \quad (1)$$

The resulting stress, σ_x, is plotted in Fig. 2, normalized to the characteristic stress, σ^*:

$$\sigma^* = \frac{2P}{Wt}. \quad (2)$$

Stress Intensity Factors for Single-Edge-Cracked Bars

The stress intensity factors for edge-cracked specimens can be computed from the stresses in the uncracked specimen by use of the fracture mechanics weight function. If σ_x is the stress normal to the prospective crack line and τ is the shear stress at the same location, the mode I stress intensity factor K_I can be computed from

$$K_I = \int_0^a \sigma_x(\eta) h_I(a,\eta)\,d\eta \quad (3)$$

using the model I weight function h_I taken from [5]. The geometric function for the mode I stress intensity factor, denoted as Y_I, is defined here by

$$K_I = \sigma^* Y_I \sqrt{W}, \quad \text{such that} \quad Y_I = \frac{K_I}{\sigma^*\sqrt{W}}. \quad (4)$$

The mode I stress intensity factor is shown in Fig. 3(*a*) as a function of a/W with d/W as a parameter. Table 1 contains values for the geometric function Y_I, defined by Eq. (4).

For the special case $d/W=1$, the geometric function Y_I is fitted from the data of Table 1 for $\alpha = a/W \leqslant 0.6$

$$Y_I = 0.905\alpha^{1/2} - 3.36\alpha^{3/2} + 3.86\alpha^{5/2} + 1.443\alpha^{7/2} - 3.87\alpha^{9/2}. \quad (5)$$

In special applications it may be important to know the stress field over a longer distance from the crack tip. This can be done by including higher order stress terms. Taking into consideration the singular stress term and the first regular term, the near-tip stress field of a cracked body can be described by

Contributed by the International Gas Turbine Institute (IGTI) of THE AMERICAN SOCIETY OF MECHANICAL ENGINEERS for publication in the ASME JOURNAL OF ENGINEERING FOR GAS TURBINES AND POWER. Paper presented at the International Gas Turbine and Aeroengine Congress and Exhibition, Amsterdam, The Netherlands, June 3–6, 2002; Paper No. 2002-GT-30507. Manuscript received by IGTI, Dec. 2001, final revision, Mar. 2002. Associate Editor: E. Benvenuti.

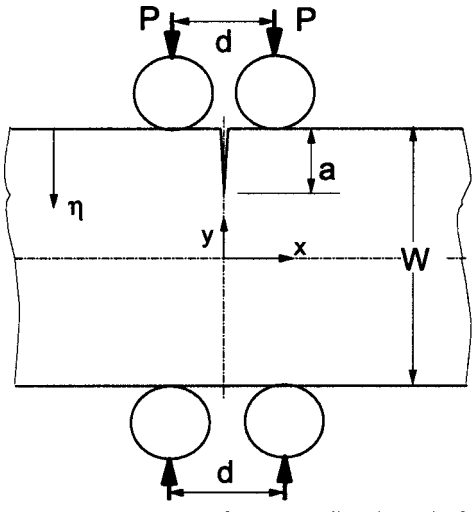

Fig. 1 Controlled fracture test device with force application via four symmetrical rollers

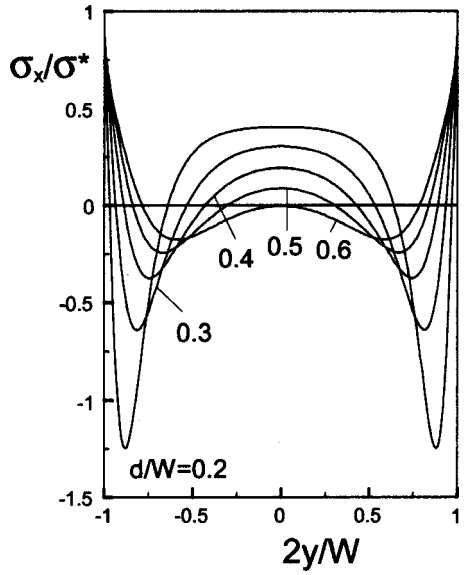

Fig. 2 Axial stresses, σ_x, along the symmetry line $x=0$ for two pairs of concentrated opposite forces

Table 1 Geometric function Y_I according to Eq. (4)

a/W	$d/W=0.6$	0.8	1.0	1.2	1.4
0.05	0.2234	0.2066	0.1686	0.1279	0.0916
0.1	0.1997	0.2196	0.1942	0.1538	0.1136
0.15	0.1346	0.1971	0.1903	0.1578	0.1199
0.2	0.0836	0.1660	0.1746	0.1510	0.1176
0.25	0.0526	0.1384	0.1556	0.1389	0.1103
0.3	0.0403	0.1186	0.1377	0.1250	0.1003
0.35	0.0414	0.1068	0.1224	0.1110	0.0891
0.4	0.0506	0.1011	0.1101	0.0977	0.0774
0.45	0.0641	0.0991	0.0998	0.0850	0.0658
0.5	0.0791	0.0984	0.0902	0.0727	0.0542
0.55	0.0931	0.0968	0.0804	0.0606	0.0431
0.6	0.1041	0.0924	0.0693	0.0483	0.0322
0.65	0.1094	0.0838	0.0564	0.0359	0.0221
0.7	0.1064	0.0703	0.0422	0.0239	0.0132

$$\sigma_{ij}=\frac{K_I}{\sqrt{2\pi r}}f_{ij}(\varphi)+\sigma_{ij,0} \tag{6}$$

$$\sigma_{ij,0}=\begin{pmatrix}\sigma_{xx,0} & \sigma_{xy,0}\\ \sigma_{yx,0} & \sigma_{yy,0}\end{pmatrix}=\begin{pmatrix}T & 0\\ 0 & 0\end{pmatrix} \tag{7}$$

where f_{ij} are the known angular functions for the singular stress contribution. The constant stress term is called the "T-stress."

In Fig. 3(*b*) the T-stress is represented by the biaxiality ratio, β, which is given by the ratio of the T-stress and stress intensity factor according to

$$\beta=\frac{T\sqrt{\pi a}}{K_I}. \tag{8}$$

The curve given in Fig. 3(*b*) can be described by (see [4])

$$\beta=\frac{-0.469+1.8589\alpha+34.527\alpha^2-133.477\alpha^3+127.994\alpha^4}{\sqrt{1-\alpha}}. \tag{9}$$

Knowledge of the stress intensity factor solution enables prediction of the crack growth under increasing force. For a material without an R-curve effect, the crack propagation regions are illustrated in Fig. 4 for the special case of $d/W=1$.

If the initial crack depth, a_0, is shorter than the value a_m corresponding to the maximum stress intensity factor (Fig. 4(*a*), crack extension is unstable up to crack length a_1. Then, stable

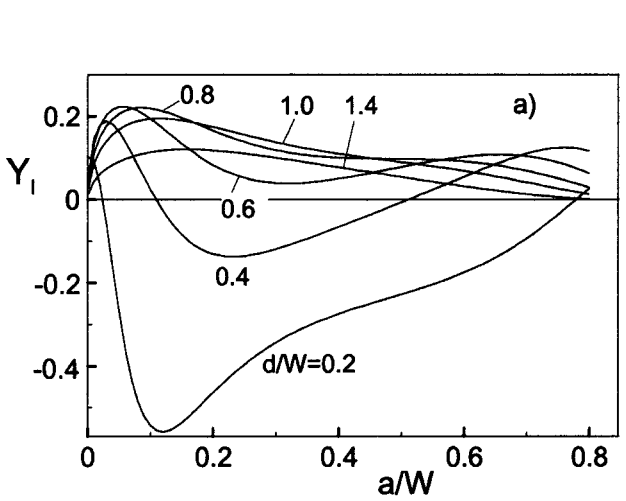

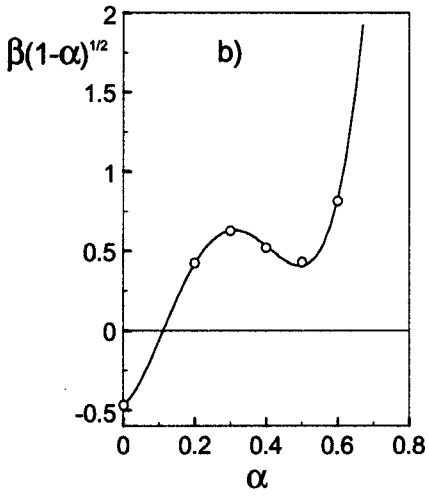

Fig. 3 (*a*) Geometric function Y_I according to Eq. (4); (*b*) biaxiality ratio β for $d/W=1$

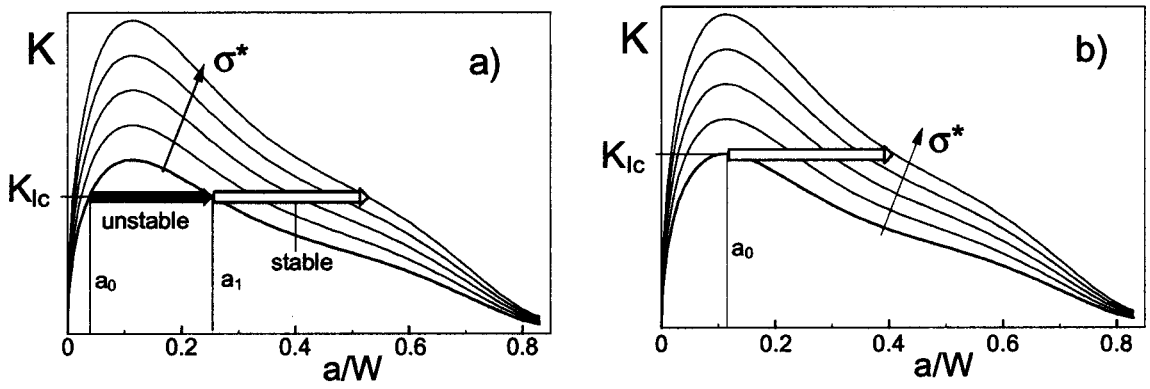

Fig. 4 Crack growth under increasing load; (*a*) initial crack size $a_0 < a_m$, (*b*) $a_0 = a_m$ ($d/W = 1$)

crack propagation takes place. For an initial crack depth $a_0 \geq a_m$, exclusively stable crack growth occurs (Fig. 4(*b*)).

Experimental Setup

An experimental setup for a fracture mechanics test is shown in Fig. 5. A pre-notched bar is loaded via four rollers in order to create a sharp crack. The force $P_{appl} = 2P$ is applied by a half-sphere to the upper rollers. As rollers, cylindrical pins (e.g., hardened steel) may be used. A simple procedure allows the estimation of the R-curve without further equipment.

Pre-notched flexure bars are monotonically loaded. From a force versus time record, the moment of first crack extension can be detected as a "pop-in" (sudden change) of the force. After a further increase of force, the test is suspended. After removing the force, the crack length can be estimated from its intersection at the side surfaces of the test specimen using an optical microscope. In addition, application of a dye penetrant to the cracked but unfractured test specimen allows measurement of the crack depth by observation of the stained fracture surface of the broken test specimen. From the applied force, P, at the instant of unloading, the corresponding crack depth, a, and the respective geometric function, Y_I, the stress intensity factor, K_{IR}, present at the instant of unloading can be computed from Eq. (4). A series of tests suspended at different loads then provides the R-curve $K_{IR} = f(\Delta a)$.

Experimental Results

In order to demonstrate the applicability of the four-roller test device, measurements of crack growth resistance were carried out with a commercial soft PZT ceramic (PIC 151, PI Ceramic, Lederhose, Germany) and an alumina containing about 4 wt% glass phase with a mean grain size of about 5 μm (V38, CeramTec, Plochingen, Germany).

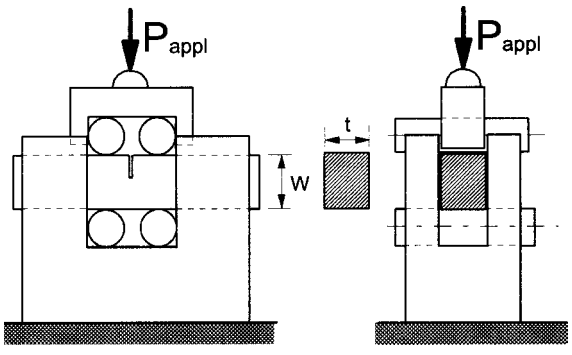

Fig. 5 Device for a four-roller crack extension test

Results on PZT. In the case of the PZT ceramic, V-notches within a range of depths of $a = 0.5-0.55$ mm were introduced into the unpoled test specimens of $3\times4\times45$ mm^3 by use of the razor blade procedure, [6], (see also [7]) and then annealed above the Curie temperature. Then, the test specimens were loaded to different forces in the four-roller testing device, with $d/W = 1$ up to different forces. After unloading, the cracks generated were marked with a dye penetrant so that the crack length a could be easily measured under the optical microscope following fracturing. In Fig. 6(*a*) the typical curvature of the crack front is visible

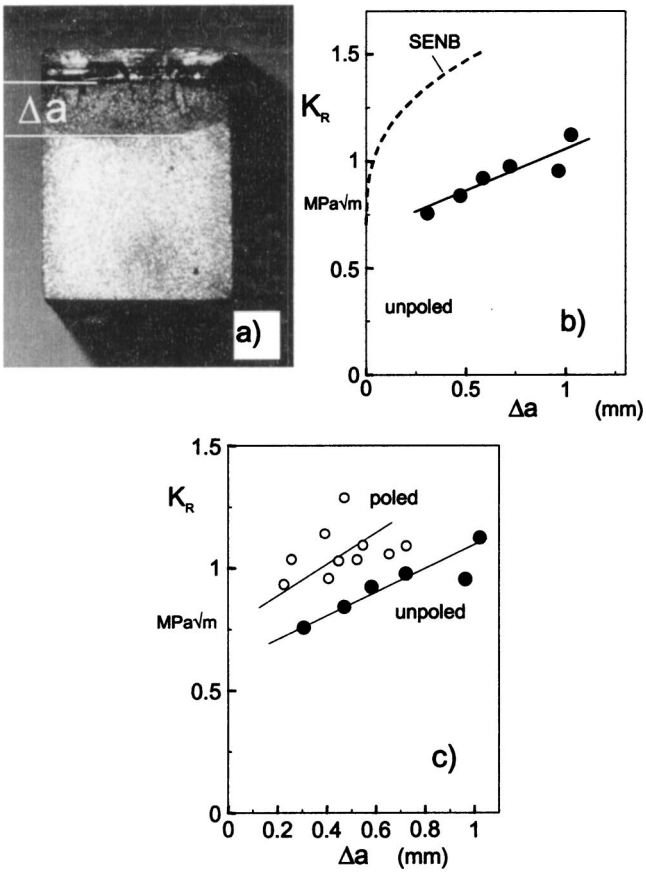

Fig. 6 (*a*) Fractured test specimen, (*b*) crack resistance K_R (R-curve) for unpoled PZT PIC 151 as a function of crack extension (dashed curve: result from controlled bending test, [8]), (*c*) ⊥-poled specimens

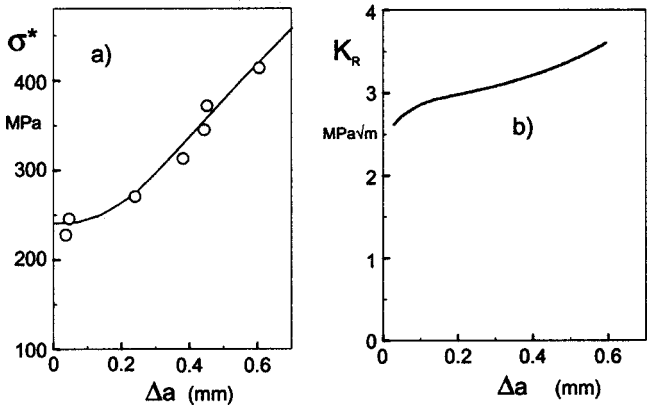

Fig. 7 (*a*) Crack extension as a function of the stress σ^*, (*b*) R-curve for alumina with 4% glass content

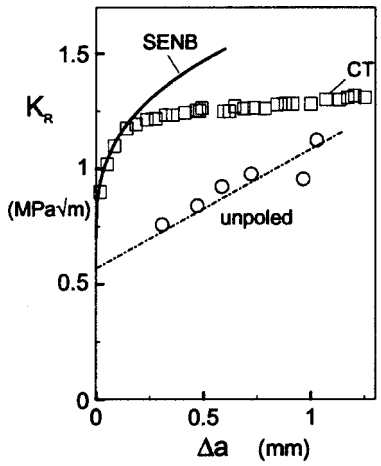

Fig. 8 Comparison of R-curves for poled and ⊥-poled PIC 151 measured with different specimens (results with CT-specimens from Lucato et al. [10])

which is similar to those of metallic materials. This behavior reflects the change of plane-strain conditions in the center of the test specimen to plane stress at the surface.

From the total maximum force $F_{max}=2F$ and the related crack length a, the stress intensity factor K_R was computed according to Eq. (4) with the geometric function Y_I taken from Table 1 by use of a cubic spline interpolation. The results are plotted in Fig. 6(*b*). In addition, the R-curve obtained in a controlled bending fracture test, [8], is shown as a dashed line. The typical result for ceramics is that the R-curve is not a material property but depends on the test specimen and the loading mode (for examples see, e.g., [9]) is also illustrated for this material. A theoretical interpretation of the strongly different R-curves was given in [8].

In Fig. 6(*c*) the influence of the poling state on K_R is shown. The measured test specimens were poled perpendicular to the length axis with the electrodes on the 4×45 mm surfaces. The fact, that the ⊥-poled material exhibits a greater resistance to crack growth is in agreement with results of Lucato et al. [10].

Results on Al_2O_3. Edge-notched bars with an initial relative notch depth of $\alpha_0=a_0/W=0.187$ (standard deviation=0.003) were loaded in the four-roller device up to different stress values σ^*. The crack extensions Δa measured on the fracture surface are plotted in Fig. 7(*a*) versus σ^*. The smoothing curve was used to compute the crack growth resistance K_R. Introducing σ^* and Δa into Eqs. (4) and (5) yields the R-curve $K_R=f(\Delta a)$ which is plotted in Fig. 7(*b*).

Comparison of the R-Curve Results

In Fig. 8 the results from Fig. 6(*b*) obtained with the opposite roller arrangement are compared with results obtained by Lucato et al. [10] with the compact tension (CT) specimen. It can be seen that strongly different R-curves are obtained from two different types of tests.

Experimental evidence of differently pronounced domain switching effects for different test specimens have been found, [8,11]. These differences are explained in [8] by the strongly different σ_x-stresses which have a strong influence on domain switching. Figure 9 shows the σ_x-stresses for the three test specimens. The σ_x-stresses (and especially the T-stress defined as the σ_x-stress at $x-a=0$) are greater by a factor 10 than these obtained by the cylinder loading test.

Conclusions

Rectangular bars loaded by opposite concentrated forces via rollers are appropriate test specimens for the determination of the fracture toughness and the crack resistance curve (R-curve). In the paper the stress solution for the proposed four-roller loading device is provided. For fracture mechanics test specimens containing edge cracks, stress intensity factor solutions as well as a solution for the T-stress term are given in the form of figures and tables. Due to the continuously decreasing stress intensity factor with

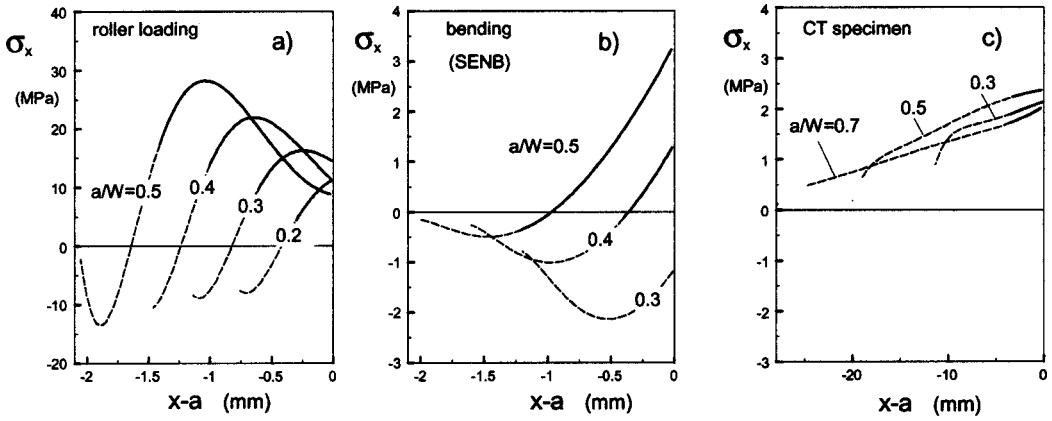

Fig. 9 σ_x-stresses for several relative crack depths a/W ($K_I=1$ MPa$\sqrt{m}$). Solid parts of curves: region of crack propagation, dashed parts: region of the initial notch [8].

increasing crack depth (under constant load), unstable crack propagation is completely prevented. As practical applications, R-curves are determined for a soft PZT ceramic and an alumina with 4% glass content. It should be mentioned that for the R-curves obtained under roller loading and those from different tests may be differences. It is well known that R-curves for ceramics depend on the test specimen geometry, the initial crack length, and on the loading mode (bending, tension, roller loading, etc.). These effects are well understood especially in the case of R-curves based on bridging effects in the wake of a crack.

Acknowledgments

The authors have to thank the Deutsche Forschungsgemeinschaft DFG for financing this work within the SFB 483.

References

[1] Warren, R., and Johannesson, B., 1984, ''Creation of Stable Cracks in Hard Metals Using 'Bridge' Indentation,'' Powder Metall., **27**, pp. 25–29.
[2] Nose, T., and Fujii, T., 1988, ''Evaluation of Fracture Toughness for Ceramic Materials by a Single-Edge-Precracked-Beam Method,'' J. Am. Ceram. Soc., **71**, pp. 328–333.
[3] Filon, L. N. G., 1903, ''On an Approximate Solution for the Bending of a Beam of Rectangular Cross-Section Under any System of Load, With Special Reference to Points of Concentrated or Discontinuous Loading,'' Philos. Trans. R. Soc. London, Ser. A, **201**, pp. 63–155.
[4] Fett, T., Munz, D., and Thun, G., 2001, ''A Toughness Test Device With Opposite Roller Loading,'' Eng. Fract. Mech., **68**, pp. 29–38.
[5] Fett, T., and Munz, D., 1997, *Stress Intensity Factors and Weight Functions*, Computational Mechanics Publications, Southampton, UK.
[6] Nishida, T., Pezzotti, G., Mangialardi, T., and Paolini, A. E., 1996, ''Fracture Mechanics Evaluation of Ceramics by Stable Crack Propagation in Bend Bar Specimens,'' Fract. Mech. Ceram., **11**, pp. 107–114.
[7] Kübler, J., 1997, ''Fracture Toughness Using the SEVNB Method: Preliminary Results,'' Ceram. Eng. Sci. Proc., **18**, pp. 155–162.
[8] Fett, T., Glazounov, A., Hoffmann, M. J., Munz, D., and Thun, G., 2001, ''On the Interpretation of Different R-Curves for Soft PZT,'' Eng. Fract. Mech., **68**, pp. 1207–1218.
[9] Munz, D., and Fett, T., 1999, *CERAMICS, Failure, Material Selection, Design*, Springer-Verlag, Heidelberg.
[10] Lucato, S. L., Lupascu, D. C., and Rödel, J., 2000, ''Effect of Poling Direction on R-Curve Behavior in PZT,'' J. Am. Ceram. Soc., **83**, pp. 424–426.
[11] Glazounov, A. E., Fett, T., Reszat, J. T., Hoffmann, M. J., Munz, D., and Wroblewski, T., 2001, ''Influence of Domain Switching State on R-Curves Interpreted by Using X-Ray Diffraction Study,'' J. Mater. Sci. Lett., **20**, pp. 877–880.

Trend Shift Detection in Jet Engine Gas Path Measurements Using Cascaded Recursive Median Filter With Gradient and Laplacian Edge Detector

Ranjan Ganguli
Assistant Professor,
Department of Aerospace Engineering,
Indian Institute of Science,
Bangalore 560003, India
Mem. ASME

Budhadipta Dan
Student,
Department of Engineering Physics,
Indian Institute of Technology,
Mumbai 400076, India

Trend shift detection is posed as a two-part problem: filtering of the gas turbine measurement deltas followed by the use of edge detection algorithms. Measurement deltas are deviations in engine gas path measurements from a "good" baseline engine and are a key health signal used for gas turbine performance diagnostics. The measurements used in this study are exhaust gas temperature, low rotor speed, high rotor speed and fuel flow, which are called cockpit measurements and are typically found on most commercial jet engines. In this study, a cascaded recursive median (RM) filter, of increasing order, is used for the purpose of noise reduction and outlier removal, and a hybrid edge detector that uses both gradient and Laplacian of the cascaded RM filtered signal are used for the detection of step change in the measurements. Simulated results with test signals indicate that cascaded RM filters can give a noise reduction of more than 38% while preserving the essential features of the signal. The cascaded RM filter also shows excellent robustness in dealing with outliers, which are quite often found in gas turbine data, and can cause spurious trend detections. Suitable thresholding of the gradient edge detector coupled with the use of the Laplacian edge detector for cross checking can reduce the system false alarms and missed detection rate. Further reduction in the trend shift detection false alarm and missed detection rate can be achieved by selecting gas path measurements with higher signal-to-noise ratios. [DOI: 10.1115/1.1635400]

Introduction

Gas turbine performance diagnostics involves the accurate detection, isolation, and estimation of engine module performance, engine system problems, and instrumentation problems using measurements from the engine gas path, [1–5]. Changes in gas path measurements from a baseline ''good engine'' are used to detect changes in engine performance from the baseline state. Typically, Kalman filter, [1–3], or weighted least-square, [4,5], type methods are used to identify the condition of the engine from gas path measurements as it deteriorates over time. In recent years, Kalman filter [6], neural network, [7–9], fuzzy logic, [10], and Bayesian, [11], methods have been used for fault isolation in gas turbine engines following a sharp trend shift.

Often, a step change in measurements has been found to be a precursor to a reliability event causing in-flight shutdowns, delays, and cancellations or unscheduled engine removals, [7]. Such trend changes in the gas path measurements of a given engine are hard to detect manually because of the large number of engines in the fleet that need to be monitored, and humans being prone to error in manual and repetitive tasks. Therefore, computational methods such as those involving exponential smoothing, [7], auto-associative neural networks, [8,9], and nonlinear median hybrid filters, [12], have been investigated to automate the process of trend shift detection.

A major problem with fault detection and isolation using gas turbine measurement deltas is that they contain considerable noise. The presence of this noise, which is typically high frequency noise, causes problems in trend shift detection. To address this issue, some researchers have looked at methods to reduce the noise levels in gas path measurements. Typically, moving averages such as the ten-point moving average are used to smooth data in the gas turbine industry, [7]. However, moving averages are special cases of linear FIR (finite impulse response) filters, which tend to remove noise, but also smooth out important features in the signal such as trend shifts, [12]. Depold and Gass [7] proposed the use of exponential average, an IIR (infinite impulse response) filter, to simultaneously reduce noise while reducing the response time of the filter to a trend shift. However, IIR filters are also linear filters and are not multiscale in nature. As such linear filters have problems in removing noise while preserving the features. On the other hand, nonlinear filters are multi-scale in nature and allow simultaneous noise reduction with feature preservation.

Another problem in gas turbine signals is the presence of outliers. Outliers are an observation, which appears to be inconsistent with the remainder of the set of data. If not adequately addressed they can cause false alarms in engine diagnostics systems. Depold and Gass [7] proposed some statistical rules to detect outliers in the measurement deltas. These rules were based on the logic that if one measurement changed and others did not change, the data point might be an outlier. However, in such cases, it can be difficult to select thresholds as to what qualifies as an appropriate ''change'' in the measurements versus changes caused by an outlier.

Lu et al. [8] suggested the use of an auto-associative neural network (AAAN) to reduce the noise level in gas path measurement deltas. The AAAN was trained using simulated fault samples with various levels of trend changes. Noise filtering and trend shift detection were done simultaneously using the AAAN. To simulate outliers, some large deviants or ''wild points'' were implanted into the signals. These ''wild points'' were successfully rejected by the AAAN filter.

Contributed by the IGTI of THE AMERICAN SOCIETY OF MECHANICAL ENGINEERS for publication in the ASME JOURNAL OF ENGINEERING FOR GAS TURBINES AND POWER. Manuscript received by the IGTI July 2002; final revision received March 2003. Associate Editor: A. Volponi.

Using an alternative approach from the image-processing field, Ganguli [12] suggested the use of FIR median hybrid filters for decreasing noise in measurement deltas, and a fuzzy decision system to detect trend shifts. He showed that linear FIR and IIR filters widely used in the industry smooth out the trend shifts that contain crucial information about the temporal location of the fault. However, the FIR median hybrid filter performed very well in removing noise while keeping the edge of the signal intact. Median-type filters are also able to remove outliers, [13].

However, the above study, [12], had some shortcomings. The FIR median hybrid filter worked well only when the length of the window was quite large and had a ten-point delay in processing a newly arriving point. Such a system would be useful if the data was received at over ten points per flight by the monitoring system. In general, more than two comparable readings in a single aircraft flight are very unusual. Timely alerting would require a near real time mode of transmission that can be very expensive.

In the current paper, the authors use the cascaded recursive median filter to remove noise from signals. Unlike the nonrecursive filter, the recursive filters converge very fast and do not need repeated passes. They are also good at removing outliers like other median filters. The use of recursive median filters in cascades is a recent research development in the field of nonlinear signal processing. In addition, the authors used a gradient and Laplacian based edge detector, to minimize false alarms and missed detections.

Problem Formulation

Consider the four basic (cockpit) measurements from an aircraft gas turbine engine—EGT, WF, N1, N2. Almost all engines, including older engines, have these measurements. Some newer engines may be fitted with additional pressure and temperature sensors. Therefore, we concentrate on these four measurements. Deltas for each of these are obtained by subtracting the baseline measurements for a good engine from the actual measurement. The baseline measurements often come from an engine model, and various correction factors are used to reduce the measured data to standard sea level conditions, [14]. But these gas path measurement deltas contain high levels of uncertainty due to sensor errors, high-frequency noise, and modeling assumptions.

For a typical engine the measurement deltas slowly increase with time due to deterioration as the number of flights increases. While deterioration accumulates over many flights, faults are more abrupt or step changes. For a trend shift to be detectable, it must show up beyond the scatter band caused by noise for the measurements. In general, the trend shift can be any amount depending on the impending fault. For this study, a step change in measurement deltas of 2% or more is interpreted as a large-enough trend shift implying a single fault event. Thus, we can write the measurement deltas as follows:

$$z = z^0 + \theta \tag{1}$$

where θ is noise and z^0 is the baseline measurement delta. Hence given the real noisy measurement deltas, our problem is: fast detection of trend shift in the presence of noise in the data. Noise is added to the simulated measurement deltas using the typical standard deviations for ΔEGT, ΔWF, ΔN1, and ΔN2 as 4.23C, 0.50%, 0.25%, and 0.17%, respectively. These values are representative of airline data and are obtained from Lu et al. [8,9]. It is also possible that there are non-Gaussian outliers or ''wild points,'' as stated by Lu et al., in the data.

Note that the problem formulation above is idealized and does not account for engine-to-engine variation, measurement bias, and gradual engine deterioration among others, which should be addressed in future work. However, the problem allows for simple illustration of the algorithms used in this study.

Image Processing Concepts

Our objective is to detect trend shifts in gas turbine measurement deltas. To do so, we borrow ideas from image processing, [15]. Images are two-dimensional signals composed of pixels with different levels of brightness. Images are often contaminated with Gaussian as well as impulsive noise. The need for detection of edges (pixels with higher brightness than the neighborhood) has led to significant research on nonlinear filtering and edge detection.

Typical edge detection methods, [16–18], use gradient (first derivative) or Laplacian (second derivative) operators to detect edges in images that are essentially discontinuities in the pixel values. In many machine vision applications, it is useful to separate out the regions of the image corresponding to the objects of interest, from the regions of the image corresponding to the background. At the edge, the magnitude of the gradient peaks and the Laplacian goes through a zero crossing. Thresholding the gradient is a way to perform the segmentation of the image on the basis of different regions or colors in the foreground and background of the image. Thus a grayscale image can be interpreted in black and white.

However, in order to use such derivative operators for edge detection, the image needs to be preprocessed using some smoothing filter to suppress noise. This is because noise in the image gets amplified due to derivative operations. Unfortunately, linear smoothing methods blur the sharp edges in the image, and are not good at removing impulsive noise. Therefore, nonlinear filters such as median filters are often used to preprocess images, [19–32].

This image processing research is applicable to our health-monitoring problem because the gas turbine measurement delta signal can be viewed as a one-dimensional image. In the following sections, we introduce the concepts of the cascaded recursive median filters and edge detection in greater detail.

Median Filter

Median filters are an important class of nonlinear filters, [19]. Nonlinear filters are multiscale in nature and possess the special ability of reducing noise without affecting the various features of the signal, which may represent a fault in the engine. An N-point median filter takes N points surrounding the central point and gives their median as the output, i.e., if z_k denotes the input signal, then the output of the median filter is

$$y_k = \text{median}(z_{k-n}, z_{k-n+1}, \cdots, z_k, \cdots, z_{k+n-1}, z_{k+n})$$

where $N = 2n+1$ is the window length of the filter. Since the median does not cause much blurring to edges, it can be applied iteratively. However, a very large number of iterations can be required by the median filter to converge to a root signal, [20]. A root signal is a signal that does not change on further passes of the median filter, which means that

$$z_k = \text{median}(z_{k-n}, z_{k-n+1}, \cdots, z_k, \cdots, z_{k+n-1}, z_{k+n}).$$

In addition, individual spikes do not affect the median value so median filters remove impulsive noise quite well, [21]. For example, the median filter can discard gross outliers. Since a median filter takes previous as well as future input values for calculating a particular output, it has an associated time lag. But at the same time it is much more effective, as compared to a linear filter, in eliminating high-frequency Gaussian noise while preserving the essential signal features.

Recursive Median Filter

A modified version of these median filters is the recursive median (RM) filter, [23–25]. Recursive median filters possess superior noise attenuation capability compared to their nonrecursive

counterparts, [24]. An RM filter uses some previous output values, instead of previous values for arriving at the next output, i.e., for an RM filter

$$y_k = \text{median}(y_{k-n}, y_{k-n+1}, \cdots, x_k, \cdots, z_{k+n-1}, z_{k+n})$$

where $N = 2n+1$ is the window length of the filter. Some fundamental properties of RM filters are

1. Any input signal reduces to a ''root'' signal after one or very few RM filter steps or equivalently the output will not be modified by further application of the same filter. The RM filter is therefore more efficient than the median filter that can require many iterative passes to converge to the root. Recursive filters also ease hardware implementation.
2. The RM filter output is always made up of monotone sequence (''edges'') linked together with ''constant neighborhoods'' having a length of at least $n+1$ if the window length of the filter is $2n+1$.

Recursive median filters also have a higher immunity to impulsive noise or outliers in the data than median filters. Recursive median filters can be improved further when they are arranged in a cascade of increasing order.

Cascaded Recursive Median Filter

Bangham [26] observed that better noise removal is possible, compared to the recursive median filter, if we apply more than one RM filter sequentially on the same set of data points with the window lengths of the filter increasing. These are called cascaded RM filters and also the recursive median sieve, [26–31]. Cascaded recursive median filters also make for easier software, [27], and hardware implementation, [28]. Alliney [29] gives analytical results showing the advantages of the cascaded RM filters. Consider one *m*-point RM filter and one *n*-point RM filter cascaded together. Passing the input signal through the *m*-point RM filter and the corresponding output through the *n*-point RM filter gives the final output signal, with quite large noise reduction and at the same time maintaining good feature representation. The results obtained are best if we use RM filters of increasing window size, i.e., $2n+1$, $n=1,2,\ldots$, arranged in a cascade. For example, a three-point and five-point recursive median filter can be cascaded as follows:

$$y_k^1 = \text{median}(y_{k-1}^1, z_k, z_{k+1})$$

$$y_{k+1}^1 = \text{median}(y_k^1, z_{k+1}, z_{k+2})$$

$$y_{k+2}^1 = \text{median}(y_k^1, z_{k+2}, z_{k+3})$$

$$y_k^2 = \text{median}(y_{k-2}^2, y_{k-1}^2, y_k^1, y_{k+1}^1, y_{k+2}^1).$$

The use of median filters of increasing order, arranged in a cascade, is especially profitable when one wants to remove disturbances superimposed on rectangular impulse trains or sharp changing signals. However, the use of the five-point RM filter results in a three-point time delay. This can be observed by considering the following logic:

1. The five-point RM output y_k^2 is a function of y_{k+2}^1.
2. The output y_{k+2}^1 from the three-point RM filter is a function of z_{k+3}.

Recently, Yli-Harja et al. [32] have shown that cascaded median filters can be implemented in hardware in a straightforward and compact manner. They are therefore useful for online applications also. Alliney [29] also mentions that the resulting signals after passing through the cascaded recursive median filters appear to be very satisfactory from a visual point of view. He speculates that some relationship could exist between the nonlinear filtering algorithms and the human visual cognition process. The human visual system tends to give very high importance to edges in images and signals, in a manner similar to the nonlinear filters.

Edge Detection

Edge detectors are a collection of image preprocessing methods used to locate changes in the image intensity function. Images are composed of pixels, and edges are pixels where this function (brightness) changes abruptly. There are many methods for edge detection in images. However, among them the most widely used are the ''gradient based edge detector'' and the ''Laplacian edge detector.'' These methods allow us to locate changes in the intensity function using derivatives. The gradient and Laplacian edge detectors are defined below.

Gradient Edge Detector. An edge is a monotone sequence surrounded by constant neighborhoods of different values. As a result, a sharp peak in the gradient characterizes an edge. In general, comparing the magnitude of the gradient to a threshold can identify candidate edge points in a signal. Thresholding ensures that all points having a local gradient above the threshold must represent an edge. Thresholds are typically set based on an estimated signal to noise ratio. The Canny edge detector, [16], for example, uses gradients for edge detection. If the threshold is set low, then all edge points in a signal will be detected. However, nonedge points, including regions of high noise, will also be falsely detected. These false alarms can be minimized by using a ''filtering'' operation that removes noise but leaves the edge intact.

Laplacian Edge Detector. The gradient at an edge reaches a maximum. Similarly, the Laplacian at an edge equals zero. Therefore, there is a change in the sign of the Laplacian before and after the edge occurs. In general, it is much easier and more precise to find a zero crossing than a maximum point. In addition, while the gradient depends on the steepness of the edge, the Laplacian does not. The Marr edge detector, [17], uses the zero crossing of the Laplacian for edge detection.

A key problem in edge detection is that the gradient and Laplacian tend to amplify the effect of high-frequency noise in the data. In addition, the presence of impulsive noise or outliers can cause spurious edges to be detected. Therefore, a smoothing or filtering method is generally used on the signal before performing edge detection. We will use the cascaded recursive median filter for smoothing the gas path measurement deltas in our study. We also use the gradient and Laplacian edge detector simultaneously for improved edge detection accuracy. Chou and Bennamoun [18] recently suggested the use of such a hybrid edge detector combining the first and second order differential edge detectors. They showed that for two-dimensional medical images their combination of two differential edge detectors gave accurate edge localization and showed robustness to noise.

Numerical Experiments

Simulated data for the test signal are used to test the cascaded RM filter for noise reduction. The filtered test signal is then used to test the combination of the gradient edge detector and the Laplacian edge detector for trend shift detection.

Test Signal. The test signal stretches over 20 discrete time points and it assumes that some fault arises in the engine at discrete time $k=11$ and continues until $k=20$, resulting in an individual 2% change in the ΔWF, ΔN1 and ΔN2 measurement and a 13.6°C change in ΔEGT. The ΔEGT signal is selected in terms of actual temperature, as percent changes are unavailable from the literature. A 13.6°C change in ΔEGT corresponds to a 2% HPC performance loss using faults defined in Lu [8], Volponi [6], and Ganguli [10]. The ideal test signals, along with a signal with added Gaussian noise, are shown in Figs. 1–4. The standard deviation for the Gaussian noise added to ΔWF, ΔN1, ΔN2, and ΔEGT are 0.5%, 0.25%, 0.17%, and 4.23°C, respectively. These numbers are obtained from a comprehensive study of airline data and are reported by Lu [8] and Ganguli [10].

Noise Reduction. Figures 1–4 also show the results of pass-

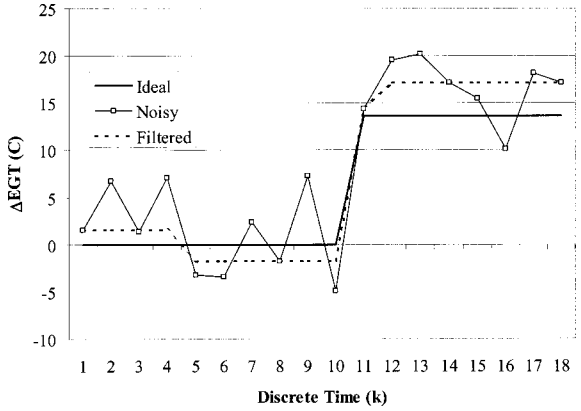

Fig. 1 Ideal, noisy, and cascaded recursive median filtered signal for ΔEGT

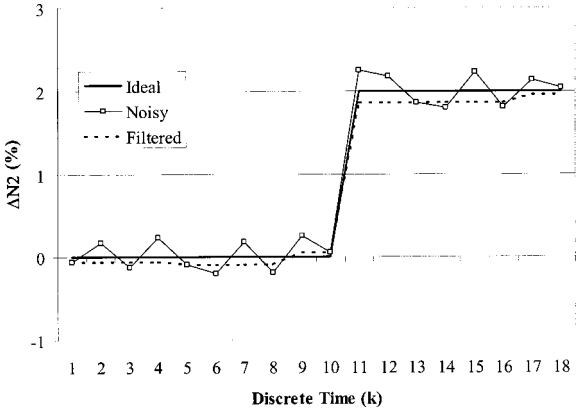

Fig. 4 Ideal, noisy, and cascaded recursive median filtered signal for ΔN2

ing the noisy data through the three-point RM filter and the five-point RM filter, cascaded together. It is clear that the cascaded RM filter, of increasing order, removes a considerable amount of high frequency noise, while preserving the sharp trend shifts. Since a trend shift can identify the temporal location of a fault, preserving them is very important for fault detection. In addition, by removing noise while preserving signal features, the cascaded RM filter enables better visualization of the signal.

Figures 1–4 give a qualitative idea of noise reduction in the data due to passage through the cascaded recursive median filter.

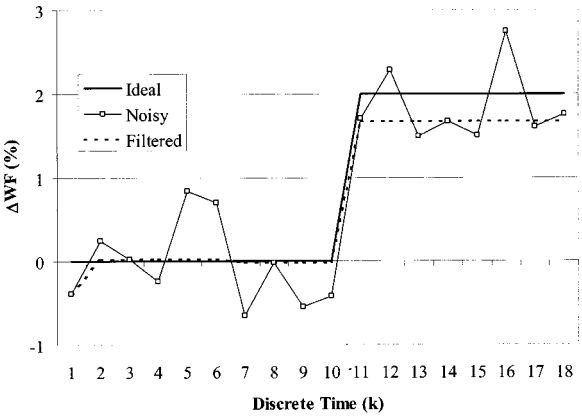

Fig. 2 Ideal, noisy, and cascaded recursive median filtered for ΔWF

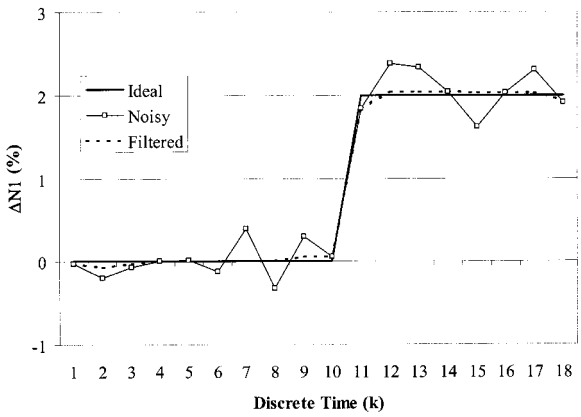

Fig. 3 Ideal, noisy, and cascaded recursive median filtered signal for ΔN1

To obtain a quantitative idea of the noise reduction, we look at the root mean square (RMS) error in the signal, which is a measure of the difference between the noisy or filtered and the ideal signal and is given as

$$\Theta = \frac{1}{M}\sqrt{\sum_{i=1}^{M}(z_i - z_i^0)^2}.$$

The error is a measure of noise in the signal, M is the number of points in the signal sample, and z_i is the ith measurement delta. If Θ is zero, all the noise has been eliminated, and the real signal is identical to the ideal signal.

To obtain the error measure Θ, we create 5000 samples of noisy data for the test signal. The error is then calculated as the average value for all the noisy signals. It is found that for all four measurements there is a reduction in the noise Θ of about 38% after filtering compared to the noisy signal. It should be noted that this substantial noise reduction is obtained while preserving the trend shifts in the signal, which are needed for fault detection.

Outlier Removal. While all other results in this paper are obtained assuming Gaussian noise, we illustrate the power of the cascaded RM filter to remove outliers in Fig. 5. Outliers have been defined as "an observation, which appears to be inconsistent with the remainder of the set of data," [33]. Here the noisy signal for ΔWF in Fig. 2 is further contaminated by adding the value 1% at $k=5$ and subtracting 1% at $k=15$ to the noisy signal. Since the

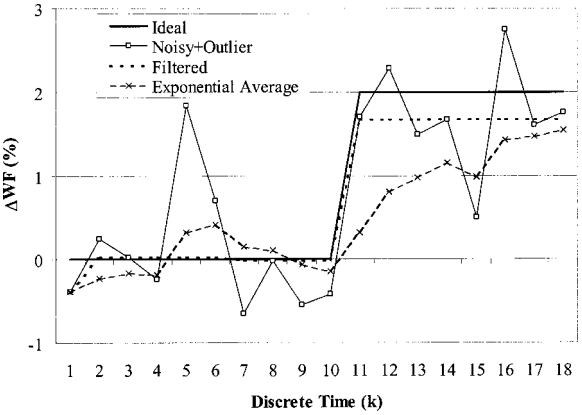

Fig. 5 Noisy signal with outliers at $k=5$ and $k=15$ along with cascaded recursive median filtered signal and exponential average filtered signal

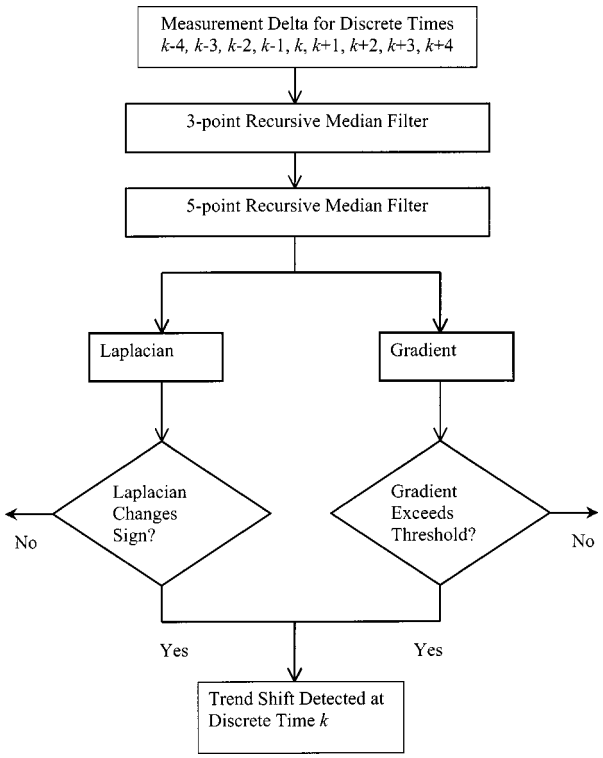

Fig. 6 A schematic view of trend shift detection algorithm

standard deviation for ΔWF is 0.5, these are equivalent to a 2σ addition and subtraction. It is clear from Fig. 5 that the cascaded RM filter discards the outlier points easily.

The results of using the exponential average filter are also shown in Fig. 5. This filter has the form ([34]):

$$y_k = az_k + (1-a)y_{k-1}.$$

The results in Fig. 5 use $a=0.25$. It can be observed that the exponential average creates a smoothing out of the trend shift. The cascaded RM filter has an advantage in removing outliers and maintaining the trend feature and temporal information in the filtered data. Note, however, that Fig. 5 does not indicate the time delay of three points in the RM filter when compared to the exponential filter.

Trend Shift Detection. A key factor in any edge detection algorithm is establishing where the detection threshold should be set, [15]. The measurement deltas entering the edge detector are preprocessed by the cascaded RM filter. For all results, we use a combined gradient/Laplacian edge detector. This edge detector detects an edge if the gradient exceeds a predetermined threshold value and the Laplacian changes sign at that point. Figure 6 shows a schematic representation of the trend shift detection algorithm.

To understand the mechanism of edge detection, consider the gradient and Laplacian of the ΔWF measurement (Fig. 2) shown in Figs. 7 and 8, respectively. Note that the trend shift takes place between discrete time $k-1$ and k of 10 and 11, respectively. For discrete signals, we need to calculate the derivative by finite difference approximation. Using a backward difference calculation of the gradient, we have

$$\nabla_k = z_k - z_{k-1}$$

where z_k and z_{k-1} are the measurement deltas at discrete time k and $k-1$. Therefore, the gradient shows a peak at $k=11$ for the trend shift. The Laplacian is then calculated as

$$\nabla_k^2 = \nabla_k - \nabla_{k-1}.$$

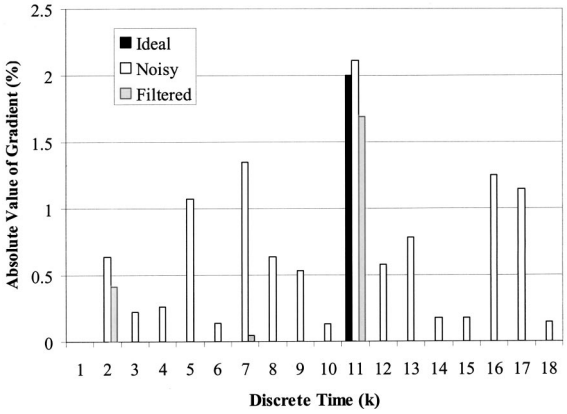

Fig. 7 Absolute value of gradient for ideal, noisy, and cascaded recursive median filtered signal in Fig. 3

The Laplacian changes sign between k and $k+1$ of 11 and 12, respectively. Therefore, we can say that a trend shift occurs at discrete time k if

$$|\nabla_k| > T \quad \text{and} \quad \text{sign}(\nabla_k^2) \neq \text{sign}(\nabla_{k+1}^2)$$

where T is a threshold selected from numerical experiments discussed later in the paper. There is an additional time delay of one point in our formulation above since ∇_{k+1}^2 is required. The use of the RM filters introduces a three-point time delay, as discussed earlier. Thus the total time delay for the edge detection algorithm is four points.

The ideal data in Fig. 7 shows a trend shift at point 11, which is validated at point 12 by the zero crossing of the Laplacian in Fig. 8. However, the noisy data shows gradient values that are nonzero at many points, and shows several zero crossings of the Laplacian. For the filtered signal, the noise is greatly reduced, and so are the spurious edge indicators for the gradient and the Laplacian. All future results are obtained with the filtered signal and the algorithm defined in Fig. 6.

Threshold Selection. To empirically obtain a threshold on the gradient edge detector, we take 5000 samples of noisy data for each measurement, assume a threshold T, and calculate the number of false alarms and the missed detections. A missed detection occurs when the trend shift, which has occurred, is not detected. A false alarm occurs when a point where the trend shift does not occur is flagged as a trend shift point. The thresholds are varied over a range of values to evaluate the number of false alarms and

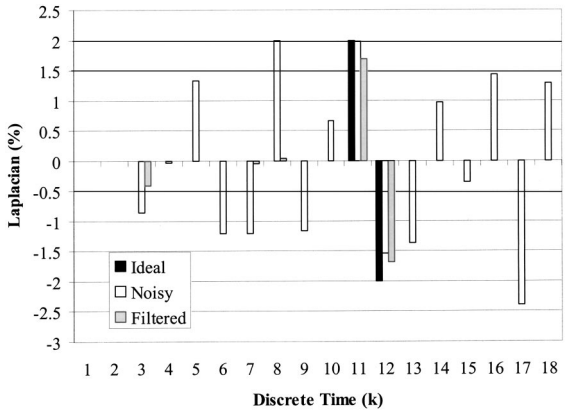

Fig. 8 Laplacian of ideal, noisy, and cascaded recursive median filtered signal in Fig. 3

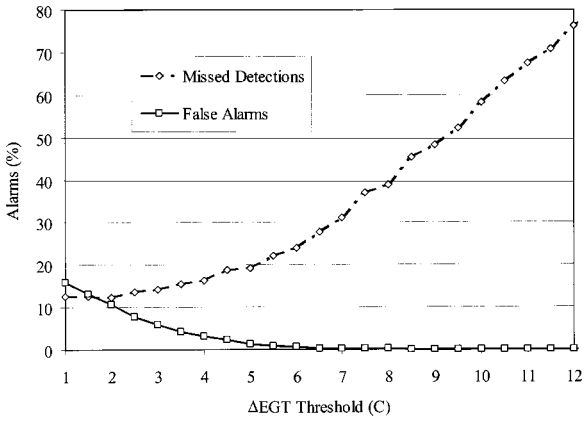

Fig. 9 Missed detections and false alarms for trend shift detection with varying values of threshold on ΔEGT

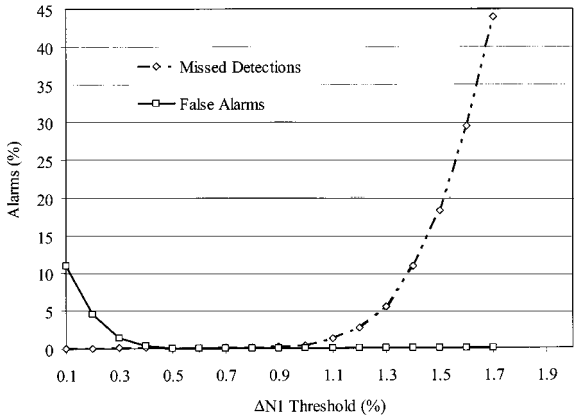

Fig. 11 Missed detections and false alarms for trend shift detection with varying values of threshold on ΔN1

missed detections given by the edge detector. The false alarms are measured by removing the trend shift in the test signal, which makes it a signal for a healthy engine with added noise.

Figures 7–10 show the results of the numerical experiments for ΔEGT, ΔWF, ΔN1, and ΔN2, respectively. As the threshold value is increased, the number of false alarms decreases but the number of missed detections increases. Measurements with better signal-to-noise ratio (S/N) can be used to obtain threshold values, which give both reduced false alarms and missed detection rates. In our study, the (S/N) for ΔEGT, ΔWF, ΔN1, and ΔN2 are 3.215, 4, 8, and 11.764, respectively. These nondimensional values are obtained by dividing the maximum trend shift magnitude by the standard deviation of a given measurement (for ΔEGT: 13.6/4.23, for ΔWF: 2/0.50, for ΔN1: 2/0.25 and for ΔN2: 2.0/0.17).

A quantitative idea of these numerical experiments can be obtained from Table 1. Analyzing Figs. 9–12 and the underlying data, a suitable threshold value is chosen for each case, such that there are no false alarms and minimum missed detections for the 5000 data sampled used in this evaluations.

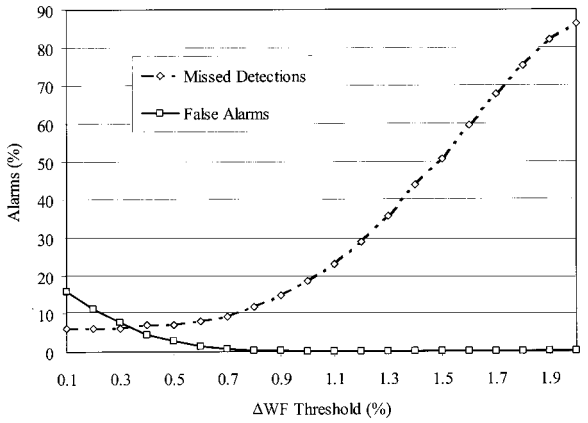

Fig. 10 Missed detections and false alarms for trend shift detection with varying values of threshold on ΔWF

Table 1 False and missed detections with thresholds obtained from numerical experiments

Measurements	Threshold	Missed Detections (%)	False Alarms (%)
EGT	11.5 (C)	70.72	0.00
WF	1.40%	43.82	0.00
N1	0.60%	0.00	0.00
N2	0.40%	0.00	0.00

Testing of Trend Detection Algorithm. Once the threshold values have been selected, the trend detection algorithm defined in Fig. 6 can be tested. Using the threshold values in Table 1, the percentage of false alarms and missed detections is calculated over 5000 new samples of noisy data and are given in the Table 1. These noisy samples are different from those used for creating the thresholds. For the ΔEGT and ΔWF measurement, there are a considerable number of missed detections, if the threshold is selected to minimize false alarms. However, for the rotor speeds ΔN1 and ΔN2, we can obtain thresholds such that the false and missed detections are both zero. The high rotor speed ΔN2 turns out to be the best measurement to monitor for trend detection.

It should be noted that other measurements besides rotor speed might provide an indication of engine distress for certain type of faults. In general, rotor speed shifts are small and so the true signal-to-noise ratio would be different for different faults. The ΔEGT and ΔWF signals are then more likely to reflect engine health. In general, the establishment of detection thresholds is a trade off between false alarms and missed detections. These thresholds can also be set or tuned by the end user or by some automated system based on historical data. Individual sensor signal to noise ratios will determine the achievable false alarm and missed detection ratio.

Finally, we point out that one of the benefits of the trend shift detection approach proposed in this paper is that it will work regardless if the trend shifts is from zero or from some other nonzero quasi-steady-state measurement value. This is because of the use of gradient information for edge detection.

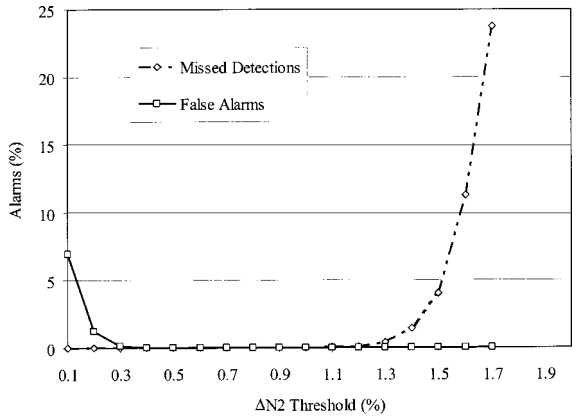

Fig. 12 Missed detections and false alarms for trend shift detection with varying values of threshold on ΔN2

It should also be pointed out that there are specific trend shift cases that the algorithm developed in this study alone would not detect. This includes intermittent shifts that the median filter would discard as outliers. It also includes gradual trend shifts that occur over several samples that the edge detector would not necessarily detect. The cascaded RM filter with edge detection is best suited for sharp trend shifts in gas path measurements.

Conclusions

Fast and effective trend shift detection requires filtering of the data for removing the high-frequency noise while preserving the sharp edges. The following conclusions are drawn from the study.

1. Among nonlinear filters, ''cascaded recursive median filters,'' of increasing order, are found to have the capability of noise removal with accurate signal feature preservation. They are also very fast converging, i.e., only one pass is required to obtain the accurate root signal, and are well suited for software and hardware implementations.
2. Simulated faulty data, indicating the effect of the fault in the engine on ΔEGT, ΔWF, ΔN1, and ΔN2 are passed sequentially through a three-point RM filter and five-point RM filter. A substantial noise reduction of about 38% is found after a single pass.
3. The task of trend shift detection is accomplished by using a combination of gradient edge detector and Laplacian edge detector. This combination is also found to be very effective. A suitable choice of threshold value for the gradient of the filtered data, along with the Laplacian edge detector used for cross checking, can be chosen to minimize false alarms.
4. For the particular faults and noise levels considered in this study, only the low rotor and high rotor speeds were found to be able to give zero false alarms and zero missed alarms. In general, measurements with less noise are more suited to trend detection.
5. One of the benefits of the trend shift detection approach proposed in this paper is that it will work regardless if the trend shifts is from zero or from some other nonzero quasi-steady-state measurement value.

Acknowledgments

The authors would like to thank the anonymous referees for their detailed and constructive comments. The second author would like to thank the Indian Institute of Science for providing facilities for conducting his research work.

Nomenclature

EGT = exhaust gas temperature
k = discrete time
N1 = low rotor speed
N2 = high rotor speed
T = threshold
WF = fuel flow
z = measurement deltas
∇ = gradient
∇^2 = Laplacian
Δ = change from baseline ''good'' engine
Θ = root mean square error
η = efficiency
σ = uncertainty as standard deviation

References

[1] Volponi, A., 1983, ''Time-Dependent Failure Mechanisms and Assessment Methodologies,'' *Gas Path Analysis: An Approach to Engine Diagnostics*, Cambridge University Press, Cambridge, UK.
[2] Volponi, A. J., and Urban, L. A., 1992, ''Mathematical Methods of Relative Engine Performance Diagnostics,'' SAE Trans., **101**, Technical Paper 922048.
[3] Luppold, R. H., Roman, J. R., Gallops, G. W., and Kerr, L. J., 1989, ''Estimating In-Flight Engine Performance Variations Using Kalman Filter Concepts,'' AIAA Paper 89-2584.
[4] Doel, D. L., 1994, ''TEMPER-A Gas Path Analysis Tool for Commercial Jet Engines,'' ASME J. Eng. Gas Turbines Power, **116**, pp. 82–89.
[5] Doel, D. L., 2003, ''Interpretation of Weighted Least Squares Gas Path Analysis Results,'' ASME J. Eng. Gas Turbines Power, **125**, pp. 624–633.
[6] Volponi, A. J., Depold, H., Ganguli, R., and Daguang, C., 2003, ''The Use of Kalman Filter and Neural Network Methodologies in Gas Turbine Performance Diagnostics: A Comparative Study,'' ASME J. Eng. Gas Turbines Power, **125**, pp. 917–924.
[7] DePold, H., and Gass, F. D., 1999, ''The Application of Expert Systems and Neural Networks to Gas Turbine Prognostics and Diagnostics,'' ASME J. Eng. Gas Turbines Power, **121**.
[8] Lu, P. J., Hsu, T. C., Zhang, M. C., and Zhang, J., 2001, ''An Evaluation of Engine Fault Diagnostics Using Artificial Neural Networks,'' ASME J. Eng. Gas Turbines Power, **123**, pp. 240–246.
[9] Lu, P. J., and Hsu, T. C., 2002, ''Application of Auto-Associative Neural Network on Gaspath Sensor Data Validation,'' J. Propul. Power, **18**(4), pp. 879–888.
[10] Ganguli, R., 2002, ''Fuzzy Logic Intelligent System for Gas Turbine Module and System Fault Isolation,'' J. Propul. Power, **18**, pp. 440–447.
[11] Romessis, C., Stamatis, A., and Mathioudakis, A. K., 2001, ''Setting up a Belief Network for Turbofan Diagnosis With the Aid of an Engine Performance Model,'' ISABE Paper 1032.
[12] Ganguli, R., 2002, ''Data Rectification and Detection of Trend Shifts in Jet Engine Gas Path Measurements Using Median Filters and Fuzzy Logic,'' ASME J. Eng. Gas Turbines Power, **124**, pp. 809–817.
[13] Ganguli, R., 2002, ''Noise and Outlier Removal From Jet Engine Health Monitoring Signals Using Weighted FIR Median Hybrid Filters,'' J. Mech. Sys. Signal Process., **16**(6), pp. 967–978.
[14] Volponi, A. J., 1999, ''Gas Turbine Parameter Corrections,'' ASME J. Eng. Gas Turbines Power, **121**, pp. 613–621.
[15] Gonzales, R. C., and Woods, R. E., 2002, *Digital Image Processing*, Addison-Wesley, Reading, MA.
[16] Canny, J., 1986, ''A Computational Approach to Edge Detection,'' IEEE Trans. Pattern Anal. Mach. Intell., **8**, pp. 679–698.
[17] Marr, D., and Hildreth, E., 1980, ''Theory of Edge Detection,'' Proc. R. Soc. London, Ser. B, **B207**, pp. 187–217.
[18] Chou, P. C., and Bennamoun, M., 2000, ''Accurate Localization of Edges in Noisy Volume Images,'' *Proceedings of the IEEE International Conference on Pattern Recognition*, IEEE Piscataway, NJ.
[19] Yin, L., Yang, M., Gabbouj, M., and Neuvo, Y., 1996, ''Weighted Median Filters: A Tutorial,'' IEEE Trans. Circuits Syst., **40**(1), pp. 147–192.
[20] Mao, M., and Gan, Z. J., 1993, ''Statistical Analysis for the Convergence Rate of Signals to Median Filter Roots,'' IEEE Trans. Signal Process., **41**, pp. 2499–2502.
[21] Senel, H. G., Peters, II, A. R., and Dawant, B., 2002, ''Topological Median Filters,'' IEEE Trans. Image Process., **11**(2), pp. 89–104.
[22] Vardavoulia, M. I., 2001, ''A New Vector Median Filter for Color Image Processing,'' Pattern Recogn. Lett., **22**, pp. 675–689.
[23] Arce, G., and Gallagher, N. C., 1988, ''Stochastic Analysis for the Recursive Median Filter Process,'' IEEE Trans. Inf. Theory, **34**, pp. 669–679.
[24] Chen, T., and Wu, H. R., 2001, ''Recursive LMS L-Filters for Noise Removal in Images,'' Signal Processing Letters, **8**(2), pp. 36–38.
[25] Shmulevich, I., and Coyle, E. J., 1997, ''The Use of Recursive Median Filters for Establishing the Tonal Context of Music,'' *IEEE Workshop on Nonlinear Signal and Image Processing*, MI.
[26] Bangham, J. A., 1993, ''Properties of a Series of Nested Median Filters, Namely the Data Sieve,'' IEEE Trans. Signal Process., **41**, pp. 31–42.
[27] Fitch, J. P., Coyle, E. J., and Gallagher, N. C., 1984, ''Median Filtering by Threshold Decomposition,'' IEEE Trans. Acoust., Speech, Signal Process., **32**, pp. 1184–1188.
[28] Richards, S. D., 1990, ''LSI Median Filters,'' IEEE Trans. Acoust., Speech, Signal Process., **38**, pp. 145–153.
[29] Alliney, S., 1996, ''Recursive Median Filters of Increasing Order: A Variational Approach,'' IEEE Trans. Signal Process., **44**(6), pp. 1346–1354.
[30] Bangham, J. A., Ling, P., and Young, R., 1996, ''Multiscale Recursive Medians, Scale-Space and Transforms with Applications to Image Processing,'' IEEE Trans. Image Process., **5**(6), pp. 1043–1048.
[31] Yli-Harja, O., Bangham, J. A., Harvey, R., and Aldridge, R., 1999, ''Correlation Properties of Cascaded Recursive Median Filters,'' *IEEE Workshop on Nonlinear Signal and Image Processing*, Antalya, Turkey, IEEE, Piscataway, NJ, pp. 491–495.
[32] Yli-Harja, O., Koivisto, P., Bangham, J. A., Cawley, G., Harvey, R., and Schmulevich, I., 2001, ''Simplified Implementation of the Recursive Median Sieve,'' Signal Process., **81**, pp. 1565–1570.
[33] Barnett, V., and Lewis, T., 1987, *Outliers in Statistical Data*, 2nd Ed., John Wiley and Sons, Norwich.
[34] Nounou, M. N., and Bakshi, B. R., 1999, ''On-Line Multiscale Filtering of Random and Gross Errors Without Process Models,'' AIChE J., **45**(5), pp. 1041–1058.

The Recuperative Auto Thermal Reforming and Recuperative Reforming Gas Turbine Power Cycles With CO_2 Removal—Part II: The Recuperative Reforming Cycle

D. Fiaschi
e-mail: danif@de.unifi.it

L. Lombardi

L. Tapinassi

Dipartimento di Energetica "Sergio Stecco",
University of Florence,
Via Santa Marta, 3,
50139 Firenze, Italy

The relatively innovative gas turbine based power cycles R-ATR and R-REF (recuperative–auto thermal reforming GT cycle and recuperative–reforming GT cycle) here proposed, are mainly aimed to allow the upstream CO_2 removal by the natural gas fuel reforming. The second part of the paper is dedicated to the R-REF cycle: the power unit is a gas turbine (GT), fuelled with reformed and CO_2 cleaned gas, obtained by the addition of several sections to the simple GT cycle, mainly: • reformer section (REF), where the reforming reactions of methane fuel with steam are accomplished: the necessary heat is supplied partially by the exhausts cooling and, partially, with a post-combustion, • water gas shift reactor (WGSR), where the reformed fuel is, shifted into CO_2 and H_2 with the addition of water, and • CO_2 removal unit for the CO_2 capture from the reformed and shifted fuel. No water condensing section is adopted for the R-REF configuration. Between the main components, several heat recovery units are applied, together with GT cycle recuperator, compressor intercooler, and steam injection into the combustion chamber. The CO_2 removal potential is close to 90% with chemical absorption by an accurate choice of amine solution blend: the heat demand for amine regeneration is completely self-sustained by the power cycle. The possibility of applying steam blade cooling (the steam is externally added) has been investigated: in these conditions, the R-REF has shown efficiency levels close to 43–44%. High values of specific work have been observed as well (around 450–500 kJ/kg). The efficiency is slightly lower than that found for the R-ATR solution, and 2–3% lower than CRGTs with CO_2 removal and steam bottoming cycle, not internally recuperated. If compared with these, the R-REF offers higher simplicity due to absence of the steam cycle, and can be regarded as an improvement to the simple GT. In this way, at least 5–6 points efficiency can be gained, together with high levels of CO_2 removal. The effects of the reformed fuel gas composition, temperature, and pressure on the amine absorption system for the CO_2 removal have been investigated, showing the beneficial effects of increasing pressure (i.e., pressure ratio) on the specific heat demand. [DOI: 10.1115/1.1639008]

Introduction

During the last ten years, special attention has been devoted by research institutions and industry to the study and development of low-CO_2 emissions power cycles. The activities in this field registered an important increase during the last five years, following the Kyoto Protocol, subscribed by many industrialized countries.

Many of the different proposals for new-concept power plants involved GT-based power cycles. Basically, two categories of solutions seem to be practicable in the short–medium term: the first, involving the downstream CO_2 removal from the CO_2 enriched exhausts, obtained by the semi-closed GT cycles, [1–9], and the second, where the upstream CO_2 removal is obtained by the fuel decarbonization amount of the combustion chamber, [10–13]. The second category is the basic guideline for the present work, where two GT power cycles with integrated fuel decarbonization and subsequent CO_2 capture are analyzed.

The CO_2 removal from the fuel is an increasingly investigated opportunity: The general approaches are those linked with CRGT (chemically recuperated gas turbine) and POGT (partial oxidation gas turbine) cycles, [10,11]. In the CRGT, the original methane fuel is converted into a mixture of H_2, CO_2, CO and steam by the steam reforming: the heat due to the related endothermic reactions can be provided by thermal recuperation from the exhausts, [11,13], or by a partial combustion into the reformer itself (auto thermal reforming, ATR, [12]). The recently studied CRGTs represent an attractive alternative to the classic GT recuperative cycles, due to the higher heat recovery levels, chemically enhanced, [14]. However, when considering its application in the field of powerplants with low CO_2 emissions, the conversion levels of methane fuel into H_2 becomes mandatory. To this aim, the operating temperature and pressure of the reformer play a key role: temperatures of 800–1000°C allow the conversion of about 60 to 95%, increasing with increasing steam/methane ratio and with decreasing pressure, [11].

Contributed by the International Gas Turbine Institute (IGTI) of THE AMERICAN SOCIETY OF MECHANICAL ENGINEERS for publication in the ASME JOURNAL OF ENGINEERING FOR GAS TURBINES AND POWER. Paper presented at the International Gas Turbine and Aeroengine Congress and Exhibition, Amsterdam, The Netherlands, June 3–6, 2002; Paper No. 2002-GT-30550. Manuscript received by IGTI, Dec. 2001, final revision, Mar. 2002. Associate Editor: E. Benvenuti.

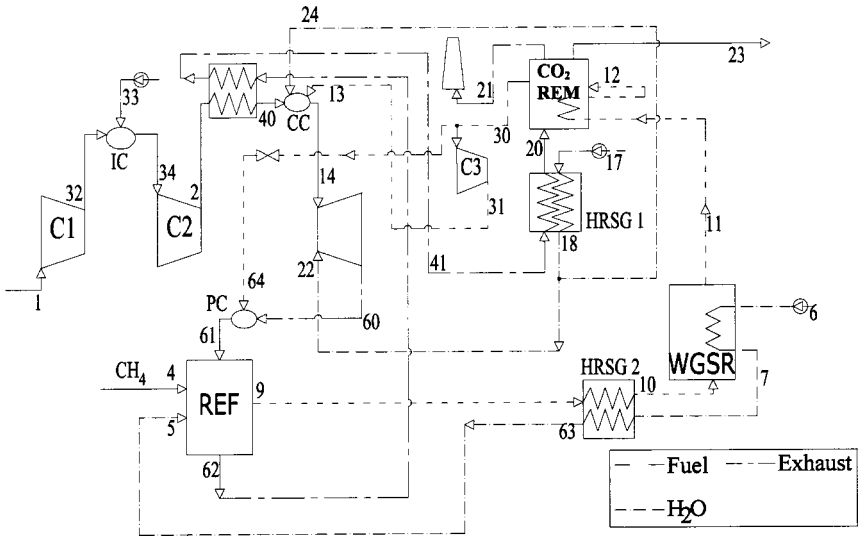

Fig. 1 Schematic representation of the steam cooled R-REF cycle

Since the temperatures of exhausts from standard GT range between 500 and 600°C, it is impossible to have high levels of conversion by the simple reforming. Then, it is supported by the water gas shift reactor (WGSR), downstream the reformer, that allows the conversion of the reformed gas into a CO_2 and H_2 rich mixture, ready to be treated by the CO_2 removal sections.

The upstream CO_2 removal by fuel decarbonization allows a consistent reduction in size for the CO_2 separation plant, with respect to the downstream CO_2 removal from the exhausts, due to the much lower mass flow rates. Chemical CO_2 separation is here investigated and discussed. Physical separation by membranes is a continuously evolving technology and has reached commercial levels, even if the presence of hydrogen is not, at present, well studied and shows, however, some evident efficiency lacks, [15]. Moreover, the membranes require high pressure levels, which contributes to reduce the reforming methane conversion. Chemical CO_2 separation by solution of ethanolamines seems thus to be a more promising technique, also in the field of upstream CO_2 capture, [1,2]. The same reasons listed in Part I, [16], of the paper lead to choose chemical absorption of CO_2 instead of physical solvents.

Description of the R-REF Power Cycle

The objective of the second part of the paper is inquiring the R-REF cycle, schematically shown in Fig. 1. It is based on a recuperative GT power cycle, but substantial differences in the fuel reforming chain have been introduced with respect to the R-ATR described in the first part of the manuscript, [16]. The heat needed by the reformer (REF) to sustain the related endothermic reactions is partially recuperated by cooling the GT exhaust. Moreover, in order to rise the reformer temperature to levels typically required by the reforming reactions to reach an appreciable conversion level of the CH_4 primary fuel, post-combustion of some CO_2-cleaned fuel in the post combustror (PC) is applied. The excess air present in the exhaust is used for this post combustion. The following reactions have been considered in modeling the REF:

$$CH_4 + H_2O \leftrightarrow CO + 3H_2$$

$$CO + H_2O \leftrightarrow CO_2 + H_2$$

$$2CO \leftrightarrow C(\text{solid}) + CO_2 .$$

Increasing temperature favors the reforming process, whereas the pressure has an opposite effect, [11].

The gas composition at the REF exit can be considered, with a satisfactory approximation, to be that resulting from chemical equilibrium if suitable catalysers are added, [13], and an adequate sizing of bed reactor catalyst with heat exchanger of 3–4 tube rows per cold side pass is adopted, [14,17,18]. The fuel temperature and composition at the REF outlet is then calculated from the energy, mass balances, and chemical equilibrium equations. The third chemical reaction must be almost completely directed toward the reactants, in order to avoid solid carbon formation: For this reason, the steam-to-methane ratio at the reformer inlet K_{steam} is always kept higher than 1.5, [13].

The reformed fuel gas is then sent to the WGSR, where the CO_2 and H_2 concentrations are enhanced to values that allow the subsequent CO_2 capture. The steam due to the reforming is produced by heat recovery from the hot reformed fuel (points 9–10) and the exothermic reactions of the WGSR, which serves as an economizer (points 6–7). Given the relatively low steam content of the reformed fuel, the water condensing heat exchanger (SEP, used in R-ATR, see Part I of the paper) downstream the WGSR is not required.

Downstream the REF (point 62), the heat content of the exhaust is partially recuperated into the GT cycle (points 62–41), partially for producing the steam needed for blade cooling in the HRSG1 and, finally, for regeneration of amine used in the CO_2 removal section (points 20–21). The water used for the intercooler compressor (33) is taken externally, while the amount of steam eventually exceeding that necessary for blade cooling can be injected into the combustion chamber. The small compressor C3 covers the pressure losses encountered by the clean reformed fuel through the heat exchangers passages.

The basic operating data of the R-REF cycle are reported in Table 1.

Performance Analysis of the Proposed Cycles

The thermodynamic calculations on the proposed R-REF cycle have been performed using a dedicated program, developed in EES software environment, on the same basis of the R-ATR, discussed in the first part of paper and the same blade cooling model. The GT cycle is the core of the proposed power plant and the GT exhaust temperature is basically a function of pressure ratio; an extensive analysis of the performance and CO_2 removal potential versus β has been thus carried out. The effects of maximum cycle temperature $T_{\max}$ have not been discussed, since an increase in this parameter should favor both the gas cycle performance and the reforming processes, leading to lower CO_2 emissions.

Table 1 Main R-REF cycle operating data

β_1	First compressor pressare ratio	$\sqrt{\beta}$
m_{comp} [kg/s]	Compressor mass flow	100
T_{max} [K]	Maximum cycle temperature	1500
T_b [K]	Turbine blade metal temperature	1100
ε_H	Turbine blade cooling efficiency	0.4
e_f	Turbine film cooling effectiveness	0.2
η_{SC}	Compressor isentropic efficiency	0.89
η_{SC}	Turbine isentropic efficiency	0.91
Lp_{CC}	Combustion chamber pressure loss $\Delta p/p$	3%
Lp_{PC}	Post-combustor pressure loss $\Delta p/p$	3%
Lp_{RIG}	Recuperator pressure loss $\Delta p/p$	5%
$Lp_{REF,c}$	Cold side reformer pressure loss $\Delta p/p$	10%
$Lp_{REF,h}$	Hot side reformer pressure loss $\Delta p/p$	1%
DT_{RIG} [K]	Recuperator approach temperature difference	30
T_{18} [K]	Exit HRSG1 temperature (R-REF cycle)	$T_{sat}+10$
η_{CO2}	CO_2 removal efficiency of the chemical absorber	90%

The maps of performance exploited by the R-REF power cycle (primary fuel LHV efficiency η_{GT} versus specific work W_{sp}) with variable β are represented in Fig. 2, for simple air and steam blade cooling.

Quite different behaviors are observed for the R-REF cycles using air or steam cooling: at very low pressure ratios, the effects of recuperation prevails, leading to higher efficiency for the steam cooling cases. With increasing β, much higher amounts of steam can be produced and injected in combustion chamber due to the lower cycle recuperation (see Figs. 3 and 4). From $\beta=8$ for steam cooling and $\beta=7$ for air cooling, this effect is dominant on the cycle efficiency, which is lead to decrease. On the whole, the R-REF shows lower efficiency levels than the R-ATR presented in Part I, [16], as well as a higher sensitivity of the efficiency to the pressure ratio. This is mainly due to the different composition and conditions of the reformed fuel sent to the CO_2 removal unit: in R-REF configuration, this determines the absorption of a consistent amount of methane (about 10%), together with the CO_2, which is lost for power production. The efficiency level is increased with decreasing post combustion temperature T_{pc}, whereas the same behaviors and optimizing β can be observed moving from $T_{pc}=1100$ to $T_{pc}=1150$ K.

The peaky shape of the performance and steam production curves for steam cooling close to the optimization point is directly

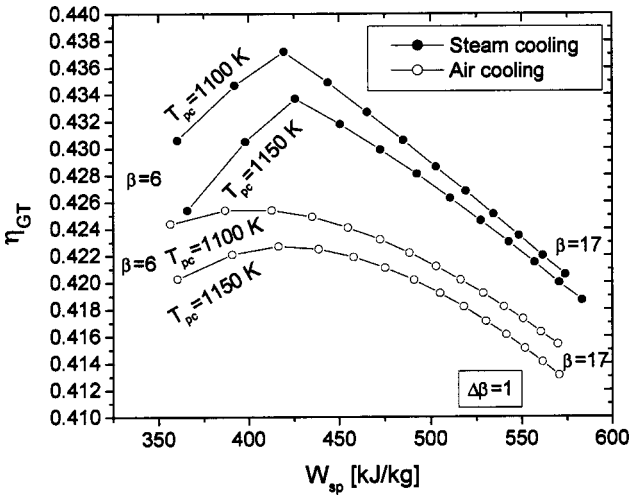

Fig. 2 Performance maps of R-REF cycle

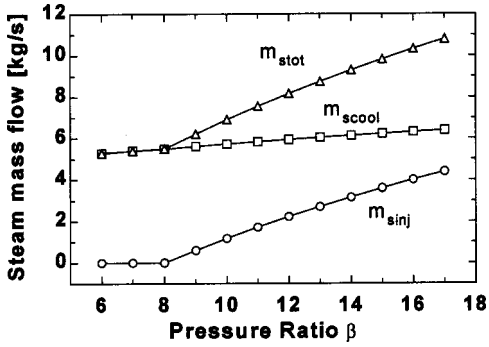

Fig. 3 Steam production versus β for the steam cooled R-REF

linked with the intercooler mass flow rate behavior: this is set to be the saturating amount only from pressure ratio values that allow the production of the necessary blade cooling steam. At very low β, the cycle recuperation level is limited by reducing the spray intercooling and allowing values of T_{41} high enough to achieve the production of the required blade cooling steam mass flow. Then, two different operating regimes are present for β values lower and higher than the optimizing value. In other words, the efficiency of the steam-cooled configurations is optimized when m_{ws} is the maximum value allowing the production of the exactly required steam cooling flow rate.

As found in R-ATR cycle in Part I, some beneficial effects of pressure ratio on performance are due also to the reduced thermal request for the CO_2 sequestration with amine solutions linked to the higher absorber operating pressure, [15,19], as will be remarked in the paragraph dedicated to the CO_2 removal section.

The Reforming Section: R-REF Power Cycle Parametric Analysis

The R-REF fuel gas composition along the main components of the fuel reforming–decarbonization line is shown in Table 2.

The CO_2 emissions of the R-REF cycles with air and steam cooling are reported in Fig. 5: At high values of β, CO_2 emissions decrease with increasing post combustion temperature. At low pressure ratios, the sensitivity to T_{pc} is less evident. This behavior is due to the opposite trend of the chemical equilibrium in the reformer and the WGSR: increasing T_{pc}, the unconverted fraction of methane in the reformer decreases, but the WGSR temperature T_{11} is increased (Fig. 6), leading to lower levels of CO-to-CO_2 conversion and, finally, to a reduction in fuel decarbonization, as shown in Figs. 7 and 8. In other words, the pressure ratio has the same effect as T_{pc} on the CO_2 removal, because, for fixed T_{max}, an increasing β leads to a reduction in T_{60} and, finally, of the

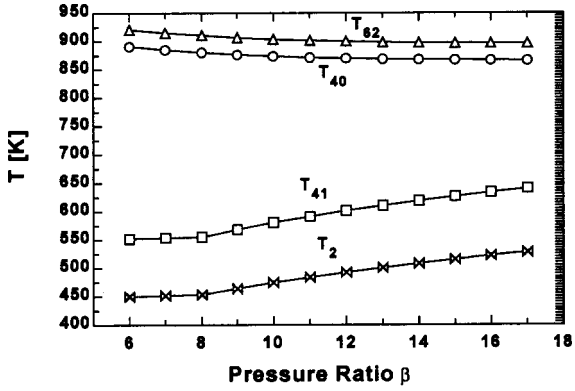

Fig. 4 Recuperator end temperatures versus β for the steam cooled R-REF

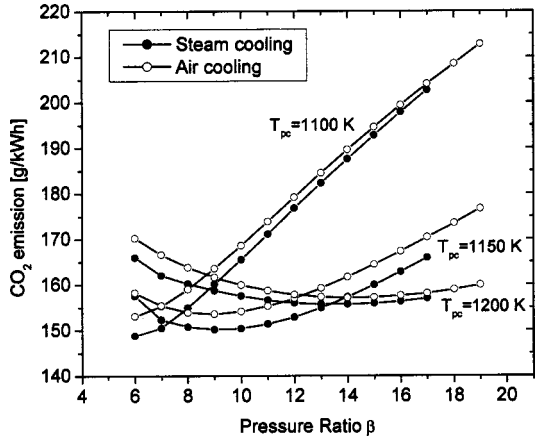

Fig. 5 Influence of β and T_{pc} on the R-REF powerplant CO_2 emission

steam reformer operating temperature. The same effects, and very similar results, have been found also for the air-cooled R-REF. This suggests the opportunity of using these cycles with low pressure ratio gas turbines or to rise T_{pc} with increasing β, in order to maintain limited CO_2 emission levels.

The combined effects of K_{steam} (defined, as in Part I, as $K_{\text{steam}} = m_{s5}/m_{pf}$) and β on the steam cooled R-REF cycle are reported in Fig. 9: the influence of this parameter is limited influence on the specific work, but consistent on the efficiency. Moving from

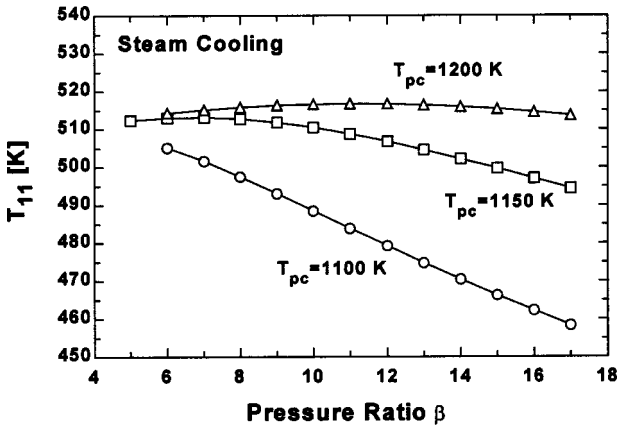

Fig. 6 WGSR exit temperature versus β and T_{pc}

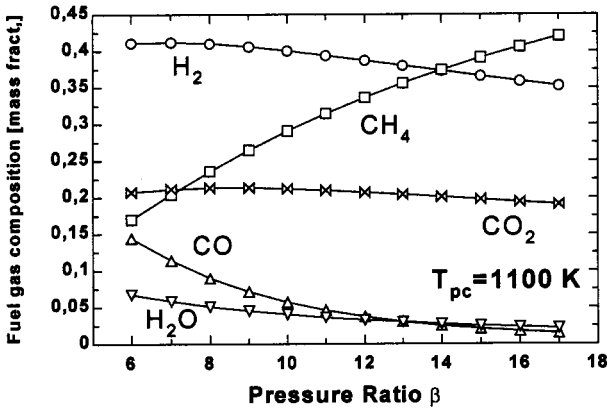

Fig. 7 Depurated fuel gas composition to the combustor versus pressure ratio (steam cooled R-REF, T_{pc}=1100 K)

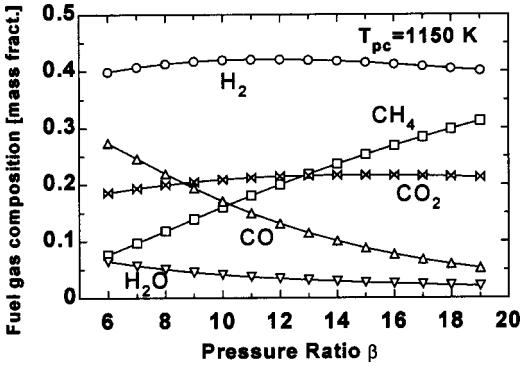

Fig. 8 Fuel gas composition to the combustor versus pressure ratio (steam cooled R-REF, T_{pc}=1150 K)

K_{steam}=2 to 2.5, an efficiency drop of about 1% is observed on almost the whole field of β. This effect is explained by the increased heat demand of the reformer with inlet steam flow rate, and by the subsequent decay of T_{62}, which brings to reduced level of cycle recuperation. The increased thermal request of the reformer with K_{steam} is due to the higher methane conversion and to the drop in reformer inlet temperature (T_5). Moreover, for low K_{steam} values it is possible to inject higher amounts of steam in the combustion chamber, due to the higher difference between the recuperator exit temperature T_{41} and the CO_2 removal system inlet temperature T_{20} (which is decreased because of lower CO_2 conversion).

The CO_2 removal potential is, instead, greatly increased with K_{steam} and reaches the 80% level only with values around 2.5 (Fig. 10).

The temperature range on the hot side (9–10) of HRSG2, is not so high as that found for the 9–51 superheater of the R-ATR (see Part I of paper [16]), but the inlet zone is likely to be interested by metal dusting conditions (Table 2). The possibility of metal dusting attack in HRSG2 has been analyzed, referring to the graphs of carbon activity as a function of gas composition and temperature (originally from [20] and reported on [21]). Referring to the average composition of the reformed fuel at the REF exit (Table 2), the following values have been calculated:

$$p_{\text{CO}} p_{\text{H2}} / p_{\text{H2O}} = 3.17$$

$$p_{\text{CO}}^2 / p_{\text{CO2}} = 2.86$$

$$p_{\text{CH4}} / p_{\text{H2}}^2 = 0.021.$$

The operating field of the HRSG2 could then fall in a dangerous zone, where, depending on the alloy used, metal dusting is likely to proceed, especially into the 500–700°C range. As pointed out

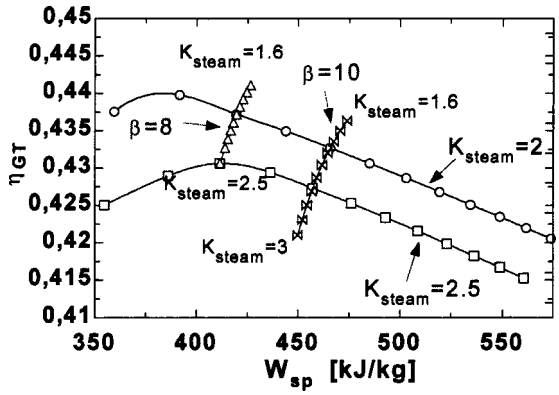

Fig. 9 Effects of K_{steam} on the R-REF cycle performance

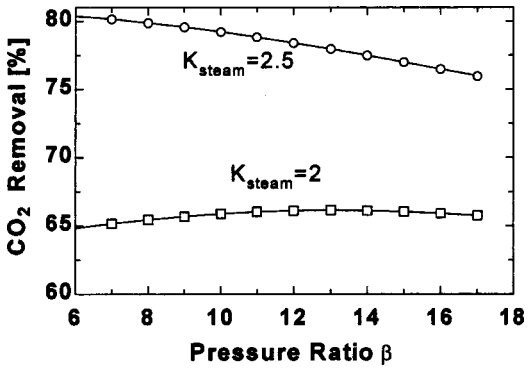

Fig. 10 Effects of K_{steam} and β on CO_2 removal

in Part I, the experience available on chemical reforming plants can drive the design of the reformer also in the field of power plants. In this way, the use of high-Cr containing materials (50/50 Cr-Ni alloy) appears to be a valuable mean against metal dusting attack, [22].

Detailed Evaluation of CO_2 Absorption Section Heat Demand

The carbon dioxide removal section is the same described and modeled in Part I of the paper for the R-ATR power cycle, [16]. The stream exiting from the top of the stripper, contains essentially carbon dioxide and it needs compression up to at least 80 bars for transportation and final storage. In calculation of the powerplant efficiency, the energetic expense for CO_2 compression (which can be estimated in about 355 kJ/kg CO_2 from [19]) has not been directly accounted as it can depend on several variables (type of disposal, transportation system, . . .).

Including this reference value, and considering that, in the optimised runs, 3.38 kg/s of CO_2 are separated for the R-REF, the efficiency drops from 43.72 to 42.47%. The mass flow rate to be treated is 5.76 kg/s with reference to the fixed compressor inlet flow rate of 100 kg/s and a CO_2 reduction of about 94% can be obtained.

The specific heat demand of the absorber unit—reported in Fig. 11 versus pressure ratio for different temperature levels of absorber inlet gas—ranges between 1750 and 2200 kJ per kg of CO_2 removed, which is slightly lower than that found for R-ATR in the first part of this work. The better removal efficiency found for the R-REF is due to the more favorable composition of the fuel gas to be treated, which has a higher concentration in CO_2 at the WGSR outlet (see Table 2), enhancing thus the gas to liquid CO_2 transfer.

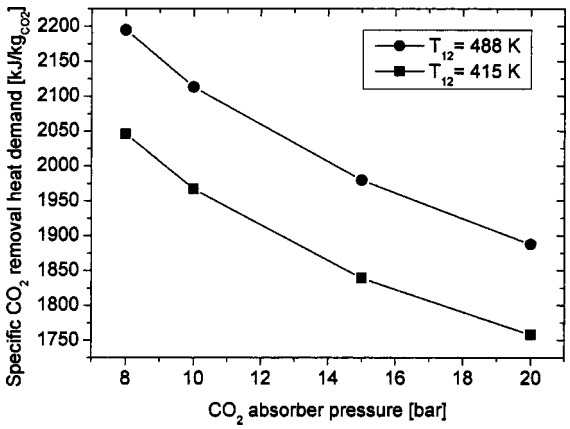

Fig. 11 CO_2 Amine absorption system heat demand

Looking at Fig. 11, for a gas temperature of 488 K, an increase in pressure from 8 to 20 bars leads to a reduction in specific heat demand of about 14%. While considering a constant pressure level (15 bar, for example) the percentage difference between the R-REF curve, at 415 K, and the R-ATR curve, at 420 K—the two temperature are almost the same—is about 14% (see the first part of paper, [16]).

With respect to the SCGT/CC case, the effects of increased operating pressure and CO_2 concentration are even higher for R-REF than for the R-ATR studied in the first part; the reduction in specific thermal request for CO_2 removal is consequently enhanced.

From Fig. 11, it is also evident that when the temperature of the absorber inlet gas increases, the specific thermal request increases as well, due to the lower efficiency in the gas-liquid CO_2 transfer.

As pointed out in Part I, [16], the eventual entrainment of corrosive amine traces (DEA and MDEA) in the fuel could bring to damage of combustion chamber and turbine blades. The results from ASPEN calculation applied to the R-REF, have shown that the possible presence of residual amine in the cleaned fuel is again marginal (pollutant level), even if somewhat higher concentrations than in the R-ATR case have been found. The estimated DEA and MDEA mass fractions for R-REF are $5.88 \cdot 10^{-7}$ and $5.90 \cdot 10^{-5}$, respectively. Here again, it can be supposed that these effects are negligible, or, anyway, that they should be evaluated by extensive test campaigns. Concerning the prevention of eventual amine droplets carryover, the same considerations reported in Part I can be applied.

Testing the R-REF Cycle on a Current-Production GT Model

As done in the first part of the work on the R-ATR, the test on a current production GT model (again, ALSTOM Cyclone) has been performed to have a preliminary verification of the adaptability of the R-REF power cycle to the current production technology: In this way, an approximate evaluation of the very short-term applicability chances of the discussed powerplant can be given.

The basic data used for the simulation and tuning of the ALSTOM Cyclone gas turbine model with the manufacturer catalogue data have been applied to the R-REF cycle. As done for the R-ATR, the compressor intercooler has eliminated from the proposed configuration of Fig. 1, since the existing engine does not include this possibility at design level. This leads to a consistent loss in performance, but the aim of this section is just to give an idea about potential of short-term application of a current production machine to R-REF cycle. Both air and steam-cooled configurations have been tested, even if the GT Cyclone model works with standard air blade cooling. For the fixed compressor inlet design mass flow rate, in cases of air blade cooling, a much higher amount of coolant mass flow should be used. On the other hand, the use of steam cooling allows a dramatic reduction in coolant mass flow, but if the steam injection in combustion chamber is maintained, a substantial increase in turbine mass flow rate is obtained with respect to the design value (Table 4). This brings to a relatively high turbine off design operation, which reflects negatively on GT efficiency, so that the values reported in Table 3 are rather optimistic. The improvement in thermodynamic efficiency (less than 2 points with steam cooling) is more limited than found for R-ATR cycle and it is due, essentially, to the missing of intercooled compression with respect to the optimized layout shown in Fig. 1. Nevertheless, a large increase in specific work is possible, due to the steam injection and to the lower compression work (coolant is pressurized in liquid state). Again, like in the R-ATR, also the blade cooling system should undergo some off design level if the coolant is changed, but this effect has not been evaluated here. Differently from R-ATR, the R-REF reformed fuel shows a higher heating value than primary fuel, which should bring to a more limited off design level of combustion chamber.

Table 2 Fuel gas composition at the main exits of the R-REF deCO$_2$ chain devices

	Composition [%] (Mass/Volume)			
SPECIE	REF exit $T=1070$ K	HRSG2 exit $T=488.6$ K	WGSR exit $T=497.5$ K	deCO$_2$ exit $T=316.9$ K
H_2	10.4/57.7	10.4/57.7	12.5/69.6	41.0/88.8
H_2O	30.6/19.0	30.6/19.0	11.5/7.17	5.09/1.23
CO	32.4/12.9	32.4/12.9	2.75/1.10	8.99/1.40
CO_2	18.6/4.72	18.6/4.72	65.2/16.6	21.3/2.12
CH_4	8.00/5.58	8.00/5.58	8.00/5.58	23.6/6.41
N_2	0.0/0.0	0.0/0.0	0.0/0.0	0.0/0.0
O_2	0.0/0.0	0.0/0.0	0.0/0.0	0.0/0.0

However, in this case, the main problem that could arise with a current production combustion chamber is the high hydrogen concentration in fuel (Table 2).

The CO_2 emission level of the ALSTOM CYCLONE GT in R-REF cycle is less than halved with respect to the simple cycle configuration, but it is more than twice that found in R-ATR mode.

Comparison of the R-ATR and R-REF Performance With Combined Cycles With Upstream CO_2 Removal

This final synthesis paragraph is aimed to find an adequate collocation to the R-REF and R-ATR power cycles proposed in this work. They actually represent two possible ways of developing powerplant with fuel decarbonization, ahead of the combustion chamber.

The basic idea of these proposals moves from the works, [10–13], and can be considered a valuable alternative to these power cycles, especially in the field of small size powerplants, due to the absence of a bottoming cycle. For this reason, they can be regarded as possible improvements to simple GT power units, as discussed in the previous paragraph, and they are ready to be applied for demonstration. When compared with that of modern combined power plants, the performance of R-ATR and R-REF is not competitive, showing an efficiency 10 to 12 points lower. Moreover, the technology of combined gas–steam power plants is well established, so the O&M costs are presumably lower (R-ATR and R-REF have, in fact, several ''new'' components in the field of power conversion like reformer, WGSR, CO_2 absorber, which need verification in terms of costs and reliability).

However, the comparison of the here-proposed solutions with those proposed by other authors (all including reforming and combined cycle) show a competitiveness in terms of performance (see Table 4).

In particular, solutions with combined cycles, [10–12], allow quite higher efficiency levels (1 to 3 points) and lower CO_2 emissions, but they are tuned on large-size combined powerplants (300–400 MW electricity). The semi-closed CRGT that uses a chemically recuperated GT without bottoming steam cycle, [13], is the most similar solution to R-REF and R-ATR, and provides

Table 4 Comparison of Performance and CO_2 emissions of R-ATR and R-REF with data from other GT cycles with reforming

Power Cycle	Efficiency [%]	W_{sp} [kJ/kg]	CO_2 emission [k/kWh]
Combined Cycle+ reforming [10,11]	46.1	505	43.4
Combined Cycle+ reforming and reheat [10,11]	48.0	575	41.5
Combined Cycle+ATR [12]	47.4	635	60.4
Semi-closed CRGT with ASU [13]	42.4	510	…
R-ATR steam cooling	45.2	430	65.5
R-REF steam cooling	43.7	425	155

efficiency and specific power levels that are 2 to 3 points lower. Finally, the relatively low sensitivity of R-REF and R-ATR efficiencies to the pressure ratio allows a noticeable degree of flexibility, as well as a consistent improvement in specific power, if modest penalties in efficiency are accepted.

Conclusions

Two GT based power cycles have been proposed, making use of fuel decarbonisation for CO_2 removal, upstream of the combustion chamber: the first inquired option involves the use of auto thermal reforming (R-ATR) and the second uses simple reforming (R-REF). Both cycles include a recuperative GT and heat recovery from the GT exhausts to the fuel reforming–cleaning chain. Both the proposed solutions make extensive use of compressor spray intercooling and steam injection in combustion chamber. Moreover, the possibility of adopting steam blade cooling has been inquired.

The trend of performance and CO_2 removal potential have been inquired versus some typical parameters of chemically recuperated GTs. In particular, the influence of GT pressure ratio has been investigated, since the gas turbine is the core of the entire cycle layout. For the studied configurations, β has a relevant influence on the cycle performance, showing generally low values for efficiency optimization. The best performance has been obtained with the adoption of steam blade cooling, even if interesting values are shown also by air cooling.

The R-REF solutions have shown lower efficiency level than those found for the R-ATR (around 42–43%), mainly due to the loss of some methane during the CO_2 capture. In this configuration, an important role is also played by the post-combustion temperature, that can be maintained at low values (for the best efficiency) when operating with small pressure ratios, whereas higher values should be used at high β in order to limit the CO_2 emissions (150–160 g/kWh).

The CO_2 removal section has shown that the particularly favorable fuel gas composition allows very low thermal requests, due to the high CO_2 concentration and pressure, in comparison to

Table 3 Main operating results for using ALSTOM Cyclone GT in R-ATR cycle

CYCLE ALSTOM Cyclone	m_c [kg/s]	β	T_{max} [K]	m_{cool} [kg/s]	$m_{sin\ j}$ [kg/s]	W_{GT} [kW]	W_{sp} [kJ/kg]	η_{GT} [%]	T_{exh} [K]	m_{exh} [kg/s]	CO_2 emiss. [g/kWh]	Fuel LHV [kJ/kg]
Standard GT	38.66	16.23	1602	8.29	0	13124	339	35.9	827	39.4	695	50009
R-REF (Steam cooling)	38.66	16.23	1602	4.75	3.03	21598	559	37.6	897	47.2	321	63543
R-REF (Air cooling)	38.66	16.23	1602	11.0	5.93	17845	462	36.6	898	45.2	427	63543

retrofit devices operating on the CO_2 concentrated exhausts released by semi-closed GT cycles. Moreover, the higher the operating pressure (i.e., GT pressure ratio), the lower the CO_2 removal heat demand.

The test of the R-REF with a current production gas turbine model has been performed, showing the possibility of a limited increase in efficiency and a consistent one in specific work. The reduction in specific CO_2 emissions is more than 50% in comparison to the simple GT. A problem is linked with the consistently higher turbine mass flow rates with respect to the design values, due substantially to the steam injected in combustion chamber and to that added for blade cooling. Another design problem of R-REF is linked to the high H_2 content in purified fuel.

Finally, comparing the results obtained by other Authors for GT cycles with steam reforming and CO_2 removal, the R-REF and R-ATR have shown to be competitive also with combined cycles and could represent valuable alternatives, especially in the field of low electrical outputs.

Nomenclature

DT = temperature difference
K_{steam} = steam-fuel mass ratio at the reformer inlet
Lp = pressure loss
m = mass flow
T = temperature
W = power

Subscripts

ATR = related to the ATR
CC = combustion chamber
CO_2 = related to CO_2 removal
comp = compressor inlet
GT = related to gas turbine cycle
exh = related to gas turbine exhaust
inj = injected
max = maximum in cycle
pc = post combustion
pf = primary fuel
REF, c = reformer cold side
REF, h = reformer hot side
RIG = Recuperator
$s5$ = steam added to the REF or ATR at point 5
sat = water-steam saturation
$s$cool = coolant steam
sin j = injected steam
s tot = total steam
ws = spray water

Greeks

β = GT cycle pressure ratio
η = efficiency

References

[1] Corti, A., Failli, L., Fiaschi, D., and Manfrida, G., 1998, ''Exergy Analysis of Two Second-Generation SCGT Plant Proposals,'' Proceedings of ASME IGTI 43rd Gas Turbine and Aeroengine Congress and Exhibition, Stockholm, Sweden.

[2] Corti, A., Lombardi, L., and Manfrida, G., 1998, ''Absorption of CO_2 With Amines in a Semi-Closed GT Cycle: Plant Performance and Operating Costs,'' Proceedings of ASME IGTI 43rd Gas Turbine and Aeroengine Congress and Exhibition, Stockholm, Sweden.

[3] Corti, A., and Manfrida, G., 1998, ''Economic Analysis of a Semi-Closed Gas Turbine/Combined Cycle (SCGT/CC) With CO_2 Removal by Amines Absorption,'' GHGT-4, ''4th International Conference on Greenhouse Gas Control Tecnologies,'' InterLaken, Switzerland, Aug. 30–Sept. 2.

[4] Corti, A., Fiaschi, D., and Manfrida, G., 1999, ''Thermo-Economic Evaluation of the SCGT Cycle,'' Energy Convers. Manage., **40**, pp. 1917–1929.

[5] Facchini, B., Fiaschi, D., and Manfrida, G., 1996, ''Semi-Closed Gas Turbine/Combined Cycle With Water Recovery,'' Proceedings of 1996 ASME IGTI Gas Turbine Conference and Exhibition, Birmingham, Paper No. 96-GT-317.

[6] Facchini, B., Fiaschi, D., and Manfrida, G., 1997, ''SCGT/CC: An Innovative Cycle With Advanced Environmental and Peakload Shaving Features,'' Energy Convers. Manage., **38**(15–17), pp. 1647–1653.

[7] Fiaschi, D., and Manfrida, G., 1999, ''A New Semi-Closed Gas Turbine Cycle With CO_2 Separation,'' Energy Convers. Manage., **40**, pp. 1669–1678.

[8] Mathieu, Ph., Dechamps, P., and Distelmans, M., 1994, ''Concepts and Applications of CO_2 Gas Turbines,'' Power-Gen Europe '94, Cologne.

[9] Mathieu, Ph., Chefneux, E., and Dechamps, P., 1995, ''Energy and Exergy Analysis of CO_2 Based Combined Cycle Plants,'' Second Law Analysis of Energy Systems: Towards the 21st Century, Roma.

[10] Lozza, G., and Chiesa, P., 2000, ''Natural Gas Decarbonization to Reduce CO_2 Emission From Combined Cycles. Part A: Partial Oxidation,'' ASME Paper 2000-GT-0163.

[11] Lozza, G., and Chiesa, P., 2000, ''Natural Gas Decarbonization to Reduce CO_2 Emission From Combined Cycles. Part B: Steam-Methane Reforming,'' ASME Paper 2000-GT-0164.

[12] Andersen, T., Kvamsdal, M., and Bolland, O., 2000, ''Gas Turbine Combined Cycle With CO_2-Capture Using Auto-Thermal Reforming of Natural Gas,'' Proceedings of ASME Turbo Expo, May 8–11, Munich, Germany.

[13] Cau G., and Cocco D., 2000, ''Performance Assessment of Semi-Closed Chemically Recuperated Gas Turbine Systems,'' Proceedings of ASME Turbo Expo, May 8–11, Munich, Germany.

[14] Carcasci, C., and Harvey, S., 1998, ''Design Issues for the Methane-Steam Reformer of a Chemically Recuperated Gas Turbine Cycle,'' ASME IGTI International Gas Turbine Congress, Stockholm.

[15] Tapinassi, L., 2001, ''Studio di impianti di potenza innovativi con turbina a gas integrati con sistemi di rimozione della CO_2 tramite conversione del metano in combustibile ad alto contenuto di idrogeno,'' Graduation thesis (in Italian) in Environmental Engineering–Università degli Studi di Firenze, Italy.

[16] Fiaschi, D., Lombardi, L., and Tapinassi, L., 2002, ''The R-ATR and the R-REF Gas Turbine Power Cycles With CO_2 Removal, Part 1: The R-ATR Cycle,'' Proceedings of 2002 ASME IGTI Gas Turbine Conference and Exhibition, Amsterdam, Paper No. GT-2002-30116.

[17] Adelman, S. T., Hoffman, M. A., and Baughn, J. W., 1995, ''A Methane-Steam Reformer for a Basic Chemically Recuperated Gas Turbine,'' ASME J. Eng. Gas Turbines Power, **117**, pp. 16–23.

[18] Carcasci, C., Facchini, B., and Harvey, S., 1998, ''Design Issues and Performance of a Chemically Recuperated Aeroderivative Gas Turbine,'' Proc. Inst. Mech. Eng., **212**, A.

[19] Lombardi, L., 2000, ''LCA Comparison of Technical Solutions for CO_2 Emissions Reduction in Power Generation,'' Ph.D. thesis, Dipartimento di Energetica ''Sergio Stecco''–Università degli Studi di Firenze, Italy.

[20] Lai, G. Y., 1990, *High Temperature Corrosion of Engineering Alloys*, ASM International, Materials Park, OH, pp. 47–72.

[21] Holland, M. L., and De Bruyn, H. J., 1996, ''Metal Dusting Failures in Methane Reforming Plant,'' Int. J. Pressure Vessels Piping, **66**, pp. 125–133.

[22] Holland, M. L., 2000, ''Practical Experience With Countering Metal Dusting in a Methane Reforming Unit,'' Mossgas (PTY) Ltd., Mossel Bay, South Africa, on http://www.mossgas.com/research/nace2000a.pdf.

A. G. Chen
United Technologies Research Center,
411 Silver Lane, MS 129-16,
East Hartford, CT 06108
e-mail: chenag@utrc.utc.com

Daniel J. Maloney
National Energy Technology Laboratory,
3610 Collins-Ferry Road,
Morgantown, WV 26507-0880
e-mail: daniel.daloney@netl.doe.gov

William H. Day
Manager,
Advanced Engine Programs,
Pratt & Whitney Power Systems, Inc.,
411 Silver Lane, Mail Stop 129-54,
East Hartford, CT 06108
e-mail: dayw@pweh.com

Humid Air NO_x Reduction Effect on Liquid Fuel Combustion

An experimental investigation was carried out at DOE NETL on the humid air combustion process using liquid fuel to determine the effects of humidity on pollutant emissions and flame stability. Tests were conducted at pressures of up to 100 psia (690 kPa), and a typical inlet air temperature of 860°F (733 K). The emissions and RMS pressures were documented for a relatively wide range of flame temperature from 2440–3090°F (1610–1970 K) with and without added humidity. The results show more than 90% reduction of NO_x through 10% humidity addition to the compressed air compared with the dry case at the same flame temperature. The substantial reduction of NO_x is due to a shift in the chemical mechanisms and cannot be explained by flame temperature reduction due to added moisture since the comparison was made for the same flame temperature.
[DOI: 10.1115/1.1615255]

Introduction

The humid air turbine (HAT) cycle was invented in the 1930s and awarded a U.S. patent in 1940, [1]. Over the years several different versions of HAT cycles have emerged. Figure 1 shows a typical intercooled HAT cycle as described by Bhargava et al. in 2000 [2]. Intercooled compressed discharge goes through an aftercooler to arrive at a saturator to get humidified. The humidified air is then heated up in a recuperator. Afterwards the hot, water vapor laden air arrives at the combustor and then the turbine.

The HAT cycle offers many advantages over simple cycles as well as combined cycles [3]. It produces more power output at higher efficiency compared to simple cycles due to less work needed for intercooled compression and more work being done in the turbine. Despite the added cost for saturator, etc., it reduces the capital cost compared to combined cycles due to the elimination of the steam cycle. It provides flexible operations like quick startup and shutdown as commonly seen in simple cycle turbines. It also minimizes the NO_x emission due to water vapor suppression of NO_x in the combustion processes. With increasingly stringent environmental requirements on pollutant emissions, production of CO_2 and other ''greenhouse'' gases and conservation of energy in the past several decades, there is a significant increase of interest in the HAT cycle.

A number of recent papers in the gas turbine literature have presented studies on the influence of water addition on NO_x and CO emissions. Lupandin [4], Dryer [5], Miyauchi et al. [6], and Blevins and Roby [7] have all investigated the subject. However, these studies only dealt with gaseous diffusion flames, premixed gaseous flames, and emulsified fuel combustion. Touchton [8] reported some results on liquid fuel combustion with steam/water injection. However, only direct steam/water injection into the combustor was investigated. Direct injection limits the amount of steam/water that can be added due to flame instability, therefore does not explore the full benefits of steam addition. Meyer and Grienche [9] investigated the steam effect to a liquid-fired engine with steam and air premixed prior to combustion. But their steam loading is relatively low. The work reported in this paper extended the investigations to liquid fuel HAT combustion with high steam content in the air before it is introduced into the combustor. Introduction of humidity to the air before combustor has been reported for natural gas fuel in [2], [9], [10], and [11], significant reduction of NO_x was achieved. In this study, partially premixed spray combustion in humid air was examined in a relatively realistic configuration for gas turbine applications with No. 2 Diesel fuel. Since liquid fuel combustion generally produces more NO_x emission than lean premixed natural gas combustion, suppression of NO_x production in liquid fuel can have a profound effect in minimizing the adverse impact on the environment.

Experimental Technique

Fuel Nozzle Design. The fuel nozzle used in the tests was a dual fuel axial swirl nozzle with a cylindrical centerbody as shown in Fig. 2. Air was introduced in an annular gap between the centerbody and an outer cylinder. Inside the annulus, 16 vanes were installed at an angle to the airflow direction to induce swirling motion in the air stream. Downstream of the vanes, there were 16 radial gaseous fuel spokes to provide distributed fuel injection. Further downstream, 16 pressure swirl liquid fuel injectors were installed. The premixed or partially premixed fuel/air mixture

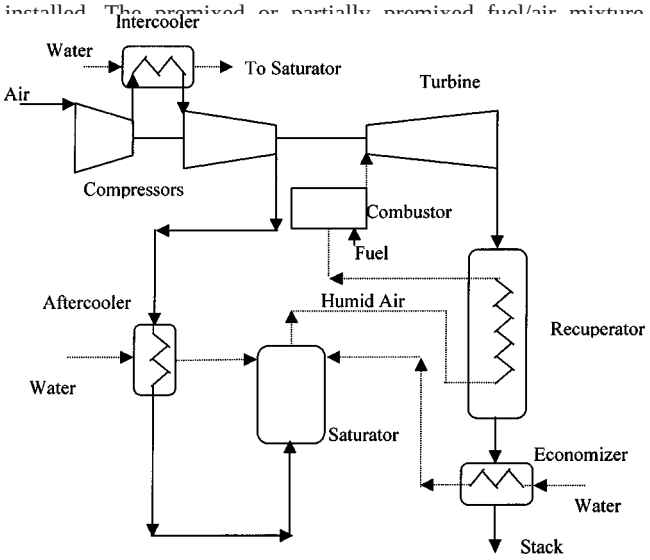

Fig. 1 A typical diagram of the HAT cycle

Contributed by the International Gas Turbine Institute (IGTI) of THE AMERICAN SOCIETY OF MECHANICAL ENGINEERS for publication in the ASME JOURNAL OF ENGINEERING FOR GAS TURBINES AND POWER. Paper presented at the International Gas Turbine and Aeroengine Congress and Exhibition, Amsterdam, The Netherlands, June 3–6, 2002; Paper No. 2002-GT-30163. Manuscript received by IGTI, December 2001, final revision, March 2002. Associate Editor: E. Benvenuti.

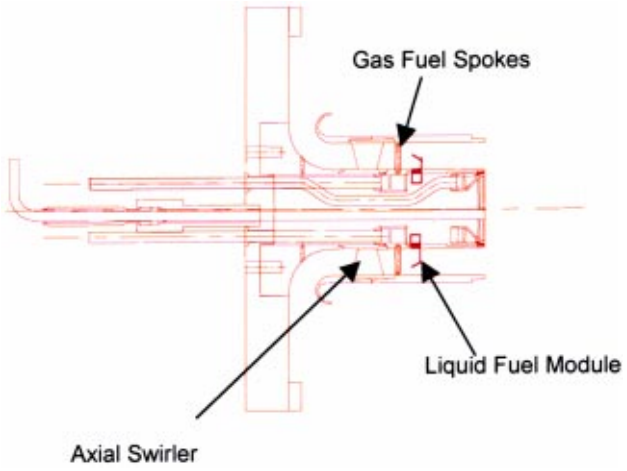

Fig. 2 Diagram of axial swirler dual fuel nozzle

traveled further downstream in the annulus until it reached the nozzle exit plane where the combustor begins. Also in the nozzle there was a diffusion flame pilot integrated in the centerbody to mitigate flame instability.

It is worth mentioning the multipoint pressure swirl liquid fuel injector incorporated here was made by an external supplier through its macrolaminate technology. Figure 3 shows a sketch illustrating the macrolaminate fuel injector. Macrolamination uses thin etchable metal sheets which are layered and bonded together to create intricate passages. It reduces the part count and the cost to make complicated parts. Liquid fuel nozzles made through macrolamination technology have demonstrated good emission performance in rig tests, [12].

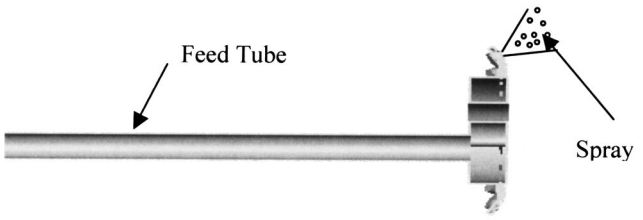

Fig. 3 Macrolaminate multipoint liquid fuel injector

The position of the injector relative to the nozzle exit plane is generally determined by balancing two factors: autoignition and mixing. Too far away from the nozzle exit plane may cause autoignition of liquid fuel in the nozzle annulus yet promote premixing and therefore decrease NO_x formation. Too close to the nozzle exit plane reduces premixing therefore increases NO_x emission but reduces the chance for autoignition. Since the main goal of this study is to investigate the humidity effect on the NO_x reduction rather than to optimize the nozzle to reduce dry NO_x emission, the balance mentioned above was shifted towards reducing the chance for autoignition to ensure the success of the experiments. As a result, the liquid injector was positioned close to the nozzle exit plane rather than far away from it. For best flame stability, sprays were directed at 60 deg away from the main nozzle centerline to ensure enough fuel was distributed towards outside diameter recirculation zone in the combustor. 0-deg nozzle was also tried and resulted in unstable combustion.

Combustion Test Rig Setup. All the experiments were carried out in the low emissions combustor test and research (LECTR) facility at U.S. Department of Energy's National Energy Technology Laboratory in Morgantown, WV. The facility has the capability to provide as much as 3 pps (1.4 kg/s) of air at 450 psia

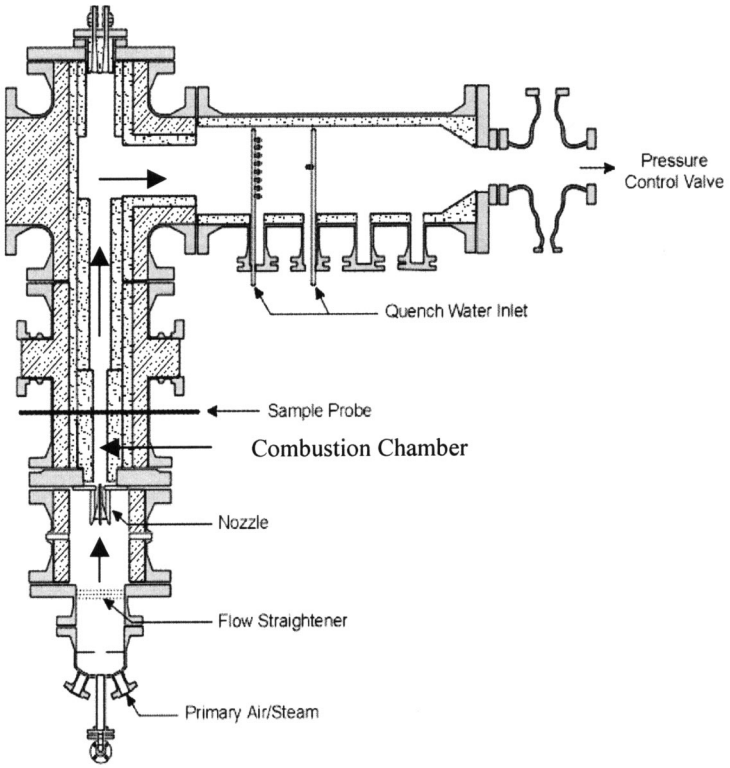

Fig. 4 Experimental setup

(3.1 MPa) and 950°F (783 K) and 0.6 pps (0.27 kg/s) of steam. It can independently control air, gas, liquid and steam flows and inlet temperature and pressure, as well as automatic ramping of these variables. The variable rate automatic ramping capability is particularly useful for the refractory liner used in the setup to minimize cracking. Figure 4 shows a diagram of the experimental setup.

Nonvitiated preheated air and steam generated by a boiler flowed through primary air/steam ports into the plenum. After going through a perforated plate acting as a flow straightener upstream to fuel nozzle, they provided uniform flow feed to the nozzle. Combustion occurred downstream to the nozzle in a 6-inch (0.15 m) diameter cylindrical refractory lined combustor which best simulates an ideal adiabatic combustion chamber. Due to the favorable refractory liner's physical properties, the need for liner cooling was eliminated. After burning, the combustion products continued to move upward and reached the water-cooled exhaust sampling probe which was located about 12 inches (0.3 m) above the nozzle exit plane. The probe sampled the exhaust in an area-averaged fashion to ensure the extracted gas samples were representative across the combustor exit plane. After passing the sampling probe, the exhaust moved further upward and reached a plenum and then turned 90 deg entering a water quench zone where temperature was reduced before the flow reached a pressure control valve and a stack.

Exhaust samples were transported through heated tubings and were dried before being analyzed. Species analyzed were NO_x, CO, CO_2, O_2 and unburned hydrocarbons (UHC). All emissions reported here are on a dry basis and have been corrected to 15% O_2. UHC was not reported here because it was only a few ppms for all the cases except when the CO was high. Excellent fuel/air ratio agreement (generally within 2%) was achieved between the emissions based fuel/air ratio and the metered fuel/air ratio.

The extent of flame temperatures examined was determined by CO emission at the lean end and NO_x emission at the rich end for the dry case. For the dry case fuel ramp stopped when CO level approached 100 ppm or when NO_x approached 430 ppm. The flame temperature range determined by the dry case was also used for the humidified case when steam was added.

For the entire test series presented here, the dynamic pressure was consistently very small. No RMS pressure above 0.3 psia (2.1 kPa) was observed. This may be partly due to the unchoked acoustic boundary conditions or less than perfect mixing in the nozzle, or both.

Results and Discussion

Figure 5 reveals the NO_x and CO emissions of Diesel fuel combustion as a function of equivalence ratio without steam addition for both the inlet pressure of 50 and 100 psia (0.34 and 0.69 MPa). The equivalence ratio is the actual fuel/air ratio divided by the stoichiometric fuel/air ratio. The inlet air temperature was 860°F (733 K) and there was 4% centerbody natural gas fuel based on total heat of combustion of all the fuels. Both CO curves exhibit U-shaped trend similar to that observed in premixed natural gas combustion, [10]. The level of CO at 100 psia (0.69 MPa) is lower than that at 50 psia (0.34 MPa). The lean stability limits moved to lower equivalence ratios as pressure increased. A similar pressure effect was also found in premixed natural gas combustion, [11]. The NO_x curves show a near linear dependence on the equivalence ratio for the range tested. This linear relationship can also be observed in most of the data presented in Ref. [12]. The 100-psia (0.69 MPa) curve displays a steeper slope and substantially higher NO_x value than the 50-psia (0.34 MPa) curve. The absolute value of NO_x is relatively high compared to well premixed liquid fuel flame rig data, [12], suggesting the vaporization and mixing of the spray is less than perfect, possibly due to short mixing time in the nozzle. However, the nozzle in Ref. [12] is a novel macrolamination nozzle which has yet to be implemented in commercial gas turbines. In the absence of water or steam, the majority of commercial liquid fuel turbine engines produce hundreds of ppm NO_x which is at a level similar to the NO_x produced in the baseline experiments here. One exception is pre-vaporized and premixed liquid fuel gas turbines. These systems face many operational challenges including thermal damage to the vaporizing elements and sensitivity to variation in fuel type. The NO_x level here is also significantly higher than those in the lean premixed gas turbine engines (typically 25 ppm). But those systems are natural gas fired and therefore cannot be compared with the system investigated here. Therefore the nozzle is suitable for the purpose of this investigation which is to study the NO_x suppression effect of humid air in liquid fuel combustors similar to real engines.

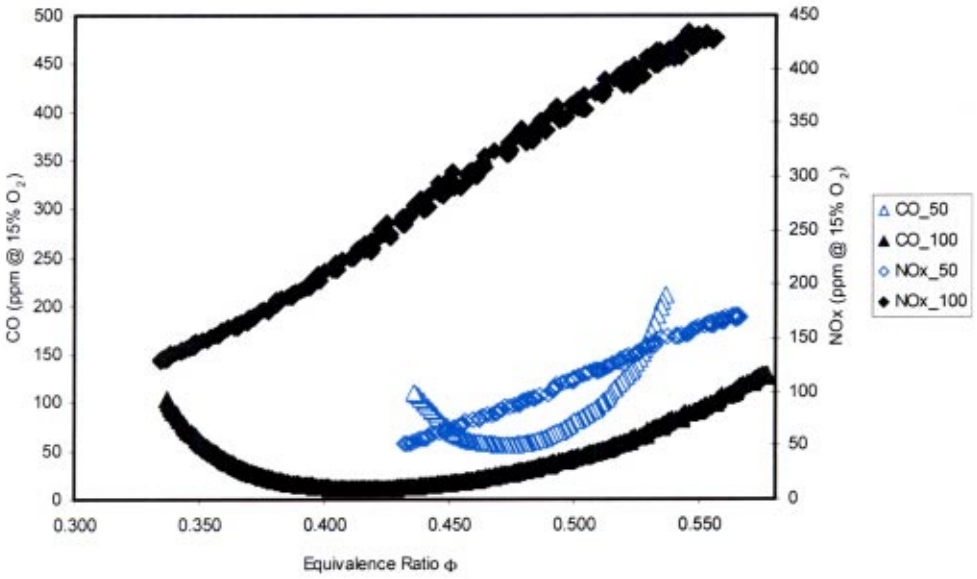

Fig. 5 Comparison of measured NO_x and CO of Diesel fuel combustion between 50 psia and 100 psia (0.34 and 0.69 MPa) dry cases. T_{air}=860°F (733 K), 4% centerbody gas fuel.

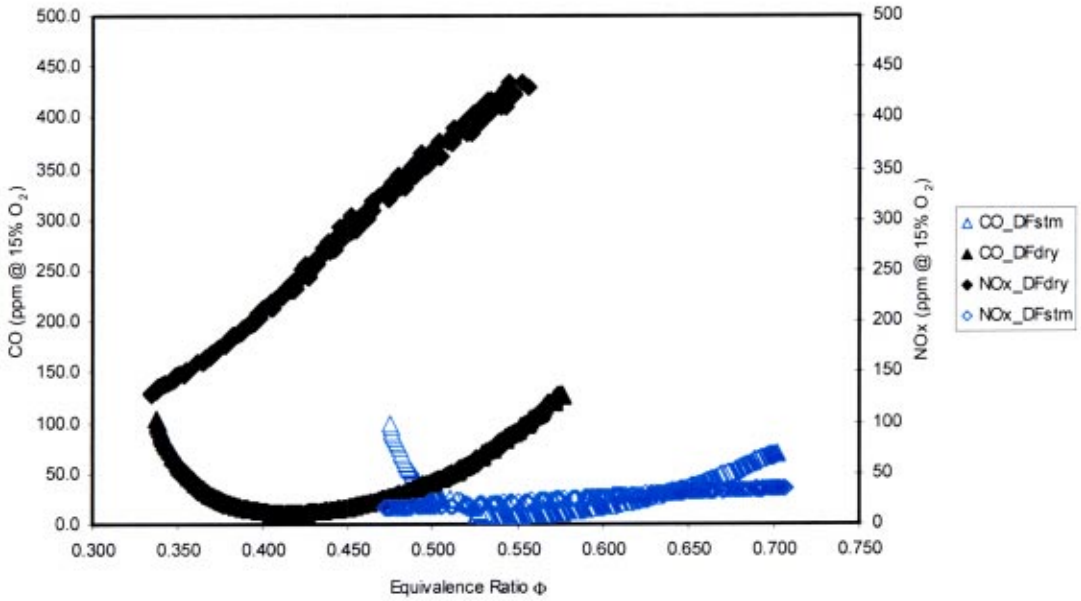

Fig. 6 Comparison of measured NO_x and CO of Diesel fuel combustion at different equivalence ratios between dry and 10% steam cases at 100 psia (0.69 MPa)

The existence of the centerbody gas pilot of 4% fuel in the test contributed a small amount of NO_x to the results. Data without pilot were not acquired during this test series. However, the small effect of pilot on NO_x can be estimated. Assuming the pilot contributes NO_x in a similar way as in a premixed natural gas flame, the pilot here would contribute about 6 ppm NO_x, [2]. Hence, if we had run cases without the pilot fuel, the NO_x level would be about 6 ppm lower.

The above 100-psia (0.69 MPa) case was then plotted with a humidified case in Fig. 6 to demonstrate the steam effect on emissions. For the humidified case, steam was 10% of the air mass flow rate, the inlet pressure was 100 psia (0.69 MPa), the inlet air temperature was 810°F (705 K) which was 50°F (28 K) lower than the dry case and there was no centerbody pilot. As discussed above, the pilot should only account for about 6 ppm NO_x difference, therefore the difference in NO_x between the two cases was mainly caused by steam addition. For the amount of steam added, typically a higher percentage of steam will bring a higher power output and efficiency to the HAT cycle. Day and Rao [3] simulated as high as 25% steam addition to a natural gas fired cycle and 45% to a syngas fired cycle and found major improvement in power output and efficiency. However, high steam addition can increase the difficulty for moisture recovery if it is needed, as well as compressor operations. Fischer et al. [13] has found that higher than 10% of steam addition may cause compressor surge. They also found that 10% steam addition would increase the HAT cycle power by about 30% and efficiency by about 15%, which are significant. From a NO_x reduction standpoint the most significant benefits are found at steam loadings on the order of 5–10% in natural gas, [2]. Above 10% steam loadings, the NO_x levels are only slightly further reduced but CO emissions begin to increase. Therefore the 10% steam content chosen in the tests here is an appropriate level for a practical HAT cycle. As it is shown in Fig. 6, the addition of steam brought a drastic reduction in the formation of NO_x similar to what was found in premixed natural gas combustion, [2]. For the same equivalence ratio NO_x was reduced more than 95% by 10% addition of the steam. For example, at an equivalence ratio of 0.47, the NO_x decreases from 323 ppm in the dry case to 15.7 ppm in the humidified case, a 95% reduction. With 10% humidity addition, the NO_x was reduced to 15–35 ppm depending on the flame temperature. These NO_x levels are comparable to those of the lean premixed natural gas fired gas turbines. Also this shows the NO_x reduction effect of humidity is insensitive to the high dry NO_x level, which indicates the wide applicability of this technique to different types of nozzles with different levels of dry NO_x. More importantly, this implies that with HAT it is not necessary to have a perfect mixer to achieve NO_x level below 25 ppm, which potentially eliminates the very destructive acoustic problem commonly associated with lean premixed systems. It is worth further researching on this subject. The CO curve for the steam case also exhibited U-shaped trend similar to that of the dry case. However, the lean stability limit moved to higher equivalence ratio as steam was added. This is due to the fact that steam addition increased the specific heat of the mixture therefore reduced the flame temperature for the same equivalence ratio. It is also due to the effect of the pilot in the dry case. The flame temperature reduction with steam addition reduced the Zeldovich or thermal NO_x formation mechanism, which partially explains the NO_x reduction effect. However, it cannot explain the entire NO_x reduction observed.

To illustrate this point, the data in Fig. 6 were plotted against adiabatic flame temperatures. The adiabatic flame temperatures were calculated through NASA CEA equilibrium code. The results are shown in Fig. 7. It is shown that even at the same adiabatic flame temperature, the 10% steam reduced NO_x by 90% for all the flame temperatures tested. For example, at a flame temperature of 2600°F (1700 K), the NO_x decreases from 223 ppm in the dry case to 19.4 ppm in the humidified case, a 91% reduction. This suggests if, through optimization of the nozzle, a 200 ppm dry NO_x is achieved, it is likely to achieve NO_x below 20 ppm in a HAT cycle at the same flame temperature. This NO_x reduction effect differs completely from the results reported by Touchton [8] in the direct steam/water injection systems where NO_x suppression is exclusively through thermal mechanism or lowering peak flame temperature. This strongly suggested that besides the NO_x reduction effect due to lowering the flame temperature through steam addition, the moisture also reduced the NO_x by other mechanisms.

Bhargava et al. [2] investigated the humid air effect on NO_x reduction in premixed natural gas combustion system and offered following explanation.

NO_x formation reactions can be categorized into three different

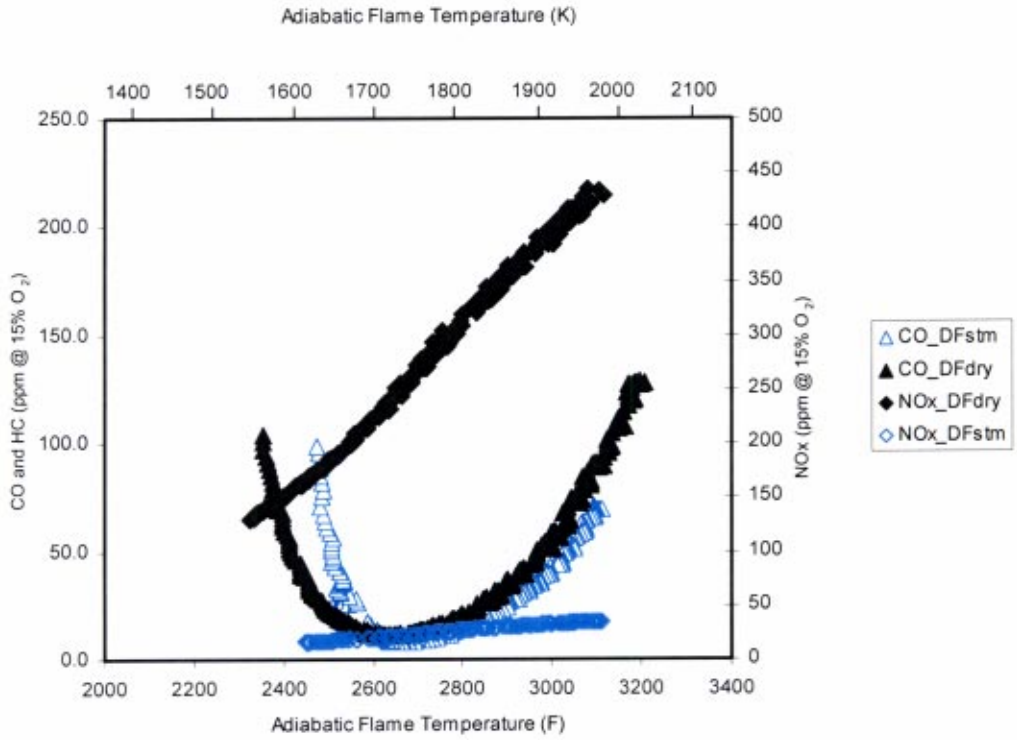

Fig. 7 Comparison of measured NO_x and CO of Diesel fuel combustion at different flame temperatures between dry and 10% steam cases at 100 psia (0.69 MPa)

groups. They are Zeldovich [14] thermal NO_x mechanism, N_2O mechanism and ''Fenimore,'' [15], or prompt NO mechanism.

Zeldovich mechanism is described by following reactions:

$$O + N_2 \rightarrow NO + N \quad (1)$$

$$N + O_2 \rightarrow NO + O. \quad (2)$$

The overall rates of NO production are controlled mainly by the first reaction since the second reaction is quicker than the first one. Due to the fact that there is abundance of N_2 available in the combustion system, the rate of the first reaction and hence the rate of NO production is strongly controlled by O concentration. A reduction of O concentration can reduce the rate of the first reaction therefore reducing NO_x production.

N_2O mechanism consists of reactions involving N_2O which form NO. NO_x formed via this mechanism can be suppressed by the reaction $N_2O + M \rightarrow N_2 + O + M$. A reduction of O concentration can promote the previous reaction therefore reduce NO_x production.

The key of ''Fenimore'' NO mechanism can be described by following reactions:

$$CH + N_2 \rightarrow HCN + N \quad (3)$$

$$CH_2 + N_2 \rightarrow HCN + NH \quad (4)$$

$$HCN + O \rightarrow CH + NO. \quad (5)$$

A reduction of CH and/or CH_2 will reduce the reaction rate in the first and/or second reactions and eventually reduce NO. A reduction of O will reduce the reaction rate in the third reaction and therefore reduce NO.

For the same flame temperature, the humidified case had higher equivalence ratio than the dry case, therefore it had lower O_2 which in turn reduced the concentration of O atoms. Humidity also promotes the $O + H_2O$ reaction therefore reduces O concentration. The reduction of O atoms lowered the NO_x formation by all the three mechanisms. In addition, humidity increases OH radical concentration which promotes the oxidation of hydrocarbon radicals therefore reduced ''Fenimore'' NO. These are the reasons why the steam addition reduced NO_x dramatically for the same flame temperature relative to a dry case.

Conclusions

Experimental data were obtained for liquid fuel combustion in dry and humid air at different pressure over a wide range of equivalence. The effect of humidity, pressure, and equivalence ratio on NO_x and CO emissions were evaluated based on the data. Introduction of 10% steam in air suppressed NO_x production by more than 90% for the same flame temperature. The dramatic suppression of NO_x is attributed to the decrease of O atoms and increase of OH radicals in the humid air combustion.

Acknowledgments

This work was supported by DOE/NETL under contract DE-AC21-96MC33084. The authors want to thank Mr. Meredith Colket for helpful discussions and Mr. Rex Harvey and Mr. Adel Mansour at Parker Hannifin Corporation for supplying the macrolaminate liquid module and support. Thanks are also expressed to Donald Kendrick for his coordination early in the planning phase for these experiments.

References

[1] Martinka, M., 1940, U.S. Patent No. 2,186,706.
[2] Bhargava, A., Colket, M., Sowa, W., Casleton, K., and Maloney, Dan, 2000, ''An Experimental and Modeling Study of Humid Air Premixed Flames,'' ASME J. Eng. Gas Turbines Power, **122**, p. 405.
[3] Day, W., and Rao, A., 1992, ''FT4000 HAT With Natural Gas Fuel,'' International Gas Turbine Institute, ASME Paper IGTI-Vol. 7, ASME Cogen-Turbo, Book No. 100333.
[4] Lupandin, V., Romanov, V., Krivutsa, V., and Lupandin, V., 2001, ''Design, Development and Testing of a Gas Turbine Steam Injection and Water Recovery System,'' ASME Paper No. 2001-GT-0111.

[5] Dryer, F. L., 1976, ''Water Addition to Practical Combustion Systems—Concepts and Applications,'' Sixteenth Symposium (International) on Combustion, The Combustion Institute, Pittsburgh, PA.
[6] Miyauchi, Y., Mori, Y., and Yamaguchi, T., 1981, ''Effect of Steam Addition on NO Formation,'' Eighteenth Symposium (International) on Combustion, The Combustion Institute, Pittsburgh, PA.
[7] Blevins, L. G., and Roby, R. J., ''An Experimental Study of NO_x reduction in Laminar Diffusion Flames by Addition of High Levels of Steam,'' ASME Paper No. 95-GT-327.
[8] Touchton, G. L., 1985, ''Influence of Gas Turbine Combustor Design and Operating Parameters on Effectiveness of NO_x Suppression by Injected Steam or Water,'' ASME Paper No. 84-JPGC-GT-3.
[9] Meyer, Jean-Louis, and Grienche, G., 1997, ''An Experimental Study of Steam Injection in an Aeroderivative Gas Turbine,'' ASME Paper No. 97-GT-506.
[10] Bhargava, A., Kendrick, D., Colket, M., Sowa, W., Casleton, K., and Maloney, D., 2000, ''Pressure Effect on NO_x and CO Emissions in Industrial Gas Turbines,'' ASME Paper No. 2000-GT-97.
[11] Mansour, A., Benjamin, M., Straub, D. L., and Richards, G. A., 2000, ''Application of Macrolamination Technology to Lean, Premix Combustion,'' ASME Paper No. 2000-GT-0115.
[12] Kendrick, D., Bhargava, A., Colket, M., Sowa, W., Maloney, D., and Casleton, K., 2000, ''NO_x Scaling Characteristics for Industrial Gas Turbine Fuel Injectors,'' ASME Paper No. 2000-GT-98.
[13] Fischer, A., Frutschi, H., and Haselbacher, H., 2001, ''Augmentation of Gas Turbine Power Output by Steam Injection,'' ASME Paper No. 2001-GT-0107.
[14] Zeldovich, J., 1946, ''The Oxidation of Nitrogen Combustion and Explosions,'' Acta Physicochim. URSS, **21**, p. 577.
[15] Fenimore, C. P., 1971, ''Formation of Nitric Oxide in Premixed Hydrocarbon Flames,'' Thirteenth Symposium (International) on Combustion, The Combustion Institute, Pittsburgh, PA.

C. Guardino

J. W. Chew

Fluids Research Center,
School of Engineering,
University of Surrey,
Guildford,
Surrey GU2 7XH, UK

N. J. Hills

Thermo-Fluid Mechanics Research Centre,
School of Engineering and Information Technology,
University of Sussex,
Falmer, Brighton BN1 9QT, UK

Calculation of Surface Roughness Effects on Air-Riding Seals

The effects of surface roughness on air-riding seals are investigated here using the Rayleigh pad as an example. Both incompressible and compressible flows are considered using both CFD analysis and analytical/numerical solutions of the Reynolds equation for various two-dimensional or three-dimensional roughness patterns on the stationary wall. A "unit-based" approach for incompressible flows has also been employed and is shown to be computationally much less expensive than the full-geometry solution. Results are presented showing the effect of surface roughness on the net lift force. The effects of varying the Reynolds number are demonstrated, as well as comparative results for static stiffness. [DOI: 10.1115/1.1619426]

1 Introduction

The effect of surface roughness on the flow in a Rayleigh step of infinite width is considered in this report. Motivation for this work arises from interest in air-riding seals from within the aeroengine industry. Air leakage through seals is an unavoidable aspect of aeroengine air system design and as discussed, for example, by Munson [1] and Hwang et al. [2], development of improved sealing techniques would give large benefits. Air-riding seals have been recognized as potential replacements for labyrinth seals, offering much better sealing performance, but their application is currently limited by problems of operation at engine conditions. To aid further development of air-riding seals there is a need for improved understanding and predictive techniques. This study is intended to advance basic understanding of the effects of surface roughness in air riding seals and the development of appropriate computational fluid dynamics (CFD) methods for such applications.

While the reader is referred to the papers by Hwang et al. and Munson for a fuller discussion of design issues for aeroengine seals, a little background will be given here. Both Hwang et al. and Munson design film-riding face seals for restricting leakage of compressor delivery air to the internal flow system, for which potential sfc savings of about 1% have been estimated for large commercial aeroengines. To achieve targets for leakage reduction in Munson's hydrodynamic seal design, operating clearances of less than 12 μm (0.0005 in.) are required. In engine operation, geometric distortions due to centrifugal, thermal, and pressure loads make such clearances difficult to maintain. Deviations in clearance are bound to occur and, as the clearance reduces, surface finish will have an influence on film lift and stiffness. Although such effects do not appear to have been discussed in the open literature on aeroengine seals, some understanding of the effects of different surface finishes would clearly be useful. The nature and height of any surface roughness will depend on manufacturing processes and design specifications. It is not clear from the published reports what the surface finish is for the seals tested, or how this might affect seal behavior. For example, while a roughness height of 0.5 μm might have negligible effect at a design condition, it could lead to reduced film lift as the clearance is reduced and greater likelihood of contact between rotating and stationary components.

Contributed by the International Gas Turbine Institute (IGTI) of THE AMERICAN SOCIETY OF MECHANICAL ENGINEERS for publication in the ASME JOURNAL OF ENGINEERING FOR GAS TURBINES AND POWER. Paper presented at the International Gas Turbine and Aeroengine Congress and Exhibition, Amsterdam, The Netherlands, June 3–6, 2002; Paper No. 2002-GT-30246. Manuscript received by IGTI, Dec. 2001, final revision, Mar. 2002. Associate Editor: E. Benvenuti.

An idealized, infinitely wide Rayleigh pad with surface roughness is illustrated in Fig. 1. Here, periodicity is assumed over the total step length $L=l_1+l_2$. The lower, smooth surface has constant velocity U. The upper, stepped surface may be rough, and the mean clearances either side of the step are, respectively, h_1 and h_2. Classic lubrication theory may be applied to this case. This is based on the Reynolds equation, which is derived by assuming a small clearance to length ratio $\varepsilon(=h_2/L)$ and that inertial effects can be neglected. In addition, the Knudsen number (which represents the ratio of the mean free path for the fluid to the mean minimum gap h_2) is assumed sufficiently small for the Navier-Stokes equations and no-slip boundary conditions to apply. Defining a Reynolds number Re based upon the minimum mean clearance h_2, i.e.,

$$\mathrm{Re}=\frac{\rho U h_2}{\mu},$$

this theory is expected to apply to smooth pads provided $\varepsilon\,\mathrm{Re}$ is small (see, for example, Acheson [3]). In this case, local departures from the Reynolds equation solution near the step will have limited effect on the overall flow behavior.

The Reynolds equation can be used even for relatively large Reynolds numbers, provided the bearing aspect ratio ε is very small according to the above condition. However, with rough surfaces, the global aspect ratio ε must be replaced by the maximum local gradient $\xi=4a/\lambda$ of the roughness peaks, where a and λ are the characteristic roughness amplitude and wavelength, respectively. This results in a more restrictive validity condition:

$$\max(\xi,\varepsilon)\mathrm{Re}\ll 1, \quad \xi=4a/\lambda. \tag{1}$$

Typical air-riding seals for aeroengine applications have clearances of order 1 to 100 μm. (It is interesting to note that these are large compared to those of order 0.1 μm achieved for the load carrying air film between a computer disk and the magnetic head.) Reynolds numbers of order 10 to 1000 are representative of aeroengine applications, so inclusion of inertial effects was considered essential for the present study. Representative Knudsen numbers are of order 10^{-5} to 10^{-2}. According to Anderson [4], the no-slip condition holds for Knudsen numbers $<\sim 0.03$, and so no account is taken of any departure from the low Knudsen number limit in this study.

As shown, for example, in the review by Dyson [5], earlier work on extending lubrication theory to rough surfaces has led to modifications of the Reynolds equation, with extra terms introduced to model the average effects of roughness. In a more recent example, Lunde and Tonder [6] obtained appropriate factors to be included in a modified Reynolds equation average flow model

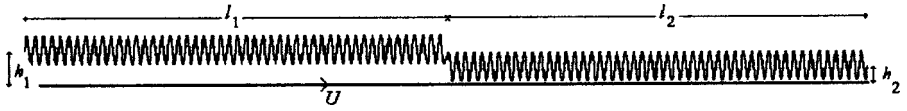

Fig. 1 Schematic of a periodic Rayleigh-pad with two-dimensional harmonic surface roughness (not to scale)

from a detailed flow model. The detailed model involved the numerical solution of the Reynolds equation over a small area of a bearing for which one surface is rough. In principal this approach might be adapted to include Reynolds number effects using numerical solutions of the Navier-Stokes equations. As the authors are not aware of any published work considering Reynolds number effects with rough surfaces, this study focuses on this aspect of the problem. Numerical solutions of the Navier-Stokes equations are presented for Rayleigh pad flow with two-dimensional and three-dimensional "structured roughness" on the stepped surface.

For completeness, a summary of lubrication theory for Rayleigh pads is given in the next section. The numerical methods used and validation of the model for smooth pads and two-dimensional roughness geometries are described in Section 3. Results of three-dimensional roughness studies are presented in Sections 4, with the main conclusions given in Section 5.

2 Theoretical Results for Smooth Rayleigh-Pads

2.1 Ideal Gas Flow. For steady compressible gas flow it is appropriate to introduce nondimensional variables as follows:

$$X=\frac{x}{L},\quad H=\frac{h}{h_2},\quad P=\frac{p}{p_0},$$

where p_0 is a reference pressure. For low Reynolds number thin film flow with uniform viscosity, the pressure distribution is given by the Reynolds equation for ideal gas flow. Assuming a steady isothermal flow in an infinitely wide pad, this is given, for example, by Szeri [7]:

$$\frac{\partial}{\partial X}\left(PH^3\frac{\partial P}{\partial X}\right)=\Lambda\frac{\partial(PH)}{\partial X}, \tag{2}$$

where the compressibility number is defined by

$$\Lambda=\frac{6\mu UL}{h_2^2 p_0}.$$

This equation may be derived from the Navier-Stokes equations with the neglect of inertial terms and derivatives in the streamwise (x) direction, and analytical integration in the direction normal to the moving wall (y). With the appropriate choice of the reference pressure p_0, the periodic boundary condition considered here gives

$$P(0)=P(1)=1.$$

This is easily modified to include pressure-driven flow, if required. Asymptotic solutions are available for incompressible flow corresponding to $\Lambda\to 0$ in the above equations. These are given in the subsection below. An important distinction between the compressible and incompressible problems is that the former is nonlinear. Solutions for the highly compressible limit $\Lambda\to\infty$ are available and are given, for example, by Szeri [7]. However, numerical solutions are required in the general case. In the present study, quantitative comparison was made with numerical results presented by Faria and Andres [8].

2.2 Incompressible Flow. For incompressible flows, the pressure P (which appears due to the equation of state) before the H on both sides of Eq. (2) disappears. In this case, it can be shown that the volume flow rate Q per unit width is given by (see, for example, Acheson [3]):

$$Q=\frac{Uh}{2}-\frac{h^3}{12\mu}\frac{dp}{dx}.$$

Since, from conservation of mass, Q is independent of x, so too is dp/dx if the clearance $h(x)$ is constant. Thus for a smooth, infinitely wide pad, the pressure decreases linearly with x in the region with smaller clearance and increases linearly in the region with larger clearance. The theory fails at the step where $h(x)$ is discontinuous but, provided $\varepsilon\ll 1$, this can be assumed to be a local effect only.

The requirement for the pressure and mass flow to be continuous at the step enables the following value of the resultant pressure increase Δp to be deduced (see, for example, Massey [9]):

$$\frac{\Delta p}{6\mu U}=\frac{h_1-h_2}{(h_1^3/l_1)+(h_2^3/l_2)}, \tag{3}$$

using the notation of Fig. 1. Note that for incompressible flow, p_0 is no longer the most useful choice of characteristic pressure. Instead, the group $\mu U/L$ is more appropriate. It can also be shown that the optimum load-carrying capacity occurs for the special case $r=h_1/h_2=1+\sqrt{3}/2\approx 1.866$ and $l_1/l_2=(5+3\sqrt{3})/4\approx 2.549$.

For convenience, this report shall focus attention only on the case $l_1=l_2=L/2$ and for a step-ratio $r=h_1/h_2=2$. In this case, the pressure increase Δp can be written as follows:

$$\frac{\Delta p}{6\mu U}=\frac{f(r)}{2}\frac{L}{h_2^2}, \tag{4}$$

where

$$f(r)=\frac{r-1}{r^3+1}. \tag{5}$$

For $r=2$, $f(r)=1/9$. It also follows from Eq. (4) that the pressure gradient is given by

$$\left|\frac{dp}{dx}\right|=\frac{6\mu U f(r)}{h_2^2}. \tag{6}$$

The load carrying force per unit width, denoted F^* for this solution, may be shown to be

$$F^*=\int_0^L (p-p_0)dx=\frac{3\mu U f(r)L^2}{2h_2^2}. \tag{7}$$

In this study, numerical results are expressed in terms of the nondimensional load-carrying capacity $\Phi=F/F^*$, where F is the actual lift force and F^* is the lift for the smooth case as determined using Eq. (7). Obviously the Reynolds equation solution for incompressible flow gives $\Phi=1$ for smooth cases. In addition, pressure distributions are plotted in terms of the nondimensional pressure κ defined by

$$\kappa=\frac{p-p_{\min}}{(\Delta p)^*},$$

Table 1 Summary of geometrical and operating parameters

Parameter	2D	3D
Length, L	0.01 m	0.0004 m
Minimum height, h_2	5×10^{-5} m	2.5×10^{-5} m
Aspect ratio, $\varepsilon=h_2/L$	0.005	0.0625
Roughness wavelength, λ	10^{-4} m	2×10^{-5} m
$\xi/\tau=4\,h_2/\lambda$	2	5
Fluid density, ρ	1.225 kg/m^3	1 kg/m^3
Fluid viscosity, μ	1.789×10^{-5} kg/ms	2×10^{-5} kg/ms
Number of roughness waves	100	20

where $p_{\min}$ is the minimum pressure and $(\Delta p)^*$ is determined using Eq. (3).

The static stiffness K can be calculated from the rate of change of load carrying force with clearance. The stiffness K^* for a smooth pad is found by differentiating Eq. (7) yielding

$$K^*=-\frac{3\mu U f(r)L^2}{h_2^3}+\frac{3\mu UL^2}{2h_2^2}\frac{df}{dr}\frac{dr}{dh_2}. \tag{8}$$

Note that the second term in the above expression is much smaller than the first for the conditions of interest in this study.

3 Results for Two-Dimensional Geometries

3.1 Numerical Procedure. In this section, sinusoidal roughness patterns are considered with various values of the roughness amplitude to mean minimum clearance ratio $\tau=a/h_2$. The geometrical and operating parameters are summarized in Table 1 below. The step ratio r was taken as 2 for all of the results shown here. It should be noted that none of the rough cases considered here have peaks which actually touch the smooth moving surface. The Reynolds and compressibility numbers were varied by changing the speed of the moving surface and/or the pressure level.

Results using FLUENT (version 5.4.8, Ref. [10]) are shown, with a comparison to a numerical solution of the Reynolds equation. All grids were generated using GAMBIT (version 1.3.0, Ref. [10]). The FLUENT results have been obtained using a second-order accurate scheme with the pressure-correction SIMPLE algorithm (see, for example, Tannehill et al. [11]). Standard fluid properties for air were used for all two-dimensional FLUENT solutions obtained here. Typically, the velocity U of the smooth wall was taken as 100 m/s, and a laminar flow was assumed throughout. All of the results presented here are believed to have converged to a steady state (for all solutions, the momentum equation residuals are reduced by at least a factor of 10^3 from their starting values). Although not shown, it has been confirmed that the net axial forces on the bearing sum up to acceptably small values. Grid independency studies were carried out and have shown that the solution does not change significantly for different meshes, provided a fine enough grid is used.

Solutions were obtained assuming either ideal gas or incompressible flow. It was found that provided Λ is small and that the overall variation in pressure was less than 5%, then these solutions were essentially the same. For convenience, some compressible flow solutions satisfying this low pressure variation condition are referred to as incompressible below.

The Reynolds equation (2.3) was solved here using a second-order accurate implicit finite-difference procedure based upon quasi-Newton iterations for arbitrary surface geometries $H=H(X)$ and bearing numbers Λ (see, for example, Burden and Faires [12]). Other researchers have used a finite element method for smooth geometries (see Faria and Andres [8] for further details). All results shown here were obtained using 5000 mesh points in order to ensure grid independency (although not shown in this report, it was verified that solutions obtained using different mesh sizes yield very similar results). In order to avoid difficulties encountered by the discontinuity at the Rayleigh-step, the upper surface $H(X)$ was taken as

$$H(X)=\frac{A+\tanh[-\sigma(X-X_{\text{step}})]}{A-1}+\frac{\eta(X)}{L},$$

where $\eta(X)$ is the perturbation due to the surface roughness and

$$A=\frac{r+1}{r-1},\quad X_{\text{step}}=0.5.$$

Here, σ is a smoothing parameter (taken here as 1000). This has the effect of slightly rounding the step, and has been shown to have negligible impact upon the global solution. It was confirmed that the numerical results obtained here for smooth cases were found to agree with those obtained by Faria and Andres [8].

Table 2 Load-carrying parameter Φ for incompressible flow with various Reynolds numbers for the smooth case

Velocity U (m/s)	Reynolds Number Re	ε Re	Φ
1	3.4	0.017	0.9889
10	34	0.17	0.9851
100	340	1.7	1.0183

3.2 Validation for Smooth Rayleigh-Pads. For smooth cases, a regular structured grid consisting of 3×10^4 mesh points was employed (50 mesh points are located across the minimum gap). The surface geometry $h_{\text{mean}}(x)$ for smooth cases was taken as

$$h_{\text{mean}}(x)=\begin{cases} rh_2, & 0\leq x\leq x_{\text{step}} \\ h_2, & x_{\text{step}}<x\leq L \end{cases},$$

where x_{step} is the location of the step, r the step ratio, and h_2 the minimum mean clearance gap.

Table 2 compares the CFD results for various velocities for the sliding wall. As might be expected, the solutions are very close to the analytical incompressible solution $\Phi=1$. It is evident that the numerical FLUENT result is in very good agreement with the expected theoretical result. As shown in Fig. 2, there is a recirculation region just upstream of the step. This weak reversed flow extends throughout the larger clearance section of the pad. Detailed comparison of the velocity profiles with lubrication theory solutions shows good agreement, including prediction of the recirculation.

3.3 Results for Harmonic Surface Roughness Patterns This section presents some results for two-dimensional Rayleigh-pads with sinusoidal surface roughness. Unless otherwise stated,

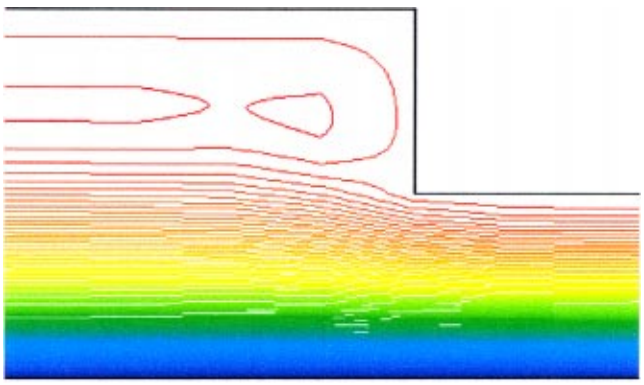

Fig. 2 Streamlines in the vicinity of the step

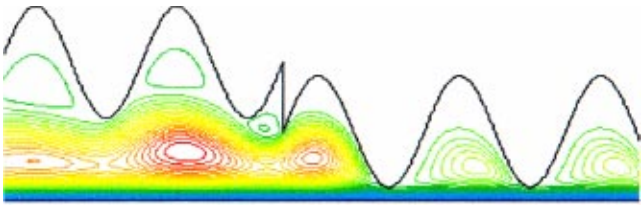

Fig. 3 Streamlines for two-dimensional flow near the step for τ=0.8 and Re=340

all results shown here for rough cases were obtained using an unstructured mesh with approximately 2×10^5 nodes. Attention is confined here to the case in which the roughness perturbation $\eta(x)$ is on the stepped (i.e., stator) surface, and for which a steady flow can be assumed. In this case, the harmonic roughness pattern $\eta(x)$ is chosen as

$$\eta(x)=h(x)-h_{\text{mean}}(x)=a\sin\left(\frac{2\pi x}{\lambda}\right),$$

where a and λ are, respectively, the characteristic amplitude and wavelength of the corrugations.

Surface roughness can have particularly dramatic effects on the streamline patterns, and can result in extensive recirculation regions, particularly for large values of τ (see Fig. 3). It is evident from the results in Fig. 4 that for τ=0.8, the CFD results differ significantly from the solution of the Reynolds equation. For the case τ=0.2 shown in Fig. 4, ξ=0.4 and hence ξRe=136, which is clearly in violation of the condition for validity of the Reynolds equation solution given by Eq. (1). Compressibility effects become significant for values of Λ greater than unity, and result in nonlinear distributions for the pressure. The comparison between the CFD and Reynolds pressure distributions for moderate values of Λ are shown in Fig. 5 for both a smooth and mild roughness case. Here, it may be noted that the Reynolds equation results are in fair agreement with the CFD solutions.

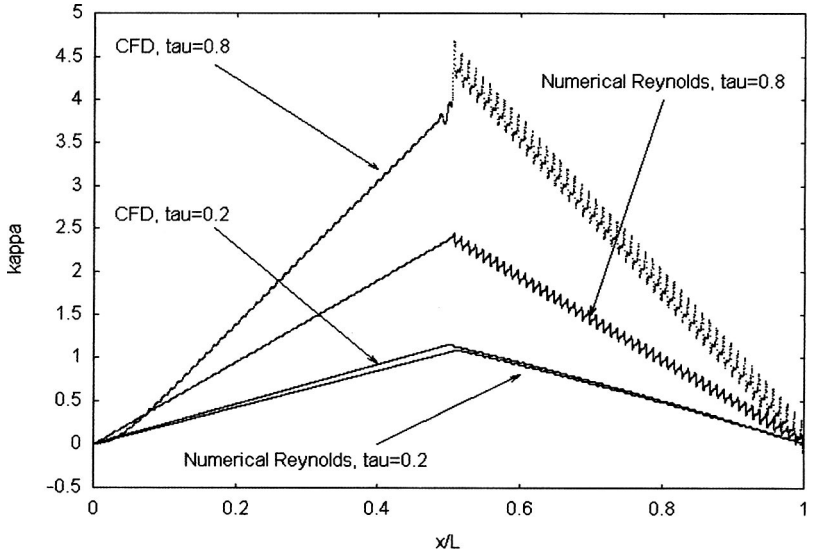

Fig. 4 Nondimensional pressures κ for Re=340 and roughness parameters τ=0.2 and 0.8 (incompressible case)

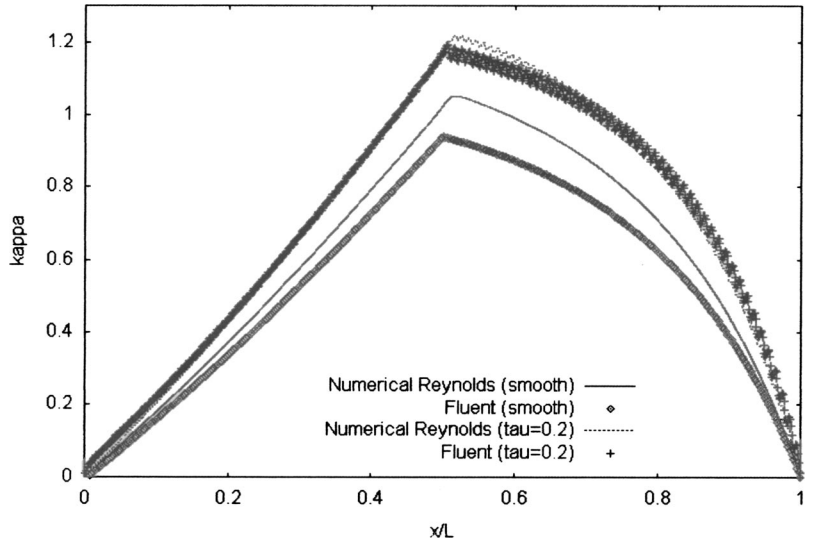

Fig. 5 Solutions for a moderate compressible smooth and rough Rayleigh-pad (smooth case: Λ=4.68 and Re=29.7, rough case: τ=0.2, Λ=5.06, Re=27.5)

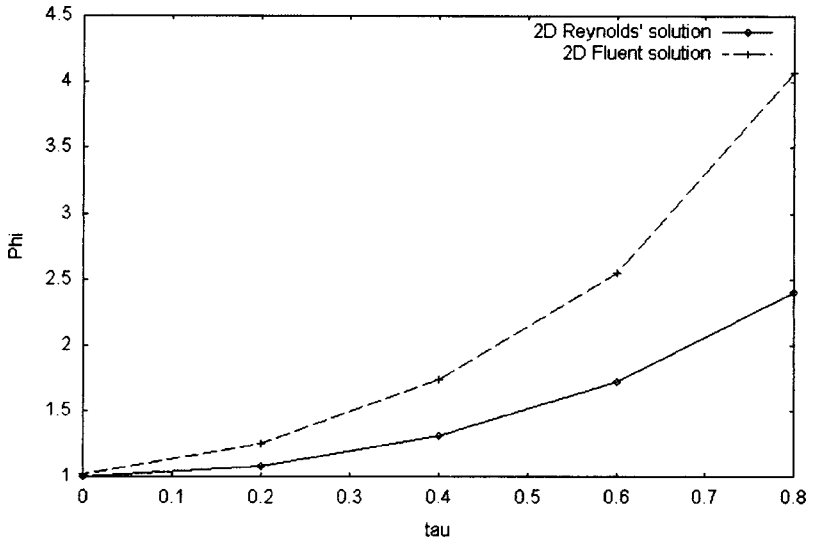

Fig. 6 Load-carrying capacities for various two-dimensional roughness parameters τ ($\xi\tau$=2, incompressible case)

Results for the nondimensional load-carrying capacity Φ are shown in Fig. 6 for two-dimensional incompressible flow with Re=340 and ξ=2. The departure of the CFD results from the Reynolds equation solutions as τ increases is clear. The effect of Reynolds number, again for incompressible flow, is shown in Fig. 7. The Reynolds equation solutions are, of course, independent of Reynolds number. It is interesting to see that only for Re>100 do the CFD solutions show significant Reynolds number dependency.

4 Results for Three-Dimensional Geometries

This section presents some results for infinite width pads with three-dimensional rough or bumpy surfaces of the form

$$\eta(x,z)=h(x,z)-h_{\text{mean}}(x)=a\cos\left(\frac{2\pi x}{\lambda}\right)\cos\left(\frac{2\pi z}{\lambda}\right),$$

where a and λ are, respectively, the amplitude and wavelength of the corrugations or ''bumps.'' All FLUENT solutions shown here were obtained for an incompressible flow with a Reynolds number of 125. The speed U of the moving surface (rotor) was taken as 100 m/s, and the other operating parameters are summarized in Table 1. As for the two-dimensional case considered in the previous section, a second-order accurate scheme with the pressure-correction SIMPLE algorithm was employed, and laminar flow conditions were assumed.

4.1 Full Three-Dimensional Rayleigh-Pad Simulation. To limit the size of the CFD mesh, the total length L of the Rayleigh-pad was chosen to give a relatively short pad with aspect ratio ε=0.0625 and a step ratio r=2. Since the surface bumps repeat themselves on every wave cycle, it suffices to consider half a wave cycle with symmetric conditions on either side (see Fig. 8). A tetrahedral unstructured grid consisting of approximately 2.3 $\times 10^5$ nodes was employed.

The numerical results for the static pressure are shown in Fig. 9 (note that gauge pressures are shown with respect to the reference pressure $p_0=10^5$ Pa). Clearly, the pressure reaches its maximum value as the flow passes from the higher to the lower sections.

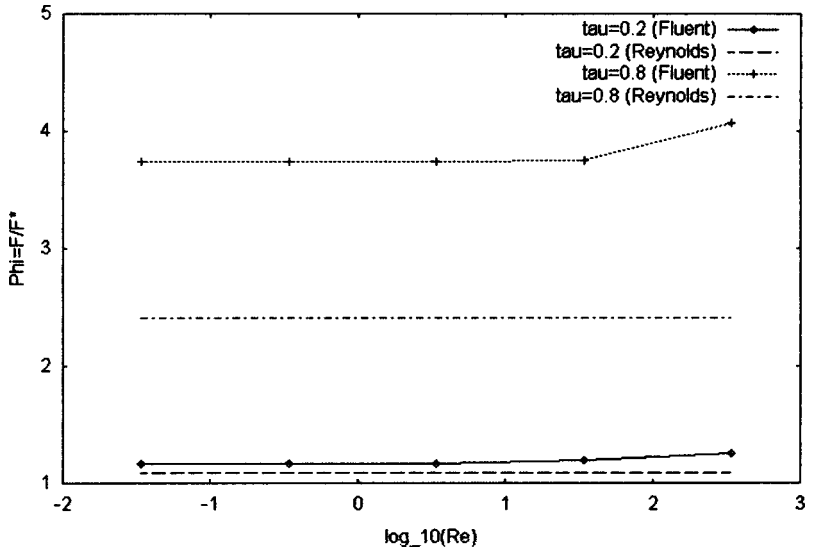

Fig. 7 Nondimensional load-carrying capacity for various Reynolds numbers (incompressible case)

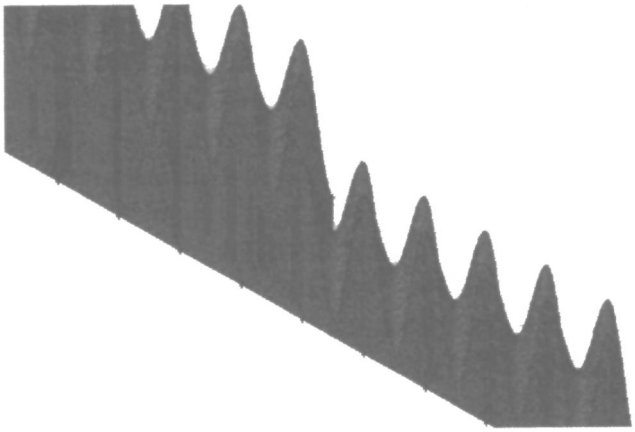

Fig. 8 Closeup of mesh for full three-dimensional Rayleigh-pad simulation

Figure 10 shows a comparison of the pressure distribution for both two-dimensional and three-dimensional cases. The steep rise in pressure at the step ($x/L=0.5$) for the two-dimensional case is associated with the greater change in flow area at the step for this case. Care must be taken in comparing the mean axial pressure gradients of the different cases due to the influence of the step on the flow. However, in the smaller clearance region, agreement between the full three-dimensional pad results and the ''three-dimensional linear unit method,'' which is described in the next section, is considered good. In the high clearance section the full three-dimensional pad results show a more variable mean pressure gradient, indicating influence due to the step.

4.2 Linear Unit-Based Method. Although solutions for short three-dimensional Rayleigh-pads have been successfully obtained here, the memory allocation and computational effort required is relatively large, and the solution on such grids can take comparatively long times to converge (see Table 3). An alternative approach (henceforth referred to here as the linear unit-based method) for incompressible flows is to make use of the linearity of

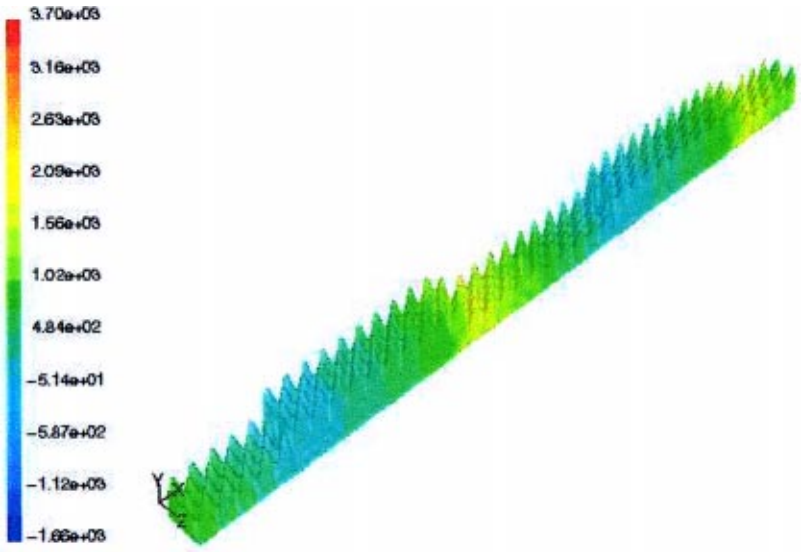

Fig. 9 Surface gauge pressure contours for a Rayleigh-step with three-dimensional harmonic surface corrugations for the case $\tau=0.8$, Re=125

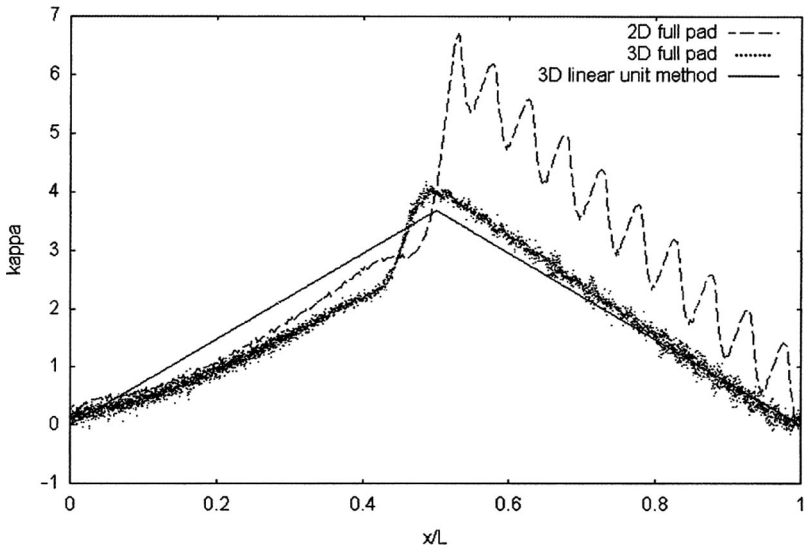

Fig. 10 Comparison of moving surface pressure distributions for both two-dimensional and three-dimensional roughness for $\tau=0.8$ and Re=125

Fig. 11 Typical tetrahedral mesh for a unit corrugation three-dimensional wavy surface (τ=0.8, Re=125)

the solution given by Eq. (6). The idea is to obtain CFD solutions for one roughness cycle (in this case one three-dimensional harmonic wave) using periodic conditions in order to simulate fully developed flow in a long channel (see Fig. 11). In order to infer the solution for a full Rayleigh-pad including the step, different solutions are obtained for the two different clearance heights, and also for various different pressure gradients. The results are then compared to each other, and the solution corresponding to the full Rayleigh-pad is obtained using the conditions for continuity of mass flow and pressure.

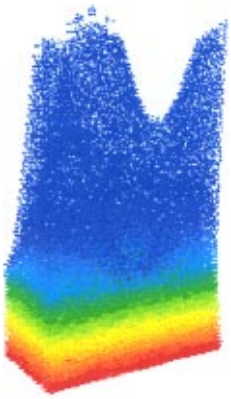

Fig. 12 Typical velocity vector plot for a unit corrugation three-dimensional wavy surface (τ=0.8, Re=125)

The comparison between the unit-based approach and a full Rayleigh-pad simulation is also shown in Fig. 10 from which it had been noted that fair agreement for the pressure gradient is obtained. Better agreement can be expected for longer Rayleigh-pads where disturbances from fully developed flow in the region of the step have less overall effect. It should be noted that the unit-based approach determines the overall pressure gradient χ, neglecting effects at the step, and is applicable for incompressible cases only. Unless stated, all other three-dimensional results presented here were obtained using this technique.

Figure 12 shows a typical velocity vector plot for the flow through a three-dimensional wave-unit. Notice the relative slow speed of the flow in or around the ''bumps.'' Figure 13 shows the effect of varying the roughness parameter τ on the load-carrying capacity Φ. In order to make a proper comparison, the geometrical and operating properties of these two-dimensional cases are the same as those for the three-dimensional case shown in Table 1. As expected, Φ increases for more severe roughness cases. The effects of the three-dimensional bumps are similar to the two-dimensional corrugations, apart from severe roughness (i.e., $\tau \approx 0.8$) for which three-dimensional bumps result in less lift force as compared to the two-dimensional case.

4.3 Static Stiffness Calculation. It follows from Eq. (6) that for Rayleigh pads with $l_1 = l_2$, the minimum clearance h_2^* for a smooth pad giving the same lift as a rough pad of the same length is given by

$$h_2^* = \sqrt{\frac{6\mu U f(r)}{\chi}},$$

where χ is the pressure gradient for the rough pad. For the case τ=0.8, the FLUENT results for χ give $h_2^*/h_2 = 0.52$. Once χ has been determined, the static stiffness K for the equivalent smooth pad can be calculated using Eq. (8).

The stiffness for the rough case can be determined by obtaining solutions with slightly reduced mean clearances h_2 between the rough and smooth. Here, the lower smooth surface was displaced upwards in increments of 1.5 μm, and steady-state results are obtained for each new case. Note that the minimum clearance

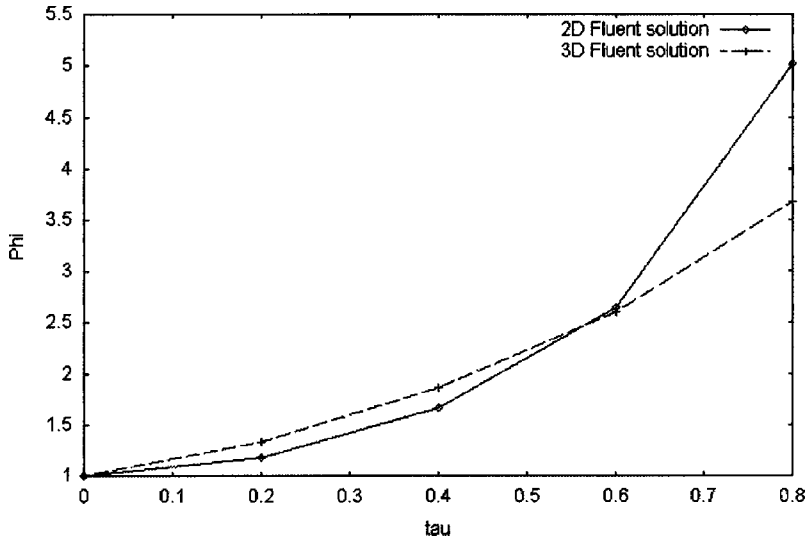

Fig. 13 Load-carrying capacities for various roughness parameters τ (ξ/τ=5, incompressible case)

Table 3 Approximate computing times (seconds per iteration) on a 1 GHz processor

Case	2D Full Pad	3D Linear Unit Method	3D Full Pad
Computing time	3	7	55

considered here between a roughness peak and the smooth surface was only 0.5 μm. From these solutions, the stiffness can be calculated for the rough case. This is found to be approximately two-thirds that for the equivalent smooth case. Thus, for a given load, surface roughness reduces the stiffness.

5 Conclusions

Numerical results using FLUENT have been successfully obtained here for air-riding Rayleigh-pads with step ratios $r=2$. The effects of roughness on the stationary surface have been investigated, and the CFD results have been compared to numerical solutions of the compressible Reynolds equation. Static stiffness results have also been obtained and compared to theoretical results for smooth bearings.

Both two-dimensional and three-dimensional cases have been considered for various roughness amplitudes and Reynolds numbers. For three-dimensional incompressible flows, a linear unit-based method has also been employed which has been shown here to be in fair agreement with the full-pad approach.

Typical computing times are summarized in Table 3.

The main conclusions from this study are:

1. the CFD and Reynolds equation solutions are in good agreement for both smooth surfaces and for low values of the roughness parameter τ.
2. at higher values of τ, the 'rough wall' Reynolds equation solutions underestimate the load-carrying capacity as compared to the more realistic CFD results.
3. even at the higher values of τ, the CFD solutions show little Reynolds number dependency for Re$<$100 (cf. Fig. 7).
4. both the two-dimensional and three-dimensional harmonic roughness patterns considered here show similar effects on the lift force. However, three-dimensional roughness yields relatively less load-carrying capacity for severe roughness cases (i.e., $\tau \approx 0.8$).
5. for a given load, surface roughness reduces the static stiffness.
6. as can be seen in Table 3, the three-dimensional linear unit method provides an efficient technique for computing the load-carrying capacity as compared to the full-pad approach.
7. there is clearly considerable scope for further investigation of roughness effects on air-riding seals using CFD. With available computing power continuing to increase, expansion of work in this area can be expected.

Nomenclature

a = roughness amplitude
C_D = drag coefficient
C_L = lift coefficient
F = load-carrying force per unit width
h_1, h_2 = mean clearance gap for high and low clearance sections
$h(x)$ = actual surface height geometry
H = nondimensional surface height geometry ($=h/h_2$)
K = static stiffness ($K=dF/dh_2$)
L = total length $L=l_1+l_2$
$l_{1,2}$ = bearing lengths for high and low sections
p = pressure
p_0 = base (operating) pressure
P = non-dimensional pressure ($=p/p_0$)
Q = volume flow rate per unit width
r = step ratio ($=h_1/h_2$)
Re = Reynolds number
S = cross-sectional surface area
U = moving surface speed
x, z = streamwise and transverse coordinates tangential to moving surface
y = coordinate normal to moving surface
X = nondimensional streamwise coordinate ($=x/L$)
γ = ratio of specific heats
Δp = pressure increase
λ = roughness wavelength
Λ = compressibility number
ε = aspect ratio h_2/L
Φ = nondimensional load-carrying capacity ($\Phi=F/F^*$)
κ = nondimensional pressure
χ = pressure gradient
η = roughness perturbations
ρ = density
μ = dynamic viscosity
σ = smoothing parameter for Reynolds equation solution
τ = ratio of roughness amplitude to clearance h_2 ($=a/h_2$)
ξ = maximum local gradient of surface roughness ($=4a/\lambda$)

Subscripts

0 = reference (base) conditions
1, 2 = high and low clearance Rayleigh-pad sections
min = minimum quantity

Superscripts

$*$ = Reynolds equation solution for incompressible flow in a smooth pad with $l_1=l_2$

References

[1] Munson, J., 1992, "Development of a High Performance Compressor Discharge Seal," *28th Joint Propulsion Conference, AIAA Paper* 92-3714.
[2] Hwang, M. F., Pope, A., and Shucktis, B., 1995, "Advanced Seals for Engine Secondary Flow Path," J. Propul. Power, **12**, pp. 794–799.
[3] Acheson, D. J., 1990, *Elementary Fluid Dynamics*, Oxford University Press, Oxford, UK.
[4] Anderson, J. D., 1989, *Hypersonic and High Temperature Gas Dynamics*, McGraw-Hill, New York.
[5] Dyson, A., 1978, "Hydrodynamic Lubrication of Rough Surfaces—A Review of Theoretical Work," *Surface Roughness Effects in Lubrication*, D. Dowson, C. M. Taylor, M. Godet, and D. Berthe, eds., Mech. Eng. Publications Ltd. London, pp. 61–70.
[6] Lunde, L., and Tonder, K., 1997, "Pressure and Shear Flow in a Rough Hydrodynamic Bearing, Flow Factor Calculation," ASME J. Tribol., **119**, pp. 549–555.
[7] Szeri, A. Z., ed., 1980, *Tribology: Friction, Lubrication and Wear*, McGraw-Hill, New York.
[8] Faria, M. T. C., and Andres, L. S., 2000, "On the Numerical Modelling of High-Speed Hydrodynamic Gas Bearings," ASME J. Tribol., **122**, pp. 124–130.
[9] Massey, B. S., 1983, *Mechanics of Fluids*, Van Nostrand Reinhold, New York.
[10] Fluent Inc., 1998, http:www.fluent.com.
[11] Tannehill, J. C., Anderson, D. A., and Pletcher, P. H., 1997, *Computational Fluid Mechanics & Heat Transfer*, 2nd Ed., Taylor & Francis, London.
[12] Burden, R. L., and Faires, J. D., 1993, *Numerical Analysis*, PWS-Kent Publishing, Boston.

Gas Turbines Design and Off-Design Performance Analysis With Emissions Evaluation

A. Andreini
e-mail: andreini@brun.de.unifi.it

B. Facchini

Dipartimento di Energetica "Sergio Stecco",
University of Florence,
Via Santa Marta, 3,
50139 Florence, Italy

Many gas turbines simulation codes have been developed to estimate power plant performance both in design and off-design conditions in order to establish the adequate control criteria or the possible cycle improvements; estimation of pollutant emissions would be very important using these codes in order to determine the optimal performance satisfying legal emission restrictions. This paper present the description of a one-dimensional emission model to simulate different gas turbine combustor typologies, such as conventional diffusion flame combustors, dry-low NO_x combustors (DLN) based on lean-premixed technology (LPC) or rich quench lean scheme (RQL) and the new catalytic combustors. This code is based on chemical reactor analysis, using detailed kinetics mechanisms, and it is integrated with an existing power plant simulation code (ESMS Energy System Modular Simulator) to analyze the effects of power plant operations and configurations on emissions. The main goal of this job is the study of the interaction between engine control and combustion system. This is a critical issue for all DLN combustors and, in particular, when burning low-LHV fuel. The objective of this study is to evaluate the effectiveness of different control criteria with regard to pollutant emissions and engine performances. In this paper we present several simulations of actual engines comparing the obtained results with the experimental published data. [DOI: 10.1115/1.1619427]

Introduction

Pollutant emissions control and reduction has now become the principal marketing matter in industrial gas turbine field. During the last 15 years, the gas turbine device subjected to the most significant modifications was probably the combustion chamber. This fact is due to the continuous reductions of governmental emission limits in most of the countries, especially for NO_x emission regulations.

Classical NO_x reduction criteria for industrial gas turbines are based on lowering of flame temperature by inert injection: generally steam or water injection. NO_x emissions below 15–20 ppm (volume dry, 15% O_2) are not easily achievable with these systems unless very high injected mass flow rates are scheduled; a worsening in CO and UHC emission and in plant thermal efficiency and a reduction in engine durability limits are expected, [1].

For these reasons, most turbine manufacturers have undertaken efforts to develop combustion systems having the potential for reducing NO_x emissions without steam or water injection: usually we refer to these new type of combustors as dry-low NO_x (DLN).

In the initial phase of DLN research, two approaches have received high levels of development attention: rich-quench-lean strategy (RQL) and lean-premixed combustors (LPC). However, at the moment, the only well defined DLN solution is based on LPC technology. RQL strategy seems to be very effective in some applications where premixed flames are not easily applicable: aircraft engines and burning of low-LHV fuels.

Using lean-premixed flames (equivalence ratio below 0.65), stoichiometric fuel-air mixtures of diffusion flames yielding the highest flame temperatures are avoided and the NO_x formation rate, which is exponentially dependent on temperature, is lowered, [1].

Lean-premixed combustion achieves low NO_x emissions only in a narrow combustion range. Values of equivalence ratio close to the stoichiometric allow stable combustion but determine high NO_x emission. Using very high excess air ratio often leads to high CO and UHC emission and determines serious problems of stability, [2]. For these reasons LPC are always equipped with some systems for the direct control of mixture composition during engine off-design. We can distinguish these devices in two main typologies: fuel/combustion staging and variable geometry.

We refer to fuel staging system when local fuel-air ratio is controlled by the means of a reduction of fuelled injectors at part-load conditions. Various combinations of switching are possible, which are based on combustor layout (annular or tubular) and size. Radial staging and circumferential staging are typical, [2]. Staged combustors are distinguished by a step-by-step combustion process. In these combustors fuel-air mixture is injected in series stages: during part load operations a reduction of fuelled stages are expected. The main advantage of this combustor is that in the downstream stages the flame develops in a region with higher temperature, widening stability limits, [2].

In variable geometry combustors, fuel-air ratio control during engine off-design, is made by the means of airflow modulation. The most common variable geometry systems is that where swirler efflux section is varied. Other variable geometry systems determines the by-pass of excess air from combustion zone to dilution zone at part-load condition, [3].

The requirements of the new DLN combustors based on lean-premixed technology, determine an appreciable change in gas turbine load regulation criteria. In fact the control devices of combustors (fuel-staging or variable geometry) are not generally sufficient to maintain combustion in the stable range. It's therefore necessary to adopt airflow modulation by the means of engine devices: compressor mass flow bleeding, and compressor inlet guide vane regulation are typical.

Contributed by the International Gas Turbine Institute (IGTI) of THE AMERICAN SOCIETY OF MECHANICAL ENGINEERS for publication in the ASME JOURNAL OF ENGINEERING FOR GAS TURBINES AND POWER. Paper presented at the International Gas Turbine and Aeroengine Congress and Exhibition, Amsterdam, The Netherlands, June 3–6, 2002; Paper No. 2002-GT-30258. Manuscript received by IGTI, Dec. 2001, final revision, Mar. 2002. Associate Editor: E. Benvenuti.

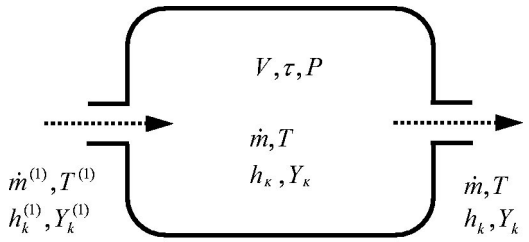

Fig. 1 PSR scheme

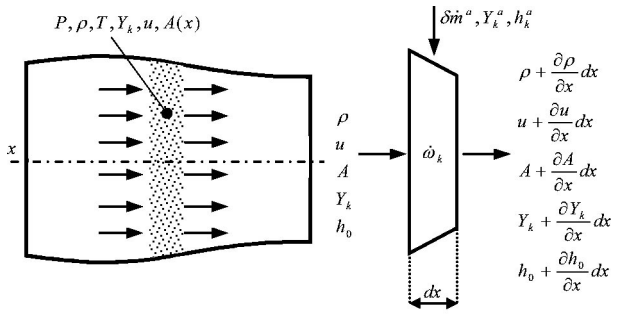

Fig. 2 PFR scheme

These observations point out the necessity to analyze gas turbine off-design performance together with a combustion process study with emissions evaluations. To reduce computational time, this type of research is possible only by introducing some form of simplification in combustion simulation. In this paper we will describe a model for the integrated plant-combustion simulation which uses a chemical reactor analysis of combustion process.

Although nowadays computational fluid dynamics (CFD) codes are valid design tools also in reactive conditions, they cannot be used in a complete analysis of gas turbine power plant because of extremely high computational costs. A simplified model based on chemical reactor, arranged with the most detailed kinetics mechanisms published in specified literature, is quickly capable to analyze the effects on pollutant emissions of the main engine operative parameters (ambient conditions, load regulations, fuel type, and so on). In this work, power plant operating conditions are evaluated with an existing simulation code based on a convenient modular approach, (ESMS Code, [4]).

Chemical Reactors

Simulation of gas turbine combustion by the means of chemical reactors is not something new. Touchton first used reactors for a complete representation of a specific combustor, [5]. Rizk and Mongia, for the first time, approached the problem in a generic manner, [6,7]. Rizk and Mongia work has been lately resumed and modified by some researchers, [8].

The main difference between Rizk and Mongia models and the one presented here consists in chemical reactors typologies and in the integration of pollutant estimation procedure with overall power plant simulation.

In this case we consider perfectly stirred (PSR) and plug flow reactors (PFR) only. These two mathematical models are widely used in kinetics analysis of flame [9]. In this work we will suggest two different reactor network for the analysis of conventional diffusion flame combustors and the new DLN combustors based on lean-premixed technology.

PSR Reactor. The chemical reactor PSR operates a zero-dimensional description of the flow and it could be described as a vessel in which *N* inlet streams are instantaneously mixed. With this type of reactor we will simulate, for the most part, the flame stabilization zones. The flux is entirely described by enthalpy conservation equation and by continuity equations for each of the chemical species, (Fig. 1).

Steady-state conditions could be determined by the time integration of the correspondent ordinary differential equations (ODE) system. Because of equations stiffness, specific numeric algorithm based on backward differentiation formulas are used, [10]. Kinetics and thermodynamics properties are evaluated using Chemkin II package, [11]. The requirements of the integration with a power plants simulation code forced us to develop a new FORTRAN code rather than adopt a commercial software.

PFR Reactor. To simulate the flame relaxation zone (typical of gas turbine combustors and called postflame, [9]) it's necessary to adopt a second type of chemical reactor called plug flow reactor. It describes the flow by a 1D approach supposing that, in the generic section, species are well mixed (Fig. 2).

The governing equations derive from the global flow equations. Written in steady-state form, they constitute an ODE system analogous to that shown for PSR reactor. Also in this case the calculation routines were developed in FORTRAN language using Chemkin II library.

Combustor Chamber Modeling

Following the same line of combustor characteristics according to flame typology, the reactors PSR and PFR will be assembled into two networks in order to model the different constructive solutions of combustion chamber. Then, two models will be described below.

The main problem for conventional combustor modeling resides in the necessity to distinguish diffusive flame features, by means of ideal chemical reactors, as they expect a homogenous reagent mixture. The chemical reaction analysis must take into account the actual reagent composition along the combustor. Then, a reactor network was made to solve the modeling problems and the solution for diffusive flame combustor is presented in Fig. 3.

The primary zone, derived from an idea of Broadwell and Lutz [12], uses two PSR reactors to simulate the jet or central region (core) and the flame sheet zone (flame sheet reactor—FSR) where chemical reactions develop in stoichiometric conditions. The diffusive flows which cause fuel-air to mix and react in stoichiometric conditions (flame sheet zone) are here reproduced by corresponding convective flows. In this initial stage the recirculation zone induced by the swirler and the flame stabilization region are simulated.

Downstream of the flame stabilization zone, the flame begins axial propagation and it develops the maximum temperature rise (postflame). The flame has a high homogeneity level, losing the core-FSR structure. Nonetheless, the flame still keeps diffusive characteristics. A PFR is used for flame zone modeling, while a

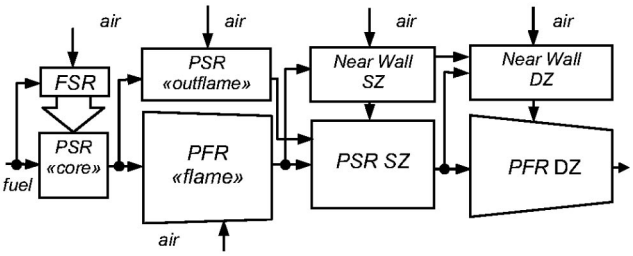

Fig. 3 Chemical reactor network for conventional diffusion flame combustors

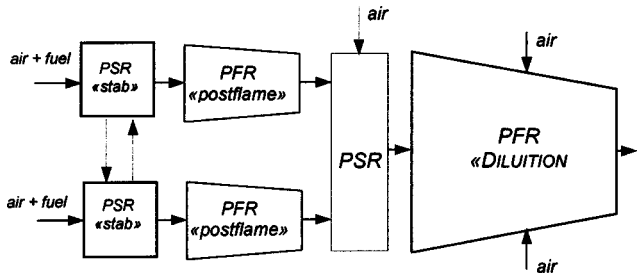

Fig. 4 Chemical reactor network for lean-premixed combustors

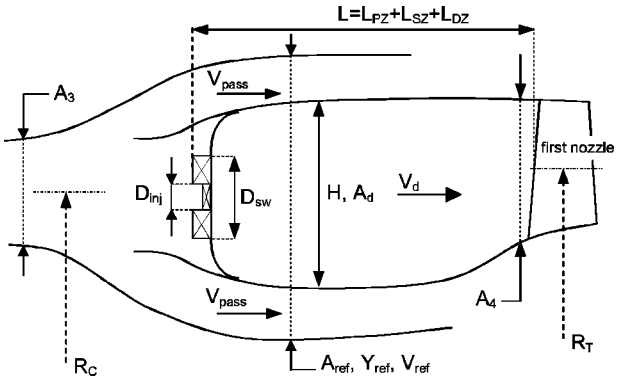

Fig. 5 Combustion chamber geometric modeling

PSR is used to out-flame, that is flame zone surroundings. In secondary zone, that is usually denoted by the first cooling holes line in the combustor wall, [2,13,14], the flame looses entirely diffusive feature and the mixture suffers a drastic homogenization, because of air cooling flow entry. In this zone a PSR can be used. But, it is necessary to take into account the small mass fraction, that reacts near to the combustor wall and it suffers quenching effects. These zones are simulated with specific PSR reactors (near-wall reactors) already introduced by Rizk and Mongia. Analogous considerations may be turned out for dilution zone, except that the best central flow representation is made with a PFR.

Modeling of lean-premixed combustors does not require a special treatment in comparison with diffusive model. In this work, we present a model based on a general scheme, in order to describe a greater number of actual combustors; this scheme is presented in the Fig. 4.

Primary zone is modeled with a PSR-PFR combination, according to typical turbulent premixed flame representation (PSR describes the flame anchorage and stabilization zone, while PFR describes the postflame zone, [9]). Multi-injectors combustors, where different flames for each injection system may be recognized, adopt a parallel arrangement of single PSR-PFR combination. Secondary zone is provided with air jets, this zone is represented with the same combustor volume reactor, where the secondary air and the primary hot gases are mixed. In dilution zone, the combustion products and external annulus air flow are mixed. In this zone hybrid air injection systems can be found, that may be used for combustor liner cooling and to obtain the required pattern-factor. A PFR with the same combustor volume is suitable to model this zone but, for compact combustors model, it is suggested to use a PSR.

ESMS: Gas Turbine Plant Simulation Code

The power plant simulations have been performed using the ESMS modular code. The reader is referred to Refs. [4] and [15] for a complete description of the code and the related theory. The most important feature of this modular code is the ability to simulate a new power plant configuration without creating a new source program. The code easily allows addition of new components. The engine configuration is defined by connecting a number of elementary components representing different unit operations such as compressors, combustion chambers, mixers and so on. Each component is defined as a black box capable of simulating a given chemical and thermodynamic transformation. The resulting set of nonlinear equations defining the power plant is then linearized (the coefficients are, however, updated in the course of the calculation). All equations are then solved simultaneously using a classic matrix method; thus the procedure is essentially that of the fully implicit linear approach. Design and off-design simulation is a two-step procedure. Off-design performance simulation requires a geometric description of the different components (e.g., the velocity triangle at mean radius and other cascade parameters for the compressor or turbine, heat exchanger surface areas, etc.). These data result from a design study. When identifying the different parameters describing the component geometry, knowledge of some plant data is important to improve simulation results (e.g., the turbine exhaust flow rate and the temperature).

Chemical Reactor Combustion (CRC) Code

The combustion models were presented in the previous section. These models, with their respective calculation tools, have been collected and put in a structured algorithm, named chemical reactor combustion (CRC). Then, this code was integrated with ESMS code by the means of a batch procedure, in order to evaluate gas turbine plant emissions both in design and off-design conditions. Firstly, CRC code comprises a detailed combustor geometric calculations, because ESMS code determines only reference geometry, [4].

To define the chemical reactor geometry, that constitutes predominantly combustor model, it is necessary to know the combustion chamber components dimensions, partially shown in Fig. 5. The method for geometry calculation are based on classical empirical correlations proposed by Lefebvre and Mellor [2,13].

Simulation of combustion is made by means of diffusive or lean-premixed combustor models, previously described. In the calculations performed in these tests we utilized some detailed chemical kinetic mechanisms developed by different research institutes. The main are the Gas Research Institute Mechanisms (GRI-Mech. 2.11 and 3.00, [16]) and the Warnatz Mechanism, developed by Klaus and Warnatz (1997).

At the same time, CRC code realizes an analogous ESMS calculation procedure for combustion chamber simulations in off-design conditions. This time geometry features are imposed and the performance parameters, i.e., thermodynamics and chemical compositions, are calculated.

Regarding ESMS and CRC linking, we had opted for a particular solution, in order to allow a certain batch procedure for automatic calculation, maintaining both codes as two independent executable programs, allowing an optional emission performance estimation, once gas turbine simulation are achieved. Figure 6 shows codes linking by a block diagram, for design and off-design simulations.

Gas Turbines Simulations

To check code reliability and to test the overall plant-combustion procedure, we performed some power plant simulations: We referred to simple Joule cycle configurations operating, when possible, a comparison with experimental data. We have tested the main combustor typology (diffusion flame, dry-low NO_x such as lean-premixed and RQL). To analyze the effects of engine operating conditions on combustion system, we studied both single shaft and double shaft gas turbines because of their different part load behavior.

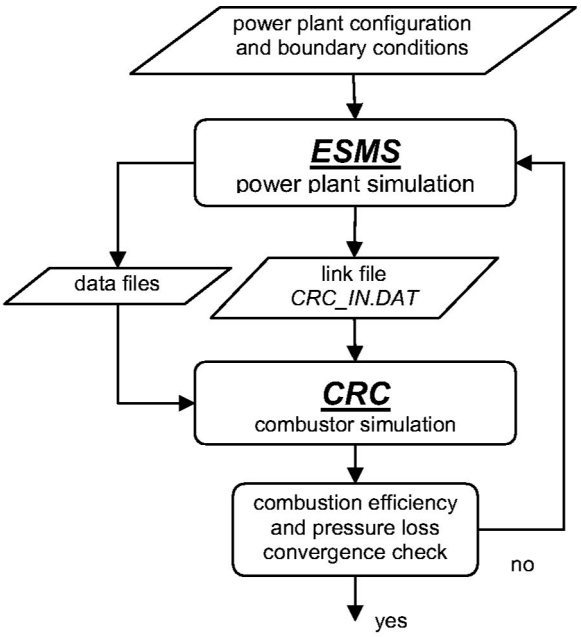

Fig. 6 Block diagram for code linkage visualization

Conventional Diffusion Flame Combustors. The first CRC-ESMS simulation with experimental data comparison was made on MS7001F gas turbine manufactured by General Electric (GE). This engine was the first installed "F" class gas turbine and its emissions have been measured during actual plant operations, [14].

This test has been performed at the Virginia Power Chesterfield station (USA), the first combined cycle plant equipped with MS7001F engine. Emission sampling was done in duct between the HRSG (heat recovery steam generator) and the stack. Many pollutant emissions have been collected: NO_x, CO, unburned hydrocarbons (UHC), volatile organic compounds (VOC), and particulate and nitrous oxide (N_2O). The reader is referred to [14] for more details about test facilities.

MS7001 engine is equipped with 14 tubular reverse flow combustors (see Fig. 7) based on conventional diffusion flames. GE has recently replaced this model with the new MS7001FA equipped with the new DLN 2.6 combustor which represent the lean-premixed solution for heavy duty gas turbine (the reader is referred to [17] for more details). Because of high NO_x emission expected for diffusion flame combustor of MS7001F engine, steam or water injection are scheduled in actual plant operations.

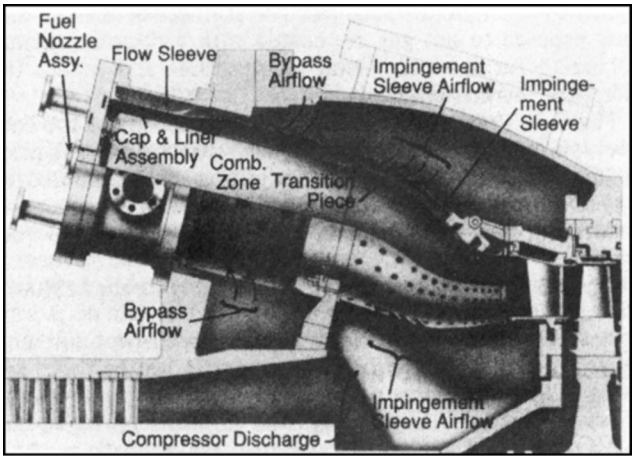

Fig. 7 Scheme of MS7001F combustor, [16]

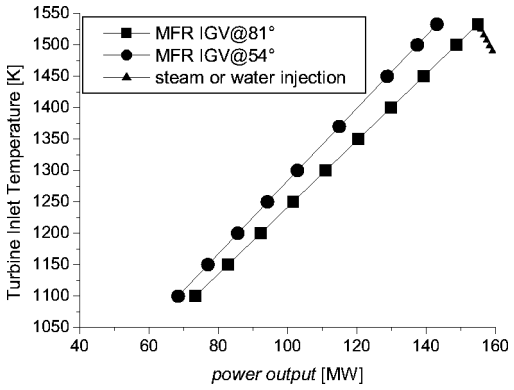

Fig. 8 MS7001 load diagram

Figure 8 shows MS-7001FA load diagram, [14]. Despite temperature values are not shown in the graph, it easy to guess that the two part-load variations are in dry conditions, i.e., without steam injection, corresponding to two different compressor inlet guide vane (IGV) angles: power output is reduced by the means of a standard mass fuel rating (MFR). Starting from some significant power values, the simulations of water and steam injection were carried on, reducing turbine inlet temperature (TIT). This procedure avoids compressor instabilities phenomena.

In this work, we reproduced published curves, in order to verify CRC-ESMS codes reliability. Figure 9 shows NO_x variation versus TIT changes, using MFR power reduction system, for the respective compressor IGV angle.

With reference to experimental values, results obtained from the simulations are close enough. There is a significant difference for low engine load, especially, regarding to partially closed compressor IGV, because of axial compressor model problems.

Figures 10 and 11 show CO and UHC versus TIT variations. The published data, in this case, are relative only to compressor IGV angle equal to 81°. We can observe, in these figures, that CRC predictions under estimate experimental data; that's because simulation devices does not correctly reproduce some real features such as reactive mixture quenching on combustor cooled walls.

The overall simulations results can be considered satisfactory: CRC code correctly reproduces CO trend at part-load conditions, both in initial zone (starting from nominal power) where CO slightly decreases and the last zone where it steeply increases.

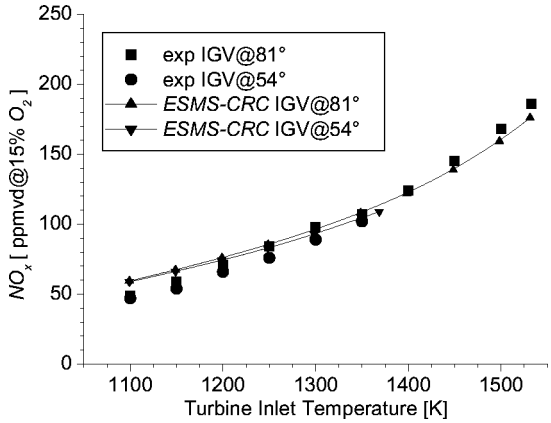

Fig. 9 Experimental and computed NO_x trend for MS 7001F GT

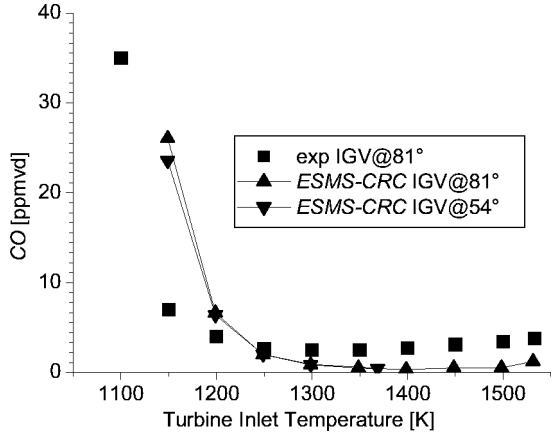

Fig. 10 Experimental and computed CO trend for MS 7001F GT

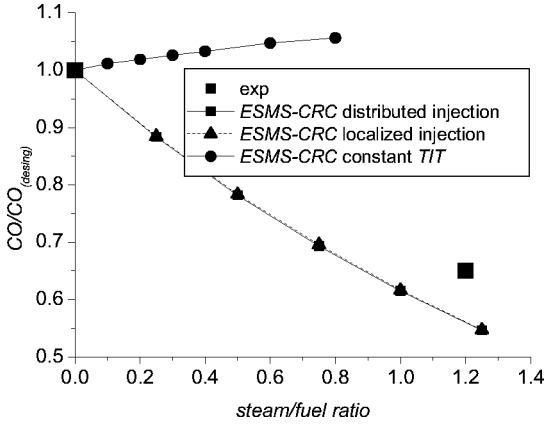

Fig. 13 Experimental and computed CO trend with steam injection

Inert (water or steam) injection effects on the main pollutant substance is described below. Figure 12 shows normalized NO_x with respect to the nominal value versus steam injection variation. Because of uncertainty about steam injection typologies, in this work two extreme types were used: distributed in combustor prediffuser and localized in primary combustion zone.

Figure 13 shows steam effects on CO production. Because of constant fuel mass flow during steam injection, CO emissions tends to decrease. In this particular case (single shaft engine, constant speed operations), steam injection determines a slight reduction in inlet air mass flow which balance the negative effects of steam on CO oxidation. To denote the importance of engine control system effects, Fig. 13 shows CO trend with constant TIT during steam injection: in this case both steam and air mass flow negatively influences CO emissions.

Figure 14 shows NO_x versus water distributed injection variations. In this case CRC code shows a good approach for experimental data reproduction, confirming the effective water action, respect to steam, for pollutant emission reduction.

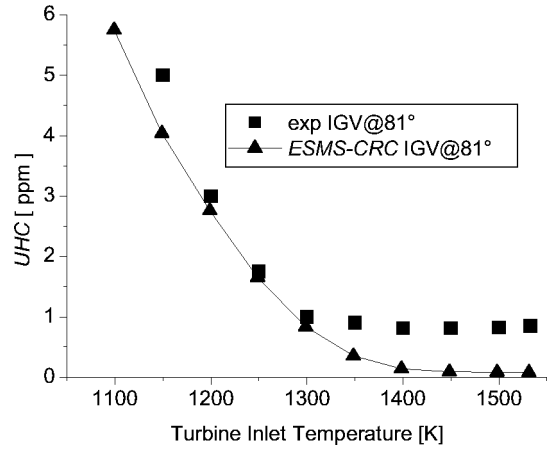

Fig. 11 Experimental and computed UHC trend for MS 7001F GT

Lean-Premixed Combustors. In order to test the validity of the proposed model for lean-premixed combustors, we report the results of two simulations. The first compares computed and experimental data of GE LM2500DLE aeroderivative gas turbine, the second shows only computed results for NP-GE PGT5B engine.

Figure 15 shows DLN combustor for GE "LM" gas turbine series. It is an annular multidome combustor based on lean-premixed technology. Its particular shape is due to two opposite demands: it must accommodate in the existing engine lay-out but it must assure an adequate residence time in order to compensate the lower flame temperature, [18,19].

The main characteristic of this combustor is its injection-premixing system (Fig. 16), called DACRS (double annular counter rotating swirler, see [18] for details). Seventy-five injectors were designed in LM2500: they are all arranged in three

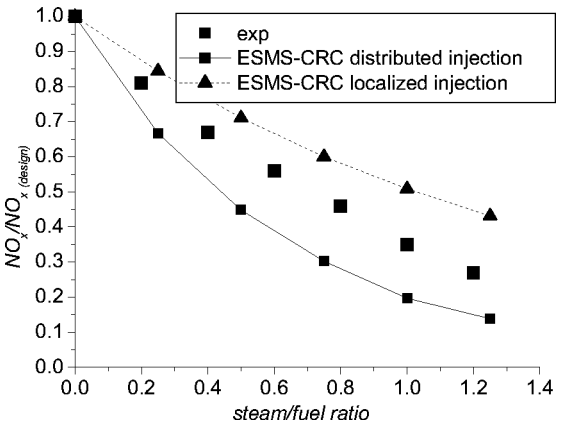

Fig. 12 Experimental and computed NO_x trend with steam injection

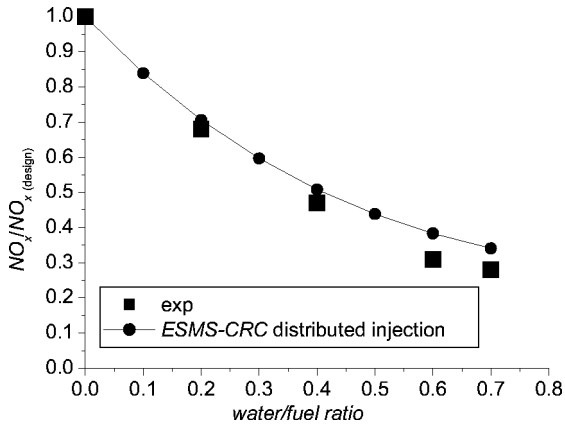

Fig. 14 Experimental and computed NO_x trend with water injection

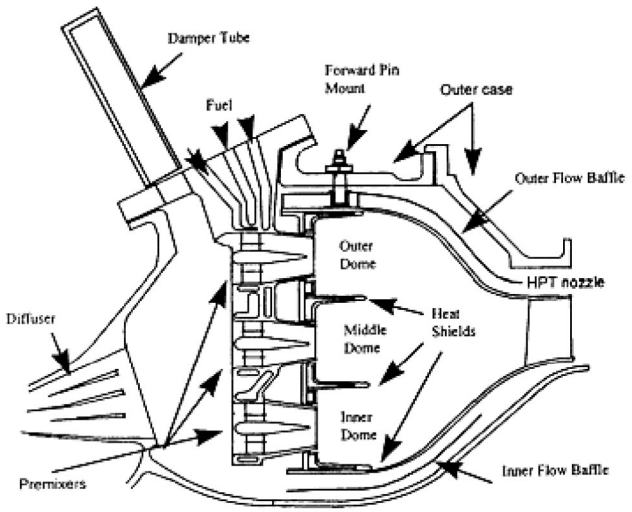

Fig. 15 Lean-premixed combustor for GE "LM" gas turbine series, [18]

concentric domes. In order to control fuel-air ratio during engine duty-cycle, several schemes of radial staging are scheduled.

PGT5B gas turbine is a heavy-duty engine based on single shaft configuration. It is equipped with an annular lean-premixed combustor distinguished by an injection-premixing system derived from GE DACRS. In this case only one row of injector is expected and fuel staging may be difficult to realize: it will be necessary to adopt circumferential staging which determines chilling of reaction at combustion zones edges and worsens exit temperature profile. We have tested two alternative solutions based on direct airflow control systems (variable geometry) which seems to be very effective especially in small engine, [3,20].

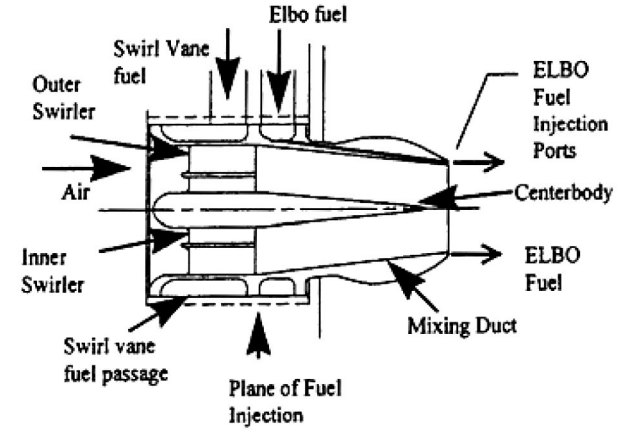

Fig. 16 DACRS injectors, [18]

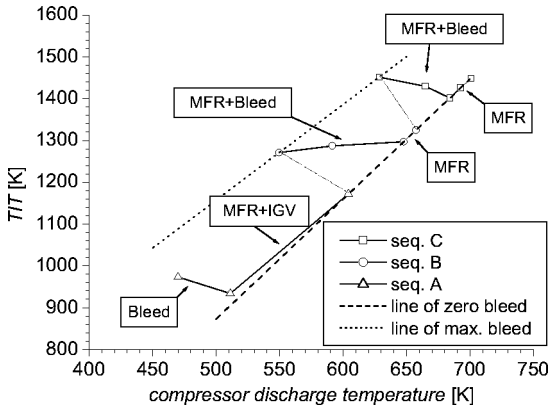

Fig. 17 LM2500DLE load diagram

GE LM 2500DLE. This simulation aims to show the complexity of engine regulation procedure required to control the DLE combustor. We will analyze regulation effects both on plant performances and pollutant emissions. LM2500 design characteristics are shown in Table 1.

As mentioned above, this combustor is equipped with fuel staging devices. Figure 17 shows the entire load diagram and Table 2 reports the various radial fuel staging sequences. The control procedure is approximately the same for any engine of "LM" series.

The purpose of this complex regulation procedure is to keep reactive mixture composition of any injector constant as much as possible during engine duty-cycle. Gas turbine load is reduced by MFR with a contemporary airflow modulation operated by air bleeding at the 8th compressor stage and by the variation of compressor IGV angles. As power output goes under a critical value, corresponding to blow-out limit for reactive mixture of any injector, the number of fueled injector is reduced (Table 2 sequences).

Figure 18 shows NO_x versus power output variation. Obtained results have an optimal approach with respect to experimental data. A progressive NO_x increment, when the power output decreases can be observed. This trend is opposed to conventional combustors: Fuel staging operations guarantee primary zone condition just above blowout limit in every load conditions. As load decreases, compressor discharge temperature and pressure decrease and blowout limit moves to a richer mixture, consequently increasing NO_x emissions.

Table 1 Simulated gas turbines design data

	GE MS 7001F	GE LM2500	NP-GE PGT5B	
Nominal power output	155	23	5.9	MW
Plant efficiency:	0.3963	0.3765	0.3266	···
COMPRESSOR				
Pressure ratio:	14	18.8	15.1	···
Discharge temperature:	631.5	700.9	680.1	K
Required power:	126920	29040	8048	kW
HIGH PRESSURE TURBINE				
Shaft speed:	···	7910	···	rpm
Inlet temperature:	···	1450	···	K
POWER TURBINE				
Inlet temperature:	1533	1078	1456	K
Discharge temperature:	873	797.16	841	K
Mass flow rate:	366.6	69	20.2	kg/s
Power output:	155000	23000	5900	kW
Shaft speed:	3600	3600	16630	rpm

Table 2 Fuel staging sequences for LM2500 GT

Fuel Staging Sequences	15 Injectors Inner Dome	30 Injectors Middle Dome	30 Injectors Outer Dome
A	fueled	fueled	unfueled
B	unfueled	fueled	fueled
C	fueled	fueled	fueled

Figure 19 shows CO versus power output variations. In this case, obtained results are not accurate as NO_x predictions, because the CRC code tends to underestimate the measured emissions. This is also presented in C and B sequences, however, the overall trend is correctly reproduced.

NP-GE PGT5B. This test case was used to check the reliability of combustion control systems based on variable geometry. These devices seem to be a valid alternative to fuel staging in DLN combustors.

As mentioned above, we have tested form this engine a reactive mixture composition control by airflow modulation based on two variable geometry systems. In the first one a bypassing of excess air during part-load operation is scheduled (we have called VG-A this regulation technique, see Fig. 20). We compared also the effectiveness of a variable geometry swirler: We adopted a swirler efflux section reduction during part load (we called this device VG-B, see Fig. 20). In Table 3 are reported design emissions value.

The graphs reported in Figs. 21 and 22 shows NO_x and CO trends versus output power. These graphs show a comparison between the standard MFR regulation (with and without compressor air bleeding) and the two-variable geometry technique. It could be seen the extreme reliability of VG-A system to maintain combustor near design emission point during plant part-load operation. VG-A regulation does not reduce in a significant manner overall plant efficiency even though it causes an increase in pressure loss.

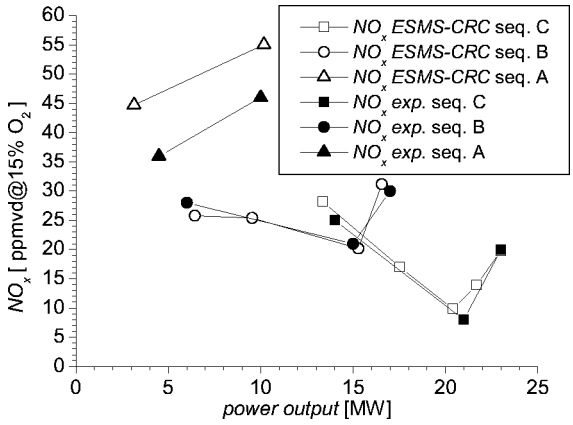

Fig. 18 Exp. and comp. NO_x in LM 2500DLE GT

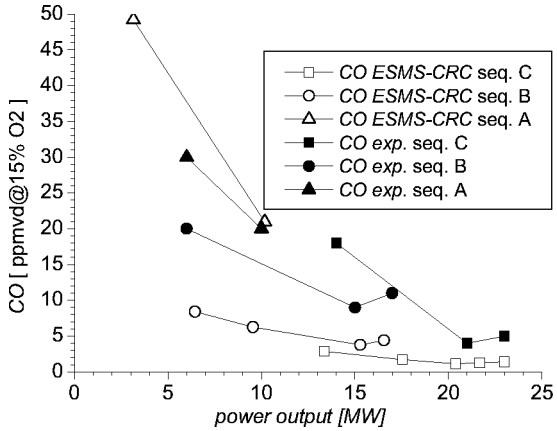

Fig. 19 Exp. and comp. CO in LM 2500DLE GT

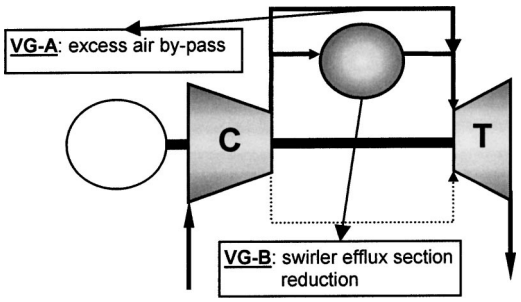

Fig. 20 Tested variable geometry systems

Table 3 PGT5B design emissions value

CO	3.02	ppmvd 15% O_2
NO_x	16.01	ppmvd 15% O_2
UHC	1.03	ppmvd 15% O_2

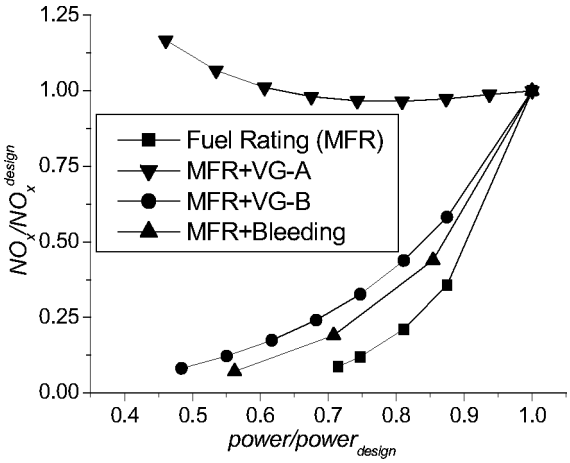

Fig. 21 NO_x emissions trend in PGT5B GT

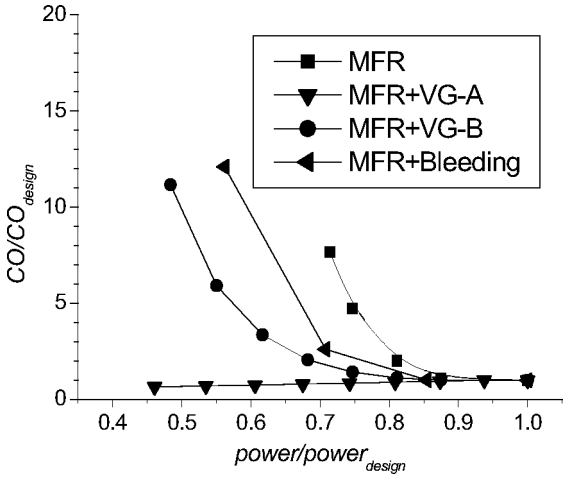

Fig. 22 CO emissions trend in PGT5B GT

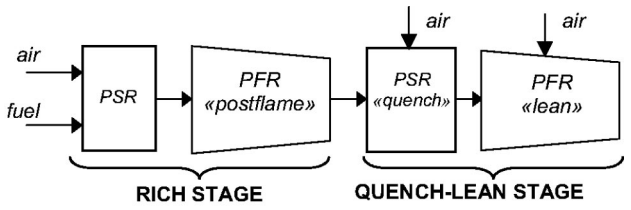

Fig. 23 Reactor network for RQL-2 combustor

Rich-Quench-Lean Combustor. In order to test the ability of the reactor network model to analyze low-LHV fuel, a simulation of RQL-2 combustor developed by General Electric was performed. As mentioned above, this combustor belongs to DLN family, but it's not based on lean-premixed technology. It is characterized by the division of combustion process in three main stages. In the first stage (Rich) a non premixed rich flame ($1.2<\phi<1.6$) with high homogenization level develops. Then follows an intermediate quenching stage, where combustion products and cool air are mixed quickly; the result is an instantaneous flame extinction.

In the last stage, residence times are higher and the mixture is very lean ($0.5<\phi<0.7$), so as to complete CO combustion, [21].

To simulate this combustor, we developed a specific reactor network (Fig. 23): Calculations were performed out of combined plant-combustion procedure because design criteria of RQL combustor are very different from that of standard combustors (premixed and non premixed flame).

RQL-2 experimental tests were performed in GE laboratories on a single, full scale, tubular combustor. Due to limited availability of low-LHV fuel during tests, a reduction in the air flow rate was necessary to achieve the target combustor exit temperature. The main goal of the tests was to evaluate the optimal air flow split between rich and quench-lean stages. Here we present only the data concerning to the 40/60% rich/quench-lean air split; This configuration determines the minimum NO_x emissions when combustor exit temperature is approximately 1550 K (''F'' class gas turbine). Actual engine off-design conditions were roughly reproduced varying fuel flow rate but keeping constant air flow and other operative parameters (pressure, inlet temperature, etc.). The reader is referred to [21] for more details about experimental tests.

Table 4 shows fuel composition and properties. It's important to note the low-LHV fuel and the stoichiometric air-fuel ratio value near to unity: Fuel mass flow cannot be neglected for the combustor design, because its value is close to air mass flow value.

Figure 24 shows NO_x versus combustor outlet temperature (or TIT) variations. The coincidence between experimental and obtained values are satisfactory, showing once again model consistency. At temperature values higher than 1600 K the model tends to overestimate experimental values. In this circumstances, the rich stage is characterized by an equivalence ratio higher than 1.5 and the Quench zone is in near stoichiometric conditions. Mostly the reaction takes place in the quench-lean stage and, here, the flame develops in diffusion manner. These conditions are not correctly reproduced by the simple PSR-PFR combination (as shown in Fig. 23): an arrangement analogous to the one previously used in conventional combustors primary zone, is probably more suitable.

Table 4 Fuel characteristics for RQL-2 combustor test, [21]

Species	Mass Fraction %
CO	10.75
H_2	1.56
CH_4	1.93
N_2	37.64
CO_2	24.76
H_2O	22.52
AR	0.54
NH_3	0.30
LHV [kJ/kg]	3920
α_s	1.14

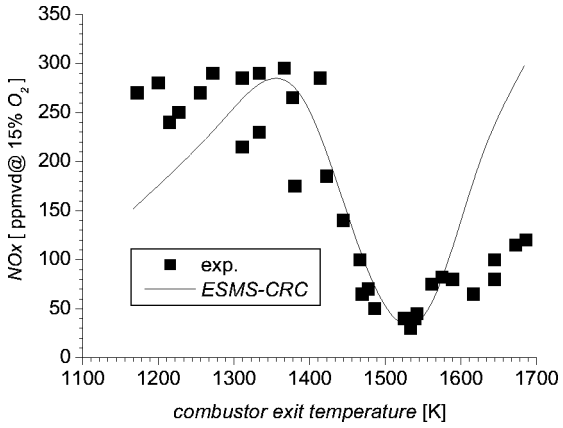

Fig. 24 NO_x emissions in RQL-2 combustor

Figure 24 confirms that, with the use of low-LHV fuel, RQL approach becomes very effective in NO_x reduction: in this particular configuration, RQL scheme guarantees NO_x emissions below 50 ppm in nominal conditions (TIT=1535 K in Fig. 24).

Figure 25 shows CO versus TIT variations. Because of experimental data scattering, it is now not significant a comparison with the calculated emission trend. To solve this problem, it is necessary to know residence time measuring devices, which are not described by Feitelberg and Lacey [21]. However, obtained results are always below 10 ppm such as in experimental data.

Conclusions

A one-dimensional emissions model has been developed. It has been integrated with an existing power plant simulation code to analyze the effects on pollutant emissions of engine operating conditions. The combustion model is based on a chemical reactor network description of the combustion chamber and it is capable to simulate the main type of combustors (conventional diffusion flame, lean-premixed and RQL combustors). The code is able to reproduce the effects of classical NO_x reduction devices, such as steam or water injection, and it can simulate the new combustor control system used in lean-premixed combustors, such as fuel-staging and variable geometry.

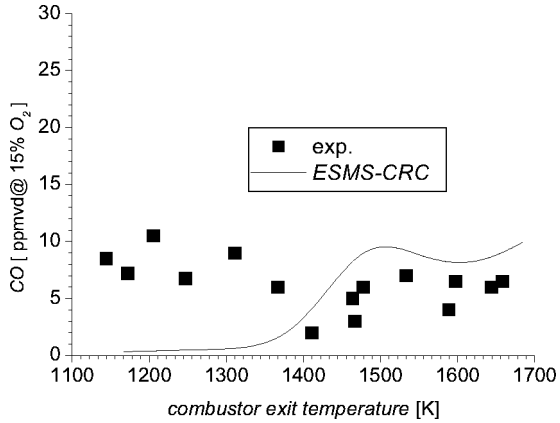

Fig. 25 CO emissions in RQL-2 combustor

Nomenclature

A_d = combustor dome section [m^2]
A_{ref} = combustor reference section [m^2]
D_{ref} = combustor reference diameter [m]
D_{sw} = swirler diameter [m]
GT = gas turbine
H = combustor liner height [m]
H = specific enthalpy [J/kg]
L = liner length [m]
LHV = lower heating value [kJ/kg]
$\dot{m}$ = mass flow rate [kg/s]
ppm = part per million
ppmvd = part per million volume dry
R = universal gas constant [kJ/(kg·K)]
TIT = turbine inlet temperature [K]
u = velocity [m/s]
V_d = dome flow velocity [m/s]
V_{pass} = combustor annulus flow velocity [m/s]
V_{ref} = combustor reference velocity [m/s]
W = molecular weight [kg/kmol]
y_k, Y_k = mass fraction [kg/kg]

Greek Letters

α = air-fuel mass ratio
α_s = stoichiometric air-fuel mass ratio
$\delta\dot{m}$ = added mass flow PFR [kg/s]
ϕ = equivalence ratio
η_b = combustion efficiency
ρ = density [kg/m^3]
τ = residence time [s]

Subscripts

k = generic chemical specie

References

[1] Puri, R., Stansel, D. M., Smith, D. A., and Razdan, M. K., 1997, ''Dry Ultralow NO_x 'Green Thumb' Combustor for Allison's 501-K Series Industrial Engines,'' ASME J. Eng. Gas Turbines Power, **119**, pp. 93–101.
[2] Lefebvre, A. H., 1999, *Gas Turbine Combustion*, 2nd Ed., Taylor and Francis, London.
[3] Yamada, H., Shimodaira, K., and Hayashi, S., 1997, ''On-Engine Evaluation of Emissions Characteristics of a Variable Geometry Lean-Premixed Combustor,'' ASME J. Eng. Gas Turbines Power, **119**, pp. 66–69.
[4] Carcasci, C., and Facchini, B., 1996, ''A Numerical Method for Power Plant Simulations,'' ASME J. Energy Resour. Technol., **118**, pp. 36–43.
[5] Touchton, G. L., 1984, ''An Experimentally Verified NO_x Prediction Algorithm Incorporating the Effects of Steam Injection,'' ASME J. Eng. Gas Turbines Power, **106**, pp. 833–840.
[6] Rizk, N. K., and Mongia, H. C., 1993, ''Semianalytical Correlations for NO_x, CO, and UHC Emissions,'' ASME J. Eng. Gas Turbines Power, **115**, pp. 612–619.
[7] Rizk, N. K., and Mongia, H. C., 1995, ''A Semianalytical Emission Model for Diffusion Flame, Rich/Lean and Premixed Lean Combustors,'' ASME J. Eng. Gas Turbines Power, **117**, pp. 290–301.
[8] Facchini, B., Ferrara, G., and Mazzilli, P., 1998, ''A Semi-Analytical Approach to Emissions Prediction in Gas Turbine Combustors,'' ASME Paper 98-GT-216.
[9] Nicol, D. G., Steele, R. C., Marinov, N. M., and Malte, P. C., 1995, ''The Importance of the Nitrous Oxide Pathway to NO_x in Lean-Premixed Combustion,'' ASME J. Eng. Gas Turbines Power, **117**, pp. 100–117.
[10] Shampine, L. F., 1994, *Numerical Solutions of Ordinary Differential Equations*, Chapman and Hall, New York.
[11] Kee, R. J., Rupley, F. M., and Miller, J. A., 1989, ''Chemkin-II: A FORTRAN Chemical Kinetics Package for the Analysis of Gas-Phase Chemical Kinetics,'' SAND89-8009, Sandia National Laboratories, Livermore, CA.
[12] Broadwell, J. E., and Lutz, A. E., 1998, ''A Turbulent Jet Chemical Reaction Model: NO_x Production in Jet Flames,'' Combust. Flame, **114**, pp. 319–335.
[13] Mellor, A. M., 1990, ''Design of Modern Gas Turbine Combustor,'' Academic Press, London.
[14] Clayes, J. P., Elward, K. M., Mick, W. J., and Symonds, R. A., 1993, ''Combustion System Performance and Field Test Results of the MS7001F Gas Turbine,'' ASME J. Eng. Gas Turbines Power, **115**, pp. 537–546.
[15] Carcasci, C., Colitto Cormacchione, N. A., and Facchini, B., 2000, ''Single Shaft Gas Turbine Comparison Using Low BTU Fuel (Biofuel) and Part Load Control Systems,'' POWER-GEN Europe 2000, Paper PGE-C-81, Helsinki, Finland, June 20–22, printed by PEI: Power Engineering International, PennWell (USA).
[16] GRI Mech, Smith, Gregory P., Golden, David M., Frenklach, Michael, Moriarty, Nigel W., Eiteneer, Boris, Goldenberg, Mikhail, Bowman, C. Thomas, Hanson, Ronald K., Song, Soonho, Gardiner, Jr., William C., Lissianski, Vitali V., and Qin Zhiwei.
[17] Vandervort, C. L., 2000, ''9 ppm NO_x /CO Combustion System for ''F'' Class Industrial Gas Turbines,'' ASME Paper 2000-GT-0086.
[18] Joshi, N. D., Mongia, H. M., Leonard, G., Stegmaier, J. W., and Vickers, E. C., 1998, ''Dry Low Emissions Combustor Development,'' ASME Paper 98-GT-310.
[19] Leonard, G., and Stegmaier, J., 1994, ''Development of an Aeroderivative Gas Turbine Dry-Low Emissions Combustion System,'' ASME J. Eng. Gas Turbines Power, **116**, pp. 542–546.
[20] Smith, K., Steele, R., and Rogers, J., 1999, ''Variable Geometry Fuel Injectors for Low Emissions Gas Turbines,'' ASME Paper 99-GT-269.
[21] Feitelberg, A. S., and Lacey, M. A., 1998, ''The GE Rich-Quench-Lean Gas Turbine Combustor,'' ASME J. Eng. Gas Turbines Power, **120**, pp. 502–508.

Microturbines and Trigeneration: Optimization Strategies and Multiple Engine Configuration Effects

S. Campanari
Research Assistant
e-mail: stefano.campanari@polimi.it

L. Boncompagni
Ph.D. Candidate
e-mail: luca.boncompagni@polimi.it

E. Macchi
Full Professor of Energy Conversion
e-mail: ennio.macchi@polimi.it

Energetics Department
Politecnico di Milano
Piza Leonardo da Vinci, 32
Milano 20133, Italy

This paper investigates energy savings and economic aspects related to the use of microturbine generators in commercial buildings either for cogeneration (electricity+heat) or for trigeneration (electricity, heat and cold). In all calculations, reference is made to a 25 kW_{el}-class commercial microturbine generator (MTG), tested by the authors. Various plant schemes are considered, based on one or several MTG sets. The possibility of generating heat and/or cold also by an electrically driven inverse-cycle air-to-water heat pump/chiller system is also considered. Calculations are based on the simulation code TRIGEN developed by the authors. The code provides detailed energy, economic and emission yearly balances. The plant operating mode is optimized in each time interval. The results indicate that, due to large load variations, (i) the optimum turbine nominal output is in the range of about 70% of the electric peak demand, (ii) energy savings are marginal, (iii) advantages related to splitting the overall capacity on more than one unit are marginal, and (iv) the addition of an absorption machine improves the plant economics. [DOI: 10.1115/1.1622410]

1 Introduction

For most industrial applications, the selection of the main design features of a cogeneration plant is a relatively straightforward procedure. Usually, when the industrial process is in operation, both thermal and electric loads are fairly constant throughout the year, so that the optimum size (both energy and cost-wise) of the cogeneration plant is generally fixed by the average thermal demand, leaving to the electric grid the role of closing the plant electricity balance, either selling or buying electricity, [1].

A totally different situation occurs in small-scale commercial applications, characterized by large fluctuations of electricity demand as well as by dramatic variations of heating and cooling demand, strictly related to climatic conditions. Although there is a diffuse consensus about the great potential of distributed cogeneration (heat+electricity) and tri-generation (heat+cold +electricity) plants, [2,3,4], actual applications are still in a limited number.[1] Simple rules for optimizing the plant design parameters are not yet established: for instance, how to select the plant size, the advantages (or disadvantages) of splitting the plant capacity on several units, the economic viability of adopting an absorption machine to recover heat released by the engine during summer, etc.

This paper investigates this matter, with reference to typical time-variable tri-generation (electricity, heat and cold) loads of medium size (5000–25,000 m^3) commercial buildings, located in areas characterized by climatic conditions that require heating in winter as well as cooling in summer and contemporary heating and cooling during half seasons. Energy savings, economic aspects are addressed: in all calculations, reference is made to a 25 kW_{el}-class commercial microturbine generator (MTG). Various plant schemes are considered, based on one or several MTG sets. Each MTG is equipped with an inverter, to generate grid frequency output, with a heat recovery unit to generate hot water and can be associated to an absorption chiller. All configurations are integrated with auxiliary boilers for back-up and peak-load heat generation. The possibility of generating heat and/or cold also by an electrically driven inverse-cycle air-to-water heat pump/chiller system is also considered.

The idea behind the presented calculations is to give an answer to several significant topics not yet clarified in the technical literature, including (i) the choice of the optimum size of the cogeneration plant for a commercial building, (ii) the rationale of splitting the plant on several modular units, and (iii) the economic advantages brought about by the use of the cogeneration plant during summer for tri-generation. Although the results found in the present analysis hold only for the specific test-case considered and their extension to different situations is not warranted, it is believed that the presented methodology, as well as the obtained general results, give an useful contribution to this relevant topic.

2 Plant Configurations

Six system configurations (Fig. 1) are considered (the first three without cooling demand):

(a) the ''basic'' configuration for cases without cooling demand, where electricity is supplied by the electric grid (EG) and heat by a natural gas boiler (NGB);
(b) an ''all electric'' case, where the EG covers the electricity as well as the electric load of a modular set of heat pump units (EHP), that supply all required heating;
(c) a cogenerative case where one (or more) microturbine generator with exhaust heat recovery boiler is added (MTG). A NGB is also present for backup;
(d) the ''basic'' case with both heating and cooling demand, that are satisfied by a NGB and an electric chiller, respectively. The chiller can act as a reversible refrigerating compressor and heat pump (ERC/EHP), thus generating cold and/or heat;

Contributed by the International Gas Turbine Institute (IGTI) of THE AMERICAN SOCIETY OF MECHANICAL ENGINEERS for publication in the ASME JOURNAL OF ENGINEERING FOR GAS TURBINES AND POWER. Paper presented at the International Gas Turbine and Aeroengine Congress and Exhibition, Amsterdam, The Netherlands, June 3–6, 2002; Paper No. 2002-GT-30417. Manuscript received by IGTI, December 2001, final revision, March 2002. Associate Editor: E. Benvenuti.

[1]The most recent information about MTG total sales is of about 1500 units, [5], but only a few of these are applied for cogeneration or trigeneration.

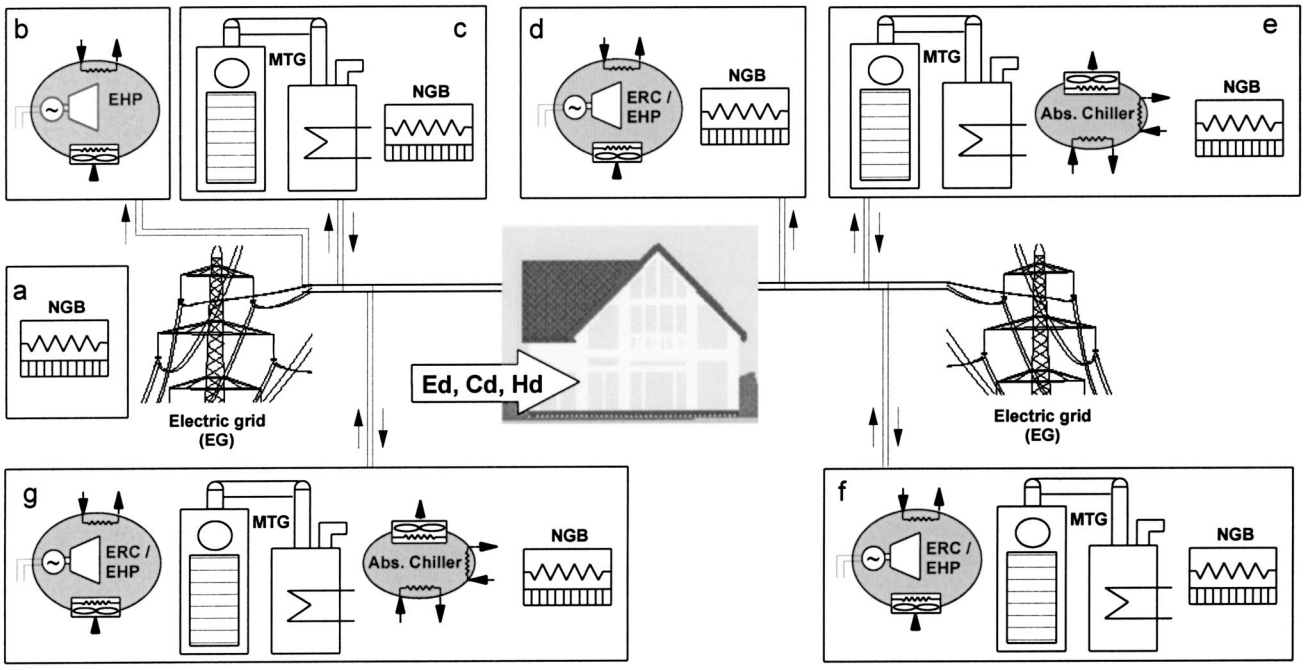

Fig. 1 Plant configurations considered in the present paper (see description in the text)

(e) an "all natural gas" case, where the MTG is coupled to an AC for cold generation; heat to AC can be supplied either by the MTG recovery unit or by the NGB;
(f) a cogenerative case, where the cooling demand is satisfied by an ERC/EHP. NGB is present for backup;
(g) a more complex cogenerative configuration, where both AC and ERC/EHP are used together with MTG and NGB.

In all cases the system:

- is connected to the EG for purchase, backup or sale of the excess electricity, when economically viable;
- fully covers the heat and cooling demand, using the natural gas boiler when necessary. The NGB and ERC/EHP capacity is always set in order to match the peak load. A redundancy in the number of ERC/EHP units is selected in order to guarantee the cooling peak load also in case of failure of one compressor.

3 Calculation Model

Calculations are performed based on a specifically developed simulation tool (TRIGEN). The code requires the assignment of a number of input data for the definition of economic assumptions, components and plant performance, load profiles, etc. (see Table 1).

TRIGEN provides detailed energy, economic and emissions yearly balances. The model optimizes the operating conditions of the trigeneration plant for each of the 8760 hours of the year. The assumption is made that the plant control system is smart enough to optimize the plant operating mode to achieve the most cost effective situation in each time step (one hour). In all cases treated in this paper, the final choice is made on an economic basis, but other optimizing strategies, say best energy saving, or minimum pollutant emissions, or any combination of economic, energetic and environmental achievement could be easily specified.

The optimization strategy is discussed below, while more details about the simulation of the main plant components (ERC/EHP, MTG, AC, and NGB) are given in the Appendix.

3.1 Optimization Strategy. Rather than relying on optimization linear techniques as the one described in [6,7], the optimization procedure is based on the simulation of all plant operating modes that could in principle be the best candidate. The code selects the option which features the minimum instant cost among different possibilities. The instant cost is defined as

$$C = C_{el,p} + C_{\mathrm{MTG},f,p} + C_{\mathrm{NGB},f,p} + C_{\mathrm{O\&M}} - V_{el,s} \qquad (1)$$

where the first four terms represent the hourly cost related to: (i) purchase of electricity, (ii) purchase of fuel for the MTG and (iii) for the NGB[2] and (iv) the cost for MTG operation and maintenance (assumed proportional to the electricity generated);[3] the last term represents the value of the electricity sold to the grid.

The following operating options are considered:

(A) Contemporary Load-Following of Electric, Thermal and Cooling Demand. The system follows all three loads (electric, thermal, cooling), by operating at partial load (same load for each engine) the minimum number of MTGs capable of meeting the demand and trying to approach zero electricity exchange with the electric grid. MTGs work at the power output necessary for covering the electric load, including ERC/EHP; heat is generated by MTG and, if necessary, by the EHP (if present); cooling is covered primarily by the AC (if present), followed by the ERC. NGB (for heating generation or for the AC heat consumption) may be used to balance the heat demand when contemporary heat and cold demand is present.

(B) All MTGs at Full Power Output. All MTGs operate at full power output (base load); cogenerated heat is used to satisfy heat demand or to feed AC, wasting the excess. Electricity is used to cover Ed and the eventual surplus is used by the EHP/ERC for the fraction of the heating and/or cooling demand not covered by cogeneration and AC. Remaining excess electricity is sold to the grid.

(C) "n" MTGs at Full Power Output. In option (a), the electric load is equally divided among "*n*" MTGs operating at partial

[2]MTG and NGB fuels may be different or have different taxation rules.
[3]According to manufacturers, a full-maintenance contract based on generated electricity is the most likely choice for MTGs users.

Table 1 Main input data of the calculation model

Economic Assumptions	
Tariff for gas purchase	One of:
Tariff for electricity purchase	1 hourly tariff for 8760 h/y 2 peak/low period charges 3 country specific tariffs
Price for electricity sold	One of: 1 hourly tariff for 8760 h/y 2 peak/low period prices 3 reverse metering factor (RMF)
Component Model	
Cogenerator performance	Variation of net electric power, net thermal power and fuel consumption versus load at different ambient temperature
Cogenerator emissions	NO_x, SO_x, CO, and CO_2 emissions versus load and ambient temperature curves
Electric heat pump/reversible compressor (EHP/ERC)	• working fluid • type of compressor • winter/summer peak sizing; internal calculation of COP
Absorption chiller (AC)	• capacity • COP versus load curve • auxiliary consumption
Natural gas boiler (NGB)	• thermal efficiency versus load curve
Heat/cooling distribution network	• winter/summer peak sizing • nominal operative temperatures
Load Definition	
Electricity, heat and cooling load profiles	three days (working, half working, holiday) for the following seven climatic conditions: • winter extremely cold • winter medium • winter extremely hot • half season • summer extremely cold • summer medium • summer extremely hot
Internal/external air temperature profiles	Distribution for the 21 day-types
Yearly days distribution	Distribution over the year of the 21 day-types

(*)Emission are not addressed in the paper

load. This option considers the possibility of operating the same number of MTGs at full load, exporting excess electricity to the grid to exploit the nominal MTGs efficiency.

(D) "n-1" MTGs at Full Power Output. This option considers the possibility of operating "n-1" MTGs at full power output (base load), importing from the grid the electricity required to fulfill the balance.

(E) Heat Following and/or Cooling Following. This option is used to operate the MTG+NGB system as "heat following," and the MTG+AC+NGB system as "cooling following," in both cases with electricity balance by EG.

The model also considers the possibility of operating with the additional plant configurations obtained by alternatively switching off, where present, the AC, the ERC/EHP, and the MTG components. The calculation is carried out for all the above-listed operating options (when applicable), aiming to investigate the most extensive as possible range of alternatives. The example described in the next paragraph clarifies the used methodology.

3.2 Example of Optimization. Let us consider the specific case of a complex plant configuration, featuring three MTGs +ERC/EHP+AC+NGB and facing the contemporary demand of electricity, cooling and heating (33, 69 and 18 kW, respectively) during an afternoon hour of a summer day. Table 2 shows all the operating options which are considered by the model while it is searching for the optimum.

- The best option (lowest cost as by Eq. (1)) chosen by the model is the operating condition featuring zero electricity exchange with EG (i.e., the above-listed operating option A), with $n=2$ MTGs in operation at part load (#1 in Table 2).
- The second best is option C) ("n" MTG at full load): it can be seen that the excess electricity sale does not overcome the increased NG consumption (#3 in Table 2).
- The third best is option E), where the engines operate at the load required to balance Hd as well as the heat demand of the AC, with ERC switched off (#11 in Table 2).

It is interesting to notice that the solutions that achieve the best economical conditions do not yield the best energy saving, as shown by the primary energy consumption (last row in Table 2), defined as the sum of the system (MTG+NGB) fuel consumption and the fuel consumption of the reference centralized power stations required to fulfill the electric balance:

$$\mathrm{PEC}=E_{f,\mathrm{MTG+NGB}}+(E_S-E_p)/\eta_{el,\mathrm{ref}} \tag{2}$$

Actually, the best option for energy saving is to shut down all MTGs and operate "all electric" (#14 in Table 2). Of course, this is not always the case, since MTGs are energy saving devices, when can operate at full load and recover all heat.

Figure 2 shows the detail of the energy flows related to the optimized solution (#1 of Table 2). In this configuration the MTG system generates 36 kWh, devoted for the majority to cover the electricity demand, and for a small fraction to the EHP/ERC system. Water is generally heated in sequence by the heat pump condenser, by the gas turbine economizer and eventually by the auxiliary boiler. In this particular case all the gas turbine exhaust heat is consumed by the AC[4] and does not contribute to water heating.

[4]The relatively low MTG exhaust gas temperature (close to 235°C at full load and lower at partial loads), makes unattractive the adoption of multistage absorption cycles; it has been therefore adopted a single-stage absorption cycle, with a nominal COP of 0.7. The absorption chiller is arranged in parallel flow with the ERC evaporator, and works with the same inlet and outlet water temperatures.

Table 2 Example of comparison of the operating options considered for hourly optimization (see option list below) option list: (1) Case A (load following) (2) Case B (MTGs at full output) (3) Case C (*n* MTGs at full output) (4) Case D (*n*−1 MTGs at full output) (5) Case A with AC switched off (6) Case B with AC switched off (7) Case C with AC switched off (8) Case D with AC switched off (9) Case A with ERC/EHP switched off (10) Case B with ERC/EHP switched off (11) Case E (heat following) with ERC/EHP switched off (12) Case C with ERC/EHP switched off (13) Case A with AC+NGB+EG (MTG and ERC switched off) (14) Case A with ERC/EHP +EG (MTG and AC switched off) (15) Case A with ERC/EHP +NGB+EG (MTG and AC switched off).

Option #	(1)	(2)	(3)	(4)	(5)	(6)	(7)	(8)	(9)	(10)	(11)	(12)	(13)	(14)	(15)
Energy balance (kWh)															
Electricity purchase	-	-	-	20	-	-	-	6	-	-	-	-	33	51	51
MTG fuel consumption	167	307	204	102	218	307	307	204	153	307	229	204	-	-	-
NGB fuel consumption	10	-	-	-	-	-	-	-	163	-	-	14	163	-	30
Total fuel consumption	176	307	204	102	218	307	307	204	316	307	229	218	163	-	30
Cost (€)															
Electricity purchase	-	-	-	248	-	-	-	75	-	-	-	-	411	635	635
Gas purchase	439	751	501	250	536	751	751	501	866	751	564	543	490	-	90
O&M	18	34	22	11	23	34	34	22	17	34	25	22	-	-	-
Electricity sale	-	-214	-53	-	-	-103	-103	-	-	-214	-103	-74	-	-	-
Total (€)	457	570	470	509	560	682	682	598	882	570	485	491	901	635	725
Number of active MTGs	2	3	2	1	3	3	3	2	2	3	3	2	-	-	-
MTGs load fraction (%)	53	100	67	33	69	100	100	67	49	100	74	67	-	-	-
Electric energy demand balance															
Ed+ERC/EHP (kWh)	36	33	36	42	47	51	51	51	33	33	33	33	33	51	51
MTG (%)	100	204.3	123.3	53.0	100	132.4	132.4	88.2	100	204.3	150.2	136.2	-	-	-
Purchase (%)	-	-	-	47.0	-	-	-	11.8	-	-	-	-	100	100	100
Sale (%)	-	104.3	23.3	-	-	32.4	32.4	-	-	104.3	50.2	36.2	-	-	-
Heat demand balance															
Hd (kWh)	18	18	18	18	18	18	18	18	18	18	18	18	18	18	18
MTG (%)	-	100	53.1	-	100	100	100	100	-	100	100.5	53.1	-	-	-
ERC/EHP (%)	68.2	-	46.9	196.8	-	-	-	-	-	-	-	-	-	436.2	-
NGB (%)	31.8	-	-	-	-	-	-	-	100	-	-	46.9	100	-	100
waste (%)	-	252.3	-	96.8	509.6	797.6	797.6	498.4	-	252.3	-.5	-	-	-	-
Cooling demand balance															
Cd (kWh)	69	69	69	69	69	69	69	69	69	69	69	69	69	69	69
ERC/EHP (%)	15.6	-	-	45.1	101.1	100	100	100	-	-	-	-	-	100	100
AC (MTG) (%)	87.2	100	100	54.9	-	-	-	-	-	100	100	100	-	-	-
AC (NGB) (%)	-	-	-	-	-	-	-	-	100	-	-	-	100	-	-
Primary Energy Consumption (kWh)	176	210	181	158	218	260	260	221	316	210	183	185	256	143	173

4 Test Case Description

4.1 Natural Gas and Electricity Tariffs. The assumptions made for tariffs for fuel and electricity purchase are presented in Table 3. They reflect, with some simplification, the Italian situation. It can be seen that the electricity cost can be as high as four or five times the NG cost in peak hours, but the tariff is much lower during low charge hours and for the electricity sold to the grid.

4.2 Cost and Investment Assumptions. The most relevant assumptions related to the cost of components and to the param-

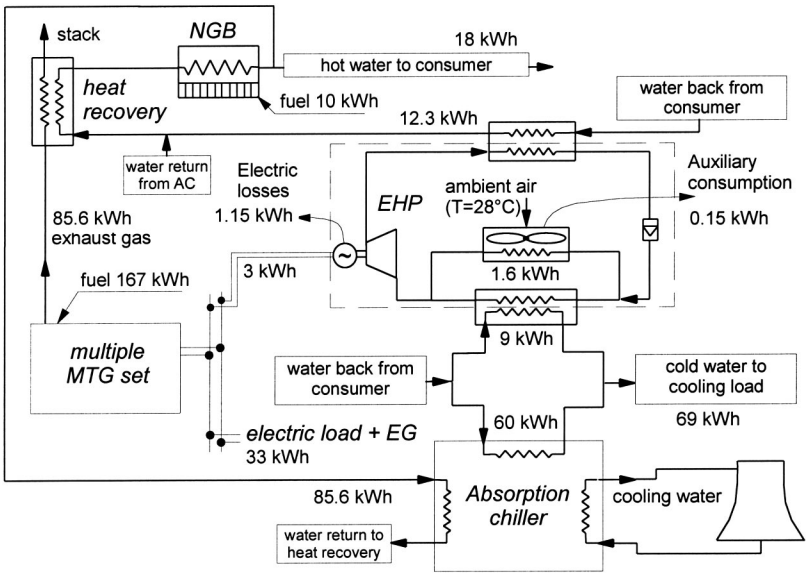

Fig. 2 Detail of the energy flows for the optimum solution (#1 of Table 2) discussed in 3.2

Table 3 NG and electricity tariff assumptions

Natural Gas Purchase		
Fixed cost, (€/kWLHV per year)		0
Variable cost, including fiscal charges (€/kW*h*LHV)		3
Tax reduction for the "fiscal" fraction of natural gas used for cogeneration (€/*k*W*h*LHV)		1
"Fiscal" fraction of natural gas used for cogeneration ($kWh_{NG}/kWh_{el,cog}$)		2.5
Electricity Purchase and Sale		
Fixed cost	Peak hours	400
(€/kW per year)	Low charge hours[1]	60
Reverse metering factor RMF		0.5
Variable cost (€/kW*h*)	Peak hours	12.5
	Low charge hours[1]	6.1

[1]Night hours (21 pm–7 am) and weekend hours

Table 4 Cost and investment assumptions

Gas turbine capital cost (€/kW_{el})	600
Gas turbine O&M cost (€/kW_h)	0.5
EHP/ERC capital cost (€/kW_c)	200
Absorption chiller capital cost (€/kW_c)	300
Natural gas boiler capital cost (€/kW_h)	15
Operating life and interest	10 years, 7%
Taxes on gross profit	43%
Inflation rate	2.7%

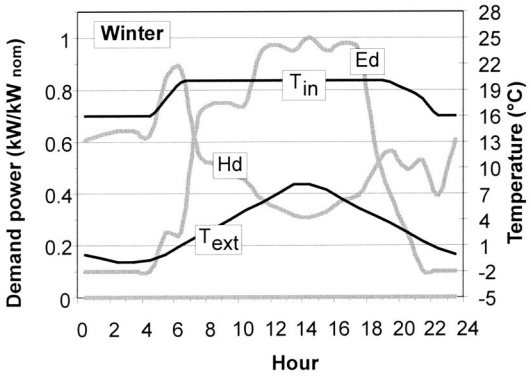

Fig. 3 Daily demand and temperature profiles for the "average cold" winter working day

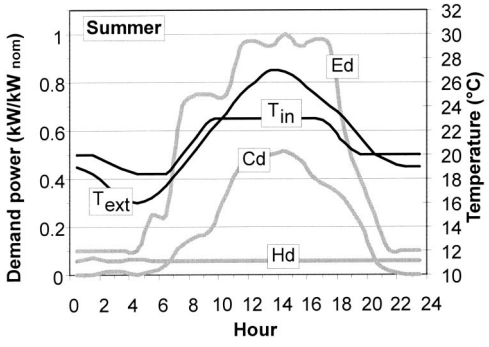

Fig. 4 Daily demand and temperature profiles for the "average hot" summer working day

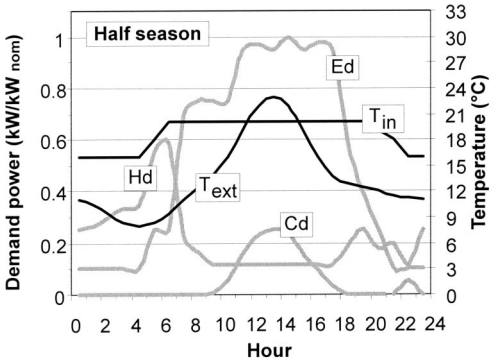

Fig. 5 Daily demand and temperature profiles for a half-season working day

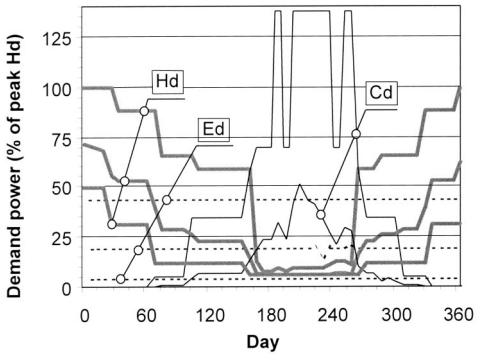

Fig. 6 Annual load profiles for the cooling, heating and electric demand (Cd,Hd,Ed), calculated on a weekly base. Each set of three curves represents maximum, average, and minimum loads, except for the cooling load where the minimum is zero.

eters involved in the financial analysis are indicated in Table 4. For the MTG "target" specific cost of 600 C/kW is assumed, [5], far lower than actual costs.

4.3 Load Profiles. The selected load profiles (specific to the unit volume) are intended representative for a tertiary building located in Northern Italy. For a total volume of 15,000 m^3 the peak electric, heating and cooling demand are respectively 97,222 and 302 kW.

Figures 3, 4, and 5 show some of the 21 day-types used for the definition of the annual load as listed in Table 1. These specific load profiles will be used throughout the paper. The yearly distribution of the three loads is shown in Fig. 6, whereas the resulting equivalent hours are listed in Table 5: It can be seen that cooling demand has the largest peak, but the involved annual energy is relatively small (about one third of the heating energy). Table 5 indicates also some interesting results on the PE annual balances related to the assumed load profiles: for a conventional plant without air conditioning equipped with a natural gas boiler (plant a of Fig. 1), electricity accounts for about 57% of the PE use (the remaining 43% being required for heating); in the "all electric solution" (plant b in Fig. 1), the use of EHP drastically cuts the primary energy consumption related to heat generation. A benefit (about 12%) is found also in terms of annual costs. When the cooling demand is added (plant d in Fig. 1), the contemporary presence of NGB and EHP allows optimizing heat generation cost

Table 5 Economic and energetic comparison of three conventional solutions considered for the coverage of electricity and heating demand (NGB+EG and EHP+EG) or electricity+heating+cooling demand (ERC+NGB+EG)

Demand Type		Load Equiv. Hours[1]	Peak Demand (W/m^3)	Annual Demand (kWh/m^3y)	NGB+EG Cost €/(m^3y)	NGB+EG PEC (kWh/m^3y)	EHP+EG Cost €/(m^3y)	EHP+EG PEC (kWh/m^3y)	NGB+EHP/ERC+EG Cost €/(m^3y)	NGB+EHP/ERC+EG PEC (kWh/m^3y)
Ed		3833	6.45	24.7	304.3	69.2	402.1	69.2	427.0	69.2
Cd		651	20.12	13.9	-	-		-		11.4
Hd	ERC	2516	14.85	37.4	-	-		28.9		3.9
	NGB				153.0	51.0	-	-	11.7	24.2
				Total	457.2	120.3	402.1	98.1	438.7	108.7
				Savings vs. NGB+EG	-	-	55.1	22.1	18.5	23.0[2]

[1]total annual energy delivered/peak demand
[2]with respect to the generation of heat and electricity only

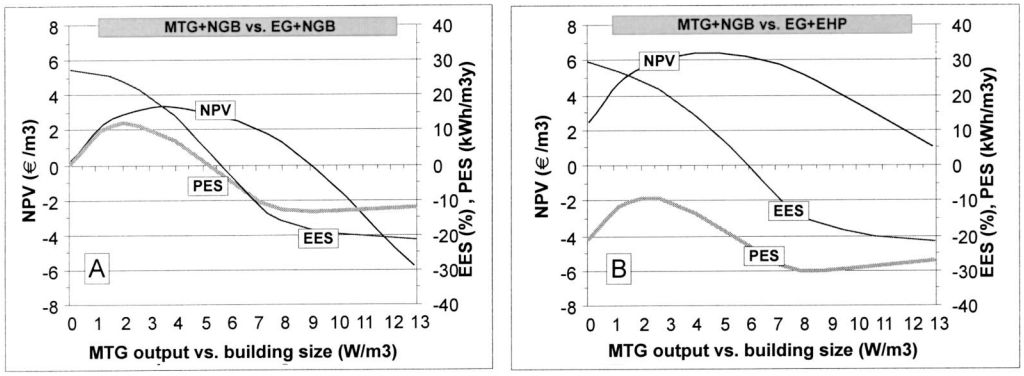

Fig. 7 Optimization of nominal MTG output versus building size for a cogenerative (heat+electricity) load, with respect to conventional solutions with (*a*) NGB and (*b*) EHP

wise: the final result is that the overall annual costs in presence of air conditioning are lower than the ones required to satisfy only electricity and heat without a EHP.[5]

5 Optimization of Building Versus MTG Size

The topic addressed in this chapter is the influence of the building size where a MTG is installed. Let's first consider the case of a building without air conditioning. Assume that the reference MTG with heat recovery boiler (plant c in Fig. 1) is installed in buildings of different size and let's compare the cogeneration plant performance versus the two reference cases (plant a and b in Fig. 1). The results of this comparison are represented in Fig. 7. The figures indicate two parameters related to the primary energy saving (PES and EES) and an economic parameter (the investment net present value, NPV).

The primary energy saving parameter PES is defined as the difference between the primary energy yearly consumption of the conventional solution and that of the cogenerative solution, referred to the unit volume:

$$\mathrm{PES} = \mathrm{PEC}_{\mathrm{conv}} - \mathrm{PEC}_{\mathrm{cog}} \tag{3}$$

The MTG relative primary energy saving EES ("engine energy savings") is expressed by the following relation:

$$\mathrm{EES} = \left(1 - \frac{E_{f,\mathrm{MTG}}}{\dfrac{E_{el,\mathrm{MTG}}}{\eta_{el,\mathrm{ref}}} + \dfrac{Q_{\mathrm{rec,MTG}}}{\eta_{th,\mathrm{ref}}}} \right) \times 100(\%) \tag{4}$$

[5]For calculating the PE related to heat and electricity, reference is made to the yearly average thermal efficiency of conventional boilers (close to 73%, according to the yearly simulation of the basic case of Fig. 1) and to a reference value for the efficiency of electric power generation of 38% with the addition of a 94% distribution efficiency to account for grid losses (these values are representative of Italian situation, [8]).

and compares the MTG primary energy consumption with that related to the separated generation of heat and electricity by NGB and by conventional electric power plants (including grid losses).

Let's consider Fig. 7(*a*): When the MTG is installed in a very large building (left in the figure) the EES parameter coincides with the value obtained at nominal load with full heat recovery: the building heat demand is so large, that the MTG operates at full load and all the heat can be recovered. When the building size decreases, also EES decreases, for two main reasons: (i) Ed decreases, so that sometimes the engine operates at part load and (ii) Hd decreases, so that sometimes part of the cogenerated heat is wasted. When the building electric peak demand reaches about 75% of the MTG output, EES becomes negatives, i.e., cogeneration is no more an energy saving solution.

Figure 7 shows also that PES reaches a maximum for a MTG nominal output/building size ratio close to 2 W/m^3, while the optimum size by the point of view of economics is 4 W/m^3 (NPV close to 3.2 €/m^3). For the 25 kW-class MTG considered, this means that the economical optimum building size is close to 7000 m^3, with NPV exceeding 145% of the required investment cost. The PES and NPV lines both start from zero when compared to the EG+NGB (Fig. 7(*a*)). When reference is made to a EHP (Fig. 7(*b*)), the cogenerative solution is considerably less capital intensive and NPV reaches higher maximum values (close to 6.2 €/m^3), even if the EHP running costs are lower than NGB (see Table 5). PES is negative all over the size range, i.e., the cogenerative solution does not save energy with respect to a heat pump system. After reaching a minimum, PES reapproaches zero outside the represented range, when the MTG cogenerated heat would be completely wasted and the MTG is never switched on.

Let's now consider the case of a trigenerative load (heat+electricity+cooling), covered with the addition of an absorption chiller and ERC (Fig. 8) or an ERC system only (Fig. 9). The

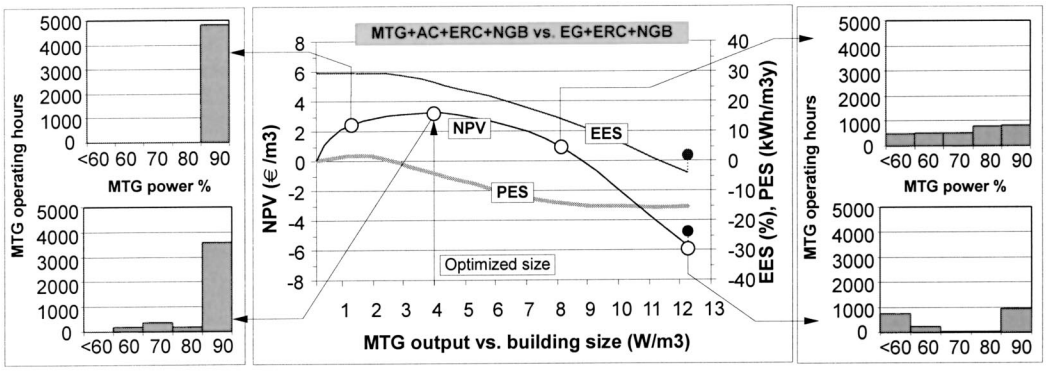

Fig. 8 Optimization of nominal MTG output versus building size for a trigenerative (heat+cooling +electricity) load. MTG operates with AC+ERC+NGB and is compared to ERC+NGB systems.

higher investment costs related to AC are more than counterbalanced by the energy savings allowed by free heat recovery, so that the first case yields higher NPV. The MTG operating hours (Fig. 8) show a constant increase moving from small (right side) to large building (left side). Due to the high energy savings already guaranteed by the reference system (EG+ERC+NGB), the PES is slightly positive only for very large building sizes, where MTGs never waste heat.

The two black dots on the right side of Fig. 8 refer to a configuration without ERC, i.e., the cooling demand is low enough to be covered by the AC only. This allows a small NPV gain (due to the lower plant capital cost) and a slight increase of EES due to the extended full load MTG operation during summer. PES instead dramatically decreases (not shown in the figure) due to the absence of ERC/EHP which frequently yields relevant energy savings.

6 Effect of a Multiple MTG Arrangement

This chapter addresses the effect of splitting the generation capacity onto several MTG units. A multiple MTG set offers higher part-load efficiency due to the possibility of switching off some engines at reduced load leaving the possibility to operate the remaining MTGs at higher load. This advantages become relevant only when a single MTG would operate at part load for a significant amount of time.

A comparison is presented between three trigenerative solutions obtained with the same overall MTG output/building size ratio (the assumed value is 8 W/m^3), considering also the adoption of two and three MTGs with a building of two and three times the original size, respectively. The results of the comparison are presented in Table 6. It can be seen that by splitting the overall capacity on more units, it is possible to increase the yearly average electrical as well as thermal efficiency of MTGs.

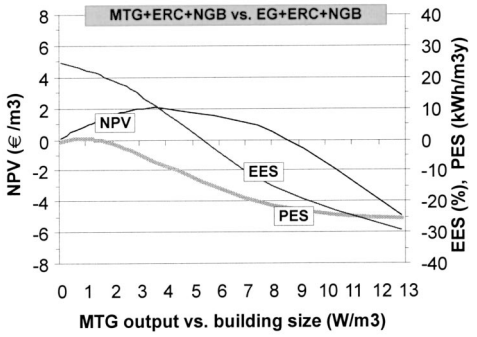

Fig. 9 Same as Fig. 8 without AC

Table 6 Comparison of the energetic and economic performance of solution adopting various MTG number

No. of MTGs	1	2	3
EE Cogenerated (kWh/m^{3}y)	18.6	18.6	19.5
Cogenerated heat (kWh/m^{3}y)	28.6	30.3	33.1
η_{el} MTG (yearly average)	0.225	0.231	0.239
η_{th} MTG (yearly average)	0.571	0.607	0.643
EES (yearly average)	0.147	0.215	0.232
NPV (€/m^{3}y)	1.45	2.19	2.38
Operating hours MTG #1	3192	2106	988
MTG #2	0	1769	1990
MTG #3	0	0	1265

As consequences, better economic (NPV) and energetic (EES) results are obtained. The same exercise applied to the economical optimum MTG output/building size ratio (4 W/m^3) indicates that the advantages brought about by multiple MTGs become marginal, since in this case a single MTG operates at full load most of the time (see Fig. 8).

7 Conclusions

The results presented in the paper indicate that, due to inherent large variability of heating, cooling and electric demand typical of commercial buildings, the optimum size of a cogeneration plant is significantly lower than the peak demand, referred to electric as well as thermal demand. In presence of cooling demand, the addition of an absorption chiller improves the plant performance, both energy and costwise. With reference to the assumed tariff scheme, the economics of these applications are only relatively attractive, even at ''target'' low specific costs assumed for the MTG. The situation would of course be more favorable if better MTG performance (for instance with net electrical efficiency of 30% as claimed by some manufacturers) are stipulated. It should also be pointed out that the economic analysis was performed without giving any prize to the significant advantages inherent in distributed generation, in particular the increased electricity availability or the possibility to overcome constraints in the expansion of urban electricity networks, as well as to decrease emissions.

Appendix

EHP/ERC Model. System capacity may be split into several ERC units,[6] with the possibility of managing the ERC units both with on/off or variable speed regulation criteria. Two possible configurations are considered, where the ERC heat exchangers are

[6]At least three units (3×50%) are always present, to insure the required redundancy.

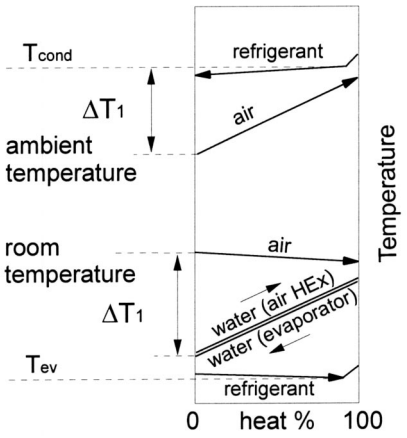

Fig. 10 Temperature distribution and heat exchanger arrangement of the EHP/ERC system. Temperature of two-phase processes varies due to pressure losses.

separated or integrated in a common block, thus exploiting the entire heat exchange surfaces also when a limited number of units is in operation.

Calculation of COP. The COP calculation is based on an iterative procedure involving the following main steps:

(a) calculation of actual refrigerant evaporating and condensing temperatures
(b) calculation of the mechanical cooling cycle performance, by means of the second-law efficiency (see Eq. (*A*2))
(c) calculation of the number of EHP/ERC units in operation
(d) calculation of ''mechanical'' COP
(e) calculation of the gross electrical COP
(f) calculation of the net electrical COP

and requires the following input data:

- number of EHP/ERC units
- working fluid
- type of compressor
- nominal unit operating conditions (either in the EHP or ERC mode), i.e., (i) refrigerating (ERC) or thermal power (EHP), (ii) ambient air temperature, (iii) evaporating and condensing temperature, (iv) water inlet/outlet temperatures
- nominal load and water temperatures of the heat/cold distribution system
- hourly load demand
- hourly external ambient temperature
- hourly internal building temperature

A brief description of the calculation steps is given in the following.

(a) Calculation of refrigerant evaporating and condensing temperatures. The temperature history of the various fluids involved in the process (ambient air, refrigerant, water, internal air) is represented in Fig. (10). All temperatures vary during the year, according to operating conditions. The following assumptions are made:

- the water-air heat exchangers (placed inside the building rooms) operate with constant $Q/\Delta T_1$, where Q is the exchanged heat and ΔT_1 is the temperature difference between room air and inlet water. This condition is representative for air heat exchangers with constant speed fan, e.g., variable speed operation of the air fan motor is not considered.
- the same assumption is made for the refrigerant-air heat exchangers (external units); in this case ΔT_1 is the difference between the refrigerant evaporation/condensation temperature and ambient air.[7]
- The refrigerant-water heat exchangers act as a constant $U \times S$ heat exchanger, where U and S are the overall average heat exchange coefficient and surface, respectively, and $\Delta T_{\rm lm}$ is the log-mean temperature difference between water and refrigerant:

$$Q = U \times S \times \Delta T_{\rm lm}. \qquad (A1)$$

The calculation requires to hypothesize the number of units in operation, as well as COP. Both variables are adjusted and recalculated during the iteration.

(b) Calculation of the mechanical cooling cycle performance, by means of the second-law efficiency. According to results of the survey of commercial ERC performance described in [9], it is possible to predict with reasonable accuracy the ''mechanical'' (i.e., referred to the mechanical power at compressor shaft) COP (at nominal conditions as well as at other operating temperatures) of state-of-the-art commercial ERC units by correlating the inverse cycle second-law efficiency $\eta_{\rm II}$, defined by

$$\eta_{\rm II} = \frac{\rm COP_c}{\rm COP_{c,id}} = \frac{T_{ev} - T_{\rm cond}}{T_{ev}} \cdot \rm COP_c \qquad (A2)$$

to the temperature difference between condensation and evaporation (larger the distance between the two temperatures, greater the difference with respect to an ideal Carnot cycle). Three curves are employed by the model, depending on the compressor type (alternative, scroll, screw compressor). Equation (*A*2) holds also when the unit operates in the heat pump mode. The relation between $\rm COP_h$ and $\rm COP_c$ is

$$\rm COP_h = COP_c + 1. \qquad (A3)$$

(c) Calculation of the number of EHP/ERC in operation. Once the evaporating and condensing temperature and COP are known, the model calculates the maximum cooling power of a unit by assuming the proper characteristic line for the compressor (for instance: constant volume flow rate), in agreement with the thermodynamic properties of the refrigerant. This result allows the selection of the proper number of units in operation. The matching of the cooling (or heating) power is done either by part-time or by variable speed operation of the units.

(d) Calculation of the gross electrical COP. The electric motors driving the compressors have a nominal power set by the load requirements, with a design-point efficiency dependent on the nominal power and reduced at partial load according to the efficiency curve for variable speed operation proposed by [10].

(e) Calculation of the net electrical COP. An auxiliary electric consumption of 1% is considered, calculated on the ERC peak thermal duty, accounting for the fan power demand. When the EHP operates at low external ambient temperatures, it is besides considered an energy penalization caused by frost formation and defrosting. Frost formation on heat transfer surface causes a decrease of evaporator temperature, due both to the reduced air flow and added thermal insulation; moreover, frost must be periodically removed, by means of energy demanding procedures. The ''dry'' COP is then reduced for ambient temperatures below 7°C with appropriate correction factors (increase of the heat exchanger ΔT_1 and increase of the ERC auxiliary consumption due to electric resistance heating, max correction at 3°C equal to 10% and 50%, respectively).

[7]There are two exceptions to this rule: (i) when the unit operates as EHP and ambient temperature is low, ΔT_1 is increased to account for frost formation; (ii) the ERC may be operated both for cooling and heating, thus requiring an additional water cooled heat exchanger (Fig. 2). The condensing temperature is then set in order to match the requirements of both useful heat generation and excess heat discharge into ambient.

Table A1 MTG nominal performances and cycle calculation assumptions (ISO ambient conditions)

MTG Nominal Performances	
Net electric power (kW)	25.6
Rotational speed (RPM)	96,000
Net electric efficiency (%)	23.3
Fuel (NG) pressure (bar)	1.05
NG compressor nominal power (kW)	1.8
Fuel lower heating value (kJ/kg)	49,070
Cycle Calculation Assumptions	
Turbine inlet temperature, °C	820
Compression ratio	3.4
$\Delta p/p$ recuperator hot/cold side, %	5/3
$\Delta p/p$ combustor, %	3
Heat loss recuperator, (% of thermal power)	2
ΔT_{min} recuperator, °C	100
Compressor isentropic efficiency	0.81
Turbine isentropic efficiency	0.86
GT mechanical efficiency	0.99
GT electric generator efficiency	0.94
GT power conditioning efficiency	0.93
Fuel compressor isentropic efficiency	0.7
Fuel compressor mech.+el. efficiency	0.9

MTG Model. The microturbine model is based on the simulation code described by [10]. The model has been calibrated with the assumptions of Table A1 to simulate the performances of a commercial 25 kW_{el} Capstone microturbine, using experimental data from [11] and from EPRI characterization tests, [12].

Partial load simulation is performed at variable speed using compressor and turbine maps given in [10] and with the assumption of a constant TIT regulation.

The calibration results of Fig. 11 show good agreement between simulated and experimental data, except for a significant difference (about 10°C) in the stack exhaust temperature at partial load, probably related to the assumption of a constant TIT regulation. Turbine inlet temperature may instead slightly decrease also for insuring the respect of maximum recuperator working temperatures, [13]. The simulation model provides also information about the ambient temperature effect on MTG performance, not discussed here. Results show a performance decay of about 2.3 percentage points on the electric efficiency at 30°C, and an efficiency gain close to 1.0% at 5°C. MTG emissions have been assumed after experimental tests, [11], as shown in Fig. 12. The existence of a low emission operating range (reflecting lean premix combustion, [14]) has suggested to limit MTG operation by switching off the unit below 60% of the nominal power output. NO_x and CO emissions remain below 8 and 20 ppmvd respectively between 90 and 100% of nominal power output.

Figure 12 shows also the microturbine EES (showing the possibility of achieving 25% energy savings when running the MTG at full load with a complete recovery of the exhaust heat)[8] as well as the first law efficiency, defined as

$$\eta_I = \frac{P_{el} + Q_{th,\text{recovered}}}{m_{\text{fuel}} \times \text{LHV}_{\text{fuel}}} \quad (A4)$$

for two different levels of stack temperature after heat recovery (70 and 90°C).

NGB and AC Efficiency. The natural gas boiler efficiency versus load curve is shown in Fig. 13. The curve account also for losses related to on/off cycles. The average yearly efficiency in the simulations of this work is close to 73%, when a single unit is in operation; better efficiencies are found when the capacity is split on more units.

[8]Two temperatures for stack gases are considered, reflecting winter and summer operation, since during summer higher heat recovery temperatures are required to drive the absorption chiller.

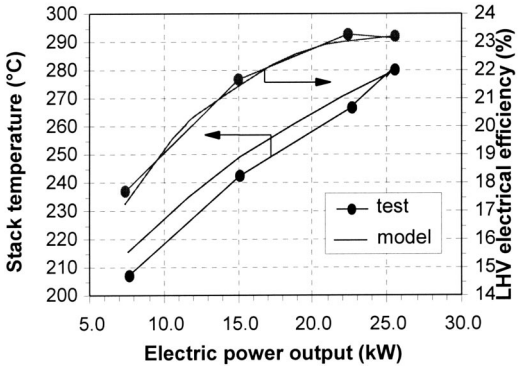

Fig. 11 Comparison of test results and simulated MTG performances

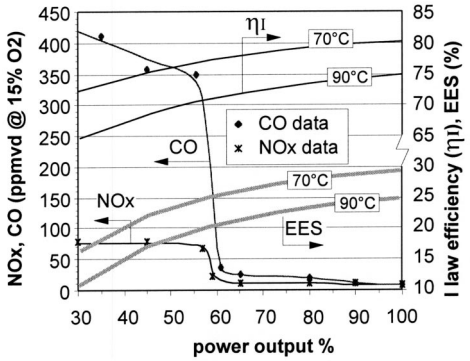

Fig. 12 Test results for MGT emissions and primary energy savings (EES)/first law efficiency versus load

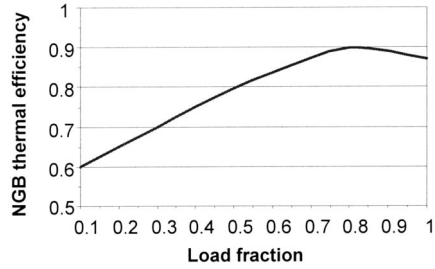

Fig. 13 NGB thermal efficiency versus load curve

AC efficiency variation versus load is computed according manufacturers' data.

Nomenclature

- AC = absorption chiller
- C = instant cost (€/kWh), Eq. (1)
- Cd = cooling demand (% or W/m^3)
- COG = cogenerator (MTG+heat recovery boiler)
- COP = coefficient of performance
- DC/AC = direct/alternating current
- E = specific yearly (or hourly) energy (kWh/m^3y)
- Ed = electricity demand (% or W/m^3)
- EG = electric grid
- EHP = electric heat pump
- ERC = electric reversible compressor
- EES = engine energy saving (%), Eq. 4

Hd = heat demand (% or W/m^3)
LHV = fuel lower heating value, kJ/kg_f
MTG = microturbine generator
NGB = natural gas boiler
NPV = specific net present value ($€/m^3$)
PE = primary energy (kWh)
PEC = specific primary energy consumption, $kWh/(m^3y)$
PES = specific primary energy saving, $kWh/(m^3y)$, Eq. (3)
P = pressure, Pa
P_{el} = electric power, kW
Qrec = MTG cogenerated heat (kWh/m^3y)
RMF = reverse metering factor, electricity sale/purchase cost ratio
rpm = revolutions per minute
T = temperature (°C or K)
TIT = turbine inlet temperature
W_{el} = electric energy (kWh)
β = pressure ratio
η_{I} = first law efficiency, Eq. (*A*4)
η_{II} = second law efficiency
η_{el} = electric efficiency
η_{th} = thermal efficiency

Subscripts

amb = ambient
c = cooling
cog = cogenerated
cond = condensation
conv = conventional solution (NGB+EG+ERC)
el = electric
ext = external (ambient)
ev = evaporator
f = fuel
h = heating
id = ideal
in = internal (room)
ng = natural gas
nom = nominal
p = purchased
ref = reference
s = sold

References

[1] Roncato, J. P., and Macchi, E., 2000, ''Report of Study Group 7.2: Comparison of Medium or Large Scale CHP and Combined Cycles, in Various Countries,'' *Woc7 Report, Proceedings of World Gas Conference 2000*, Nice, June IGUTCC, France, pp. 55–82.
[2] Kincaid, D. E., 1999, ''Distributed Generation: A Primer,'' Gas Research Institute, Diesel&Gas Turbine–Distributed power, BPA International, Oct.
[3] Green, S., 2001, ''Distributed Generation—A New Wave,'' *Power Engineering International*, PennWell, Mar.
[4] Campanari, S., and Macchi, E., 2001, ''Potential Developments in Gas-Fired Microturbines: Hybrid Cycles and Trigeneration,'' Cogeneration and On-site Power Production, **2**(2) (Mar.).
[5] De Biasi, V., 2001, ''DOE Developing Technology Base for Advanced Microturbine Designs,'' *Gas Turbine World*, Pequot, CT, **31**, (4), July.
[6] Consonni, S., Lozza, G., and Macchi, E., 1989, ''Optimization of Cogeneration Systems Operation—Part A: Prime Movers Modelization,'' *Proceedings of the 1989 ASME Cogen-Turbo Symposium*, Nice, Aug., ASME, New York, pp. 313–322.
[7] Consonni, S., Lozza, G., and Macchi, E., 1989, ''Optimization of Cogeneration Systems Operation—Part B: Solution Algorithm and Examples of Optimum Operating Strategies,'' *Proc. of the 1989 ASME Cogen-Turbo Symposium*, Nice, France, Aug. ASME, New York, pp. 323–331.
[8] Anon., 2000, ''Statistical Data on Electricity in Italy'' GRTN, Italy.
[9] Bombarda, P., 2001, ''Survey of Commercial ERC Performance,'' Technical Report, Department of Energetics, Politecnico di Milano.
[10] Campanari, S., 2000, ''Full Load and Part-Load Performance Prediction for Integrated SOFC and Microturbine Systems,'' ASME J. Eng. Gas Turbines Power, **122**, pp. 239–246.
[11] Campanari, S., and Boncompagni, L., 2001, ''Experimental Acquisition of Emission Data From a Commercial Microturbine,'' Internal Technical Note, Department of Energetics, Politecnico di Milano.
[12] Anon., 1999, ''Performance and Electrical Characterization Tests on a Microturbine Commercial Prototype,'' EPRI-TR 114270, Dec.
[13] Carnö, J., Cavani, A., and Liinanki, L., 1998, ''Micro Gas Turbine for Combined Heat and Power in Distributed Generation,'' ASME Paper 98-GT-309.
[14] Gliddon-Bush, C., 2001, ''Micro Size, Maximum Efficiency,'' *Power Engineering International*, Cogeneration supplement, PennWell, July.

Development of Operating Temperature Prediction Method Using Thermophysical Properties Change of Thermal Barrier Coatings

T. Fujii
e-mail: t-fujii@criepi.denken.or.jp

T. Takahashi

Central Research Institute of Electric Power Industry,
2-6-1 Nagasaka, Yokosuka,
Kanagawa 240-0196, Japan

Thermal barrier coatings (TBCs) have become an indispensable technology as the temperature of turbine inlet gas has increased. TBCs reduce the temperature of the base metal, but a reduction of internal pores by sintering occurs when using TBCs, and so the thermal barrier performance of TBCs is deteriorated. This in turn increases the temperature of the base metal and could shorten its lifespan. The authors have already clarified by laboratory acceleration tests that the deterioration of the thermal barrier performance of TBCs is caused by a decrease in the noncontact area that exists inside TBCs. This noncontact area is a slit space that exists between thin layers and is formed when TBCs are coated. This paper examines the relations between the decrease of the noncontact area and the exposure conditions, by measuring the thermal conductivity and the porosity of TBCs exposed to the temperatures that exist in an actual gas turbine, and derives the correlation with exposure conditions. As a result, very high correlations were found between the thermal conductivity and exposure conditions of TBCs, and between the porosity and exposure conditions. A very high correlation was also found between the thermal conductivity and porosity of TBCs. In addition, techniques for predicting TBC operating temperature were examined by using these three correlations. The correlation of diameter and exposure conditions of the gamma prime phase, which exists in nickel base super alloys, is used as a general method for predicting the temperature of parts in hot gas paths. This paper proposes two kinds of operating temperature prediction methods, which are similar to this general method. The first predicts the operating temperature from thermal conductivity measurements of TBCs before and after use, and the second predicts the operating temperature from thermal conductivity measurements of TBCs after use and porosity measurements before use. The TBC operating temperatures of a combustor that had been used for 12,000 hours with an actual E-class gas turbine were predicted by these two methods. The advantage of these methods is that the temperature of all parts with TBC can be predicted. [DOI: 10.1115/1.1619428]

Introduction

As gas turbines are being operated under increasingly high temperatures and pressures, the parts positioned in the path of hot combustion gas are thermally and mechanically subjected to severe working environments. Hot gas path parts that are especially exposed to high temperatures are combustors, transition pieces, and turbine first-stage buckets and nozzles. The surfaces of such parts are coated to protect the base metals from heat, oxidation, and corrosion. Ceramics of the zirconia system are normally used in TBCs, since compared to metals, a ceramic coating of low thermal conductivity protects the base metal from high-temperature cnvironments.

The application of TBCs has helped prolong the service life and raise the working temperature of components, however, the relationship between the raw materials and coating status of TBCs to thermal barrier performance has not yet been quantitatively evaluated. Furthermore, the temperature of parts that influence the service life of base metals under TBCs has also not yet been verified. It is therefore essential to clarify the thermophysical properties of TBCs first.

The authors measured the thermal conductivity of TBCs of an actual combustor, and have already clarified the age deterioration of the thermal barrier performance of TBCs, [1,2]. The average powder size, powder configuration, and powder components were taken as the parameters of plasma spray powder to identify the causes of age deterioration, and laboratory-scale acceleration tests were performed. As a result, it was clarified that the decrease in the noncontact area in TBCs by sintering was closely related to the deterioration in the thermal barrier performance of TBCs.

This paper examines the influence of the temperature in an actual gas turbine on the deterioration in thermal barrier performance, based on the change with age of noncontact area in TBCs. It also examines methods of predicting the operating temperature of actual TBCs based on the changes in the thermal barrier performance of TBCs and the changes in noncontact area (changes in porosity).

Experimental Samples and Equipments

Since fine spray powder is atmospheric plasma sprayed directly onto the surface of the base metal to form a coating layer, the layer contains pores. When applying TBCs, a coating layer of

Contributed by the International Gas Turbine Institute (IGTI) of THE AMERICAN SOCIETY OF MECHANICAL ENGINEERS for publication in the ASME JOURNAL OF ENGINEERING FOR GAS TURBINES AND POWER. Paper presented at the International Gas Turbine and Aeroengine Congress and Exhibition, Amsterdam, The Netherlands, June 3–6, 2002; Paper No. 2002-GT-30274. Manuscript received by IGTI, Dec. 2001, final revision, Mar. 2002. Associate Editor: E. Benvenuti.

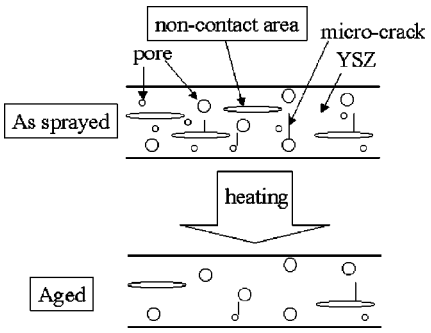

Fig. 1 Degradation mechanism of TBC

several tens of microns is formed by one pass. Therefore, TBCs are built up to the prescribed thickness by applying several coating layers. Therefore, noncontact areas resembling slits are generated between the coating layers due to incomplete fusion of plasma spray powder. In addition, microcracks are caused in the direction of thickness of TBCs because the coating layers melted by the plasma cool quickly on the surface of the base metals. Thus, there are three kinds of spaces in TBCs: pores, noncontact areas, and microcracks, as shown in Fig. 1. Especially, because the noncontact areas exist vertically in the direction of thickness of TBCs, the thermal barrier performance of TBCs is greatly affected. In this paper, we examine how the noncontact areas change with exposure conditions in an actual gas turbine. An 8wt% yttria partially stabilized zirconia (8wt%YSZ) was selected as a plasma spray powder. Table 1 shows the specifications of this powder. The thermal barrier performance was evaluated from the thermal conductivity of TBCs made from this plasma spray powder, and the amount of noncontact areas was evaluated from the porosity.

The process of manufacturing the samples is as follows. First, the plasma spray powder was atmospheric plasma sprayed onto the surface of the base metals to the thickness of 1 to 3 mm to form the TBCs. Then, only TBCs were peeled off from the surface of the base metals. Using only the TBCs portion, the coatings were prepared into sample configurations for measuring the respective thermophysical properties and establishing them as the as-sprayed TBCs.

Since it is difficult to directly measure the thermal conductivity in the hot condition, the following relation was used to calculate the thermal conductivity by measuring the thermal diffusivity, specific heat, and density:

$$\lambda = a \cdot Cp \cdot \rho.$$

Thermal diffusivity was measured by the laser flash method by using a sample of 10 mm in diameter×1 mm in thickness and specific heat by DSC (differential scanning calorimeter) by using a sample of 3 mm×3 mm×2 mm in thickness. The density was calculated from dimensional and mass measurements taken at room temperature. Density at high temperature was compensated by the measured values of thermal expansion obtained with a push rod dilatometer by using a sample of 3 mm×15 mm×3 mm in thickness.

Table 1 Specification of plasma spray powder

Range of Powder Diameter	20–75				
Average powder diameter	58.9 μm				
Powder type	Fused and crushed powder				
Thickness of coating	1–3 mm				
Component [wt%]	ZrO_2	Y_2O_3	TiO_2	Fe_2O_3	SiO_2
	91.93	7.89	0.14	0.03	0.01

Table 2 Exposure conditions

Exposure Temperature	Exposure Time
1000°C	200h
	1000h
1050°C	200h
	1000h
1100°C	200h
	1000h
1150°C	200h
	1000h

Next, the as-sprayed TBCs were exposed in an electric furnace to the temperatures that exist in an actual gas turbine to prepare simulated aged TBCs that had actually deteriorated. Table 2 shows the exposure conditions. Each of the thermophysical properties and the porosity were measured by using these as-sprayed and aged TBCs.

Sintering Start Temperature of TBCs

To determine the temperature at which the decrease in noncontact areas begins, the sintering start temperature of TBCs was examined first. Figure 2 shows the change in thermal expansion of the as-sprayed TBC. The decrease in thermal expansion which originated in sintering was confirmed at about 1000°C. To determine this sintering start temperature, the rate of change of thermal expansion at each temperature was calculated as shown in Fig. 3. As a result, it was found that the sintering began at almost 1000°C. Thus, TBCs were sintered under the conditions shown in Table 2.

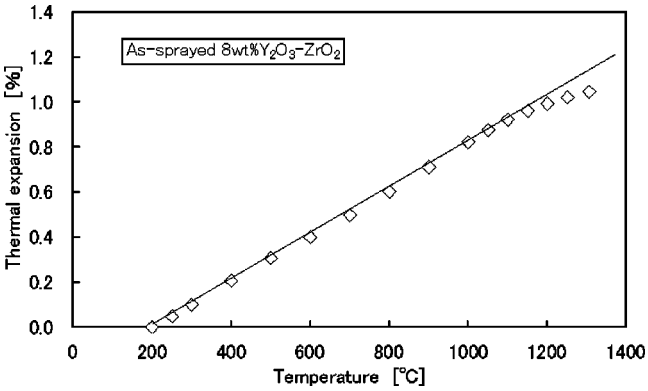

Fig. 2 Measurement result of thermal expansion

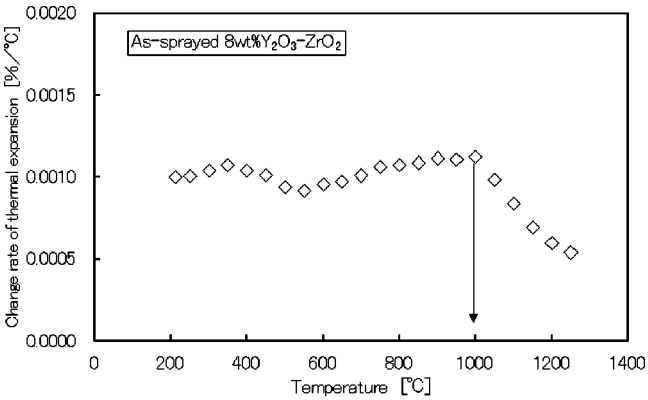

Fig. 3 Rate of change of thermal expansion

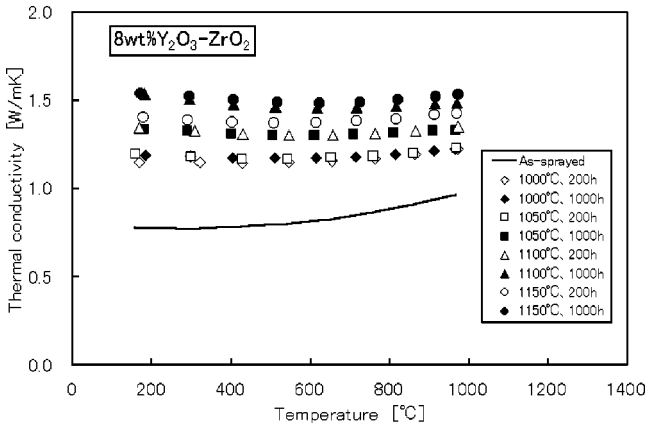

Fig. 4 Measurement results of thermal conductivity

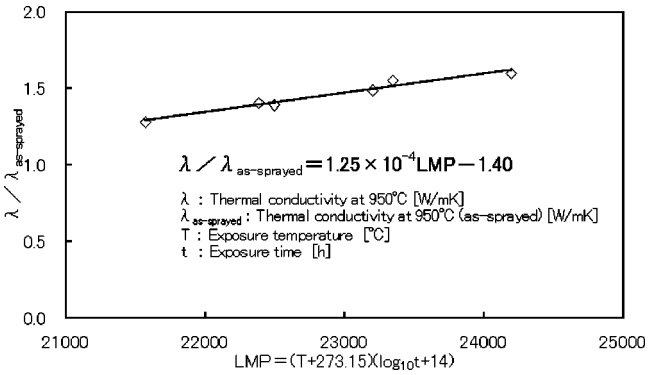

Fig. 6 Relation between thermal conductivity and exposure conditions

Effect of Exposure Conditions on Thermal Conductivity

Figure 4 shows the results of measuring the thermal conductivity after the as-sprayed TBCs were exposed under the conditions shown in Table 2. Comparing the measurement results, the thermal conductivity values of the aged TBCs were larger than those of the as-sprayed TBC in any condition. Moreover, when the exposure time was the same, the higher the exposure temperature, the larger the thermal conductivity.

Next, the rate of increase of thermal conductivity of the aged TBCs to the as-sprayed TBC was examined. Thermal conductivity values were compared at 950°C at which the measurement time does not influence the thermophysical properties because the TBCs were considered to be sintered at 1000°C or more. Figure 5 shows the result. The vertical axis represents the value of thermal conductivity at 950°C of the respective TBCs normalized by the values of thermal conductivity at 950°C of the as-sprayed TBC. The thermal conductivity values were 1.3–1.5 times higher than that of the as-sprayed TBC 200 hours later, and increased to 1.3–1.6 times that of the as-sprayed TBC 1000 hours later. Moreover, the thermal conductivity values after 200 hours and 1000 hours were almost the same, suggesting that sintering almost saturated at the exposure temperature of 1000°C. Therefore, the relation between the thermal conductivity changes and the exposure conditions at 1050°C or more was examined.

Figure 6 shows the result of examining the correlation of the thermal conductivity values at 950°C and the exposure conditions, given by the following equation:

$$\lambda/\lambda_{\text{as-sprayed}} = 1.25\times 10^{-4}\text{LMP} - 1.40$$
$$\text{LMP} = (T+273.15)(\log_{10} t + 14). \quad (1)$$

LMP is the Larson-Miller parameter used to examine the relation between the stress and the creep rupture time of metals. Equation (1) and the measurement values corresponded closely, so the thermal conductivity changes of TBCs appear to be modeled by the equation of the Larson-Miller parameter type, [3]. However, the range of T of Eq. (1) is 1000°C or more at which the thermal conductivity increases by sintering.

Effect of Exposure Conditions on Porosity

Next, to examine quantitatively the decrease in noncontact area in TBCs, the porosity of TBCs was measured by a mercury penetration porosimeter. Figure 7 shows the result of measuring the porosity. The initial porosity was about 8.8%, and the porosity tended to decrease as the exposure time or exposure temperature increased.

In the measurement result of the thermal conductivity, because sintering saturated quickly at the exposure temperature of 1000°C, the relation between the exposure conditions and the porosity values was examined at the exposure temperature of 1050°C or more. Figure 8 shows the relation between the porosity values and the exposure conditions, given by the following equation:

$$P/P_{\text{as-sprayed}} = -1.89\times 10^{-5}\text{LMP} + 1.80$$
$$\text{LMP} = (T+273.15)(\log_{10} t + 32). \quad (2)$$

Equation (2) and the measurement values corresponded closely, so the porosity changes of TBCs appear to be modeled by the equation of the Larson-Miller parameter type. However, the range of T of Eq. (2) is 1000°C or more at which the porosity decreases by sintering.

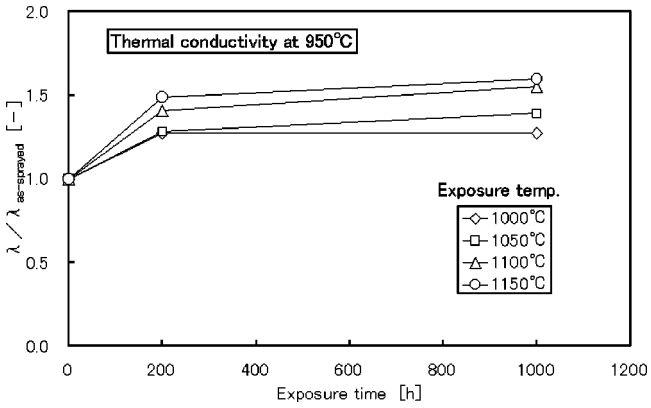

Fig. 5 Change of thermal conductivity

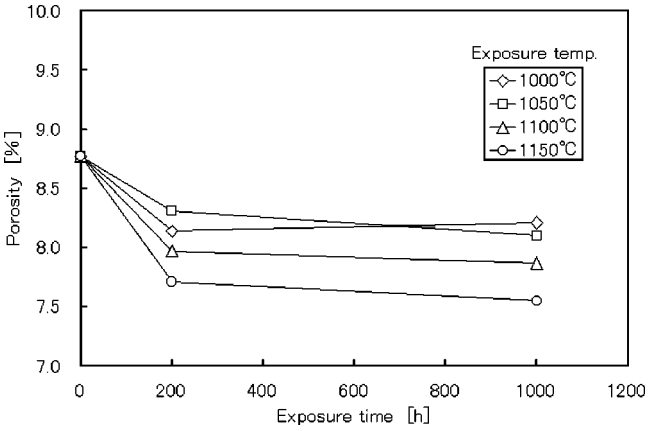

Fig. 7 Change of porosity

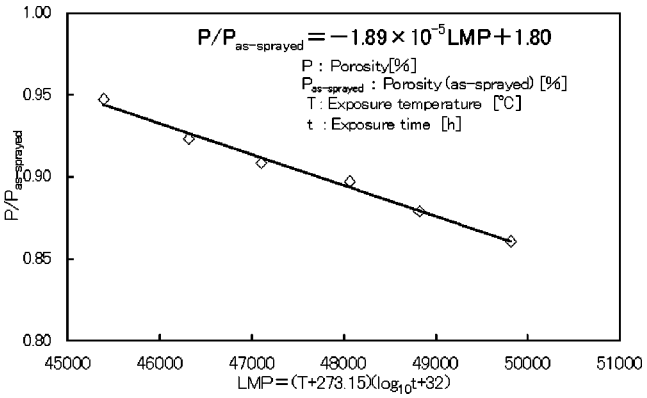

Fig. 8 Relation between porosity and exposure conditions

Correlation of Thermal Conductivity and Porosity

In addition, the correlation of the thermal conductivity values and the porosity values was examined. The following correlation was obtained by regression analysis of the thermal conductivity values at 950°C and the porosity values:

$$\lambda = -0.383P + 4.42 \quad (3)$$

P = value obtained from Eq. (2)

λ = value at 950°C

Figure 9 shows the relation between the values calculated by Eq. (3) and actual measured values, [4]. The differences between the calculated and measured values were within 5%, and thus the values were accurate.

Next, the correlation including the temperature dependency of the thermal conductivity was examined. The following correlation was obtained by multiple regression analysis of the thermal conductivity, temperature, and porosity:

$$\lambda = -0.398P - 3.01\times10^{-4}\theta + 2.64\times10^{-7}\theta^2 + 4.58 \quad (4)$$

P = value obtained from Eq. (2)

θ = temperature range 150 to 1000°C

λ = thermal conductivity value at 150 to 1000°C.

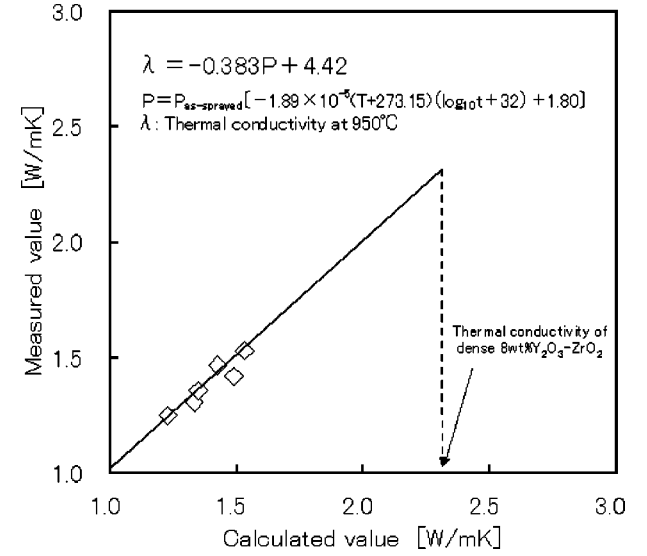

Fig. 9 Relation between calculated values and measured values

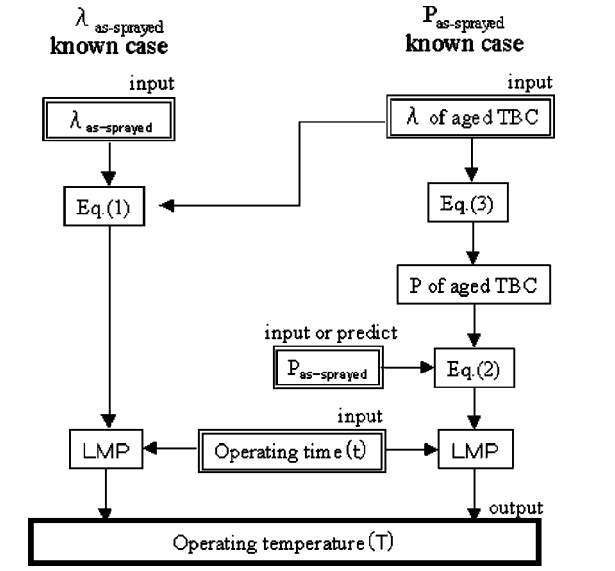

Fig. 10 Prediction flow of operating temperature of TBC

The differences between the calculated and measured values were within 5%, and thus the values were accurate. These results suggested that the thermal conductivity of exposed TBCs could be predicted from Eqs. (1), (3), and (4).

Operating Temperature Prediction Method of Actual TBC

Originally, Eq. (1) was used to predict the thermal conductivity of exposed TBC from the initial thermal conductivity and the exposure conditions. Equations (3) or (4) were used to predict the thermal conductivity of exposed TBC from the initial porosity and the exposure conditions. However, if the thermal conductivity of the as-sprayed TBC and exposed TBC, and the exposure time are known, the exposure temperature of the TBC can be predicted from Eq. (1). Moreover, if the thermal conductivity of exposed TBC, the initial porosity, and the exposure time are known, the exposure temperature of the TBC can be predicted from Eqs. (3) or (4). Figure 10 shows these prediction flows. The temperatures of TBCs are not often measured in an actual gas turbine, although it is very important for evaluating the lifespans of parts to predict the temperatures of TBCs. Therefore, these prediction methods were applied to the measurement results of the thermal conduc-

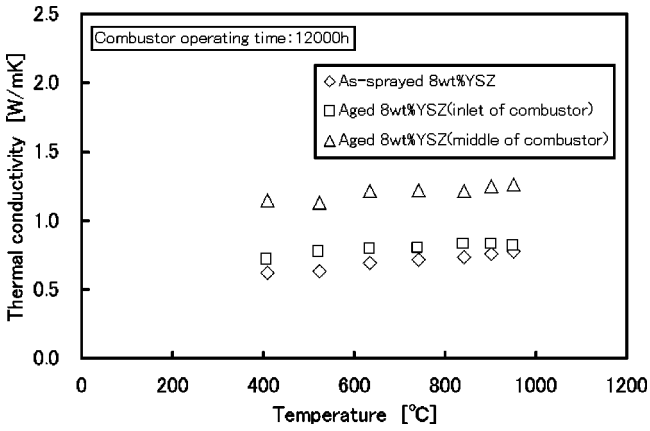

Fig. 11 Measurement results of thermal conductivity of actual TBCs

Table 3 Prediction results of TBC operating temperature ($\lambda_{as\text{-}sprayed}$ known case)

Area	$\lambda/\lambda_{as\text{-}sprayed}$ (950°C)	Operating Time	Operating Temperature (Predicted Value)
Inlet of combustor (low temperature)	1.05	12000 h	812°C
Middle of combustor (high temperature)	1.62		1062°C

Table 4 Prediction results of TBC operating temperature ($P_{as\text{-}sprayed}$ known case)

Area	λ at 950°C	Porosity (As-Sprayed)	Operating Time	Operating Temperature (Predicted Value)
Inlet of combustor (low temperature)	0.821W/mK	9.40% (predicted value)	12000 h	900°C
Middle of combustor (high temperature)	1.26 W/mK			1079°C

tivity of TBCs used for 12,000 hours for the actual combustor, and the operating temperatures of TBCs were predicted.

Figure 11 shows the results of measuring the thermal conductivity of actual TBCs. The operating temperatures of TBCs were predicted by using the thermal conductivity values at 950°C in this figure, and Eqs. (1) and (3). When Eq. (3) was used, the initial porosity value was not known. However, it was judged that the thermal conductivity of the aged TBC in the combustor inlet area was almost the same as that of the as-sprayed TBC, and did not sinter as shown in Fig. 11. Therefore, the porosity of TBC of the combustor inlet area obtained from Eq. (3) was assumed to be the initial porosity, and so the operating temperatures were predicted.

Tables 3 and 4 show the prediction results by each method. As a result, the predicted results for the combustor inlet area showed a difference of about 90°C although the predicted results for the combustor middle area agreed closely. The reason for this is that the valid range of temperature of Eqs. (1) and (3) is 1000°C or more at which sintering begins, and the error was greater in the combustor inlet area with comparatively low temperature. As a result, the operating temperature can be predicted by these methods if TBCs are used at 1000°C or more. However, the prediction results must be verified in future because the operating temperatures of actual TBCs have not been measured.

The correlation between diameter and exposure conditions of the gamma prime phase, which exists in nickel base super alloys, is commonly used to predict the temperature of parts in hot gas paths, [5]. However, our method makes it possible to predict the temperature of all TBC parts.

Conclusion

TBCs made from plasma spray powder of 8wt%YSZ with atmospheric pressure plasma spray were exposed to the temperatures assumed to exist in actual gas turbines, and the thermal conductivity and the porosity were measured. Equations for predicting the deterioration in thermal barrier performance of TBCs from the correlation among thermal conductivity, porosity, and exposure conditions were obtained. Methods for predicting the operating temperature of actual TBCs were derived from these equations, and the operating temperatures of TBCs that had been used for 12,000 hours in an actual combustor were predicted. Verification of the prediction results remains for future studies.

Nomenclature

a = thermal diffusivity (m^2/s)
Cp = specific heat (J/kg K)
H = exposure time (h)
P = porosity (%)
T = temperature (°C)
λ = thermal conductivity (W/m K)
ρ = density (kg/m^3)

References

[1] Fujii, T., and Takahashi, T., 2001, "Estimation of Thermophysical Properties and Microstructure of Aged Thermal Barrier Coatings," ASME Paper 2001-GT-417.

[2] Ishiguro, T., Makino, A., Noda, N., and Araki, N., 1992, "Transient Temperature Response of Material With Distributed Properties," JSME **B58**(556), pp. 176–182.

[3] Dinwiddie, R. B., Beecher, S. C., Porter, W. D., and Nagaraj, B. A., 1996, "The Effect of Thermal Aging on the Thermal Conductivity of Plasma Sprayed and EB-PVD Thermal Barrier Coatings," ASME Paper 96-GT-282.

[4] Ravichandran, K. S., An, K., Dutton, R. E., and Semiatin, S. L., 1997, "Microstructure and Thermal Conductivity of Layered Thermal Barrier Coatings Processed by Plasma Spray and Physical Vapor Deposition Techniques," *Proceedings of AGARD SMP Meeting on "Thermal Barrier Coatings,"* AGARD Report, **14**, pp. 1–12.

[5] Yoshioka, Y., Okabe, N., Saito, D., Fujiyama, K., and Okamura, T., 1996, "Service Temperature Estimation for Gas Turbine Buckets Based on Microstructure Change," J. Soc. Mater. Sci. Jpn., **45**, pp. 699–704.

Measurement of Void Fraction and Pressure Drop of Air-Oil Two-Phase Flow in Horizontal Pipes

J. L. Pawloski

C. Y. Ching[1]
e-mail: chingcy@mcmaster.ca

M. Shoukri

Department of Mechanical Engineering,
McMaster University,
Hamilton, ON L8S 4L7, UK

The void fractions, flow regimes, and pressure drop of air-oil two-phase flow in a half-inch diameter pipe over a wide range of test conditions have been investigated. The flow regimes were identified with the aid of a 1000 frames per second high-speed camera. A capacitance sensor for instantaneous void fraction measurements was developed. The mean and probability density function of the instantaneous void fraction signal can be used to effectively identify the different flow regimes. The current flow regime data show significant differences in the transitional boundaries of the existing flow regime maps. Property correction factors for the flow regime maps are recommended. The pressure drop measurements were compared to the predictions from four existing two-phase flow pressure drop models. Though some of the models performed better for certain flow regimes, none of the models were found to give accurate results over the entire range of flow regimes. [DOI: 10.1115/1.1619429]

Introduction

Accurate prediction of the flow regimes and pressure drop of air-oil flow is important in many industrial applications. For example, in aeroengines, air and lubrication oil are mixed in the bearing chamber, which is subsequently drained by a scavenging system comprising of a pump and piping system where the air and oil are separated. The accurate prediction of the pressure loss in the scavenge line is important to design the pressure limits of the bearing chamber to ensure no loss of lubricant with the air. The scavenge line can have several singularities such as sudden area changes, bends, and junctions in addition to straight piping. Models to predict the pressure loss in each of these components are required for the proper design of the scavenge system. However, the complex nature of two-phase flow, characterized by turbulence, deformable phase interface, phase interaction, phase slip, and compressibility of the gas phase has made it extremely difficult to obtain reliable flow models.

There have been numerous theories and correlations developed to predict pressure drop in two-phase flows in horizontal pipes. Among the more common models are the homogeneous model and the separated flow models. The homogeneous model assumes that the two-phase flow can be characterized as a single phase with one set of common properties. The homogeneous properties are determined from a weighted average of the mass flow rates of the gas and liquid. The separated flow models consider the two phases separately, with an inherent assumption that the two phases reach constant but not necessarily equal velocities. While several models of this type have been developed, the three most commonly used are the Friedel [1], Martinelli [2], and Chisholm [3] models. Each of these separated flow models has been found to be acceptably accurate under certain flow conditions.

The pressure drop models are very likely to be dependent on the flow regime, as the flow regimes significantly affect the flow characteristics. Accurate identification of the flow regime under different flow conditions can greatly simplify the flow modeling by only dealing with the specific flow regime. There are three main approaches to identifying flow regimes: visual observations, measurement of pressure or void fraction fluctuations, and tomography. All three approaches have specific advantages and disadvantages to them. Visual observations are a simple technique but subjective and difficult to make, especially at high phase velocities. A high-speed imaging system can alleviate some of the difficulties associated with visual observation. Measurement of local pressure fluctuations as a function of time has shown great success in distinguishing the points of transition between flow regimes, [4]. Hubbard and Dukler [5] first introduced the technique by using the power spectral density of the pressure fluctuations to identify the flow regimes. They found three distinct frequency distributions for separated, dispersed and intermittent flows, [5].

Similarly, the void fraction or liquid hold-up fluctuations can be used to distinguish the flow regime. For example, Jones and Zuber [6] found three distinct probability density function (PDF) distributions of the void fraction fluctuation for separated, dispersed and intermittent flows. The third approach, tomography, involves the measurement of phase distribution spatially as well as temporally. This technique produces an image of the spatial phase distribution in the channel over time. Several tomography methods have been well developed, including capacitance and X-ray techniques.

In general, void fraction and liquid holdup measurement techniques have been shown to indicate the transition boundaries with a high degree of accuracy, [4]. Visual observations combined with one or more other techniques can be used to accurately identify the flow regimes. In the current research only visual observation of the flow using a high-speed video camera is made to distinguish between flow regimes. A second technique of flow regime identification using void fraction measurements with a capacitance sensor has been developed and the results are discussed in this paper. The flow regimes are usually presented as flow regime maps, with the axes representing certain physical characteristics of the two phases. Among them, mass flow rate, superficial velocity, and momentum flux have been the most widely used mapping parameters. While as many as 31 different flow regimes have been identified for horizontal two phase flow, [4], only six main flow regimes are distinguished in this study. These are: stratified (ST),

[1]To whom Correspondence should be addressed.

Contributed by the International Gas Turbine Institute (IGTI) of THE AMERICAN SOCIETY OF MECHANICAL ENGINEERS for publication in the ASME JOURNAL OF ENGINEERING FOR GAS TURBINES AND POWER. Paper presented at the International Gas Turbine and Aeroengine Congress and Exhibition, Amsterdam, The Netherlands, June 3–6, 2002; Paper No. 2002-GT-30277. Manuscript received by IGTI, December 2001, final revision, March 2002. Associate Editor: E. Benvenuti.

wavy (W), annular (A), mist (M), plug (P), and slug (S). Due to the existence of several sub regimes in slug flow, three additional slug sub regimes are identified: slug building zone (SBZ), foam slug (FS), and blow through slug (BTS). The flow regimes and pressure drop data of air-oil two-phase flow in a half-inch diameter horizontal pie are presented in this paper.

Experimental Facilities

The experiments were performed in a new versatile air/oil flow loop designed and constructed for the present research (Fig. 1). It is designed to accommodate multiple test section geometries over a wide range of operating parameters. The facility operates at pressures up to 415 kPa, with maximum air and oil flow rates of 43.5 kg/hr and 1840 kg/hr, respectively. The oil is stored in the tank (1), which also acts as a separation chamber for the air and the oil. The oil passes through a fine mesh filter (2) before entering the rotary gear pump (3), which is driven by a three-phase, 1 HP electric motor. A programmable speed controller on the gear pump is used to vary the oil flow rate. A 100-psi house line provides the air for the system. The air is filtered and regulated (7) before entering the air/oil mixer (6). Electric heaters are installed on both the air and oil lines to permit operation at temperatures up to 150°C. The air heater is a single-phase, 4 kW heater (9) and the oil heater is a three-phase, 18 kW heater (5). The air/oil mixer is annular in design, with oil flowing around an inner perforated pipe. Air flows in the inner pipe and enters the oil stream through 380 1/32-inch diameter perforations. Once the air/oil mixture has passed through the test section (10), it can either pass through a cooler (11) or flow directly to the phase separation and oil storage tank. An oil mist filter (12) removes any remaining oil in the air stream before it is vented to the outside. The air/oil mixture passes through a 0.9 m long flow development section prior to entering the half-inch diameter, 1.0 m long test section. A 0.6 m long stabilization section follows immediately downstream of the test section. The entire test section is made of Lexan polycarbonate tubing to allow for complete flow visualization.

Two turbine flow meters (4) are used to measure the oil flow rate, with a range of 0.0036–0.51 kg/s (0.07–10.0 USGPM). Four rotameters (8) in a bank are used to measure the air flow rates, with a range 0–600 SCFH. Two Rosemount pressure transducers with an accuracy of ±0.5% full scale are used to measure the system pressure and pressure drop along the pipe. Temperature is measured at various locations throughout the loop using type K thermocouples. Five standard liquid-filled pressure gages are used to monitor pump pressure, inlet air pressure, inlet mixer conditions, and tank pressure. Flow regimes are identified by visual observation with the aid of a high-speed video camera (up to 1000 frames/s). The data is acquired using an AT-M10-16E-10DAQ board for the pressures and a PCI-6034E board with SCB-68 connection block for the temperatures. All data is processed using National Instrument's LabVIEW software in a program especially written for this research program.

Capacitance Sensor Design. A capacitance sensor was designed and developed to measure the instantaneous void fraction of the air-oil two-phase flow. The advantages of a capacitance sensor are its ability to capture fast transient phenomena without disrupting the flow while being relatively inexpensive to build. Variations in measured capacitance can be directly related to the void fraction, since this directly affects the dielectric constant of the mixture and hence the measured capacitance. The two most common capacitance sensor designs for use on round tubes are helically coiled electrodes and ring electrodes in series, [7]. The design of a helically coiled sensor is generally more complicated, due to the specific placement of the shielding required to minimize edge effects and stray capacitance. The same is not true with the coiled ring design, as the entire sensor can simply be shielded to prevent stray capacitance. Both types of sensors have been proven to produce accurate measurements of void fraction. For this study, the ring type sensor with three sets of copper electrodes connected in parallel was used (Fig. 2). The electrodes are housed in two pieces of acrylic to allow direct mounting on the test section. The sensor is shielded by completely covering the acrylic housing with copper tape, which is grounded, eliminating environmental capacitance interference. This method of shielding reduced the effect of stray capacitance on the sensor output signal from ±1–5 pF to ±0.01–0.03 pF, as measured on a Booton-72B capacitance transducer (±0.5% accuracy full scale).

Both an offline and online calibration of the capacitance sensor were performed. The effect of different flow regimes on the sensor was determined with an off-line calibration using Phenolic, a plastic material with the same dielectric constant as the oil used for the experiments. Pieces of Phenolic were machined to fit inside the tube to simulate different flow regimes. In this instance, eight annular and eleven stratified pieces with different cross-sectional

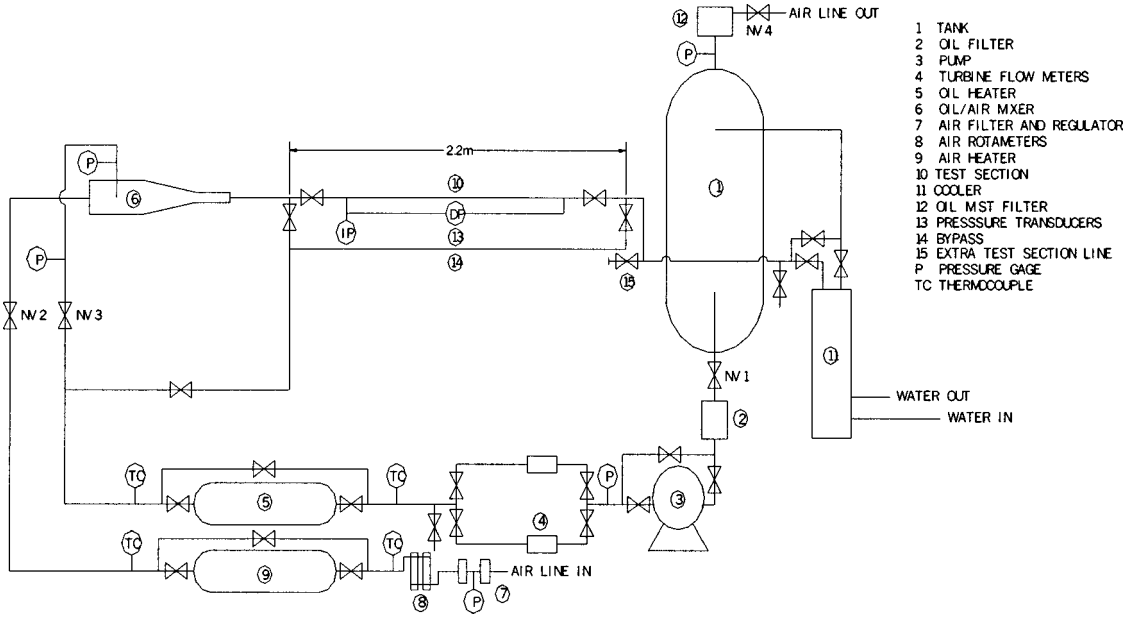

Fig. 1 Schematic of air/oil flow loop

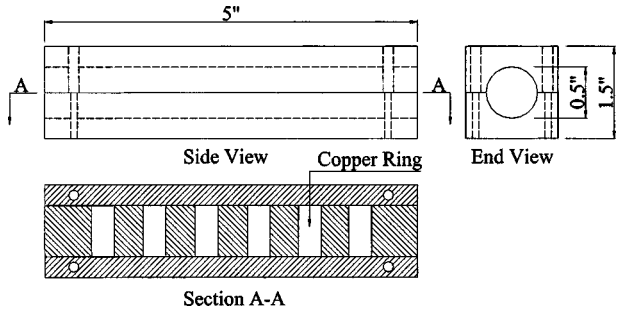

Fig. 2 Capacitance sensor design

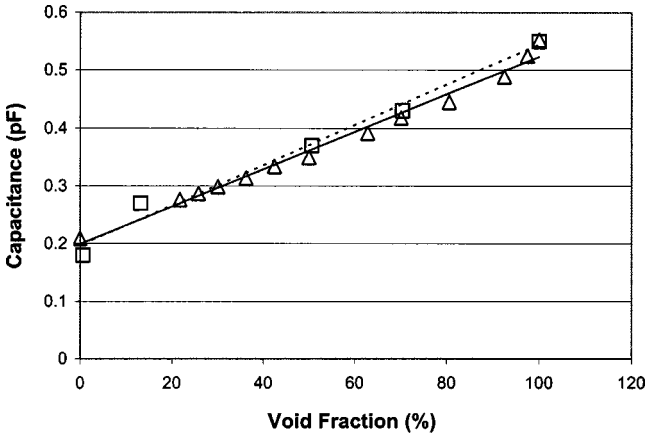

Fig. 3 On and off-line calibration of capacitance sensor. □, oil; △, phenolic; — — —, linear (oil); ——, linear (phenolic).

areas to simulate different void fractions were used to measure the range of the sensor. The sensor was then installed on the test section and measurements were obtained with the tube filled with all air and all oil. On-line static stratified flow regime data points were also taken, and the results were found to be in good agreement with the offline results (Fig. 3). Dynamic measurements for the two limiting conditions with the flow of air and oil only were obtained, and the range was found to be in complete agreement with the static calibration, indicating that the sensor is not affected by the running of the flow loop. To check the response of the sensor, tests were conducted over a wide range of flow conditions using several sampling frequencies. It was found that a sampling frequency of 1000 Hz was sufficient to resolve the dynamic characteristics of the flow in this instance.

Results and Discussion

Capacitance Sensor Results. The void fraction can be obtained from the capacitance signal using the relation:

$$\alpha = \frac{C_{\text{oil}} - C_{\text{measured}}}{C_{\text{oil}} - C_{\text{air}}} \tag{1}$$

where C_{oil} and C_{air} are the capacitance when the tube is filled with oil only and air only, respectively. The values for C_{oil} and C_{air} in this instance are 0.55 pF and 0.18 pF, respectively. While the instantaneous capacitance signal showed distinct patterns for certain flow regimes, allowing for relatively easy identification, this was not always the case. In order to better interpret the instantaneous capacitance signal, the power spectral density (PSD) and probability density function (PDF) of the signal were examined. The range and location of the peaks of the PSD and PDF can be used to identify the flow regimes. The signals for transitions from slug to plug, slug to wavy, and slug to annular are presented to illustrate the flow regime identification technique. These three transitions were chosen due to the ease of identifying each flow regime visually, which allows confirmation of the capacitance sensor results. For each transition case, three measurements were obtained, two within the flow regimes, and the third within the transitional zone.

The time traces for transition between slug and plug flow (Fig. 4) are similar in appearance and indicate that both flow regimes exhibit some periodicity, with capacitance mean values increasing from 0.4 to 0.5 pF as the transition progresses. The PSD and PDF of the time traces, however, clearly show very distinct characteristics. Plug flow exhibits a small frequency peak at about 20 Hz, while the transitional PSD (middle) shows a slightly higher peak at about 30 Hz and elements of the other two PSD graphs. For the PDF of slug flow, two peaks are observed: a larger one at a void fraction of about 0.5, and a smaller one at a very low void fraction. Plug flow has a much larger single peak at a very low void fraction (approximately 0.1). The transitional PDF shows characteristics of both regimes, with two peaks at void fractions of about 0.1 and 0.45. Lowe and Rezkallah [8] observed very similar results from capacitance signals in vertical upwards two-phase slug flow. This suggests that a slug flow PDF can be characterized as having two peaks, a small one at low void fraction, and a much larger one at higher void fractions. The low void fraction peak represents the tube when filled with oil, which occurs when a slug passes the sensor. The higher void fraction represents the flow regime the rest of the time, when the tube contains both air and oil in a stratified type of flow. By similar interpretation, the plug flow PDF has a peak at low void fraction as a result of the tube being filled with oil most of the time.

A transition from slug to wavy flow is presented in Fig. 5, with the time trace for the wavy flow showing a significant difference to that of the slug flow. The slug flow characteristics were discussed in the previous section; and therefore are not addressed here. The mean capacitance decreases from 0.4 to 0.3 pF as the transition occurs, which is expected because air is the larger phase by volume in wavy flow. The PSD reflects the uniformity of the wavy flow, showing no dominant frequency. For this transition, the PDF is more useful than the PSD, as it provides more detail on the flow regimes. The wavy flow has a single large peak with low variance at an approximate void fraction of 0.6, while the transition shows a dominant peak at a void fraction of about 0.5, but with a much wider variance over lower values. The transition from slug to wavy flow results in an increase in the amount of air present in the tube, and therefore an increase in the void fraction.

The transition from slug to annular flow is examined in Fig. 6. As with the previous two flow transitions, the same slug flow data is being used to provide consistency in the comparisons. The annular flow regime, which is predominantly air, is clearly shown in the time trace and PSD results. The time trace signal is steady with a very low variance. The mean capacitance of the annular flow is 0.27 pF, which is approaching the lower limit of 0.18 pF for all air. There is no dominant frequency, as shown in the PSD; and the PDF shows only one, very pronounced peak at a void fraction of about 0.75. As expected, the transition regime has characteristics of both flow regimes, with a slightly dominant frequency of 20 Hz (with slug flow having 10 Hz and annular flow having no dominant frequency) on the PSD. The peak void fraction for the transitional zone occurs at about 0.65, which lies between the 0.5 of slug flow and the 0.75 of annular flow. Unlike annular flow, which has a very narrow PDF variance, the transitional flow has a wider variance similar to the slug PDF. These results clearly indicate that the instantaneous void fraction can be used to effectively identify the different flow regimes.

Air/Oil Flow Regime Maps. The flow regimes of the present data are compared to the flow regime maps of Mandhane [9], Taitel and Dukler [10], and Spedding and Nguyen [11] based on air-water properties. This provides consistency between all three maps, as air-oil property corrections are not available for all three maps. The slug flow regime is well predicted by the flow map of

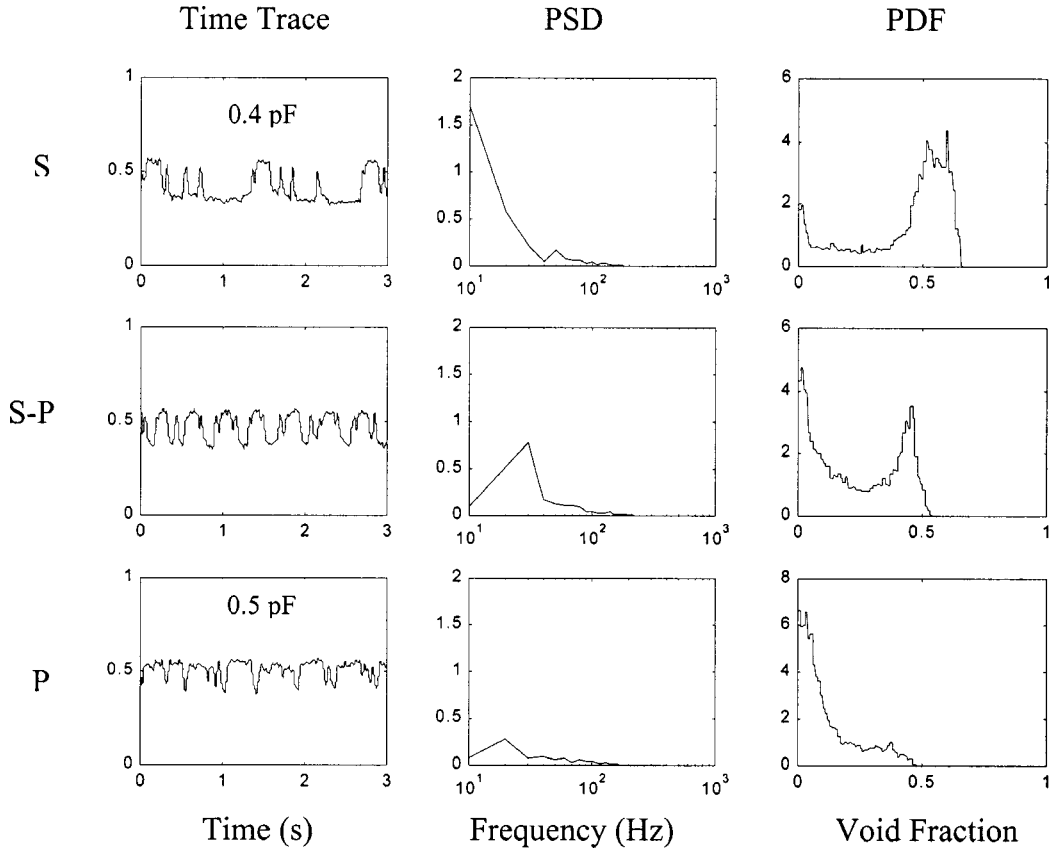

Fig. 4 Slug to plug transition

Mandhane (Fig. 7), with all data points falling within the suggested ''slug area'' of the map. Transition between slug flow and annular flow is represented by the blow through slug data, which occurs at air superficial velocities in the range of 6–20 m/s. This transition is clearly overpredicted by the map, which suggests the transition occurs at higher air superficial velocities of 11–70 m/s (with increasing oil velocity). The map also poorly predicts the plug to slug transition; with the current data indicating the transition occurs at higher superficial gas velocities (1.2–2.5 m/s) over the range of liquid superficial velocities (0.25–4.3 m/s) than suggested by the map. All of the other transition boundaries are found to have transition data points on both sides of the predicted line. This does not necessarily indicate a problem with the transition boundary, as transition between flow regimes occurs more gradually than suggested by most flow regime maps, [12].

The Taitel and Dukler [10] flow regime map (for a 2.5 cm dia. pipe) is presented using superficial velocities (Fig. 8). The transition boundaries between plug and slug flow, and annular and mist flow, were not developed by Taitel and Dukler [10] and therefore cannot be evaluated. The transition between slug and annular flow, as represented by the blow through slug flow regime, is accurately predicted at oil velocities in the range of 0.3–0.7 m/s. At velocities greater than 0.7 m/s, the present data indicates transition occurs at lower gas velocities than those predicted by the map. Transition between wavy and annular flow regimes also appears to be well predicted at oil velocities below 0.1 m/s. All the other transitional boundaries require adjustment to better predict the transition between flow regimes. For example, the stratified to plug transition is predicted to occur at oil superficial velocities of 0.12–0.16 m/s, but plug flow was observed at an oil superficial velocity of 0.08 m/s. Similarly, the slug to dispersed flow regime transition range for the oil superficial velocity is overpredicted by 1.5 m/s.

The dimensionless plotting parameter map of Spedding and Nguyen [11] is compared with the present data in Fig. 9. In order to compare their flow map to other maps, Spedding and Nguyen [11] used air and water two-phase flow results to obtain the transition boundaries. The definitions for the flow regions of this map are different than those of the previous two maps. For example, the blow through slug flow regime is represented as a flow region and not a transitional boundary. The same is true for the wavy to slug flow transition. The map predicts the blow through slug and annular flow regime data with a great deal of accuracy; however, the slug region is not well predicted by the flow regime map. Unlike the other two flow maps presented here, the dimensionless numbers used for the plotting parameters rely on the physical properties of the two phases indirectly. However, Spedding and Nguyen [11] suggest that transitional boundary prediction errors are more likely to result from differences in test facilities than from use of different two-phase systems.

In order to evaluate the overall usefulness of the three flow regime maps, the maps were compared against one another. The ability of each map to correctly predict the flow regimes was calculated using the method suggested by Mandhane et al. [9]. The number of correctly predicted points in an individual flow regime is divided by the number of total observed points in the flow regime and converted to a percentage. The total number of correctly predicted points and the average accuracy of the whole map can then be determined (Table 1). Several flow regimes have a limited number of collected data points, and are therefore included in the table but not considered in the comparison. The Mandhane et al. [9] and Taitel and Dukler [10] flow regime maps predict the slug region with 100% accuracy. While Taitel and Dukler [10] do not define a transition boundary between plug and slug flow, most of the plug points still lie within the defined ''intermittent'' region. In comparison the Spedding and Nguyen [11] flow regime map performs poorly in the slug region but has a high accuracy in predicting the blow through slug and annular flow regimes. Overall the Taitel and Dukler [10] flow regime map is

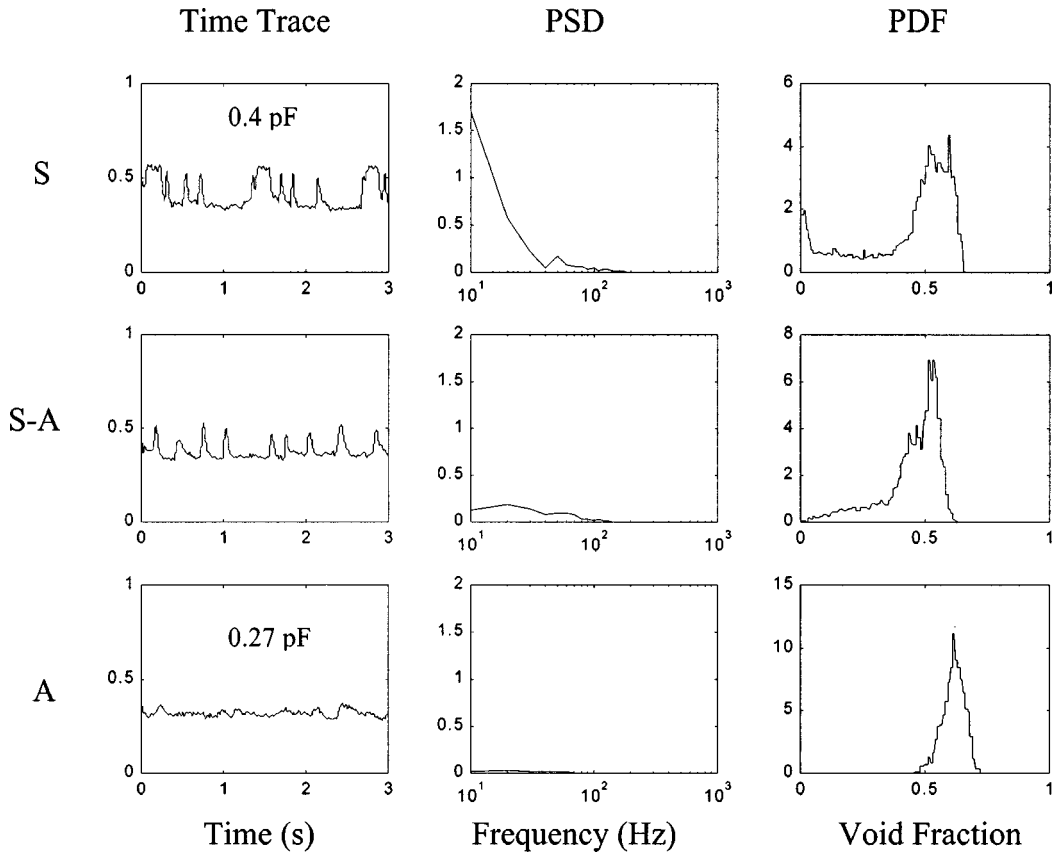

Fig. 5 Slug to wavy transition

found to have the highest prediction accuracy at 53%, which can be partly attributed to the high accuracy in predicting the flow regimes where the most data was collected.

The preceding comparison of the three flow regime maps was based on the transition boundaries for air-water properties. However, both the Mandhane et al. [9] and Taitel and Dukler [10] transition boundaries can be converted for air and oil properties. Mandhane et al. [9] proposed two correction factors based on early work by Glover and Aziz [13] and with the addition of viscosity terms. To account for changes in physical properties, the superficial velocity coordinate is multiplied by the suggested physical property correction (M) as listed in Table 2.

$$j_i = \frac{G_i}{\rho_i}\ (\text{m/s}) \tag{2}$$

$$j_i' = M j_i \tag{3}$$

where X' and Y' are given by

$$X' = \left(\frac{\rho_g}{0.0808}\right)^{0.2}\left(\frac{72.4\rho_l}{62.4\sigma}\right)^{0.25}\left(\frac{\mu_g}{0.018}\right)^{0.2} \tag{4}$$

$$Y' = \left(\frac{\mu_l}{1.0}\right)^{0.2}\left(\frac{72.4\rho_l}{62.4\sigma}\right)^{0.25}. \tag{5}$$

The constants in the above equations are based on imperial units, and all physical properties should be in these units. Applying the physical property corrections only marginally improved the accuracy of the map (Fig. 10). For example, the plug to slug transition is more accurately predicted in the 0.25–1 m/s range. However, the slug to dispersed transition accuracy observed in the original map (Fig. 7) is lost. It is apparent that more study is required on the form the physical property factors should take in order to obtain more accurate transition boundaries. As a first recommendation, a combination of the correction factors suggested by Mandhane et al. [9], Glover and Aziz [13], and Pawloski [14] is suggested (Table 3). The resulting flow map (Fig. 11) is an improvement of the original Mandhane et al. [9] flow regime map.

The Taitel and Dukler [10] flow map transitional boundaries were recalculated to reflect the properties of oil instead of water by assuming turbulent flow for both phases. For the oil used in the current investigation, the viscosity was sufficiently high to result in large errors for the stratified to wavy transition, and this is not included in the corrected map (Fig. 12). Overall, the corrected map showed a decrease in prediction accuracy. The slug to annular transition shifted upwards by a factor of 1.5, and the slug to dispersed transition shifted to the left by a factor of 0.1, resulting in a much lower prediction of these two transitions. It can be speculated that the corrections to the map are affected by the viscosity of the oil, resulting in the large errors. Comparison of the two corrected maps against the two original map results is shown in Table 4, with the corrected Mandhane et al. [9] map predicting with 75% accuracy.

Pressure Drop Measurements. Four frictional pressure drop models (homogeneous, Martinelli, Chisholm, and Olujic) were compared against the measured pressure drop data over the entire range of flow regimes. The overall results for the homogeneous model were found to underpredict the pressure drop by an average of 41% (Fig. 13). An analysis of the pressure drop results by flow regimes indicate that the mist flow and annular flow regimes are the best predicted by the homogeneous model. Figure 14 shows the pressure drop data for these two flow regimes, with an average underprediction of about 26%. This is expected given the inherent assumptions in the homogeneous model.

The Martinelli model was found to consistently underpredict the pressure drop by an average of 47% across all flow regimes

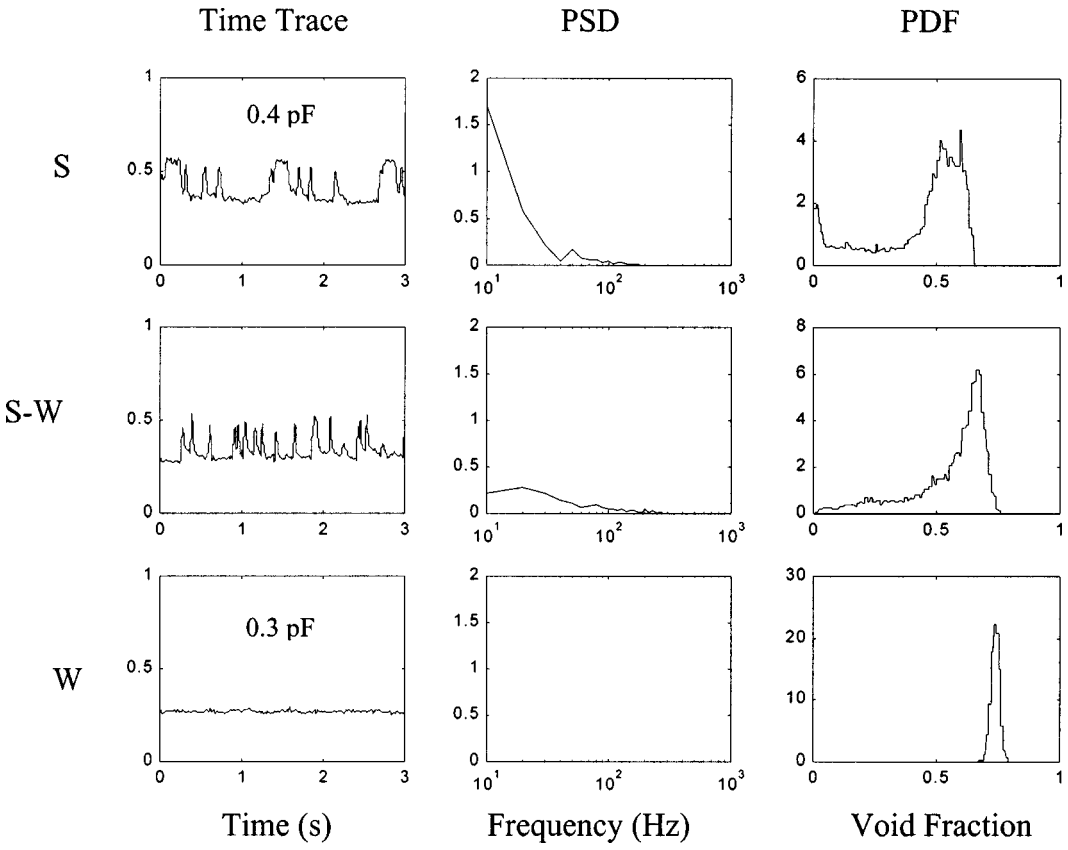

Fig. 6 Slug to wavy transition

(Fig. 15). The best prediction from the Martinelli model was for the slug-building zone, which averaged a 35% underprediction (Fig. 16). The annular flow regime was the most poorly predicted, which averaged a 56% underprediction (Fig. 16). The relatively small scatter in the data from the Martinelli model allows for a simple single correction factor to be applied for all flow regimes. Taking the inverse of the slope of the trendline, the model is multiplied by a factor of 1.9, resulting in the data distribution shown in Fig. 17. The corrected model predicts the frictional pressure drop within ±30% of the measured pressure drop. The accuracy improves to ±15% for pressure drops above 15000 $N/m^2/m$.

The Chisholm model (Fig. 18) predicted the pressure drop with

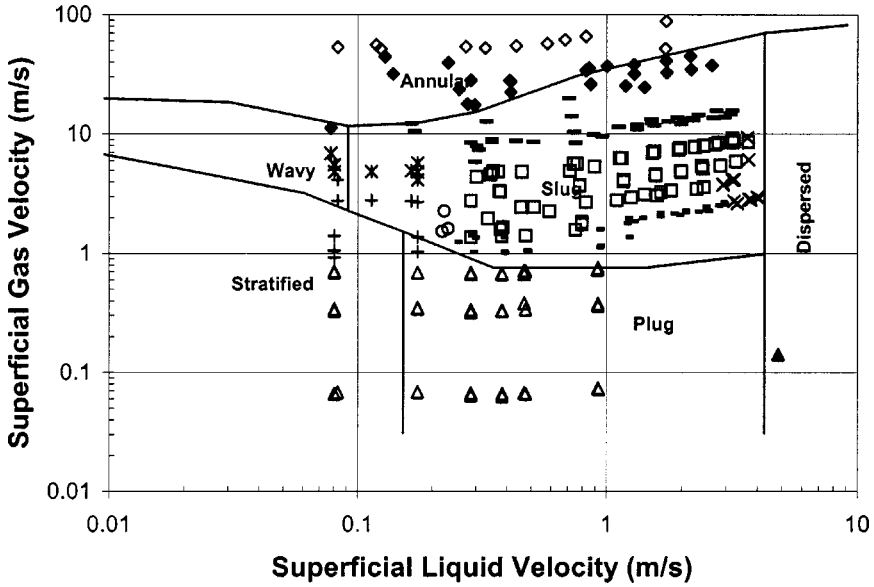

Fig. 7 Mandhane [9] flow regime map. ♦, annular; -, BTS transition; ▲, dispersed; ◇, mist; △, plug; −, P-S transition; □, slug; ×, S-D transition; +, P-ST-W transition; *, wavy; ○, W-S transition;—transition boundaries.

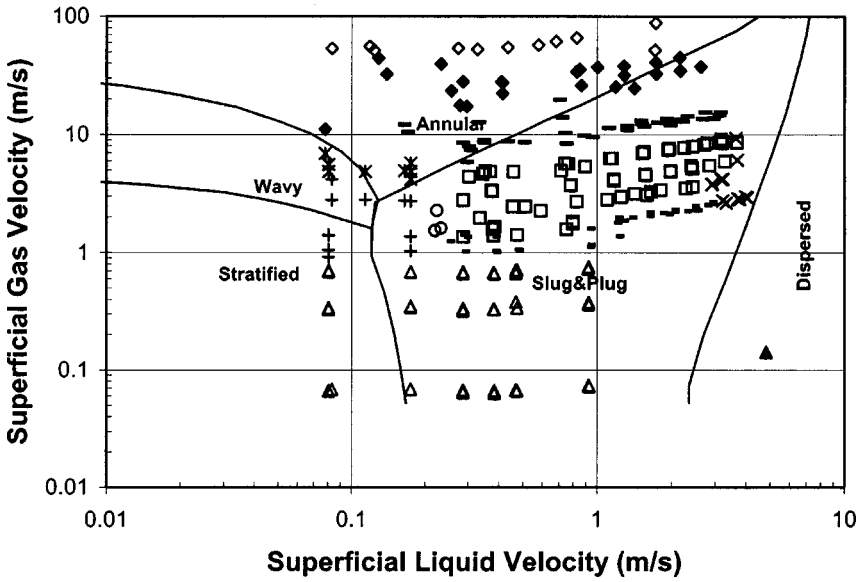

Fig. 8 Taitel and Dukler [10] flow regime map. ♦, annular; -, BTS transition; ▲, dispersed; ◇, mist; △, plug; −, P-S transition; □, slug; × S-D transition; +, P-ST-W transition; *, wavy; ○, W-S transition;—transition boundaries.

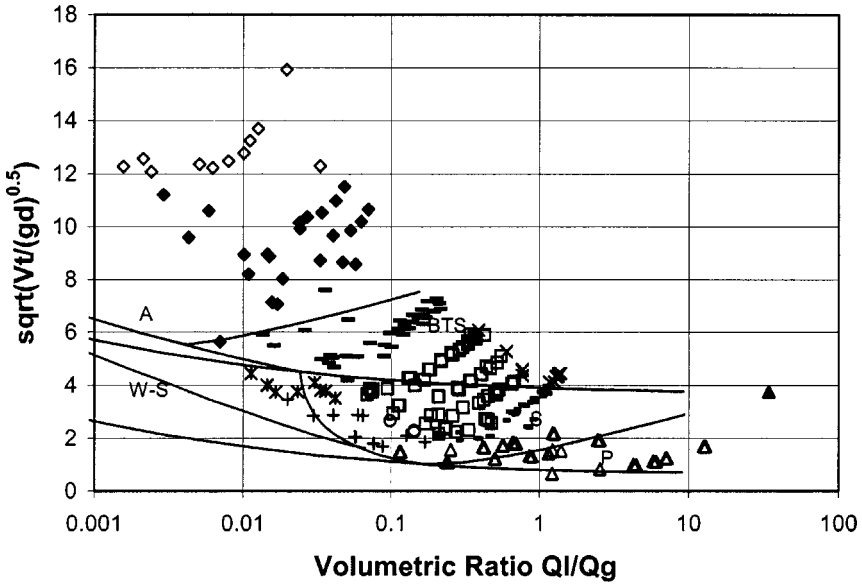

Fig. 9 Spedding and Nguyen [11] flow regime map. ♦, annular; -, BTS transition; ▲, dispersed; ◇, mist; △, plug; −, P-S transition; □, slug; ×, S-D transition; +, P-ST-W transition; *, wavy; ○, W-S transition;—, transition boundaries.

an average of 43% underprediction; however, several of the flow regimes were predicted with a much higher accuracy (<30%). The flow regimes predicted with higher accuracy include plug, slug, slug building zone and the slug to plug transition. Figure 19 shows the four regimes, with the slug building zone flow regime having almost no deviation from the measured values. Unlike the Martinelli frictional pressure drop model, the Chisholm model does not closely follow one trendline, making a simple correction to the model difficult. The relatively accurate prediction (within 35%) of many of the flow regimes also indicates correction of the model may not be necessary. This model may be useful as a first step in developing a new model that predicts pressure drop based on flow regime.

Ferguson and Spedding [15] examined the accuracy of 14 different frictional pressure drop models with respect to indivi-

Table 1 Comparison of flow regime maps

Flow Regime	Number of Points	Mandhane Correct (%)	Taitel & Dukler Correct (%)	Spedding & Nguyen Correct (%)
A	24	54.2	66.7	**95.8**
M	11	**100.0**	90.9	0.0
S	60	**100.0**	**100.0**	48.3
W	9	33.3	33.3	44.4
P	35	**82.9**	**82.9**	54.3
BTS	38	2.6	15.8	**97.4**
P-S	34	0.0	0.0	0.0
P-ST-W	12	16.7	0.0	0.0
S-D	12	8.3	16.7	0.0
W-BTS	2	0.0	0.0	100.0
W-S	3	0.0	0.0	0.0
W-A	2	0.0	100.0	100.0
Total	242	50.4	**53.3**	47.5

Table 2 Coordinates for Mandhane map transition boundaries

Transition Boundary	j_g (ft/s)	j_l (ft/s)	Physical Property Correction M
Stratified to plug	0.1	0.5	Y'^{-1}
	5.0	0.5	Y'^{-1}
Wave to slug	7.5	0.3	Y'
	40.0	0.3	Y'
Plug and slug to dispersed	0.1	14.0	Y'
	230.0	14.0	Y'
Stratified and plug to wave and slug	35.0	0.01	X'
	14.0	0.1	X'
	10.5	0.2	X'
	2.5	1.15	X'
	2.5	4.8	X'
	3.25	14.0	X'
Wave and slug to annular mist	70.0	0.01	X'
	60.0	0.1	X'
	38.0	0.3	X'
	40.0	0.56	X'
	50.0	1.0	X'
	100.0	2.5	X'
	230.0	14.0	X'
Dispersed to annular mist	230.0	14.0	X'
	269.0	30.0	X'

Table 3 Suggested transition boundary correction factors for Mandhane map, [14]

Transition Boundary	Physical Property Correction Equation
Stratified to plug	$j_i' = Y'^{-1} j_i$
Wave to slug	$j_l' = Y' j_l$
	$j_g' = 0.5X' j_g$
Plug and slug to dispersed	no change
Stratified and plug to wave and slug	$j_i' = X j_i$
Wave and slug to annular mist	$j_l' = 1.2Y' j_l$
	$j_g' = 0.4X' j_g$
Dispersed to annular mist	$j_l' = Y' j_l$
	$j_g' = 0.4X' j_g$

dual flow regimes, and found the Olujic [16] model to perform the best over the largest number of identified flow regimes. The Olujic model was therefore selected as the fourth model investigated using the current air-oil data. The Olujic model attempts to separate the flow regimes into two regions, based on the Froude number and phase volume flow ratio, and uses different models in the two different regions. When the gas phase velocity is much greater than the liquid phase velocity, the region is designated as alpha. When the velocities are approximately equal, the region is designated as beta. In terms of flow regimes, the beta region represents plug and dispersed flow, and the alpha region all others. The pressure drop in the two regions are given by

$$\left(\frac{dP}{dz}\right)_F = f\left[\frac{(Gx)^2}{2d\rho_g}\right]\left[1+\frac{(1-x)}{x\varepsilon R}\right]^{19/8} \qquad \text{alpha model}$$

$$\left(\frac{dP}{dz}\right)_F = f\left(\frac{G^2}{2d\rho_l}\right)[1+x(R-1)] \times[1-x(R-1)(K_2-1)] \qquad \text{beta model}$$

where the friction factors for the models are defined as

$$f = 0.3164\left(\frac{Gxd}{\mu_g}\right)^{-1/4} \qquad \text{alpha} \tag{6}$$

$$f = \frac{64}{\mathrm{Re}} \quad \text{if Re}<2000 \qquad \text{beta} \tag{7}$$

$$f = \frac{3.164}{\mathrm{Re}^{0.25}} \quad \text{if Re}<2000 \quad \text{beta.} \tag{8}$$

The alpha model requires the calculation of the two-phase parameters ε and Γ_o, defined as

$$\Gamma_o = \left(\frac{1-x}{x}\right)\left[\frac{G^2(1-x)^2}{\rho_l g d}\right]^{-1/4} R^{-1/2}\theta^{-1/8} \tag{9}$$

$$\varepsilon_1 = 0.77R^{-0.55}\Gamma_o^X$$

$$\varepsilon_2 = 2.19R^{-0.61}\Gamma_o^Y$$

$$X = 0.266R^{0.057}$$

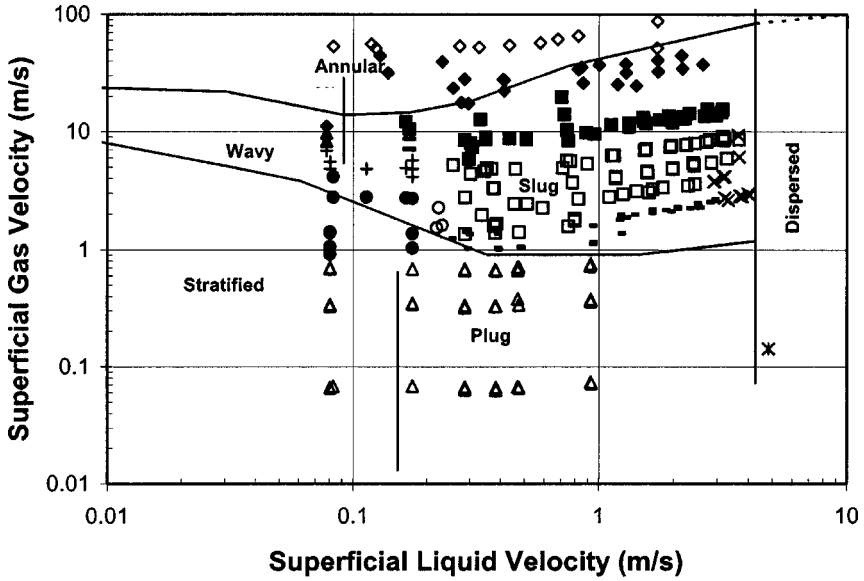

Fig. 10 Mandhane [9] map for air-oil properties. ♦, annular; ■, BTS transition; ◇, mist; △, plug; −, P-S transition; □, slug; ×, S-D transition; ●, P-W transition; ○, W-S transition; +, wavy; *, dispersed; ▲, W-A transition.

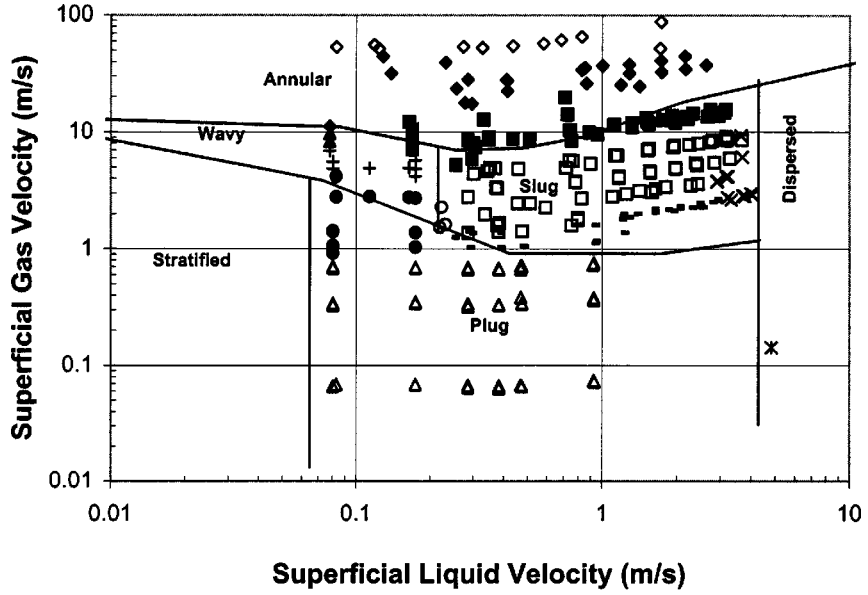

Fig. 11 Suggested air-oil property correction for Mandhane [9] map. ♦, annular; ■, BTS transition; ◇, mist; △, plug; −, P-S transition; □, slug; ×, S-D transition; ●, P-W transition; ○, W-S transition; +, wavy; *, dispersed; ▲, W-A transition.

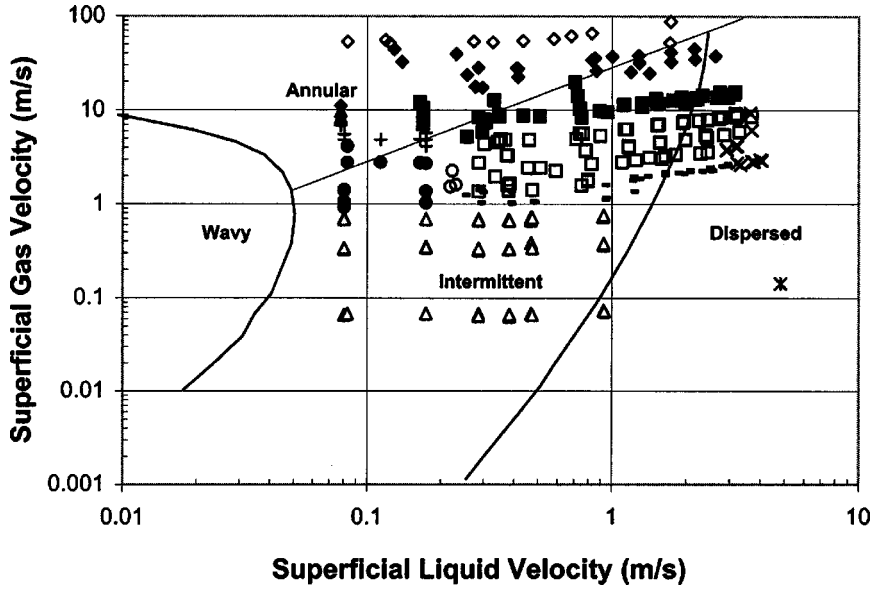

Fig. 12 Taitel and Dukler [10] map for air-oil properties. ♦, annular; ■, BTS transition; *, dispersed; ◇, mist; △, plug; −, P-S transition; □, slug; ×, S-D transition; ▲, P-W transition; +, wavy; ●, W-A transition; ○, W-S transition.

Table 4 Comparison of property corrected flow regime maps

Flow Regime	Number of Points	Mandhane Correct (%)	Taitel & Dukler Correct (%)	Corrected Mandhane Correct (%)	Corrected Taitel & Dukler Correct (%)
A	24	54.2	66.7	**95.8**	66.7
M	11	**100.0**	90.9	**100.0**	**100.0**
S	60	**100.0**	**100.0**	**100.0**	75.0
W	9	33.3	33.3	**100.0**	0.0
P	35	82.9	82.9	**100.0**	94.3
BTS	38	2.6	15.8	**60.5**	10.5
P-S	34	0.0	0.0	**29.4**	0.0
P-ST-W	12	16.7	0.0	**25.0**	0.0
S-D	12	8.3	**16.7**	8.3	0.0
W-BTS	2	0.0	0.0	**100.0**	0.0
W-S	3	0.0	0.0	**100.0**	0.0
W-A	2	0.0	**100.0**	0.0	0.0
Total	242	50.4	53.3	**74.6**	45.0

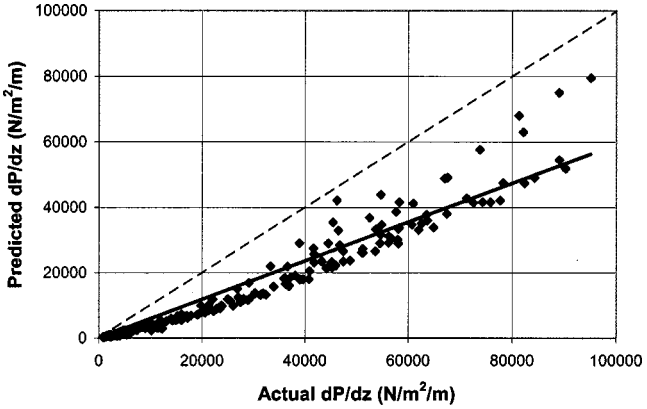

Fig. 13 Comparison with the homogeneous model. ♦, data;—, $y=0.5915\times$.

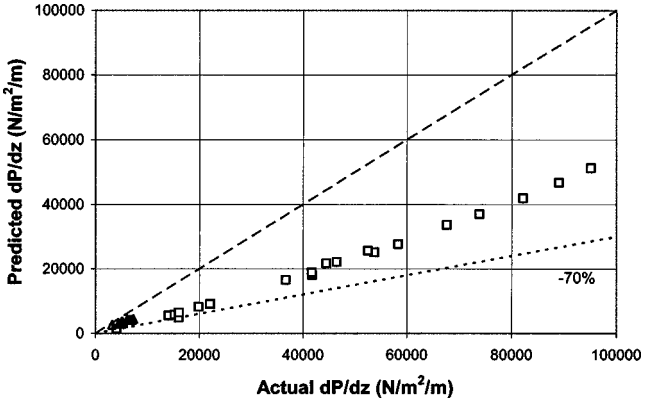

Fig. 16 Comparison of slug building zone data with Martinelli model

$$Y=1.78R^{-0.078}$$

$$\varepsilon=(\varepsilon_1^{-3}+\varepsilon_2^{-3})^{-1/3}. \tag{10}$$

In the beta model, the value K_2 was defined by Olujic [16] to be

$$K_2=1.2\left[\frac{(7+8n)(7+15n)}{(7+9n)(7+16n)}\right] \tag{11}$$

$$n=\left(\frac{0.671}{\beta}\right)[1+(1+0.907\beta)^{1/2}]. \tag{12}$$

In the beta region, the model underpredicted the data by an average of 45% (Fig. 20). In the alpha region, the model produced relatively good results for pressure drops below 25000 $N/m^2/m$ (Fig. 21). Above this value, the alpha region model greatly overpredicted the pressure drop, with all overpredicted points representing data in the blow through slug, annular, or mist flow regimes. It was determined that some flow regimes contained points falling in both the alpha and beta regions, suggesting that the model was not correctly identifying the specific flow regimes. Therefore, it is speculated that the criteria used to select the flow

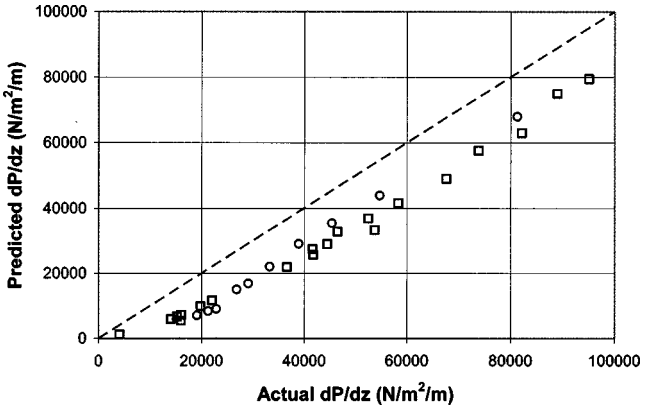

Fig. 14 Comparison of mist and annular flow data with homogeneous model

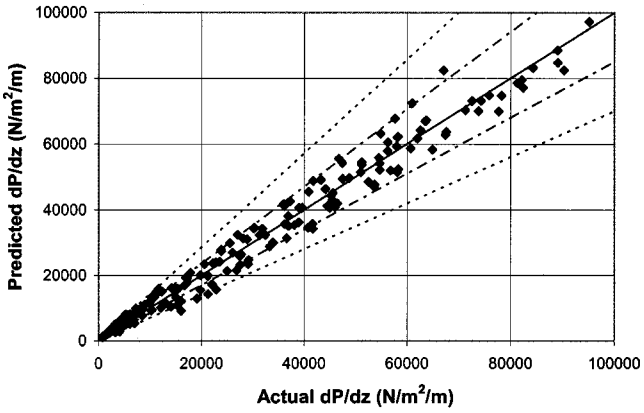

Fig. 17 Corrected Martinelli model. ♦, data; ------, +/−30%; — - — -, +/−15%.

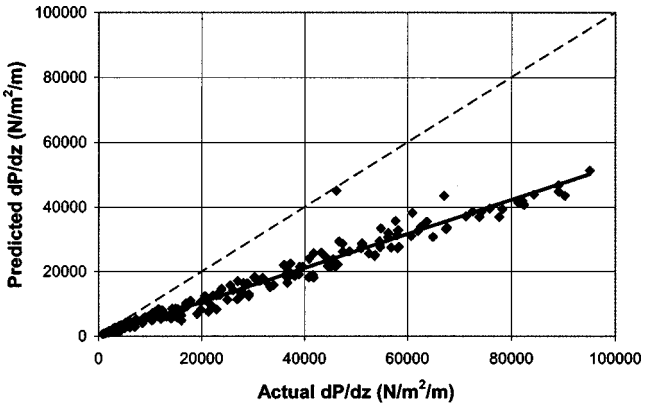

Fig. 15 Comparison with the Martinelli model. ♦, data;—, $y=0.05279\times$.

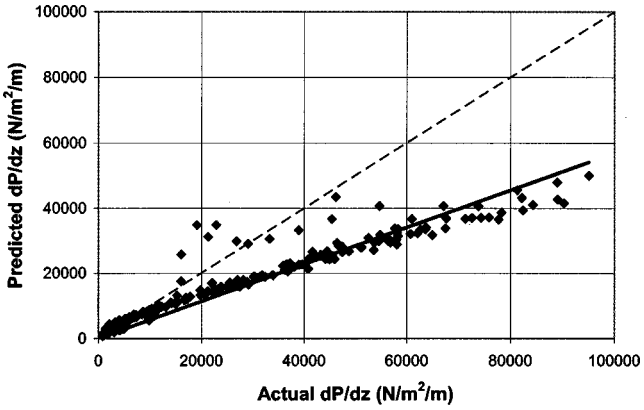

Fig. 18 Comparison with the Chisolm model. ♦, data;—, $y=0.5684\times$.

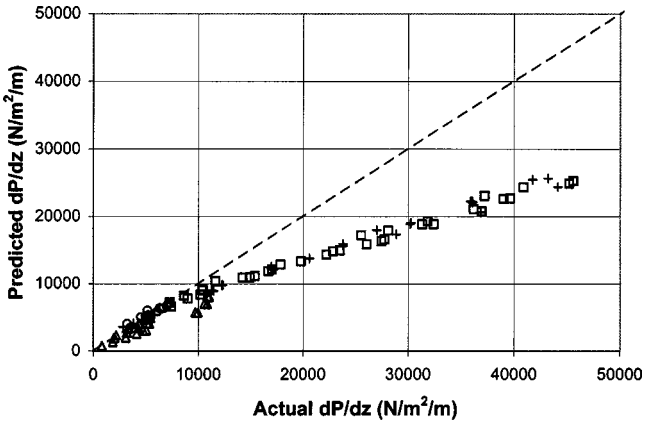

Fig. 19 Comparison with Chisolm model

region model is not accurately separating the data by flow regimes. The Olujic model is, however, an useful example of a pressure drop model based on flow regimes.

In order to evaluate the different pressure drop models, the root mean square error of each model was computed and compared against the other models (Table 5). For each flow regime, the model that best predicts the pressure drop has been highlighted. The foam slug and slug-dispersed regimes are predicted to the same accuracy by the homogeneous and Martinelli models, while the plug flow regime is predicted with almost the same accuracy by the Chisholm and Martinelli models. Of the 16 flow regimes, the Chisholm model most accurately predicts ten. These include the intermittent (plug and slug) flow regimes, as well as the high-speed air flow rate (annular, mist, and blow through slug) flow regimes. All regimes associated with high oil flow rates, including foam slug, dispersed flow, and the slug-dispersed transition, are well predicted by the Martinelli model. The homogeneous model also predicted the foam slug and slug-dispersed transition well.

Table 5 Pressure drop percentage root mean square error

Flow Regime	Homogeneous	Chisholm	Martinelli	Olujic
A	42	**38**	56	78
BTS	52	**40**	52	53
M	42	**39**	57	311
FS	**44**	45	**44**	49
P	65	**26**	**27**	84
P-S	64	**29**	36	67
P-ST-W	74	49	**31**	87
S	60	**33**	43	59
SBZ	70	**9**	35	72
S-D	**43**	45	**43**	47
W	59	76	**35**	72
W-A	60	84	**49**	62
W-BTS	59	**19**	47	65
W-S	80	**8**	45	84
Total	55	**35**	**40**	79

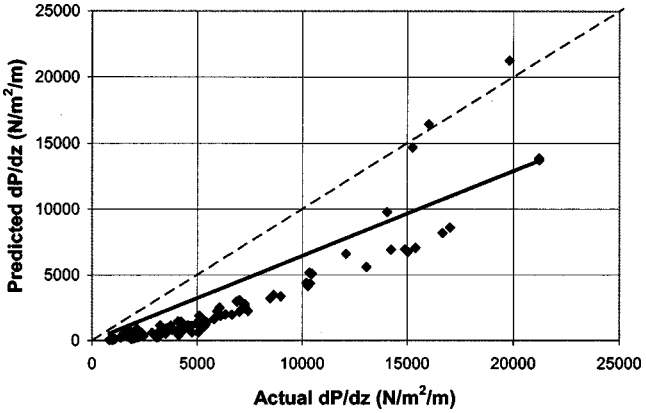

Fig. 20 Comparison with the Olujic model (beta region). ♦, alpha region data;—, $y=0.6432\times$.

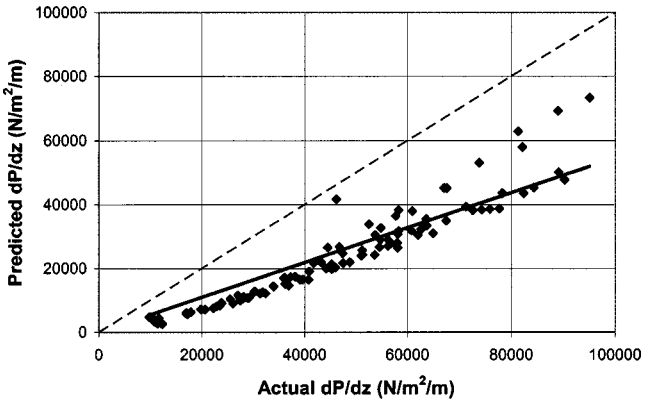

Fig. 21 Comparison with the Olujic model (alpha region). ♦, beta region data;—, $y=0.5464\times$.

Concluding Remarks

Void fraction, flow regime, and pressure drop measurements for air-oil two-phase flow in a half-inch diameter horizontal pipe have been obtained. The instantaneous void fraction signal can be used to effectively identify the flow regime. The probability distribution function (PDF) of the void fraction signal is particularly useful, which shows very distinct distributions for the different regimes. The current flow regime data, collected from visual observations, were compared with the flow maps of Mandhane et al. [9], Taitel and Dukler [10], and Spedding and Nguyen [11]. While the current flow regime data exhibit the same trends of these flow maps, there are significant differences in the transition boundaries. For example, slug flow occurs over a narrower range of gas and liquid superficial velocities than that predicted by the maps. Overall, the Taitel and Dukler air-water map was found to predict the flow regimes most accurately. Correcting the transition boundaries of the Mandhane et al. [9] and Taitel and Dukler [10] maps for air-oil properties improved the prediction accuracy of the former to 75%. Due to the influence of the viscosity of the oil being used, the corrected Taitel and Dukler [10] map was found to have decreased prediction accuracy. The corrected Mandhane et al. [9] map is therefore recommended. The pressure drop data was compared against several existing empirical models, including the homogeneous model, the separated flow models of Martinelli and Chisholm, and the Olujic model. Though some of the models performed better for certain flow regimes, none of the models were found to give accurate results over the entire range of flow regimes. Overall, the Martinelli and Chisholm models predicted with the lowest error (40% and 35%, respectfully) and are therefore recommended as a starting point in developing a more accurate prediction model based on flow regimes.

Acknowledgments

The support of the Natural Sciences and Engineering Research Council (NSERC) of Canada and Pratt and Whitney Canada is gratefully acknowledged.

Nomenclature

C = capacitance (pF)
d = tube inner diameter (m)
dP/dZ = pressure gradient ($N/m^2/m$)

f = friction factor
g = gravity (m/s^2)
G = mass flux ($kg/m^2.s$)
j = superficial velocity (m/s)
K_2 = Martinelli and Chawla variable
M = Mandhane correction variable
n = Olujic variable
R = density ratio
Re = Reynolds number
x = quality
X' = Mandhane plotting parameter
Y' = Mandhane plotting parameter

Subscripts

air = air properties
F = friction
g = gas phase
i = phase
l = liquid phase
oil = oil properties

Greek

ρ = density (kg/m^3)
σ = surface tension (N/m)
μ = viscosity (Pa.s)
α = void fraction
β = volume flow rate ratio
θ = viscosity ratio
ε = Olujic variable
Γ_o = Olujic variable

Defined Flow Regimes

A = annular
BTS = S to A transition
D = dispersed
FS = foam slug
M = mist
P = plug
S = slug
SBZ = slug building zone
ST = stratified
W = wavy

References

[1] Friedel, L., 1979, ''Improved Friction Pressure Drop Correlations for Horizontal and Vertical Two Phase Pipe Flow,'' European Two Phase Flow Group Meeting, Paper E2, Ispra, Italy.
[2] Martinelli, R. C., and Nelson, D. B., 1948, ''Prediction of Pressure Drop During Forced-Circulation Boiling of Water,'' Trans. ASME, **70**, pp. 695–702.
[3] Chisolm, D., 1973, ''Pressure Gradient due to Friction During Flow Evaporating Two-Phase Mixtures in Smooth Tubes and Channels,'' Int. J. Heat Mass Transfer, **16**, pp. 347–348.
[4] Hand, N. P., and Spedding, P. L., 1993, ''Horizontal Gas-Liquid Flow at Close to Atmospheric Conditions,'' Chem. Eng. Sci., **48**, pp. 2283–2305.
[5] Hubbard, M. G., and Dukler, A. E., 1966, ''The Characterization of Flow Regimes for Horizontal Two-Phase Flow: I. Statistical Analysis of Wall Pressure Fluctuations,'' *Proc. Heat Transfer and Fluid Mechanics Institute*, Stanford, CA, pp. 385–400.
[6] Jones, A. B., and Zuber, N., 1975, ''The Interrelation Between Void Functions Fluctuation and Flow Patterns in Two-Phase Flow,'' Int. J. Multiphase Flow, **2**, pp. 273–306.
[7] Abdul-Razzak, A., Shoukri, M., and Chang, J. S., 1995, ''Characteristics of Refrigerant R-134A Liquid-Vapor Two-Phase Flow In A Horizontal Pipe,'' ASHRAE Trans., **101**, pp. 1–13.
[8] Lowe, D., and Rezkallah, S., 1999, ''A Capacitance Sensor for the Characterization of Microgravity Two-Phase Liquid-Gas Flow,'' Meas. Sci. Technol., **10**, pp. 965–975.
[9] Mandhane, J. M., Gregory, G. A., and Aziz, K., 1974, ''A Flow Pattern Map for Gas-Liquid Flow in Horizontal Pipes,'' Int. J. Multiphase Flow, **1**, pp. 537–553.
[10] Taitel, Y., and Dukler, A. E., 1976, ''A Model for Predicting Flow Regime Transitions in Horizontal and Near Horizontal Gas-Liquid Flow,'' AIChE J., **22**, pp. 47–55.
[11] Spedding, P. L., and Nguyen, V. T., 1980, ''Regime Maps for Air-Water Two Phase Flow,'' Chem. Eng. Sci., **35**, pp. 779–793.
[12] Barnea, D., Shoham, O., Taitel, Y., and Dukler, A. E., 1979, ''Flow Pattern Transition for Gas-Liquid Flow in Horizontal and Inclined Pipes: Comparison of Experimental Data With Theory,'' Int. J. Multiphase Flow, **5**, pp. 217–225.
[13] Glovier, G. W., and Aziz, K., 1972, *The Flow of Complex Mixtures in Pipes*, Van Nostrand Reinhold, New York.
[14] Pawloski, J. L., 2001, ''A Study of Air-Oil Two-Phase Flow in a Horizontal Straight Pipe,'' M.A.Sc. thesis, McMaster University, Hamilton, Ontario.
[15] Ferguson, M. E., and Spedding, P. L., 1995, ''Measurement and Prediction of Pressure Drop in Two-Phase Flow,'' J. Chem. Technol. Biotechnol., **62**, pp. 262–278.
[16] Olujic, Z., 1985, ''Predicting Two-Phase Flow Friction Loss in Horizontal Pipes,'' Chem. Eng. Sci., **92**, pp. 45–50.

F. G. Elliott
University of Virginia,
Charlottesville, VA
and Solar Turbines Incorporated,
9330 Skypart Court,
San Diego, CA 92123

R. Kurz

C. Etheridge

Solar Turbines Incorporated,
9330 Skypark Court,
San Diego, CA 92123

J. P. O'Connell
University of Virginia
Charlottesville, VA

Fuel System Suitability Considerations for Industrial Gas Turbines

Industrial Gas Turbines allow operation with a wide variety of gaseous and liquid fuels. To determine the suitability for operation with a gas fuel system, various physical parameters of the proposed fuel need to be determined: heating value, dew point, Joule-Thompson coefficient, Wobbe Index, and others. This paper describes an approach to provide a consistent treatment for determining the above physical properties. Special focus is given to the problem of determining the dew point of the potential fuel gas at various pressure levels. A dew point calculation using appropriate equations of state is described, and results are presented. In particular the treatment of heavier hydrocarbons, and water is addressed and recommendations about the necessary data input are made. Since any fuel gas system causes pressure drops in the fuel gas, the temperature reduction due to the Joule-Thompson effect has to be considered and quantified. Suggestions about how to approach fuel suitability questions during the project development and construction phase, as well as in operation are made. [DOI: 10.1115/1.1619424]

Introduction

The quality and composition of fuel burned in a gas turbine impacts the life of the turbine, particularly its combustion system and turbine section. The fuel specified for a given application is usually based on availability and price. Natural gas is a typical fuel of choice for gas turbines due to its low cost, widespread availability and low resulting emissions. However, the composition of fuel gas can widely vary, from gas with significant amounts of heavier hydrocarbons[1] (butane and heavier), to pipeline quality gas consisting mostly of methane, to fuel gas with significant amounts of dilutants (such as nitrogen, or carbon dioxide).

The unique situation at each site requires a thorough evaluation of the delivery system. Issues include the choice of fuel, fuel gas sources, transmission, handling, storage, conditioning, seasonal variations, mixing, turbine package location, fuel supply line configuration, fuel system component selection, combustion process, and turbine life. It is important to review them as a whole in determining appropriate equipment configurations and reasonable protection schemes.

Gas Fuels

Gaseous fuels can vary from poor quality wellhead gas to high quality consumer or ''pipeline'' gas. Typically, the major sources of contaminants within these fuels are:

- solids
- water
- heavy gases present as liquids
- oils typical of compressor oils
- hydrogen sulfide (H_{2S})
- hydrogen (H_2)
- carbon monoxide (CO)
- carbon dioxide (C_{O2})
- siloxanes

Other factors that will affect turbine or combustion system life and performance include lower heating value (LHV), specific gravity (SG), fuel temperature, and ambient temperature. Some of these issues may co-exist and be interrelated. For instance, water, heavy gases present as liquids, and leakage of machinery lubricating oils, may be a problem for turbine operators at the end of a distribution or branch line, or at a low point in a fuel supply line.

Water in the gas may combine with other small molecules to produce a hydrate—a solid with an ice-like appearance. Hydrate production is influenced, in turn, by gas composition, gas temperature, gas pressure, and pressure drops in the gas fuel system. Liquid water in the presence of H_2S or CO_2 will form acids that can attack fuel supply lines and components. Free water can also cause turbine flameouts or operating instability if ingested in the combustor or fuel control components.

Heavy hydrocarbon gases present as liquids provide many times the heating value per unit volume than they would as a gas. Since turbine fuel systems meter the fuel based on the fuel being a gas, this creates a safety problem, especially during the engine startup sequence when the supply line to the turbine still may be cold. Hydrocarbon liquids can cause:

- turbine overfueling, which can cause an explosion or severe turbine damage,
- fuel control stability problems, because the system gain will vary as liquid slugs or droplets move through the control system,
- combustor hot streaks and subsequent engine hot section damage,
- overfueling the bottom section of the combustor when liquids gravitate towards the bottom of the manifold, and
- internal injector blockage over time, when trapped liquids pyrolyze in the hot gas passages.

With a known gas composition, it is possible to predict dew point temperatures for water and hydrocarbons. However, the prediction methods for dew points may not always be accurate. In fact, it is known that different equations of state will yield different calculated dew points under otherwise identical conditions. Furthermore, the temperature in an unheated fuel line will drop, because the pressure drop due to valves and orifices in the fuel line causes a temperature drop in the gas (Fig. 1). This effect is known as the Joule-Thompson effect. Most fuel gases (except hydrogen) will exhibit a reduction in temperature during an adia-

Contributed by the International Gas Turbine Institute (IGTI) of THE AMERICAN SOCIETY OF MECHANICAL ENGINEERS for publication in the ASME JOURNAL OF ENGINEERING FOR GAS TURBINES AND POWER. Paper presented at the International Gas Turbine and Aeroengine Congress and Exhibition, Amsterdam, The Netherlands, June 3–6, 2002; Paper No. 2002-GT-30592. Manuscript received by IGTI, Dec. 2001, final revision, Mar. 2002. Associate Editor: E. Benvenuti.

[1]Hydrocarbons in fuel gas are usually alkanes, with the summary chemical formula C_nH_{2n+2}.

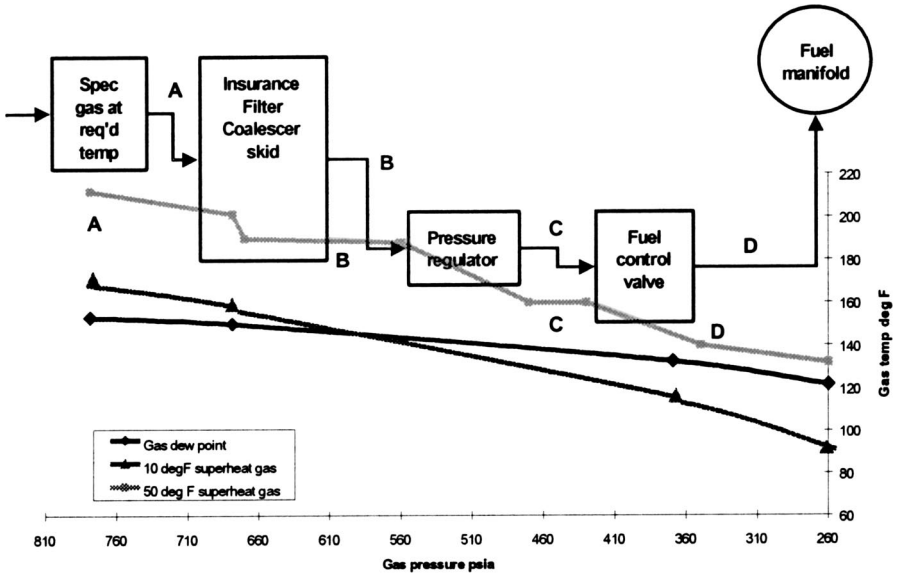

Fig. 1 Schematic of a gas fuel system, showing the pressure drop in various devices. If the gas is not superheated sufficiently, its temperature will eventually fall below the dew point temperature.

batic pressure drop. Hydrogen, on the other hand, actually shows an increased temperature when the pressure drops, which is a potential explosion hazard.

Protection against heavy gases and water present as liquids can be achieved by heating the fuel downstream of knockout drums and coalescing filters (Fig. 2). The idea is to have a saturated gas at the exit of the knockout drum and filters and then raise the temperature to the necessary superheat to prevent subsequent liquid dropout. The system shown in Fig. 2 is typical for fuel systems on oil or gas platforms, where the gas produced is usually wet. For dry gas of well known composition, such as from gas plants or for pipeline applications, a less complex system may be feasible.

Figure 1 illustrates the necessity for a superheat of about 50°F (28 K) over the dew point to ensure that no liquid dropout appears in the fuel system components downstream of the heater. A superheating requirement of 50°F (28 K) is currently acknowledged as a tacit industry standard, [1].

A gas analysis alone may not be entirely sufficient for the detection of heavy hydrocarbons, because it may only include the gases, but not the liquids in the stream. Also, it is common practice to lump all hydrocarbons from hexane and heavier into one number. While this is perfectly acceptable for the calculation of the lower heating value as long as the hexane and heavier hydrocarbons constitute a minute fraction of the gas, it will lead to a wrong estimate of the dew point. $C_{14}H_{30}$, even in parts-per-million amounts has a significant impact on the dew point of the gas mixture, as we will show later. Certainly a gas analysis has to be used in the project stage to allow for equipment sizing. Also, fuel systems usually limit the gas supply temperature due to temperature limits of its components. If the necessary superheat temperature exceeds the fuel system temperature limits, additional gas treatment may be necessary.

Lower heating value, specific gravity, fuel temperature, and ambient temperature are important parameters since they influence the energy of the fuel flowing in the system. From the lower

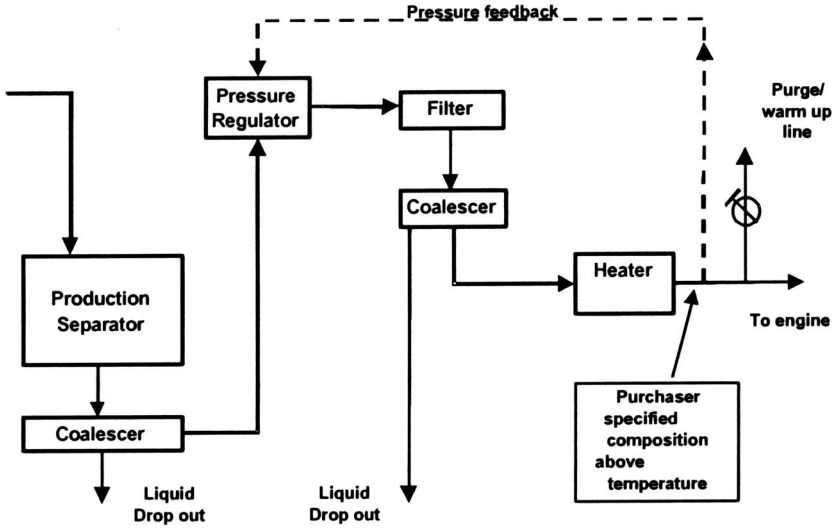

Fig. 2 Schematic of typical oil or gas platform fuel conditioning system

heating value (LHV) in Btu/scf [kJ/Nm^3] and the specific gravity (SG), the Wobbe Index (WI) of the gas can be calculated:

$$\mathrm{WI}=\frac{\mathrm{LHV}}{\sqrt{\mathrm{SG}}}. \tag{1}$$

Because the fuel supply temperature T_f has an impact on the actual volumetric fuel flow, a temperature corrected Wobbe Index is often used, where the reference temperature T_{ref} is usually 520°R or 288 K:

$$\mathrm{WI}=\frac{\mathrm{LHV}}{\sqrt{\mathrm{SG}}}\cdot\sqrt{\frac{T_{\mathrm{ref}}}{T_f}}. \tag{2}$$

If two different fuel gas compositions have the same Wobbe Index, the pressure drop in a given fuel system will be the same for both gases. The Wobbe Index is thus an indication of energy flow in the system at the same gas pressures and pressure drops.

A standard fuel system may for example be designed for a Wobbe Index of 1220±10% Btu/scf (48,031±10% kJ/Nm^3) based on the LHV of the fuel. Different gas compositions can yield the same Wobbe Index, but they may have widely different hydrocarbon dew points. Minimum engine flameout fuel flows will also vary if the fuel contains high percentages of noncombustible gases. High fuel gas or ambient temperatures can cause problems if the temperature capability of elastomeric seals, electrical devices or other system components are exceeded. Low fuel gas or ambient temperatures can cause water or heavy hydrocarbon condensation.

Protection against these factors includes analyzing the variations in the fuel composition, fuel temperature, and ambient temperature so that the required modifications to the fuel treatment system and turbine fuel system can be made. A turbine expected to operate with gaseous fuels exhibiting a wide Wobbe Index range will need to be configured differently than one that will only operate with a small variance in Wobbe Index. The fuel supply contract should include the allowable variations in composition and temperature. The probability of upset conditions needs to be evaluated and fuel treatment systems and turbine fuel systems need to be designed for the upset conditions. Gas fuel supply and package lines may need to be heat traced to keep the gas fuel supply above the gas dew point during periods when the engine is not operating. Low point drains are also recommended if liquids may be present in the gas fuel. This precludes burying the gas fuel supply lines underground when liquids may be present.

Equation of State

To develop a streamlined method to model the fuel system based on local pressures and temperatures in the system, various equations of state (EOS) were examined, and the preferred EOS methodology was developed for use in the model.

The dew point temperature of a gas is the temperature at a given pressure at which the first drop of liquid forms in equilibrium with the gas. The basis for performing a dew point calculation is the understanding that it is an equilibrium state. The fundamental thermodynamic relation for phase equilibria, such as the dew point, is that the fugacity of each component in the vapor phase is equal to the fugacity of the same component in the liquid phase. This arises because the fugacity is a measure of the ''escaping tendency'' for a component to leave its phase. Thus, when a component's fugacity is the same in two or more homogeneous phases in contact, there will be no net mass transfer, i.e., equilibrium. In equation form for C components in a vapor-liquid system, this is

$$f_i^V(T,P,\mathbf{y})=f_i^L(T,P,\mathbf{x}) \tag{3a}$$

where

$$f_i^V(T,P,\mathbf{y})=y_iP\phi_i(T,P,\mathbf{y}) \tag{3b}$$

and

$$f_i^L(T,P,\mathbf{x})=x_iP\phi_i(T,P,\mathbf{x}). \tag{3c}$$

The fugacity coefficient (ϕ_i) is calculated from the desired equation of state. The full equation is given in Appendix A, where the equation of state used in this project is discussed.

The other criterion to be met is that in the final solution, the liquid phase mole fractions must sum to one.

$$\sum_i^C x_i=1. \tag{4}$$

There are C unknowns (T and $C-1$ values of $\mathbf{x}$) and C equations. Therefore, the system can be solved, but an iterative method will be needed. The chosen method includes a nested loop. The inner loop uses successive substitution to converge $\mathbf{x}$ towards stability. Once this is done, Newton's method is used to move T a step towards the solution, after which new $\mathbf{x}$ are calculated. This is repeated until the second criterion has been satisfied.

Before the calculations can be started initial guesses must be made of T and $\mathbf{x}$. The user is only required to guess T, though, since $\mathbf{x}$ can be calculated from estimated K-values. The K-values are predicted from the equation:

$$K_i=\left(\frac{P_{ci}}{P}\right)\exp\left(\frac{\frac{1}{T}-\frac{1}{T_{Bi}}}{\frac{1}{T_{ci}}-\frac{1}{T_{Bi}}}\right) \tag{5}$$

where

$$K_i=\frac{y_i}{x_i}. \tag{6}$$

With the guessed temperature and the estimated liquid phase mole fractions, the fugacity of both phases can be calculated. New liquid phase mole fractions are calculated from the ratio of the fugacity coefficients.

$$x_i=y_i\frac{\phi_i^V}{\phi_i^L} \tag{7}$$

If this is the first time through, the temperature is changed by a small amount, δt, and the fugacities and new x_i are recalculated. If not, and the difference of the new Σx_i and the Σx_i of the previous run is greater than epsilon, the fugacities are recalculated and a new x_i got from that. If the difference of the two Σx_i is within epsilon, then the next check is to see if the second criterion is met. If so, the calculation is done. Otherwise, a new temperature must be calculated from the difference of the Σx_i divided by δt. The process is then repeated from Eq. (5).

A temperature and set of x_i that meet these criteria are assumed to be a solution to the dew point problem. However, this method can converge to a trivial solution. A trivial solution is when the vapor and liquid phase are calculated to have the same composition and compressibility factor.

$$\mathbf{y}=\mathbf{x} \tag{8}$$

and

$$Z^V=Z^L \tag{9}$$

If this occurs, the calculation has to be repeated with different initial guesses. For more on compressibility, please refer to Appendix A.

If water is present in the gas, then the problem becomes more complex. Though the systems of interest are mostly alkanes and, in some cases, nonpolar inorganic gases, an aqueous phase may be formed at a higher T than the organic phase. The aqueous phase fugacity expression is assumed to be

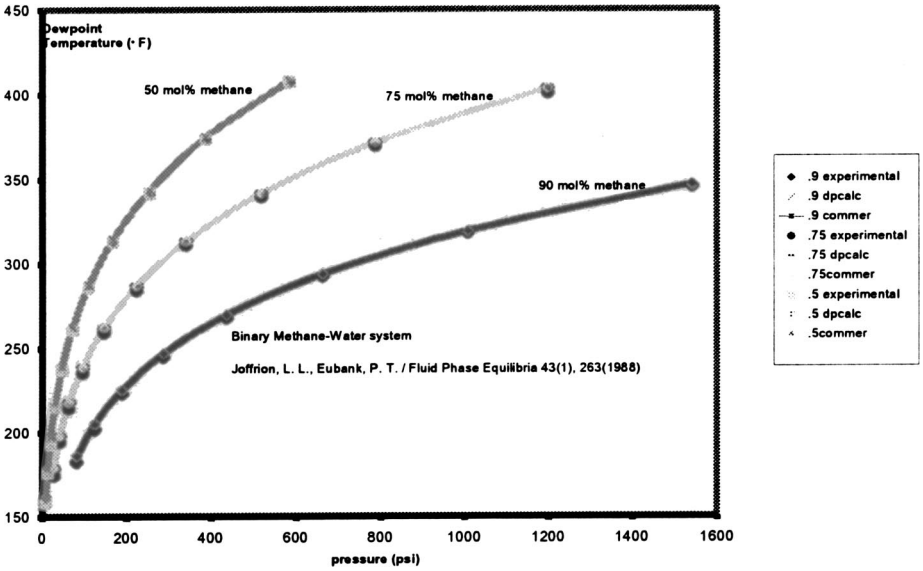

Fig. 3 Comparison of a experimental data, a commercial code, and the presented code (dpcalc) for the dewpoint calculation of a binary methane-water system. Experimental data from Joffrion and Eubank [3].

$$f_w^V(T,P,\mathbf{y}) = P_w^{\text{sat}}(T). \tag{10}$$

Since this is a one equation, one unknown system, it can be solved with an approximate method such as Newton-Raphson scheme. The dew point calculated is not necessarily the correct one, since it is possible for the organic phase to drop out first. The preferred method is to calculate both the dew point where the organic phase drops out first and the dew point where the aqueous phase drops out first, and then to choose whichever T is larger.

The Joule-Thomson effect is the temperature change that accompanies a pressure change under constant-enthalpy conditions. This effect is for example associated with a temperature drop across an isenthalpic throttling valve. The effect can be calculated by integrating the Joule-Thomson coefficient, which is

$$\left(\frac{\partial T}{\partial P}\right)_H = \frac{-\mathbf{V}\left(1 - T\left(\frac{\partial \mathbf{V}}{\partial T}\right)_P\right)}{C_p}. \tag{11}$$

Since the cubic equations of state are written in terms of P, this equation cannot be solved directly but instead is rearranged to

$$\left(\frac{\partial T}{\partial P}\right)_H = \frac{-\mathbf{V}\left(1 + T\left(\frac{\partial P}{\partial T}\right)_{\mathbf{v}}\left(\frac{\partial \mathbf{V}}{\partial P}\right)_T\right)}{C_p} \tag{12}$$

for a direct solution.

The partial derivatives are derived from the desired equation of state. The heat capacity is calculated from

$$C_p = C_p^{IG} + (C_p - C_v) + (C_v - C_v^{IG}) - R \tag{13}$$

where

$$C_p - C_v = \frac{-T\left(\frac{\partial P}{\partial T}\right)_{\mathbf{V}}^2}{\left(\frac{\partial P}{\partial \mathbf{V}}\right)_T} \tag{14}$$

and

$$C_v - C_V^{IG} = \int_\infty^V \left(\frac{\partial^2 P}{\partial T^2}\right)_{\mathbf{V}} d\mathbf{V} \tag{15}$$

and

$$C_p^{IG} = \sum_1^C y_i C_{pi}^{IG}(T). \tag{16}$$

There are many different formulas for $C_{pi}^{IG}(T)$; most chemistry reference books will have one. Most of the formulas are fourth or fifth-order polynomials with respect to temperature and with component-dependent coefficients. When all terms are substituted in, Eq. (12) becomes a rather complicated ordinary differential equation, which cannot be solved by analytical methods. Therefore, a fourth-order Runge-Kutta numerical method is used.

The procedure described above was validated against various cases found in the literature (Voulgaris [2] and Joffrion and Eubank [3]) as well as against commercially available codes (Hyprotech [4]). Calculated dew lines as a function of pressure and temperature for a mixture of methane and water vapor are shown in Fig. 3. The results show a good correlation between the commercial code, the present code and the experimental data.

Application of the Model

The procedures described in this paper are applied to avoid liquid dropout in gas turbine fuel systems. Many gas turbine installations operate with very simple fuel supply systems, especially if the fuel composition and supply temperature and pressure are constant. If the fuel analysis determines that there will not be any liquid dropout under any operating condition with sufficient superheat margin, the system as outlined in Fig. 4 should be sufficient. In applications where the fuel quality is subject to significant change, or where a sufficient margin of superheat cannot be ensured, a fuel system as outlined in Fig. 2 is more appropriate.

In such a fuel system with a separator and subsequent heater, the fuel will leave the separator in a saturated state (either saturated with water or heavy hydrocarbons). The temperature increase in the heater is thus equal to the amount of superheat of the gas. On a side note, for a given required amount of superheating, the required heat input of the heater P_H is approximately

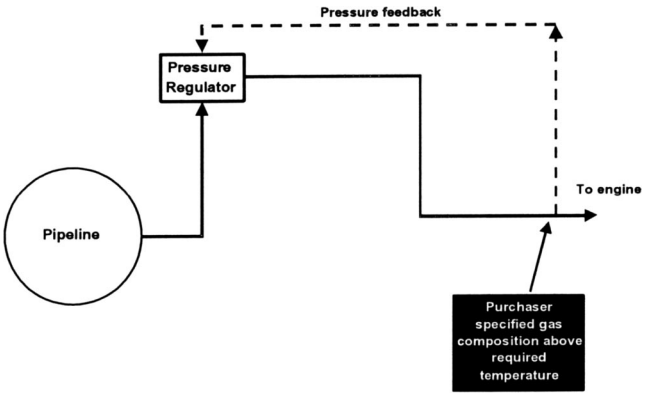

Fig. 4 Schematic of gas pipeline fuel delivery system with gas at greater than minimum superheat

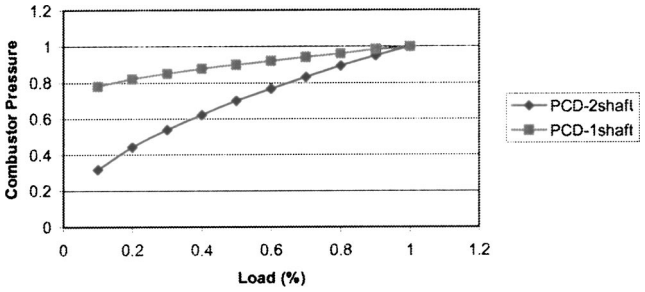

Fig. 5 Engine compressor discharge pressure (PCD) as a function of engine load

$$P_H = W \cdot c_p \cdot \Delta T. \tag{17}$$

To determine whether the system will be capable of avoiding liquid drop out, the enthalpy of the fuel gas has to be calculated at the skid edge. Knowing the gas composition, the gas pressure, and the gas temperature at skid edge allows to calculate the enthalpy of the gas. The pressure in the combustor depends on the engine load (Fig. 5). The exact slope of combustor pressure versus load depends on the design of the engine; in particular whether it is a single or two-shaft engine, and the type of engine controls used. We further assume that the velocities in the fuel system stay low (i.e., there is no significant difference between the static and the total enthalpy). The necessary condition to avoid liquid drop out in an adiabatic fuel system is, that for all pressure levels that may occur in this fuel system, the enthalpy of the vapor at the dew point is lower than the enthalpy of the gas at the skid edge (Fig. 6)[2]. It is noteworthy that the dew point in Fig. 6 is mostly driven by the water contained in the gas.

This approach does obviously not account for the effect of high velocities in the fuel system, as they can occur in partially closed valves. These high velocities can lead to a significant drop in the enthalpy (by $w^2/2$), and can easily cause a situation where liquids drop out. However, this situation is not as critical as it looks at the first glance. First, the velocities will drop again after the valve. The static enthalpy will therefore increase, so even if droplets may have formed, they will evaporate again. Secondly, it is known (Gyarmathy [5]) that in situations with rapidly accelerated gas there is a time lag between the condition where the state of the gas would indicate liquid droplets and the actual formation of droplets. This effect is frequently experienced in steam turbines,

[2]The Joule-Thompson effect manifests itself in the fact, that for the condition of a pressure drop at constant enthalpy, the temperature of the gas will change. For an ideal gas in the same situation, temperature and enthalpy would remain constant.

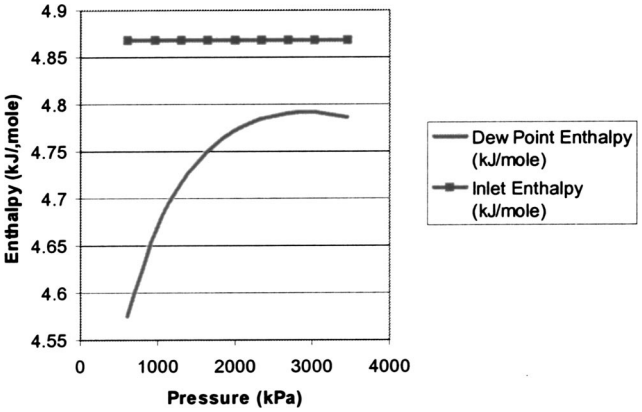

Fig. 6 Enthalpy of the dewpoint must always be below the entahlpy of the fuel gas at inlet conditions. Gas composition is: methane 75.4%, ethane 13.8%, propane 5.25%, I-butane .86%, n-butane 1.12%, I-pentane 0.63%, n-hexane 0.21%, n-heptane 0.08%, n-octane .03%, n-nonane 0.01%, nitrogen 0.5%, carbon dioxide 1.86%, water 0.23%.

where, during the rapid acceleration of the steam in the nozzles, steam can be substantially supercooled without forming liquids.

Under quasi-stationary conditions, we can easily describe the change of states from skid edge to the exit of the fuel injector into the combustor. The conditions at skid edge are known, and the pressure at the injector exit can be either approximated by the engine compressor exit pressure or the actual combustor pressure. The path in a Mollier diagram is shown in Fig. 6. The dewline, which is typical for hydrocarbon fuel gas, shows a distinct maximum $\delta H/\delta_p = 0$ at a pressure of 2930 kPa. The shape of the dew line thus suggests, that the highest chance of liquid dropout occurs not necessarily at the lowest pressure in the system. The example in Appendix B outlines a situation, where the liquid dropout would become likely at part load operation of the engine.

In evaluating these fuel systems, one must take into account that the highest pressure drops in the fuel system may not occur at full load, but rather during the starting of the engine, when the combustor pressure is lowest (Fig. 5). In other words, the system has to be evaluated for the highest pressure that the gas can have at skid edge, and the combustor pressure at light-off conditions, as well as for any load condition between idle and full load.

Additionally, unless the fuel lines are heat traced, they may be colder than the fuel especially during start up. Therefore, a significant safety margin between the dew point temperature, and the lowest possible fuel temperature is necessary.

Necessary Information

To conduct a successful determination of the fuel system capability, the fuel gas composition, possible contaminants, the fuel supply pressure and temperature need to be known. As part of this study, it became obvious that the dewpoint of a hydrocarbon gas mixture is highly dependent on the heavier hydrocarbons. The common practice to report hydrocarbons individually only up to pentane, and lump all heavier hydrocarbons into one C6+ number may yield sufficient information about the lower heating value and the Wobbe Index of the fuel. It will not yield an accurate dew point, however. In Fig. 7, a typical situation is evaluated: A fuel gas composition has 0.71% of its constituents lumped together as C6+. Then, dewpoints are calculated assuming these constituents are either all hexane, all octane or all undecane. As Fig. 7 shows, even small amounts of heavier hydrocarbons have a significant effect on the dewpoint of the gas mixture. Campbell [6] suggests therefore to determine the individual constituents of the gas composition up to C_{14}.

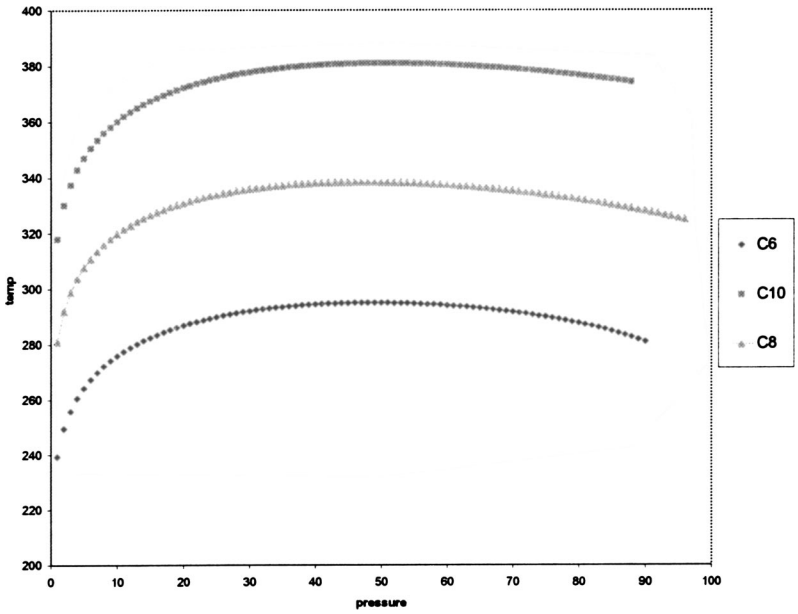

Fig. 7 Dewline for different gas mixtures in a pressure (bar)-temperature (K) diagram. Gas composition is: methane 73.8%, ethane 8.2%, propane 3.23%, I-butane .28%, n-butane 0.78%, I-pentane 0.24%, n-pentane 0.18%, n-hexane 0.18%, Cxx 0.71%, nitrogen 0.93%, carbon dioxide 11.68%. Cxx represents either hexane (C6), octane (C8), or decane (C10). Despite the fact that Cxx represents only 0.71% of the gas, it has a significant impact on the dew point.

Arguably, the practice to remove all liquids in a separator, and then to heat the gas portion by, say 50°F (28 K), will insure that the gas supplied to the gas turbine will indeed be superheated by 50°F (28 K). However, a proper sizing of the heater is not possible without knowing (at least approximately), the required end temperature. Also, fuel system components usually have maximum allowable temperatures. Without prior knowledge of the necessary gas temperature, the fuel system temperature limits may not allow the necessary superheat.

It must be noted that all the prior statements assume an adiabatic fuel system. Heat loss in the fuel system will occur, however, if the system is not insulated and the surrounding temperature is significantly lower than the fuel supply temperature. In particular during startup at low ambient temperatures, when the fuel system is still cold liquids can form. A system without heat tracing needs to be evaluated assuming the lowest surrounding temperature. However, standard heat transfer methods allow to approximate the heat loss of a fuel system under arbitrary surrounding conditions, and using the first law of thermodynamics, to calculate the fuel gas enthalpy at any point of the fuel system. As described above, this enthalpy has to be higher than the enthalpy of the vapor at the dew point.

Conclusion

An approach to determine the compatibility of a fuel system and the desired fuel gas has been presented. The key points regarding fuel gas system suitability are

- the influence of the Wobbe Index,
- the proper treatment of the Joule-Thompson cooling,
- the use of equations of state to calculate the enthalpy-pressure-temperature relationships and the dew point, and
- the importance of accounting for heavy hydrocarbons in a fuel analysis.

Applying the thoughts outlined in this paper will help to avoid problems with fuel systems on gas turbine packages.

A procedure is developed to model the fuel system in detail to determine fuel superheat and clean-up requirements, in order to enhance the reliability of operation.

Nomenclature

$a(T,x)$ = cubic EoS attraction term
$b(x)$ = cubic EoS covolume term
C = total number of components
c_p = heat capacity at constant pressure
C_p^{IG} = constant pressure ideal gas heat capacity
C_{pi}^{IG} = constant pressure ideal gas heat capacity of component I
c_v = heat capacity at constant volume
C_V^{IG} = constant volume ideal gas heat capacity
f_i^L = fugacity of component i in liquid phase
f_i^V = fugacity of component i in vapor phase
f_w^V = vapor phase fugacity of water
H = enthalpy
k_{ij} = Peng Robinson binary interaction parameter
K_i = ratio of vapor-phase mol fraction to liquid-phase mol fraction
LHV = lower heating value
N_i = number of moles of species i
N = total number of moles
p = pressure
P_{ci} = critical pressure of component i
P_w^{sat} = saturated vapor pressure of water
P_i^{sat} = saturated vapor pressure of component i
P_H = heating power
R = universal gas constant
SG = specific gravity
T = temperature
T_{Bi} = boiling temperature of component i
T_{ci} = critical temperature of component I
V = molar volume
w = flow velocity
W = mass flow
WI = Wobbe Index
x_i = mole fraction of component i in liquid phase
$\mathbf{X}$ = all liquid mol fractions

y_i = mole fraction of component i in vapor phase
$\mathbf{Y}$ = all vapor mol fractions
Z^V = vapor phase compressibility factor
Z^L = liquid phase compressibility factor
ω = accentric factor
ϕ_i^L = fugacity coefficient of component i in liquid phase
ϕ_i^V = fugacity coefficient of component i in vapor phase

Appendix A

Equation of State Used in This Study. The generalized form for a cubic equation of state is

$$P=\frac{RT}{\mathbf{V}-b}-\frac{(\mathbf{V}-\eta)\theta}{(\mathbf{V}-b)(\mathbf{V}^2+\delta\mathbf{V}+\varepsilon)}. \tag{18a}$$

The main equation of state used in this project was the Peng-Robinson [7] equation of state where

$$\theta=a(T,\mathbf{x}); \quad \eta=b(\mathbf{x}); \quad \delta=2b(\mathbf{x}); \quad \delta=0. \tag{18b}$$

The full equation is

$$P(T,\mathbf{V},\mathbf{x})=\frac{RT}{\mathbf{V}+b(\mathbf{x})}+\frac{a(T,\mathbf{x})}{\mathbf{V}^2+2\mathbf{V}\mathbf{b}(\mathbf{x})-(b(\mathbf{x}))^2}. \tag{19}$$

$a(T,x)$ and $b(x)$ are calculated using a mixing rule. The one used for this paper is the Van Der Waals one-fluid mixing rule, where

$$a(T,\mathbf{x})=\sum_{i=1}^{C}\sum_{j=1}^{C}x_i x_j a_{ij}(T) \tag{20}$$

$$a_{ij}(T)=\sqrt{a_i(T)a_j(T)}(1-k_{ij}) \tag{21}$$

$$a_i(T)=0.45724\frac{R^2T_{ci}^2}{P_{ci}}\alpha_i(T) \tag{22}$$

$$\alpha_i(T)=\left(1+\kappa_i\left(1-\sqrt{\frac{T}{T_{ci}}}\right)\right)^2 \tag{23}$$

$$\kappa_i=0.37464+1.54226\omega_i-0.26992\omega_i^2 \tag{24}$$

and

$$b(\mathbf{x})=\sum_{1}^{C}b_i \tag{25}$$

$$b_i=0.07780\frac{RT_{ci}}{P_{ci}}. \tag{26}$$

k_{ij} is the binary interaction parameter between species i and j for the Peng-Robinson [7] equation of state only. These can be derived by performing a fitting to experimental data or can simply be looked up.

The Peng-Robinson [7] equation falls in the category of cubic equations of state since it is cubic with respect to volume and compressibility. Using the equation for compressibility factor,

$$Z=\frac{P\mathbf{V}}{RT}, \tag{27}$$

the volume term can be substituted for and the equation itself rearranged to give

$$Z^3+(B-1)Z^2+(A-3B^2-2B)Z+(B^2+B^3-AB)=0 \tag{28}$$

where

$$A=\frac{a(T,\mathbf{x})P}{R^2T^2} \quad \text{and} \quad B=\frac{b(\mathbf{x})P}{RT}. \tag{29}$$

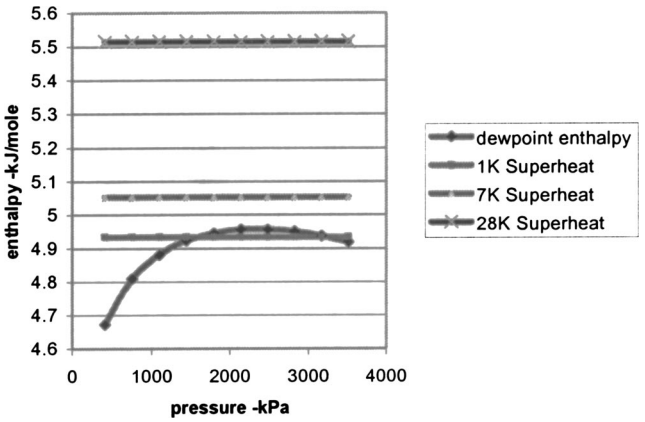

Fig. 8 Dewpoint enthalpy for gas fuel and process path for adiabatic expansion starting with different degrees of superheat. Fuel gas composition is: methane 83%, ethane 8%, propane 3%, I-butane 0.3%, n-butane 0.8%, I-pentane 0.3%, n-pentane 0.3% n-hexane 0.4%, n-heptane 0.2%, n-octane 0.08%, n-nonane 0.02%, n-decane 0.01%, nitrogen 1.9%, carbon dioxide 1.69%.

Cubic equations can be solved analytically using Cardano's method. A given cubic will have either one or three real roots. If there are three roots, the largest represents the ZV, the smallest represents the ZL, and the middle root is of no consequence. If there is only one root, it may be either liquid or vapor phase.

The fugacity coefficient of a component in a mixture in the vapor phase is found using the equation

$$\ln\phi_i^V(T,P,y)=\frac{1}{RT}\int_{V=\infty}^{V=Z^VRT/P}\left[\frac{RT}{\mathbf{V}}-N\left(\frac{\partial P}{\partial N_i}\right)_{T,V,N_{j\neq i}}\right]d\mathbf{V} - \ln Z^V. \tag{30}$$

A similar equation is found for the liquid phase fugacity coefficient.

$$\ln\phi_i^L(T,P,\mathbf{x})=\frac{1}{RT}\int_{\mathbf{V}=\infty}^{\mathbf{V}=Z^LRT/P}\left[\frac{RT}{\mathbf{V}}-N\left(\frac{\partial P}{\partial N_i}\right)_{T,V,N_{j\neq i}}\right]d\mathbf{V} - \ln Z^L. \tag{31}$$

When these are evaluated, the equation for the vapor phase fugacity coefficient of a component in a mixture is

$$\ln\phi_i^V(T,P,\mathbf{y})=\frac{b_i}{b}(Z^V-1)-\ln\left(Z^V-\frac{bP}{RT}\right)-\frac{a}{2\sqrt{2}bRT} \times\left(\frac{2\Sigma_j y_j a_{ij}}{a}-\frac{b_i}{b}\right)\ln\left(\frac{Z^V+(1+\sqrt{2})\frac{bP}{RT}}{Z^V+(1-\sqrt{2})\frac{bP}{RT}}\right) \tag{32}$$

The liquid-phase coefficient is

$$\ln\phi_i^L(T,P,\mathbf{x})=\frac{b_i}{b}(Z^L-1)-\ln\left(Z^L-\frac{bP}{RT}\right)-\frac{a}{2\sqrt{2}bRT} \times\left(\frac{2\Sigma_j x_j a_{ij}}{a}-\frac{b_i}{b}\right)\ln\left(\frac{Z^L+(1+\sqrt{2})\frac{bP}{RT}}{Z^L+(1-\sqrt{2})\frac{bP}{RT}}\right) \tag{33}$$

Appendix B

Sample Calculation for Dew Point in a Fuel System. The following example shows the considerations for a given, typical gas fuel composition.

The fuel supply pressure is 510 psia (kPaa). In Fig. 8, the dew point as a function of pressure is calculated. The combustor pressure may vary between 300 psia (2070 kPaa) at full load and 100 psia (690 kPaa) at idle. Based on three different levels of superheat (1K, 7K, 28K), the expansion of the gas in the fuel system is traced. It can be seen that little or no superheat will cause liquid dropout at the pressures, where the process path fall below the dew line. At 7K superheat, no liquid dropout is expected. However, the ''safety margin'' is fairly small. Considering reality of changing fuel compositions, the usual uncertainty in calculating the dewpoint, the 28 K superheated gas will provide adequate safety.

References

[1] ASME B133.7, 1992, ''Gas Turbine Fuels,'' ASME, New York.
[2] Voulgaris, M., 1995, ''Prediction and Verification of Hydrocarbon Liquid Drop Out of Lean Natural Gas,'' dissertation, TU Delft.
[3] Joffrion, L. L., and Eubank, P. T., 1988, Fluid Phase Equilib., **43**(1), p. 263.
[4] Hyprotech, 1998, *HYSYS Process Manual*, Calgary, Canada.
[5] Gyarmarthy, G., 1962, ''Grundlagen Einer Theorie der Nassdampfturbine,'' dissertation, ETH Zuerich.
[6] Campbell, J. M., 1998, ''Gas Conditioning and Processing.''
[7] Peng, D. Y., and Robinson, D. B., 1976, ''A New Two-Constant Equation of State,'' Ind. Eng. Chem. Fundam., **15**, pp. 59–64.
[8] Kurz, R., Brun, K., and Legrand, D. D., 1999, ''Field Performance Testing of Gas Turbine Driven Compressor Sets,'' *Proc. 28th Texas A&M Turbomachinery Symposium*.
[9] Poling, B. E., Prausnitz, J. M., and O'Connell, J. P., 2001, *The Properties of Gases and Liquids*, 5th Ed. McGraw-Hill, New York.
[10] Sandler, S. I., ed., 1993, *Models for Thermodynamic and Phase Equilibria Calculations*, Marcel Dekker, New York.
[11] Soave, G., 1972, Chem. Eng. Sci., pp. 27–1197.
[12] Starling, K. E., 1973, *Fluid Thermodynamic Properties for Light Petroleum Systems*, Gulf, Houston, TX.

Stress Redistribution for Increased Creep Life in the GE MS6001 B Second-Stage Blade

P. E. DiCristoforo
Principal Engineer,
TurboCare,
2140 Westover Road,
Chicopee, MA 01022

M. Elledge
Rotating Equipment/Reliability Supervisor,
BP Amoco Chemicals,
510 Old Bayou Drive,
Dickinson, TX 77539

When a hot end blade for a gas turbine is designed, several failure criteria must be considered to insure reliability. The criteria include (but are not limited to) creep rupture, low-cycle fatigue, high-cycle fatigue, and creep deflection. This paper will focus on the second-stage turbine blade for the GE MS6001 industrial gas turbine. BP Amoco has experienced failure of this blade due to excessive creep deflection. Creep deflection rate is a function of stress level and metal temperature. A typical approach to reducing creep deflection is to reduce the bulk temperature in the blade. In this paper a design is reviewed that has had the stress redistributed, so that the high-temperature regions of the airfoil are at a lower stress level, thereby reducing the creep rate to an acceptable level.
[DOI: 10.1115/1.1498271]

Introduction

The GE MS6001B has had several second-stage turbine blade designs. The first design was made of equiaxed Inco 738LC alloy and was cooled with four smooth STEM (shaped tube electrochemical machining) drilled radial cooling holes. The next iteration was the same as the original, except that the Z-lock interface on the shroud was modified to prevent binding and additional material was added to the fillet radius at the shroud to airfoil interface (this iteration is called the original design in this paper). A more recent design being supplied by the OEM (original equipment manufacturer) is similar to the previous design, except it now has seven radial cooling holes, two smooth and five turbulated between 40% and 70% of the radial span. The trailing edge region has been thickened and it is assumed that this was done to reduce the stress in this region and to allow adequate stock for the two trailing edge cooling holes that were added.

BP Amoco's Texas City, TX refinery has had both of the four-hole designs installed in their Frame 6 gas turbine, operating on base load at a firing temperature of up to 1104°C. The first design performed adequately, with an operating life exceeding 50,000 fired hours without any failures. With the next iteration, the unit experienced a failure in the second stage in 1995 at 49,000 hours. The authors are not aware of any failures with the current OEM design.

The failure of the original design can be attributed to tip creep deflection, which caused the Z-shrouds to ''shingle'' at the interface until the deflection was so great that the contact was lost. The ''shingling'' is due to a higher creep rate in the leading and trailing edges of the airfoil near the radial pitchline which causes the airfoil to lean toward the suction side. Because of the thin, twisted shape of this airfoil, it is impossible to put cooling holes closer to these regions and so they are essentially uncooled. The design relies on the cooler middle section of the airfoil (near the cooling holes) to carry the centrifugal load. Creep is a function of temperature and stress. The temperature cannot be reduced in the high creep regions so the life of this part will be increased by redistributing the stresses so that the stress is reduced in the high-temperature leading and trailing edge and increased in the region of the airfoil that is cooled. This results in a significant increase in the life without a significant increase in cooling flow.

Stress Redistribution

The strategy for reducing the creep deflection in this stage was to reduce stresses in regions of high temperature. This was accomplished by restacking of the airfoil. The direction of the centrifugal forces in the blade due to the rotation of the rotor will be radially outward from the centerline of the shaft. In restacking, the center of gravity of each section of the airfoil is shifted so that a favorable bending moment is imposed at the radial location of the highest temperature. The redesigned blade used the same airfoil sections used in the current OEM blade.

It was determined from the analysis of the original blade, that the region of highest temperature was at the leading and trailing edge of the airfoil at the pitchline. The blade stresses were minimized in this region by an iterative process, using a parametric three-dimensional finite element model. Since STEM drilled holes must be straight, excessive twist or bow could not be tolerated. It was found that the best solution was the combination of bowing the airfoil tangentially toward the pressure (concave) side and leaning the entire airfoil tangentially toward the suction (convex) side. The stresses in the original four-hole design, the current OEM seven-hole turbulated design and the restacked redesign were evaluated and are compared in Figs. 1–3. The current OEM design has a more uniform stress than either the original or the restacked design. This design relies on the cooler mid span section to hold back the hotter leading edge and trailing edge. From the

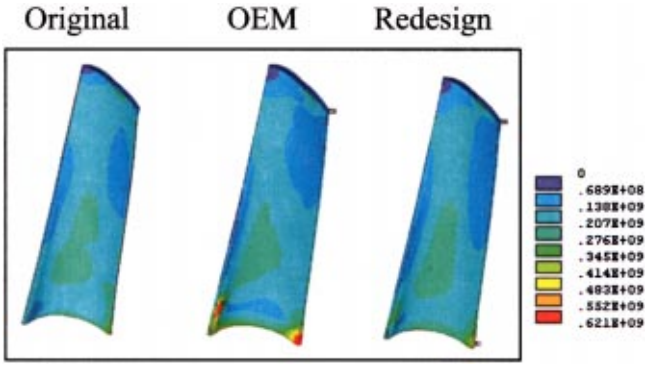

Fig. 1 Pressure side stress comparison (Mpa)

Contributed by the International Gas Turbine Institute (IGTI) of THE AMERICAN SOCIETY OF MECHANICAL ENGINEERS for publication in the ASME JOURNAL OF ENGINEERING FOR GAS TURBINES AND POWER. Paper presented at the International Gas Turbine and Aeroengine Congress and Exhibition, New Orleans, LA, June 4–7, 2001; Paper 01-GT-279. Manuscript received by IGTI, December 2000, final revision, March 2001. Associate Editor: R. Natole.

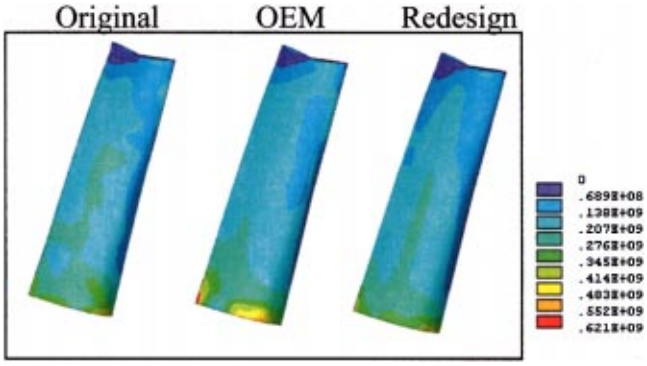

Fig. 2 Suction side stress comparison (MPa)

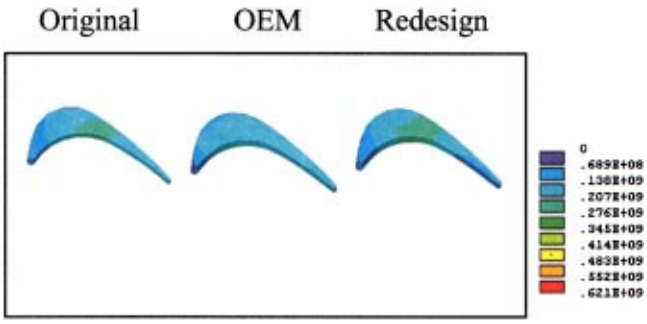

Fig. 3 Pitchline stress comparison (MPa)

restacking, the stresses in the hotter leading and trailing edges are reduced, resulting in a lower creep rate, while the stresses in the cooler mid span are higher, resulting in a higher creep rate. This results in a more uniform creep rate across the airfoil which reduces the ''shingling.''

Heat Transfer Evaluation

In order to perform the heat transfer analysis of this stage, it was necessary to evaluate the aerodynamic flow around the airfoil. Detailed airfoil geometry data was acquired through reverse engineering techniques; spares of the rotating parts were measured on a stationary coordinate measuring machine (CMM) while the stationary parts were measured at the customer's turbine installation, with a portable CMM, during a planned maintenance outage.

Operating parameters, such as mass flow, compressor discharge temperature and pressures, and wheelspace temperatures were tabulated from the user's operating database. Cooling flow and exit temperature for the first-stage turbine blade was taken from a previous analysis by Jaqueway et al. [1]. The cooling flow and temperatures for the other stages was estimated. A two-dimensional through-flow analysis was performed and stage temperatures, pressures and flows were derived. The results of this analysis were used for a rotor blade aerodynamic loading analysis of the second stage blade to determine the Mach number distribution around the airfoil at five radial locations.

A program was written that calculates the external boundary conditions around the airfoil. It uses the convection correlation for a cylinder in crossflow at the leading edge and a turbulent flat-plate correlation for the remainder of the airfoil using methods presented by White [2]. The film coefficients were calculated at various bulk temperatures for input into a finite element analysis as a variable.

Three designs were evaluated, the original (four smooth holes), the current OEM (five turbulated, two smooth holes) and the restacked redesign (six smooth holes). Three-dimensional finite element models of the blades were created, using thermal-fluid pipe elements to model the heat transfer of the radial STEM drilled cooling holes. For the current OEM blade evaluation, adjustments were made to the heat transfer calculations in the thermal-fluid pipe element, using the methods of Webb et al. [3] to account for the turbulation used in this design.

The internal and external convection rates will vary based on the temperature of the surface of the airfoil and cooling hole as well as the heat pickup and flow rate of the cooling air as it flows through the cooling hole. For this reason, an iterative process is required until the calculated temperatures are approximately equal to the values that were used in the convection calculations. By evaluating the external boundary conditions as a function of surface temperature and providing a flow network that includes the convection calculation in the finite element model the iterations are handled by the FEA program. This greatly reduced the effort required for each case.

The steady-state temperatures for the three designs are shown in Figs. 4–6. It is clear from the figures that the original four-hole

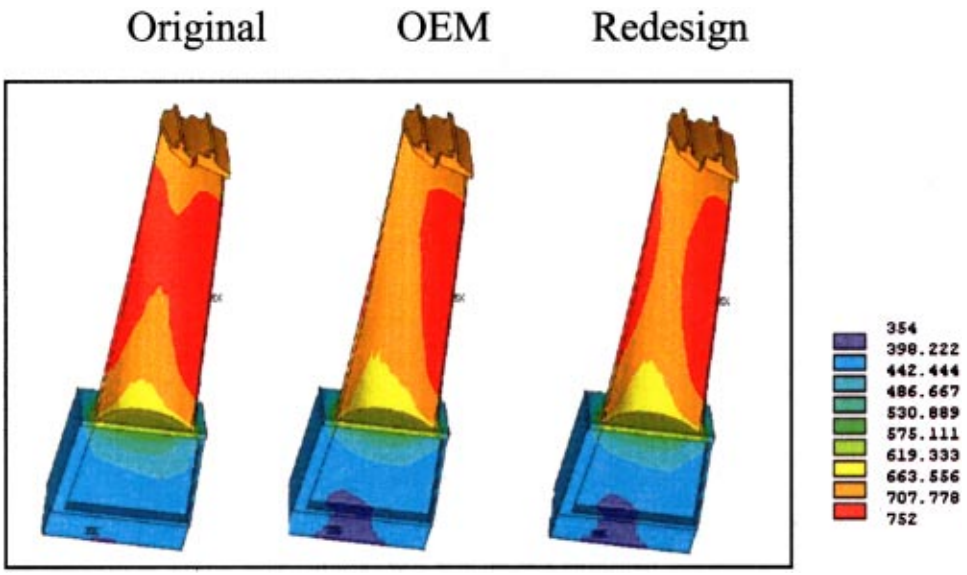

Fig. 4 Pressure side temperature comparison (°C)

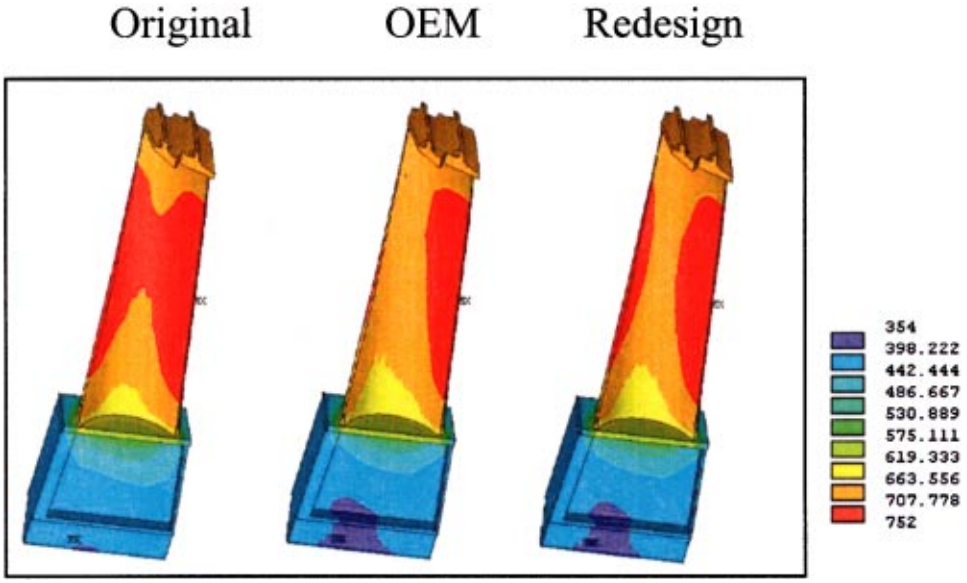

Fig. 5 Suction side temperature comparison (°C)

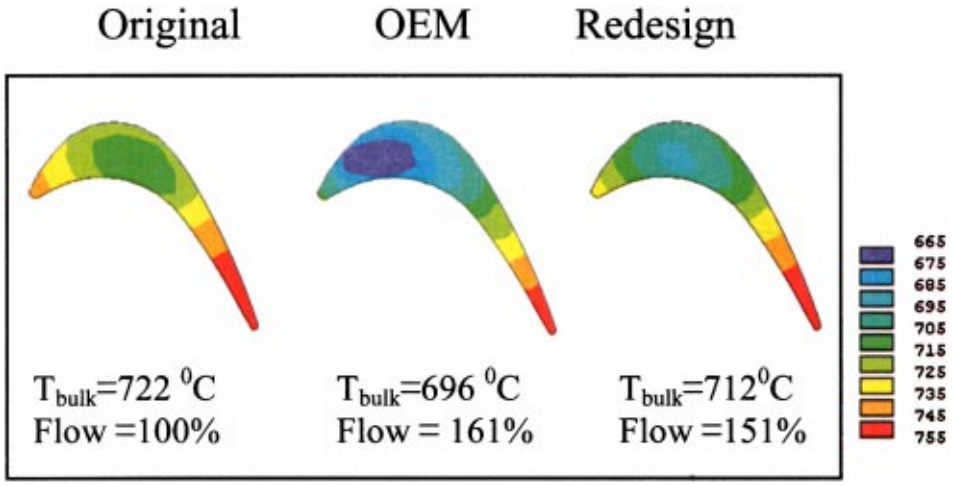

Fig. 6 Pitchline temperature comparison (°C)

design runs much hotter than either the current OEM design or the restacked redesign. It should be noted that although the current OEM design runs 16°C cooler than the restacked redesign, the trailing edge temperature is still quite high (it is a max of about 752°C for all three designs). The flow rate for each design was extracted as output from the flow network in the finite element analysis model. If the original four-hole design is used as a baseline, the current OEM design used 61% more cooling air while the restacked redesign uses 51% more. Since the restacked design requires less airflow than the current OEM design and it is assumed that the OEM design has adequate backflow margin, there was no attempt evaluate this for any of the three designs.

Creep Evaluation

Creep Rupture. The creep rupture life for each design was determined from a Larson-Miller parameter curve presented by Jaqueway et al. [1]. The life at the pitchline, which is assumed to be the worst case, is much greater than 100,000 hours for all cases (Table 1). It is clear that this is not the limiting criterion in the life of this blade.

Creep Deflection. The creep deflection was evaluated using the same three-dimensional models that were used in the stress evaluation. A user-defined subroutine was written that included constitutive equations for creep strain that would be calculated

Table 1 Creep rupture comparisons

	Original	Current OEM	Restacked
Bulk Temperature (°C)	722	696	712
Net Section Stress (MPa)	169.5	170.5	170.4
Life (hrs.)	≫100 K Hrs.	≫100 K Hrs.	≫100 K Hrs.

Table 2 Creep deflection summary at 48,000 hours

	Original	Current OEM	Restacked
Shroud lifting (mm)	2.54	1.12	0.813
Improvement		56%	68%
Maximum radial deflection (mm)	2.54	.820	0.973

Fig. 7 Shroud mismatch after 48,000 hours

over time by the finite element program. The equations were derived from relationships developed by Granacher and Preussler [4] for IN738LC superalloy. Although there is some permanent strain due to primary creep, the majority of the permanent strain is due to secondary creep. In this evaluation only secondary creep is considered.

A creep deflection analysis was performed on the three designs considered. The blades were run at speed and temperature for a period of 48,000 hours and then a final load step at zero speed and room temperature was run to determine the permanent creep deflection (Table 2). To evaluate the shroud lifting, the permanent deflection at each end of the Z-shroud was determined and the difference between these deflections was calculated. The maximum radial deflection is also tabulated, since this would indicate the amount that the radial clearances would be decreased. It should be noted that the calculated shroud lifting value of 2.64 mm is within the scatter of reported actual shroud mismatch of blades that have been in service for 48,000 hours.

The shroud lifting causes a mismatch in the contact area of the Z-shroud (Fig. 7) that will eventually result in a loss of contact. This will result in a change in the frequencies and response of the blades and would potentially result in catastrophic failure of the stage.

The standard time between hot gas path inspections is 24,000 hours. If, during an outage, it was determined that there would not be adequate engagement by the time of the next outage, the blades would need to be taken out of service. With the original design the shrouds had a mismatch of approximately 2.5 mm when inspected after 48,000 hours of service. Since the contact surface is approximately 3.8 mm, if the same rate of creep is assumed, there would be almost no contact by the time the unit had run for 72,000 hours. Because of the risk of disengagement and the potential for failure, the original design blades needed to be retired after 48,000 hours. If the same evaluation is done for the current OEM design and the restacked redesign, both would last at least 72,000 hours without risk of Z-shroud disengagement.

Operational Data

The first set of the new restacked redesign second stage blades was installed in a unit at the BP Amoco refinery on April 12, 2000. These blades went into service on April 19, 2000 and have been running at base load ever since. The next planned inspection of these blades is during a major overhaul, sometime in 2003. It is expected that these blades will have over 24,000 operating hours at that time.

Conclusion

Based upon the relative differences, the restacked redesign has been analytically proven to meet the design life expectations of the gas turbine user community. The Z-shroud mismatch has been reduced by 68% while using approximately 7% less cooling air than the current OEM design. It is felt that this blade is a viable alternative to the OEM offering.

Acknowledgments

The authors would like to thank Michael Mindock of Demag DeLaval Turbomachinery for his help in performing the performance and aerodynamic evaluation work, which was required to evaluate this blade. We would also like to thank John Bryan of BP-Amoco for providing access to Frame 6 stationary components during a planned maintenance outage.

References

[1] Jaqueway, J. K., and Pistor, R. J., 1997, "Redesign of the MS6001 First Stage Bucket for Improved Cooling and Extended Life," presented at IGTI Turbo Expo in Orlando, FL, June.
[2] White, F. M., 1984, *Heat Transfer*, Addison-Wesley, Reading, MA.
[3] Webb, R. L., Eckert, E. R. G., and Goldstein, R. J., 1971, "Heat Transfer and Friction in Tubes with Repeated-Rib Roughness" Int. J. Heat Mass Transf., **14**, pp. 601–617.
[4] Granacher, J., and Preussler, T., 1987, "Creep of Some Gas Turbine Materials," *Advances in Materials Technology for Fossil Powered Plants*, pp. 511–518.

Local/Global Effects of Mistuning on the Forced Response of Bladed Disks

A. J. Rivas-Guerra

M. P. Mignolet
Fellow ASME
e-mail: marc. mignolet@asu.edu

Department of Mechanical and Aerospace Engineering,
Arizona State University,
Tempe, AZ 85287-6106

The focus of the present investigation is on the assessment and modeling of the local (spanning only a few blades) and global (encompassing the entire disk) effects of mistuning on the forced response of bladed disks. To this end, the concept of localization is first revisited and a new measure of this effect is introduced in terms of the number of blades the mistuning of which actually affects the forced response of a central blade. Using this new metric, it is demonstrated that high responding blades typically exhibit a high level of localization and that the reverse is not necessarily true. Thus, localization is not only disk dependent but also varies from blade-to-blade on the same disk. This observation is then used to validate a partial mistuning approach to the determination of the maximum amplitude of response over the entire population of disks. The results of this study indicate that the largest amplification due to the mistuning occurs at very strong blade-to-blade coupling levels, at the contrary of a general perception, but is associated with large mistuning levels. Finally, the above phenomenological observations are used to devise a modeling technique of both local and global components of mistuning. An example of application is presented that demonstrates the high accuracy of this approach through the entire blade-to-blade coupling domain. [DOI: 10.1115/1.1581898]

Introduction

The prediction of the effects of mistuning on the response of bladed disks is a particularly challenging problem as clearly indicated by the vast body of literature on this topic (see, for example, Ref. [1–13]). The difficulties in accomplishing this task stem from two main factors: (i) the random nature of blade-to-blade variations in their structural properties, and (ii) the fact that mistuning corresponds to fluctuations in the *system* properties, i.e., stiffnesses, masses, and damping factors.

The importance of this latter characteristic can be assessed by noting that the equations of motion of a mistuned bladed disk parallel those of parametrically excited systems, i.e., they resemble Mathieu and Hill's equations (see [10,14]), which are well known to exhibit complex behavior. The inclusion of randomness in the mistuning further adds to the complexity and transforms the problem into one of parametric random vibration, see [15].

The qualitative and quantitative aspects of the prediction of the mistuning effects have very often gone hand in hand, i.e., the development of computational tools has been based on the physical properties expected of the solution. For example, the work of Wei and Pierre [5,6] has demonstrated that the response of a mistuned bladed disk resembles its tuned counterpart at large blade-to-blade coupling levels. Accordingly, a series of numerical algorithms have been proposed that rely on tuned response features (see, for example, [6] (regular perturbation), [7,8] (large coupling case), and [12]). In the opposite limit, i.e., for very low blade-to-blade coupling levels, other techniques have been proposed (see [6] (modified perturbation), [8] (small coupling case), and [11] that rely on the localized nature of the response, [5].

The present investigation will proceed in reverse of the above trend, i.e., the successes and failures of well understood computational methods in accurately predicting the forced response of mistuned bladed disks will be relied upon to provide some clarification of phenomenological issues associated with mistuning. For example, it has been successfully argued by Wei and Pierre [5,6] that the mistuning-related increase in forced response of the blades stems from a localization of the modes of the mistuned disks. Yet the localization factor introduced by these authors is a monotonic decreasing function of the blade-to-blade coupling while the forced response appears to peak at an intermediate value of this parameter (see [9]). In this context, the present effort will focus on answering the following questions:

(Q.1) Is there a direct relationship between the localization of the free/forced response and an increase of the amplitude of blade vibration with respect to its tuned value?

(Q.2) If yes, is the localization factor of Wei and Pierre [5] an appropriate measure of localization for this purpose?

(Q.3) Is there a genuine peak of the forced response at an intermediate blade-to-blade coupling level and what is/are the change(s) in the physics of the problem creating the peak?

Another goal of the present investigation is to improve the characterization of the largest amplitude of blade response that can be observed on the entire population of bladed disks. A simple upper bound of this amplitude has been provided by Whitehead [2,16] as $(1+\sqrt{N})/2$, where N is the number of blades but many investigations have reported values substantially lower than this limit. Accordingly, it is desired to:

(Q.4) Investigate the largest amplitude of blade response, assess the conditions under which it occurs, and evaluate the reliability of Whitehead's estimate of this quantity.

As a final objective, it is desired to provide some perspective on the characterization of the forced response when the coupling level is neither very large nor very small. This issue is directly related to the long standing question:

(Q.5) Can a single approximation method/computational algorithm provide reliable estimates of the mistuned forced response through the entire range of blade-to-blade coupling levels?

Answering the five questions enunciated above in connection with an arbitrary bladed disk dynamic model would be a formidable task well beyond the scope of this paper. Rather, it is desired here to answer them first in the context of the single-degree-of-

Contributed by the International Gas Turbine Institute (IGTI) of THE AMERICAN SOCIETY OF MECHANICAL ENGINEERS for publication in the ASME JOURNAL OF ENGINEERING FOR GAS TURBINES AND POWER. Paper presented at the International Gas Turbine and Aeroengine Congress and Exhibition, New Orleans, LA, June 4–7, 2001; Paper 2001-GT-0289. Manuscript received by IGTI, Dec. 2000, final revision, Mar. 2001. Associate Editor: R. Natole.

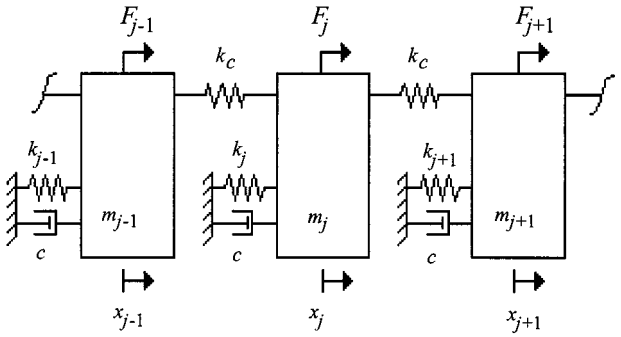

$m_j = 0.0114$ kg (all j); $k_t = 430{,}000$ N/m; $c = 1.443$ Ns/m;

$$F_j = F_o \cos\left(\omega t + \frac{2\pi r(j-1)}{N}\right);\ N = 24 \text{ blades};\ F_o = 1\text{ N};\ r = 3$$

k_j: Gaussian distribution with mean k_t and standard deviation 8,000 N/m

Fig. 1 Single degree-of-freedom per blade disk model

freedom per blade model of Fig. 1 in which mistuning affects only the blade alone stiffnesses (modeled here as Gaussian random variables, see Fig. 1). Next, a confirmation of some of these findings will be obtained on the reduced-order model (see Castanier et al. [17]) of the blisk shown in Fig. 2 (see Bladh et al. [18]).

As stated above, questions (Q.1)–(Q.5) will be addressed by studying the benefits and shortcomings of two previously published approximation techniques of the response of mistuned bladed disks, i.e., the adaptive perturbation method, [8], and the partial mistuning modeling, [11]. For completeness, these techniques are briefly reviewed next.

Review of Approximation Techniques

Partial Mistuning Modeling. Generally speaking, a disk is said to be partially mistuned if mistuning affects only a small portion of it, i.e., a limited number of degrees-of-freedom. The analysis of such systems was motivated by the expectation at low blade-to-blade coupling that the response of a specific blade would only be affected by a few of its neighbors and thus the remaining blades could be taken as tuned. Partially mistuned bladed disks have recently been considered by Mignolet et al. [11] and have been shown to lead to a forced response determination much simpler than the one corresponding to full mistuning (the reduction in complexity is a direct consequence of the limited extent of the mistuning as also observed more recently by Petrov et al. [13]). The simplification arises as follows. Let the bladed disk be described by the equations of motion

$$M\ddot{\mathbf{X}} + C\dot{\mathbf{X}} + K\mathbf{X} = \mathbf{F}e^{i\omega t} \tag{1}$$

where M, C, and K are the symmetric mass, damping, and stiffness matrices of the disk model. Then, assuming the steady-state response in the form $\mathbf{X}(t) = \mathbf{x}e^{i\omega t}$ yields the set of algebraic equations

$$H\mathbf{x} = \mathbf{F} \tag{2}$$

where $H = K - M\omega^2 + i\omega C$ is the impedance matrix at the excitation frequency ω. In the presence of mistuning, H can be separated into its tuned counterpart $\bar{H}$ and a mistuned component ΔH. In a partially mistuned bladed disk, the number of nonzero elements of ΔH is very small and it is convenient to partition Eq. (2)

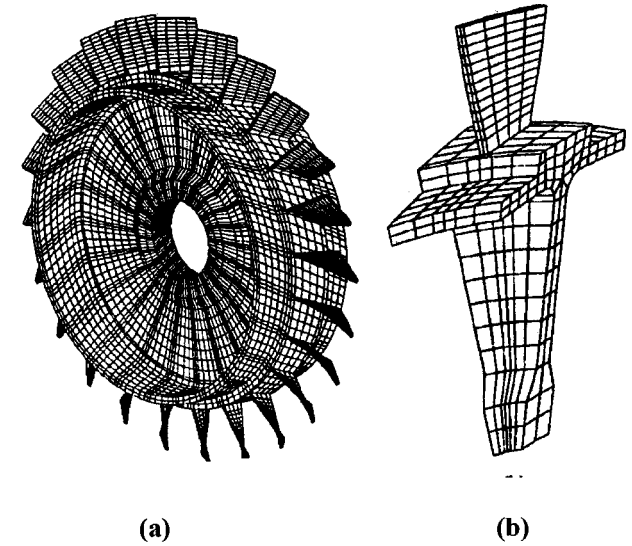

(a) (b)

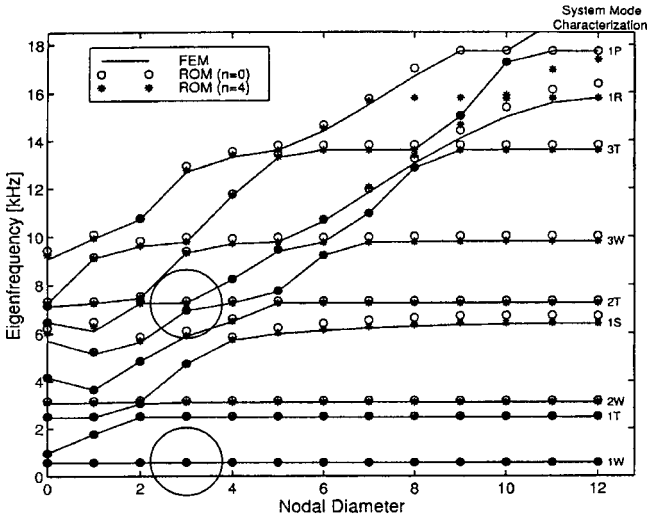

(c)

Fig. 2 Blisk example: (*a*) blisk view, (*b*) blade sector finite element mesh, and (*c*) natural frequency versus nodal diameter plot

into n_m degrees-of-freedom directly (subscript d) affected by mistuning and those that are only indirectly subjected to it (subscript i). That is

$$\mathbf{x} = \begin{bmatrix} \mathbf{x}_d \\ \mathbf{x}_i \end{bmatrix};\quad H = \begin{bmatrix} H_{dd} & H_{di} \\ H_{id} & H_{ii} \end{bmatrix};\quad \text{and}\quad \mathbf{F} = \begin{bmatrix} \mathbf{F}_d \\ \mathbf{F}_i \end{bmatrix}. \tag{3}$$

In view of the partial mistuning assumption, the matrices H_{di}, H_{id}, and H_{ii} are equal to their tuned counterparts $\bar{H}_{di}$, $\bar{H}_{id}$, and $\bar{H}_{ii}$ and $H_{dd} = \bar{H}_{dd} + \Delta H_{dd}$. In an effort to rewrite the equations of motion (2) in a form that is reminiscent of the tuned system, introduce the "mistuned force" $\mathbf{F}_m = \Delta H_{dd}\mathbf{x}_d$ and note that Eq. (2 then becomes

$$\bar{H}_{dd}\,\mathbf{x}_d + \bar{H}_{di}\,\mathbf{x}_i = \mathbf{F}_d - \mathbf{F}_m \tag{4a}$$

and

$$\bar{H}_{id}\,\mathbf{x}_d + \bar{H}_{ii}\,\mathbf{x}_i = \mathbf{F}_i\,. \tag{4b}$$

If the vector $\mathbf{F}_m$ was known, Eqs. (4*a*) and (4*b*) would in fact be the equations of motion of a *tuned* system subjected to the combined action of the forces $\mathbf{F}$ and $\mathbf{F}_m$. Thus, by linearity, the response vector $\mathbf{x}$ can be written as the sum of the tuned solution $\mathbf{x}^{(t)}$ (response to the force $\mathbf{F}$) and of a mistuned component $\mathbf{x}^{(m)}$ (response to the force $\mathbf{F}_m$). The determination of this second part is achieved by rewriting $\mathbf{F}_m$ as

$$\mathbf{F}_m = \Delta H_{dd}\mathbf{x}_d = \sum_{j=1}^{n_m}\left[\sum_{k=1}^{n_m}(\Delta H_{dd})_{jk}(\mathbf{x}_d)_k\right]\mathbf{E}_j \tag{5}$$

where $\mathbf{E}_j$ denotes the vector whose components are all zero except the *j*th one which equals one. The term $[\Sigma_{k=1}^{n_m}(\Delta H_{dd})_{jk}(\mathbf{x}_d)_k]\mathbf{E}_j$ thus physically corresponds to a force of magnitude $[\Sigma_{k=1}^{n_m}(\Delta H_{dd})_{jk}(\mathbf{x}_d)_k]$ applied on the *j*th degree-of-freedom of the set $\mathbf{x}_d$ of the *tuned* system. Next, introducing $\mathbf{h}_d^{(j)}$ and $\mathbf{h}_i^{(j)}$ as the response of the *tuned* system on the degree-of-freedom *d* and *i*, respectively, to a single, unit force acting on the degree-of-freedom *j* of the set $\mathbf{x}_d$, it can be shown that

$$H_{pm}\mathbf{x}_d = \mathbf{x}_d^{(t)} \tag{6}$$

where the subscript *pm* refers to partial mistuning and the element *kl* of the matrix H_{pm} is

$$(H_{pm})_{kl} = \delta_{kl} + \sum_{j=1}^{n_m}(\Delta H_{dd})_{jk}(\mathbf{h}_d^{(j)})_l \tag{7}$$

in which δ_{kl} denotes the Kronecker symbol. Once the response $\mathbf{x}_d$ of the degrees-of-freedom that are directly affected by the mistuning has been determined from Eq. (6), the motion of the remaining degrees-of-freedom can be determined from Eq. (4) and (5), i.e.,

$$\mathbf{x}_i = \mathbf{x}_i^{(t)} + \mathbf{x}_i^{(m)} = \mathbf{x}_i^{(t)} - \sum_{j=1}^{n_m}\left[\sum_{k=1}^{n_m}(\Delta H_{dd})_{jk}(x_d)_k\right]\mathbf{h}_i^{(j)}. \tag{8}$$

Equations (7) and (8) demonstrate that the determination of the response of a bladed disk that involves mistuning on only n_m degrees-of-freedom requires the solution of a system of equations of size $n_m \times n_m$ only and the determination of some tuned responses, i.e., the vectors $\mathbf{h}^{(j)}$.

Adaptive Perturbation Method. It has recently been argued, see [8], that the analysis of the *n*-degree-of-freedom bladed disk model given by Eq. (1) or (2) should be achieved not in the physical coordinates, $\mathbf{X}(t)$, as in Eq. (1), but rather in terms of a set of variables $\mathbf{Q}(t)$ that accurately represent the contributions of the various mode shapes in the response. These new coordinates would be related to the physical ones by the relation

$$\mathbf{X}(t) = T\mathbf{Q}(t) \tag{9}$$

where T denotes a $N \times N$ transformation matrix the columns of which are the exact mode shapes of the mistuned bladed disk or reliable approximation thereof. Introducing the above change of variables, Eq. (9), in Eq. (2) and premultiplying the resulting relations by T^T leads to the transformed steady-state equations of motion

$$\tilde{H}\mathbf{q} = \tilde{\mathbf{F}} \tag{10}$$

where the components of $\mathbf{q}$ are the complex amplitudes of response of the coordinates $\mathbf{Q}(t)$ and $\tilde{H} = T^T H T$ and $\tilde{\mathbf{F}} = T^T\mathbf{F}$ denote the corresponding impedance matrix and force vector.

Considering the magnitude of the different terms $\tilde{H}_{jl}$, it is first noted that if the columns of the matrix T are close approximations of the mistuned bladed disk modes, the off-diagonal terms $\tilde{H}_{jl}$, $j \neq l$, are close to zero. Further, the magnitude of $\tilde{H}_{jj}$ is "small" when the excitation frequency is close to one of the approximate natural frequencies ω_l associated with T, i.e., $\omega_l^2 = (T^T K T)_{ll}/(T^T M T)_{ll}$, but is otherwise "large." On this basis, it was suggested to partition the response vector $\mathbf{q}$ in terms of the components $\mathbf{q}_S$ and $\mathbf{q}_L$ which are associated with small and large diagonal elements of $\tilde{H}$, respectively. That is,

$$\mathbf{q} = [\mathbf{q}_S^T\ \mathbf{q}_L^T]^T \tag{11}$$

where $\mathbf{q}_S$ and $\mathbf{q}_L$ are vectors of dimensions $d \times 1$ and $(N-d) \times 1$, respectively. The above partition can be achieved by selecting the transformation matrix T to be

$$T[\Phi_S\ \Phi_L] \tag{12}$$

where Φ_S and Φ_L denote the $N \times d$ and $N \times (N-d)$ matrices whose columns are the approximate mode shapes associated with the natural frequencies ω_l that are close to (for Φ_S) and far from (for Φ_L) the excitation frequency ω.

Proceeding with this partitioning, it is found that the linear system of Eq. (10) becomes

$$\begin{bmatrix}\tilde{H}_{SS} & \tilde{H}_{SL}\\ \tilde{H}_{LS} & \tilde{H}_{LL}\end{bmatrix}\begin{bmatrix}\mathbf{q}_S\\ \mathbf{q}_L\end{bmatrix} = \begin{bmatrix}\tilde{\mathbf{F}}_\mathbf{S}\\ \tilde{\mathbf{F}}_\mathbf{L}\end{bmatrix} \tag{13}$$

where the matrices $\tilde{H}_{SS}$, $\tilde{H}_{SL}$, $\tilde{H}_{LS}$, and $\tilde{H}_{LL}$ are of respective dimensions $d \times d$, $d \times (N-d)$, $(N-d) \times d$, and $(N-d) \times (N-d)$ while the vectors $\tilde{\mathbf{F}}_\mathbf{S}$ and $\tilde{\mathbf{F}}_\mathbf{L}$ have d and $(N-d)$ components.

The computation of the steady-state components $\mathbf{q}_S$ and $\mathbf{q}_L$ can now be performed. Specifically, it is found that

$$\mathbf{q}_S = G_{SS}[\tilde{\mathbf{F}}_\mathbf{S} - \tilde{H}_{SL}\tilde{H}_{LL}^{-1}\tilde{\mathbf{F}}_\mathbf{L}] \tag{14}$$

and

$$\mathbf{q}_L = \tilde{H}_{LL}^{-1}[\tilde{\mathbf{F}}_\mathbf{L} - \tilde{H}_{LS}\mathbf{q}_S] \tag{15}$$

where

$$G_{SS} = [\tilde{H}_{SS} - \tilde{H}_{SL}\tilde{H}_{LL}^{-1}\tilde{H}_{LS}]^{-1}. \tag{16}$$

Up to this point, the formulation is exact and the results are independent of the selection of the transformation matrix T. Relying on the expected large separation between the excitation frequency ω and the approximate natural frequencies ω_l corresponding to Φ_L, it can be argued (see [8]) that $\tilde{H}_{LL}^{-1}$ can be approximated as the Taylor series

$$\tilde{H}_{LL}^{-1} = (\overline{\tilde{H}_{LL}} + \Delta\tilde{H}_{LL})^{-1} = \overline{\tilde{H}_{LL}^{-1}} - \overline{\tilde{H}_{LL}^{-1}}\Delta\tilde{H}_{LL}\overline{\tilde{H}_{LL}^{-1}} + \cdots \tag{17}$$

where the matrices $\overline{\tilde{H}}$ and $\Delta\tilde{H}$ are the tuned and mistuned components of $\tilde{H}$, respectively. Introducing a truncated form of this series in Eq. (14)–(16) leads to the required approximation of the forced response of the mistuned disk considered.

The above procedure was referred to as adaptive as its accuracy can be increased or decreased by varying the number d of modes retained in the set $\mathbf{q}_S$ ($d = N$ yields the exact solution) and the number of terms kept in the Taylor series (17). Following the discussion of Lin and Mignolet [8], only the first term, i.e., $\tilde{H}_{LL}^{-1} = \overline{\tilde{H}_{LL}^{-1}}$ was kept here to ensure a technique accurate to first order in mistuning.

Another factor that affects the accuracy of the forced response estimate is the selection of the columns of the transformation matrix T. The choice of these vectors as the exact mode shapes of the mistuned bladed disk leads of course to a set of variables $\mathbf{q}$ that correspond exactly to the system's modal coordinates and to a diagonal impedance matrix $\tilde{H}$ (assuming classical damping). However, this selection requires the evaluation of the mode shapes of the mistuned disk, a problem more complex than the forced response estimation. Thus, it was suggested in [8] that the columns of T should be selected as the mode shapes of a *fixed* system that is "close" to the bladed disk considered. In view of the comprehensive qualitative analysis performed by Wei and Pierre [5,6], it was proposed to choose the columns of the transformation matrix T to be the mode shapes of the tuned system when the blade-

to-blade coupling is large (with respect to the mistuning) and those of the decoupled system when this coupling is small (with respect to the mistuning). Since the present investigation will rely on the adaptive perturbation method only for large blade-to-blade coupling levels, the columns of the matrix T were taken as the tuned modes of the disk.

Localization Study (Questions Q.1 and Q.2)

The present study of the localization of the forced response of mistuned bladed disks was prompted by the recent criticisms of Castanier and Pierre [19,20], Cha and Morganti [21], and LaBorde [22] of the commonly accepted measure of localization proposed by Wei and Pierre [5]. Specifically, these former authors have suggested that the mean localization factor, as specified by Wei and Pierre [5], is inappropriate because (i) it is dominated by damping effects not by mistuning and (ii) it does not account for the disk-to-disk variability of the localization of the forced response. In view of these comments, it was felt that a reliable answer to questions (Q.1) and (Q.2) would require an assumption-free estimator of the level of localization of the forced mistuned response of bladed disks (not chains). The partial mistuning model provides a perfect basis for this assessment as it relies on no other assumption or approximation that the existence of a localization of the response. In fact, there is a direct relationship between the level of localization and the number of blades (sector width, s) that must be considered mistuned to obtain an accurate matching of the partially and fully mistuned disks, i.e., the higher the localization the smaller s needs be. On this basis, a comprehensive analysis of the adequacy of partial mistuning as a representation of full disk mistuning was undertaken for the entire range of coupling levels (k_C), for various damping ratios (c) and excitation patterns, i.e., engine orders (r). Specifically, for each set of values of (k_C,c,r) considered, a thorough Monte Carlo simulation (10,000 fully mistuned disks) was performed to obtain the first statistics, i.e., mean and standard deviation, (i) of the response of a typical blade (blade 1) at the tuned natural frequency corresponding to the given engine order, (ii) of the maximum responding one at that frequency, and (iii) of the maximum responding one over a frequency sweep. In addition, the maximum amplitude of vibration of the entire population of disks was also recorded. These seven sets of values were first estimated by determining the exact steady-state response of each disk at the appropriate frequency(ies). Then, these computations were repeated by assuming that the disks were not fully mistuned but rather that the variations in blade properties were limited to blades j-p, ...,j, ...,$j+p$, the other ones being considered tuned. The corresponding value of the amplitude of response of the central blade, j, was then considered as its partial mistuning estimate of order $s=2p+1$. Note that since each blade is modeled as a single-degree-of-freedom system, $n_m=s$. The process was repeated for each blade on the disk, $j=1,...,N=24$, for each disk of the population of 10,000, and for several values of s. Such a study was performed for 13 different values of the blade-to-blade coupling (stiffness k_C), and several different combinations of damping constant (coefficient c) and engine order (parameter r of the forcing function).

The results shown in Figs. 3–9 correspond to $r=3$ and $c=1.443$ Ns/m but many of these computations were also repeated for $r=3$ and $c=0.7215$ Ns/m and 2.886 Ns/m, and $c=1.443$ Ns/m and $r=0$, 6, 10, and 12. The results shown in Figs. 3–9 are representative of all these computations and can serve as a basis for the following important and/or surprising observations:

1. The physical model of partial mistuning is completely justified at small coupling levels for all types of responses considered.
2. The reliability of the partial mistuning model in predicting the means and the standard deviations of the maximum responses on the disk is similar. Further, this observation is valid for both sweep and no-sweep analyses.

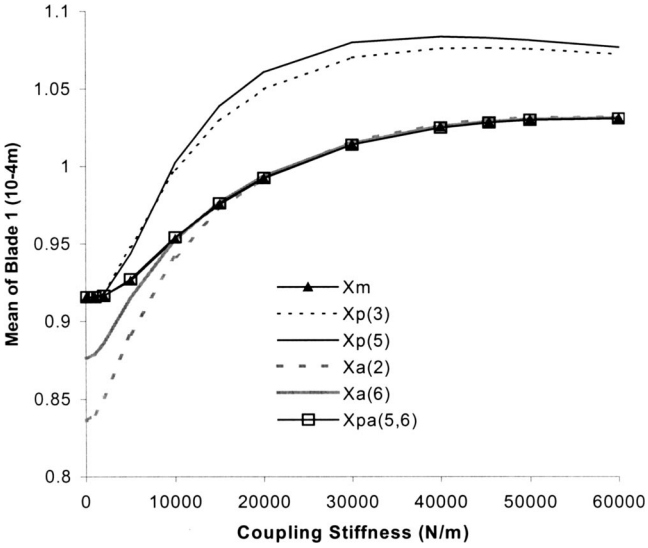

Fig. 3 Mean value of the response of blade 1 (typical blade) by Monte Carlo simulation (Xm), three-blade and five-blade partial mistuning models (Xp(3) and Xp(5)), adaptive perturbation method with two and six modes (Xa(2) and Xa(6)) and local +global approximation with s=5 and d=6 (Xpa(5,6))

3. The partial mistuning model, with s fairly small, i.e., $s=3$–5, provides very reliable estimates of the maximum blade response over the entire population of disks over a broad range of coupling levels. From Fig. 9, it would be estimated that this reliability extends till the peak shown at $k_C \approx 20{,}000$ N/m but the discussion below suggests that it is in fact valid for all coupling levels.
4. The range of coupling stiffness in which the partial mistuning model is valid is not uniform across the types of responses considered, i.e., a given width s of partial mistuning leads to a better approximation of the maximum amplitude obtained on the entire population than of the maximum response on a specific disk in a sweep (compare Figs. 7–8 and 9), which is itself better estimated than its no-sweep coun-

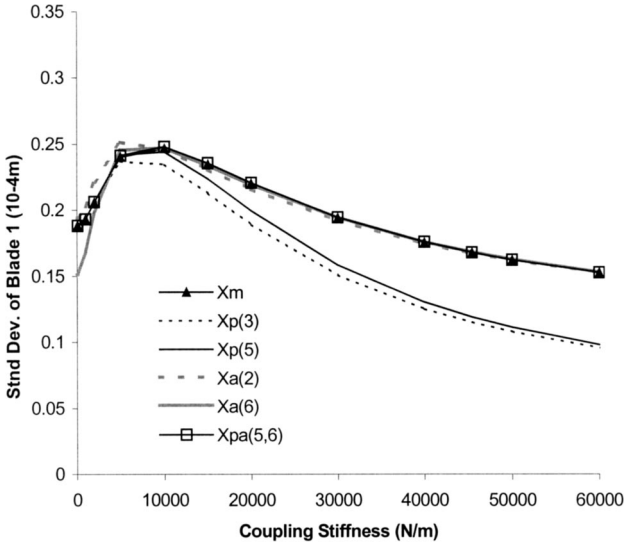

Fig. 4 Standard deviation of the response of blade 1 (typical blade) by Monte Carlo simulation (Xm), three-blade and five-blade partial mistuning models (Xp(3) and Xp(5)), adaptive perturbation method with two and six modes (Xa(2) and Xa(6)) and local+global approximation with s=5 and d=6 (Xpa(5,6))

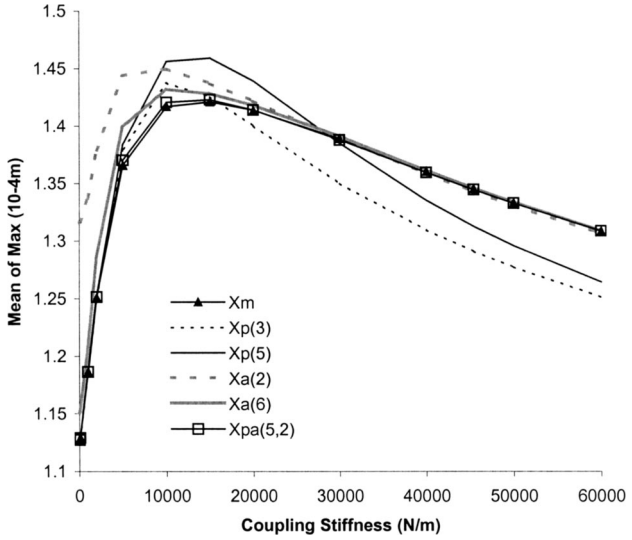

Fig. 5 Mean value of the maximum response on the disk by Monte Carlo simulation (Xm), three-blade and five-blade partial mistuning models (Xp(3) and Xp(5)), adaptive perturbation method with two and six modes (Xa(2) and Xa(6)) and local+global approximation with *s*=5 and *d*=2 (Xpa(5,2))

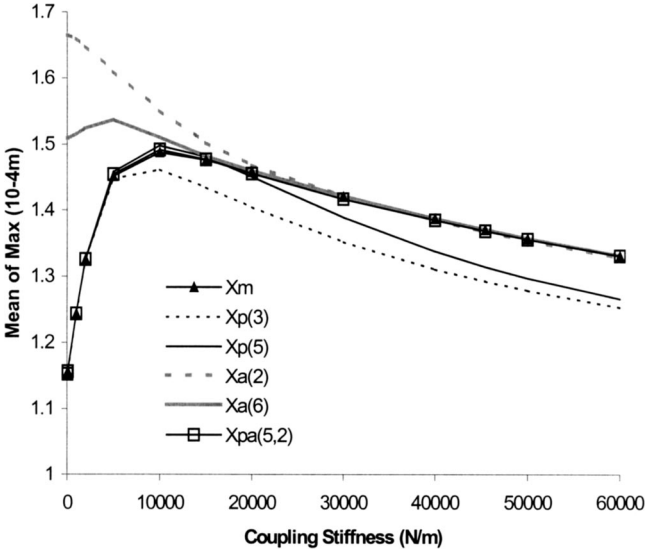

Fig. 7 Mean value of the maximum response on the disk in a sweep by Monte Carlo simulation (Xm), three-blade and five-blade partial mistuning models (Xp(3) and Xp(5)), adaptive perturbation method with two and six modes (Xa(2) and Xa(6)) and local+global approximation with *s*=5 and *d*=2 (Xpa(5,2))

terpart (compare Figs. 5–6 and 7–8), in turn better than the amplitude of vibration of blade 1 (compare Figs. 3–4 and 5–6).

The observation (4) is in fact very important as it has far reaching consequences:

(4.1) Since the maximum amplitude obtained on the entire population is clearly larger than (or equal to) the maximum response on a specific disk in a sweep, which is itself larger than (or equal to) its no-sweep counterpart also larger (or equal to) the amplitude of vibration of its blade 1, it can be concluded that the accuracy/reliability of the partial mistuning model generally increases with the level of response of the blade considered. This finding is confirmed by the results of Figs. 10–12 which show the minimum value of *s* required for the partial mistuning model to yield an estimate of the blade response to within 10% of the exact value. Note in particular the "triangular wedge" formed by these points and that the highest amplitudes are well estimated with only *s*=3 or 5. These three scatter plots were produced with the 120 blades of 5 random disks as follows. First, the amplitude of response of each blade of the five fully mistuned disks was determined (the "exact" value). Next, each of the 120 blades was considered as the center of mistuned sectors of *s*=1,3,5,...,23 blades and the estimate of the amplitude of response of the center blade corresponding to each value of *s* was compared to the exact value. The lowest value of *s* for which the partial mistuning estimate was within 10% of the exact value was recorded. The plots

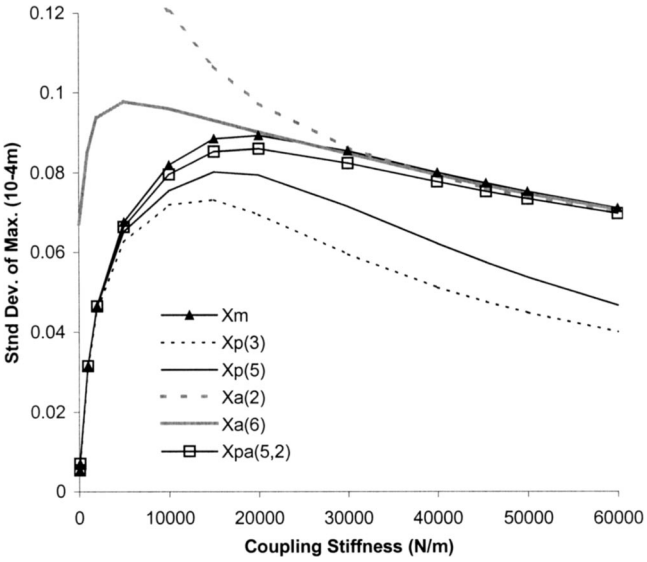

Fig. 6 Standard deviation of the maximum response on the disk by Monte Carlo simulation (Xm), three-blade and five-blade partial mistuning models (Xp(3) and Xp(5)), adaptive perturbation method with two and six modes (Xa(2) and Xa(6)) and local+global approximation with *s*=5 and *d*=2 (Xpa(5,2))

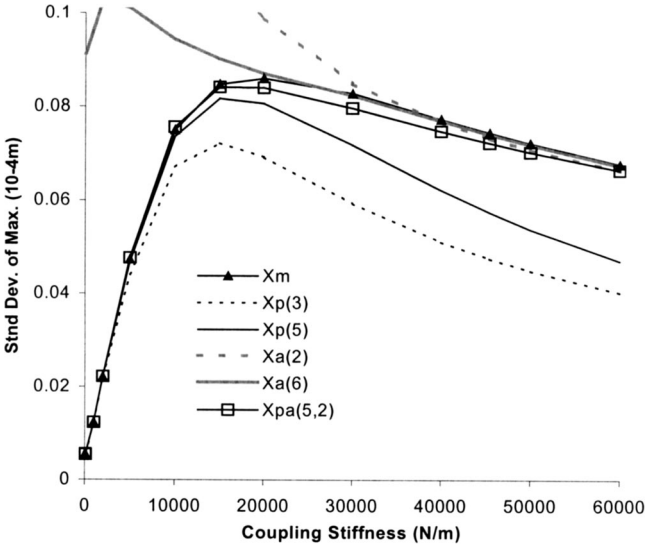

Fig. 8 Standard deviation of the maximum response on the disk in a sweep by Monte Carlo simulation (Xm), three-blade and five-blade partial mistuning models (Xp(3) and Xp(5)), adaptive perturbation method with two and six modes (Xa(2) and Xa(6)) and local+global approximation with *s*=5 and *d*=2 (Xpa(5,2))

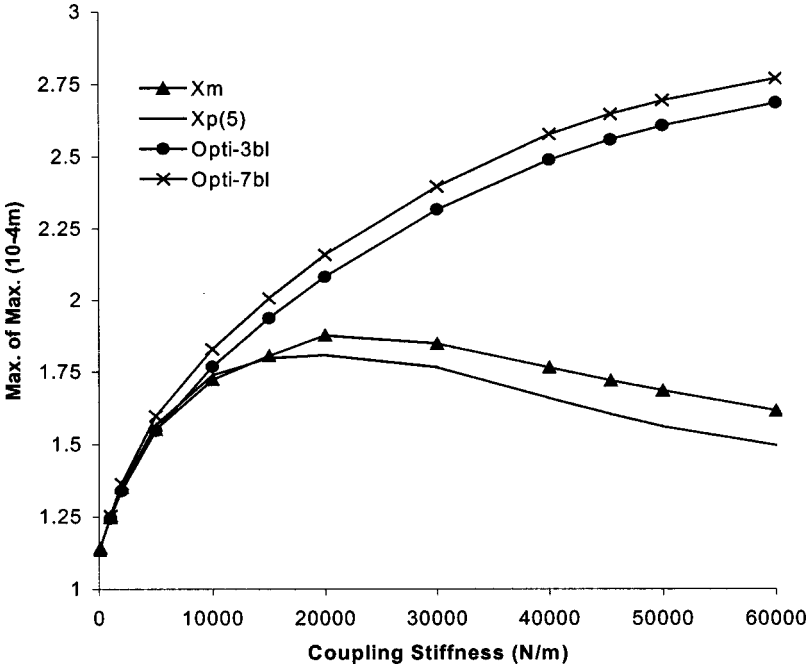

Fig. 9 Maximum response on the population of disks by Monte Carlo simulation (Xm), five-blade partial mistuning model (Xp(5)), and by optimization of three and seven-blade mistuning models (Opti-3bl and Opti-7bl)

of Figs. 10–12 were then obtained by using these values of s as abscissas and the exact amplitudes of response as ordinates.

(4.2) Since the applicability/reliability of the partial mistuning model is directly related to the localization of the forced response, it is concluded here that the disk behavior is *on average* more localized around the blades that exhibit a large response than around those having a smaller amplitude of vibration. Note, however, that a high level of localization does not necessarily imply large amplitudes, some of the very low responses are also well captured with $s=3$ or 5.

(4.3) The above conclusion on the nonuniformity around the disk of the localization of the forced response adds to the recent criticisms of Castanier and Pierre [19,20], Cha and Morganti [21], and LaBorde [22] stated above. The present investigation demonstrates that, in addition to the disk-to-disk variations of such a measure, one should also account for blade-to-blade differences.

The Maximum Response and Its Peak—(Questions Q.3 and Q.4)

The determination of the blade-to-blade coupling level at which the maximum amplitude of response achieves a peak is an issue that has been brought up in a variety of previous mistuning efforts and has never received a fully satisfactory answer (see the recent paper by Ottarsson and Pierre [23] for a discussion). An analysis of Fig. 9 would suggest that an explanation of this peculiarity should be related to the apparent breakdown of the partial mistuning model of the maximum response over the entire population of disks in the neighborhood of $k_C \approx 20{,}000$ N/m. In fact, the decrease in accuracy of the partial mistuning approximations appears consistent with the reduction in the maximum amplitude of blade vibration and suggests a general decrease in the localization of the forced response per observation (4.2). This answer, however, brings out the question of why do highly localized disks exhibit some large amplitudes of response at small coupling levels but do not for large values of k_C? To address this follow-up question, the stiffness of the N blades that yield the amplitudes of response shown in Fig. 9 were recorded for all values of k_C considered. It was then observed that the stiffness of several of the blades located near the maximum responding one were growing rapidly as a function of the coupling stiffness k_C and were surpassing the tuned value by several standard deviations even for k_C as small as 1000 N/m. Accordingly, it can be expected that the probability of obtaining such cases would be very small and that the simulation results shown in Fig. 9 could be biased by the size of the population selected (10,000 disks). To remedy this situation, it was decided to proceed with an optimization effort in which the stiffnesses of three and seven-blade mistuning models were selected to achieve the maximum response of the central blade. This undertaking was quite successful and led to the very large amplitudes of response also shown in Fig. 9 (curves Opti) which were obtained with some large mistuned stiffnesses (thereby confirming the approximate analysis of Sinha [24]). Note in this context that several (at least two) maxima of the forced response were obtained for most values of k_C but the results discussed above and shown in Fig. 9 correspond to the highest maximum.

At this point, a comparison of the above results with those of Whitehead [16] is in order. First, the maximum amplitude estimate obtained by this author, i.e., $(1+\sqrt{N})/2=2.95$ times the tuned value, corresponds well to the present results at high coupling levels. Indeed, for $k_C=60{,}000$ N/m the optimization effort yields a magnification factor of 2.55 and this number increases to 2.69 at $k_C=120{,}000$ N/m. In regards to the mistuned stiffnesses required to achieve these high amplitudes, a very good qualitative agreement with Whitehead's analysis is also obtained. Indeed, it can be shown that the optimum pattern of stiffnesses obtained by this author's approach for the bladed disk model of Fig. 1 reduces to a three-blade partial mistuning with large values of the stiffnesses of the blades directly next to the maximum responding one as noted in the present effort. The excellent qualitative match of the present results with the upper bound analysis of Whitehead [16] further supports again the very localized nature of the forced response around highly responding blades (see observation 4.2). Some further discussions regarding the largest amplitude of blade response within the population can be found in [25].

These optimization results confirm the suspicion that the peak

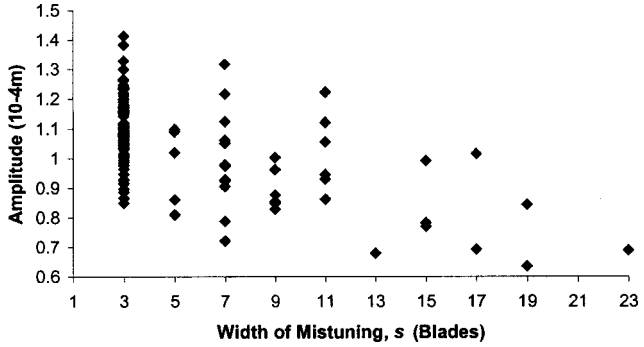

Fig. 10 Scatter plot of the width of partial mistuning required to achieve an accuracy of 10% on the amplitude of response of the blades of five randomly mistuned disks, k_C=45,430 N/m

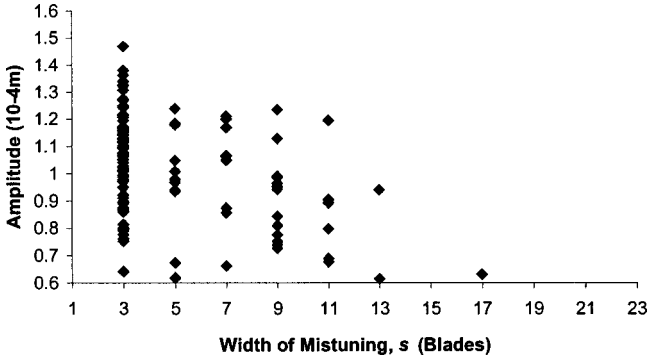

Fig. 11 Scatter plot of the width of partial mistuning required to achieve an accuracy of 10% on the amplitude of response of the blades of five randomly mistuned disks, k_C=20,000 N/m

shown in Fig. 9 is in fact an artifice of the finite population size used. They also shed some light on the genuine peaks of the mean and standard deviations of the maximum response on a disk shown in Figs. 5–8. Specifically, they demonstrate that these peaks are associated with a ''large tail event.'' That is, as the coupling stiffness increases, the magnitude of the largest response also increases (see Fig. 9) but its probability of occurrence decreases as the stiffnesses associated with this configuration rapidly shift away from their mean (tuned) value. The effect of this tail event on the mean and standard deviation of the maximum response (see Figs. 5 and 6 for the no-sweep data and Fig. 7 and 8 for the sweep results) can be quantified by $A_{\max}p_A(A_{\max})$ and $A^2_{\max}p_A(A_{\max})$, respectively, where $p_A(A_{\max})$ denotes the probability density function of the amplitude evaluated at the maximum amplitude $A_{\max}$. An increase in the coupling stiffness can then be seen to create two opposite effects. First, it yields an increase in the maximum amplitude that can be obtained $A_{\max}$, which would promote higher values of the mean and standard deviations of the maximum response on a disk. But this increase in $A_{\max}$ requires larger deviations from the tuned value which are associated with a lower probability density function so that $p_A(A_{\max})$ decreases. Eventually, the fast decay of the Gaussian probability density function of the stiffnesses assumed here overwhelms the slow increase in $A_{\max}$ and the effect of the maximum response on both means and standard deviations diminishes leading generally to a decrease of these curves at high coupling levels.

It is interesting to observe that the contributions of the largest possible amplitude to the standard deviation of the maximum involves $A^2_{\max}$ vs $A_{\max}$ for the mean of this variable. Since the amplitude $A_{\max}$ increases with the coupling stiffness k_C, it could be expected that its effect would be felt more strongly and up to larger values of k_C on the standard deviation than it would on the mean. This conclusion is in fact easily confirmed: the peak in the standard deviation plots, see Figs. 6 and 8, occurs at a larger coupling value than its counterpart in the mean value plots, see Figs. 5 and 7. In fact, the same reasoning could be repeated to justify that the peaks of the 50th, 60th,..., 90th, 95th percentiles of the maximum amplitude of response on a disk would all occur at different (increasing) values of the blade-to-blade coupling. Since the peak is governed by a ''tail event,'' it is also suggested here that the location of this maximum would in fact also be dependent on the distribution of the stiffness, i.e., Gaussian versus triangular or uniform. In a more general perspective, the above discussion demonstrates that there is no single coupling level at which a *well-defined maximum* occurs, rather one should define a *transition zone* in which the *various* peaks occur. Interestingly. it has been observed in the same region that the behavior of the mistuned mode shapes changes from generally global to generally local (results not presented here for brevity).

Local+Global Modeling Strategy—(Question Q.5)

It remains to address question (Q.5), i.e., determining what is missing to the partial mistuning model to fully account for the behaviors shown in Figs. 3–9. Clearly, and expectedly, the discrepancy between the exact statistics and their partial mistuning estimates increases steadily as the coupling level is increased. However, are these differences simply representative of a general decrease in the localization of the forced response so that the width of partial mistuning s should be slowly increased as a function of the coupling level, k_C, or are they symptomatic of the existence of another type of response, i.e., of a *global* component? It is suggested here that the latter explanation is the correct one. Indeed, it has been argued in many previous investigations of mistuning that the wavelike response of the tuned disk is still very much present in mistuned disks exhibiting a large coupling level. This observation was in fact the basis for the adaptive perturbation strategy (large coupling) of Lin and Mignolet [8] (see above) which can be seen in Figs. 3–8 to yield an excellent prediction of the response of the entire bladed disk for large k_C. The presence of a global component of the response can also be confirmed from plots similar to Figs. 10–12 but corresponding to smaller error levels, 3% say, see Fig. 13. Note in this figure that the triangular nature of the physical domain (A,s) has mostly disappeared and that large widths of mistuning are required for most amplitudes giving way to an almost rectangular domain as could be expected from a response correlated over the entire set of blades. A final confirmation of the existence of such a global component stems from efforts to model the response of the entire mistuned bladed disk as originating from an ''equivalently'' tuned disk subjected to both the physical engine order excitation and a white noise mistuning-based correction (see [26]). The success obtained with

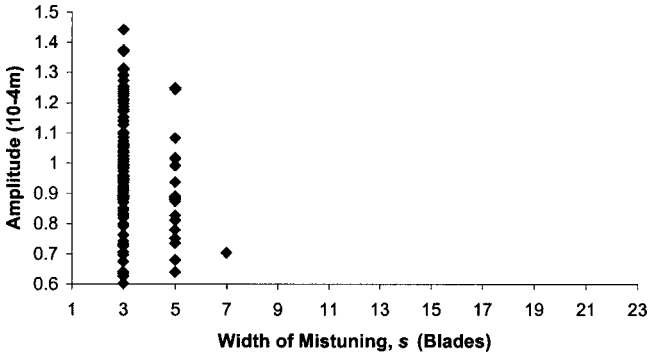

Fig. 12 Scatter plot of the width of partial mistuning required to achieve an accuracy of 10% on the amplitude of response of the blades of five randomly mistuned disks, k_C=5,000 N/m

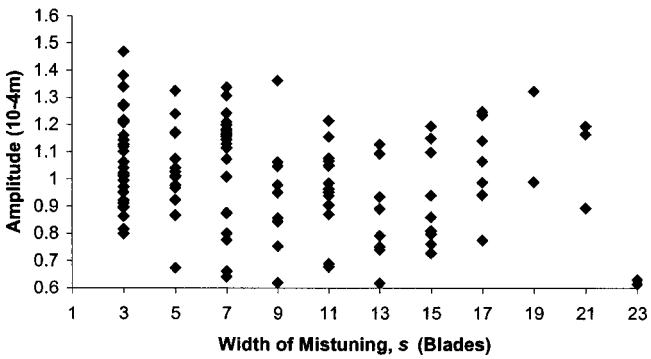

Fig. 13 Scatter plot of the width of partial mistuning required to achieve an accuracy of 3% on the amplitude of response of the blades of five randomly mistuned disks, k_C=20,000 N/m

this model through the entire range of coupling stiffness clearly indicates that the response of bladed disks does exhibit short range, i.e., local, effects accounted for in that paper by the spatial white noise term in addition to a global component which is associated with an approximately tuned disk.

The above discussion clearly demonstrates that a successful modeling of the disk response must include both local and global components in a manner somewhat akin to multiple scale problems (see [27] for a discussion). A strategy that is based on a separate modeling of both components *concurrently* can be developed on the basis of a combination of the partial mistuning modeling and the adaptive perturbation method. Clearly, the partial mistuning modeling relies on the local features of the response but does not include any global component. On the contrary, the adaptive perturbation technique represents the response as a sum of global components and the local character only appears by including all terms. These strengths and weaknesses are clearly reflected in the results of Figs. 3–8.

The proposed local+global modeling strategy proceeds as follows. First, let the response vector be written as the sum of its local and global components, i.e.,

$$\mathbf{x}=\mathbf{x}^{(L)}+\mathbf{x}^{(G)} \tag{18}$$

so that, from Eq. (2)

$$H(\mathbf{x}^{(L)}+\mathbf{x}^{(G)})=\mathbf{F}. \tag{19}$$

The estimation of the separate components $\mathbf{x}^{(L)}$ and $\mathbf{x}^{(G)}$ can then be achieved by assuming that the local component $\mathbf{x}^{(L)}$ is dominant and estimate it from a partial mistuning model of the disk disregarding the global term $\mathbf{x}^{(G)}$. This computation yields

$$\mathbf{x}^{(L)}=(H^{-1}\mathbf{F})_{pm(s)} \tag{20}$$

where the subscript $pm(s)$ indicates the use of the partial mistuning model with a total of s mistuned degrees-of-freedom/blades. Since this approach does not provide the exact response (because $s<N$), there exists a remainder in Eq. (19) which must correspond to the global effects. That is, one has

$$Hx^{(G)}=\mathbf{F}-H\mathbf{x}^{(L)}=\mathbf{F}-H(H^{-1}\mathbf{F})_{pm(s)}. \tag{21}$$

Given the global nature of the expected result, Eq. (21) will be solved by relying on the adaptive perturbation strategy so that

$$\mathbf{x}^{(G)}=\{H^{-1}[\mathbf{F}-H(H^{-1}\mathbf{F})_{pm(s)}]\}_{ap(d)} \tag{22}$$

where the notation $ap(d)$ denotes the use of the adaptive perturbation technique with d ''small'' modes. Summing the contributions of Eq. (20) and (22) yields a local+global estimate of the response of the disk considered.

An alternative local+global modeling strategy is the exact reverse of the one shown above, i.e., the global solution is computed first so that

$$\mathbf{x}^{(G)}=(H^{-1}\mathbf{F})_{ap(d)} \tag{23}$$

and then the local correction is evaluated as

$$\mathbf{x}^{(L)}=\{H^{-1}[\mathbf{F}-H(H^{-1}\mathbf{F})_{ap(d)}]_{pm(s)}. \tag{24}$$

In assessing the reliability of the above two formulations, it should first be noted that they yield very small errors at both small and large blade-to-blade coupling levels. Indeed, when the blade-to-blade coupling is large, the adaptive perturbation technique provides an excellent approximation of the exact response so that the residual should be negligible. Further, at very low coupling levels, the partial mistuning becomes exact for very small width of mistuning independently of the excitation characteristics. Moreover, it is seen from Figs. 3–8 that the prediction of all forced response statistics is also very accurate in the transition zone even with small values of d and s (the curves corresponding to these approaches are almost indistinguishable from their exact counterparts).

Confirmation to a Blisk Reduced-Order Model

The above discussion has been accomplished on the basis of the single-degree-of-freedom per blade model of Fig. 1. While past studies have clearly demonstrated that this simple system exhibits many of the phenomenological features of mistuning, it was deemed desirable to obtain a confirmation of some of the above findings on a more complex bladed disk model, e.g., the blisk of Fig. 2. Much of the above discussion has relied on the partial mistuning concept which may not be surprising with a nearest neighbor interaction as in the system of Fig. 1 but is not easily justifiable for the blisk model of Fig. 2. Accordingly, the focus of the present confirmation effort was placed on the assessment of the partial mistuning approach and the amplitude versus partial mistuning width scatter plots.

As Figs. 3–9 indicate, the partial mistuning approximation can only be expected to be reliable when the blades are weakly coupled or equivalently for modal families that exhibit a very flat frequency versus nodal diameter curve. Accordingly, it was decided to assess the accuracy of the partial mistuning strategy in predicting the blade response to a r=3 excitation at the frequency ω=577.1486 Hz, which corresponds to the lowest circle on Fig. 2, with damping ratio 0.125%. For simplicity, it was assumed that the relative variations of the different blade alone natural frequencies were the same for any given blade thereby reducing the number of mistuning parameters to one per blade, i.e., to

$$\delta_j=\frac{(\omega_{i,j}^2)_{\text{mist}}-(\omega_{i,j}^2)_{tun}}{(\omega_{i,j}^2)_{tun}} \quad \text{for any } i \text{ and } j=1,...,N. \tag{25}$$

In the above equation, $(\omega_{i,j})_{tun}$ and $(\omega_{i,j})_{mist}$ denote the ith tuned and mistuned blade alone natural frequencies of blade j.

Shown in Fig. 14 is the error on the maximum amplitude of response of a typically mistuned disk as a function of the mistuning strength for three and five-blade partial mistuning. As observed in connection with the single-degree-of-freedom blade model, partial mistuning does provide a very good approximation of the blade response for weak blade-to-blade coupling which further improves as the mistuning width is increased.

Having established the validity of the partial mistuning technique, it is now appropriate to proceed with the amplitude versus mistuning width (A,s) scatter plots. The two resonance conditions circled on Fig. 2, i.e., r=3, ω=577.1486 Hz, damping ratio =0.025% (case 1) and r=3, ω=6989.65 Hz, damping ratio =0.125% (case 2) were selected. The corresponding plots, shown in Figs. 15 and 16, exhibit as before peaks at the low values of s demonstrating again that the highest amplitudes of response are

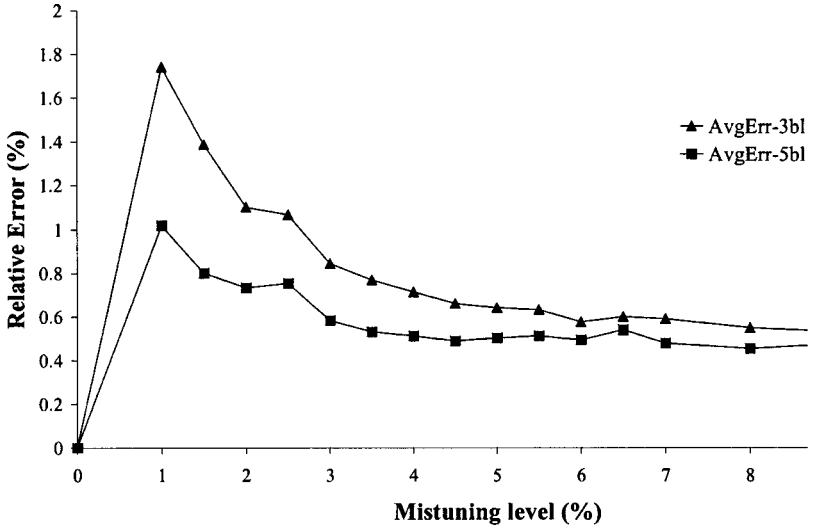

Fig. 14 Maximum response prediction error with partial mistuning versus mistuning level, blisk on lower third EO mode 0.125% damping

typically attained with a strong localization as already noted in connection with the single-degree-of-freedom blade model.

Summary

The present investigation focused on the assessment and prediction of the local and global effects of mistuning on the forced response of bladed disks. Local effects are those that span only a few blades while their global counterparts encompass the entire disk. Thus, local effects are appropriately captured by the partial mistuning model in which only a few blades are assumed to be mistuned (mistuning width $=s$) while the remaining ones are tuned. Similarly, the global component of the forced response is well represented by a modal approximation with few tuned modes, i.e., by the adaptive perturbation method corresponding to the high coupling case. The successes and shortcomings of the partial mistuning and adaptive perturbation approaches are directly related to the relative strengths of the local and global effects on the mistuned forced response. For example, the width s of the disk sector that must be considered mistuned to obtain a reliable estimate of the forced response of the blade located at the center of the sector is a direct measure of localization. Indeed, the need for a large sector is indicative of a long spatial correlation between blades and thus of a weakly localized response. On this basis, it was proposed to use the mistuning width s as an indicator of localization. With this tool and the partial mistuning and adaptive perturbation approaches, the five phenomenological and modeling questions enunciated in the introduction were answered as follows.

(Q.1) Is there a direct relationship between the localization of the free/forced response and an increase of the amplitude of blade vibration with respect to its tuned value?

There is *not a one-to-one* relationship between localization of the forced response and amplification of blade vibration but there is a definite trend. The triangular wedge shapes of Figs. 10–12 and 15–16 clearly indicate that the highest amplitudes of response are typically associated with a high localization around that blade but the reverse is not true. Further, the differential accuracy of the partial mistuning in predicting (in increasing order of accuracy) the response of a typical blade, the highest response at a given frequency, the highest response in a sweep, and the highest re-

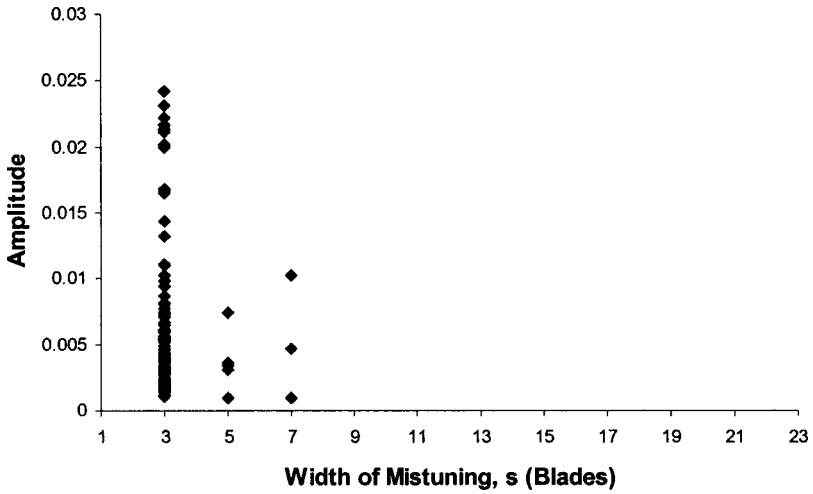

Fig. 15 Scatter plot of the width of partial mistuning required to achieve an accuracy of 10% on the amplitude of response of the blades of five randomly mistuned disks, blisk on lower third EO mode. 0.025% damping, 0.5% mistuning.

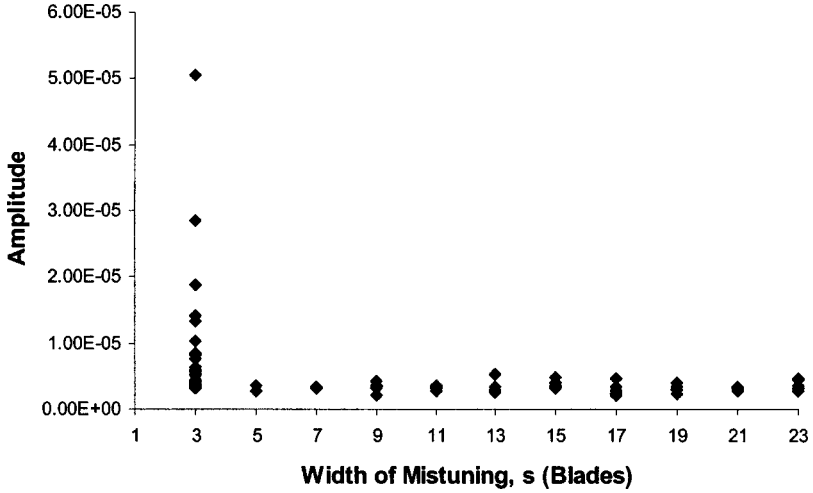

Fig. 16 Scatter plot of the width of partial mistuning required to achieve an accuracy of 10% on the amplitude of response of the blades of five randomly mistuned disks, blisk in veering 2 (third EO modes). 0.125% damping, 4% mistuning.

sponse in the entire population of disks clearly suggests that the *highest amplitudes of blade vibrations are obtained for very localized responses at all blade-to-blade coupling levels.*

(Q.2) If yes, is the localization factor of Wei and Pierre [5] an appropriate measure of localization for this purpose?

No. In addition to existing criticisms of this measure of localization, i.e., that it is dominated by damping and does not account for disk-to-disk variations, in localization, the present investigation has demonstrated, see Figs. 10–12 and 15–16, a need to account for *blade-to-blade* variations of the localization factor.

(Q.3) Is there a genuine peak of the forced response at an intermediate blade-to-blade coupling level and what is/are the change(s) in the physics of the problem creating the peak?

Figures 5–8 demonstrate that the means and standard deviations of the maximum amplitudes on a disk (at a given frequency and in a sweep) all exhibit peaks but the peaks of the means occur at a lower coupling level than they do for the standard deviations. Further, the maximum amplitude on the population of disks does not exhibit a peak. This behavior was justified by noting that the largest amplitude of blade response is associated with mistuning that increases with the blade-to-blade coupling level. Accordingly, it was demonstrated that the peaks of the 50th, 60th, 90th, 95th, etc. percentiles of the response would all occur at different coupling levels and thus no specific peak (''worse case coupling level'') can be defined. Rather, these different peaks are located in a transition zone in which the mistuned mode shapes change from generally global to generally local (results not shown here for brevity).

(Q.4) Investigate the largest amplitude of blade response, assess the conditions under which it occurs, and evaluate the reliability of Whitehead's estimate of the quantity.

The answer to question (Q.1) clearly indicated that the response around the blade exhibiting the largest amplitude in the entire population should be very localized. Accordingly, an optimization effort to determine this largest amplitude was undertaken by using three and seven-blade partial mistuning models. Several maxima (at least two) were consistently observed but the one associated with the largest amplitude of blade response was found to correspond to mistuning of the neighboring blades that increases rapidly with the blade-to-blade coupling level. Surprisingly, it was found that this largest amplitude of response increases monotonically, i.e., is the highest at high coupling levels. Finally, a comparison of these results with those published by Whitehead [16] revealed interesting similarities. First, the amplification factor, defined as the largest amplitude divided by its tuned value, obtained from the present optimization effort at high blade coupling levels was close to the upper bound of Whitehead, i.e., 2.69 versus 2.95. Further, the application of his analysis to the present bladed disk model, see Fig. 1, yielded the optimum mistuning pattern as having only three mistuned blades and mistuning in the stiffnesses of the order of or larger than the tuned value, in close agreement with the present optimization strategy. A more thorough discussion of the behavior of the maximum amplification factor can be found in [25].

(Q.5) Can a single approximation method/computational algorithm provide reliable estimates of the mistuned forced response through the entire range of blade-to-blade coupling levels?

Yes. In view of the presence of both local and global components in the forced response of mistuned bladed disks for most blade-to-blade coupling levels, it was argued that a combination of the partial mistuning modeling and the adaptive perturbation method should be used. In fact, two novel modeling schemes were presented that *cascade*, see Eqs. (20) and (22) and (23), (24), the partial mistuning modeling and the adaptive perturbation method. Accordingly, these two local+global approximation techniques are expected to yield extremely small errors in both weak and strong coupling limits. More surprisingly, however, they are very accurate (almost indistinguishable from the exact curves) through the entire range of blade-to-blade coupling levels, see Figs. 3–8 even for very small number of modes (d) and mistuning width (s). To the authors' knowledge, Eqs. (20) and (22) and (23), (24) are the first approximation methods ever proposed that yield such a consistent matching for all blade-to-blade coupling levels.

Acknowledgments

The financial support of this investigation by the NASA grant NAG-1-2233 is gratefully acknowledged. In addition, the authors wish to express their gratitude to the University of Michigan group, Prof. C. Pierre and Drs. M. P. Castanier and R. Bladh, for the use of both REDUCE and the blisk example geometry.

References

[1] Ewins, D. J., 1969, ''The Effects of Detuning Upon the Forced Vibrations of Bladed Disks,'' J. Sound Vib. **9**, pp. 65–79.
[2] Whitehead, D. S., 1966, ''Effect of Mistuning on the Vibration of Turbomachines Blades Induced by Wakes,'' J. Mech. Eng. Sci. **8**, pp. 15–21.

[3] Kielb, R. E., and Kaza, K. R. V., 1984, ''Effects of Structural Coupling on Mistuned Cascade Flutter and Response,'' ASME J. Eng. Gas Turbines Power **106**, pp. 17–24.
[4] Basu, P., and Griffin, J. H., 1986, ''The Effect of Limiting Aerodynamic and Structural Coupling in Models of Mistuned Bladed Disk Vibration,'' ASME J. Vib., Acoust., Stress, Reliab. Des. **108**, pp. 132–139.
[5] Wei, S. T., and Pierre, C., 1988, ''Localization Phenomena in Mistuned Assemblies With Cyclic Symmetry—Part I: Free Vibrations,'' ASME J. Vib., Acoust., Stress, Reliab. Des. **110**(4), pp. 429–438.
[6] Wei, S. T., and Pierre, C., 1988, ''Localization Phenomena in Mistuned Assemblies With Cyclic Symmetry—Part II: Forced Vibrations,'' ASME J. Vib., Acoust., Stress, Reliab. Des. **110** (4), pp. 439–449.
[7] Sinha, A., and Chen, S., 1989, ''A Higher Order Technique to Compute the Statistics of Forced Response of a Mistuned Bladed Disk,'' J. Sound Vib. **130**, pp. 207–221.
[8] Lin, C. C., and Mignolet, M. P. 1997, ''An Adaptive Perturbation Scheme for the Analysis of Mistuned Bladed Disks,'' ASME J. Eng. Gas Turbines Power **119**, pp. 153–160.
[9] Wei, S.-T., and Pierre, C., 1990, ''Statistical Analysis of the Forced Response of Mistuned Cyclic Assemblies,'' AIAA J. **28**(5), pp. 861–868.
[10] Mignolet, M. P., Hu, W., and Jadic, I., 2000, ''On the Forced Response of Harmonically and Partially Mistuned Bladed Blisks. Part I: Harmonic Mistuning,'' International Journal of Rotating Machinery **6**(1), pp. 29–41.
[11] Mignolet, M. P., Hu, W., and Jadic, I., 2000, ''On the Forced Response of Harmonically and Partially Mistuned Bladed Disks. Part II: Partial Mistuning and Applications,'' International Journal of Rotating Machinery **6**, (1), pp. 43–56.
[12] Yang, M.-T., and Griffin, J. H., 2001, ''A Reduced Order Model of Mistuning Using a Subset of Nominal System Modes,'' ASME J. Eng. Gas Turbines Power **123**(4), pp. 893–900.
[13] Petrov, E., Sanliturk, E., Ewins, D. J., and Elliott, R., 2000, ''Quantitative Prediction of the Effects of Mistuning Arrangement on Resonant Response of a Practical Turbine Bladed Disc,'' *5th National Turbine Engine High Cycle Fatigue (HCF) Conference*, Chandler, AZ, Mar. 7–9.
[14] Kenyon, J. A., and Griffin, J. H., 2000, ''Intentional Harmonic Mistuning for Robust Forced Response of Bladed Disks,'' *5th National Turbine Engine High Cycle Fatigue (HCF) Conference*, Chandler, AZ, Mar. 7–9.
[15] Ibrahim, R. A., 1985, *Parametric Random Vibration*, Research Studies Press, John Wiley and Sons, New York.
[16] Whitehead, D. S., 1998, ''The Maximum Factor by Which Forced Vibration of Blades Can Increase Due to Mistuning,'' ASME J. Eng. Gas Turbines Power **120**, pp. 115–119.
[17] Castanier, M. P., Ottarson, G., and Pierre, C., 1997 ''A Reduced Order Modeling Technique for Mistuned Bladed Disks,'' ASME J. Vibr. Acoust. **119**, pp. 439–447.
[18] Bladh, R., Castanier, M. P., and Pierre, C., 2001, ''Component-Mode-Based Reduced Order Modeling Techniques for Mistuned Bladed Disks—Part II: Application,'' ASME J. Eng. Gas Turbines Power **123**(1), pp. 100–108.
[19] Castanier, M. P., and Pierre, C., 1993, ''Individual and Interactive Mechanisms for Localization and Dissipation in a Mono-Coupled Nearly Periodic Structure,'' J. Sound Vib. **168**(3), pp. 479–505.
[20] Castanier, M. P., and Pierre, C., 1997, ''Predicting Localization via Lyapunov Exponent Statistics,'' J. Sound Vib. **203** (1), pp. 151–157.
[21] Cha, P. D., and Morganti, C. R., 1994, ''Numerical Statistical Investigation on the Dynamics of Finitely Long, Nearly Periodic Chains,'' AIAA J. **32**(11), pp. 2269–2275.
[22] LaBorde, B. H., 1999, ''*Assessment of Predictive Capabilities of Mistuning Effects on the Resonant Response of Bladed Disks*,'' M.S. thesis, Arizona State University, AZ, Dec.
[23] Ottarsson, G., and Pierre, C., 1995, ''On the Effects of Interblade Coupling on the Statistics of Maximum Forced Response Amplitudes in Mistuned Bladed Disks,'' *Proceedings of the 36th Structures, Structural Dynamics, and Materials Conference and Adaptive Structures Forum*, New Orleans, LA, Apr. 10–13, **5** 3070–3078.
[24] Sinha, A., 1997, ''Computation of the Maximum Amplitude of a Mistuned Bladed Disk Assembly via Infinity Norm,'' *Proceedings of the 1997 ASME International Mechanical Engineering Congress and Exposition*, ASME, New York, Vol. AD-55, pp. 427–432.
[25] Rivas-Guerra, A. J., and Mignolet, M. P., 2003, ''Maximum Amplification of Blade Response due to Mistuning: Localization and Mode Shapes Aspects of the Worst Disks,'' ASME J. Turbomach **125**(3), pp. 442-454.
[26] Rivas-Guerra, A. J., Mignolet, M. P., and LeBorde, B. H, 2000, ''On the Value of Tuned-Like Systems for Mistuned Forced Response Analyses,'' *5th National Turbine Engine High Cycle Fatigue (HCF) Conference*, Chandler, AZ, Mar. 7–9.
[27] Nayfeh, A. H., 1981, *Introduction to Perturbation Techniques*, John Wiley and Sons, New York.

A. Kenny

A. Palazzolo

Department of Mechanical Engineering,
Texas A&M University,
College Station, TX 77843-3123

G. T. Montague

A. F. Kascak

NASA Lewis Research Center,
Cleveland, OH

Theory and Test Correlation for Laminate Stacking Factor Effect on Homopolar Bearing Stiffness

The effect of the laminate stacking factor on homopolar magnetic bearing performance is examined. Stacked laminates are used on the bearing rotor and in the stator. These laminate stacks have anisotropic permeability. Equations for the effect of the stacking factor on homopolar bearing position stiffness are derived. Numerical results are calculated and compared to measurements. These results provide an answer for the common discrepancy between test and theory for homopolar magnetic bearing position stiffnesses.
[DOI: 10.1115/1.1615258]

Introduction

Magnetic bearings often use lamination stacks in the stator poles and on the rotor. They reduce eddy current losses generated both by the rotor turning in the magnetic field and by time variation of the magnetic field. In homopolar magnetic bearings, the bias flux field travels axially through the rotor which is normal to the laminate stacks on the rotor. Figure 1 shows how the bias flux path crosses the laminated cross section of a homopolar bearing. The bias flux travels tangential to the laminates in the stator stacks, [1].

Laminate Stack Permeability

In 1980, M. L. Barton [2] published a derivation giving equations for the anisotropic relative permeability of a stack of laminates. The derivation of the relative permeability normal to the stack starts with Gauss's law, Eq. (1).

$$\nabla \cdot \mathbf{B} = 0 \tag{1}$$

This equation requires the normal flux density, B_n, at the laminate surfaces be continuous. Equation (2) then follows since the laminates are separated by a thin layer of air or adhesive.

$$B_{\text{stack}n} = \mu_o H_{\text{air}n} = \mu_{\text{lam}} \mu_o H_{\text{lam}n} \tag{2}$$

From Ampere's law an equation relating the normal magnetic field in the laminate and layer of adjoining air is given by Eq. (3).

$$l_{\text{total}} H_{\text{stack}n} = l_{\text{lam}} H_{\text{lam}n} + l_{\text{air}} H_{\text{air}n} \tag{3}$$

The definition of the stacking fraction, $f = l_{\text{lam}}/l_{\text{total}}$, combined with Eqs. (2) and (3) leads to Eq. (4). This is the dependence of the normal relative permeability of the stack on the stacking factor.

$$\mu_{\text{stack}n} = \frac{1}{\mu_o}\frac{B_{\text{stack}n}}{H_{\text{stack}n}} = \frac{\mu_{\text{lam}}}{(1-f)\mu_{\text{lam}} + f} \tag{4}$$

A similar derivation using the tangential field boundary condition leads to the relative tangential permeability of the stack given by Eq. (5).

$$\mu_{\text{stack}t} = \frac{1}{\mu_o}\frac{B_{\text{stack}t}}{H_{\text{stack}t}} = [f\mu_{\text{lam}} + (1-f)] \tag{5}$$

For a stack made out of any ferromagnetic material, the relative permeability tangential to the stack is practically given by $f\mu_{\text{lam}}$ because the stacking factor, f is just slightly less than one.

There is a dramatic difference between the relative permeability of the stack tangential and normal to the stack. Only the normal permeability is highly sensitive to the stacking factor. Figure 2 is a plot of the relative permeability of a stack versus stacking factor. Laminate stacks usually have a stacking factor less than .995 and have low values of normal permeability. These are used in the three-dimensional finite element analysis of electric machinery. For example, Timothy and Preston [3] report a using normal stack relative permeability of 20 in the finite element analysis of a large turbine generator.

Table 1 shows numerical values for the permeability normal to two stacks made from two different materials. Metal A has a value for the relative permeability μ_{lam} of 500, while metal B has a value of 5000. The effect of stacking is to make the normal permeability for both laminated stacks very much lower and almost equal. For a stacking factor of 0.99 the normal permeabilities of the two stacks differ by only 15% even though the permeabilities of the laminate metals differ by a factor of ten.

The stacking factor is affected by pressure on the laminates, laminate thickness, and the adhesive bonding technique used, [4]. Some laminate alloys require high temperature heat treatments, [5], which can affect the surface roughness and oxide thickness.

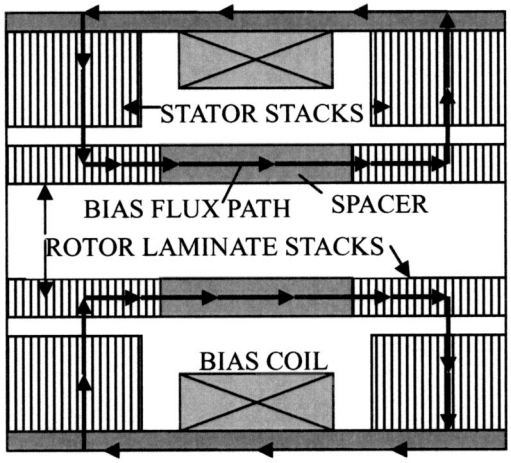

Fig. 1 Laminated bias flux path in a homopolar magnetic bearing

Contributed by the International Gas Turbine Institute (IGTI) of THE AMERICAN SOCIETY OF MECHANICAL ENGINEERS for publication in the ASME JOURNAL OF ENGINEERING FOR GAS TURBINES AND POWER. Paper presented at the International Gas Turbine and Aeroengine Congress and Exhibition, New Orleans, LA, June 4–7, 2001; Paper 2001-GT-0294. Manuscript received by IGTI, December 2000, final revision, March 2001. Associate Editor: R. Natole.

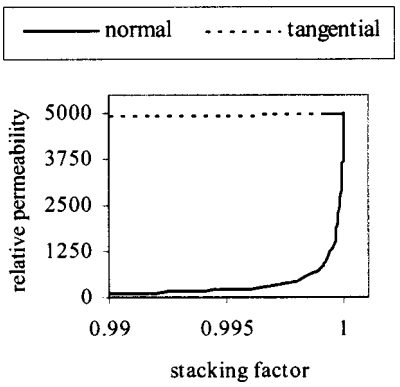

Fig. 2 Relative permeability of laminate stack

The stacking factor can be measured from the stack weight, volume, and laminate material density using Eq. (6).

$$f = \frac{\text{mass}_{\text{stack}} - \rho_a \text{vol}_{\text{stack}}}{(\rho_{\text{lam}} - \rho_a)\text{vol}_{\text{stack}}} \tag{6}$$

For cold rolled metal the surface roughness varies between 1.25 and 4.9 microns (32 and 125 micro inches), [6,7]. As shown in Fig. 3, stacking factors between .997 and .989 would result from stacked layers of .15 mm (.006 in.) cold rolled metal laminates assuming the rough regions on both sides of the laminates are air.

We made measurements on two stacks of rotor laminates made from 17.8 mm (.7 in.) and 8.8 mm (.35 in.) thick stacks of.15 mm (.006 in.) thick adhesive bonded laminates with a diameter of 44.5 mm (1.75 in.). The measurements included the stack dimensions and weight. Using the known density of the metal, the stacking factors were determined to be .981 and .987.

The stacking factor of tape wound cores tends to be lower than that of flat stacks of laminates. Table 2, [8], shows stacking factors for tape wound cores reported by one manufacturer. It indicates the average separation distance between tape wound laminates is 12 to 20 microns (.0003 to .0005 in.). The stacking factor of a core wound from 80 micron (.002 in.) thick metal tape, could be as low as 0.75.

Table 1 Numerical values of relative permeability of laminate stack

Stacking Factor	Metal A $\mu_{\text{stack}n}$	Metal B $\mu_{\text{stack}n}$
1.0	500	5000
.995	143	192
.99	83	98
.95	19	20
.92	12.2	12.5
.90	9.8	9.98
.85	6.6	6.7
.70	3.3	3.3
.50	2.0	2.0

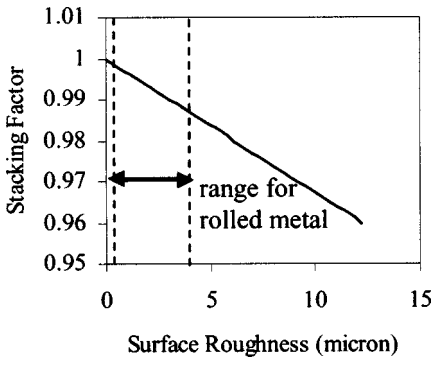

Fig. 3 Simple theoretical relation between .15-mm thick plate surface roughness and stacking factor

Table 2 Stacking factor of tape wound cores

Tape Thickness micron (in.)	Stacking Factor
205 (.012)	.95
153 (.006)	.90
102 (.004)	.90
50.8 (.002)	.85

Derivation of Position Stiffness Equations Including Stacking Factor

The homopolar bearing bias flux path circuit model is illustrated in Fig. 4. The bias flux flows normal to the rotor stack laminations which have the reluctances denoted by R_{rnp_j} and R_{rns}. These reluctances are relatively high since the laminates are normal to the flux path. The bias flux travels across a variable number of rotor laminates, depending on which laminate in the stator stack it originated. Therefor there is a specific rotor reluctance, R_{rnp_j}, Eq. (7), for each laminate, j, in the stator stack.

$$R_{rnp_j} = \frac{\frac{j}{k} l_{rnp}}{\mu_{\text{stack}n} \mu_o A_{\text{lam}}} \tag{7}$$

In Fig. 4, there is a reluctance denoted by R_{rns}, for the spacer that separates the laminated rotor sections under the left and right side poles. Because the bias flux is not time varying, sometimes the spacer is not laminated. The spacer may be a laminated stack if there is a need to minimize the eddy current power loss in the bearing. The laminates reduce the eddy currents generated because the spacer is a rotating conductor in the bias flux path. Equations (8) and (9) give the reluctance for the unlaminated and laminated spacer. The cross-section area of the back iron is often designed to equal that of the rotor spacer so that they will both magnetically saturate at once. This is the reason for the same cross-section areas, A_{lam}, in both Eqs. (8) and (9).

$$R_{rs} = \frac{l_s}{\mu_{\text{lam}} \mu_o A_{\text{lam}}} \tag{8}$$

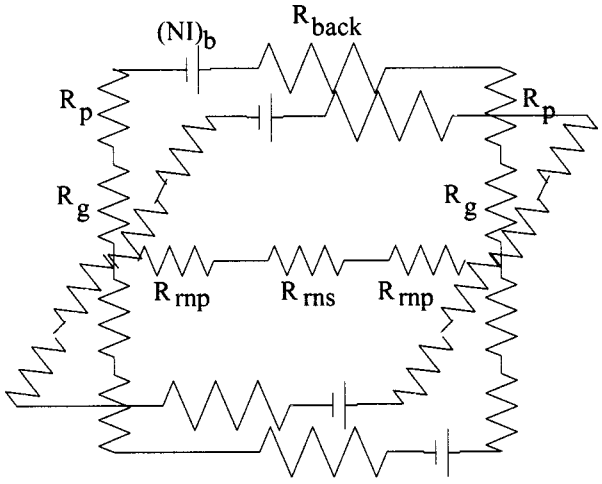

Fig. 4 Homopolar bearing bias path circuit model

$$R_{rns}=\frac{l_s}{\mu_{\text{stack}n}\mu_o A_{\text{lam}}} \tag{9}$$

The flux path width is wider in the gap since it includes the whole cross section of the laminate and the stacking factor layer. The gap cross section is therefore larger than the pole laminate by the factor $1/f$ as shown in Eqs. (10) and (11).

$$R_g=\frac{l_g}{\mu_o A_{\text{lam}}/f} \tag{10}$$

$$R_p=\frac{l_p}{\mu_{\text{lam}}\mu_o A_{\text{lam}}} \tag{11}$$

The bearing position stiffness is the ratio of the change in force on the rotor to the change in radial displacement of the shaft. Movement of the shaft alters the gap reluctance which in turn alters the bias flux and the force. The bias flux through each laminate in the pole stack is calculated via Eq. (12). For very small movements of the rotor the gap bias flux varies according to Eq. (13)–(14).

$$\Phi_{b_j}=\frac{(NI)_b}{2R_p+2R_g+R_{rns}+R_{\text{back}}+2R_{rnp_j}} \tag{12}$$

$$\Phi_{(bg+)_j}=\Phi_{b_j}\frac{l_g}{l_g+\Delta x} \tag{13}$$

$$\Phi_{(bg-)_j}=\Phi_{b_j}\frac{l_g}{l_g-\Delta x} \tag{14}$$

The magnetic force on the rotor is due to the flux density under each laminate, and the total force on the rotor is the sum of the forces from all the laminates as given by Eq. (15). The factor of two comes from the force under the two planes of the two laminated stators in this homopolar bearing. Thus the position stiffness is calculated from the limit of Eq. (16). As shown by Eq. (17), it is proportional to the square of the bias flux which is reduced by the stacking effect.

$$F_{b\text{rotor}}=2\sum_{j=1}^{k}\left(\frac{f^2\eta^2\Phi_{b+_j}^2}{2\mu_o A_{\text{lam}}}-\frac{f^2\eta^2\Phi_{b-_j}^2}{2\mu_o A_{\text{lam}}}\right) \tag{15}$$

$$K_p=\Delta x \xrightarrow{\lim} 0\ \frac{F_{b\text{rotor}}}{\Delta x} \tag{16}$$

$$Kp=\frac{4\eta^2 f^2}{l_g\mu_o A_{\text{lam}}}\sum_{j=1}^{k}\Phi_{b_j}^2 \tag{17}$$

Combining Eqs. (7)–(12) and Eq. (17) results in Eq. (18) which is the position stiffness including the effect of the stacking factor. The terms in the denominator have the greatest effect on the position stiffness. As the stacking factor decreases, the effective length of the laminated rotor spacer, l_s, and the rotor stack under the poles, l_{rnp}, increases. The squared f term in the numerator also contributes to the position stiffness decrease.

$$K_p=\frac{4(NI)_b^2 f^2\eta^2\mu_{\text{lam}}^2\mu_o A_{\text{lam}}}{l_g}\sum_{j=1}^{k}\left[\frac{1}{2\cdot l_p+l_{\text{back}}+2\cdot l_g f\mu_{\text{lam}}+\left(l_s+\frac{2j}{k}l_{rnp}\right)((1-f)\mu_{\text{lam}}+f)}\right]^2 \tag{18}$$

The bearing current stiffness is also dependent on the stacking factor. As Eq. (19) shows, it is directly proportional to the bias flux. It is reduced less by stacking than the position stiffness, since the control flux path is only tangent to the laminates.

$$K_i=\frac{8f^2\eta^2}{\mu_o A_{\text{lam}}}\frac{\partial(\phi_c)}{\partial(i)}\frac{1}{k}\sum_{j=1}^{k}\Phi_{bg_j} \tag{19}$$

The achievable bearing stiffness is affected by stacking by both the position stiffness and the current stiffness as shown by Eq. (20).

$$K_a=K_i K_{pa} K_c-K_p \tag{20}$$

Measurements and Results

Measurements of the position stiffness were made on a homopolar bearing designed for a low drag torque application. The rotor on this bearing was entirely laminated. There was no unlaminated spacer between rotor stacks under the fore and aft poles. A photograph of this bearing is shown in Fig. 5.

The measured position stiffness of this bearing was compared to the position stiffness predicted by Eq. (18). A three-dimensional magnetostatic model of the bearing was also used to predict the stiffnesses. The anisotropic relative permeability of the laminated rotor and stator was used in the FEA model rotor and stator stacks shown in Fig. 6. The relative permeabilty normal to the laminate stacks was calculated using Eq. (4), and the tangential relative permeability was calculated using Eq. (5).

The position stiffnesses that were measured and predicted are shown in Table 3. The one-dimensional circuit prediction calculated by Eq. (18) was very close to the measured value when a reasonable value for the stacking factor was used. The difference between the measured value and the one-dimensional circuit prediction was only 6.8% based on a stacking factor of .992. The

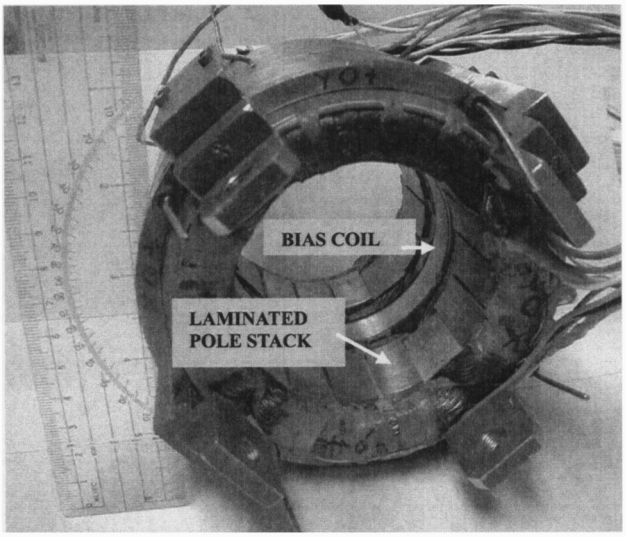

Fig. 5 Homopolar bearing for position stiffness measurements

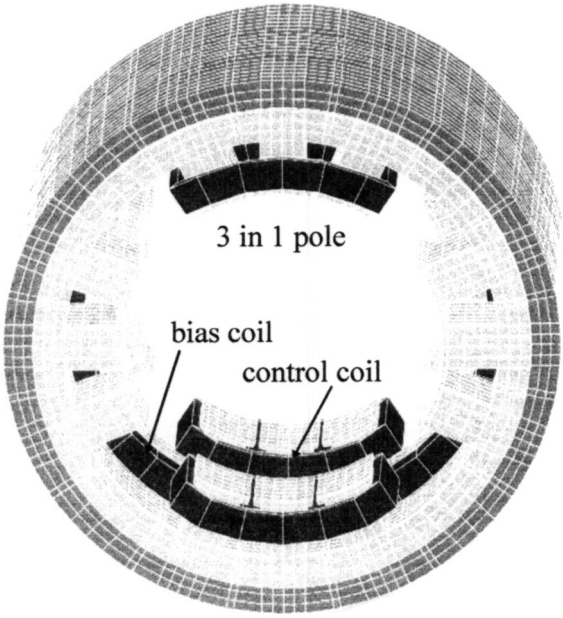

Fig. 6 Finite element model of bearing

FEA model showed similar accuracy. The difference between the FEA prediction and the measured value was only 3.3% based on a stacking factor of .993. To see the importance of including the effect of lamination, the stiffness predicted by Eq. (18) with an unlaminated rotor which would have a stacking fraction of 1.00 is included. In this case the difference between the measured value and the prediction is 153%. In other words a prediction that does not include that stacking factor cannot be expected to be close to the true value of stiffness.

Conclusions

The position stiffness in homopolar bearings is affected by the bias flux density. Since part of the bias flux path passes through the rotor normal the rotor laminate stacks, the bias flux is reduced by the low anisotropic permeability of the stack normal the laminates. The relative permeability normal to the laminate stack can be calculated using the laminate stacking factor. Then the normal relative permeability can be included in magnetic circuits and finite element models to better predict the homopolar bearing position stiffness.

Table 3 Comparison of position stiffnesses

	Position Stiffness	Percent Difference
Measured value	−1.49 MN/m −8500 LB/in	–
One-dimensional circuit Eq. (25) with $f=1.00$	−3.76 MN/m −21500 LB/in	153
One-dimensional circuit Eq. (25) with $f=.992$	−1.59 MN/m −9076 LB/in	6.8
Three-dimensional FEA model with $f=.993$	−1.44 MN/m −8218 LB/in	−3.3

Acknowledgments

The authors gratefully acknowledge the funding for this project from the Machinery Dynamics Branch and from Ray Beach each of the Space Power Systems Division at NASA Glenn Research Center. The authors also thank Mr. John Poles of NASA GRC for his excellent support in Power Electronics for the testing. The authors also gratefully acknowledge funding for this project from Tom Calvert, Lyn Peterson, and Glenn Bell of the U.S. Naval Surface Warfare Center. The authors thank Dr. David Carpenter of Vector Fields, Inc., for his expert assistance with the FEA modeling.

Nomenclature

A_{lam} = area of pole laminate flux cross section
B_g = flux density through air gap
$B_{\text{stack}n}$ = flux density normal to stack laminates
$B_{\text{stack}t}$ = flux density tangential to stack laminates
f = stacking factor
F_b = force on one pole due to bias flux
F_{bg+} = bias flux force on pole with incrementally larger gap
F_{bg-} = bias flux force on pole with incrementally smaller gap
$H_{\text{air}n}$ = magnetic field in air normal to laminate
$H_{\text{lam}n}$ = field in laminate normal to laminate
$H_{\text{stack}n}$ = field normal to stack of laminates
$H_{\text{stack}t}$ = field tangential to stack of laminates
H_t = tangential field
i = control current
j = jth laminate in stack
k = number of laminates in stack
K_a = achievable bearing stiffness
K_c = controller feedback gain
K_i = current stiffness
K_p = position stiffness of bearing
K_{pa} = power amplifier gain
l_{air} = separation distance between laminates
l_g = length of air gap
l_{lam} = laminate thickness
l_p = length of laminated pole
l_{rnp} = length of normal flux path in rotor laminates under pole
l_s = length of rotor spacer
l_{total} = total length of flux path
$\text{mass}_{\text{stack}}$ = mass of all metal and adhesive in stack
η = gap flux density fringe factor
$(NI)_b$ = bias coil current and bias coil turns
$\Phi_{(bg+)_j}$ = bias flux in larger gap under jth laminate
$\Phi_{(bg-)j}$ = bias flux in smaller gap under jth laminate
ϕ_c = control flux in gap
R_{back} = reluctance of solid back iron
R_{b_j} = reluctance of bias flux path through jth laminate
R_g = reluctance of air gap
R_p = reluctance of one laminate in pole
R_{rnp_j} = reluctance of rotor from pole laminate j to stack edge
R_{rns} = reluctance of laminated spacer on rotor
ρ_a = density of interlaminate air or adhesive
ρ_{lam} = density of ferromagnetic laminate
μ_o = permeability of air
μ_{lam} = relative permeability of ferromagnetic laminate
$\mu_{\text{stack}n}$ = relative permeability of stack normal to laminate
$\mu_{\text{stack}t}$ = relative permeability of stack tangential to laminate
$\text{vol}_{\text{stack}}$ = volume of laminate stack
Δx = incremental movement of shaft to open or close gap

References

[1] Fukata, S., Yutani, K., and Kouya, Y., 1998, ''Characteristics of Magnetic Bearings Biased With Permanent Magnets in the Stator,'' JSME Int. J., Ser. C, **41**(2), pp. 206–213.

[2] Barton, M. L., 1980, ''Loss Calculation in Laminated Steel Utilizing Anisotropic Magnetic Permability,'' IEEE Trans. Power Appar. Syst., **PAS-99**(3), pp. 1280–1287.

[3] Timothy, M. A., and Preston, T. W., 1995, ''Finite Element Modeling of Laminated Structures in Electrical Machines,'' *Proceedings IEE, 7th International Conference on Electrical Machines and Drives*, Institution of Electrical Engineers, London, pp. 121–125.

[4] De Weese, R. T., 1996, ''A Comparison of Eddy Current Effects in a Single Sided Magnetic Thrust Bearing,'' thesis, Texas A&M University, College Station, TX.

[5] Kondoleon, A. S., 2000, ''Soft Magnetic Alloys for High Temperature Radial Magnetic Bearings,'' *Proceedings 7th International Symposium on Magnetic Bearings*, ETH-Zurich (Swiss Federal Institute of Technology), Zurich, Switzerland, pp. 111–116.

[6] Beausmeister, T., et al., ed., 1978, *Mark's Standard Handbook for Mechanical Engineers*, 8th Ed., McGraw-Hill, New York.

[7] Rastogi, P. K., 1988, ''Lamination Steel Technology for Appliance Industry,'' IEEE Trans. Ind. Appl., **24**(6), pp. 982–986.

[8] Magnetic Metals Inc., 2000, *Tape Wound Core Design Manual*, Westiminister, CA.

Deterministic Micro Asperities on Bearings and Seals Using a Modified LIGA Process

L. S. Stephens
e-mail: stephens@engr.uky.edu

R. Siripuram

M. Hayden

B. McCartt

Bearing and Seals Laboratory,
University of Kentucky,
151 Ralph G. Anderson Building,
Lexington, KY 40506

Deterministic micro asperities show potential for enhancement of lubrication in conformal contacts as found in many bearing and seal designs. Several manufacturing methods have been proposed for deterministic micro asperities. Of these, laser texturing has emerged as the most viable option. This paper proposes the LIGA MEMs manufacturing method as an alternative. Using LIGA, surfaces with patterned micron sized surface features of arbitrary cross section (cylindrical, hex, triangular, etc.) can be fabricated from electroplated nickel, gel-cast silicon nitride, or plastic. The resulting asperities can be positive (protuberances) or negative (recesses) and can have heights (depths) from 1–1000 microns and be patterned over surface areas up to about 150 mm×150 mm. In this paper, the LIGA method is used to fabricate a sample thrust bearing surface with a hexagonal array of positive asperities. The resulting asperities are 550 μm in average diameter, 165 μm in edge-to-edge spacing and have heights of 3–100 μm. Surface metrology indicates submicron accuracy of form and 13 nm Ra roughness on the asperity tops (land). Tribology testing in a nonpressurized oil bath indicates full film conditions and shows a 14–22% reduction in friction coefficient for a thrust surface covered with the micro asperities. A model confirms the experimental trends and indicates the potential to further reduce the friction coefficient by about 60% through optimization of the asperity geometry and layout. [DOI: 10.1115/1.1619430]

Introduction

Micro asperities are the micro and nano-sized peaks and valleys on a surface that constitute the surface roughness. Depending on the size, shape, and distribution of these asperities, the hydrodynamic lubrication characteristics of the surface can vary significantly. On fluid bearings and seals, control of the lubrication properties using micro asperities can alter load capacity, friction torque, dynamic stiffness, and damping coefficients, among others. This, in turn, significantly affects energy consumption, reliability, and vibration in rotating machines.

A literature search has found extensive work that demonstrates the potential benefits of micro asperities to bearings and seals. Early research primarily focused on stochastic surface roughness, which occurs naturally during manufacture. The manufacturing processes are commonly engineered to create stochastic features including preferential groove orientations during machining, [1,2], controlled porosity or optimum asperity statistical distribution during ceramic forming, [3,4], or an array of microvanes that occur due to elastomer deformation in rotary lip seals, [5].

Deterministic asperities are patterned surface features with arbitrarily specified geometries that are controllable and repeatable. An important distinction is that of deterministic *micro* asperities versus deterministic *macro* asperities. Macro asperities are typically large area surface features with extremely low height to diameter (aspect) ratios (<0.0001). Unlike micro asperities, macro asperities have found widespread application since the 1970s. Examples include the use of sinusoidal waves, [6,7], radial grooves, [8], spiral grooves, [9], and hydropads, [10], on mechanical seal faces. Macro surface features are typically few in number and therefore can be manufactured with comparative ease using processes including grinding and chemical etching. By contrast, deterministic micro asperities are orders of magnitude smaller in average diameter, significantly greater in number and have larger aspect ratios (0.001–10). These properties make it extremely difficult to cost effectively manufacture large fields of asperities with controllable and repeatable geometry. One approach that has recently emerged as a viable option is that of laser texturing, [11,12], and has found application to end face mechanical seals, [13], and reciprocating automotive components, [14]. In laser texturing, negative asperities (recesses) are cut into the surface using a focused laser. The emergence of laser texturing in the mid 1990s has enabled an increase in the number of experimental studies on the effects of micro asperities on lubrication. These works have built on the early work of Hamilton, Anno, and Walowit [15–17], and confirm that the addition of patterned asperities of the appropriate size and layout can increase the hydrodynamic effect.

This paper describes the LIGA micro fabrication technique and proposes it as an alternative to laser texturing for manufacturing large fields of deterministic micro asperities on the load bearing surfaces of conformal bearings and seals. A sample thrust-bearing surface is fabricated with a hexagonal pattern of hexagonal asperities. The quality of these surface features is characterized using scanning electron microscopy and three-dimensional surface profilometry. The coefficient of friction of the thrust surface is then measured using a thrust washer rotary tribometer to demonstrate a change in lubrication properties with asperity height. Finally, a discussion is included that compares experimental and theoretical results.

Thrust Ring Fabrication

A stainless steel thrust ring was fabricated with a field of electrodeposited nickel micro asperities of hexagonal cross section on the end face. Figure 1 shows the thrust ring and the resulting asperities in a hexagonal array and Table 1 summarizes their properties. The asperities shown have a 550 μm average diameter, 165 μm edge-to-edge spacing and a height of 14 μm. This corresponds to an aspect ratio of 0.026 (height-to-diameter), an asperity area fraction of 0.59 (ratio of asperity area to total area, including spacing, associated with one asperity) and 2.5 asperities/mm^2. Mi-

Contributed by the International Gas Turbine Institute (IGTI) of THE AMERICAN SOCIETY OF MECHANICAL ENGINEERS for publication in the ASME JOURNAL OF ENGINEERING FOR GAS TURBINES AND POWER. Paper presented at the International Gas Turbine and Aeroengine Congress and Exhibition, Amsterdam, The Netherlands, June 3–6, 2002; Paper No. 2002-GT-30289. Manuscript received by IGTI, December 2001, final revision, March 2002. Associate Editor: E. Benvenuti.

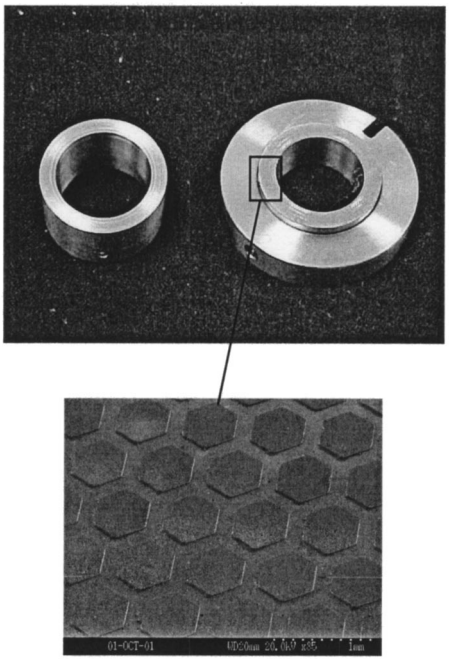

Fig. 1 Thrust ring (28.6 mm OD) with hex asperities

crohardness tests of the surface indicate that the nickel asperities have a hardness in excess of 400 Knoop (Kg/mm^2) as compared to 250 Knoop for bulk electrodeposited nickel. This increase is attributable to the smaller grain size that results from electroplating the small features [18]. On the left in Fig. 1 is the mating thrust ring made of soft bronze with a hardness of approximately 100 Knoop. This ring rotates against the sample thrust ring during tribology testing. Due to its significantly lower hardness, any wear that occurs will be on the bronze ring.

Fabrication of the micro asperities on the stainless steel thrust ring is accomplished using the LIGA process that has been at the leading edge of MicroElectroMechanical systems (MEMs) development. LIGA is a three-step process comprised of X-ray lithography, electroforming, and molding, [19,20], as illustrated in Fig. 2. Several aspects of LIGA are distinct from the more common silicon microfabrication techniques. X ray radiation, rather than visible or ultraviolet light, is used to pattern thick layers of resist with sharp corners and vertical sidewalls. The LIGA process proceeds by bonding a sheet of poly-methyl-methacrylate (PMMA)

Table 1 Properties of experimental thrust surface

Description	Symbol	Units	Value
Stationary ring material	—	—	Stainless steel
Asperity material	—	—	Electroplated nickel
Thrust ring OD	D_o	mm	28.6
Thrust ring ID	D_i	mm	25.4
Asperity cross section	—	—	Hexagonal
Asperity pattern	—	—	Hexagonal
Asperity height	h_1	μm	3–100
Asperity average diameter	d_{asp}	μm	550
Edge-to-edge spacing	E	μm	165
Asperity density	N_{asp}	Asp/mm^2	2.5
Area fraction	δ^2	—	0.59
Aspect ratio	$\alpha = h_1/R_o$	—	0.006–0.182
Asperity hardness	—	Knoop	400

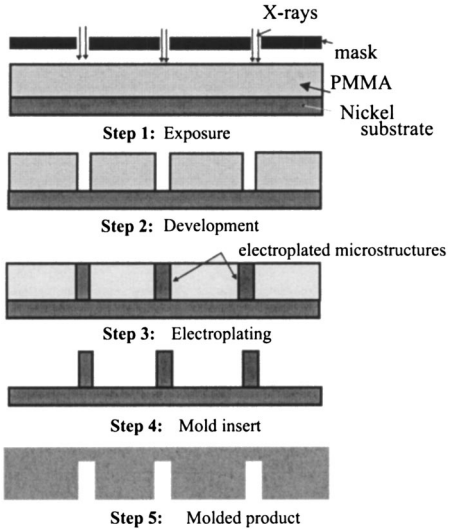

Fig. 2 LIGA microfabrication process

resist to a conductive metal substrate. The thickness of the PMMA is typically equal to the desired height of the microstructure. The PMMA metal substrate laminate is positioned behind a mask, and exposed to a collimated X-ray beam. A synchrotron provides the source of X-ray radiation with a characteristic wavelength of approximately 0.5 nanometers and is a principal resource of microsystem development. The molecular weight of the PMMA decreases in irradiated area. After the PMMA sheet is exposed to the proper radiation dose, it is immersed in a developer that dissolves the irradiated areas with low molecular weights. The resulting PMMA template is used to electroplate microstructures on the substrate. After the electroplating process is completed, the remaining PMMA is removed (dissolved), resulting in a metal surface covered with microstructures. The microstructure-covered sheet sometimes represents the final product, or it may serve as a mold that can be inserted into an injection molding or hot embossing machine to repeatedly reproduce a secondary polymer template with geometry identical to the primary PMMA template, [21]. This molding process is the step that makes LIGA MEMS cost effective when applied to mass-produced components. It essentially decouples the manufacturing process from the X-ray source for all manufactured components except the initial one, allowing for the initial cost to be shared by the subsequent components. Recent modifications, [22], to the latter steps in the LIGA process allow fabrication using gel cast silicon nitride and moldable plastic.

Figure 3(*a*) shows the polymer template (PMMA) used for electrodeposition of the hexagonal array of micro asperities in this study. This template is 1000 μm thick and therefore can be used to electroplate hexagonal asperities up to 1000 μm tall. Shorter asperities are obtained by simply terminating electrodeposition at the desired height. The polymer template is clamped to the end face of the thrust ring using a special jig. The entire jig is immersed into the electroplating solution and nickel is electrodeposited into the through holes of the polymer sheet and onto the end face of the thrust ring. Figure 3(*b*) shows an aerial view of the resulting micro asperities.

Experimental

Surface Metrology. One key factor in determining the effects of micro asperities on lubrication properties is the controllability and repeatability of micro asperity geometry. In fact, [16] hypothesized the reason for a large difference in experimental versus theoretical load capacity in their work was an error in the resulting asperity geometry. (The authors assumed the asperity lands were

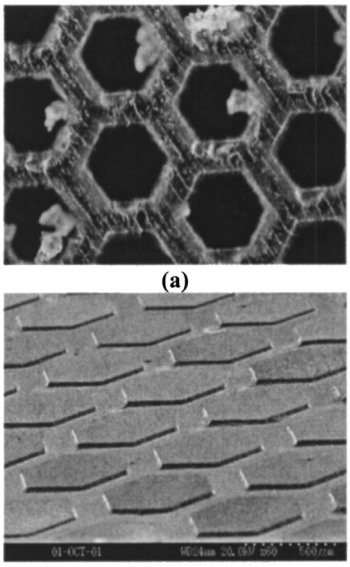

Fig. 3 (*a*) **PMMA template used for electroplating process;** (*b*) **electroplated nickel hexagonal asperities** (**550** μ**m avg diameter, 165** μ**m edge-to-edge, 14** μ**m tall**)

perfectly flat but later hypothesized that they were actually tilted, creating a converging wedge. However, at the time of the work the surface metrology was unavailable to verify this claim.) With the advent of scanning electron microscopy and three-dimensional optical surface profilometry this limitation no longer exists at the micro/nano scale.

The thrust ring sample of Fig. 1 was lapped and polished such that the asperity surface was flat to within 2 helium light bands as measured using monochromatic light source and optical flats. An analysis of the surface using SEM was then performed. Figure 4(*a*) shows a detail of a typical asperity from the surface and indicates there is a small radius of curvature of approximately 1.2 μm where the bottom of the asperity meets the substrate. Also, on the asperity top (the land), very small scratches can be seen that resulted from lapping and polishing. Figure 4(*b*) shows a close up of one such scratch that is measured at 800 nm in width. Finally, the asperity sidewalls are found to be vertical to submicron accuracy.

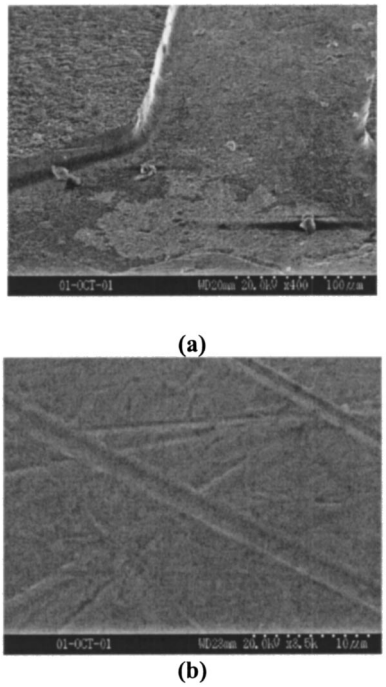

Fig. 4 (*a*) **SEM detail of hexagonal micro asperity,** (*b*) **800 nm wide scratch on asperity land**

To further characterize the surface, the ring was mounted in a noncontacting three-dimensional surface profiler and several topographical features were measured. The measurements indicated a surface roughness of 13 nm Ra and 15 nm RMS on the asperity top (land), an average asperity height of 25.3 μm, and a tilt (inclination) of the land of 3.9 μm/mm. Since the asperity height is the least controllable parameter in the electroplating process, it is adjusted by electroplating to a slightly larger than desired height and successively lapping and measuring until the desired height is reached.

Tribology Testing. At issue is the effect of the micro asperities on lubrication properties. To observe this, the coefficient of friction between the thrust ring with asperities and the soft bronze rotary ring was measured using an ASTM Standard D3702 thrust washer rotary tribometer. The test procedure consists of sample surface preparation, complete characterization of the sample surfaces, controlled testing of each specimen, and computerized data logging and storage.

Sample surface preparation and characterization are critical for correct interpretation of results. The specimen surfaces are lapped (with not more than 6890 N/m^2 (1 psi) of pressure to eliminate damage to the specimen) to the desired post height and flatness. The surfaces are then polished, ultrasonically cleaned and washed with acetone.

The thrust washer tribometer is presently capable of recording temperature, friction moment, applied load, and rotational speed. Figure 5 is a schematic of the setup and illustrates the 5:1 lever arm used to apply an axial load to the specimen, an interface load cell used to measure the load and a 10:1 moment arm that measures the frictional moment. Proper alignment is critical when attaching the specimen holders to the tribometer. This is accomplished through alignment springs and setscrews to lock the holder in place. A damping pad is placed under the stationary specimen to reduce any vibrations that may occur. Similar test rigs have been developed to measure the effects of surface features on friction coefficient and load support, [12,13,23,24]. Some of these rigs have used air bearings or other precision components to increase the resolution of the friction coefficient measurement. These setups are optimal for hydrodynamic conditions where the friction torque is very low like that found in water-lubricated studies. Most of these rigs use a pressurized lubricant chamber to simulate conditions similar to those found in end face mechanical seals. The present test rig is similar to that found in [23] without a pressurized lubricant chamber. Such a configuration removes from the measurement any hydrostatic lubrication effect that occurs due to Poiseuille flow in the radial direction.

A wear-in period is required for the soft bronze rotating ring to ensure that proper mating occurs between the surfaces during testing. After the wear-in step is complete the rotating specimen is then re-polished and the surface is characterized using SEM and profilometry. The sample thrust ring with micro asperities is placed into the tribometer and a baffled lubricant cup filled with a nonpressurized oil is placed around the system. Thermocouples are used to record the temperature during testing at different locations in the lubricant. Finally, a computer based data acquisition system is used to record the data. A medium weight oil with a viscosity of 42–110 cP over the test temperature range was used during the tribology tests. In all tests the applied face load was 0.1 N/mm^2 (14.4 psi).

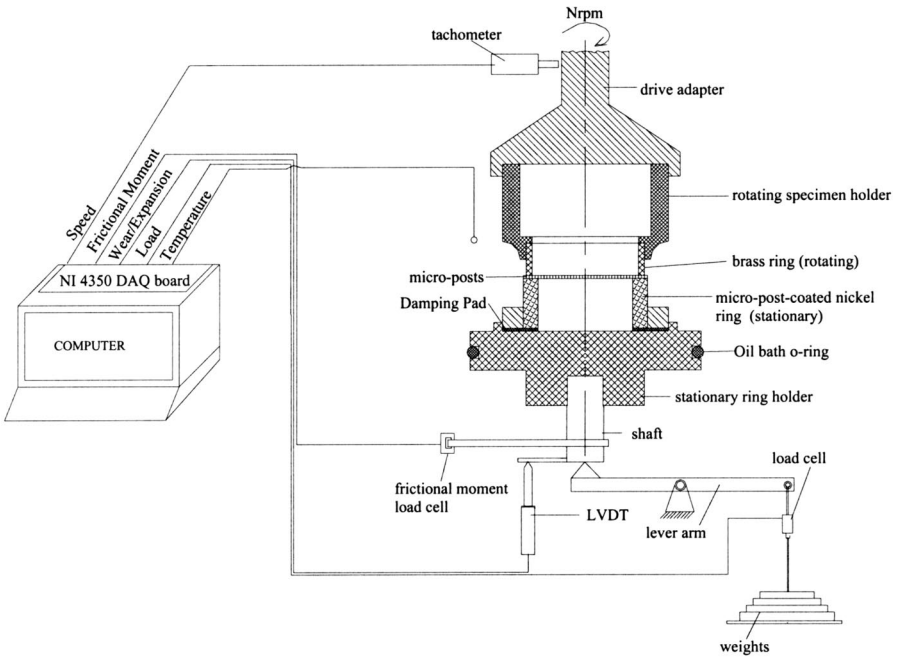

Fig. 5 Tribometer schematic

Figure 6 shows the friction coefficient at different rotational speeds between 700 and 4000 rpm for an asperity height of 7 μm (aspect ratio of 0.013). This is compared to the friction coefficient for a thrust ring constructed of the same material (stainless steel ring with electroplated nickel coating) but with no surface features (plain) and a surface roughness of 120 nm Ra after lapping. This figure shows that the friction coefficient increases with speed, which is consistent with hydrodynamic lubrication at higher bearing numbers (ZN/P). Figure 6 also indicates that the addition of the micro asperities results in a moderate reduction in friction coefficient of approximately 14.2% over all speeds. One factor that was not controlled during the first experiment was the temperature of the lubricant, which ranged from 21.1°C to 40.6°C. A second group of experiments were performed in which the temperature was held constant during testing. In these experiments, the asperity height was varied by subsequent lapping and polishing of the surface features. For all cases, the applied face load was again 0.1 N/mm^2 and the rotational speed was 2500 RPM (surface velocity of 3.5 m/s (694 ft/min) and PV of 0.35 MPa-m/s).

Figure 7 shows the resulting friction coefficients at various increases in lubricant temperature over ambient for asperity heights of 0, 3.0 μm, 7.0 μm, 14 μm, and 100 μm. (The 100 μm specimen was fabricated separately.) The values for coefficient of friction are the average of 30 data points per bar with a standard deviation less than 0.004 in all cases. Also shown in Fig. 7 is the measured friction coefficient (0.75) for the plain ring under boundary-lubricated conditions (no fluid lubrication). The experimental trends of Figs. 6 and 7 are consistent with the transition from hydrodynamic to mixed lubrication, indicating that the plain, 3 μm, 7 μm, and 14 μm specimens are operating in the hydrodynamic lubrication regime and the 100 μm specimen is operating in the mixed regime. Further, Fig. 7 illustrates the existence of an optimal asperity height for a given array geometry and operating condition resulting in a 14–22% reduction in friction coefficient as compared to the plain specimen.

Theoretical

To aid in the discussion of the experimental results, a hydrodynamic model is taken from the literature, [15]. This model considers a *unit cell* of the asperity pattern, which consists of a single

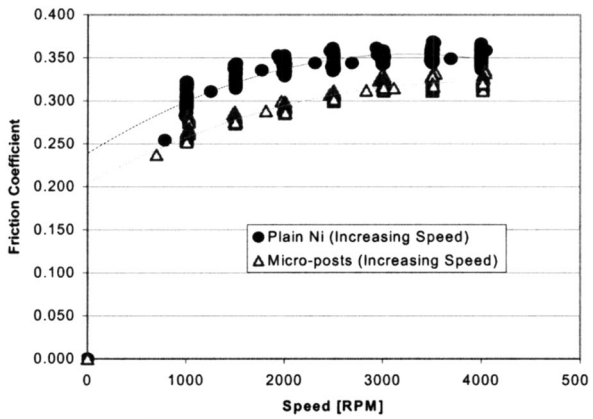

Fig. 6 Exp. friction coefficients (7 μm tall asperities)

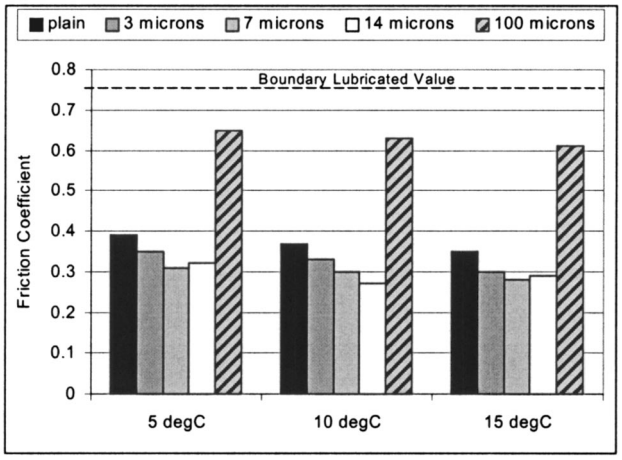

Fig. 7 Exp. friction coefficient versus asperity height

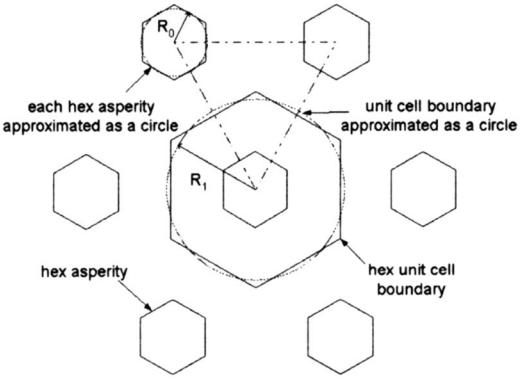

Fig. 8 Asperity pattern and isobars

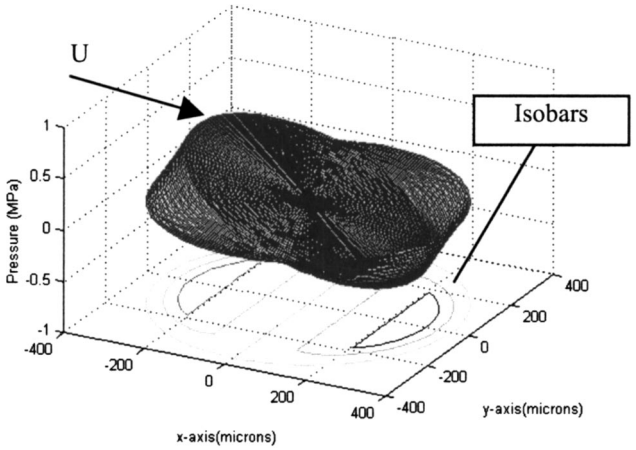

Fig. 10 Pressure distribution over unit cell

asperity and its surrounding cavity (area between asperities). Figure 8 shows a single unit cell and the adjacent asperities for the hexagonal pattern. All asperities are equally spaced, therefore each asperity has a hexagonal unit cell as shown. Each vertex of the hexagonal unit cell is the circumcenter of an equilateral triangle formed by the centers of the corresponding three asperities. The pressure distribution at these vertices and at the midpoints between any two asperities is equal to the ambient pressure, P_∞. The hexagonal unit cell boundary is therefore an isobar. Taking the approach as in [15], both the hex boundary and asperity are approximated as circles with radii, R_1 and R_0, respectively. Figure 9 shows the interaction of the rotating surface (slider) with a single asperity of height, h_1. The lubricant has absolute viscosity, μ, film thickness, h_0, and the rotating ring has an average linear velocity, U. Assuming a perfectly flat asperity land, the film thickness is then

$$h(r)=\begin{cases} h_0 & r<R_0 \quad \text{(above asperity)} \\ h_1+h_0 & r>R_0 \quad \text{(between aperities)} \end{cases}. \tag{1}$$

Further, assuming laminar flow of a thin film, no pressure variation across the film, no slip at the film boundaries, negligible body forces, and a Newtonian fluid with constant density and constant viscosity across the film, Reynolds equation governs the steady-state pressure distribution in both the region above the asperities and between the asperities. Since the film thickness is constant in both regions, Reynolds equation reduces to Laplaces equation, [15]:

$$\frac{\partial}{\partial r}\frac{r\partial P}{\partial r}+\frac{1}{r}\frac{\partial^2 P}{\partial \theta^2}=0 \tag{2}$$

where $P(r,\theta)$ is the hydrodynamic pressure. Note that Reynolds equation is limited to smaller values of h_1/h_0 where the laminar flow and negligible fluid inertia assumptions remain valid, and to lower shear rates where the Newtonian fluid assumption remains valid. The solution for the steady-state pressure distribution both above and between the asperities and including the interaction of adjacent asperities is then (see [15] for details)

$$P(r,\theta)=p(r)\cos\theta \tag{3}$$

where

$$p(r)=\frac{-6\mu U R_0 h_1}{h_0^3+\left(\dfrac{1+\delta^2}{1-\delta^2}\right)(h_0+h_1)^3}\psi \tag{4}$$

and

$$\psi=\begin{cases} \dfrac{r}{R_0} & 0\leqslant r/R_0\leqslant 1 \quad \text{(above asperities)} \\ \dfrac{\left(\dfrac{R_0}{r}-\delta^2\dfrac{r}{R_0}\right)}{(1-\delta^2)} & 1\leqslant r/R_0\leqslant R_1/R_0 \quad \text{(between asperities)} \end{cases}. \tag{5}$$

The parameter δ^2 is the asperity area fraction, which is defined as the ratio of the asperity area to the total unit cell area or $(R_0/R_1)^2$.

Figure 10 shows the resulting pressure distribution over a unit cell for the thrust ring sample geometry with asperity height, $h_1=14\ \mu$m and a slider speed of 2500 rpm (3.5 m/s). It is well known that the hydrodynamic load generating mechanism for surface asperities is the local cavitation effect, which limits the lower bound on the pressure distribution to the cavitation pressure (either the fluid vapor pressure or the pressure at which the fluid is saturated with the gas dissolved in it.) For simplicity, the load support per unit area of the thrust ring is computed using the approach in [11,15,25] that assumes the half Sommerfeld cavitation condition. While this assumption results in a lower bound on the actual load capacity, this is sufficient for discussion since the trends are largely preserved. Using the half Sommerfeld condition the pressure $P(r,\theta)$ is replaced with the cavitation pressure, P_c, whenever $P(r,\theta)\leqslant P_c$. The resulting total load support per unit area of thrust ring surface area is calculated as

$$W=\frac{\delta^2}{\pi R_0^2}\int_0^{2\pi}\int_0^{R_1}P(r,\theta)r\,dr\,d\theta. \tag{6}$$

In addition to the pressure distribution and load capacity, an

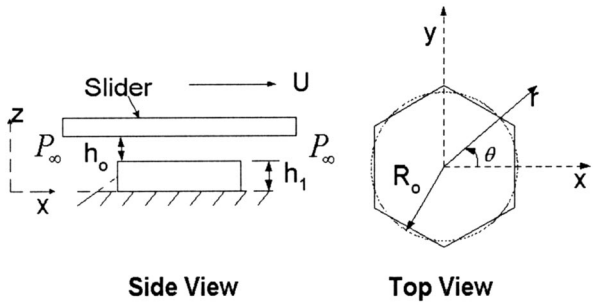

Fig. 9 Asperity layout

Table 2 Experiment versus theory for 0.1 N/mm^2, 2500 rpm

Asperity Height h_1	Experiment		Theory	
	Friction Coeff.	Film Thickness h_o	Friction Coeff.	Film Thickness h_o
Plain	0.39	8.8 μm	—	—
3 μm	0.34	9.3 μm	0.40	8.0 μm
7 μm	0.30	9.7 μm	0.37	7.8 μm
14 μm	0.32	8.1 μm	0.52	4.8 μm
100 μm	0.65	—	—	—
Boundary	0.75	—	—	—

expression for the friction coefficient is arrived at by considering the total frictional force over the thrust ring surface:

$$F_f = \int \tau dA \tag{7}$$

where the shear stress is approximated by

$$\tau \cong \frac{\mu U}{h}. \tag{8}$$

Using the film thickness of Eq. (1) in (7) and (8) yields an expression for the coefficient of friction as

$$f = \frac{\mu U}{W}\left[\frac{\delta^2}{h_0} + \frac{(1-\delta^2)}{h_0 + h_1}\right]. \tag{9}$$

Clearly, for very large asperity area fractions, δ^2, the area above the asperity dominates the friction coefficient, and for very low values the area between asperities will dominate.

Discussion

Comparison of Theory and Experiment. The experimental friction coefficients presented in Fig. 8 were used directly in Eq. (9) to compute an experimental film thickness. A theoretical film thickness was estimated by using the experimental values for applied load, viscosity, asperity height, surface velocity, and geometry in the hydrodynamic model. The theoretical film thickness was then used in Eq. (9) to compute a theoretical friction coefficient for comparison.

Table 2 compares the experimental and theoretical friction coefficients. The theoretical results are consistent with the experimental ones, predicting full film load support for 3 μm, 7 μm, and 14 μm asperity heights and no load support (mixed lubrication) for the 100 μm tall asperities. The theoretical friction coefficients are somewhat larger than the experimental ones but on the same order. The trends are similar and both indicate that an optimal asperity height of around 7 μm minimizes friction over the test conditions. Finally, a drastic increase occurs in the experimental friction between the 14 μm and 100 μm cases (from 0.32 to 0.65, which is close to the boundary lubricated value of 0.75). This is consistent with a loss of full film lubrication conditions. As a further comparison, the magnitudes of the friction coefficients reported in this study are in the range of those reported in [16] for oil lubricated positive asperities operating at similar bearing numbers (friction coefficients there were as high as 0.8 in full film operation). This is in contrast to more recent work, [23,24], where friction coefficients significantly less than 0.1 were reported for water lubricated seals with deterministic asperities. Table 2 also summarizes the theoretical and experimental film thickness. The theoretical values are slightly lower than the experimental values but within about 20%. Further, both sets of data indicate that the average film thickness (which includes the asperity height) increases as the friction coefficient decreases, as one would expect from Eq. (9).

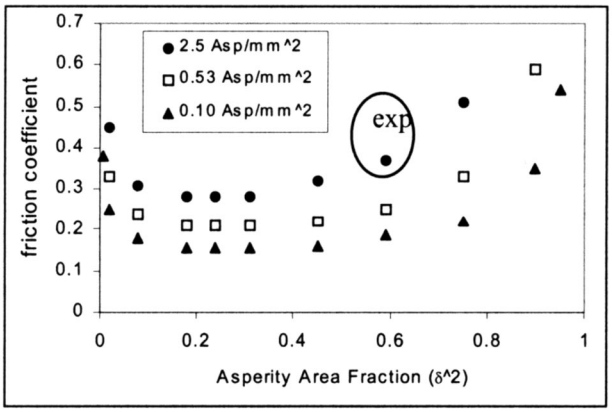

Fig. 11 Theoretical friction coefficient for 7 μm height

The model is used further to investigate the existence of an asperity geometry and layout that would result in a lower friction coefficient than those measured for the same operating conditions. Figure 11 shows the friction coefficient versus asperity area fraction for 7 μm tall asperities. The friction coefficient is plotted for 2.5, 0.53, and 0.10 asperities/mm^2. The point corresponding to the experiment is also indicated. This figure shows that with proper asperity pattern geometry, the friction coefficient can be reduced by more than 60% over the plain thrust ring (from 0.39 to 0.15). The figure also indicates that friction increases drastically if the asperity area fraction is at either extreme. This trend was also found in Ref. [11] for negative asperities. Finally, Fig. 11 indicates that the friction coefficient decreases with a smaller number of asperities/mm^2. Physically, this means that for the medium weight oil the optimal asperity distribution is a small number of large diameter asperities (aspect ratios of around 0.004). This is consistent with the trend found in [11] that showed the optimal asperity size increases with fluid viscosity.

Practical Considerations. The results of this study clearly demonstrate that the addition of LIGA micro asperities to a thrust surface leads to an increase in hydrodynamic lubrication and results in lower friction coefficients. This benefit, however, comes at the expense of a larger average film thickness, which leads to an increase in bulk fluid flow through the asperity field. In the case of a bearing this increases the oil supply flow rate through the surface. In the case of a seal this increases the leakage rate and calls into question the effectiveness of using surface features in these applications. However, there are several arguments in favor of asperities on seal faces. First, the increased leakage can be alleviated somewhat by using negative asperities which results in a smaller average film thickness. A second approach is to use designs such as those in [26,27] that use positive upstream pumping features to limit leakage. Finally, the increased lift due to asperities allows the use of a higher spring load in seal applications that can reduce the film thickness to a point with acceptable leakage and friction torque. (In the case of positive asperities this is less effective.) The increased spring load has the added benefit of reducing the tendency of secondary seals to hang up during operation.

The results demonstrate that the LIGA manufacturing method is capable of producing large fields of very accurate, deterministic surface features on thrust surfaces. Using information from Refs. [12, 13, 14, 24], Table 3 was compiled as a comparison between LIGA and the laser texturing method. LIGA can produce either positive (proturberances) or negative (recesses) asperties of any cross section, where laser texturing can produce only negative asperities of spherical or conical geometry. Negative asperities are advantageous in many sealing applications, [11–14], because the leakage across the seal face is minimized for the same film thick-

Table 3 LIGA Comparison

Property	Laser Texturing	LIGA
Asperity convexity	Negative	Negative and positive
Asperity shape	Spherical or conical	Any arbitrary cross section; vertical sidewalls
Asperity height (depth)	1–30 μm	800 nm–2 mm
Asperity diameter	95–250 μm	2–1000 μm
Aspect ratio	0.004–0.3	0.001–20
Edge-to-edge spacing	No appreciable limit	No appreciable limit
Specimen size	No appreciable limit	No appreciable limit
Asperity quality	Heat effected zone & cracking	Excellent

ness. However, positive asperities are advantageous in other designs, [26,27], because they can be used for upstream pumping. LIGA clearly has more flexibility in fabricating a significantly larger range of different asperity geometries, offering the opportunity for many more designs.

One present limitation with LIGA is in generating asperities with other than vertical sidewalls. Reference [28] discussed two possible mechanisms that may be the cause of enhanced lubrication when using asperities: (1) the hydrodynamic lift at each asperity is increased; and (2) the asperity cavities serve as reserviors that supply an even distribution of fluid to a larger number of asperities (less lubricant starvation). In the case of the former, laser texturing has an advantage over LIGA due to the spherical or conical shape which enables a continuously converging wedge. In the case of the latter effect, the LIGA asperities with vertical sidewalls would be just as effective. The author is aware of at least one research effort with LIGA that is making progress towards tapered (nonvertical) sidewalls and may alleviate this limitation.

From a materials perspective LIGA is capable of producing asperities in electrodeposited metals (predominantly nickel), gelcast ceramics such as silicon nitride and molded plastic or rubber parts. This places LIGA somewhat at a disadvantage to laser texturing which machines asperities directly into the native component material. The laser process, however, may result in a heat effected zone with localized cracks around the asperities, [24]. This effectively decreases the fatigue resistance of the material.

Finally, the relative manufacturing cost of the two processes depends upon the component being produced. LIGA is more expensive at the front end of the process, requiring a synchrotron radiation source. However, progress is being made in the use of photolithography using UV light in place of X-rays that will significantly reduce this cost. Secondly, since LIGA is a molding process, the cost of the initial exposure can be spread out over many mass produced units. In the final analysis, each manufacturing technique has its own advantages and disadvantages depending upon the specific design goal.

Conclusions and Summary

This paper described the LIGA fabrication method that was recently configured to produce large fields of deterministic micro asperities on bearing and seal geometries. A sample bearing surface was fabricated, and SEM and three-dimensional surface profilometry demonstrated that the LIGA method was successful in producing controllable and repeatable deterministic micro asperities with submicron accuracy of form, 13 nm Ra surface roughness on the asperity tops (land) and flatness to within 3.9 μm/mm. A series of tribology tests in an oil bath indicated that the presence of the deterministic micro asperities reduced the coefficient of friction between 14–22%. The experimental results also demonstrated the existence of an optimal asperity height for a given array geometry. Finally, theoretical results indicated that a further decrease in friction coefficient is achievable if asperity geometry and layout are optimized.

Acknowledgments

The authors wish to express their appreciation to the Zygo Corporation of Orlando, Florida, the University of Kentucky Materials Characterization Facility and the University of Kentucky 2D/3D Micro/Nano Fabrication Facility for assistance with the metrology measurements. The authors also thank the Louisiana State University μSET Team and Center for Advanced Microstructures and Devices for supplying the PMMA templates used for electroplating.

References

[1] Tonder, K., 1987, ''Effects of Skew Unidirectional Striated Roughness on Hydrodynamic Lubrication,'' Wear, **115**, pp. 19–30.
[2] Davies, M. G., 1961, ''The Generation of Lift by Surface Roughness in a Radial Face Seal,'' International Conference on Fluid Sealing, British Hydromechanics Research Association, Harlow, Essex, UK.
[3] Divakar, R., 1994, ''Sintered Silicon Carbides with Controlled Porosity for Mechanical Face Seal Applications,'' Lubr. Eng., **50**(1), pp. 75–80.
[4] Cusano, C., 1972, ''Lubrication of Porous Journal Bearings,'' J. Lubr. Technol., pp. 69–73.
[5] Day, Kevin, and Salant, Richard F., 1999, ''Thermal Elastohydrodynamic Model of a Radial Lip Seal—Part 1: Analysis and Base Results,'' ASME J. Tribol., **121**, pp. 1–10.
[6] Burton, R. A., 1963, ''Effect of Two-Dimensional, Sinusoidal Roughness on the Load Support Characteristics of a Lubricant Film,'' J. Basic Eng., **85**, pp. 258–264.
[7] Young, L. A., and Lebeck, A. O., 1989, ''The Design and Testing of a Wavy-Tilt-Dam Mechanical Face Seal,'' Lubr. Eng., **45**(5), pp. 322–329.
[8] Shellef, R. A., and Johnson, R. P., 1992, ''A Bi-Directional Gas Face Seal,'' Tribol. Trans., **35**(1), pp. 53–58.
[9] Pecht, G. G., and Carter, D., 1989, ''System Design and Performance of a Spiral Grove Gas Seal for Hydrogen Service,'' Tribol. Trans., **46**(9), pp. 607–612.
[10] Kojabashian, C., and Richardson, H. H., 1967, ''A Micropad Model for the Hydrodynamic Performance of Carbon Face Seals,'' *Proceedings of the Third International Conference on Fluid Sealing*, A. L. King, B. S. Nau, and H. S. Stephens, eds., British Hydromechanics Research Association, UK, pp. E4-41—E4-71.
[11] Etsion, I., and Burstein, L., 1996, ''A Model for Mechanical Seals With Regular Microsurface Structure,'' Tribol. Trans., **39**(3), pp. 677–683.
[12] Etsion, I., Halperin, G., and Greenberg, Y., 1997, ''Increasing Mechanical Seals Life With Laser-Textured Seal Faces,'' *Proc., 15th Int'l. Conference on Fluid Sealing*, BHR, pp. 3–11.
[13] Etsion, I., Kligerman, Y., and Halperin, G., 1999, ''Analytical and Experimental Investigation of Laser-Textured Mechanical Seal Faces,'' Tribol. Trans., **42**(3), pp. 511–516.
[14] Ronen, A., Etsion, I., and Kilgerman, Y., 2001, ''Friction-Reducing Surface-Texturing in Reciprocating Automotive Components,'' Tribol. Trans., **44**(3), pp. 359–366.
[15] Hamilton, D. B., Walowit, J. A., and Allen, C. M., 1996, ''A Theory of Lubrication by Microirregularities,'' J. Basic Eng., pp. 177–185.
[16] Hamilton, D. B., Walowit, J. A., and Allen, C. M., 1968, ''Microasperity Lubrication,'' J. Lubr. Technol., pp. 351–355.
[17] Anno, J. N., Walowit, J. A., and Allen, C. M., 1969, ''Load Support and Leakage From Microasperity-Lubricated Face Seals,'' J. Lubr. Technol., pp. 726–731.
[18] Stephens, L. S., Simhadri, S., McCandless, A. B., Kelly, K. W., and Meletis, E. I., 2001, ''Mechanical Property Evaluation and Failure Analysis of Cantilevered LIGA Nickel Microposts,'' J. Microelectromech. Syst., **10**(3), pp. 347–359.
[19] Becker, E. W., Ehrfeld, W., Hagmann, P., Maner, A., and Munchmeyer, D., 1986, ''Fabrication of Microstructures With Extreme Structural Heights by Synchrotron Radiation Lithography, Galvanoforming and Plastic Moulding (LIGA Process),'' Microelectron. Eng., **4**, pp. 35–56.
[20] Hagmann, P., Ehrfeld, W., and Vollmer, H., 1987, ''Fabrication of Microstructures With Extreme Structural Heights by Reaction Injection Molding,'' Makromolkulare Chemie-Macromolecular Symposia, **24**, pp. 241–251.
[21] Marques, C., Desta, Y., Rogers, J., Murphy, M., and Kelly, K., 1997, ''Fabrication of High Aspect Ratio Microstructures on Planar and Nonplanar Surfaces Using a Modified LIGA Process,'' J. Microelectromech. Syst., **6**(4), pp. 329–336.
[22] Kelly, K. W., Harris, C., Stephens, L. S., Marques, C., and Foley, D., 2001, ''Industrial Applications for LIGA-Fabricated Micro Heat Exchangers,'' SPIE 2001 Symposium on Micromachining and Microfabrication, Proc. 4559, San Francisco, CA, Oct.
[23] Lubbinge, H., Schipper, D. J., and Bakx, S., 1997, ''A Test Rig for Measuring Friction and Load Carrying Capacity for Mechanical Face Seals,'' *Proc., 15th International Conference on Fluid Sealing*, BHR, pp. 539–551.

[24] Wang, X., Kato, K., Adachi, K., and Aizawa, K., 2001, ''The Effect of Laser Texturing of SiC Surface on the Critical Load for the Transition of Water Lubrication Mode from Hydrodynamic to Mixed,'' Tribol. Int., **34**, pp. 703–711.
[25] Burstein, L., and Ingman, D., 1999, ''Effects of Pore Ensemble Statistics on Load Support of Mechanical Seals With Pore-Covered Faces,'' ASME J. Tribol., **121**, pp. 927–932.
[26] Muller, H. K., Schefzik, C., Wallace, N., and Evans, J., 1997, ''Laserface Sealing Technology: Analysis and Application,'' *Proc., 15th International Conference on Fluid Sealing*, BHR, pp. 13–25.
[27] Otto, D. L., Allen, C. M., and Walters, C. T., 1971, ''Wear Surface and Seal Construction,'' United States Patent # 3,586,340.
[28] Lo, S. W., and Horng, T. C., 1999, ''Lubricant Permeation From Micro Oil Pits Under Intimate Contact Condition,'' ASME J. Tribol., **121**, pp. 633–638.

G. R. Leverant
H. R. Millwater
R. C. McClung
M. P. Enright

Southwest Research Institute,
6220 Culebra Road,
San Antonio, TX 78238-5166

A New Tool for Design and Certification of Aircraft Turbine Rotors

This paper summarizes recent enhancements to a probabilistic damage tolerance software code, DARWIN™, that can be used for design certification of aircraft jet engine titanium disks/rotors that may contain melt-related anomalies. Evaluations of DARWIN™ by engine manufacturers are also discussed, including comparisons with existing codes for accuracy and time efficiency. In addition, relevant test results, including various fatigue tests on material containing melt-related anomalies, are summarized.
[DOI: 10.1115/1.1622409]

Introduction

A probabilistically based damage tolerance software code called DARWIN™ (Design Assessment of Reliability With Inspection) has been developed to supplement the current safe-life approach for low-cycle fatigue design of titanium disks/rotors in aircraft gas turbine engines. DARWIN™ is a computer program that integrates finite element stress analysis, fracture mechanics analysis, nondestructive inspection simulation, and probabilistic analysis to assess the risk of rotor failure. It computes the probability of fracture as a function of flight cycles, considering random defect occurrence and location, random inspection schedules, and several other random variables. Both Monte Carlo and advanced, fast integration methods are integral to the probabilistic driver. A fracture mechanics module, called Flight_Life, is also incorporated in the code. In addition, a user-friendly graphical user interface (GUI) is available to handle the otherwise difficult task of setting up the problem for analysis and viewing the results.

Previous papers, [1–3], and a report, [4], have reported on the detailed ingredients contained within DARWIN™ and the methodology used in performing a probabilistic analysis with this code. With the Federal Aviation Administration (FAA) having recently stated that DARWIN™ is an acceptable tool to conduct risk analyses for certification of new titanium rotor designs in compliance with Advisory Circular 33.14, the purpose of this paper is to describe several recent enhancements to DARWIN™ that ensure risk convergence and substantially reduce the total engineering time needed to reach convergence; to summarize the results to date of industry evaluations of the code; and to describe several supplementary tasks that address fatigue crack growth (FCG) behavior from hard alpha (HA) anomalies in titanium.

The developments summarized in this paper represent the collective contributions of the program team: Southwest Research Institute, General Electric, Honeywell, Pratt & Whitney, and Rolls-Royce as well as the Rotor Integrity Subcommittee (RISC) of the Aerospace Industries Association.

Enhanced DARWIN™ Capabilities

Previous versions, [5,6], of DARWIN™ provided the capability to predict the risk of fracture associated with hard alpha defects in titanium disks. The risk solution obtained from the zone-based methodology, however, is dependent upon the discretization of the risk zones (i.e., size and number of zones). A zone refinement methodology was recently implemented in DARWIN™ (version 3.5) to assist the user with zone discretization. The methodology, shown in Fig. 1(*a*) can be summarized as follows:

1. Define initial zones (initial discretization).
2. Execute DARWIN™ risk assessment code.
3. Evaluate results. If total risk is less than or equal to design target risk or if a converged solution (i.e., small change in disk failure probability) is obtained, analysis is complete (code terminated).
4. If further analysis is required, the user selects zones to be refined based on zone risk contribution factors (i.e., relative contribution of each zone to the total risk of the disk). Selected zones are automatically subdivided based on the centroid of each zone.
5. User defines fracture mechanics parameters associated with newly subdivided zones (return to step 2).

Since the zone-based risk methodology requires that hard alpha defects be placed in the life-limiting location of each zone, the total disk risk decreases with increasing discretization (i.e., probability of fracture decreases as the number of zones is increased) because the location of the defect in most of the subdivided zones is less severe than the original life limiting location in the parent zone.

The red zones in Fig. 1(*a*) indicate the zones whose contribution to the disk risk exceeds a specified percent threshold, e.g., 2%. When a zone is subdivided, its percent contribution is reduced because the volume of the zone is reduced, thus, the probability of the zone containing a defect is reduced. Also, as mentioned above, the location of the defect in most subdivided zones is less severe than the original life limiting location. Typically, refinement continues until all zones fall below the threshold value.

When using a zone-based risk method, the zone boundaries often conflict with the existing element boundaries defined in the original finite element (FE) mesh (e.g., optimum zone smaller than a single finite element). The solution is to refine the mesh for setting zone boundaries for risk integration. The refined mesh is not used for further analysis; the FE results are merely interpolated for the new mesh. Several new features are provided in DARWIN™ (version 3.5) to assist the user with element discretization. Two of these new features, element refinement and onion skinning, are shown in Figs. 1(*b*) and (*c*), respectively. The element refinement feature allows the user to subdivide any element(s) into a 2×2 set of four elements. Onion skinning divides any element on the surface of the model into two elements—an element of user specified depth normal to the surface and an element containing the remaining material.

Contributed by the International Gas Turbine Institute (IGTI) of THE AMERICAN SOCIETY OF MECHANICAL ENGINEERS for publication in the ASME JOURNAL OF ENGINEERING FOR GAS TURBINES AND POWER. Paper presented at the International Gas Turbine and Aeroengine Congress and Exhibition, Amsterdam, The Netherlands, June 3–6, 2002; Paper No. 2002-GT-30303. Manuscript received by IGTI, Dec. 2001, final revision, Mar. 2002. Associate Editor: E. Benvenuti.

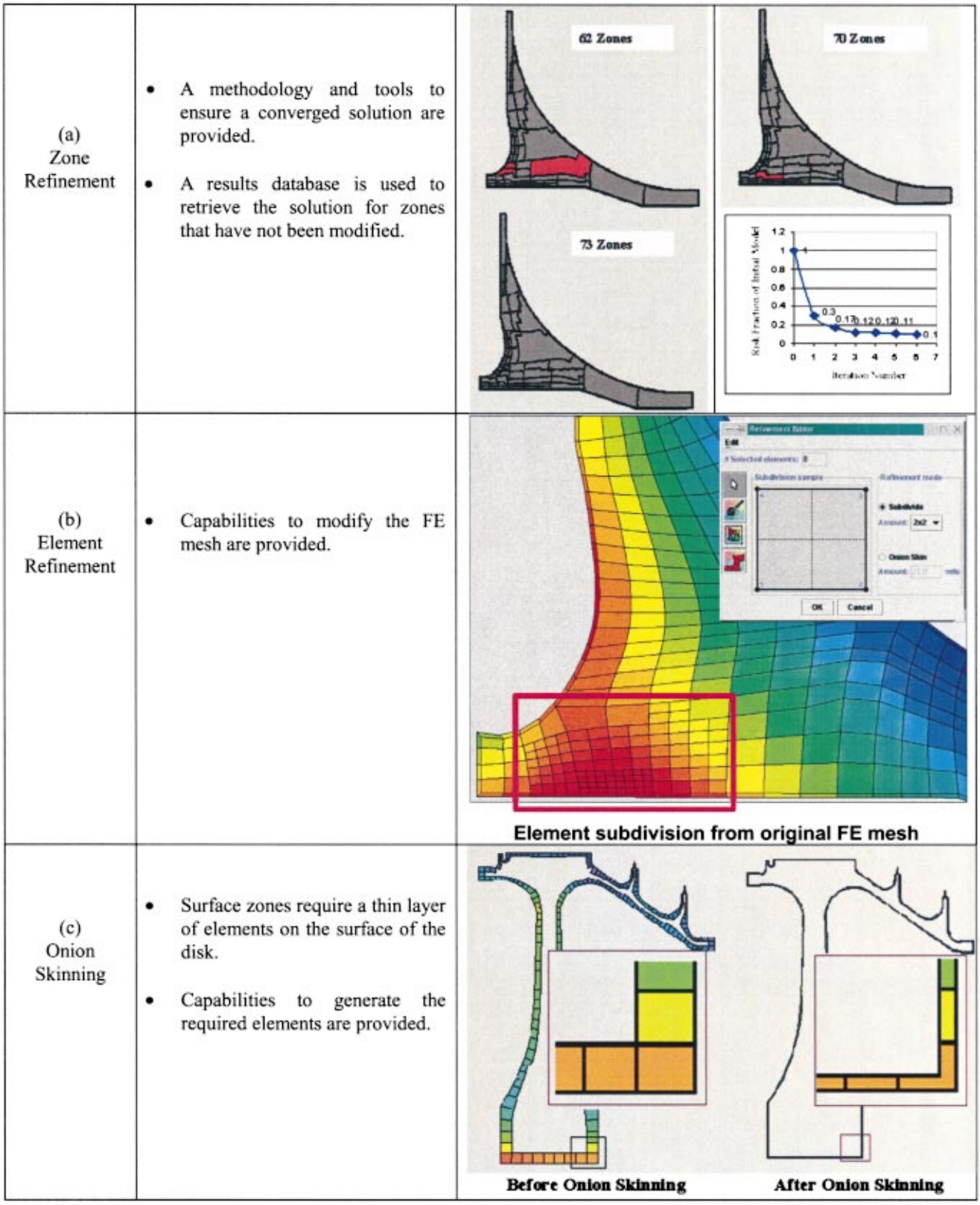

Fig. 1 Summary of element and zone discretization features associated with DARWIN™ (3.5 release)

Further details on the zone and element refinement capabilities are contained in Ref. [7].

Enhanced Fracture Mechanics Capabilities. The Flight_Life fracture mechanics module in DARWIN™ currently contains a limited but sophisticated set of stress intensity factor (K) solutions focused on rotor geometries. In addition to the original polynomial formulations, the code now contains new weight function formulations for semielliptical surface and elliptical em-

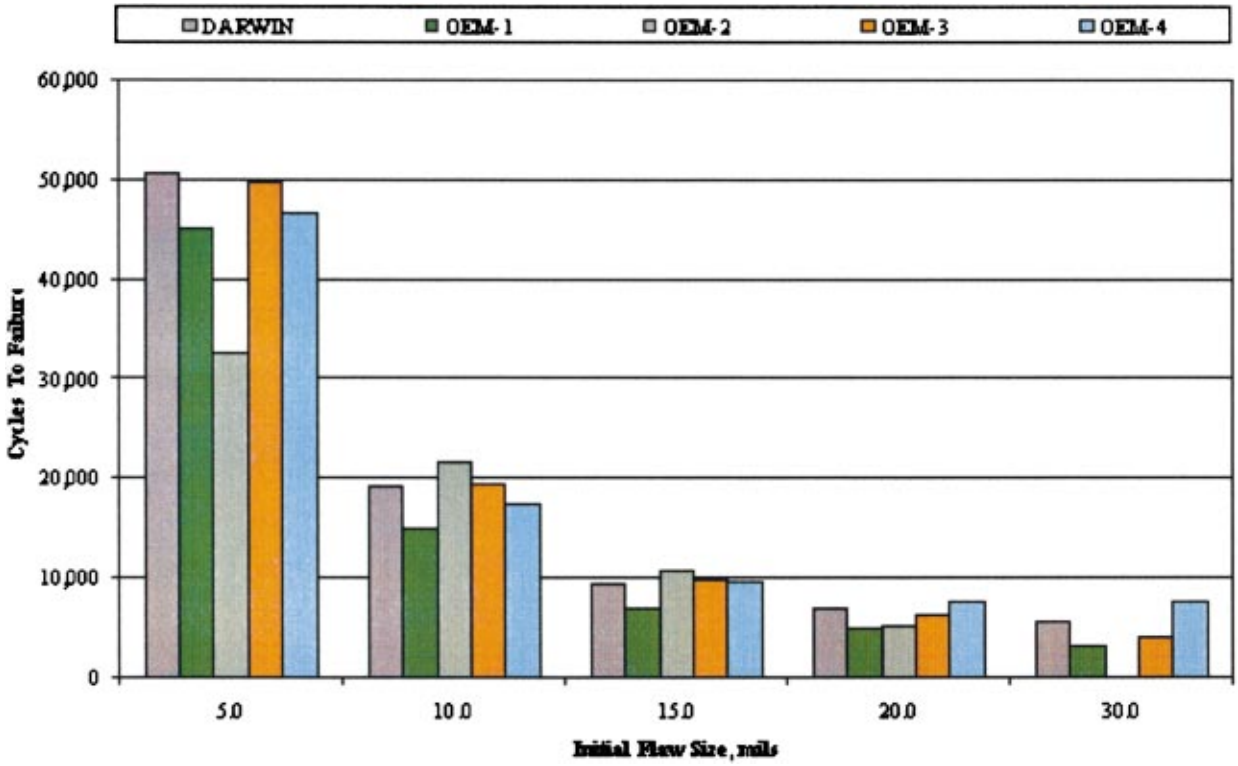

Fig. 2 Cycles to failure vs. initial flaw size for the Flight_Life fracture mechanics module in DARWIN™ compared to OEM fracture mechanics codes

bedded cracks in rectangular plates under univariant stress gradients. Both sets of solutions can address off-center cracks with crack aspect ratios from near 0 up to 2.0. A corner crack plate solution for uniform and linear bivariant stress gradients is also available.

Extension of DARWIN™ to address surface damage issues required implementation of K solutions for corner, surface, and through cracks growing from holes. A new set of weight function solutions for univariant stress gradients have recently been developed, based on a large matrix of reference solutions generated with the FADD-3D boundary element code, [8]

DARWIN™ Evaluation by Industry

Various DARWIN™ capabilities have been independently evaluated by aircraft gas turbine manufacturers (OEMs) that are members of the program team or members of the AIA Rotor Integrity Subcommittee. The evaluations included one-to-one comparisons with their own codes as well as assessments of DARWIN™ predictions compared to actual field experience.

The first set of evaluations involved the prediction of low-cycle fatigue crack propagation lives for different locations in a hypothetical Ti-6A1-4V rotating ring. Comparisons were made between the Flight_Life fracture mechanics code that is embedded in DARWIN™ (but can be run as a stand-alone code) and various fracture mechanics codes in use by the manufacturers. Results of the analyses for one disk location are shown in Fig. 2. It can be seen that the Flight_Life results are typically bracketed by the results obtained by the OEMs

A second set of evaluations for the rotating ring was a comparison of the probability of failure in 20,000 cycles for certain loading conditions. This comparison is shown in Fig. 3 where it can be seen that DARWIN™ compares very favorably with the risk values computed independently by one manufacturer using their own code and by other OEM's using the DARWIN™ probabilistic algorithms with their own fracture mechanics modules.

In addition, one manufacturer assessed the field experiences of over 50 engine disks of varying levels of maturity using DARWIN™. This included various titanium alloys with different disk and hub geometries. The computed probability of fracture predictions for a subset of a fleet involving 2 billion part cycles was combined with the representative fleet population and accumulated cycles to predict the number of fractures and finds (HA detection prior to fracture). The probability of fracture predictions were reasonably consistent with earlier results used by the AIA Rotor Integrity Subcommittee to set the initial HA defect distributions [9].

Another manufacturer performed a one-to-one comparison between their own code and DARWIN™ predictions for a compressor disk. The risk predictions compared favorably, and the DARWIN™ analyses could be completed in less than half the total engineering time required by the corresponding OEM tool.

Characterization and Verification of Material Behavior

Vacuum Fatigue Crack Growth Behavior. DARWIN™ includes a library of FCG rate properties for rotor materials. Only minimal data are provided for air environments, since most DARWIN™ users (engine companies) have their own proprietary databases. However, DARWIN™ will provide more extensive databases for FCG behavior in vacuum environments, which are relevant to embedded cracks growing in isolation from the atmosphere. Because FCG rates in vacuum can be substantially different from FCG rates in air, especially at low ΔK, characterization of vacuum behavior is especially important since most HA defects are in subsurface locations.

Since extensive vacuum data are not commonly available, the TRMD program is conducting a testing program to generate vacuum FCG data on select rotor alloys. Tests are being conducted in engine company labs following their conventional test protocols: surface crack tension and single edge notch button head

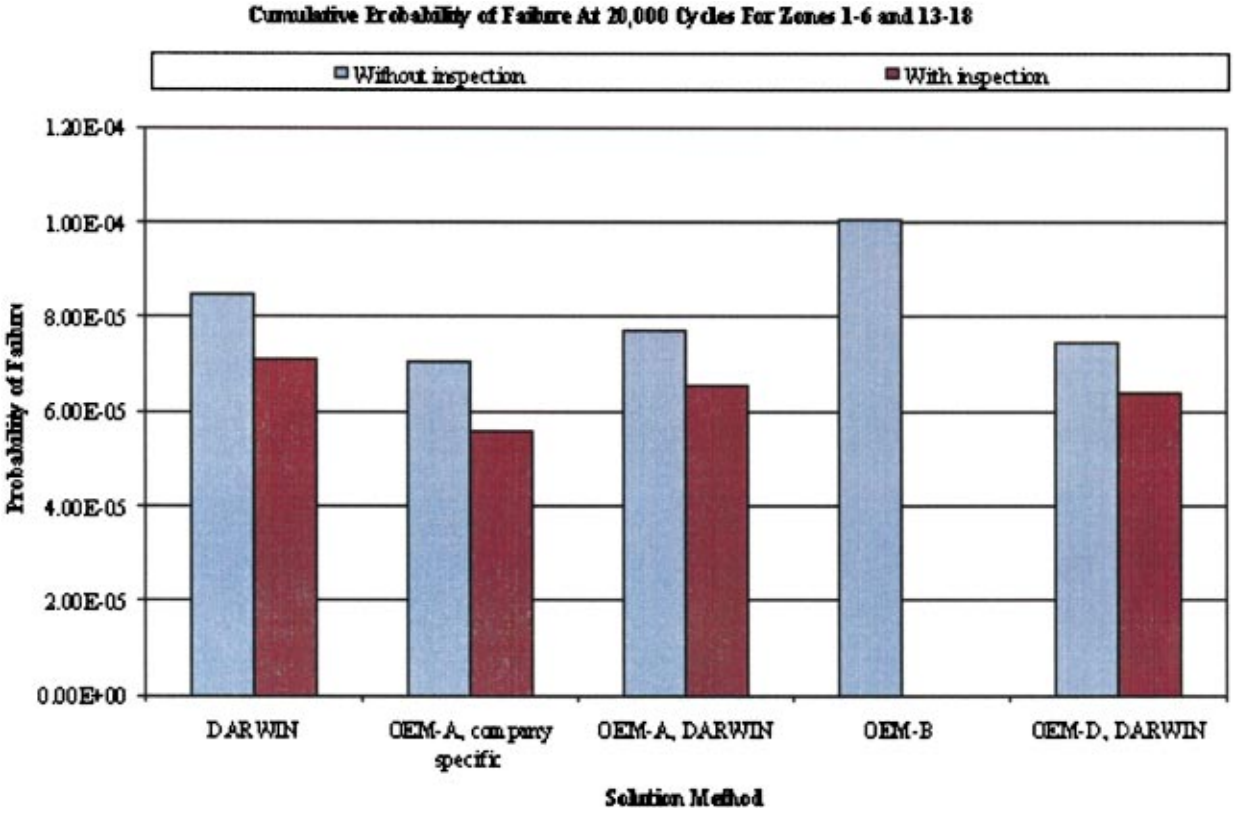

Fig. 3 Summation of the probability of failure for 12 zones computed entirely using DARWIN™ and by OEMs using DARWIN™ in conjunction with their own fracture mechanics codes

specimens, and DCPD crack length monitoring. Vacuum levels are greater than 10^{-7} Torr and test frequencies are 0.33 to 1 Hz. Stress ratios range from 0.05 to 0.75.

Experiments at relevant temperatures have been completed on three titanium alloys, Ti-6Al-4V, Ti-6Al-2Sn-4Zr-2Mo+Si, and Ti-17β. Early results were documented in [10]. Testing is currently underway on two conventional nickel-base rotor alloys, Inconel 718 and Waspaloy, and limited tests are planned on representative powder metallurgy nickel-base alloys.

Static and Fatigue Behavior of Hard Alpha Defects

Laboratory Tests. The AC33.14 risk assessment procedure assumes that HA defects are cracked during the forging process and that FCG from the defect into the surrounding titanium matrix begins essentially on the first cycle of service loading. In order to assess the potential conservatism of this assumption, laboratory tests were conducted on coupons containing artificial or natural HA defects. Test procedures and early results were documented previously, [11]. Acoustic emission methods were used to sense cracking in embedded defects. High stress ratio fatigue marker bands were applied to assist in post-test fractographic interpretation of results.

Static tests showed that HA defect cores and the surrounding diffusion zones exhibited multiple cracking at very low static stresses (5–40 ksi) when the defects were surface-connected. When the defects were embedded, substantial cracking apparently did not occur until static stresses exceeded 90–100 ksi.

Fatigue tests with embedded defects exhibited somewhat longer lives and higher threshold stresses than expected, and this was apparently due to delays in FCG into the matrix. Diffusion zones exhibited some resistance to fatigue crack growth, albeit a lower resistance than matrix material. Marker banding of cracks that had grown into the matrix well beyond the defect showed that crack growth rates agreed with predictions based on vacuum data. Synthetic and natural defects behaved similarly.

Spin Pit Tests. Three forgings with simple sonic shapes that were manufactured for separate studies of the forging deformation process were also spin pit tested in conjunction with evaluation of the fracture mechanics model. All forgings contained a single significant HA defect located by design in a high stress region of the disk. One forging contained a synthetic defect, and two forgings contained natural defects obtained from an independent NDE study of a contaminated billet. As in the coupon tests, the disks exhibited higher threshold stresses than anticipated. After applied stresses were increased, cracks in two of the disks grew to rupture; the third test was halted prior to rupture and the disk sectioned. Crack growth predictions using Flight_Life showed general agreement with measured behavior at these higher stresses.

Analysis of Residual Stresses Around Hard Alpha. HA defects and the surrounding matrix material contain residual stresses due to differential thermal contraction of defect and matrix during cool down from the final heat treatment. A brief analytical study of these residual stresses was conducted to evaluate their potential contribution to the enhanced static and fatigue strengths of embedded defects. The study employed simple elastic models of spherical and cylindrical defects, [12], and values of the coefficient of thermal expansion for both HA and matrix material that were experimentally measured for the program at GE CR&D. The models successfully explained the observed experimental behavior in the laboratory tests. Parameter studies indicated that residual stress effects could be substantial at lower applied stresses but might be negligible at higher applied stresses. Ignoring these residual stresses is conservative.

Summary

Recent progress in the development of a probabilistic damage tolerance software code, DARWIN™, has been highlighted, including a zone refinement methodology for risk convergence, automated creation of thin surface zones, ability to modify the original finite element mesh, and enhancements to the fracture mechanics capabilities. Successful, independent evaluations of DARWIN™ by engine manufacturers were also discussed in terms of comparative crack propagation lives and risk assessments as well as engineering time required to perform an analysis. The fatigue behavior of titanium containing hard alpha (HA) anomalies was also determined to evaluate the assumption that cracks immediately start to propagate from precracked HA on the first flight cycle. It is shown that this is generally a conservative assumption.

Acknowledgments

This work was supported by the Federal Aviation Administration (FAA) under Grants 95-G-041 and 99-G-016. The authors wish to thank the FAA Technical Center project managers, Bruce Fenton and Joe Wilson, for their continued diligence and encouragement and Tim Mouzakis of the FAA Engine and Propeller Directorate for his continued support. The authors also wish to acknowledge the contributions of the industry steering committee: Darryl Lehmann (Pratt & Whitney), Sandeep Muju (Honeywell), Jon Tschopp (General Electric), and Geoff Ward (Rolls-Royce).

References

[1] Leverant, G. R. et al., 1997, ''A Probabilistic Approach to Aircraft Turbine Rotor Material Design,'' ASME Paper No. 97-GT-22.

[2] Enright, M. P., and Wu, Y.-T., 2000, ''Probabilistic Fatigue Life Sensitivity Analysis of Titanium Rotors,'' Proceedings, 41st Structures, Structural Dynamics, and Materials Conference, Atlanta GA, Apr. 3–6.

[3] Millwater, H. R. et al., 2000, ''A Probabilistically-Based Damage Tolerance Analysis Computer Program for Hard Alpha Anomalies in Titanium Rotors,'' ASME Paper No. 2000-GT-0421.

[4] Leverant, G. R. et al., 2000, ''Turbine Rotor Material Design,'' Federal Aviation Administration Report DOT/FAA/AR-00/64.

[5] Wu, Y.-T., Millwater, H. R., and Enright, M. P., 2000, ''Efficient and Accurate Methods for Probabilistic Analysis of Titanium Rotors,'' Proceedings, 8th ASCE Specialty Conference on Probabilistic Mechanics and Structural Reliability, South Bend, IN, July 24–26, CD-ROM Proceedings Paper PMC2000-221.

[6] Wu, Y.-T., Enright, M. P., Millwater, H. R., Chell, G. G., Kuhlman, C. J., and Leverant, G. R., 2000, ''Probabilistic Methods for Design Assessment of Reliability With Inspection (DARWIN™),'' Proceedings, 41st Structures, Structural Dynamics, and Materials Conference, Atlanta GA, Apr. 3–6.

[7] Millwater, H. R., Enright, M. P., Fitch, S., 2002, ''A Convergent Probabilistic Technique for Risk Assessment of Gas Turbine Disks Subject to Metallurgical Defects,'' 43rd Structures, Structural Dynamics, and Materials Conference, Denver, CO, Apr. 22–25.

[8] Li, S., Mear, M. E., and Xiao, L., 1998, ''Symmetric Weak-Form Integral Equation Method for Three-Dimensional Fracture Analysis,'' Comput. Methods Appl. Mech. Eng., **151**, pp. 435–459.

[9] Subteam to the Aerospace Industries Association Rotor Integrity Subcommittee, 1997, ''The Development of Anomaly Distributions for Aircraft Engine Titanium Disk Alloys,'' 38th AIAA/ASME/ASCE/AHS/ASC SDM Conference, pp. 2543–2553.

[10] McClung, R. C., Lawless, B. H., Gorelik, M., Date, C., Gill, Y., and Piascik, R. S., 1999, ''Fatigue Crack Growth of Titanium Rotor Alloys in Vacuum and Air,'' *Fatigue Behavior of Titanium Alloys*, R. R. Boyer, D. Eylon, and G. Lutjering, eds., The Minerals, Metals, and Materials Society, pp. 211–218.

[11] McKeighan, P. C., Nicholls, A. E., Perocchi, L. C., and McClung, R. C., 2001, ''Sensing Crack Nucleation and Growth in Hard Alpha Defects Embedded in Ti-6Al-4V Alloy,'' *Nontraditional Methods of Sensing Stress, Strain and Damage in Materials and Structures: Second Volume, ASTM STP 1323*, G. F. Lucas, P. C. McKeighan, and J. S. Ransom, eds., American Society for Testing and Materials, pp. 15–35.

[12] Brooksbank, D., and Andrews, K. W., 1972, ''Stress Fields Around Inclusions and Their Relation to Mechanical Properties,'' Journal of the Iron and Steel Institute, **210**, pp. 246–255.

Fatigue Crack Growth Life Prediction for Surface Crack Located in Stress Concentration Part Based on the Three-Dimensional Finite Element Method

Y. Yamashita
Structure and Strength Department,
Research and Development,
Ishikawajima-Harima Heavy Industries Co. Ltd.,
1-banchi, Shinnakahara-cho,
Yokohama 235-8501, Japan

M. Shinozaki

Y. Ueda

Aeroengine and Space Operations,
Research and Engineering Division,
Engine Technology Department,
Ishikawajima-Harima Heavy Industries Co. Ltd.,
3-5-1 Mukodai-cho, Nishitokyo-shi,
Tokyo 188-8555, Japan

K. Sakano
Structure and Strength Department,
Research and Development,
Ishikawajima-Harima Heavy Industries Co. Ltd.,
1-banchi, Shinnakahara-cho,
Yokohama 235-8501, Japan

Fatigue crack growth prediction methods using three-dimensional finite element analyses were investigated to improve the predictability of part-through surface crack growth life. First, a direct analysis method of cyclic finite element analysis was adopted. Fatigue crack growth was predicted on a step by step basis from the Paris' law using stress intensity factor range (ΔK) calculated by the three-dimensional finite element method. This method takes the procedure of cyclic operation of finite element analysis modeled with crack tip elements, crack growth increment calculation and remeshing of the finite element model. Second, a method based on the influence function method for the ΔK calculation directly using three-dimensional finite element method analysis result has been developed and applied. It was found that crack growth prediction based on the step by step finite element method and the method based on the influence function method showed good correlation with the experimental results if Paris' law coefficient C, determined by CT specimen, was appropriately used for a semi-elliptical surface crack. [DOI: 10.1115/1.1619425]

Introduction

Predictability of fatigue crack growth life is a key term in damage tolerance design as well as crack inspection ability of a nondestructive test. The material surface of stress concentration part is a major site of fatigue crack initiation and in many cases the crack configuration is a part-through surface crack such as a semicircle or semi-elliptical shape. Therefore, part-through surface crack growth analysis is a major problem in damage tolerance design of turbomachinery.

In this study, fatigue crack growth prediction methods using three-dimensional finite element analysis were investigated to improve the predictability of surface crack growth life by taking into account the stress distribution in a crack section as exact as possible.

First, a direct fatigue crack growth analysis method using the step by step finite element analysis procedure was investigated. The method takes the step by step operation of three-dimensional finite element method analysis with crack tip elements to calculate the stress intensity factor range ΔK, crack growth increment calculation, and remeshing of the finite element model corresponding to a new location of a crack front, [1–3].

Second, a simplified method of fatigue crack growth analysis based on the influence function method, [4,5], for ΔK calculation was investigated. The method uses the database of influence coefficients for a semi-elliptical surface crack developed by Shiratori et al. and uses the three-dimensional finite element analysis result. The authors developed a crack growth analysis system based on the influence function method for ΔK calculation by the direct use of three-dimensional finite element method input data and three-dimensional finite element method result, [6].

With the above-stated two methods it is possible to calculate ΔK under an arbitrary distributed stress field. And fatigue crack growth tests were conducted with specimens that have the stress concentration part derived from the rib on the specimen's main plate to investigate the effectiveness of the methods. The specimens were designed to have a stress concentration part producing an arbitrary distributed stress field not only in the plate thickness direction but also in the plate width direction. In this point, the above-mentioned two methods are desired to be more effective for fatigue crack growth life prediction than the linear approximation method that takes into account the nonlinear stress distribution only in the thickness direction of the center of plate width.

Fatigue Crack Growth Tests

Aluminum alloy A5083-O was used for the specimen. Its mechanical properties and the chemical composition are shown in Table 1 and Table 2, respectively.

Tensile and bending plate specimens with a stress concentration part caused by the rib on the main plate were used in the fatigue crack growth tests. All tests are conducted at room temperature. In the first step, to introduce the fatigue crack in the specimen, the specimen has a crack starter notch as shown in Fig. 1. And after the part-through surface crack was introduced in the center of the specimen by fatigue loading, the starter notch was removed. The maximum fatigue pre-cracking load was within the maximum load level of the fatigue crack growth test after pre-cracking. Specimen size and configurations for cyclic tensile and bending loading crack growth tests are shown in Fig. 2. And the detailed dimensions are shown in Table 3. The geometrical definitions of a surface crack are shown in Fig. 3. Initial crack sizes introduced by the pre-cracking starter notch and stress range condition for crack

Contributed by the International Gas Turbine Institute (IGTI) of THE AMERICAN SOCIETY OF MECHANICAL ENGINEERS for publication in the ASME JOURNAL OF ENGINEERING FOR GAS TURBINES AND POWER. Paper presented at the International Gas Turbine and Aeroengine Congress and Exhibition, Amsterdam, The Netherlands, June 3–6, 2002; Paper No. 2002-GT-30304. Manuscript received by IGTI, December 2001, final revision, March 2002. Associate Editor: E. Benvenuti.

Table 1 Mechanical properties (R.T.) of A5083-O used

Yield stress (0.2%) (MPa)	Tensile strength (MPa)	Elongation (gauge length: 50 mm)
155	315	20.6%

growth tests are shown in Table 4 and Table 5, respectively. All tests are set at the stress ratio(minimum stress/maximum stress) $R=0.1$. Tensile and four-point bending test facilities are shown in Fig. 4. And the dimensions of the propagating surface crack were measured by the beach mark caused by changing the stress range. Fracture surfaces are shown in Fig. 5.

Crack Growth Analysis Procedure

Paris' law $da/dN=C(\Delta K)^m$ was adopted for the crack growth rule and the material constants C and m were determined from the crack growth test with the CT specimen based on the ASTM E647 method. The constants $C=8.692\times10^{-11}$ and $m=3.17$ were employed (da/dN is measured in the m/cycle and ΔK in MPa$\sqrt{\text{m}}$) under stress ratio $R=0.1$. The obtained $da/dN\sim\Delta K$ curve is shown in Fig. 6.

It has been assumed that fatigue cracks grow in an almost semi-elliptical shape, that is, the semi-minor and major axes suffice in defining the crack front. Paris' law for semi-elliptical surface crack can be defined independently at points A and C at the crack front,

$$da/dN=C_a(\Delta K_a)^m \text{ for crack deepest (A) point} \quad (1)$$

$$dc/dN=C_c(\Delta K_c)^m \text{ for plate surface (C) point.} \quad (2)$$

However, in fatigue crack growth analysis for semi-elliptical surface crack, Newman and Raju [7], Jolles and Tortoriello [8], and A. Hosseini and M. A. Mahmoud [9] suggested that $C_c=(0.9)^m C_a$. This suggestion was based on experiments reported by Corn [10] showing that for surface cracks under tension and bending fatigue loads show that small semicircular surface cracks tend to grow semicircular for low a/t ratios. Because the stress intensity factor solution for the semicircular crack shows that the stress intensity factor at point C is about 10% higher than the value at point A, so the coefficient C_c was assumed to be $C_c=(0.9)^m C_a$ so that a small semicircular crack would be predicted to initially retain its shape. One reason C_a is not equal to C_c may be the changing relationship between the stress intensity factor and the crack growth rate as the stress state changes from plane stress on the front surface to plane strain at the maximum depth point, [7]. In crack growth analysis, for simplicity, following three cases were investigated:

$$①\ C_a=C_c=C \quad (3)$$

$$②\ C_a=C, C_c=(0.9)^m C_a \quad (4)$$

$$③\ (C_a+C_c)/2=C, C_c=(0.9)^m C_a \quad (5)$$

Step by Step Finite Element Method

A direct method to simulate fatigue crack growth using the three-dimensional finite element method was investigated. Fatigue crack growth was predicted on a step by step basis from the Paris'

Table 2 Chemical composition of A5083-O used (mass %)

Si	Fe	Cu	Mn	Mg	Cr	Zn	Ti
0.13	0.19	0.03	0.68	4.61	0.09	0.01	0.02

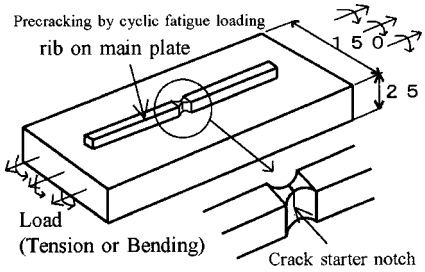

Fig. 1 Specimen with crack starter notch

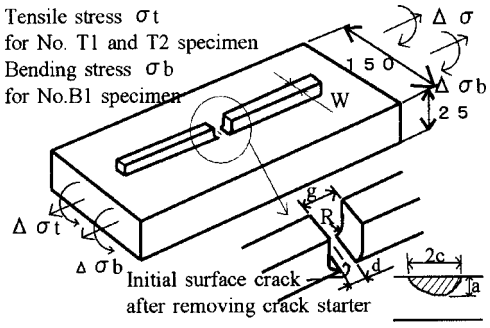

Fig. 2 Fatigue crack growth test specimen

Table 3 Dimensions for tensile and bending specimens

Specimen No.	d (mm)	g (mm)	R (mm)	W (mm)
No. B1 and No. T1	7	10	1.5	10
No. T2	10	15	2.5	20

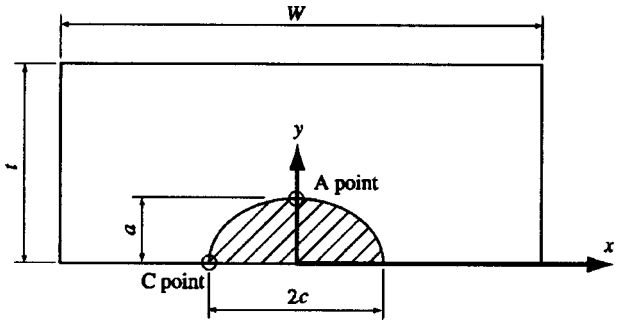

Fig. 3 Geometrical definition of surface crack

Table 4 Initial fatigue crack sizes

Specimen No.	a_0 (m)	$2c_0$ (m)
B1	0.0025	0.004
T1	0.0025	0.005
T2	0.0051	0.0082

Table 5 Stress range condition (stress ratio $R=0.1$)

Specimen No.	Nominal Tensile Stress Range $\Delta\sigma_t$ (MPa)	Nominal Bending Stress Range $\Delta\sigma_b$ (MPa)
B1	—	70
T1	60	—
T2	60	—

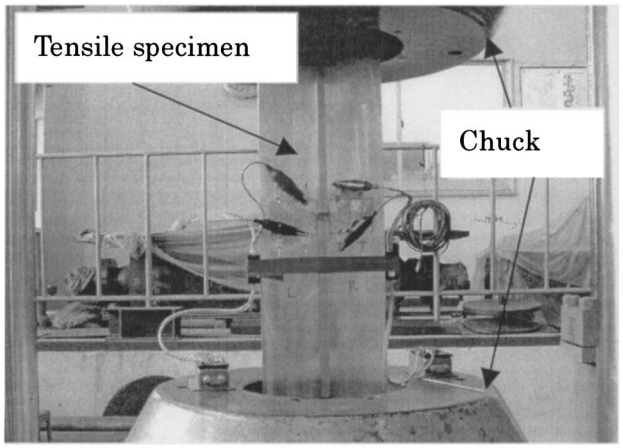

(*a*)

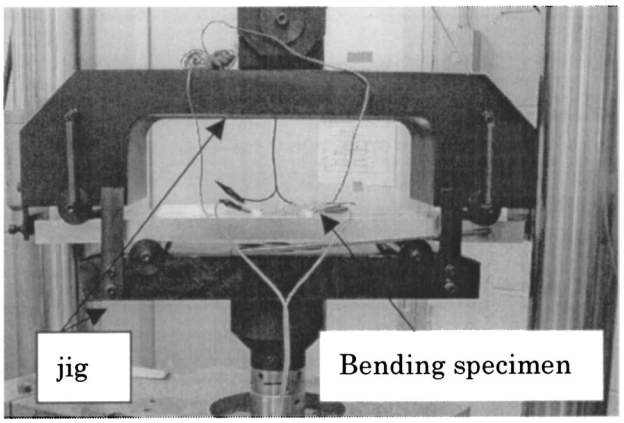

(*b*)

Fig. 4 Fatigue crack growth test facilities; (*a*) tensile test facility, (*b*) four-point bending test facility

law using ΔK calculated by the finite element method. This method has wide applicability to real complicated shape cracks in a real engineering structure for it is based on three-dimensional finite element analysis, [1–3]. The method takes the procedure of cyclic operation of finite element analysis modeled with crack tip elements for ΔK calculation, crack growth increment calculation, and finite element re-meshing step by step. Both the quarter-point-node crack opening displacement method proposed by Barsom [11] et al. and the three-dimensional J-integral methods are used to calculate the stress intensity factors. The determination of the stress intensity factor is due to the conversion method from J-integral calculated by ABAQUS code. In plane-strain condition, the stress intensity factor and J-integral have the relationship

$$K = \sqrt{\frac{JE}{1-\nu^2}} \tag{6}$$

where E is Young's Modulus, ν is Poisson's ratio, J is the J-integral and K is the mode I stress intensity factor.

The crack growth increment procedure is based on Paris' law. The number of increment cycles ΔN corresponding to controlled crack depth increment Δa is determined by Eq. (7). The corresponding crack half-length increment Δc is determined by Eq. (8).

$$\Delta N = \Delta a/(C_a \Delta K_a^m) \tag{7}$$

$$\Delta c = C_c(\Delta K_c)^m \cdot \Delta N \tag{8}$$

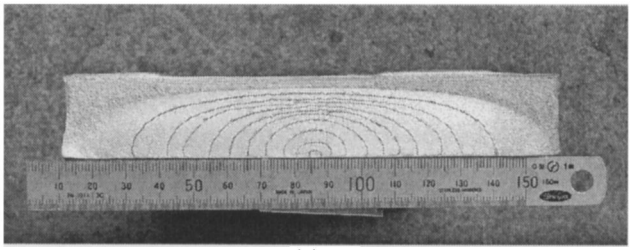

(*a*)

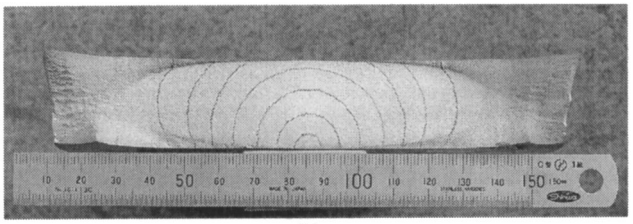

(*b*)

Fig. 5 Fracture surface of bending and tension specimen; (*a*) bending specimen (No. B1), (*b*) tensile specimen (No. T1)

After this procedure, the re-meshing procedure of the finite element model to a new position which defines the new crack front enables the next step finite element analysis. A finite element mesh example is shown in Fig. 7 for a No. T2 specimen.

Influence Function Method Directly Using the Three-Dimensional Finite Element Method Result

The influence function method take an effective procedure to calculate stress intensity factor at the deepest (A) point and at the plate surface (C) point of semi-elliptical surface crack under arbitrary distributed stress field, [4,5]. The K-value at the crack deepest point and at the plate surface point can be found from the arbitrary distributed stress field over a virtual crack surface according to the following equation:

$$K_i = \sum_{j=1}^{n} K_{ij}\sigma_j \tag{9}$$

where K_{ij} is the influence coefficient that is the stress intensity factor of a surface crack acted on by a unit force at one node on a crack surface. In Eq. (9), n denotes the number of nodes on crack surfaces at which K_{ij} are defined, and K_i are the K-values at nodes on the crack front of a surface crack. In this study, they are denoted as K_a at a node on the crack bottom and K_c on the plate surface. A benefit of influence function method is that it is not necessary to model crack tip elements if influence coefficients are prepared. The values of K_{ij} have been established as a database by

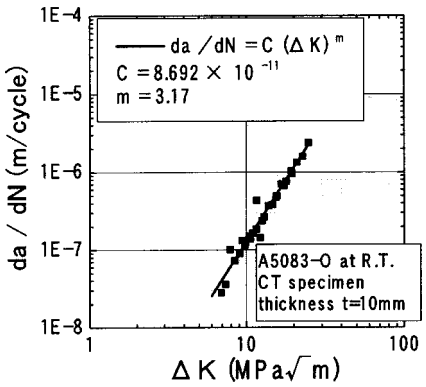

Fig. 6 Material properties of fatigue crack growth with CT specimens

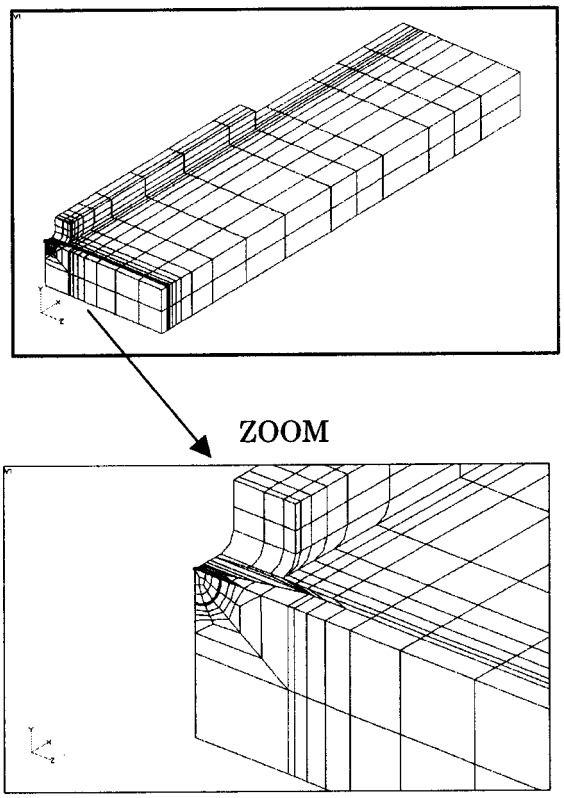

Fig. 7 Example finite element mesh used in step by step finite element method (No. T2 specimen, $\frac{1}{4}$ model)

Shiratori et al. for various types of surface cracks, [5]. For simplification of the analysis, the authors developed a system performing K-value calculation by the influence function method and crack growth analysis. In the system, the values of σ_j in Eq. (9) can be directly determined from the three-dimensional finite element method input data and nodal stress of three-dimensional finite element method results, [6].

In order to determine nodal stress σ_j, three-dimensional finite element method analyses were conducted. The finite element method model is not needed to include crack tip configurations in the influence function method. For example, the finite element model used for the influence function method is shown in Fig. 8.

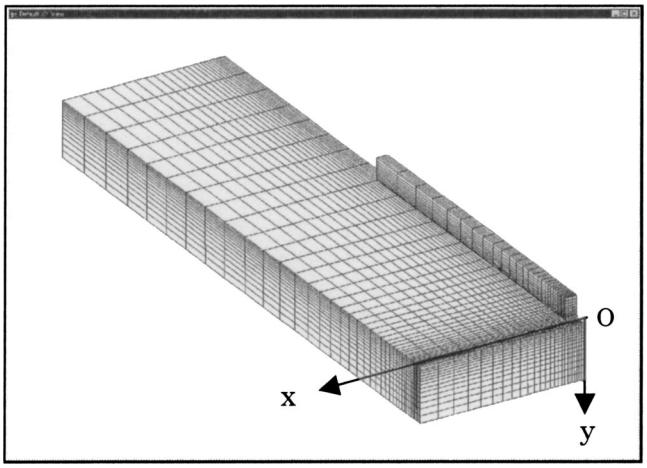

Fig. 8 Finite element model used for influence function method (specimen No. B1, $\frac{1}{4}$ model)

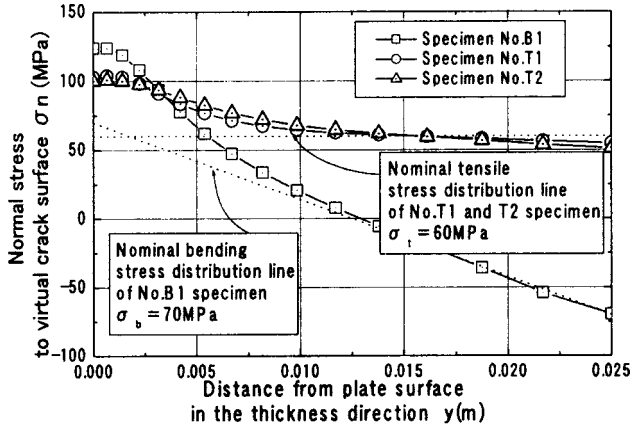

(*a*)

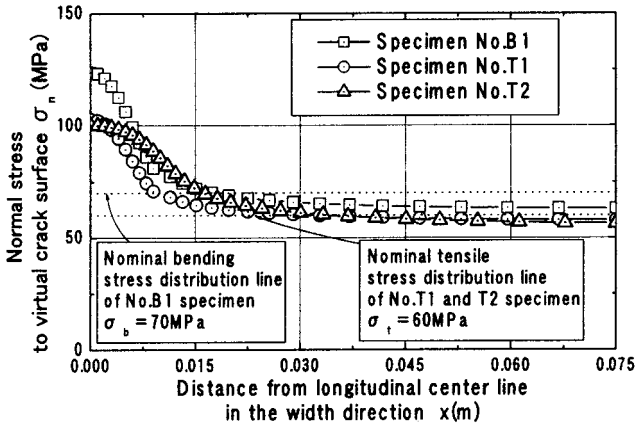

(*b*)

Fig. 9 Stress distribution by finite element analysis with no crack; (*a*) stress distribution along thickness direction, (*b*) stress distribution along plate width direction

And Fig. 9 shows the arbitrary distributed stresses σ_n normal to the virtual crack surface in each specimens calculated by the three-dimensional finite element method.

Linear Approximation Method

In conventional crack growth analysis for a semi-elliptical surface crack according to the method of ASME Code Sec. XI or other standards, the nonlinear stress distribution along plate thickness will be normalized to the linear approximation and decomposition into tensile and bending stress components. This study also employed this linear approximation method, as a conventional method (called the linear approximation method). For linear approximation of stress range, the stress value at the surface and that at the bottom of the crack are connected by a straight line as shown in Fig. 10. σ_t represents the nominal tensile stress component and σ_b the nominal bending stress component. After σ_t and σ_b are determined for update of the surface crack size, the crack growth analysis was performed according to the K-value calculation by the Newman and Raju equation, [12]. In this method nonlinear stress distribution was determined from three-dimensional finite element method analysis for each specimen as already shown in Fig. 9.

Predicted Results and Discussions

Crack growth analysis are conducted and appropriate Paris' law coefficients of Eqs. (3)–(5) are investigated.

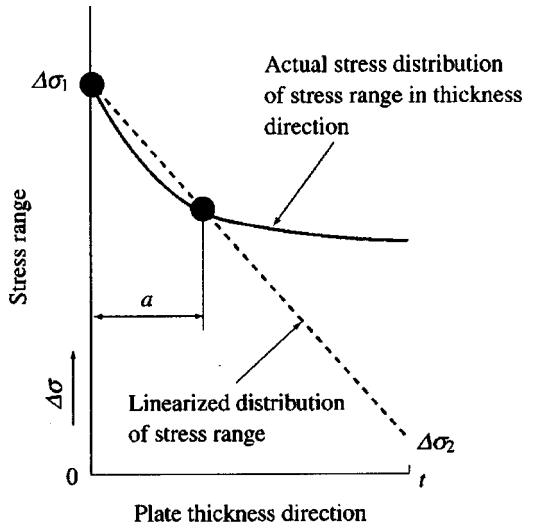

Tensile stress range $\Delta\sigma_t = \frac{\Delta\sigma_1 + \Delta\sigma_2}{2}$

Bending stress range $\Delta\sigma_b = \frac{\Delta\sigma_1 - \Delta\sigma_2}{2}$

Fig. 10 Linear approximation method

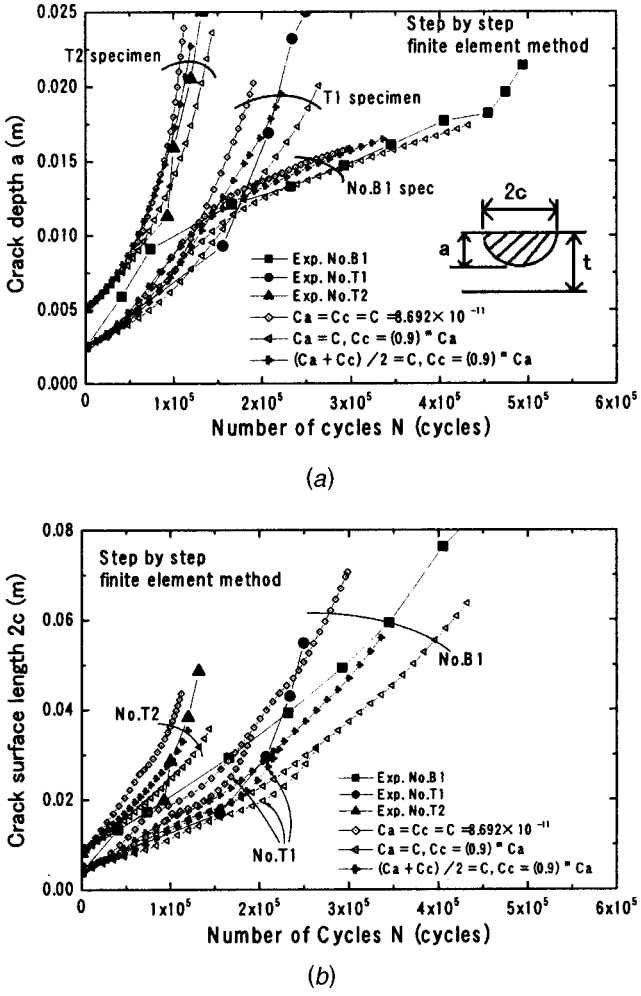

Fig. 11 Comparison between predicted results by step by step finite element method; (*a*) crack depth *a*, (*b*) crack surface length 2*c*

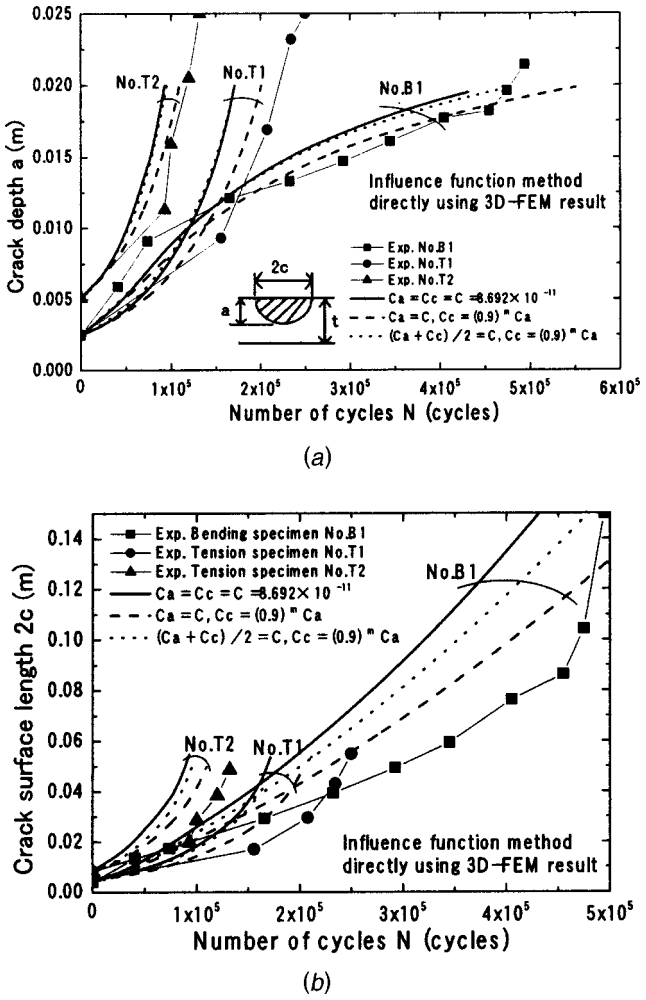

Fig. 12 Comparison between predicted results by influence function method and experiments; (*a*) crack depth *a*, (*b*) crack surface length 2*c*

Figure 11 shows crack depth (a) and crack surface length ($2c$) predicted results, respectively, of the step by step finite element method in comparison with experimental data. The results have generally good correlation with experimental results for each specimen. And the Paris' law coefficients of Eq. (5) for crack growth rule gives the best predicted results. The Paris law coefficients of Eq. (4) gives a little unsafe side predicted results.

Figure 12 shows crack depth (a) and crack surface length ($2c$) prediction of the method by the influence function method directly using the three-dimensional finite element method results. The results of the influence function method have good correlation with experimental data, especially for crack depth prediction. In the influence function method, the Paris' law coefficients of Eq. (4) for crack growth rule gives the best predicted results.

By these results, it has been found that analysis precision can be tuned if the coefficient C_a for the deepest point and C_c for plate surface point were appropriately used based on the relationship of $C_c = (0.9)^m C_a$. In the step by step finite element method, the relationship $(C_a + C_c)/2 = C, C_c = (0.9)^m C_a$ gives the best correlation with test data. In the influence function method, $C_a = C, C_c = (0.9)^m C_a$ gives the best correlation with test data.

Figure 13 shows the predicted results of the conventional method based on linear approximation of nonlinear stress distributed in the thickness direction. The linear approximation method gives very conservative results. This tendency is remarkable for deep cracks of each specimen and especially for bending speci-

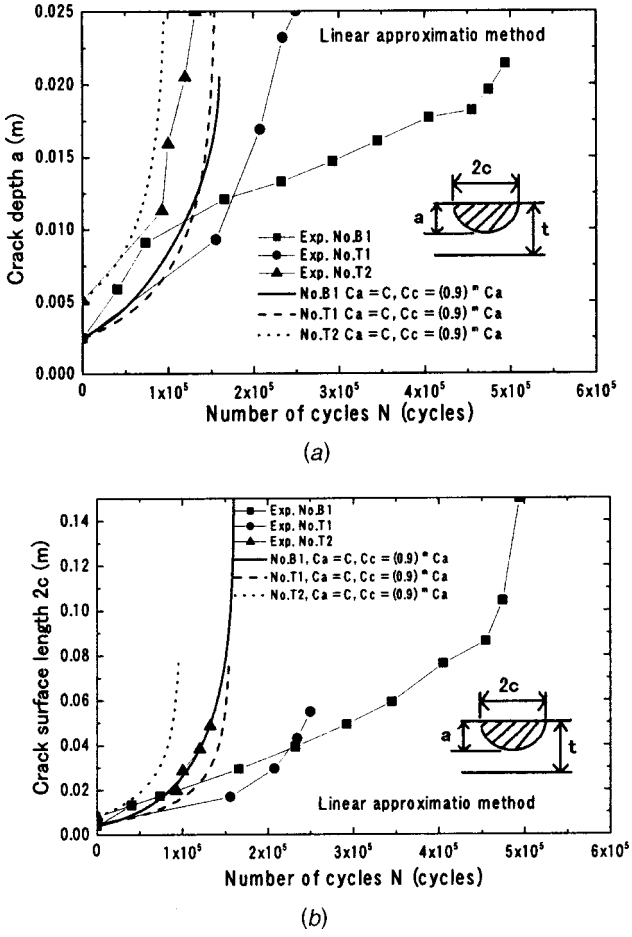

Fig. 13 Comparison between predicted results by linear approximation method and experiments; (*a*) crack depth *a*, (*b*) crack surface length 2*c*

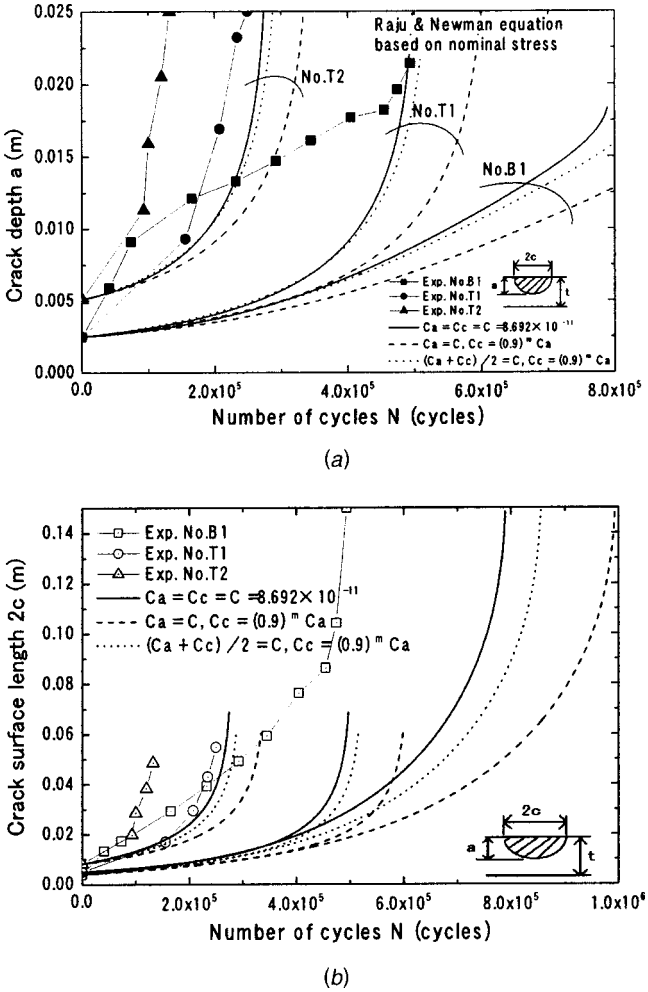

Fig. 14 Comparison between predicted results by the method using Newman and Raju equation based on nominal stress and experiments; (*a*) crack depth *a*, (*b*) crack surface length 2*c*

men. In the specimens, a nonlinear stress distribution builds up not only along plate thickness but also along plate width under the influence of stress concentration by the rib on main plate. Therefore, ΔK-value determined from the approximated linear distribution in the thickness direction tends to be evaluated on the safe side, especially for the bending stress state.

On the other hand, fatigue crack growth analyses were conducted using nominal stress shown in Table 5 based on the Newman and Raju equation. This method only takes into account nominal stress and ignores a rising stress component from the nominal stress derived from the stress concentration part. Figure 14 shows that the result gives unsafe side prediction. This indicates the significance of the appropriate consideration in the stress concentration effect on fatigue crack growth life prediction.

It can be able to interpret the above four predicted results by the change trend of stress intensity factor as crack growth. For instance, the change trend of the stress intensity factor at the deepest point K_a and at the surface point K_c in the case of specimen No. B1 and Paris' law coefficients $(C_a+C_c)/2=C, C_c=(0.9)^m C_a$ are shown in Fig. 15.

Conclusions

Fatigue crack growth prediction methods using three-dimensional finite element analysis were investigated to improve the predictability of the surface crack growth life by taking into account the stress distribution in the crack section as exact as possible. Fatigue crack growth tests were conducted with the specimens that have a stress concentration part derived from the rib on the main plate to investigate the effectiveness of the above-mentioned methods. Conclusions of this study are given as follows.

1. It was found that predicted results of the step by step finite element method have generally good correlation with experimental results for each cyclic tension and bending specimen.
2. A crack growth analysis system based on the influence function method for K value calculation by the direct use of three-dimensional finite element method input data and three-dimensional finite element analysis results was developed. Using this system, it was found that fatigue crack growth predicted results by the influence function method have good correlation with test data, especially for crack depth prediction.
3. Analysis precision can be tuned if Paris' law coefficients C_a for the deepest point and C_c for the plate surface point were appropriately used according to the relationship of $C_c=(0.9)^m C_a$. In the step by step finite element method, the relationship $(C_a+C_c)/2=C, C_c=(0.9)^m C_a$ gives the best correlation with the test data. In the influence function method, $C_a=C, C_c=(0.9)^m C_a$ gives the best correlation with test data.
4. Fatigue crack growth analysis by the step by step finite element method and that by the influence function method turned out to be more effective for growth analysis of surface cracks located in the stress concentration part than the conventional linear approximation method.

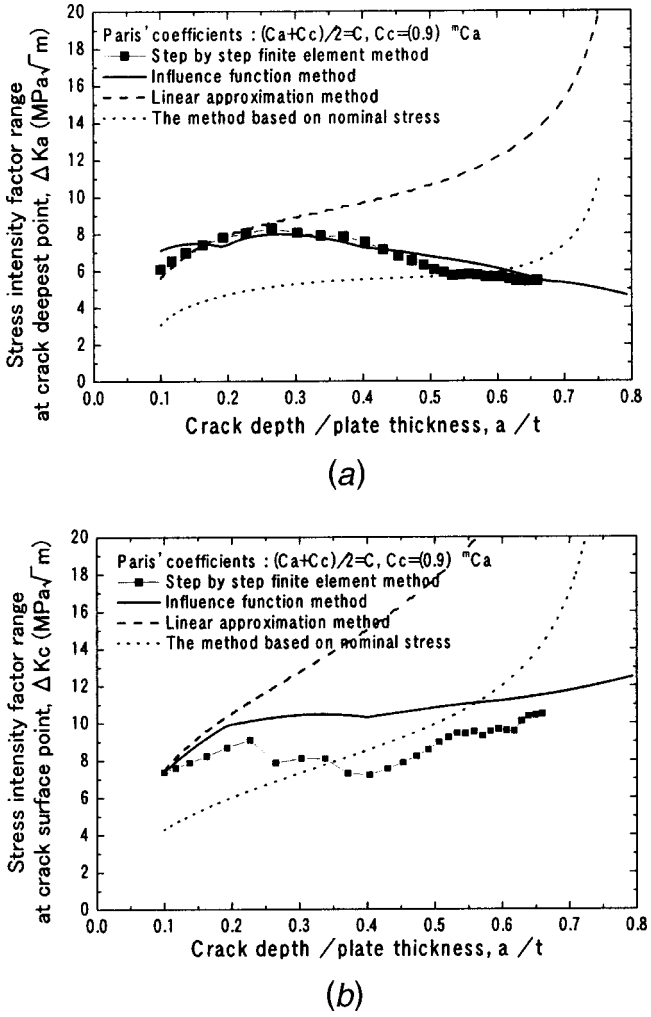

Fig. 15 Change trend of stress intensity factor range in each prediction method; (*a*) change trend of K_a, (*b*) change trend of K_c

Acknowledgments

The authors thank the Agency of Industrial Science and Technology (AIST), Ministry of International Trade and Industry (MITI), for funding this work as a part of the ''Research and Development of Environmentally Compatible Propulsion System for Next-Generation Supersonic Transport (ESPR)'' project. And the authors give great thanks to Shiratori Laboratory of Yokohama National University for its permission to use the database of influence coefficients which enables K calculation based on the influence function method. And the authors would like to extend their sincere appreciation to K. Kamata and T. Kimura at Ishikawajima Inspection & Instrumentation Co. Ltd.

Nomenclature

a = depth of semi-elliptical surface crack
c = plate surface half-length
t = plate thickness, m
C_a = Paris' law coefficient for crack deepest point
C_c = Paris' law coefficient for plate surface point
ΔK_a = stress intensity factor range at deepest point
ΔK_c = stress intensity factor range at surface point
J = J-integral
K_{ij} = influence coefficients used for influence function method
N = number of loading cycles

References

[1] Lin, X. B., and Smith, R. A., 1997, ''An Improved Numerical Technique for Simulating the Growth of Planar Fatigue Cracks,'' Fatigue Fract. Eng. Mater. Struct., **20**(10), pp. 1363–1373.
[2] Lin, X. B., and Smith, R. A., 1998, ''Fatigue Growth Simulation for Cracks in Notched and Unnotched Round Bars,'' Int. J. Mech. Sci., **40**(5), pp. 405–419.
[3] Lin, X. B., and Smith, R. A., 1998, ''Fatigue Shape Analysis for Corner Cracks at Fastener Holes,'' Eng. Fract. Mech., **59**(1), pp. 73–87.
[4] Shiratori, M., Miyoshi, T., and Tanigawa, K., 1985, ''Analysis of Stress Intensity Factors for Surface Cracks Subject to Arbitrary Distributed Surface Stresses,'' Trans. Jpn. Soc. Mech. Eng., **51**(467), pp. 1828–1835 (in Japanese).
[5] Shiratori, M., Miyoshi, T., Yu, Q., Terakado, T., and Matsumoto, T., 1999, ''Development of a Software System Estimating Stress Intensity Factors and Fatigue Crack Propagation for Three-Dimensional Surface Cracks by an Influence Function Method,'' *Computer Technology-1999* ASME, New York, PVP-Vol. 385, pp. 299–309.
[6] Yamashita, Y., Sakano, K., and Shiratori, M., 2001, ''Improvement of Predictability of Fatigue Crack Growth Analysis—A Simplified Method of Fatigue Crack Growth Analysis Using Database of Influence Coefficients,'' IHI Eng. Rev., **34**(3), pp. 67–74.
[7] Newman, Jr., J. C., and Raju, I. S., 1981, ''An Empirical Stress-Intensity Factor Equation for the Surface Crack,'' Eng. Fract. Mech., **15**, pp. 185–192.
[8] Jolles, M., and Tortoriello, V., 1983, ''Geometry Variations During Fatigue Growth of Surface Flaws,'' *Fracture Mechanics*, ASTM-STP-791, Vol. I, pp. I-297–I-307.
[9] Hosseini, A., and Mahmoud, M. A., 1985, ''Evaluation of Stress Intensity Factor and Fatigue Growth of Surface Cracks in Tension Plates,'' Eng. Fract. Mech., **22**, pp. 957–974.
[10] Corn, D. L., 1971, ''A Study of Cracking Techniques for Obtaining Partial Thickness Cracks of Pre-selected Depths and Shapes,'' Eng. Fract. Mech., **3**(1), pp. 45–52.
[11] Barsoum, R. S., 1976, ''On the Use of Isoparametric Finite Elements in Linear Fracture Mechanics,'' Int. J. Numer. Methods Eng., **10**, pp. 25–37.
[12] Raju, I. S., and Newman, Jr., J. C., 1979, ''Stress-Intensity Factors for a Wide Range of Semi-Elliptical Surface Cracks in Finite-Thickness Plates,'' Eng. Fract. Mech., **11**, pp. 817–829.

Effect of Optimization Criteria on Direct-Injection Homegeneous Charge Compression Ignition Gasoline Engine Performance and Emissions Using Fully Automated Experiments and Microgenetic Algorithms

M. Canakci
Technical Education Faculty,
Kocaeli University,
Izmit 41100, Turkey

R. D. Reitz
Engine Research Center,
Department of Mechanical Engineering,
University of Wisconsin-Madison,
Madison, WI 53706

Homogeneous charge compression ignition (HCCI) is a new low-emission engine concept. Combustion under homogeneous, low equivalence ratio conditions results in modest temperature combustion products, containing very low concentrations of NO_x and PM as well as providing high thermal efficiency. However, this combustion mode can produce higher HC and CO emissions than those of conventional engines. Control of the start of combustion timing is difficult with pre-mixed charge HCCI. Accordingly, in the present study charge preparation and combustion phasing control is achieved with direct injection. An electronically controlled Caterpillar single-cylinder oil test engine (SCOTE), originally designed for heavy-duty diesel applications, was converted to a direct-injection gasoline engine. The engine features an electronically controlled low-pressure direct injection-gasoline (DI-G) injector with a 60 deg spray angle that is capable of multiple injections. The use of double injection was explored for emission control, and the engine was optimized using fully automated experiments and a microgenetic algorithm optimization code. The variables changed during the optimization include the intake air temperature, start of injection timing, and the split injection parameters (percent mass of fuel in each injection, dwell between the pulses) using three different objective (merit) functions. The engine performance and emissions were determined at 700 rev/min with a constant fuel flow rate at 10 MPa fuel injection pressure. The results show the choice of merit or objective function (optimization goal) determines the engine performance, and that significant emission reductions can be achieved with optimal injection strategies. Merit function formulations are presented that minimized PM, HC, and NO_x emissions, respectively. [DOI: 10.1115/1.1635395]

Introduction

The US Environmental Protection Agency (EPA) and California's Air Resources Board (CARB) are instituting mandates for reducing the exhaust emissions from stationary and mobile IC engines. The exhaust emissions standards phasing in for 2007 for heavy-duty engines will be 0.25 g/kW-hr NO_x+HC and 0.01 g/kW-hr PM, [1]. It will not be easy to reach these low emissions levels for heavy-duty engines. Therefore, engine exhaust emissions reduction studies are receiving a great deal of attention.

The HCCI mode is an alternative combustion concept for the internal combustion engine. Like in SI engines, the fuel is homogeneously premixed with air if early injection is used (but with a high proportion of air) and when the piston reaches top dead center (TDC) this lean mixture autoignites as in a diesel engine. Because mixing occurs before the combustion starts, cooler burning occurs, and this causes reductions in NO_x and PM emissions. However, high unburned hydrocarbon (HC) and carbon monoxide (CO) emissions can be produced due to incomplete combustion. At the same time, it should be noted that there are other shortcomings of current HCCI engine concepts, such as low maximum power output, and difficulties in engine startup.

In direct injection spark ignition (DISI) gasoline engines, the fuel is injected directly into the cylinder and stratified near the spark plug. This allows for a flame to propagate, and fuel to be consumed with excess oxygen around the flammable fuel charge. The high-temperature flame produces NO_x emissions similar to those of a stoichiometric homogeneously charged engine. Due to the fuel stratification, locally rich fuel regions can also produce particulate matter (PM) emissions, [2]. Therefore, the current limitations on NO_x and particulate emissions of DISI engines have stimulated further investigation in alternative combustion systems like HCCI, which produces significantly lower emissions through overall lean operation, [3]. However, only a few studies on gasoline engines have been performed using the DI-HCCI combustion mode. A detailed review of previous HCCI engine research is given by Canakci and Reitz [4]. Marriott [2,5] studied the effect of SOI on HCCI combustion for different engine speeds and equivalence ratios, and concluded that SOI would be an effective and useful needed parameter to control ignition timing for transient engine applications. In that study, the study of double injection found that multiple injections were able to reduce NO_x emission

Contributed by the Internal Combustion Engine Division of THE AMERICAN SOCIETY OF MECHANICAL ENGINEERS for publication in the ASME JOURNAL OF ENGINEERING FOR GAS TURBINES AND POWER. Manuscript received by the ICE Division, March 2002; final revision received January 2003. Associate Editor: D. Assanis.

levels by up to 80% as compared to single injections with increased engine speed and constant intake air temperature.

In Marriott and Reitz's study, [6], the first injection took place early in the cycle (e.g., during the intake stroke) to allow time for the formation of a lean homogeneous mixture. This lean mixture was such as to avoid self-ignition during the compression stroke. The second injection occurred during the compression stroke and provided a locally rich mixture to serve as the ignition source. In that study, especially the effect of individual parameters on the engine performance and emissions was investigated. To further explore this concept, in the present study, a HCCI direct-injection gasoline engine was used to investigate and optimize the effects of double injections and intake air temperature on the engine performance and emissions.

Experimental and computational studies to simultaneously investigate the effects of different input parameters on the emissions and performance of the Caterpillar 3400 series heavy-duty DI diesel engine used here have been reported in Refs. [7–10]. The results have shown that NO_x and PM emissions, as well as fuel consumption can be reduced over the entire engine operating range by optimizing engine inputs such as start of injection (SOI), injection pressure, amount of EGR, boost pressure, and split-injection rate shape, multiple injections, and EGR. This may also be true for HCCI combustion. However, there are many options to control the ignition timing of HCCI combustion, and little research has been conducted to simultaneously investigate the effects of different engine input parameters on the emissions and performance of HCCI combustion. Therefore, the objective of this study was to explore HCCI engine performance and emissions using double injections and inlet air temperature variation with various optimization criteria.

Experimental Setup

A fully instrumented, single cylinder oil test engine (SCOTE) was used after converting it to an HCCI direct-injection gasoline engine. The engine was connected to a 68 kW Westinghouse direct current dynamometer. The SCOTE is capable of producing 62 kW at 1800 rpm when operated as a diesel engine. The basic specifications of the engine are provided in Table 1 and a schematic of the engine test cell is shown in Fig. 1.

Table 1 Test engine specifications, [2]

Engine	Caterpillar 3401 SCOTE (single-cylinder oil test engine)
Bore×stroke	137.2 mm×165.1 mm
Compression ratio	16.1:1
Displacement	2.44 liters
Connecting rod length	261.62
Squish height	1.57 mm
Combustion chamber	In-piston Mexican hat with sharp edged crater
Valve train (four-valve)	EVC=−355 deg ATDC IVC=−143 deg ATDC EVO=130 deg ATDC IVO=335 deg ATDC
Piston	Articulated
Charge mixture motion	Quiescent

A data acquisition system was used to generate all digital information regarding the engine experiments by averaging 50 engine cycles in 0.5 deg CA increments. For the purpose of running the automated genetic algorithm experiments in the laboratory, specialized data acquisition and analysis software (AutoOpt GA), [10], found using National Instruments LabWindows/CVI programming software, was used. To control the engine and its subsystems for the automated experiments, both RS-232 serial and analog communication was established between a laboratory PC, (for acquisition, analysis, and control) and each of the process controllers and measurement instruments, which included

- dynamometer controller,
- injector controller,
- intake and exhaust tank pressure controller,
- gaseous emission analyzer,
- AVL DPL particulate analyzer,
- temperature scanner,
- EGR pump drive, and
- various pressure transducers.

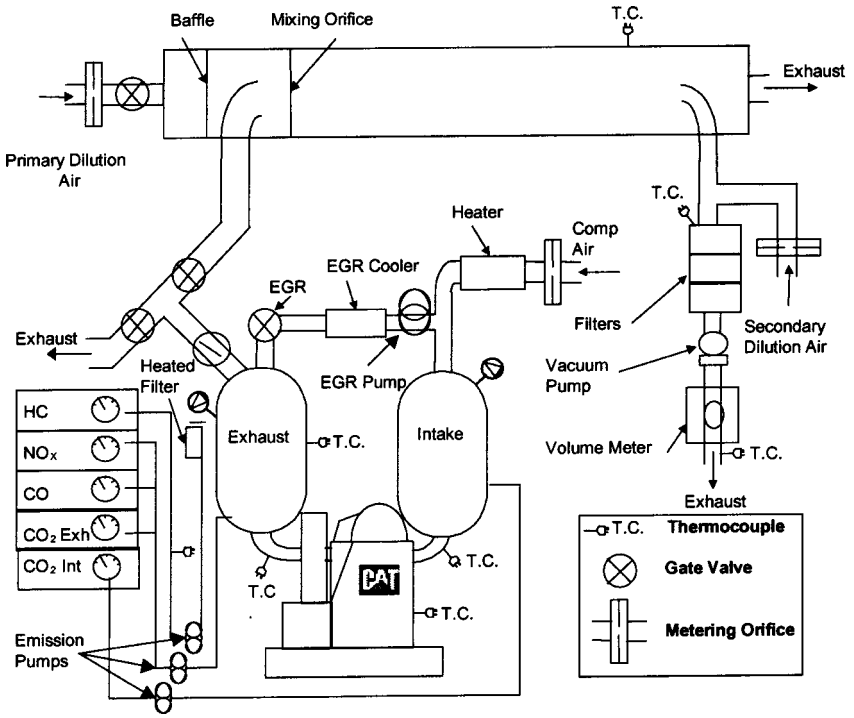

Fig. 1 Engine laboratory setup

Table 2 Fuel system specifications, [2]

Injector type	Delphi electronically controlled DI-G injector
Injection pressure	10 MPa
Poppet valve motion	Outwardly opening
Nozzle type	Pressure swirl atomizer
Spray geometry	Hollow cone
Spray orientation	Coaxial with the cylinder
Spray angle (included)	60 deg
Maximum continuous flow rate	11 g/sec
Valve opening response time	~0.5 msec
Valve closing response time	~0.2 msec

During the experiments, a temperature-controlled intake surge tank was used, as shown in Fig. 1. The intake air temperature was regulated by a closed-loop control system operating the two 220 V, three-phase, 4.5 kW intake air heaters placed in series within the intake air flow stream. All engine temperatures were monitored using type K dual element thermocouples. Engine fluid pressures were measured using a variety of gages and transducers.

A prototype, low-pressure, direct injection-gasoline (DI-G) injector supplied by Delphi Energy and Engine Management Systems was used. The injector creates a hollow cone sheet spray for good atomization. The injector was designed to operate with a rail pressure of 10 MPa and for injections into a gas with pressures less than 2 MPa. This restriction allows for an end of injection (EOI) timing as late as −25 deg ATDC for the SCOTE under normally aspirated operation. The basic specifications are shown in Table 2. Detailed information about the fuel injection system is given in Ref. [2]. The fuel used in the present study was Amoco Indolene. Fuel analysis results provided by the manufacturer are given in Table 3.

Emissions data recorded during the engine tests include unburned HC, CO, CO_2, NO_x, and PM. Analyzer calibration was done before the tests. Dry NO_x, CO, and CO_2 emissions were measured after a particulate filter and ice bath. Unburned HC was measured after a heated filter, heated transport line, and heated diaphragm pump, all of which were maintained at 190°C to prevent UHC condensation. The instruments used in the measurements of the engine exhaust emissions are summarized in Table 4.

Table 3 Fuel analysis results, [15]

Fuel	Amoco Indolene
Carbon (by mass)	86.38%
Hydrogen (by mass)	13.28%
C/H ratio	1.83
Lower heating value (LHV)	42.90 MJ/kg
Sulfur content	3 ppm
Research octane number (RON)	97.1
Motor octane number (MON)	89.0
API gravity @ 60°F	59.0
Reid vapor pressure, (kPa)	63.43
Distillation, (°C)	
Initial boiling point	31.7
10% evaporation	54.4
50% evaporation	105.0
90% evaporation	159.4
endpoint	197.2

Table 4 Exhaust emission measurement equipment

NO/NO_x	Chemiluminescent detector/California Analytical Inc., Model 400-CLD
CO	Infrared gas analyzer/California Analytical Inc., Model 3300A
CO_2	Infrared gas analyzer/Horiba, Model VIA-510
UHC	Flame ionization detector (FID)/Siemens, Model FIDAMAT 5E-IM
Soot	Dynamic Particulate analyzer/AVL, Model DPL 482

Genetic Algorithm and Optimization Methodology

Genetic algorithms can be divided into two distinct types, the simple GA and the micro-GA (μGA). Though the basic principles of natural selection are common to both types, including evaluation of citizen merit and breeding of the fittest individuals, differences in the application of mutations allow for beneficial changes in the structure of the μGA. The simple GA utilizes a population size of roughly 200 individuals and intersperses random mutations, [11]. With such an algorithm, only a few generations pass before thousands of function evaluations are made. With time-consuming evaluations, such as those required for three-dimensional combustion simulations or experimental engine runs, this method proves to be prohibitive. A μGA on the other hand utilizes only a small number of citizens per generation. Because there are only roughly five individuals in each generation, the population is likely to converge (all citizens consist of the same genes) relatively quickly. To ultimately reach an optimum, the μGA randomly disperses the micropopulation when convergence occurs, with the exception that the fittest citizen from the converged generation is kept. This characteristic is called elitism. With elitism, when the population converges again, it will have a maximum fitness that is equal to or greater than the fitness experienced during four the last convergence. In this manner, significant fitness improvements are obtained in steps, but the number of required function evaluations is reduced considerably, [12].

A baseline design, parameters of interest, a merit function, and its evaluation method must be selected for an optimization study. A genetic algorithm code was used in the present optimization study that was originally developed by Senecal and Reitz [8]. The code uses the microgenetic algorithm (μGA) technique based on the GA code of Carroll [13]. The optimization methods used in this experimental work are also discussed and compared with other algorithms in detail in Refs. [8] and [14].

Baseline Design and Parameters of Interest. The baseline operating conditions are presented in Table 5. The engine speed was 700 rev/min with parameters from the double injection study of Marriott [2]. The intake air temperature was 99°C; 69% of the fuel mass was injected in the first injection with an equivalence ratio of 0.26. The start of injection timings (SOI) for the first and second injections were −289 and −107 deg CA ATDC, respectively.

The nomenclature used in defining multiple injections was of the form 50(110)50 where 50% of the fuel is injected in the first pulse followed by a 110 deg CA dwell and 50% of the fuel injected in the second pulse.

As stated earlier, for the present study the optimization parameters were the intake air temperature, start-of-injection timing, and split injection parameters (percent mass of fuel in each injection, and the dwell between the pulses). The considered engine optimization variables and ranges are presented in Table 6. The optimization target values are given in Table 7. These values were defined as 80% of the EPA's 2004 emission regulations for heavy-duty engines since to set a safety factor and it improves upon the regulation.

Table 5 Operating conditions for the baseline engine case

Engine speed (rpm)	700
Intake pressure (MPa)	0.1
Exhaust pressure (MPa)	0.1
Injection pressure (MPa)	10
Equivalence ratio	0.26
Intake temperature (°C)	99
1st SOI (deg CA ATDC)	−289
2nd SOI (deg CA ATDC)	−107
Fuel mass in first pulse (%)	69.0

Table 6 Engine optimization variables and ranges for 700 rpm

Variable	Range
Inlet air temperature (°C)	80→120
Start of injection (deg CA ATDC)	−320→−115
Fuel mass in first pulse (%)	10→90
Dwell between pulses (deg CA)	5→160

Objective Function and Its Evaluation. The purpose of the present study was to reduce pollutant emissions of the engine by varying operating parameters. Therefore, a general merit function should contain exhaust emission measurements, including NO_x, HC, CO, and PM, as well as fuel consumption. However, the choice of merit function is not well defined. For example, PM is usually reduced at the expense of an increase in NO_x. However, with HCCI, high levels of unburned HC (relative to target values) contribute to PM, which mostly consist of soluble organic fraction (SOF). The unburned HC and CO in the exhaust also directly affect BSFC. Clearly, NO_x+HC, NO_x, and BSFC should appear in the merit function. But it is not clear whether PM is relevant because it is largely determined by the HC. Similar objective functions have been used for diesel optimizations that also include PM in Refs. [8–10], but in this study it was felt that inclusion of PM would be misleading since the carbonaceous fraction of the particulate was small. Since CO and HC emissions are also of interest, it could be argued that they should also appear as parameters in the optimization. This motivated the use and comparison of several objective functions. Specifically, the objective functions used in this study were

$$f_1(\mathbf{X}) = \frac{2*10^3}{R_1^2+R_2^2+R_3^2+R_5} \tag{1}$$

$$f_2(\mathbf{X}) = \frac{10^3}{R_1^2+R_5} \tag{2}$$

$$f_3(\mathbf{X}) = \frac{10^3}{R_4^2+R_5} \tag{3}$$

where

$$R_1 = \frac{NO_x+HC}{(NO_x+HC)_t} \tag{4}$$

$$R_2 = \frac{CO}{(CO)_t} \tag{5}$$

$$R_3 = \frac{PM}{PM_t} \tag{6}$$

$$R_4 = \frac{NO_x}{(NO_x)_t} \tag{7}$$

$$R_5 = \frac{BSFC}{BSFC_t}. \tag{8}$$

The parameter vector **X** is the array of control factors, (SOI, Air Temp, dwell, etc.). For the current study, the target values were 2.68 g/kW-hr NO_x+HC, 16.63 g/kW-hr CO and 0.11 g/kW-hr PM, as given in Table 7. The BSFC target value was 200 g/kW-hr, which is the baseline fuel consumption of the SCOTE at the engine speed of 700 rpm with an equivalence ratio of 0.26.

Table 7 Optimization target values

Emission	Target Value (g/kW-hr)
$(NO_x+HC)_t$	2.68
$(NO_x)_t$	2.14
CO_t	16.63
PM_t	0.11
$BSFC_t$	200

The motivation for the squared dependence on emissions and the linear dependence on BSFC is that this formulation promotes fast convergence initially on the emission targets, and once they are met, the fuel consumption becomes weighted in the optimization, [9]. After inserting the measured values in Eqs. (1), (2) or (3), the optimum search provides a higher merit value for those members of each generation with lower exhaust emissions and fuel consumption. Since it is more convenient to work with integer merit values, the factor of 10^3 was included in the numerator of the function. The additional factor of 2 in Eq. (1) ensures that all merit formulations have a value of $f=500$ when the target values have all been reached.

The physical constraints on the engine included a maximum intake pressure of 276 kPa, a dP/dt of 5 bar/degree, a maximum exhaust temperature of 1023 K, and peak combustion pressure of 15.2 MPa. Cases that violated these constraints were rejected.

Results and Discussion

The optimization ranges were first determined for each variable. The values used in the present study are given in Table 6. Starting with a random number seed, the algorithm was run for 16 generations (i.e., $16\times4=64$ test conditions) using the full optimization goal, Eq. (1). Figure 2 and Table 8 present, respectively, the in-cylinder combustion characteristics and operating conditions of the baseline and optimum cases.

The optimum was found to have an intake air temperature of 110°C, and 31.3% of fuel mass injected in the first injection. The SOI for the first and the second injections were −143.5 and −116 deg CA ATDC, respectively.

As seen in Fig. 2, the peak cylinder pressure for the f_1 optimum case are higher than those of the baseline case as a result of the different operation conditions. The air-fuel mixture is less homogeneous than in the baseline case since the first SOI is 145.5 deg later than the first SOI of the baseline case and there is a shorter dwell between injections. 68.7% of the total fuel injected was used in second injection. However, the higher intake air temperature helps the vaporization process. Note that the dwell between injections was close to the minimum dwell allowed by the injection hardware. This suggests that this merit function formulation, function f_1, selects an injection that is similar to a single injection.

Figure 3 shows the merit value of each citizen as a function of generation number where the maximum merit value for the generation is shown by the solid line. Throughout the optimization, the maximum merit value increased only two times, suggesting that convergence may not have been achieved by the 16th generation. As shown in Table 8, the unburned HC and particulate is much higher than the target values, and the merit value is correspondingly very low.

Figures 4 and 5 present the BSFC versus NO_x and PM versus NO_x data points, respectively, for all the runs. The data show that the choice of variables in the merit function is very important, since in this case PM is reduced at the expense of a sizeable increase in NO_x. Note that very high levels of unburned HC (relative to the target value) are also found. The unburned HC and CO amounts in the exhaust are reflected in the BSFC and, as can be seen, the f_1 optimization has improved HC and CO emissions relative to the baseline, and hence the improved BSFC.

The above results suggest that the objective function should contain only NO_x, and BSFC for improved optimization. Figure 5 shows that very high PM's (relative to the target) were found in the optimization. However, the AVL dynamic particulate analyzer results showed that around 95% of the measured value was soluble organic fraction (SOF). This is consistent with the high measured HC concentration, as seen in Table 8.

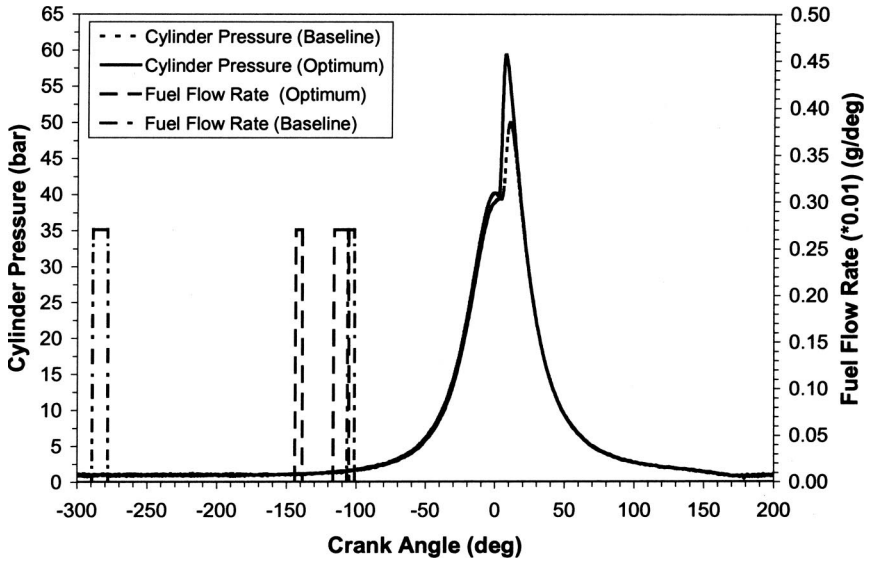

Fig. 2 Comparison of the in-cylinder characteristics of the baseline and optimum case with merit from Eq. (1)

-

Table 8 Target values, operating conditions, and emission results for the baseline and optimum engine cases

			Optimum After Using		
Operating Conditions	**Target**	**Baseline**	**Eq. (1)**	**Eq. (2)**	**Eq. (3)**
Intake temperature (°C)	–	99	110	120	115
1st SOI (deg CA ATDC)	–	−289	−143.5	−142.5	−245.5
2nd SOI (deg CA ATDC)	–	−107	−116	−121	−133
Fuel mass in first pulse (%)	–	69	31.3	58	69
Emissions (g/kW-hr)					
NO_x	2.14	0.02	0.73	0.73	0.01
HC	0.54	10.85	7.09	3.24	10.14
NO_x+HC	2.68	10.87	7.82	3.97	10.15
PM	0.11	1.59	0.58	0.24	1.30
CO	16.63	21.24	17.31	17.85	17.96
BSFC	200	261.65	254.24	286.31	257.13
Combustion efficiency (%)	–	94.21	97.10	97.59	94.64

Unburned HC also effects the BSFC and the relationship between combustion efficiency and NO_x+HC emission is shown in Fig. 6. Because of the choice of merit function, the optimum point has higher NO_x than the baseline (see also Fig. 4), and a higher combustion efficiency. Of course, other parameters also appear in the merit function of Eq. (1) (i.e., species other than NO_x), and their influence is included in the optimization. As can be seen in Table 8, the target values were not reached. Accordingly, a revised optimization was considered.

Clearly, the optimum reached depends on the choice of parameters selected in the merit function. As an alternative, the merit function was changed to deemphasize the contribution of unburned HC and soluble particulates, as shown in Eq. (2), which now only considers NO_x+HC and BSFC. Starting with a random number seed, the algorithm was run for 33 generations (i.e., $33 \times 4 = 132$ test conditions). Figure 7 and Table 8 present, respectively, the in-cylinder combustion characteristics and operating conditions of the baseline and the new optimum for the case where f_2 (Eq. (2)) is used.

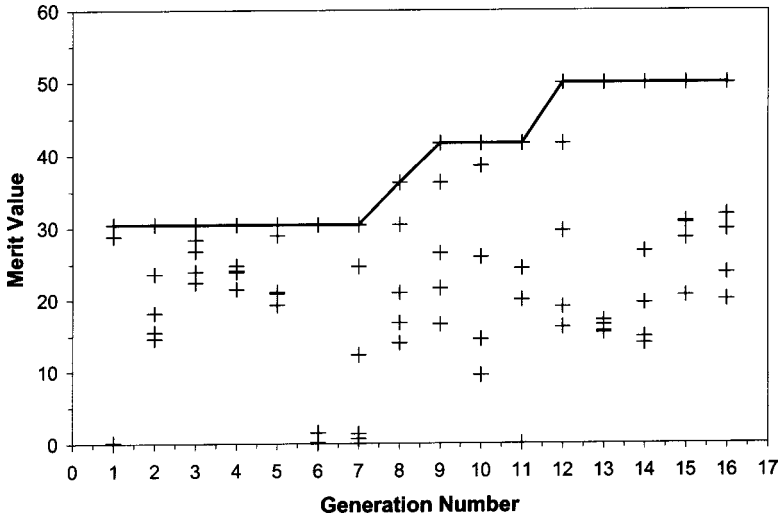

Fig. 3 Merit value versus generation number for merit determined from Eq. (1)

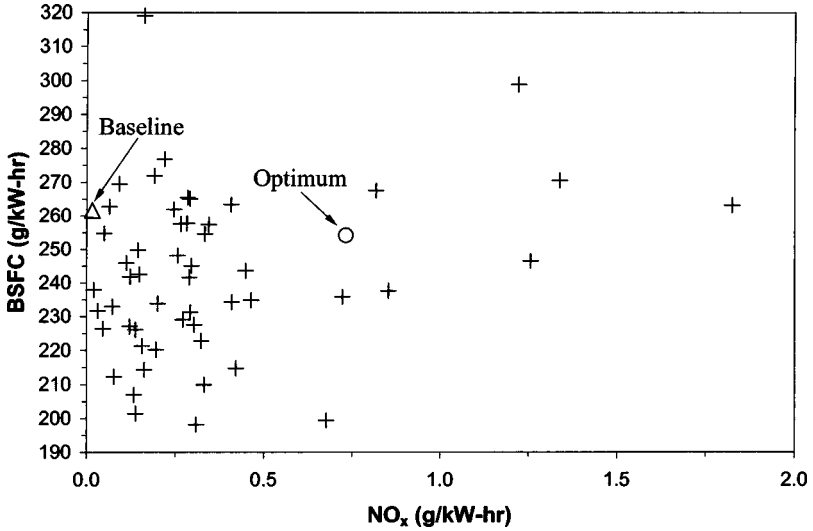

Fig. 4 BSFC versus NO_x data with merit from Eq. (1)

After convergence, the optimum conditions were found to be an intake air temperature of 120°C, 58% of fuel mass injected in the first injection and the SOI for the first and the second injections were −142.5 and −121deg CA ATDC, respectively.

As seen in Fig. 7, the peak cylinder pressure for the optimum case is higher than that of the baseline case. The air-fuel mixture is less homogeneous than in the baseline case since the first SOI is 146.5deg later than the first SOI of the baseline case and there is a shorter dwell (i.e., reduced time for mixing) between the injections. In fact, the dwell between injections (10°) is the minimum allowed by the injection hardware. 42% of the total fuel injected was used in second injection but a single injection would probably have been preferred.

Figure 8 shows that the merit value is much improved compared to these of Fig. 3. Throughout the optimization, the maximum merit value increased only three times, but it stayed constant from generation 23 to 33, suggesting that convergence was achieved. However, as shown in Table 8, the unburned HC and particulate is still higher than the target values, although they are significantly improved relative to the Eq. (1) optimum and the baseline case. However, exhaust gas after treatment could be used with this engine concept to remove unburned HC.

Figures 9 and 10 present the BSFC versus NO_x and PM versus NO_x data, respectively. The data show that the HC and PM is reduced with similar NO_x to the Eq. (1) optimization. Figure 10 shows that very high PM was found in the baseline, low NO_x case. The optimized case had much improved PM levels, albeit higher than the target (0.11 g/kW-hr). However, the AVL dynamic particulate analyzer results again showed that around 95% of the measured value was soluble organic fraction (SOF) in the PM.

The relationship between combustion efficiency and the NO_x + HC emissions is shown in Fig. 11. Because of the choice of merit function, the optimum point has higher NO_x but lower NO_x + HC than the baseline (see Fig. 9), and it has significantly higher combustion efficiency.

When comparing the optimum case to the baseline case, the air-fuel mixture is evidently less homogeneous due to the later injection of the first pulse and the larger fuel amount in the second pulse. As seen in Table 8, reduced PM and NO_x + HC emissions were obtained at the expense of significantly increased fuel con-

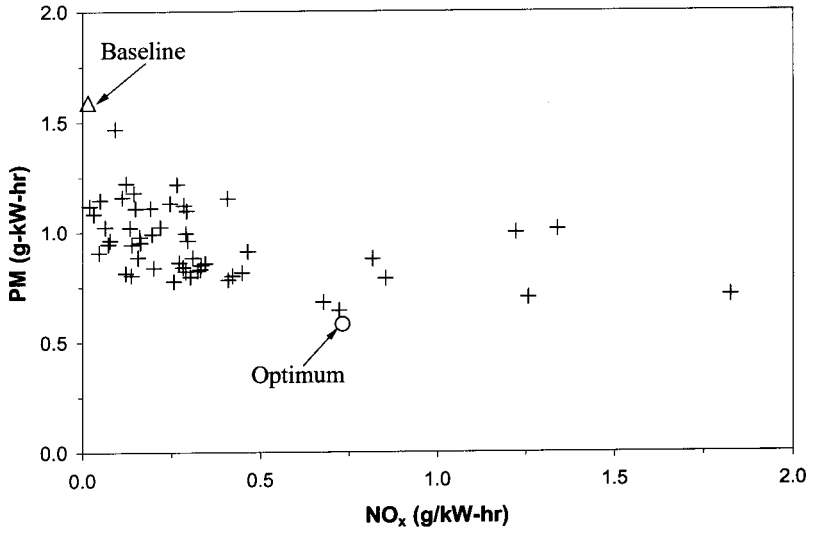

Fig. 5 PM versus NO_x data with merit from Eq. (1)

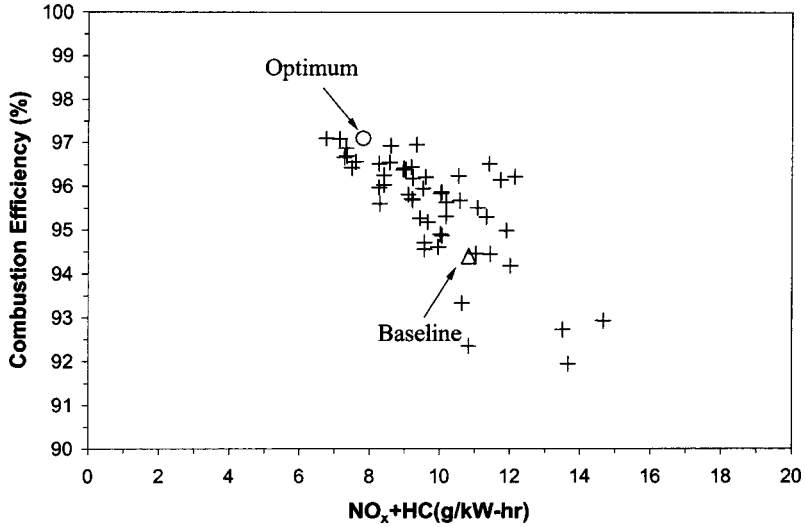

Fig. 6 Combustion efficiency versus NO_x+HC data with merit from Eq. (1)

sumption. The reduction in the PM for the optimum case was likely due to the higher intake air temperature (120°C) which helps the vaporization process. The higher intake temperatures required retarded SOI timing and unburned HC emission decreased with retarded SOI timing in first injection, which caused increased fuel stratification. This reduction in HC emission improved the combustion efficiency and CO emission relative to baseline. The NO_x emission increased with retarded SOI timing, suggesting that the optimum case has higher local combustion temperatures. This indicates that SOI timing has significant effect on the combustion. Table 8 also presents a comparison of the target and optimum values. As can be seen, the target values were not reached, except for NO_x.

In order to further deemphasize HC in the optimization, a third objective function formulation was also considered that contained only NO_x and BSFC (Eq. (3)). Starting the from the baseline case, the algorithm was run for 26 generations (i.e., $26\times4=104$ test conditions). Figure 12 and Table 8 show, respectively, the in-cylinder combustion characteristics and operating conditions of the baseline and optimum cases. The optimum conditions were found to be an intake air temperature of 115°C, with 69% of fuel mass injected in the first injection and the SOI for the first and the second injections were −245.5 and −133 deg CA ATDC, respectively. In this case the optimum consisted of two distinct widely spaced injections, similar to those used in the baseline case.

A higher peak cylinder pressure was obtained for this optimum case than that of the baseline case as a result of the different operating conditions. The higher intake air temperature helps the vaporization process, and the air-fuel mixture is less homogeneous than in the baseline case since the first SOI is 43deg later than the first SOI of the baseline case, and there is a shorter dwell between the injections. 31% of the total fuel injected was used in second injection.

Figure 13 shows the evaluation of the merit value of each citizen as a function of generation number after using the alternative objective function. The maximum merit value slightly increased only one time and stayed constant from generation 5 to 26 throughout the optimization. However, as shown in Table 8, the unburned HC and PM are still higher than the target values, but slightly improved relative to the baseline case. This is not surpris-

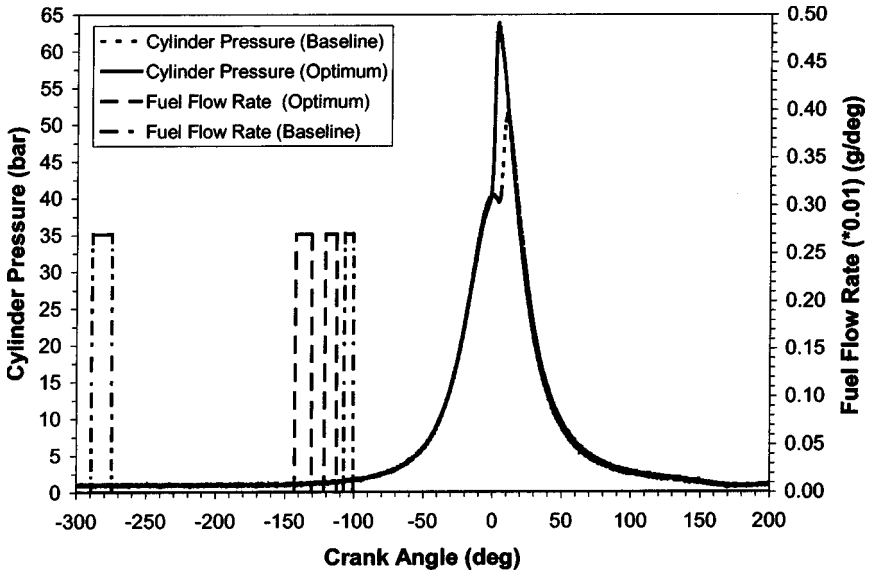

Fig. 7 Comparison of the in-cylinder characteristics of the baseline and optimum cases from Eq. (2)

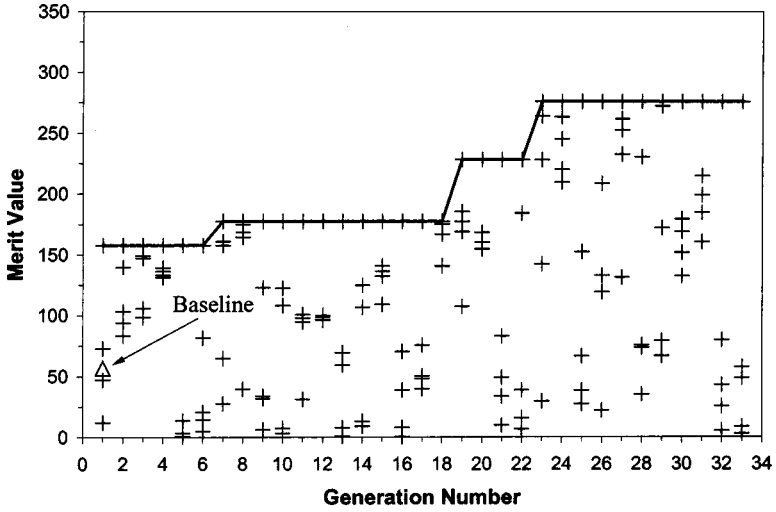

Fig. 8 Merit value versus generation number from Eq. (2)

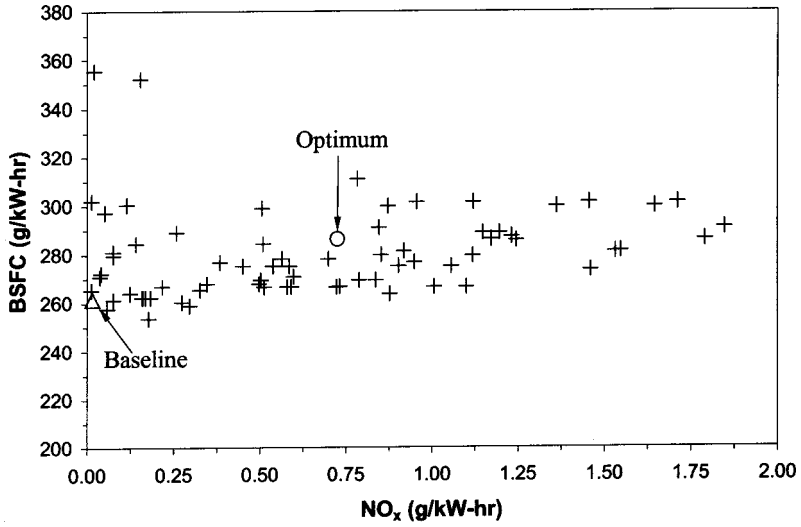

Fig. 9 BSFC versus NO_x data from Eq. (2)

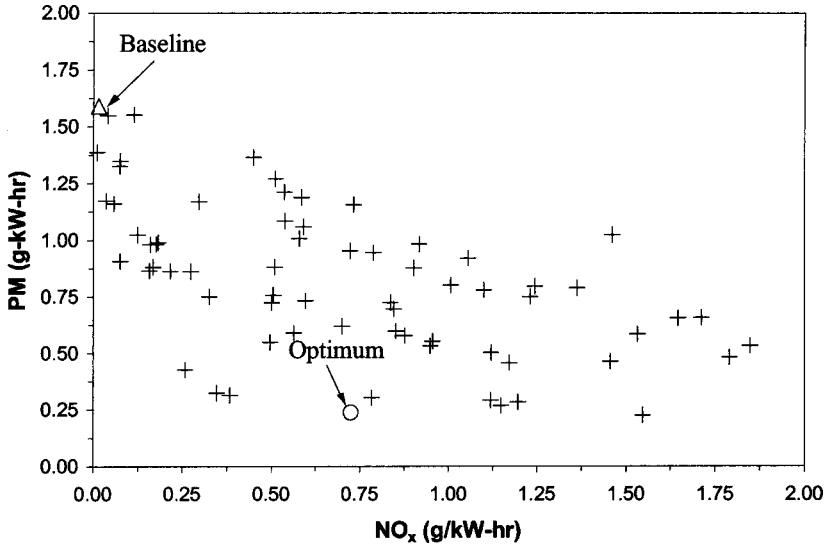

Fig. 10 PM versus NO_x data from Eq. (2)

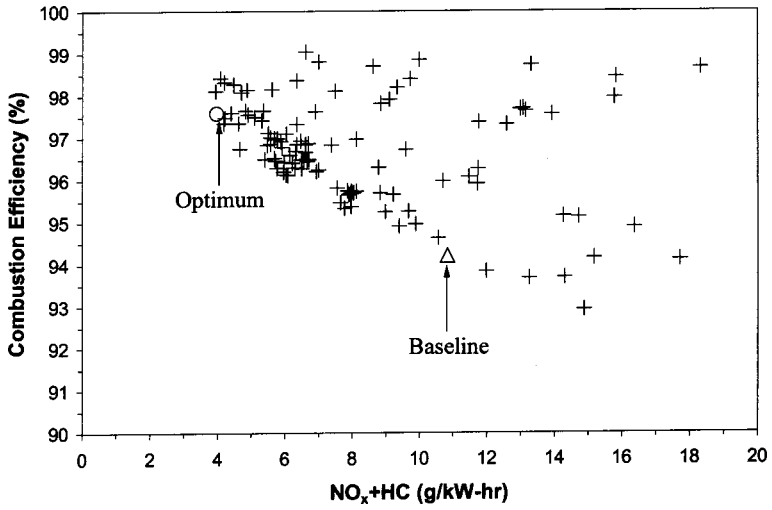

Fig. 11 Combustion efficiency versus NO_x+HC data from Eq. (2)

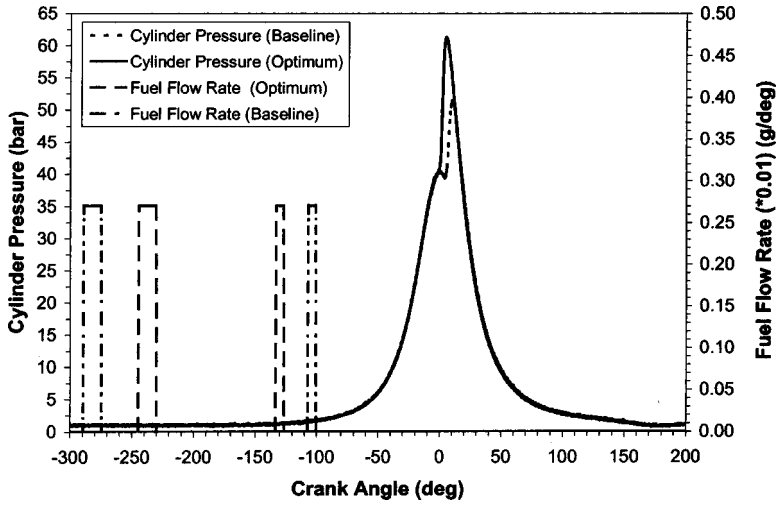

Fig. 12 Comparison of the in-cylinder characteristics of the baseline and optimum cases with merit from Eq. (3)

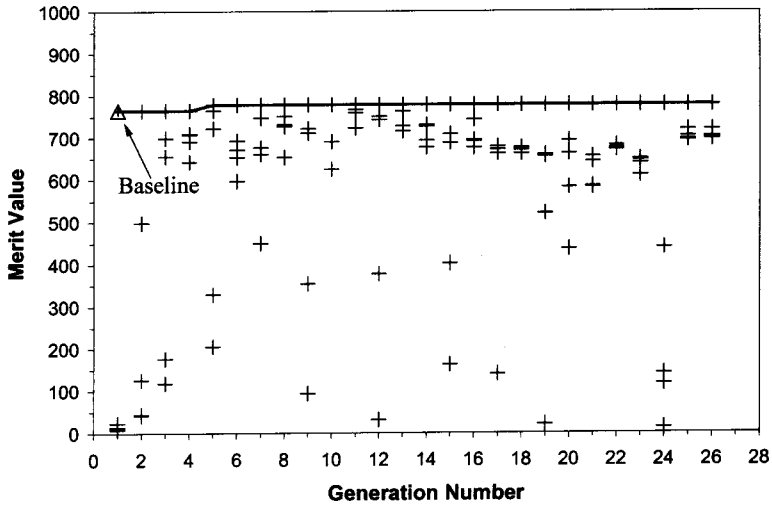

Fig. 13 Merit value versus generation number for merit determined from Eq. (3)

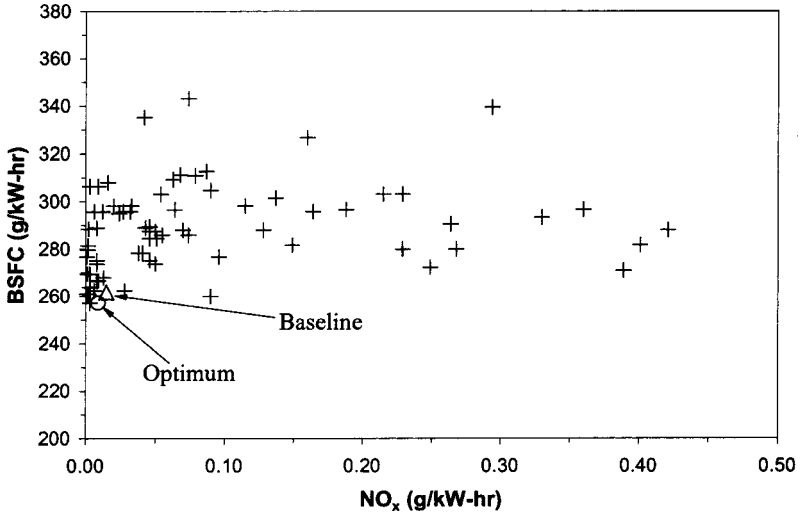

Fig. 14 BSFC versus NO_x data with merit from Eq. (3)

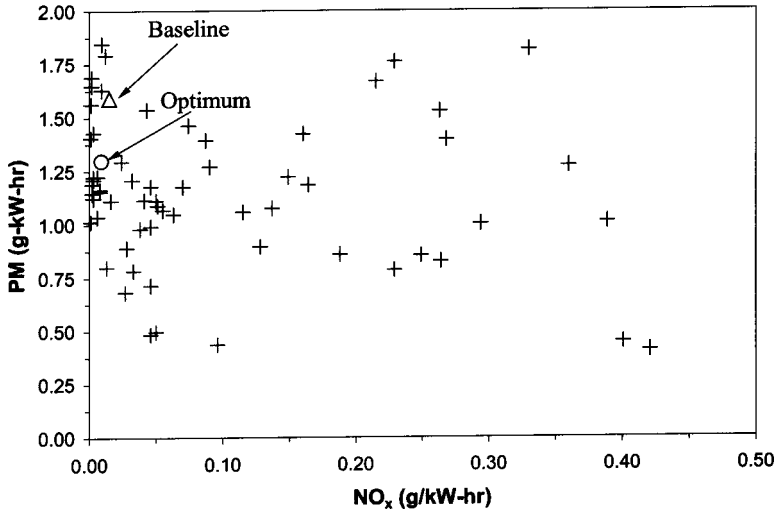

Fig. 15 PM versus NO_x data with merit from Eq. (3)

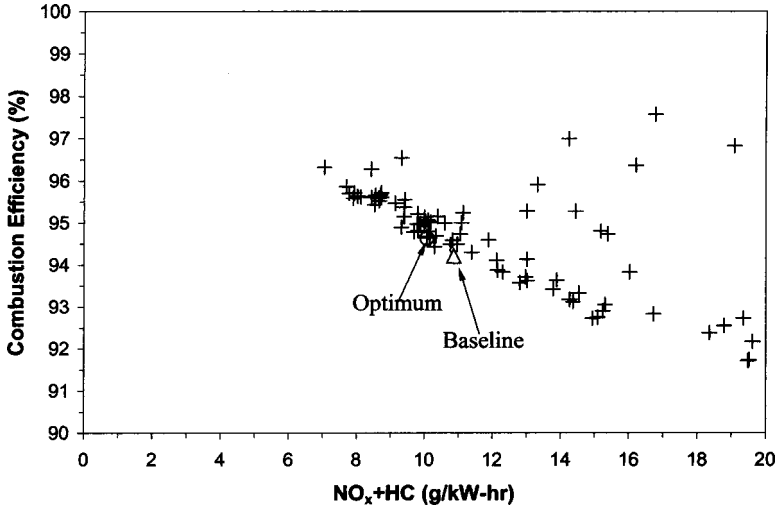

Fig. 16 Combustion efficiency versus NO_x+HC data with merit from Eq. (3)

ing since Marriott and Reitz [6] emphasized NO_x reduction in their study, and the merit formulation in Eq. (3) concentrates on NO_x reduction.

Figures 14 and 15 present the BSFC versus NO_x and PM versus NO_x data, respectively. The data show that the injection timing choice of Marriott [2] for split injection is very reasonable for an inlet air temperature of 99°C. As seen in Fig. 15, high PM's were found in the baseline case. However, the optimized case had improved PM levels, but still higher than the target (0.11 g/kW-hr). Again the AVL dynamic particulate analyzer results showed that around 95% of the measured PM was soluble organic fraction (SOF).

The relationship between combustion efficiency and the NO_x + HC emissions is shown in Fig. 16. The optimum point has slightly higher combustion efficiency than the baseline.

It is evident from the results of this study shown in Table 8 that the emission and BSFC results for the cases depend on the objective function since it determines the operating parameters to achieve the optimum case.

Summary and Conclusions

An electronically controlled Caterpillar single-cylinder oil test engine (SCOTE) was configured as a direct-injection gasoline engine. The use of double injections was explored for emission control, and the engine was optimized using fully automated experiments and a microgenetic algorithm optimization code. The variables changed during the optimization included the intake air temperature, start of injection timing, and the split injection parameters (percent mass of the fuel in each injection, dwell between the pulses) using three different objective functions. The chosen objective functions emphasized PM, HC, and NO_x reduction, respectively. The engine performance and emissions were determined at 700 rev/min with a constant fuel flow rate at 10 MPa fuel injection pressure. The results show that significant emissions reductions are possible with the use of optimal injection strategies. The fully automated experiments and optimization methodology provides a useful tool for engine designers investigating the effects of a large number of input parameters on emissions and performance. This technique efficiently determined input parameters that resulted in significantly lower emissions and BSFC compared to a baseline case. The results also show that the appropriate selection of the merit function is crucial in the search for optimum engine parameters for improved emissions and BSFC in HCCI combustion. As can be seen in Table 8, the target values were not also reached for all cases. However, by using catalytic exhaust after treatment technology, the vehicle-out HC emissions could likely be reduced to the target values.

Acknowledgments

This research was funded by Caterpillar Inc. and the DOE/Sandia National Laboratories. The authors would like to thank Eric Hruby for his contribution, and other individuals at Caterpillar who were involved in making this work possible.

References

[1] EPA Document, 2000, ''Heavy-Duty Engine and Vehicle Standards and Highway Diesel Fuel Sulfur Control Requirements,'' EPA Document #: EPA420-F-00-057, Dec.
[2] Marriott, C. D., 2001, ''An Experimental Investigation of Direct Injection for Homogeneous and Fuel-Stratified Charge Compression Ignited Combustion Timing Control,'' M.S. thesis, University of Wisconsin, Madison, WI.
[3] Kong, S-C., Marriott, C. D., Reitz, R. D., and Christensen, M., 2001, ''Modeling and Experiments of HCCI Engine Combustion Using Detailed Chemical Kinetics with Multidimensional CFD,'' SAE Paper 2001-01-1026.
[4] Canakci, M., and Reitz, R. D., 2002, ''Experimental Optimization of a DI-HCCI-Gasoline Engine Using Split Injections With Fully-Automated Micro-Genetic Algorithms,'' Int. J. of Engine Research, **4**(1), pp. 47–60.
[5] Marriott, C. D., Kong, S-C., and Reitz, R. D., 2002, ''Investigation of Hydrocarbon Emissions From Direct Injection-Gasoline Premixed Charge Compression Ignited Engine,'' SAE Paper 2002-01-0419.
[6] Marriott, C. D., and Reitz, R. D., 2002, ''Experimental Investigation of Direct Injection-Gasoline for Premixed Compression Ignited Combustion Phasing Control,'' SAE Paper 2002-01-0418.
[7] Montgomery, D. T., and Reitz, R. D., 1996, ''Six-Mode Cycle Evaluation of the Effect of EGR and Multiple Injections on Particulate and NO_x Emissions from a D.I. Diesel Engine,'' SAE Paper 960316.
[8] Senecal P. K., and Reitz, R. D., 2000, ''Simultaneous Reductions of Engine Emissions and Fuel Consumption Using Genetic Algorithms and Multi-Dimensional Spray and Combustion Modeling,'' SAE Paper 2000-01-1890.
[9] Montgomery, D. T., and Reitz, R. D., 2001, ''Effects of Multiple Injections and Flexible Control of Boost and EGR on Emissions and Fuel Consumption of a Heavy-Duty Diesel Engine,'' SAE Paper 2001-01-0195.
[10] Thiel, M. P., 2001, ''Application of Automated Experiments to the Optimization of a Heavy-Duty Direct Injected Diesel Engine for the Simultaneous Reduction of NO_x and Particulate Emissions,'' M.S. thesis, University of Wisconsin, Madison, WI.
[11] Goldberg, D. E., 1989, ''Genetic Algorithms In Search, Optimization and Machine Learning,'' Addison-Wesley, Reading, MA.
[12] Senecal, P. K., 2000, ''Development of a Methodology for Internal Combustion Engine Design Using Multi-Dimensional Modeling With Validation Through Experiments,'' Ph.D. thesis, University of Wisconsin, Madison, WI.
[13] Carroll, D. L., 1996, ''Genetic Algorithms and Optimizing Chemical Oxygen-Iodine Lasers,'' Developments in Theoretical and Applied Mechanics, **18**, p. 411.
[14] Thiel, M. P., Klingbeil, A. E., and Reitz, R. D., 2002, ''Experimental Optimization of a Heavy-Duty Diesel Engine Using Automated Generic Algorithms,'' SAE Paper 2002-01-0960.
[15] BP Amoco Indolene Manufacturer Test Sheet.

A. A. Al-Farayedhi
Mechanical Engineering Department,
King Fahd University of Petroleum and Minerals,
Dhahran 31261, Saudi Arabia

A. M. Al-Dawood
Mechanical Technology Department,
College of Technology at Dammam,
Dammam 31472, Saudia Arabia

P. Gandhidasan
Mechanical Engineering Department,
King Fahd University of Petroleum and Minerals,
Dhahran 31261, Saudi Arabia

Experimental Investigation of SI Engine Performance Using Oxygenated Fuel

The current experimental study aims to examine the effects of using oxygenates as a replacement of lead additives in gasoline on performance of a typical SI engine. The tested oxygenates are MTBE, methanol, and ethanol. These oxygenates were blended with a base unleaded fuel in three ratios (10, 15, and 20 vol.%). The engine maximum output and thermal efficiency were evaluated at a variety of engine operating conditions using an engine dynamometer setup. The results of the oxygenated blends were compared to those of the base fuel and of a leaded fuel prepared by adding TEL to the base. When compared to the base and leaded fuels, the oxygenated blends improved the engine brake thermal efficiency. The leaded fuel performed better than the oxygenated blends in terms of the maximum output of the engine except in the case of 20 vol.% methanol and 15 vol.% ethanol blends. Overall, the methanol blends performed better than the other oxygenated blends in terms of engine output and thermal efficiency. [DOI: 10.1115/1.1615254]

Introduction

The anti-knock quality of the gasoline fuel used in spark-ignition internal combustion engines can be enhanced by the addition of lead alkyls but this results in the formation and emission of toxic lead compounds. A recent practice is to enhance the anti-knock property of the fuel by using certain high-octane oxygen-containing organic compounds called oxygenates. The use of oxygenates to replace the lead additives in gasoline is considered now as an alternative. The aim of this experimental work is to help in understanding the effect of the most popular oxygenates on the performance of typical automotive engines. The most commonly used oxygenates are MTBE (methyl tertiary butyl ether, $C_4H_9-O-CH_3$), methanol (CH_3-OH), and ethanol (C_2H_5-OH). MTBE is manufactured from isobutane ($(CH_3)_3CH$) and methanol, while methanol is manufactured from natural gas or synthesized from a variety of materials such as coal, municipal wastes, and biomass. Ethanol is derived from the direct fermentation of sugars, fermentation of starches and cellulose after chemical or enzymatic pretreatment, or made from petroleum sources.

These three oxygenates have different chemical and physical properties when compared to gasoline. These differences are expected to influence the performance and combustion products of gasoline-oxygenate blends. The study offers a comparison between the oxygenated and leaded fuels in terms of engine performance.

Experimental Setup

The experiments were conducted using a six-cylinder engine. This engine is manufactured by Mercedes-Benz and has a swept volume of 2960 cm^3. It has a bore of 88.5 mm, a stroke of 80.2 mm, a compression ratio of 9.2, and a maximum power of 132 kW at 5700 rpm. The engine is equipped with the KE-Jetronic continuous fuel injection system. The engine has an electronic ignition system with an electronic spark timing adjustment. The temperatures of cooling water and lubrication oil are controlled by two fitted heat exchangers. The engine is coupled to an eddy-current dynamometer. This eddy-current dynamometer is electronically controlled and water cooled. It has a maximum power of 257 kW, a maximum torque of 1400 Nm, and a maximum speed of 8000 rpm. The effects of blending the oxygenates with unleaded gasoline on exhaust emissions of SI engines are presented in [1,2]. The detailed description of the test equipment used in this study is given in [3].

Test Fuels

A base fuel was prepared by mixing 20% of naphtha with 80% of reformate on volumetric basis. A leaded fuel was prepared by adding tetra ethyl lead (TEL) to the base fuel. The addition of TEL brought the lead concentration in the fuel to 0.4 g pb/liter. The tested oxygenates are the MTBE (methyl tertiary butyl ether), methanol, and ethanol. Each one of the three oxygenates is blended with the base fuel in three ratios: 10, 15, and 20 vol.%. The MTBE/base blends were designated MTBE10 (10 vol.% MTBE+90 vol.% base), MTBE15, and MTBE20. The methanol/base blends were designated METH10, METH15, and METH20. The ethanol/base blends were designated ETH10, ETH15, and ETH20.

The purity of the MTBE was 98.71 wt.%, and the purity of methanol was 99.99 wt.%. The ethanol had a purity of 91.0 wt.%, and contains 7.8 wt.% of water. The presence of water is known to affect the miscibility of alcohol in gasoline. A blend of alcohol and gasoline tolerates the presence of water up to certain percentage, then any additional water will cause the alcohol to separate from the gasoline. Ethanol is known to have appreciably more tolerance to water than methanol. In the case of the ethanol/base blends prepared in the current study, the phase separation was

Table 1 Properties of the oxygenates tested in this study

Property	MTBE	Methanol	Crude Ethanol
Weight percent oxygen	18	50	39
Reid vapor pressure (kPa)	61.2	37.1	17.5
Boiling temperature, °C	53.3	63.5	75.6
Specific gravity @ 15.56°C	0.7461	0.7954	0.816
Research octane number	116*	133*	129*
Lower heating value (MJ/kg)	35.2**	20.0**	24.77***
Latent heat of vaporization (kJ/kg)	340**	1160**	950***
Stoichiometric A/F ratio	11.76	6.47	8.3****

*Obtained from SAE handbook [9] for pure MTBE, methanol, and ethanol.
**Obtained from Ref. [10].
***Obtained from Ref. [10] for ethanol and adjusted for the presence of water.
****Calculated for ethanol and adjusted for the presence of water.

Contributed by the Internal Combustion Engine Division of THE AMERICAN SOCIETY OF MECHANICAL ENGINEERS for publication in the ASME JOURNAL OF ENGINEERING FOR GAS TURBINES AND POWER. Manuscript received by the ICE Division, Nov. 2002; final revision received May 2003. Associate Editor: D. Assanis.

Table 2 Properties of the test fuel

Fuel Property	Base	Leaded	MTBE10	MTBE15	MTBE20	METH10	METH15	METH20	ETH10	ETH15	ETH20
Specific gravity @ 15.56°C	0.7697	0.772	0.7638	0.7633	0.7628	0.7692	0.7697	0.7707	0.775	0.775	0.777
Rvp, kPa	35.0	33.6	41.0	41.6	42.4	57.4	61.6	66.5	59.5	58.1	54.6
Research octane number	84.7	92	87.9	89.8	91.7	88.2	91.6	94.4	88.4	91.5	93.4
Heat of vaporization, kJ/kg*	350	350	349	349	348	428	466	505	413	445	476
Weight percent oxygen*	0	0	1.77	2.66	3.55	5.15	7.71	10.27	4.08	6.10	8.11
Heating value, MJ/kg*	44	44	43.144	42.715	42.283	41.528	40.298	39.073	41.97	40.97	39.97
Stoichiometric A/F*	14.6	14.6	14.33	14.19	14.05	13.77	13.35	12.94	13.95	13.62	13.3
Hydrocarbon types, vol.%**											
N-Paraffins	8.78	8.78	7.91	7.47	7.03	7.91	7.47	7.03	7.91	7.47	7.03
Iso-Paraffins	43.60	43.60	39.24	37.06	34.88	39.24	37.06	34.88	39.24	37.06	34.88
Naphthenes	3.83	3.83	3.45	3.26	3.07	3.45	3.26	3.07	3.45	3.26	3.07
Aromatics	42.54	42.54	38.28	36.16	34.03	38.28	36.16	34.03	38.28	36.16	34.03

*Typical or calculated values and, if applicable, adjusted for the presence of added oxygenate.
**Analysis was conducted on reformate and naphtha then calculated and, if applicable, adjusted for the presence of oxygenates.

encountered only with the ETH10 blend (10 vol.% ethanol+90 vol.% base) at a room temperature of about 20°C. No signs of phase separation were noticed beyond that temperature. In order to emulsify ethanol with base blends during operation, a circulation pump was fitted in the fuel tank to ensure continuous mixing of the fuel.

The relevant physical and chemical properties of the test fuels were determined. Tables 1 and 2 list those properties for the oxygenates and the test fuels, respectively. Some of the listed properties were not measured but rather obtained from the cited literature.

Test Conditions

All the performance tests were carried out with the spark timing being manually adjusted to the maximum brake torque (MBT) timing, and the engine operating with a stoichiometric mixture.

The temperatures of the cooling water and the lubrication oil were controlled by two fitted heat exchangers. In all the tests, the cooling water temperature was kept at 80±5°C. The temperature of the lubrication oil was kept at 80±2°C during the exhaust emission tests, and ranged from 80°C to 95°C during the performance tests. The test room temperature was kept at 25±2°C during the exhaust emission tests and ranged from 20°C to 30°C during the performance tests. The recorded atmospheric pressure in the test room ranged from 99.4 kPa to 100.9 kPa. The engine performance results were corrected to the reference conditions (standard dry-air absolute pressure=99 kPa, standard temperature =25°C).

Results and Discussion

The performance was evaluated in terms of the maximum output and the brake thermal efficiency of the engine. The maximum output was measured in a wide-open throttle variable-speed test. In the same test, the corresponding values for the brake thermal efficiency were evaluated. The brake thermal efficiency was also evaluated at a constant-speed constant-load test as a function of the equivalence ratio. The MBT timing values and the exhaust gas temperatures were closely examined in order to help in understanding the performance results and explaining the variations between the fuels.

Variable-Speed Test. The engine maximum output and brake thermal efficiency were evaluated as a function of engine speed. During the test, the spark timing was adjusted to maximum brake torque (MBT) timing and the mixture was set to stoichiometric. Table 3 shows the values of the MBT timing versus engine speed for all the tested fuels. These values represent the MBT timing at wide-open throttle and stoichiometric mixture. The MBT timing is given in terms of crankshaft degrees before the top center (btc).

Figures 1, 2, and 3 show the variation of exhaust gas temperature corresponding to the current test for all the tested fuels. These exhaust temperatures were measured near the outlet of the exhaust manifold. In general, the highest exhaust temperature is observed with the base fuel, and the lowest with the leaded fuel. In addition, the exhaust temperature decreases as the oxygenate ratio in the blend increases. These variations in exhaust temperatures can be attributed to the increase in thermal efficiency and/or the decrease in the combustion temperatures. The increase in thermal efficiency means that a larger portion of combustion heat has been converted into work and therefore lower exhaust temperatures are expected. In addition, the lower combustion temperatures characterizing the oxygenated blends are expected to result in lower exhaust temperatures.

Maximum Engine Output. The engine maximum output was measured in terms of the maximum brake torque exerted by the engine at different engine speeds. The brake mean effective pressure (bmep) is usually used instead of the brake torque to represent the engine output. The bmep is a more universal term than the brake torque since it is independent of the engine.

The maximum brake torque and bmep results versus engine speed for all the tested fuels are shown in Figs. 4, 5, and 6. The points indicate the measured values while the lines indicate the least-squares polynomial fit. Consistent and persisting fluctuations in the maximum torque measurements were observed. These fluctuations were closely examined and eventually linked to abnormal vibrations in the test setup. To reduce the fluctuation error, the

Table 3 MBT spark timing at wide-open throttle and Φ=1.0

Speed, RPM	Base	Leaded	MTBE10	MTBE15	MTBE20	METH10	METH15	METH20	ETH10	ETH15	ETH20
1000	6	13	9	10	12	12	13	14	10	13	14
1500	13	20	15	16	20	18	19	20	17.5	22	23
2000	18	28	23	25	28	25	25	27	24	27	28
2500	21	31	26	28	31	28	29	30	26	31	32
3000	24	33	28	32.5	33	31	31	32	30	34	35
3500	25	35	31	32	35	33	33	33	32	35	36.5

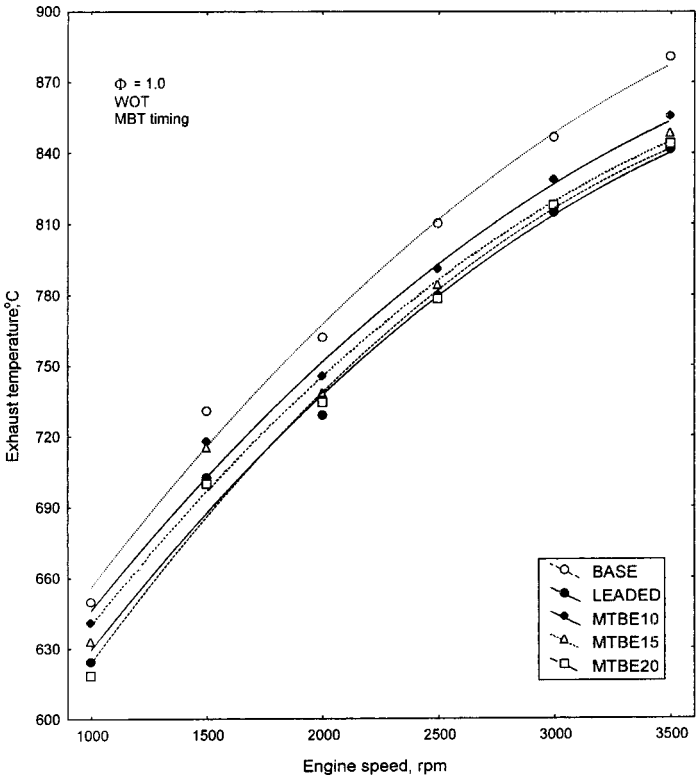

Fig. 1 Exhaust gas temperatures at wide-open throttle for the MTBE blends

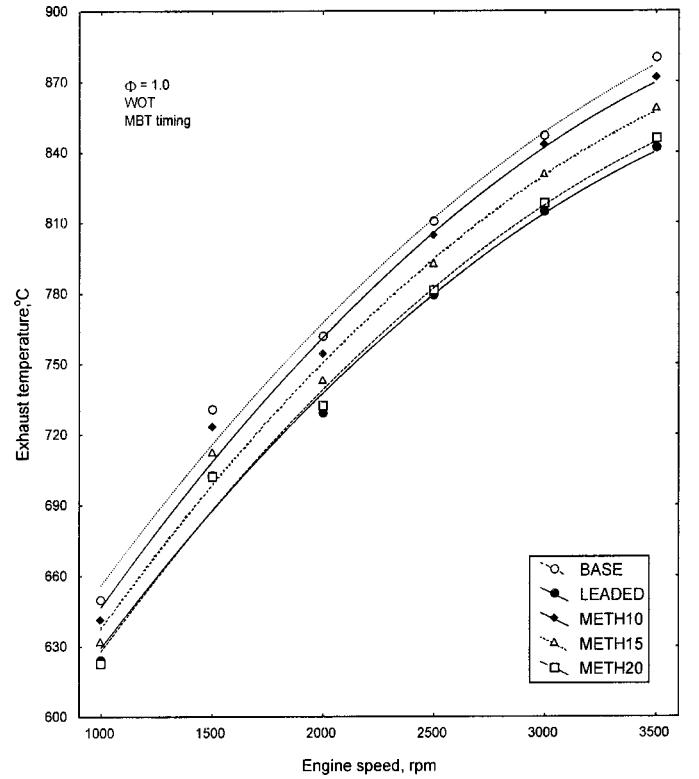

Fig. 2 Exhaust gas temperature at wide-open throttle for the methanol blends

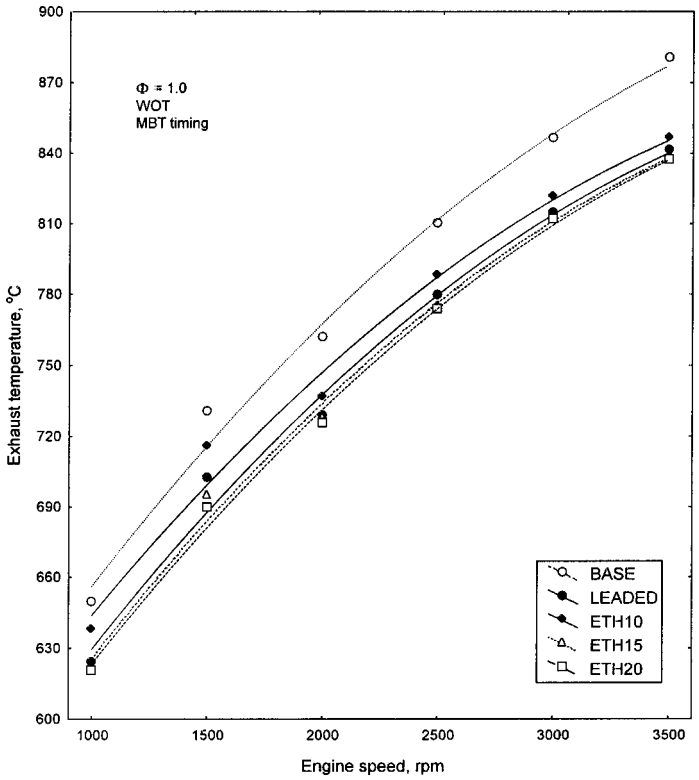

Fig. 3 Exhaust temperature at wide-open throttle for the ethanol blends

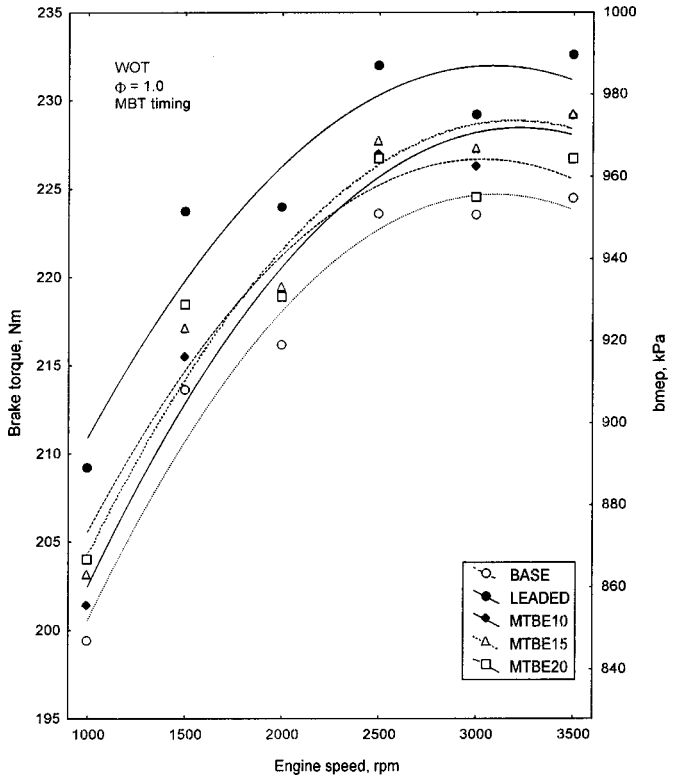

Fig. 4 Brake torque and mean effective pressure at wide-open throttle for the MTBE blends

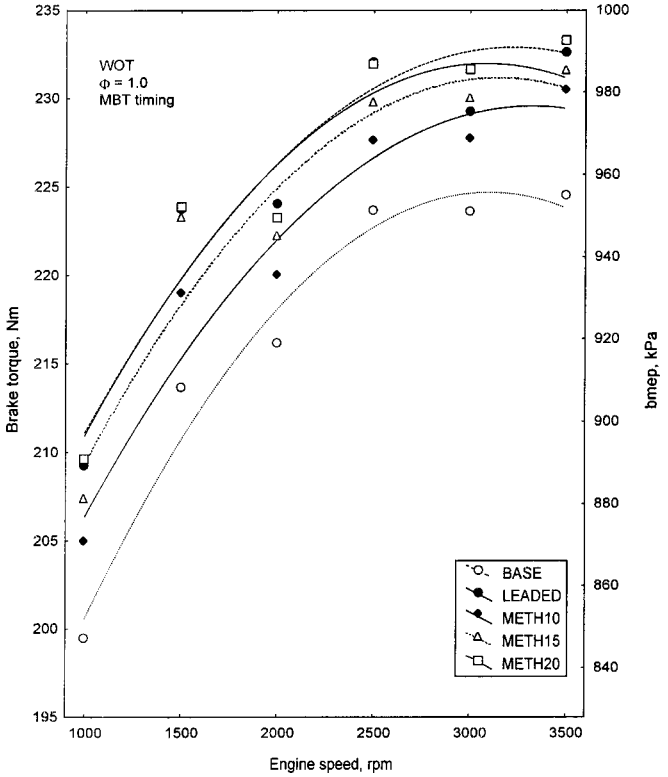

Fig. 5 Brake torque and mean effective pressure at wide-open throttle for the methanol blends

average of three readings of each test condition is recorded. The confidence of torque measurement is found to be 95%. A possible cause of these abnormal vibrations is a misalignment of the shaft connecting the engine with the dynamometer.

The base fuel produced the lowest brake torque among all the tested fuels. The leaded fuel exhibited a substantial increase in the brake torque with respect to the base fuel. This substantial increase is a result of the improved anti-knock behavior due to the addition of TEL, which raised the octane number from 84.7 for the base fuel to 92 for the leaded fuel. The improved anti-knock behavior allowed a more advanced MBT timing that results in higher combustion pressure and thus higher exerted torque (and bmep).

Generally, the results of MTBE blends (Fig. 4) indicate an increase in brake torque with respect to the base fuel. The significance of this increase varied with engine speed and MTBE ratio in the blend. At lower speeds, increasing MTBE ratio in the blend resulted in a gradually slight increase in the brake torque. At higher speeds, however, a considerable increase in the brake torque was obtained with the blend containing 10 vol.% of MTBE (MTBE10), but further addition of MTBE eventually led to the decline of brake torque. The gain in brake torque obtained with MTBE blends can be attributed to the improvement in anti-knock behavior, which allows more advanced MBT timing and thus higher output. As the MTBE ratio in the blend increases, the variation in the instantaneous oxygen/fuel equivalence ratio due to the change of fuel oxygen content in the combustion chamber and decreasing heating value of the fuel tend to affect the combustion flame temperature which in turn offset the improvement in performance. The positive effect of MTBE on maximum brake power has been reported also by Wang et al. [4].

The results for the methanol blends (Fig. 5) indicate an increasingly improving brake torque with the increasing methanol ratio in the blend. The improvement in the brake torque persists over the whole range of the tested engine speed. This gain in brake torque obtained with methanol blends can be attributed to the better anti-knock behavior of these blends and the improvement in engine volumetric efficiency. The research octane numbers (RON) for the methanol blends are significantly higher than that of the base fuel (Table 2). This improved anti-knock behavior allows a more advanced MBT timing, as evident from Table 3, and thus a higher engine output. The improvement in engine volumetric efficiency is a result of the higher latent heat of vaporization characterizing the methanol blends. The latent heat of vaporization is the amount of heat required to vaporize the liquid molecules of the fuel prior to the combustion process. Most of this latent heat is provided by the air accompanying the fuel in its way to the engine cylinder, particularly in the case of port fuel injection systems. The absorption of heat from the air cools it and makes it denser. This allows more air mass to be admitted into the cylinder during the induction process and thus increasing the volumetric efficiency. Alcohols in general are characterized by their higher latent heat of vaporization when compared to the typical gasoline. Increasing alcohol ratio in a gasoline-alcohol blend will increase the latent heat of vaporization of the blend and thus improve the engine volumetric efficiency. Alcohols, on the other hand, have lower heating values when compared to gasoline, which means a lower energy release during combustion and a lower work transfer during expansion process. However, the gain in brake torque due to the improvement in anti-knock behavior and the volumetric efficiency seems to overweigh the losses due to the lower heating. The gain in maximum brake power due to the addition of methanol was reported also by Tsao and Lee [5].

The results for the ethanol blends (Fig. 6) show that there is a significant improvement in brake torque with the 10 vol.% ethanol blend (ETH10) when compared to the base fuel. At low engine speeds, further increase of ethanol ratio had no effect on the brake torque. At high speeds, the 15 vol.% ethanol blend (ETH15) performed slightly better but further addition of ethanol resulted in a decline in the brake torque. Similar to the methanol blends, the gain in brake torque can be attributed to the improvement in anti-knock behavior and volumetric efficiency. However, the improve-

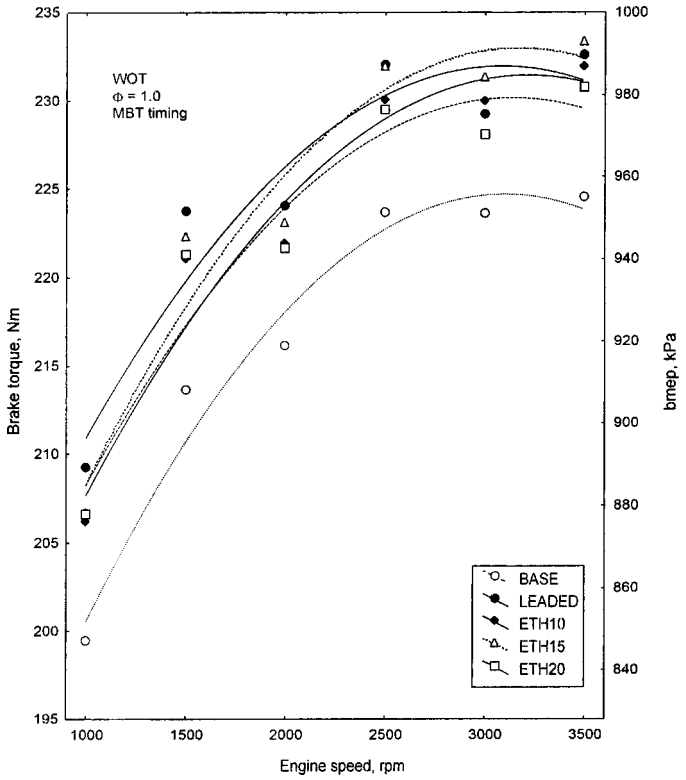

Fig. 6 Brake torque and mean effective pressure at wide-open throttle for the ethanol blends

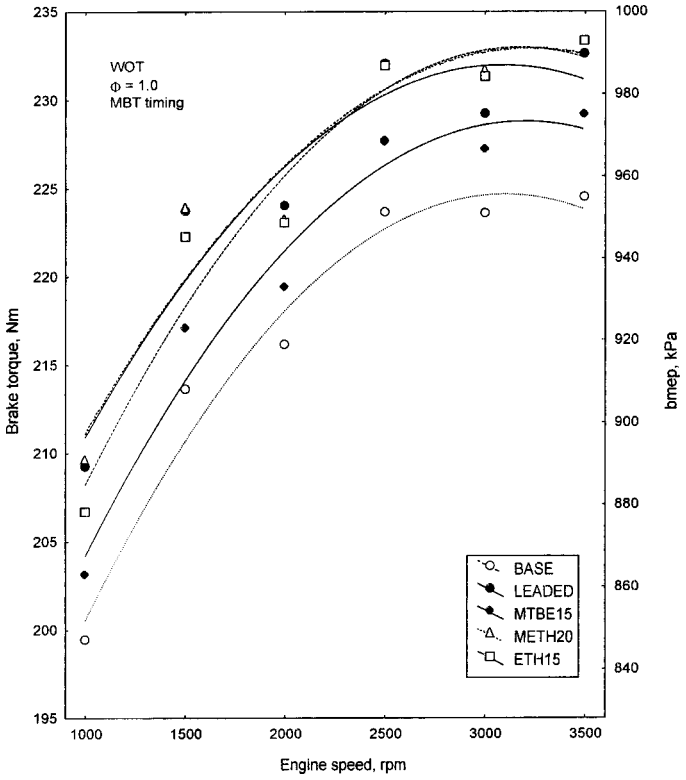

Fig. 7 Brake torque and mean effective pressure at wide-open throttle for the best performing blends compared to the base and leaded fuels

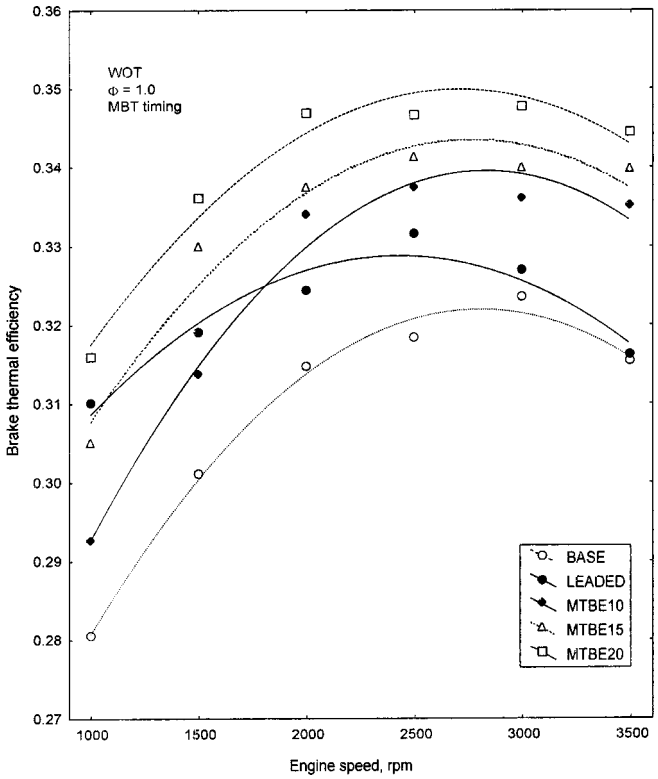

Fig. 8 Brake thermal efficiency at wide-open throttle for the MTBE blends

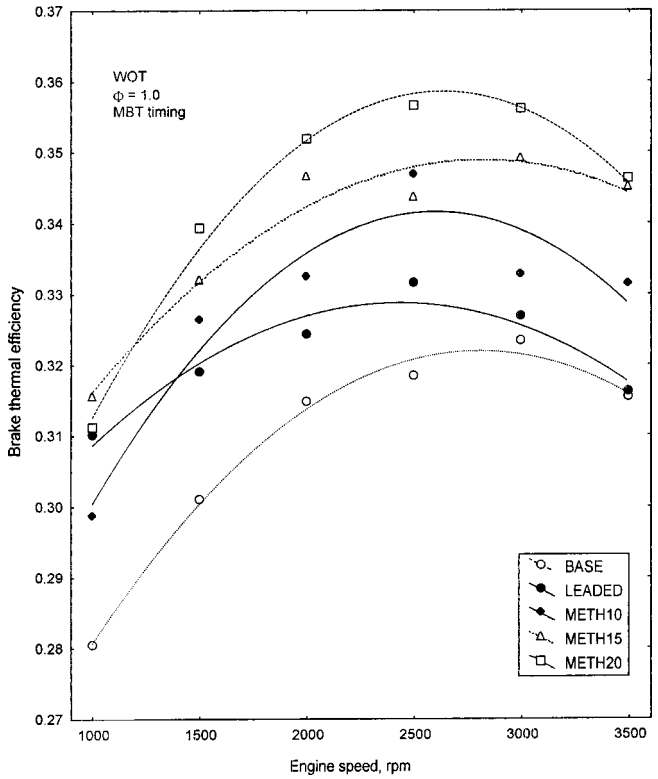

Fig. 9 Brake thermal efficiency at wide-open throttle for the methanol blends

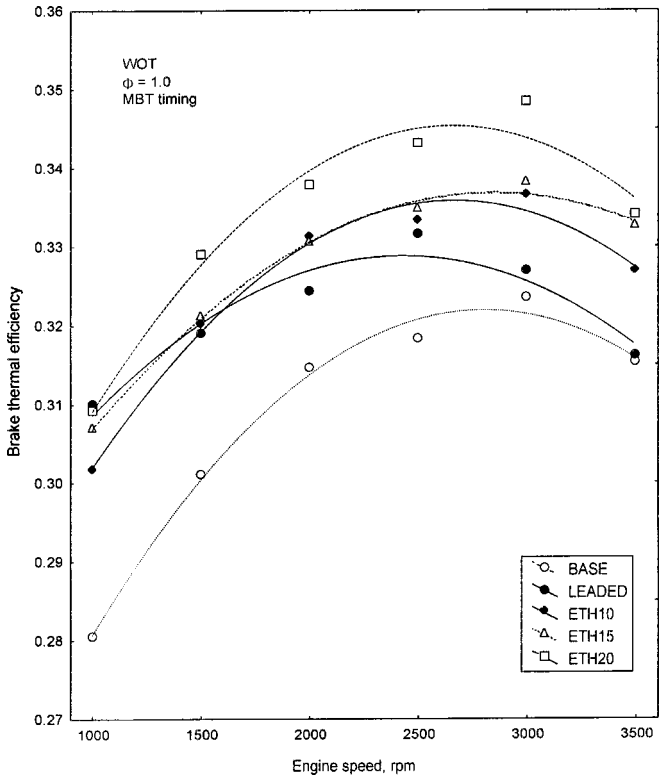

Fig. 10 Brake thermal efficiency at wide-open throttle for the ethanol blends

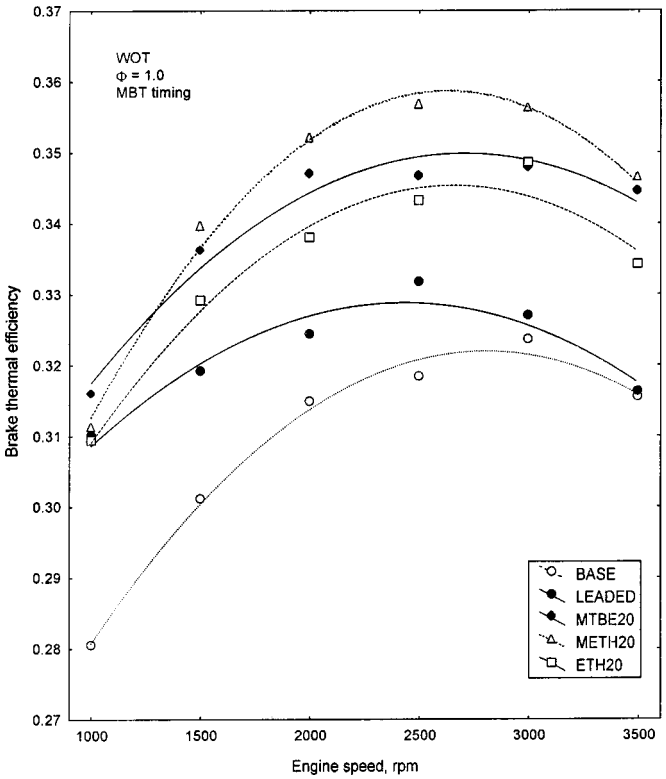

Fig. 11 Brake thermal efficiency at wide-open throttle for the best performing blends compared to the base and leaded fuels

Table 4 MBT spark timing at 2000 rpm and bmep=680 kPa

Φ	Base	Leaded	MTBE10	MTBE15	MTBE20	METH10	METH15	METH20	ETH10	ETH15	ETH20
0.8	32	37.5	36	37	37.5	36	37	37.5	34	35	37
0.9	29	32	31	32	33	31	32	33	31	32	34
1.0	28	30	29	30	31	28	29	30	29	30	31
1.1	26	28	27	28	29	27	28	29	27	28	30
1.2	25	26	26	27	28	26	27	28	26	27	29

ments seem to be significant only with low ethanol ratios (up to 15 vol.% in this case). As the ethanol ratio in the blend increases, the variation in the instantaneous oxygen/fuel equivalence ratio due to the change of fuel oxygen content in the combustion chamber and decreasing heating value of the fuel tend to affect the combustion flame temperature which in turn offset the improvement in performance. In general, the three ethanol blends resulted in higher brake torque than the base fuel. This result does not agree with the results reported by Rajan [6]. Rajan reported a sharp decrease in engine output in the case of 20 vol.% hydrated ethanol (about 6% water in ethanol).

The results for the best performing blends in terms of the maximum brake torque compared to the base and leaded fuels are shown in Fig. 7. The performance of METH20 and ETH15 is comparable with that of leaded fuel and represents a gain of about 5% in the brake torque when compared to the base fuel. The best performing MTBE blend, which is the MTBE15, shows a gain of only about 2%.

Brake Thermal Efficiency. Brake thermal efficiency is defined as the ratio between the engine brake power and the rate of fuel energy input.

Figures 8, 9, and 10 show the brake thermal efficiency results for the variable-speed test at wide-open throttle, stoichiometric mixture, and MBT timing. In general, the brake thermal efficiency improves with increasing speed up to about 2500 rpm where it becomes maximum then starts to decline as the speed increases. Among all the tested fuels, the base fuel obtained the lowest brake thermal efficiency along the whole range of the test speed. The results for the leaded fuel show a significant improvement in the brake thermal efficiency at lower speeds with respect to the base fuel (about 10.7%). As the speed increases, however, this improvement continues to decline and eventually vanishes. This indicates that the effect of improved anti-knock behavior of the leaded fuel on the thermal efficiency lessens as the engine speed increases.

The results for the MTBE blends, shown in Fig. 8, indicate a significant improvement in brake thermal efficiency. As the MTBE ratio in the blend increases, the brake thermal efficiency continues to improve achieving a maximum gain of about 12.5% with respect to the base fuel at low speeds (1000 rpm).

The improvement in the brake thermal efficiency with the three MTBE blends persists over the whole range of test speed. This improvement can be attributed to the more advanced MBT timing allowed by the improved anti-knock behavior, and the lower heat losses due to the lower combustion temperatures. The MTBE blends have lower heating values than that of the base fuel and, therefore, their combustion temperatures are expected to be also lower, [7]. The improvement in thermal efficiency observed here agrees qualitatively with the results reported by Wang et al. [4].

The results for the methanol blends, Fig. 9, show a continuous

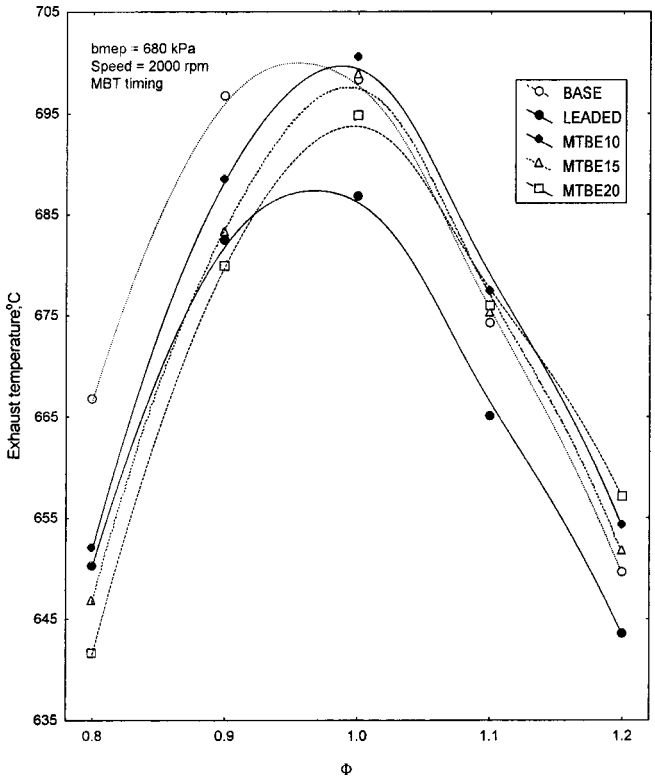

Fig. 12 Effect of equivalence ratio on exhaust gas temperature for the MTBE blends

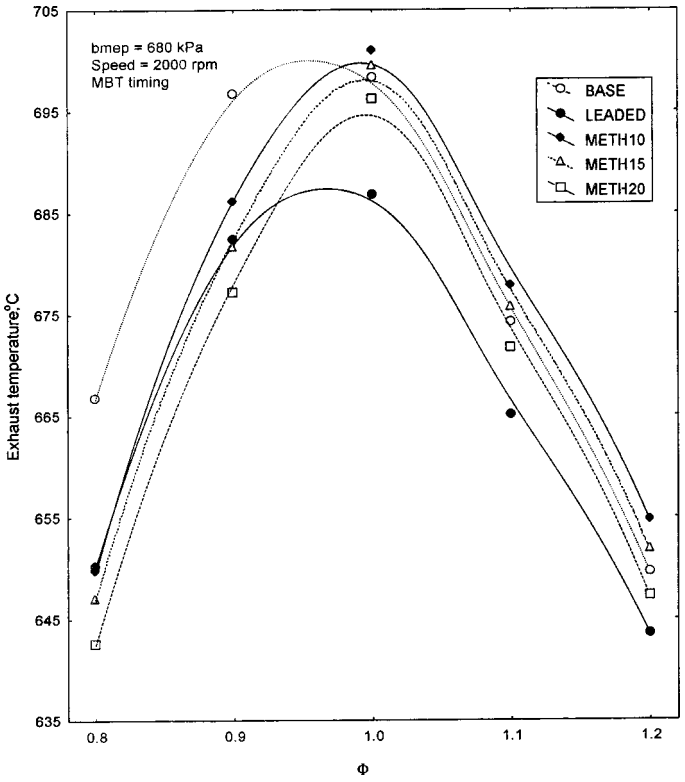

Fig. 13 Effect of equivalence ratio on exhaust gas temperature for the methanol blends

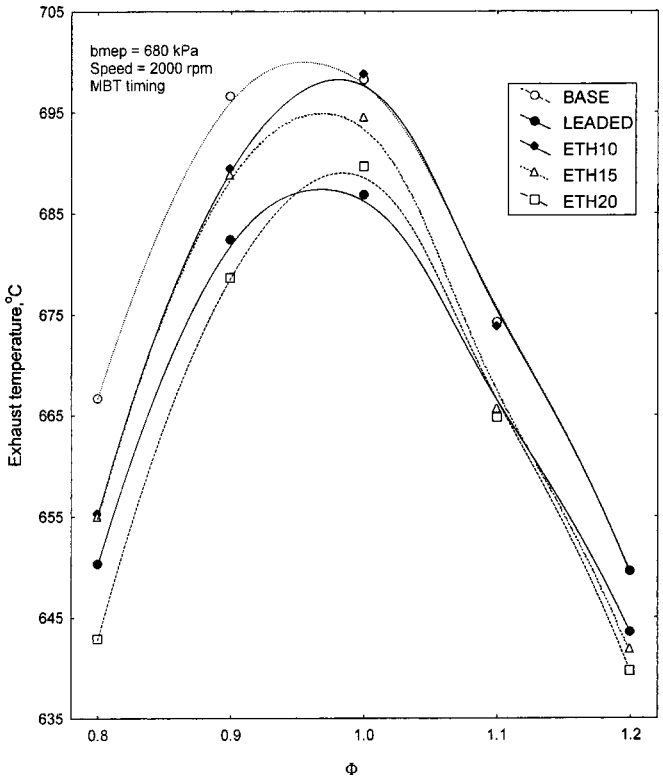

Fig. 14 Effect of equivalence ratio on exhaust gas temperature for the ethanol blends

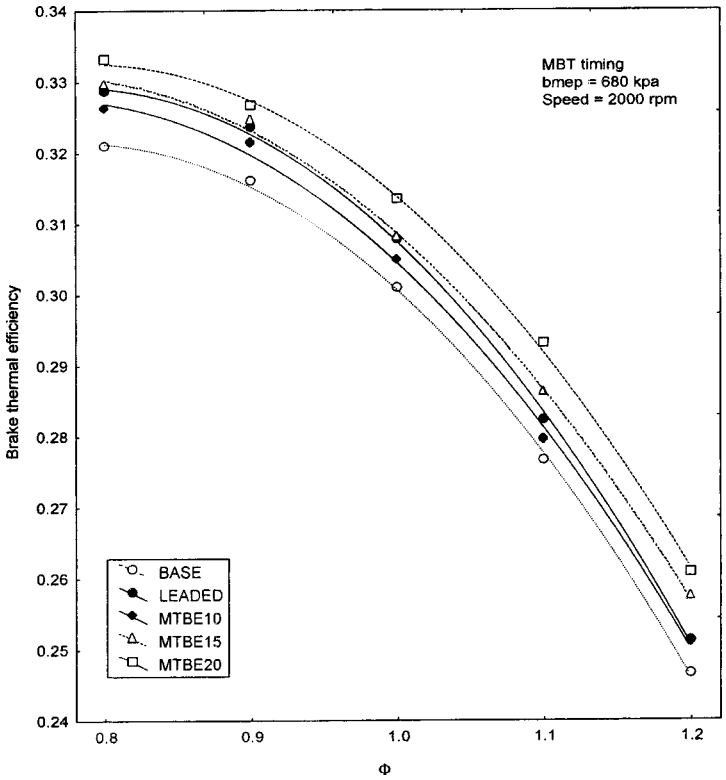

Fig. 15 Effect of equivalence ratio on brake thermal efficiency for the MTBE blends

improvement in brake thermal efficiency as the methanol ratio in the blend increases. The improvement is maintained over the entire speed range and is maximum (about 12.5%) at midrange speed (about 2500 rpm). The improvement in brake thermal efficiency associated with the methanol blends is also due to the more advanced MBT timing and the lower heat losses. The heating values for the methanol blends are noticeably less than that of the base fuel due to the extremely low heating value of methanol, which is less than 50% of that of typical gasoline, [8]. The improvement in brake thermal efficiency due to the addition of methanol was also reported by Tsao and Lee [5] and Kowalewicsz [8].

The results for the three ethanol blends, Fig. 10, also show an improvement in the brake thermal efficiency. A maximum gain of about 9% is achieved at midrange speeds with the ETH20 blend. The improvement in brake thermal efficiency noticed here can be also explained by the improvement in anti-knock behavior that allows a more advanced MBT timing, and the expected lower heat losses due the lower combustion temperatures. Rajan [6] reported an improvement in the thermal efficiency with blends containing up to 10 vol.% hydrated ethanol (about 4% water in ethanol). Beyond this limit, however, Rajan reported a substantial decrease in the thermal efficiency. This contradicts the results in the current study which indicate a noticeable improvement in thermal efficiency in the case of 20 vol.% ethanol blend (which contains about 7% of water in ethanol).

Figure 11 shows the results of brake thermal efficiency for the best performing blends compared to the base and leaded fuels. The highest efficiency was obtained with METH20 blend followed by MTBE20 then ETH20. At low speeds, the improvement associated with the three blends is comparable to that of leaded fuel. As the speed increases, however, the brake thermal efficiency continues to improve in the case the three blends while declining in the case of leaded fuel.

Variable Equivalence Ratio Test. The effect of equivalence ratio on the brake thermal efficiency was evaluated at a constant speed (2000 rpm), constant load (680 kPa), and MBT timing. The values for MBT timing corresponding to this test are given in Table 4. In general, the MBT timing retards towards the top center as the mixture is enriched. This can be attributed to the effect of equivalence ratio on the burning rate and therefore on the time required to complete the combustion. Usually, the maximum burning rate occurs at about 10% rich mixture (i.e., $\Phi=1.1$). Lean mixtures and extremely rich mixtures have low burning rates, and therefore, they need more advanced spark timing to attain the maximum brake torque. The results show also that the MBT timing advances as the oxygenate ratio in the blend increases. This is probably due to the improvement in anti-knock behavior of the blends due the addition of oxygenates.

The exhaust gas temperatures, shown in Figs. 12, 13, and 14, peak at about stoichiometric ($\Phi=1.0$) and sharply drop with lean and rich mixtures. This indicates that the flame temperature during combustion and the prevailing gas temperature at the end of the expansion process are higher in the case of stoichiometric than in lean or rich mixtures. Consequently, for stoichiometric mixture at the same exhaust flow rate, the heat loss is maximum. In general, the exhaust temperatures for the oxygenated blends were comparable to those of the base fuel in the case of rich mixtures but noticeably lower in the case of lean mixtures. The leaded fuel exhibited a consistent decrease in exhaust temperature with respect to the base fuel over the entire test range. The decreased exhaust temperature is a result of lower combustion temperature and/or improved thermal efficiency.

Figures 15, 16, and 17 show the brake thermal efficiency at different equivalence ratios for all the test fuels. The results indicate that the brake thermal efficiency is significantly influenced by the equivalence ratio. The efficiency drastically deteriorates with increasing richness of the mixture ($\Phi>1.0$). On the other hand, the efficiency improves as the mixture is leaned out up to about $\Phi=0.9$ after which the improvement slows down.

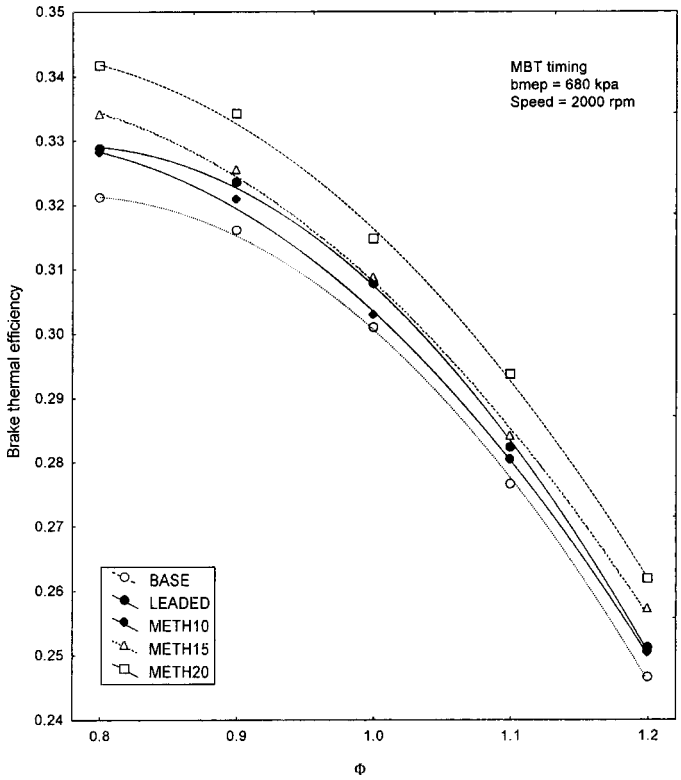

Fig. 16 Effect of equivalence ratio on brake thermal efficiency for the methanol blends

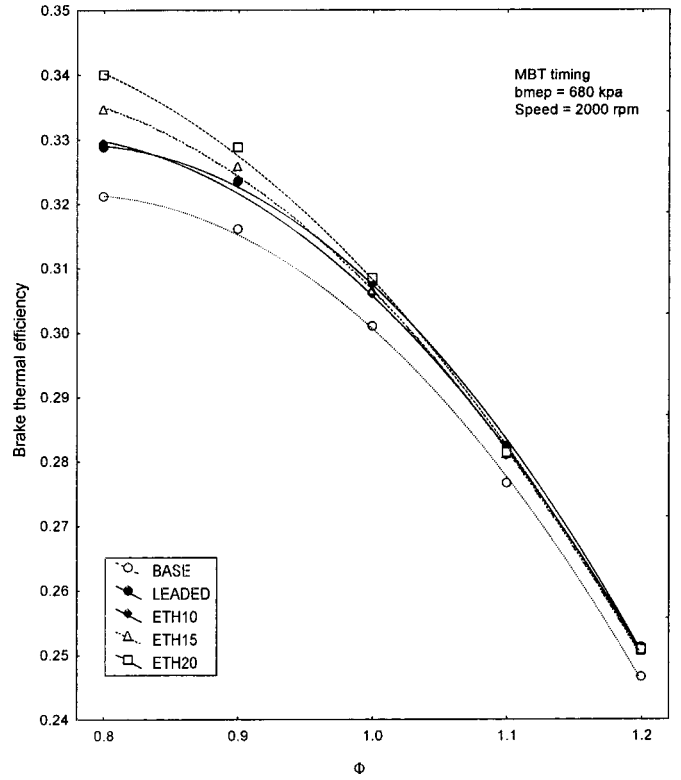

Fig. 17 Effect of equivalence ratio on brake thermal efficiency for the ethanol blends

Among all the tested fuels, the base fuel attained the lowest brake thermal efficiency values in the whole test range. In general, the addition of oxygenates resulted in a noticeable improvement in the brake thermal efficiency. The results here indicate, however, less significant differences between the test fuels at part load than in the case of wide-open throttle tests.

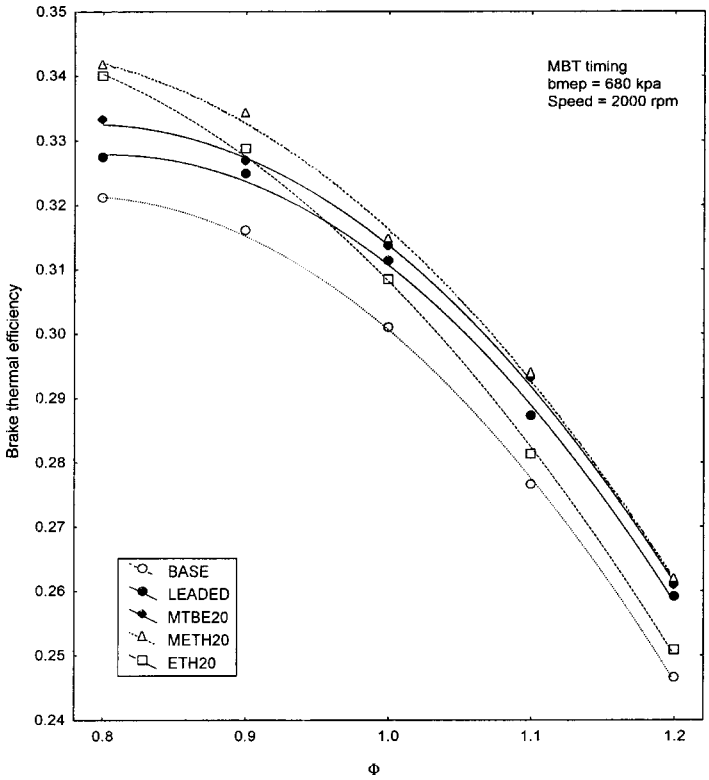

Fig. 18 Effect of equivalence ratio on brake thermal efficiency for the best performing blends compared to the base and leaded fuels

The results for the MTBE blends, shown in Fig. 15, indicate a continuous improvement in the efficiency as the MTBE ratio increases. This improvement is sustained over the entire tested range of equivalence ratio. The maximum gain in efficiency with respect to the base fuel is observed at the rich side ($\Phi=1.2$) and is about 6%. The gain in efficiency decreases as the mixture is leaned out reaching about 3.8% at $\Phi=0.8$. In the case of the methanol blends, the efficiency also continues to improve as the methanol ratio increases in the blend at all equivalence ratios as shown in Fig. 16. However, the gain in efficiency in this case is almost constant at all equivalence ratios and is about 6%. Different from the MTBE and methanol blends, the ethanol blends at rich equivalence ratios ($\Phi>1.0$) show a slight gain in efficiency (about 1.5%) with respect to the base fuel (Fig. 17). Furthermore, this slight gain in efficiency is not affected by the increase of ethanol ratio in the blend. As the mixture is leaned out, however, the gain in efficiency increases and the variation between the three ethanol blends becomes more noticeable. A maximum gain in efficiency of about 6% is observed for ETH20 at $\Phi=0.8$.

Similar to the previous test, the improvement in efficiency noticed in this test can be attributed to the more advanced MBT timing allowed by the improved anti-knock behavior, and/or the lower heat losses due to the lower combustion temperatures.

The brake thermal efficiency values as a function of equivalence ratio for the best performing blends compared to the base and leaded fuels are shown in Fig. 18. Again, the METH20 is the best performer at the whole test range. At the rich side ($\Phi>1.0$), the results for the MTBE blends are comparable to those of METH20. At the lean side ($\Phi<1.0$), the METH20 outperforms all other test fuels and is approached only by the ETH20 blend at $\Phi=0.8$. The performance of the leaded fuel at rich equivalence ratios is comparable to the best performing blend, but fall behind at the lean side.

Conclusions

• The results from the variable-speed wide-open throttle (WOT) tests show that the leaded and oxygenated fuels performed better than the base fuel in terms of maximum brake mean effective pressure (bmep). The improvement in performance persists along the entire tested speed range. For leaded fuel, the average increase of maximum bmep with respect to the base fuel is about 4%. The improvement due to the addition of oxygenates varies with the oxygenate type and ratio in the blend but generally is less than that noticed with leaded fuel except in the case of the 20 vol.% methanol and 15 vol.% ethanol blends. The reduced knock propensity of the oxygenated fuel is significant in the engine performance over the base fuel.

• For lower ratios of oxygenates (up to 15 vol.%), the ethanol blends perform better than methanol and MTBE blends. For higher ratios, however, the methanol is the best oxygenate in terms of maximum bmep of the engine.

• The results show that the oxygenated fuels resulted in higher brake thermal efficiency than the base fuel and than leaded fuel particularly at higher engine speeds. Although less than the oxygenated fuels, the thermal efficiency improves with leaded fuel but this improvement declines as the engine speed increased until eventually vanishes at high speed of 3500 rpm.

• At midrange speed of 2500 rpm, the methanol blends are the best performers followed by MTBE, then ethanol blends. Methanol blends result in maximum increase in thermal efficiency of about 12.3% with respect to base fuel. The maximum increase in thermal efficiency is about 8.8% in the case of MTBE blends, and about 7.9% in the case of ethanol blends. Overall, the methanol blends are the best performers in terms of brake thermal efficiency at practical wide-open throttle conditions.

• The results from variable-equivalence ratio tests show that

the differences between fuels are less significant at part-load than in the wide-open throttle condition. With all the tested fuels, the brake thermal efficiency improves significantly as the equivalence ratio is decreased (i.e., as the mixture is leaned out).

• At stoichiometric mixture ($\Phi=1.0$), constant load of 680 kPa, and constant speed of 2000 rpm, the best oxygenate in terms of brake thermal efficiency is ethanol for low oxygenate ratio (up to 10 vol.%) and methanol for higher ratio (15 and 20 vol.%). The maximum increase in thermal efficiency with respect to the base fuel is about 4.7% in the case of methanol, about 4.0% in the case of MTBE, about 2.3% in the case of ethanol, and about 3.3% in the case of leaded fuel.

Acknowledgments

The authors are grateful for the financial support and facilities provided by the King Fahd University of Petroleum and Minerals. Ras Tanura refinery of Saudi Aramco, Saudi Petrochemical Company (SADAF), and National Methanol Company (Ibn Sina) are gratefully acknowledged for their support in this research.

References

[1] Al-Farayedhi, A. A., Al-Dawood, A. M., and Gandhidasan, P., 2000, ''Effects of Blending MTBE With Unleaded Gasoline on Exhaust Emissions of SI Engines,'' ASME J. Energy Resour. Technol., **122**, pp. 239–247.
[2] Al-Farayedhi, A. A., Al-Dawood, A. M., and Gandhidasan, P., ''Effects of Blending Crude Ethanol With Unleaded Gasoline on Exhaust Emissions of SI Engine,'' Proceedings of the International Fall Fuels and Lubricants Meeting and Exposition, Baltimore, MD, Oct. 16–19, SAE Paper No. 2000-01-2857.
[3] Al-Dawood, Ali M., 1998, ''Effects of Blending MTBE, Methanol, or Ethanol With Gasoline on Performance and Exhaust Emissions of SI Engines,'' M.S. thesis, Mechanical Engineering Department, King Fahd University of Petroleum & Minerals, Dhahran.
[4] Wang, X. et al., 1987, ''Study of the Performance of MTBE Blended Unleaded Gasoline,'' SAE Paper No. 871268.
[5] Tsao, K. C., and Li, C., 1984, ''Performance Comparison of Gasoline-Methanol Emulsions as Spark Ignition Engine Fuels,'' SAE Paper No. 840241.
[6] Rajan, S., 1984, ''Water-Ethanol-Gasoline Blends Physical Properties, Power, and Pollution Characteristics,'' ASME J. Eng. Gas Turbines Power, **106**, pp. 841–848.
[7] Piel, W. J., and Thomas, R. X., 1990, ''Oxygenates for Reformulated Gasoline,'' Hydrocarbon Process., **69**, July, pp. 68–73.
[8] Kowalewicz, A., 1994, ''Efficiency of the SI Engine Fueled With Methanol-Gasoline Blends,'' Proc. Inst. Mech. Eng., Part D (J. Automob. Eng.), **208**, Part D: Journal of Automotive Engineering.
[9] SAE Handbook, 1992, ''Alternative automotive fuels,'' SAE J1297 JUN90, Vol. 3, Society of Automotive Engineers, Warrendale, PA.
[10] Heywood, J. B., 1988, *Internal Combustion Engine Fundamentals*, McGraw-Hill, New York.

Characteristic and Computational Fluid Dynamics Modeling of High-Pressure Gas Jet Injection

Y. Li
A. Kirkpatrick
C. Mitchell
B. Willson

Engines and Energy Conversion Laboratory,
Mechanical Engineering Department,
Colorado State University,
Fort Collins, CO 80523

The topic of this paper is the computational modeling of the gas injection process in a large-bore natural gas fueled engine. At high injection pressures, the overall gas injection and mixing process includes compressible flow features such as rarefaction waves and shock formation. The injection geometries examined in the paper include both a two-dimensional slot and an axisymmetric nozzle. The computations examine the effect of the supply pressure/cylinder stagnation pressure ratio, with ratios ranging from 3 to 80, on the velocity and pressure profiles in the near field region. Computational fluid dynamics modeling was compared with results obtained from a two-dimensional analytical method of characteristics solution and experimental results. The comparison process evaluated factors such as pressure and Mach number profiles, jet boundary shape, and shock location. [DOI: 10.1115/1.1635398]

Introduction

The objective of this paper is to assess the ability of a commercial computational fluid dynamics (CFD) code to compute the velocity and pressure profiles in high pressure gas flow from simple sonic nozzles. A sonic nozzle is a convergent or straight nozzle with an exit Mach number equal to one. Two types of nozzles were investigated, a two-dimensional nozzle, and an axisymmetric nozzle. The axisymmetric nozzle is a geometry used in direct injection natural gas fueled engines.

The main parameters determining the type of the flow exiting from a sonic nozzle are the ratio of the supply stagnation pressure to the cylinder stagnation pressure and the nozzle geometry. As the injection pressure increases, a condition is reached for convergent nozzles where the exit velocity reaches the speed of sound. This pressure ratio is the critical pressure ratio for the nozzle. For an ideal gas with a specific heat ratio of 1.35, the critical pressure ratio is 1.86. At higher pressure ratios, the exit Mach number remains equal to one, but the exit static pressure is greater than the ambient or cylinder pressure, so that substantial gas expansion from the exit pressure to the cylinder pressure is required downstream of the nozzle. This type of nozzle outflow produces an underexpanded jet.

As a consequence of the nozzle exit–cylinder static pressure difference, when an underexpanded jet emerges from a nozzle or orifice, an expansion fan originating at the corners of the orifice is generated. As shown in Fig. 1 (Pai [1]), the expansion waves are subsequently reflected at the jet boundary as compression waves, so that the jet boundary pressure remains equal to the cylinder pressure. At higher pressure ratios the compression waves coalesce into intercepting shocks, which meet at the symmetry axis forming diamond-shaped cells. At relatively low pressure ratios above the critical pressure ratio, the boundary reflection process need not include shocks and can repeat until the waves are dissipated by viscosity. The velocity of the gas increases to supersonic speed as it passes through the expansion fan, with a corresponding decrease in the static pressure and density. Likewise, as the gas passes through the compression and shock structures, its velocity decreases, and the static pressure and density increase.

As the pressure ratio is increased, the intercepting shocks can no longer reflect at the axis and instead are connected by a normal shock, or Mach disk as shown in Fig. 2 (Adamson and Nicholls [2]). For sonic nozzles, calculations by Owen and Thornhill [3] showed that along the jet centerline downstream of the nozzle, the local nondimensional static pressure, P/P_n, and the local Mach number depend only on the nondimensional axial distance x/d and are independent of the supply-cylinder stagnation pressure ratio as long as the pressure ratio is sufficiently high. For pressure ratios large enough for a Mach disk to exist, Adamson and Nicholls [2] extended this region of self-similar flow all the way to the Mach disk.

Since the mean flow velocities are very large relative to characteristic diffusion velocities, the flow structures in the near field of the nozzle, such as the location of the first normal shock or Mach disk are primarily a function of the nozzle exit–cylinder pressure ratio, with little dependence on viscous or turbulent effects. Adamson and Nicholls [2] compared various experimental measurements of the Mach disk location in air jets from sonic nozzles reported by various researchers, including Love et al. [4], for nozzle exit–cylinder static pressure ratios from 2 to 100.

It is important to compute the initial outflow from the nozzle accurately, as it governs the subsequent mixing of the gas jet with the cylinder air. A virtual nozzle has been used in internal combustion engine modeling as an alternative to computing the detailed near-field fluid mechanics (Mather and Reitz [5]). With a virtual nozzle, the computation of the flow field begins downstream of the Mach disk, assuming a perfectly expanded nozzle with the same mass flow rate and a nozzle area based on expansion of the jet to cylinder pressure. This approach decreases the grid density requirements at the nozzle, but requires information about the Mach disk size and location.

Computational Methodology

There are numerous specialized compressible gas dynamics computer packages used for this class of problem. Current research in this area examines the fine scale structure and interaction of the various flow structures. For example, Gribben et al. [6] used a CFD solver to compute the hysteresis of the shock reflection. Representative computations of the complex wave structure in underexpanded jets has been reported by Cumber et al. [7] and Hsu and Liou [8] for aerospace applications. The texts by Laney [9] and Ferguson and Kirkpatrick [10] discuss various discretization and modeling methods for compressible flow problems. In this paper, a general purpose commercial CFD solver, Fluent Version 5.0 [11], was used for the gas dynamics computations, in

Contributed by the Internal Combustion Engine Division of THE AMERICAN SOCIETY OF MECHANICAL ENGINEERS for publication in the ASME JOURNAL OF ENGINEERING FOR GAS TURBINES AND POWER. Manuscript received by the ICE Division, April 2002; final revision received December 2002. Associate Editor: D. Assanis.

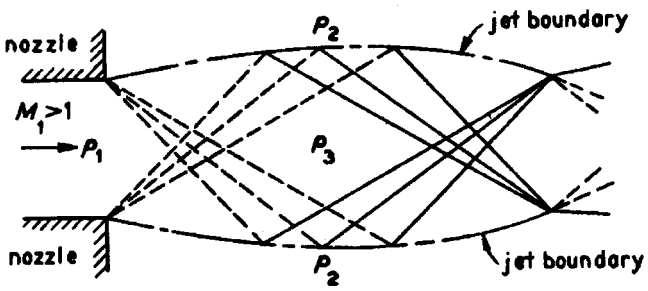

Fig. 1 Supersonic flow from a simple orifice at low pressure ratios (Pai [1])

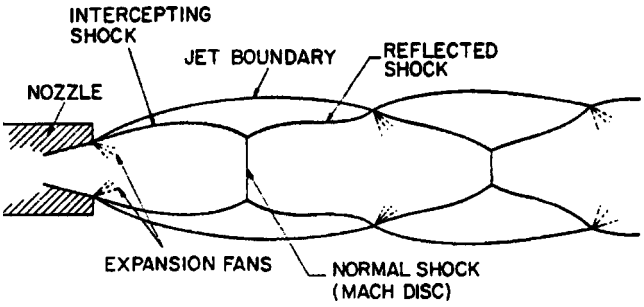

Fig. 2 Supersonic flow from a simple diverging orifice at high pressure ratios (Adamson and Nicholls [2])

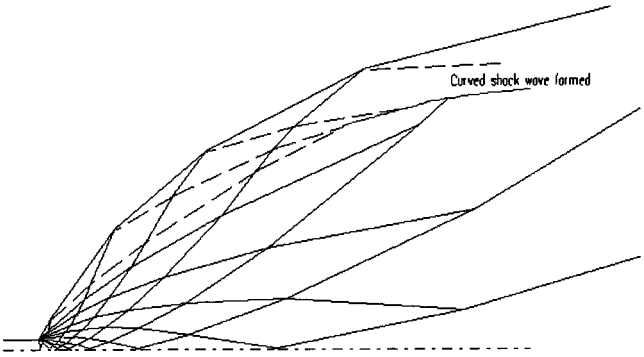

Fig. 3 Characteristic net and jet boundary for pressure ratio of 81.4:1

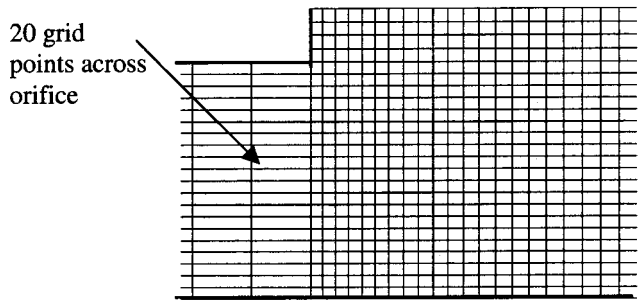

Fig. 4 Close up of computational grid near the orifice outlet

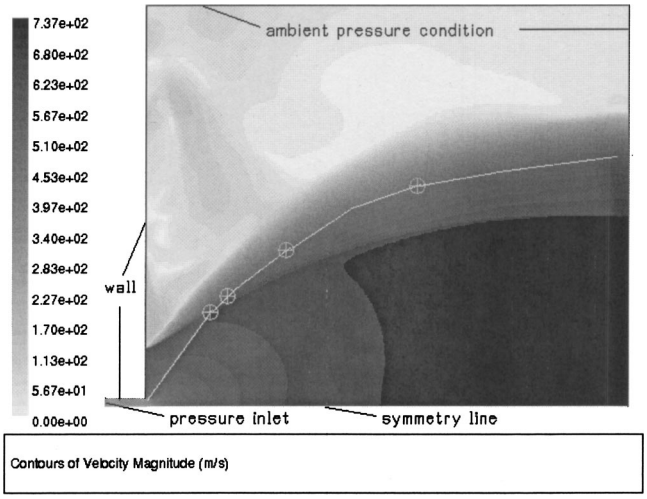

Fig. 5 Comparison of two-dimensional jet velocity contours (m/s) of for pressure ratio of 35:0.43

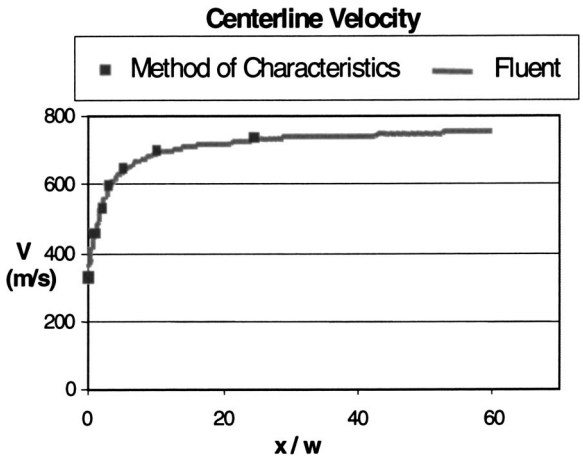

Fig. 6 Two-dimensional centerline velocity profile in axial direction

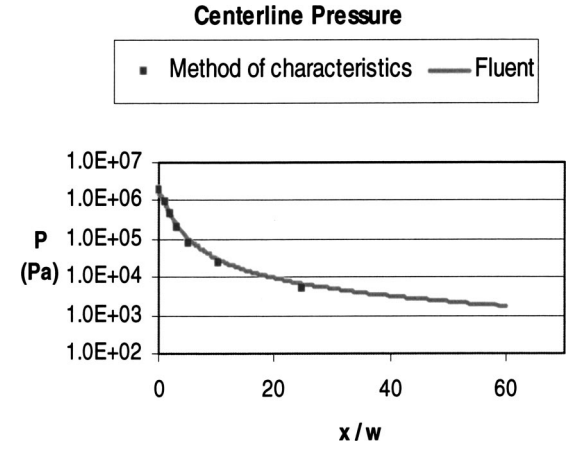

Fig. 7 Two-dimensional jet centerline pressure in axial direction

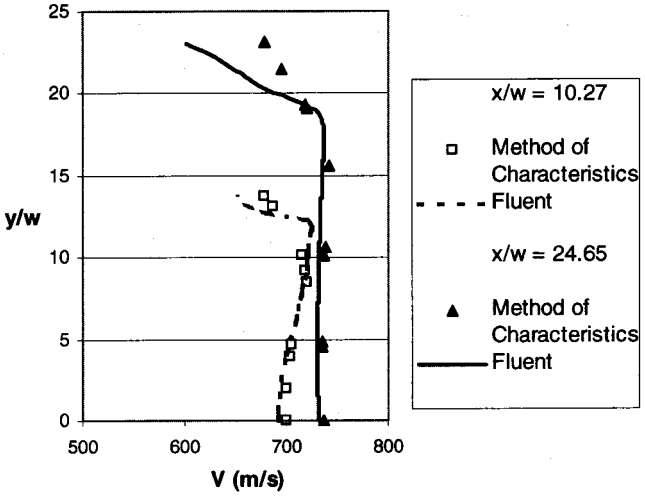

Fig. 8 Two-dimensional jet velocity profile in transverse direction at two axial locations

order to assess how accurately a general purpose CFD solver could capture the details of the compressible flow structures. The Fluent CFD solver uses a finite volume technique for discretization of the governing equations. The computations presented in this paper are part of a broader effort in modeling the in-cylinder flow of natural gas fueled engines.

A quadratically spaced mesh for both the two-dimensional and axisymmetric computations was used to discretize the computational mesh. The numerical scheme was explicit in time and first-order upwind in space. Grid adaptation was used to refine the mesh and locate the rapidly varying shock structures. Grid sensitivity computations indicated that at least ten grid points across the nozzle orifice were required to reduce the sensitivity to grid size in the nozzle region. Twenty grid points were used across the two-dimensional orifice and 15 grid points were used across the axisymmetric orifice to resolve the immediate expansion fan region. This grid resolution is consistent with the orifice grid recommendations of Abraham [12]. The outlet flow from the nozzle was assumed to be steady, simulating the fully open steady-state flow condition of a fuel injector. A pressure boundary condition was imposed at the inlet to the nozzle. The cylinder pressure was held constant, corresponding to the case where the time scale for fuel injection was much smaller that for pressure changes due to piston motion. The steady-state jet flow was computed, since for electronically controlled natural gas injectors, the time period for steady-state operation is much longer than the transient opening and closing times. Both inviscid and turbulent computations were performed. The turbulence model employed was the standard k-ε model, with the intent of assessing the performance of this turbulence model in the near field of the jet. Post et al. [13] note that the performance of the k-ε model is suitable for gas jet entrainment computations.

Comparison of Computational Fluid Dynamics (CFD) and Method of Characteristics Solutions for Two-Dimensional Jets

The jet flows for high pressure fuel injection in direct injection engines can be highly underexpanded with supply stagnation pressure to combustion chamber pressure ratios as large as 80 or more. In practice the jets of interest are approximately axisymmetric or (more accurately) three-dimensional. Application of an appropriate CFD solver to simulate and model the gas injection process is thus attractive. The question of whether existing commercial codes could capture adequately the supersonic and compressible flow features of these jets was of concern, however. As a first step

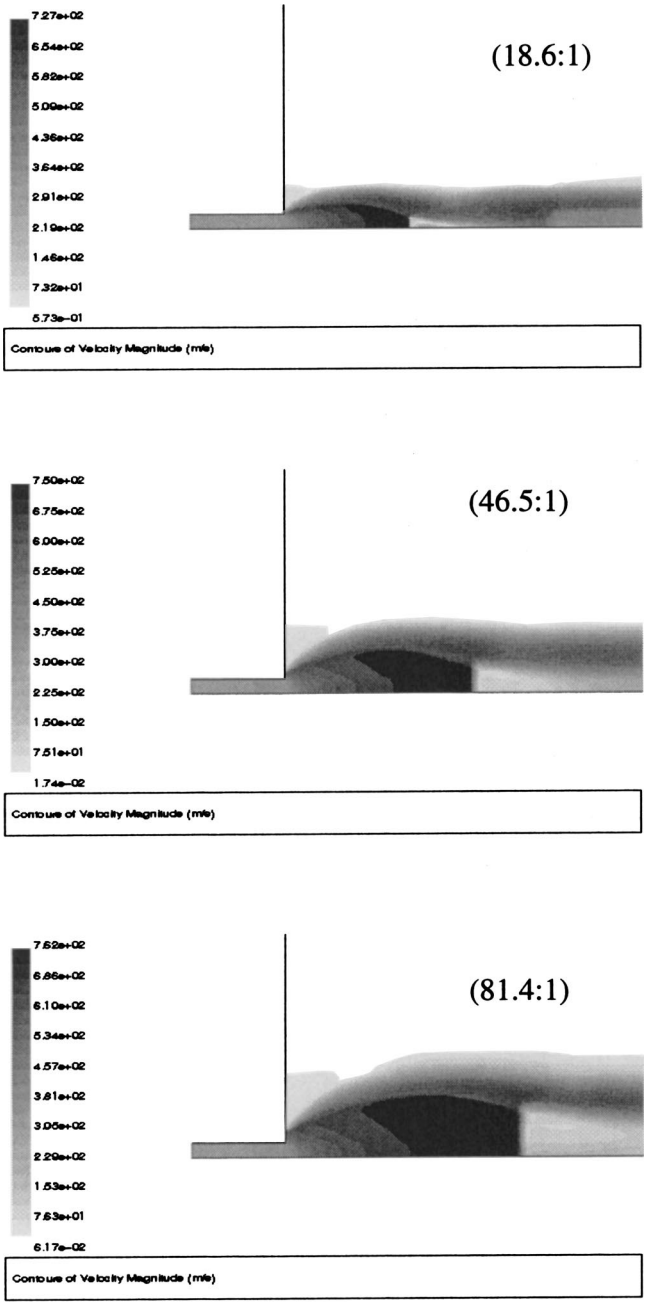

Fig. 9 Velocity contours at the three higher pressure ratios

in evaluating the predictive capability of the Fluent CFD solver in this type of application, a simple two-dimensional jet problem for the same pressure ratio range was examined. This simpler problem could be treated by a straightforward application of the method of characteristics. The method of characteristics is a classic analytical technique for the solution of hyperbolic equations. Before the advent of digital computation, it was the primary technique used for solution of the inviscid Euler equations used to represent two dimensional and axisymmetric jets (Shapiro [14]).

The two-dimensional jet treated in this comparison study was assumed to issue from a simple slot in the wall of a two-dimensional chamber. The supply stagnation pressure was taken to be 35 bar and the chamber pressure to be 0.43 bar, giving a pressure ratio, P_o/P_∞ of approximately 81.4. The gas was assumed to be air and was modeled as a calorically perfect gas. For the application of the method of characteristics the flow was assumed to be isentropic, irrotational and inviscid as well. In addition, for the

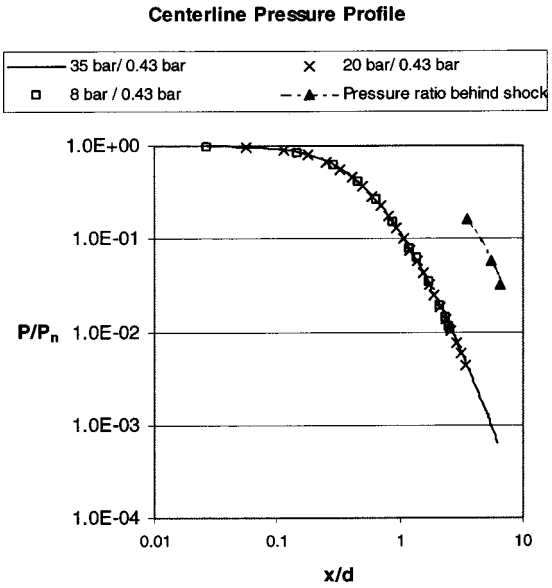

Fig. 10 Effect of overall pressure ratio on the local nondimensional pressure profile along jet centerline

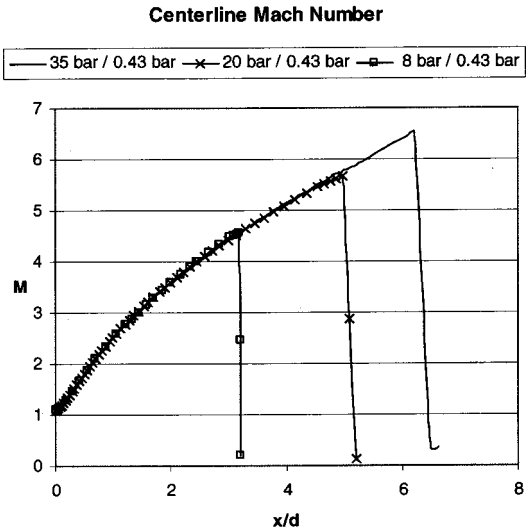

Fig. 11 Effect of overall pressure ratio on the Mach number profile along jet centerline

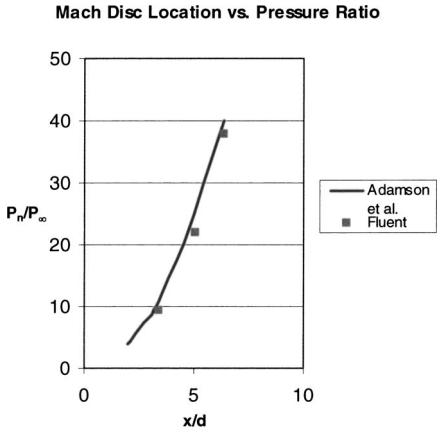

Fig. 12 Effect of pressure ratio on location of Mach disk

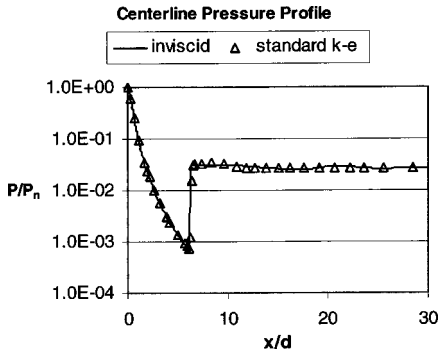

Fig. 13 Comparison of viscous effects on centerline pressure profile (pressure ratio=81.4:1)

characteristic calculations the sonic surface ($M=1$) was assumed to be planar and located at the interface between the injection slot and the perpendicular wall of the combustion chamber.

A computer code was developed and used to generate the characteristic net and compute the required values of P, M, V, and T at the net points. A plot of the characteristic net and the jet boundary is shown in Fig. 3. Because the jet is symmetrical, only the upper half-plane is shown. Solid lines indicate expansion waves and dashed lines are the compression waves reflected from the jet boundary. The formation of a curved shock caused by the convergence and intersection of the compression waves is indicated. Additional computations performed with a finer characteristic net showed that the change in the jet boundary was minimal. Downstream of the curved shock, the inviscid form of the method of characteristics is not strictly valid since the flow becomes rotational, and vorticity generation need to be included, as discussed by Chang and Chow [15]. Figure 4 shows the detailed CFD mesh structure at the nozzle exit region. For the CFD calculations, the length of the injection nozzle upstream of the exit plane) was 5 slot half-widths and the entire computational domain was 60 $\times$50 slot half-widths.

The general shapes of the jet predicted by the two methods are compared in Fig. 5. The black line indicates the jet boundary predicted from the method of characteristics, while the jet shape from the CFD computations can be inferred from the shaded velocity contours. The shapes predicted are qualitatively similar, though the thickened jet edge predicted by the computations is apparent. Since this particular set of CFD calculations were inviscid, the thickening results from numerical diffusion.

Velocity and pressure profiles along the jet centerline computed with the two methods are compared in Fig. 6 and Fig. 7, respectively. For both the velocity and pressure profiles, the agreement appears to be quite good. The nondimensional axial coordinate x/w in Figs. 6 and 7 is the distance x from the exit divided by the slot half-width w. There is a decrease in the jet centerline pressure to pressures less than the cylinder pressure, and a corresponding increase in the jet velocity.

Transverse profiles of axial velocity at two axial distances from the jet exit are shown in Fig. 8. Here, the transverse y-coordinate is nondimensionalized by the slot half-width w. Agreement between the two methods is again quite good except near the edge of the jet, consistent with the jet shape differences shown in Fig. 5. Note that the jet velocity increases slightly in the transverse direction, opposite to the velocity decrease characteristic of perfectly expanded jets in which viscous effects play a larger role in jet mixing.

Computation of Underexpanded Axisymmetric Jets

Since the general shape of direct injection nozzles and combustion chambers is cylindrical, the high-pressure injection process in a direct injection engine is classified as an underexpanded axisym-

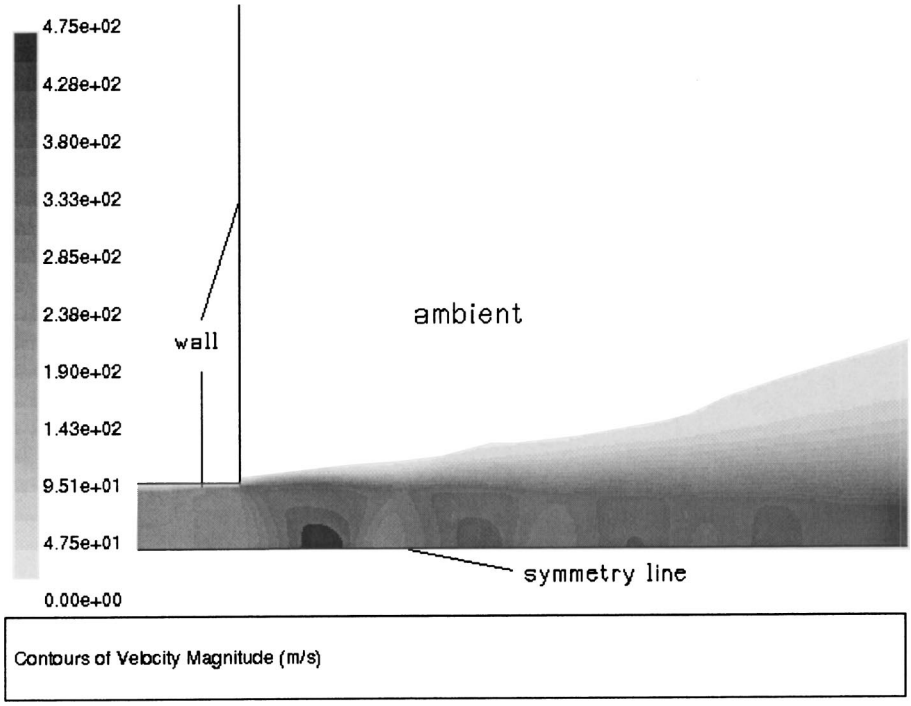

Fig. 14 Velocity contours for 3:1 pressure ratio

metric nozzle flow. Computations of the flow field of air flowing from an axisymmetric nozzle were also performed as part of this study. The physical domain for these computations was a 127 mm (5 inch)×25 mm (1 inch) diameter nozzle connected to a 1,524 mm (60 inch) long×762 mm (30 inch) diameter adjacent chamber.

The jet flow field for three cases of high supply–cylinder stagnation pressure ratios of 81.4:1, 46.5:1, and 18.6:1 were computed. The three cases used supply pressures of 35 bar, 20 bar, and 8 bar, respectively, and a cylinder pressure of 0.43 bar, large enough to produce Mach disk structures. The 0.43 bar cylinder pressure was chosen as a representative cylinder pressure in a throttled engine at the start of gas injection. The effects of the pressure ratio on centerline pressure profile, Mach number profile, and location of the Mach disk were computed. The flow field at these three pressure ratios was modeled as inviscid. In addition, viscous and turbulent effects for the supply–cylinder stagnation pressure ratio case of 81.4:1 were also computed, using the standard k-ε turbulence model.

A low supply–cylinder stagnation pressure ratio (3 bar:1 bar) turbulent jet flow from a sonic nozzle was also computed. The computational domain for the low pressure ratio case was composed of a 127 mm (5 inch)×25 mm (1 inch) nozzle connected to a 762 mm (30 inch) long×254 mm (10 inch) diameter adjacent chamber. In this low-pressure ratio case, a one-equation turbulent model was used so that effects due to viscous and turbulent dissipation were included.

Results and Discussion for Underexpanded Axisymmetric Jets

Figure 9 shows the velocity contours for the three high-pressure ratios. These contours clearly show the Mach disc structure

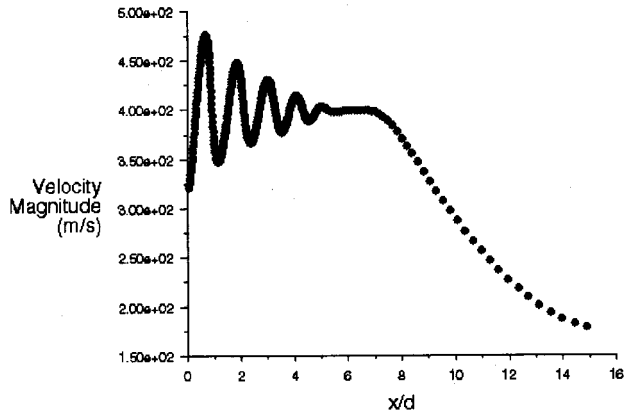

Fig. 15 Centerline velocity oscillation and decay for 3:1 pressure ratio

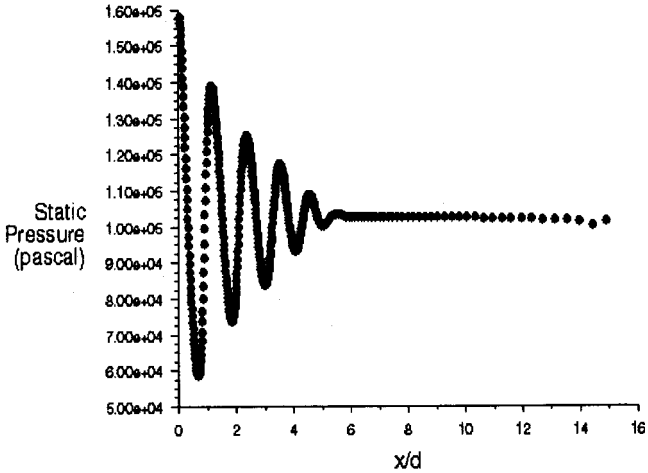

Fig. 16 Centerline static pressure oscillation and decay for 3:1 pressure ratio

formed. As the pressure ratio is increased, the Mach disk increases in size and is positioned farther away from the nozzle exit. The intercepting or barrel shock at the boundary of the jet is also evident. The contours show that the axial velocity increases in the transverse direction, similar to the two-dimensional slot computations.

The dimensionless local pressure P/P_n and Mach number M profile along the jet centerline resulting from the CFD computations for the three high-pressure ratio cases are shown in Fig. 10 and Fig. 11, respectively. The nondimensional x/d coordinate in these figures is the axial distance divided by the nozzle diameter. The results indicate that upstream of the Mach disk the decrease in the dimensionless local pressure is the same for the three pressure ratios. The pressure behind or downstream of the shock for the three supply–cylinder stagnation pressure ratios is also plotted in Fig. 10, indicating that the pressure rise across the shock is dependent on the overall supply–cylinder stagnation pressure ratio.

In Fig. 11, the Mach number profiles are the same until the onset of a Mach disk. The sudden decrease of Mach number for the three high pressure ratio cases indicates the presence of the Mach disk. Figure 12 is a plot of the distance between the Mach disk and the nozzle exit versus the static pressure/ambient pressure ratio. Also plotted are the experimental results presented in Adamson and Nicholls [2]. There is good agreement between the computational and the experimental results. As the pressure ratio increases, the distance of the Mach disk from the nozzle increases nonlinearly.

Figure 13 compares the dimensionless centerline static pressure variation between the inviscid model and standard k-ε model variation for a pressure ratio of 81.4:1. The results show that for high injection/cylinder pressure ratios, the viscous and turbulent stresses on the jet structure are insignificant relative to the jet kinetic energy. The assumption of inviscid flow in the near field of the jet is reasonable, and justifies the use of the method of characteristics in this region.

As discussed in the Introduction, with a slightly underexpanded nozzle, the injection/back pressure is not large enough for the gas to form a Mach disk, so the intercepting shocks will meet at the centerline axis forming diamond shaped cells. Velocity contours in Fig. 14 shows repeating diamond shapes for the supply–cylinder stagnation pressure ratio of 3:1. The effect of viscous dissipation on the diamond structure is also shown.

Centerline velocity and pressure profiles for the same pressure ratio of 3:1 are shown in Fig. 15 and Fig. 16, respectively. The x-coordinate, the axial distance to the nozzle exit, is nondimensionalized by the nozzle diameter d. The oscillation of pressure and velocity in Figs. 15 and 16 are a consequence of the repeating expansion and compression wave structure in the jet, and the decay of the oscillation amplitude is due to the viscous dissipation. At a distance about seven nozzle diameters to the nozzle exit, jet is fully expanded and then subsonic velocity decay is observed.

Conclusions

The outlet jet flow structure from underexpanded two-dimensional and axisymmetric nozzles has been numerically investigated. The CFD results show good agreement with the results from the method of characteristics applied to two-dimensional jets. Mach disk structures were observed from computational results for axisymmetric jets with high pressure ratios. Pressure and Mach number variation along the centerline and location of Mach disk are in good agreement with previous results. For low pressure ratios, a repeating diamond-shape cell structure downstream of the nozzle exit was computed.

Acknowledgments

This research was supported by the Pipeline Research Committee International (PRCI).

Nomenclature

d = nozzle diameter, mm
M = Mach number
P_o = supply stagnation pressure, bar
P_∞ = cylinder stagnation pressure, bar
P = static pressure along centerline, bar
P_n = static pressure at nozzle exit, bar
T = temperature, K
V = velocity, m/s
V_n = velocity at nozzle exit, m/s
w = nozzle half-width, mm

References

[1] Pai, S. H., 1954, *Fluid Dynamics of Jets*, D. Van Nostrand Co., New York.
[2] Adamson, T. C., and Nicholls, J. A., 1959, ''On the Structure of Jets From Highly Underexpanded Nozzles Into Still Air,'' J. Aerosp. Sci., **26**, pp. 16–24.
[3] Owen, P., and Thornhill, C., 1952, ''The Flow in an Axially-Symmetric Supersonic Jet From a Nearly Sonic Orifice Into a Vacuum,'' Brit. A. R. C. Technical Report, R and M 2616.
[4] Love, E., Grigsby, C., Lee, L., and Woodling, M., 1959, ''Experimental and Theoretical Studies of Axisymmetric Free Jets,'' NASA Technical Report R-6.
[5] Mather, D., and Reitz, R., 2000, ''Modeling the Effects of Auxiliary Gas Injection on Diesel Engine Combustion and Emissions,'' SAE Paper 2000-01-0657.
[6] Gribben, B., Badcock, K., and Richards, B., 2000, ''Numerical Study of Shock-Reflection Hysteresis in an Underexpanded Jet,'' AIAA J., **38**(2), pp. 275–283.
[7] Cumber, P., Fairweather, M., Falle, S., and Giddings, J., 1995, ''Predictions of the Structure of Turbulent Highly Underexpanded Jets,'' ASME J. Fluids Eng., **117**, pp. 599–604.
[8] Hsu, A., and Liou, M., 1991, ''Computational Analysis of Underexpanded Jets in the Hypersonic Regime,'' J. Propul. Power, **7**(2), pp. 297–299.
[9] Laney, C., 1998, *Computational Gasdynamics*, Cambridge University Press, New York.
[10] Ferguson, C., and Kirkpatrick, A., 2001, *Internal Combustion Engines: Applied Thermosciences*, John Wiley and Sons, New York.
[11] FLUENT, 2001, Fluent Incorporated, Hanover, NH.
[12] Abraham, J., 1997, ''What is Adequate Resolution in the Numerical Computations of Transient Jets?,'' SAE Trans., **106**, pp. 141–151.
[13] Post, S., Iyer, V., and Abraham, J., 2000, ''A Study of the Near-Field Entrainment in Gas Jets and Sprays Under Diesel Conditions,'' ASME J. Fluids Eng., **122**, pp. 385–395.
[14] Shapiro, A., 1953, *The Dynamics and Thermodynamics of Compressible Fluid Flow*, Vol. 1, John Wiley and Sons, New York.
[15] Chang, I., and Chow, W., 1974, ''Mach Disk From Underexpanded Axisymmetric Nozzle Flow,'' AIAA J., **12**(8), pp. 1079–1082.

Journal of Engineering for Gas Turbines and Power

Book Review

Engineering Fundamentals of the Internal Combustion Engine, 2nd Ed., Willard W. Pulkrabek. Prentice-Hall, Englewood Cliffs, NJ, 2003.

REVIEWED BY JIM S. COWART[1]

The new second edition internal combustion engine text by Professor Pulkrabek is an excellent undergraduate engineering text book. This book is well suited for a one semester senior level elective course on engines. It provides a broad introductory coverage of the relevant theory and practice surrounding spark ignition (SI) and compression ignition (CI) internal combustion engines. As appropriate, general descriptions of current engine technology (e.g., fuel injection practice) are also presented.

This text covers the fundamental elements of SI and CI internal combustion engines. This includes operating characteristics, ideal cycles, thermochemistry, as well as details on the specific engine strokes: intake and fluid motion, combustion and exhaust processes. Additionally, the topics of heat transfer, emissions and friction/lubrication are presented in individual chapters. Numerous example problems are placed in the text and relevant problems (including design problems) at the end of each chapter will be useful for students.

Pulkrabek's text also includes numerous and frequent historical notes throughout the book. These notes are sure to create interest in both students and professionals who may use this text. A few examples of these historical notes include a discussion of how compression ratios have changed over the years, a description of when automobiles ran on charcoal, and ignition system history. These notes are a wonderful complement to the study of engine technology.

For practicing engineers in the field of engines this text is likely to be less useful than *Internal Combustion Engine Fundamentals* by J. B. Heywood (McGraw-Hill, 1988). Heywood's text generally provides more detail on the engine topics covered by Pulkrabek as well as specific chapters on the properties of engine working fluids, widely used engine models (both physical and phenomenological), and detailed engine operating behavior. Pulkrabek's text is targeted toward undergraduate students and thus, for example, discusses qualitatively the effects of engine operation on heat transfer but does not contain Heywood's detailed analysis and data.

[1]Sloan Automotive Laboratory, M.I.T., Cambridge, MA 01760.

Journal of Engineering for Gas Turbines and Power

Erratum

Erratum Redux: "Effect of Biodiesel Utilization of Wear of Vital Parts in Compression Ignition Engine" [ASME J. Eng. Gas Turbines Power, 125, pp. 604–611]

A. K. Agarwal, J. Bijwe, and L. M. Das

The title of this paper should read ''Effect of Biodiesel Utilization on Wear of Vital Parts in Compression Ignition Engine'' (''Effect of Biodiesel Utilization on Wear . . . '' instead of ''Effect of Biodiesel Utilization of Wear . . . '').